

UC San Diego

UC San Diego Electronic Theses and Dissertations

Title

Engineering virus-based nanocarriers for human and plant health

Permalink

<https://escholarship.org/uc/item/2965v9nk>

Author

Chariou, Paul Laurent

Publication Date

2020

Peer reviewed|Thesis/dissertation

UNIVERSITY OF CALIFORNIA SAN DIEGO

Engineering plant virus-based nanocarriers for human and plant health

A dissertation submitted in partial satisfaction of the requirements for the degree Doctor of
Philosophy

in

BioEngineering

by

Paul Laurent Chariou

Committee in charge:

Professor Nicole F. Steinmetz, Chair
Professor Geert W. Schmid-Schoenbein
Professor Ester J. Kwon
Professor Jon K. Pokorski
Professor Gerald M. Sidel

2020

The dissertation of Paul Laurent Chariou is approved, and it is acceptable in quality and form for publication on microfilm and electronically:

Chair

University of California San Diego

2020

Epigraph

The success or failure of your deeds does not add up to the sum of your life.

Oma Desala

Table of Contents

Signature Page	iii
Epigraph.....	iv
Table of Contents.....	v
List of Figures.....	xiii
List of Tables	xvi
List of Supplementary Information.....	xvii
List of Abbreviations	xxi
Acknowledgments.....	xxvi
Vita.....	xxx
Abstract of the Dissertation	xxxii
Chapter I: Introduction: Nanocarriers for Agricultural, Veterinary, and Medical Applications	1
1.1. Opening.....	1
1.2. From idea to commercial product.....	4
1.2.1. Trends in active ingredient delivery.....	4
1.2.2. Ingredients delivered by nanocarriers.....	7
1.3. Liposomal nanocarriers.....	15
1.4. Polymeric nanocarriers.....	23
1.5. Micellar nanocarriers.....	30

1.6. Inorganic nanocarriers.....	34
1.7. Proteinaceous nanocarriers.....	36
1.8. Virus-based nanocarriers.....	39
1.9. Conclusions.....	42
Chapter II: Aims of the Dissertation Work.....	44
Chapter III: Delivery of Pesticides to Parasitic Nematodes using TMGMV.....	46
3.1 Introduction.....	46
3.2. Experimental methods.....	50
3.2.1. Crystal Violet (CV) loading into TMGMV.....	50
3.2.2. Bioconjugation of TMGMV glutamic/aspartic acid residues.....	50
3.2.3. Bioconjugation of TMGMV tyrosine residues.....	51
3.2.4. UV/Visible spectroscopy.....	52
3.2.5. Denaturing gel electrophoresis (SDS-NuPAGE).....	52
3.2.6. Western blotting.....	52
3.2.7. Size exclusion chromatography (SEC).....	53
3.2.8. Transmission electron microscopy (TEM).....	53
3.2.9. CV release profile from $_{cv}$ TMGMV.....	53
3.2.10. Caenorhabditis elegans nematode culture.....	53
3.2.11. Bioavailability of $_{cv}$ TMGMV and free CV to C. elegans.....	54
3.2.12. Soil mobility of $_{cv}$ TMGMV and free CV.....	55

3.3. Results and discussion.....	56
3.3.1. Synthesis and characterization of TMGMV-encapsulated crystal violet (CV).....	56
3.3.2 cvTMGMV toxicity and interactions with <i>C. elegans</i> nematodes.....	66
3.3.3. Soil mobility of cvTMGMV and free CV.	72
3.4. Conclusions.....	73
Chapter IV: Soil Mobility of Synthetic and Virus-based Model Nanopesticides.....	75
4.1. Introduction.....	75
4.2. Experimental methods.....	76
4.2.1. Expression and purification of nanoparticles	76
4.2.2. Bioconjugation of Cy5 to TMGMV tyrosine residues.....	77
4.2.3. Bioconjugation of Cy5 to PhMV/CPMV lysine residues.....	78
4.2.4. Bioconjugation of Cy5 to MSNP carboxylate residues.....	78
4.2.5. Encapsulation of Cy5 into TMGMV/CPMV/PhMV/MSNP particles.....	78
4.2.6. UV/Vis spectroscopy.....	78
4.2.7. Denaturing gel electrophoresis.....	79
4.2.8. Agarose gel electrophoresis.....	79
4.2.9. Transmission electron microscopy.....	79
4.2.10. Dynamic light scattering.....	80
4.2.11. Size exclusion chromatography.....	80
4.2.12. Fluorescent-dye release profiling.....	80

4.2.13. Soil mobility of TMGMV, CPMV, PhMV, PLGA, MSNP and free Cy5.	80
4.3. Computational methods.....	82
4.4. Results and discussion.....	87
4.4.1. Nanopesticide characterization.....	88
4.4.2. Soil transport behaviour.....	90
4.4.3. Computational modelling of pesticide delivery.....	94
4.4.4. Testing the nanopesticide model in a real-life scenario.	99
4.5. Conclusions.	101
Chapter V: Chemical and UV Light Inactivation of TMGMV for Environmental Applications	103
5.1. Introduction.	103
5.2. Materials and methods	106
5.2.1. TMGMV inactivation using UV-light, β -propiolactone, and formalin.....	106
5.2.2. Plant inoculation with native and inactivated TMGMV	106
5.2.3. Viral RNA extraction	107
5.2.4. Reverse transcription polymerase chain reaction (RT-PCR).....	107
5.2.5. Agarose gel electrophoresis.....	108
5.2.6. UV/Vis spectroscopy.....	108
5.2.7. Dynamic light scattering.....	109
5.2.8. Transmission electron microscopy	109
5.2.9. Size exclusion chromatography.....	109

5.2.10. Denaturing gel electrophoresis	109
5.3. Results and discussion.....	110
5.3.1. Infectivity or lack thereof of inactivated TMGMV	115
5.4. Conclusions	124
Chapter VI: Diffusion and Uptake of a High Aspect Ratio Nanocarriers in Tumor Tissue	125
6.1. Introduction.	125
6.2. Theoretical methods.	128
6.2.1. TMV dynamics.	130
6.2.2. Model transformation.	130
6.2.3. Model parameter values.....	131
6.2.4 Diffusion coefficients.	131
6.3. Experimental methods.....	133
6.3.1. Rate of cellular uptake.	133
6.4. Results and discussion.....	134
6.4.1. Effect of tumor spheroid radius on TMV diffusion (without cellular uptake).	135
6.4.2. Effect of cell density on TMV diffusion (without cellular uptake).	137
6.4.3. Effect of TMV aspect ratio on diffusion (without cellular uptake).	139
6.4.4. Effects of TMV characteristics on the rate of cell uptake.	140
6.4.5. Model simulated uptake of TMV.	144
6.5. Conclusions.	146

Chapter VII: Targeted Photodynamic Therapy Using High Aspect Ratio Plant Viral

Nanoparticles	147
7.1. Introduction.....	147
7.2. Results and discussion.....	148
7.3. Conclusions.....	164
Chapter VIII: <i>In situ</i> vaccine application of inactivated CPMV nanoparticles	165
8.1 Introduction.....	165
8.2. Materials and methods	167
8.2.1. Preparation of native CPMV	167
8.2.2. CPMV inactivation using UV-light, β -propiolactone, and formalin.....	167
8.2.3. Black-eyed pea plants inoculation with native and inactivated CPMV	167
8.2.4. Viral RNA extraction.....	167
8.2.5. Reverse transcription polymerase chain reaction (RT-PCR).....	168
8.2.6. Bioconjugation of Cyanine 5 (Cy5) to CPMV	169
8.2.7. UV/Vis spectroscopy.....	169
8.2.8. Dynamic light scattering (DLS)	170
8.2.9. Transmission electron microscopy (TEM)	170
8.2.10. Size exclusion chromatography (SEC).....	170
8.2.11. Agarose gel electrophoresis.....	170
8.2.12. Denaturing gel electrophoresis	171

8.2.13. Virus overlay binding protein assay (VOBPA).....	171
8.2.14. Tissue culture.....	172
8.2.15. Flow cytometry.....	172
8.3. Results and discussion.....	174
8.3.1.Nanoparticle characterization.....	174
8.3.2. Treated CPMV particles exhibit diminished infectivity.....	180
8.3.3. Effect of inactivation on the chemical reactivity of CPMV.....	185
8.3.4.Effect of inactivation on the biological activity of CPMV.....	185
8.4. Conclusions and future directions.....	188
Chapter IX: Conclusions and Outlooks.....	189
9.1. Scope of this work.....	189
9.2. TMGMV as a nanocarrier for the delivery of pesticides to nematode infested crops.....	190
9.3. TMGMV as a nanocarrier for the delivery of therapeutics to cancer.....	198
9.4. Cancer <i>in situ</i> vaccination using inactivated CPMV.....	201
9.5 Final remark.....	203
Appendix I: Supplementary Information of Chapter I.....	204
Appendix II. Supplementary Information of Chapter III.....	213
Appendix III: Supplementary Information of Chapter IV.....	221
Appendix IV: Supplementary Information of Chapter V.....	281
Appendix V: Supplementary Information of Chapter VI.....	290

Appendix VI: Supplementary Information of Chapter VII.....	297
Appendix VII: Supplementary Information of Chapter VIII.....	300
References.....	314

List of Figures

Figure 1.1. Nanocarriers in human medicine, veterinary medicine, and agriculture.....	6
Figure 1.2. Size and structure of nanocarriers (approved and in development)	12
Figure 3.1. Structure of TMGMV.....	56
Figure 3.2. cvTMGMV conjugation and characterization.....	59
Figure 3.3. Characterization of cvTMGMV particles.....	63
Figure 3.4. Evaluation of CV drug release from TMGMV	66
Figure 3.5. C. elegans motility assay	68
Figure 3.6. C. elegans ingestion of TMGMV	71
Figure 3.7. Soil mobility of cvTMGMV and free CV	73
Figure 4.1. Combined experimental and computational nanopesticide transport through soil	87
Figure 4.2. Cargo release from nanoparticles during dialysis	89
Figure 4.3. Experimental transport of nanopesticides and pesticides through soil.....	92
Figure 4.4. Theoretical transport of nanoparticles through soil.....	95
Figure 4.5. Theoretical transport of Cy5 through soil	98
Figure 4.6. Theoretical treatment of crops infected with nematodes.....	101
Figure 5.1. Comparing the effect of UV light, β PL, and Formalin on TMGMV	110
Figure 5.2. Characterization of inactivated TMGMV: part 1	112
Figure 5.3. Characterization of inactivated TMGMV: part 2	113
Figure 5.4. Infectivity of TMGMV v. inactivated TMGMV against Tn86	119

Figure 5.5. Infectivity of TMGMV v. inactivated TMGMV against Samsun-NN.....	120
Figure 5.6. Infectivity of TMGMV v. inactivated TMGMV against TSA	121
Figure 6.1. Theoretical diffusion of TMV through a tumor spheroid.....	129
Figure 6.2. Effects of spheroid radius on TMV's distribution.....	137
Figure 6.3. Effects of cell density on TMV's distribution	138
Figure 6.4. Effects of the TMV aspect ratio on TMV's distribution	140
Figure 6.5. Experimental rate of cellular uptake.....	142
Figure 6.6. Effects of cellular uptake on on TMV's distribution.....	143
Figure 6.7. Effects of aspect ratio on TMV-PEG's distribution.....	145
Figure 7.1. Evaluation of Zn-Por loading and release from TMV and TMGMV	150
Figure 7.2. In vitro treatment of B16F10 cells.....	157
Figure 7.3. Synthesis of targeted TMVlys-F3 particles	160
Figure 7.4. Uptake of TMVlys-F3 particles by HeLa cells in vitro.....	162
Figure 8.1. CPMV viral inactivation.....	174
Figure 8.2. Structural integrity of UV, β PL, and Formalin inactivated CPMV particles.	176
Figure 8.3. CPMV RNA integrity following UV, β PL, and Formalin treatment of CPMV	178
Figure 8.4 Gel electrophoretic mobility of native and inactivated CPMV	180
Figure 8.5. Infectivity of native and inactivated CPMV against Black eyed peas	183
Figure 8.6. Chemical and biological reactivity of inactivated CPMV	184
Figure 9.1. Avermectin synthesis schemes	195

Figure 9.2. Conjugation and characterization of TMGMV-avermectin 196

List of Tables

Table 1.1. FDA and EMA approved medical nanocarriers.	13
Table 1.2. Novel medical nanocarriers in clinical trials	20
Table 1.3. EPA approved pesticide nanocarriers	28
Table 5.1. RT-PCR conditions.....	108
Table 5.2. Leaf infectivity as per visual inspection	122
Table 5.3. Pros and cons of TMGMV inactivation by UV, β PL, and formalin.....	123
Table 6.1. Parameters used for the model simulations in Figures 6.2, 6.3 and 6.4	135
Table 6.2. Rate of cellular uptake of three aspect ratios of TMV-PEG and TMV-RGD	141
Table 8.1. RT-PCR conditions.....	169

List of Supplementary Information

Supporting Table 1.1. Gene therapy nanocarriers undergoing clinical trials.	204
Supporting Table 1.2. Viral nanocarriers undergoing clinical trials.....	205
Supporting Table 1.3. FDA and EMA approved polymer-protein conjugates.	209
Supporting Table 1.4. Polymer-protein conjugates undergoing clinical trials.	210
Supporting Table 1.5. FDA and EMA approved inorganic nanoparticles.....	212
Supporting Figure 3.1. TMV and TMGMV sequence and structural comparisons.....	213
Supporting Figure 3.2. Positioning of cysteine, tyrosine, and lysine residues on TMGMV	214
Supporting Figure 3.3. Positioning of cysteine, tyrosine, and lysine residues on TMV	215
Supporting Figure 3.4. Structure of TMV	216
Supporting Figure 3.5. Size distribution analysis from TEM images.....	217
Supporting Figure 3.6. Reactivity of ASP/GLU/TYR residues on TMV and TMGMV	218
Supporting Figure 3.7. Characterization of modified TMGMV	219
Supporting Figure 3.8. C. elegans neutralization assay with TMGMV alone	220
Supplementary Table 4.1. Comparison of conventional pesticides to the model drug Cy5.....	221
Supporting Figure. 4.1. Cy5 conjugation to TMGMV, PhMV, CPMV and MSNP.....	222
Supporting Figure. 4.2. Nanoparticle characterization	223
Supporting Figure. 4.3. Characterization of Cy5-labelled viruses.....	227
Supporting Figure. 4.4. SEC and SDS-PAGE analysis of Cy5-labelled viruses.....	228

Supporting Table 4.2. Soil composition.	229
Supporting Table 4.3. Soil particle size distribution.....	230
Supporting Figure. 4.5. SDS-PAGE and dot blot analysis of nanoparticle elution fractions.	231
Supporting Figure 4.6. Distribution of free Cy5 in the soil.....	242
Supporting Table 4.4. Tables of virus recovery from the empty elution samples.....	243
Supporting Figure. 4.7. TEM images of viruses that were leached through soil.....	244
Supporting Figure. 4.8. Reaction mechanisms of nanoparticles and pesticides in soil.	245
Supporting Equation 4.1. model of nanopesticide transport through the soil.....	246
Supporting Code 4.1. MATLAB code.....	251
Supporting Table 4.5. Optimized parameters.	273
Supporting Figure. 4.9. Free Cy5 from experimental (left) and model output (right).....	277
Supporting Figure. 4.10. Nanoparticle soil transport prediction using a 4 cm soil column	277
Supporting Figure. 4.11. Q β characterization.....	278
Supporting Figure 4.12. Q β transport through soil.....	279
Supporting Figure. 4.13. Parameter correlation.....	280
Supporting Figure 5.1. Size exclusion chromatography of TMGMV after UV treatment	281
Supporting Figure 5.2. Size exclusion chromatography of β PL-TMGMV	282
Supporting Figure 5.3. Size exclusion chromatography of form-TMGMV	282
Supporting Figure 5.4. Surface exposition of various amino acids on the surface of TMGMV prone to β PL and Formalin treatment.	283

Supporting Table 5.1. Tobacco mild green mosaic virus complete genome	285
Supporting Figure 5.5. Agarose gels from the RT-PCR ran on RNA extract from Tn86.	287
Supporting Figure 5.6. Agarose GE from the RT-PCR ran on RNA extract from Samsun-NN.	288
Supporting Figure 5.7. Agarose gels from the RT-PCR ran on RNA extract from TSA.	289
Supporting Equations 6.1. Characteristic rates of diffusion and cellular uptake.....	290
Supporting Table 6.1. Computation of the order of magnitude difference between the rate of endocytosis and the rate of diffusion of TMV.	291
Supporting Table 6.2. Computation of the order of magnitude difference between the rate of TMV diffusion in the surrounding medium and the spheroid interspace.	292
Supporting Equations 6.2. Model transformation.	292
Supporting Equations 6.3. Method of lines.	292
Supporting Equations 6.4. Characteristic axial and transverse velocity of TMV.....	294
Supporting Table 6.3. Computation of the axial and transverse velocity of specified TMV dimensions	294
Supporting Equations 6.5. Diffusion coefficients in the surrounding medium and in the spheroid	295
Supporting Table 6.4. Diffusion coefficients of TMV in the surrounding medium (D_{rt}), and in the presence of ECM proteins (D_{int})	295
Supporting Table 6.5. Diffusion coefficient of TMV in the porous spheroid containing cells ..	296
Supporting Figure 7.1. Chemical structure of the monocationic, dicationic, tricationic and tetracationic Zn-Porphyrin molecules.....	297

Supporting Figure 7.2. Evaluation of Zn-Por loading and release from TMV and TMGMV	298
Supporting Figure 7.3. Characterization of fluorescently labeled TMV and TMGMV	299
Supporting Figure 7.4. MTT viability assay of HeLa cells treated with TMVlys-F3 particles..	299
Supporting Figure 8.1. Nucleotide sequence of the RNA-1 and RNA-2.....	300
Supporting Figure 8.2. Chemical addressability of various amino acids on CPMV	300
Supporting Figure 8.3. TEM images of native and UV inactivated CPMV	307
Supporting Figure 8.4. Size exclusion chromatography of CPMV treated with β PL.....	307
Supporting Figure 8.6. CPMV treated with low concentrations of UV.....	309
Supporting Figure 8.7. CPMV treated with low concentrations of formalin.....	310
Supporting Figure 8.8. UV-CPMV infection on black-eyed peas leaves, and corresponding RT-PCR amplicons.....	311
Supporting Figure 8.9. β PL-CPMV infection on black-eyed peas leaves, and corresponding RT-PCR amplicons.....	312
Supporting Figure 8.10. Form-CPMV infection on black-eyed peas leaves, and corresponding RT-PCR amplicons	313

List of Abbreviations

2D	two-dimensional
3D	three-dimensional
AAV	adeno-associated virus
ADC	antibody-drug
ASC	ascorbic acid
AMG	aminoguanidine
ASP	aspartic acid
AVMA	American veterinary medical association
BBB	blood brain barrier
β PL	β -propiolactone
CCMV	cowpea chlorotic mosaic virus
CP	coat protein
CPMV	cowpea mosaic virus
CV	crystal violet
CY5	sulfo-Cyanine5 azide
CYS	cysteine
DAPI	4',6-diamidino-2-phenylindole
DCC	n',n'-dicyclohexylcarbodiimide
DCM	dichloromethane
DLS	dynamic light scattering
DMAP	4-dimethylaminopyridine

DMEM	Dulbecco's modified Eagle medium
DMF	dimethylformamide
DMSO	dimethyl sulfoxide
DNA	deoxyribonucleic acid
dsRNA	double-stranded ribonucleic acid
ECM	extracellular matrix
EDC	1-Ethyl-3-(3-dimethylaminopropyl)carbodiimide
EDTA	ethylenediaminetetraacetic acid
EMA	European medical agency
EPA	environmental protection agency
EPR	enhanced permeability and retention
FACS	fluorescence-activated cell sorting
FBS	fetal bovine serum
FDA	food drug administration
FPLC	fast protein liquid chromatography
GFP	green fluorescence protein
GI	gastrointestinal
GLU	glutamic acid
GMP	good manufacturing practice
HEPES	4-(2-hydroxyethyl)-1-piperazineethanesulfonic acid
HIV	human immunodeficiency virus
HRP	horseradish peroxidase
HSV	herpes simplex virus

IFN	interferon
ISO	international organization for standardization
KP	potassium phosphate
LDL	low-density lipoprotein
LYS	lysine
mAb	monoclonal antibody
miRNA	micro ribonucleic acid
MOPS	morpholinepropanesulfonic acid
MW	molecular weight
N. benthamiana	Nicotiana benthamiana
NHS	N-hydroxysuccinimide
OAS	origin of assembly site
PAL	polyacrylate
PAMAM	polyamidoamine
PBS	phosphate buffered saline
PCL	polycaprolactone
PDT	photodynamic therapy
PEG	polyethylene glycol
penstrep	penicillin-streptomycin
PGA	polyglycolic acid
PLA	poly(lactic acid)
PRINT	particle replication in nonwetting templates
PS	photosensitizer

PVX	potato virus X
RCNMV	red clover necrotic mosaic virus
RGD	arginylglycylaspartic acid
RNA	ribonucleic acid
RT	room temperature
RT-PCR	reverse transcription polymerase chain reaction
SDS-PAGE	sodium dodecyl sulfate polyacrylamide gel electrophoresis
SEAP	secreted alkaline phosphatase
SEC	size exclusion chromatography
siRNA	silencing ribonucleic acid
ssRNA	single stranded ribonucleic acid
TBE	tris-borate-EDTA
TBST	tris-buffered saline, tween
TEA	triethylamine
TEM	transmission electron microscopy
THF	tetrahydrofuran
THPTA	tris(3-hydroxypropyltriazolylmethyl)amine
TLR	toll-like receptor
TMGMV	tobacco mild green mosaic virus
TMV	tobacco mosaic virus
TRAIL	Tumor Necrotic Factor-related apoptosis- inducing ligand

TSA	tropical soda apple
USDA	United States department of agriculture
UV	ultra violet
UV/vis	UV/visible
v/v	volume by volume
VLP	virus-like particle
VNP	viral nanoparticle
VOBPA	virus overlay binding protein assay
w/v	weight by volume
WGA	wheat-germ agglutinin

Acknowledgments

First, I would like to thank my advisor Dr. Nicole Steinmetz for her support and guidance throughout my PhD. None of this would have been possible if Dr. Steinmetz did not believe in my potential back in 2011, when she hired me as a college freshman. Since then, she kindly and patiently mentored me to become a critical thinker, an independent scientist, and a better individual in general. In particular, I would like to thank Dr. Steinmetz for supporting my career goals to become a leader in the industry sector by giving me countless opportunities for presenting my research at national and international conferences, writing manuscripts, and letting me train and mentor talented undergraduate students.

Next, I would like to thank the current and past members of my dissertation committee for their advice and support over the years: Dr. Giuseppe Strangi, Dr. David Schiraldi, Dr. Colin Drummond, Dr. Robert Kirsch, Dr. Gerald Saidel, Dr. Jon Pokorski, Dr. Ester Kwon, and Dr. Geert schmid-Schoenbein. Their knowledge and expertise have been invaluable.

It has been my pleasure to grow with the Steinmetz lab and to work with my past and current lab-mates: Dr. Amy Wen, Dr. Karin Lee, Dr. Neetu Gulati, Dr. Anna Czapar, Dr. Abner Murray, Dr. Sourabh Shukla, Dr. Michael Bruckman, Dr. Patricia Lam, Dr. Andrzej Pitek, Dr. Brylee Tiu, Dr. Duc Le, Dr. Andy Hu, Dr. Hui Cai, Dr. Chao Wang, Dr. Jooneon Park, Dr. Veronique Beiss, Dr. Isaac Marks, Dr. Shuai Shao, Dr. Oscar Ortega-Rivera, Dr. Soo Khim Chan, Dr. Christine Boone, Dr. Sayoni Ray, Frank Veliz, Dan Kernan, Christina Franke, Bindi Patel, Richard Lin, Lu Wang, Matthew Shin, Torus Washington, Yvonne Ma, and Eric Chung. Each one of them has contributed to the positive lab atmosphere that has made the Steinmetz lab such a great place to work at, even during the occasional stressful and frustrating times. I am especially grateful for Richard Lin, who navigated the grad school experiences with me, as well as being such a great

friend and suitemate. Thank you to the students I had the opportunity to mentor over the years for working so hard and for keeping me sane when I was swamped in work: Alan Dogan, Alex Welsh, Cian Desai.

I would like to thank all my collaborators, in no particular order, who have been invaluable over the years to expose me to different research fields and to complete the work presented here: Dr. Jonathan Pokorski (NanoEngineering, UCSD), Dr. Gerald Saidel (Biomedical Engineering, CWRU), Dr. Harihara Baskaran (Chemical and Biomolecular Engineering, CWRU), Dr. Reza Ghiladi (Chemistry, NCSU), Dr. Leanna Robbins (Chemistry, NCSU), Dr. Raghavan Charudattan (Plant Pathology, Univ. Florida), Dr. Erin Rosskopf (U.S. Horticultural Research Laboratory, USDA), Dr. Hema Masarapu (Virology, Sri Venkateswara University), Dr. Miguel Correa-Duarte (Physical Chemistry, Universidade de Vigo), Dr. Jacky Wallat (Macromolecular Science and Engineering, CWRU), Laura Marín-Caba (Physical Chemistry, Universidade de Vigo), Justin Hochberg (NanoEngineering, UCSD), Kristen S. Wek (Macromolecular Science and Engineering, CWRU), Bradley L. Carpenter (Macromolecular Science and Engineering, CWRU).

I would like to thank all the administrative assistants in Biomedical Engineering and the Case Center for Imaging Research at Case Western Reserve University: Debra Rudolph, Carol Adrine, Carol Rice, Barbara Richards, Cena Hilliard, and Kacie Beck. I would like to thank the administrative assistants in NanoEngineering and BioEngineering at UC San Diego: Jan Lenington and Dana Jimenez; and all the staff members that work behind the scenes.

I also appreciate the members of the Karathanasis lab, Exner lab, and Pokorski lab, for letting me borrowing reagents when I was in need: Dr. Efstathios Karathanasis, Dr. Agata Exner, Dr. Jon Pokorski, Dr. Pubudu Peiris, Dr. Derek Church, Dr. Chris Hernandez, Elizabeth Doolittle, Gil Covarrubias, Peter Bielecki, Selva Jeganathan, Justin Hochberg, Yi Zheng, and David Wirth.

I would like to thank the National Science Foundation for supporting my work with the CAREER DMR 1452257 and DMR 1841848 (to N.F.S.) grant.

I would also like to thank all my friends, although you are too many to name here. While it has been hard to stay in touch, you have always been there when I needed to socialize or talk about anything but science. Thank you for reminding me to have fun outside of the lab and for making me a better human being.

I would like to thank my family for their emotional and financial support, none of this adventures would have been possible without them. My family helped me fulfilling my dream of moving to the United States. Even though the distance to France makes it hard to be close, my family always finds the time to visit me during the important moments of life. I thank them for always believing in me.

Chapter I, in full, is a reprint of the material as it appears in ACS Nano, 2020. Chariou, P. L, Ortega-Rivera O.A, Steinmetz N.F. *Nanocarriers for the delivery of medical, veterinary, and agricultural active ingredients*. DOI: <https://doi.org/10.1021/acsnano.0c00173>. The dissertation author was the primary investigator and author of this paper.

Chapter III, in full, is a reprint of the material as it appears in ACS Nano, 2017. Chariou, P.L., Steinmetz, N.F. *Delivery of Pesticides to Plant Parasitic Nematodes using Tobacco Mild Green Mosaic Virus as a Nanocarrier*. 11, 4719-4730. The dissertation author was the primary investigator and author of this paper.

Chapter IV, in full, is a reprint of the material as it appears in Nature Nanotechnology, 2019. Chariou, P.L., Dogan, A.B., Welsh, A.G., Saidel, G.M., Baskaran, H., Steinmetz, N.F. *Soil mobility of synthetic and virus-based model nanopesticides*. DOI: <https://doi.org/10.1038/s41565-019-0453-7>. The dissertation author was the primary investigator and author of this paper.

Chapter V, in full, is in preparation for submission to a peer-reviewed journal, 2020. Chariou, P.L. Roskopf, E.N., Hong, J.C, Charudattan, R., Steinmetz, N.F. *Chemical and UV Light Inactivation of TMGMV for Environmental Applications*. The dissertation author was the primary investigator and author of this paper.

Chapter VI, in full, is a reprint of the material as it appears in the Journal of Physical Chemistry B, 2016. Chariou, P.L., Lee, K.L, Pokorski, J.K, Saidel, G.M, Steinmetz, N.F. *Diffusion and Uptake of Tobacco Mosaic Virus as Therapeutic Carrier in Tumor Tissue: Effect of Nanoparticle Aspect Ratio*. 120, 6120-6129. The dissertation author was the primary investigator and author of this paper.

Chapter VII, in full, is a reprint of the material as it appears in Macromolecular Biosciences, 2019. Chariou, P.L., Wang L., Desai C., Park J., Robbins L.K., von Recum H.A., Ghiladi R.G., Steinmetz N.F. *Let there be light: targeted photodynamic therapy using high aspect ratio plant viral nanoparticles*. 1800407. The dissertation author was the primary investigator and author of this paper.

Chapter VIII, in full, is in preparation for submission to a peer-reviewed journal, 2020. Chariou, P.L. Beiss, V., Steinmetz, N.F. *In Situ Vaccine Application of Inactivated CPMV Nanoparticles*. The dissertation author was the primary investigator and author of this paper.

Vita

2011-2015 Undergraduate Research Assistant, Case Western Reserve University

2012-2019 Health and Safety Officer of the Steinmetz Lab

2014 Undergraduate Research Assistant, Rice University

2013-2018 Teaching Assistant, Case Western Reserve University

2015 Bachelor of Science, Case Western Reserve University

2015-2018 Graduate Research Assistant, University of California San Diego

2018 Master of Science, Case Western Reserve University

2018-2020 Graduate Research Assistant, University of California San Diego

2020 Doctor of Philosophy, University of California San Diego

Publications

“*” indicates co-authorship.

Chariou, P.L.*, Lee, K.L*, Wen, A.M, Steinmetz, N.F. (2015). *Detection and imaging of aggressive cancer cells using an epidermal growth factor receptor (EGFR)-targeted filamentous plant virus-based nanoparticle*. *Bioconjugate Chemistry*. 201526(2):262-269.

Chariou, P.L., Lee, K.L, Pokorski, J.K, Saidel, G.M, Steinmetz, N.F. (2016). *Diffusion and Uptake of Tobacco Mosaic Virus as Therapeutic Carrier in Tumor Tissue: Effect of Nanoparticle Aspect Ratio*. *Journal of Physical Chemistry B*. 120, 6120-6129.

Chariou, P.L., Steinmetz, N.F (2017). *Delivery of Pesticides to Plant Parasitic Nematodes using Tobacco Mild Green Mosaic Virus as a Nanocarrier*. *ACS Nano*. 11, 4719-4730.

Wallat J.D., Wek K, Chariou P.L, Carpenter B.L, Ghiladi R.A, Steinmetz N.F., Pokorski J.K. (2017) *Fluorinated Polymer-Photosensitizer Conjugates enable Improved Generation of ROS for Anticancer Photodynamic Therapy*. *Polymer Chemistry*. 8, 3195-3202.

Masarapu, H., Patel, B.K., Chariou, P.L., Hu, H., Gulati, N.M., Carpenter, B.L., Ghiladi, R.A., Shukla, S., Steinmetz, N.F. (2017). *Physalis Mottle Virus-Like Particles as Nanocarriers for Imaging Reagents and Drugs*. *Biomacromolecules*. DOI: 10.1021/acs.biomac.7b01196

Marin-Caba L., Chariou P.L., Pesquera C., Correa-Duarte M., Steinmetz N.F. (2018) *Tobacco Mosaic Virus-Functionalized Mesoporous Silica Nanoparticles, a Wool-Ball-like Nanostructure*

for Drug Delivery, Langmuir, DOI: 10.1021/acs.langmuir.8b03337

Chariou P.L., Wang L., Desai C., Park J., Robbins L.K., von Recum H.A., Ghiladi R.G., Steinmetz N.F. (2019) Let there be light: targeted photodynamic therapy using high aspect ratio plant viral nanoparticles. *Macromol. Biosci.* 1800407

Chariou, P.L, Dogan, A.B., Welsh, A.G., Saidel, G.M., Baskaran, H., Steinmetz, N.F. (2019). *Soil mobility of synthetic and virus-based model nanopesticides*. *Nature Nanotechnology*. DOI: <https://doi.org/10.1038/s41565-019-0453-7>

Fields of Study

Major Field: BioEngineering

Studies in nanomedicine, drug delivery, and precision farming
Professor Nicole F Steinmetz

Abstract of the Dissertation

Engineering plant virus-based nanocarriers for human and plant health

by

Paul Laurent Chariou

Doctor of Philosophy in BioEngineering

University of California San Diego, 2020

Professor Nicole F. Steinmetz, Chair

Nanocarrier-based delivery systems can be used to increase the safety and efficacy of active ingredients in medical, veterinary or agricultural applications, particularly when such ingredients are unstable, sparingly soluble, or cause off-target effects. To this day, the majority of nanocarriers that are commercially available or in the development pipeline are spherical in shape. However, recent data suggests that high aspect ratio nanoparticles possess unique fluid transport properties (*e.g.* enhanced margination and tumor homing) and physiological interactions (*e.g.* decreased phagocytosis). Non-mammalian viruses are on the rise as economically and environmentally viable alternative to synthetic nanoparticles. Therefore I turned towards the study of high aspect ratio plant virus-based nanocarriers, and my dissertation focused on their development and testing for applications as pesticide carriers for precision farming as well as drug carriers and

immunotherapies for nanomedicine applications. Specifically, I focused on the high aspect ratio viruses tobacco mosaic virus (TMV), and its U2 strain tobacco mild green mosaic virus (TMGMV). The central part of my thesis focused on the development and evaluation of TMGMV as a pesticide nanocarrier for the treatment of crops infected with endoparasitic nematodes. I report the formulation and characterization of TMGMV loaded with anthelmintic pesticides using non-covalent and covalent loading methods, the bioavailability and treatment efficacy of the TMGMV nanopesticide vs nematodes in liquid cultures, the superior soil mobility of TMGMV compared to free pesticides and other contemporary nanoparticle-based formulations, and the successful development of non-infectious TMGMV particles for safe use in agricultural applications. In addition, I have applied the knowledge I have gained from my precision farming studies to the field of cancer nanomedicine. I developed a mathematical model to quantify diffusion and uptake of TMV in a spheroid system approximating a capillary-free segment of a solid tumor. I determined that TMV and TMGMV could be stably loaded with cationic photosensitizer drugs via non-covalent interactions for application as photodynamic therapy targeting cancer. Lastly, I developed non-infectious cowpea mosaic virus nanoparticles for use as an *in situ* cancer vaccine. Overall, my research enhanced the understanding of high aspect ratio viral nanoparticles and has laid groundwork toward their use as drug carriers for food safety and security as well as cancer treatment.

Chapter I: Introduction: Nanocarriers for Agricultural, Veterinary, and Medical Applications

1.1. Opening.

Over the past 30 years, nanoparticle engineering has led to the development of novel delivery systems for active ingredients with medical, veterinary, and agricultural applications. The increasing cost of research and development combined with the growing number of competitive manufacturing entities, short patent cycles, and the tightening regulatory guidelines for active ingredients, have made it difficult to bring new formulations from the bench to the market.^{1,2} Furthermore, the efficacy of many drugs is limited by their low solubility and/or stability, as well as off-target effects following systemic delivery. For example, cancer therapy is often unsuccessful due to the toxicity of cancer drugs towards healthy cells and/or the development of resistant cells overexpressing efflux transporters and multidrug-resistance proteins.^{3,4} The resulting low bioavailability of the active ingredient in the tumor requires the administration of larger doses to ensure the drug concentration stays within the therapeutic window, which in turn increases off-target toxicity. Nanocarriers can address this challenge by delivering active ingredients via the enhanced permeability and retention (EPR) effect, a well-established phenomenon based on the combination of leaky vasculature and poor lymphatic drainage at the tumor site.⁵ The EPR effect only increases the tumor homing of nanoparticles by two-fold compared to normal tissue,⁶ so nanoparticles can also be functionalized with targeting ligands, aptamers, antibodies, or antibody fragments to promote their binding to receptors overexpressed on tumor cells or in the surrounding extracellular matrix.^{7,8} The entrapment of active ingredients in nanocarriers also reduces the clearance rate via renal elimination and phagocytosis, which increases the active ingredient circulation time and therefore its therapeutic longevity.

The medical and veterinary applications of nanocarriers are analogous, but only experimental veterinary applications have been reported.⁹ Most research in veterinary drug delivery has focused on diseases in animals that can be translated to humans. However, the importance of animal welfare *per se* is increasingly important to consumers, and nanocarriers that improve the efficacy and safety of active ingredients are demanded in the context of companion animals such as cats, dogs and horses, as well as farm animals such cattle, sheep, swine and poultry.¹⁰ Pet owners consider companion animals as an extension of the family and are willing to pay their bills, including the high cost of cancer treatment, with the cost of veterinary care in the USA therefore rising from \$7 billion in 2001 to \$19 billion in 2019.¹¹ This increase most likely reflects a combination of inflation, high drug costs, better treatment options (with higher survival rates), and an increased willingness to care for pets. In contrast, the food industry works with low profit margins and would only treat animals suffering from temporary and low-risk diseases, such as infections.¹² Veterinary nanocarriers must therefore combine low costs with the release of active ingredients for sustained periods to minimize the frequency of animal handling and improve therapeutic efficacy. For example, animals are often subject to bacterial infections, and a nanomedicine approach could achieve the targeted delivery of drugs to pathogens, killing them on demand. This avoids the unnecessary use of antibiotics, which can encourage the emergence of resistant strains.

The controlled delivery of agrochemicals and nutrients to plants is conceptually similar to drug delivery in humans and animals. However, agricultural delivery takes place in an open field, with variable weather and geographic features and no specific transport pathway to the target, in contrast to the closed and regulated nature of the bloodstream. Nanocarriers can be administered via the foliage, where they are taken up passively through stomata and any wounds, or can be

transported through the soil and taken up via the roots.¹³ Among the agrochemicals that can be delivered using nanoparticles, pesticides are particularly suitable candidates because they are effective at very low doses (grams per acre) but are difficult to apply in such small amounts due to their non-uniform distribution in the field.¹⁴ To compensate, the active ingredient can be diluted within a mixture of liquid or solid diluents. However, the active ingredient is often unstable, sparingly soluble, and binds with high affinity to soil particles, thus reducing its efficacy against target pests and increasing the amount required to achieve an effective dose.¹⁵ In an analogous manner to the off-target effects caused by systemic drugs, the persistence of large quantities of pesticides in the environment is toxic to other species, and contaminates the soil and groundwater leading to health problems in domestic animals and humans, including cancer and infertility.^{16,17} Governments have therefore started to prohibit many pesticides or strictly regulate their use. In one strategy, the active ingredient is enveloped in organic or inorganic coatings (microencapsulation) for protection against photolysis or biodegradation, allowing the controlled release of the ingredient.¹⁸ But even microencapsulation is limited by the poor chemical and thermal stability of the capsules, and degradation promotes the acidification of soil, which can impair its fertility. As discussed in more detail below, these drawbacks can be addressed by a new generation of nanocarriers based on polymers, lipids and other materials.

The definition of a nanomaterial is not yet harmonized, but the International Organization for Standardization (ISO) defines nanoparticles as objects with dimensions of 1–100 nm, because the physicochemical properties of the material at this scale differ from the bulk material. Unfortunately, this ISO definition excludes most nanomaterials that are relevant in the medical, veterinary, and agricultural sectors. A less stringent definition would include any materials with at least one dimension in the range 1–100 nm, thus including nanowires and nanotubes.¹⁹ In this

introduction, I considered nanocarriers with at least one dimension smaller than 1000 nm and their use for the targeted delivery of active ingredients (drugs or pesticides) to achieve greater efficacy. I will focus on the translation of nanocarriers from the bench to the market in the medical, veterinary, and agricultural industries in order to describe the current landscape and potential future directions for active ingredient delivery systems. Specifically, I discuss research articles (retrieved from PubMed and the Web of Science), patents (retrieved from Orbit Express using Questel software), clinical trials (listed in the clinicaltrials.gov database), and commercially available nanocarrier formulations approved by: (1) the US Food and Drug Administration (FDA) and/or European Medicines Agency (EMA) for medical use; (2) the American Veterinary Medical Association (AVMA) for use in animals, *i.e.* products listed in the Approved Animal Drug Products (Green Book) and/or AVMA Animal Health Studies database; and (3) the US Environmental Protection Agency (EPA), *i.e.* products listed in the National Pesticide Information Center database. Nanoparticles have also been used for diagnosis, drug discovery, gene delivery, immunotherapy, photothermal/photodynamic therapy, and biosensor applications, which are reviewed elsewhere.^{20–25}

1.2. From idea to commercial product.

1.2.1. Trends in active ingredient delivery.

The term “nanotechnology” was coined in 1974 by the Japanese scientist Norio Taniguchi,²⁶ but the worldwide proliferation of nanotechnology started in the 1990s and has thus far led to the publication of more than 60,000 research articles in the pharmaceutical and environmental sciences. More than 93% of these articles relate to medical research, whereas nanoparticles in agriculture and veterinary research emerged later in the 2010s and represent only

~4% and ~3% of the publications, respectively (**Figure 1.1 A**). Even so, the growing political and consumer interest in global food security and environmental protection is likely to drive additional research in the use of nanocarriers in agriculture and veterinary research in the future. Nanoparticle-based innovations also account for more than 150,000 patents (**Figure 1.1 B**). Since the Bayh-Dole (Patent and Trademark Law Amendments) Act was ratified in the United States, allowing small businesses, non-profit institutions, and universities to own inventions created via research funded by the federal government, the majority of these patents have been filed by universities. The University of California is the largest patent holder in this field, with more than 1200. Interestingly, 16% of all nanotechnology patents (~24,000) are held by the pharmaceutical sector, highlighting the growing interest in nanoparticles for drug delivery, diagnosis, and imaging.

Nanocarriers for medical and veterinary applications are regulated by the FDA in the United States and the EMA in Europe. Since 1990, the FDA and EMA have approved 19 nanocarriers (**Table 1.1**), and more candidates are undergoing pre-clinical and clinical testing (**Table 1.2**). Most of these nanocarriers are administered orally or intravenously, and some transdermally. The materials used in these formulations include polymers, micelles, liposomes, proteins and viruses. Most clinical trials (48%) involve micellar formulations, whereas viruses account for only 1% (**Figure 1.1 C**). In contrast, most approved nanocarriers are based on liposomes (47%), followed by viral (19%), micellar (14%), polymeric (10%), and proteinaceous (10%) formulations (**Figure 1.1 D**). Most of these nanocarriers have demonstrated lower toxicity rather than improved efficacy compared to the active ingredient alone.²⁷ Accordingly, novel nanocarriers may not survive clinical trials because they do not achieve greater efficacy and because the reduction in toxicity might be achieved using an already-approved nanocarrier formulation.

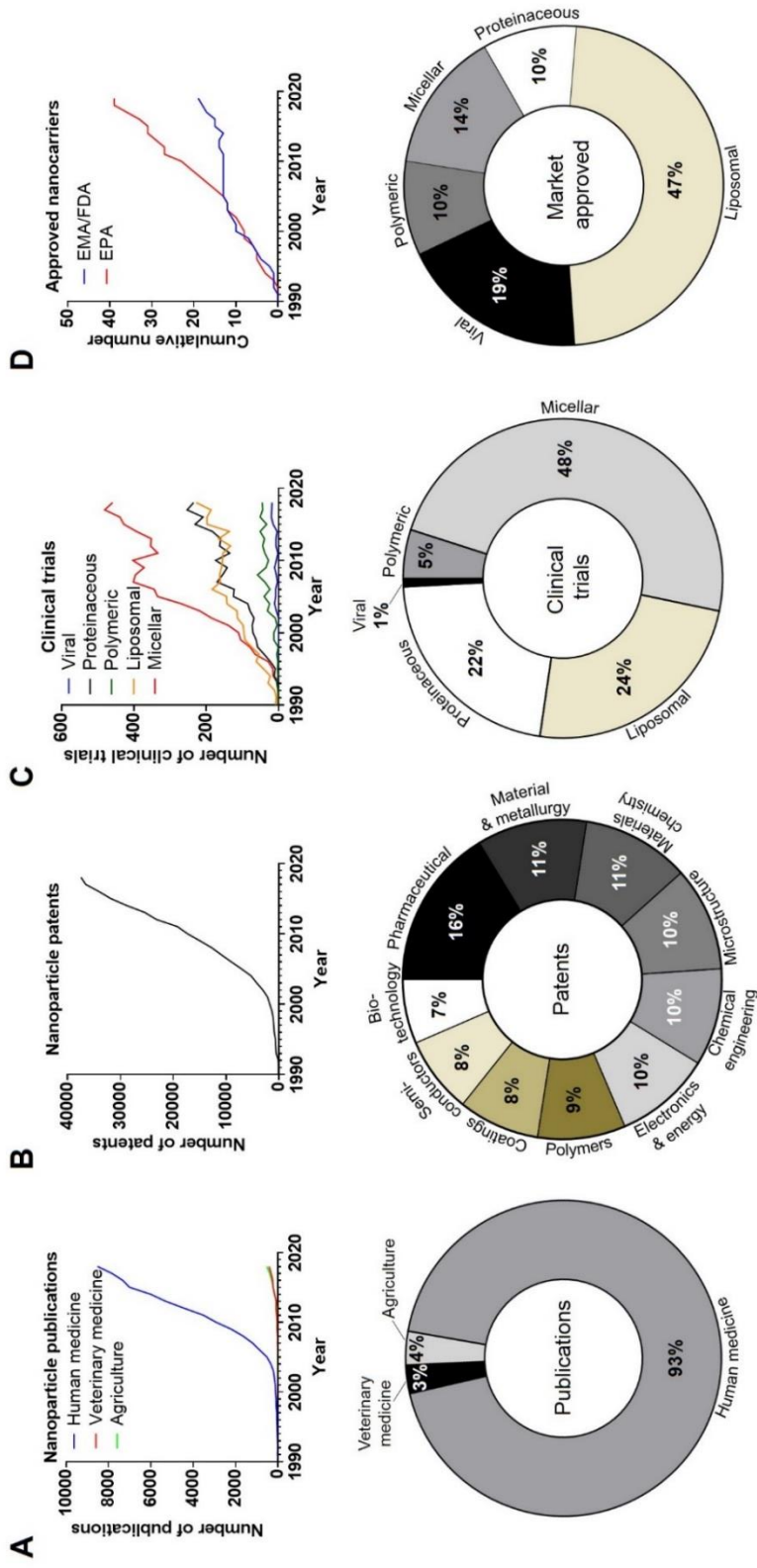


Figure 1.1. Nanocarriers in human medicine, veterinary medicine, and agriculture. The timeline and corresponding distribution of: (A) peer-reviewed publications involving nanoparticles in the medical, veterinary, and agricultural fields; (B) patent applications involving nanoparticles; (C) clinical trials using nanocarriers based on different materials; and (D) market approved nanocarrier formulations.

The regulation of nanocarriers for agricultural applications is not yet harmonized because a clear definition of agricultural nanocarriers has not yet been agreed, which makes it difficult to determine how many products are already commercialized. Such products are overseen by the EPA in the United States and the European Commission in Europe. In 2011, the EPA became the first regulatory agency to approve a nanopesticide, but this nanosilver-based product was approved as an antimicrobial agent for use in clothing, not for agricultural applications. The first true agricultural product was a nanoparticle formulation based on Tobacco mild green mosaic virus (TMGMV), which was approved by the EPA as a herbicide in the state of Florida for the treatment of tropical soda apple, an invasive weed.^{28,29} No commercialized agricultural nanoformulations for pesticide or fertilizer delivery are yet branded as nanocarriers. This is most likely a marketing strategy to deal with the unclear regulation of agricultural nanocarriers while ensuring public acceptance. However, 42 microencapsulated products (including microscale and nanoscale carriers) have been approved by the EPA (**Table 1.3**). Although most of these formulations are used as herbicides or insecticides, a growing body of literature has demonstrated the usefulness of nanocarriers based on clay, chitosan, silica, or zeolites for the delivery of fertilizers, as discussed elsewhere.³⁰

1.2.2. Ingredients delivered by nanocarriers.

The cargos delivered by nanocarriers include small molecules, peptides and proteins, nucleic acids, or combinations of the above. Small molecules are low-molecular-weight organic compounds with beneficial biological activities, such as cancer drugs, antibiotics, fertilizers and pesticides. Relevant examples in clinical and veterinary medicine include the antimetabolites paclitaxel and vincristine, the DNA intercalator doxorubicin, and the antibiotic amphotericin B.³¹⁻

³⁴ When delivered systemically, hydrophobic small molecules are rapidly metabolized and eliminated, narrowing their therapeutic window. Large doses are therefore required for therapeutic efficacy, which in the case of cancer drugs can lead to off-target effects such as cardiotoxicity and nephrotoxicity.^{35,36} Similarly, only a small fraction of pesticides and fertilizers applied to fields ever reach their target, due to leaching, evaporation, photolysis, chemical hydrolysis, and biodegradation. To feed the growing world population, today's yields must increase by 60–100%, and this must be achieved in part by more effective treatment methods to eliminate pests and by increasing the efficiency of fertilizers.³⁰

Peptide and protein pharmaceuticals may act as receptor agonists, essentially fulfilling the functions of endogenous molecules, whereas others act as antagonists. Neuroprotective proteins such as nerve growth factor and brain-derived neurotrophic factor are examples of agonists. They may help to combat Alzheimer's disease and Parkinson's disease, although they remain at the preclinical development stage.³⁷ The blood brain barrier (BBB) remains a major hurdle to deliver these proteins to the central nervous system, and nanocarriers have been engineered to deliver proteinaceous active ingredients across the BBB.³⁸ Small peptides and proteins are often unstable *in vivo* due to the presence of proteases, and may also be removed by renal filtration, reducing their bioavailability. Nanocarriers can also overcome this challenge. For example, the antimicrobial peptide HPA3P^{His} was delivered using aptamer-targeted gold nanoparticles, which led to the complete inhibition of *Vibrio vulnificus* colonization in infected mice.³⁹ As well as stabilizing peptide and protein drugs with nanocarriers, multivalent display can be used as a strategy to enhance therapeutic efficacy, as demonstrated by the delivery of TNF-related apoptosis-inducing ligand (TRAIL) using liposomal and plant viral nanoparticle formulations.^{40,41} Monoclonal antibodies (mAbs) are a large class of protein drugs that often act as antagonists. For

example, Herceptin is a mAb approved by the FDA for the treatment of HER2⁺ breast, gastric, and esophageal cancers by blocking HER2 receptor signaling.⁴² Herceptin is one of 59 therapeutic mAbs that have been approved since 1992, when the first mAb formulation was launched.⁴³ Four antibody–drug conjugates (ADCs) have also been approved, with another 22 currently undergoing clinical trials.⁴⁴ Antibody–nanoparticle conjugates can be targeted to specific cells using the properties of nanocarrier, the antibody, or both. Similarly, the target specificity of the antibody can be combined with the cargo-loading capacity of nanoparticles, which has proven effective in many research studies but has yet to be deployed successfully in the clinic.⁴⁵ Nanoparticle-mediated antibody delivery is particularly useful when the target is intracellular.⁴⁶ For example, a liposomal nanocarrier was designed to display CD44-specific antibodies on the surface in order to target CD44⁺ cells but to carry a second IL6R-specific antibody as a cargo, which was taken up by the target cells to inhibit the intracellular IL6R-Stat3 signaling pathway in mice with triple-negative breast cancer. The treated mice showed a significant reduction in metastatic events.⁴⁷

Like antibodies, peptides and proteins can also be used as targeting ligands to direct nanoparticles to disease sites. Such ligands displayed on nanoparticles promote cell binding, internalization and endosomal escape, allowing the nanoparticles to accumulate and release their active ingredient within target cells while sparing healthy tissue from damage.⁴⁸ However, actively targeted nanocarriers developed for the treatment of cancer have yet to progress beyond clinical trials.⁴⁹ Targeted nanoparticles are more complex than their passive counterparts, which makes them more difficult to produce according to good manufacturing practice (GMP) and significantly increases the cost of therapy. Furthermore, it is unclear whether active targeting improves therapeutic efficacy. A meta-analysis of the literature over the past 10 years has shown that, on

average, 0.9% of each dose of active nanocarriers reaches its target, compared to 0.6% for the passive nanocarriers.⁵⁰

Finally, nucleic acids can be used as active agents in medical, veterinary and agricultural applications, particularly DNA, microRNA (miRNA) and short interfering RNA (siRNA).³⁰ Gene therapy in humans and domestic animals involves the delivery of DNA to the nucleus in order to augment or repair malfunctioning genes, whereas gene transfer to crops can introduce new functionalities, such as resistance to pests and diseases, or pesticide tolerance.^{20,45} MicroRNA is non-coding RNA ~20 nucleotides in length that regulates endogenous genes, and the delivery of miRNA to the cytoplasm of target cells can be used to suppress the expression of disease-causing genes.⁵¹ The delivery of non-coding double-stranded dsRNA or siRNA derived from it promotes the assembly of a protein complex that binds complementary mRNA, leading to its cleavage and the targeted suppression of gene expression. The systemic delivery of miRNA and siRNA is generally ineffective because such molecules are rapidly degraded and cleared, and often trigger an innate immune response, the exact nature of which is sequence dependent. Furthermore, miRNA and siRNA are hydrophilic and cannot penetrate the hydrophobic cell membrane to reach the cytoplasm. In the cytoplasm, they are rapidly degraded by nucleases and multiple doses are therefore needed to suppress gene expression enough for a therapeutic effect. The drawbacks of conventional nucleic acid therapies can be addressed by encapsulating them in nanocarriers (**Supporting Tables 1.1 and 1.2**) and five such carriers have already reached the market (**Table 1.1**).

Genetic engineering has facilitated significant advances in human and veterinary medicine, and has also helped to improve the yield of crops by enhancing pest and disease resistance and abiotic stress tolerance.⁵² Most genetically engineered plants are produced by transformation using

the soil bacterium *Agrobacterium tumefaciens*, which introduces DNA via a type IV secretion system, or by biolistic delivery systems, which introduce DNA by physically penetrating the cell wall using high-velocity metal particles.^{53,54} Nanocarrier-based delivery systems would need to find an alternative strategy to pass through the cell wall, and current research is focusing on the size, charge and surface properties of metallic, liposomal, silicon-based, and polymeric nanocarriers to enable cell wall penetration.⁵²

The limitations of small molecules, peptides, proteins, and nucleic acids can be overcome by using nanocarriers to achieve three key goals: (1) enhance the aqueous solubility and therefore bioavailability of active ingredients; (2) increase the stability of active ingredients by inhibiting their degradation *in vivo* or in the environment, effectively increasing their half-life; and (3) promote the accumulation of the active ingredient at the target site. If all three goals are achieved, the dose of active ingredient required for efficacy is greatly reduced, thus limiting overall costs and avoiding off-target effects. These goals can be achieved using nanocarriers made from a wide range of materials (**Figure 1.2**), which are discussed in more detail below.

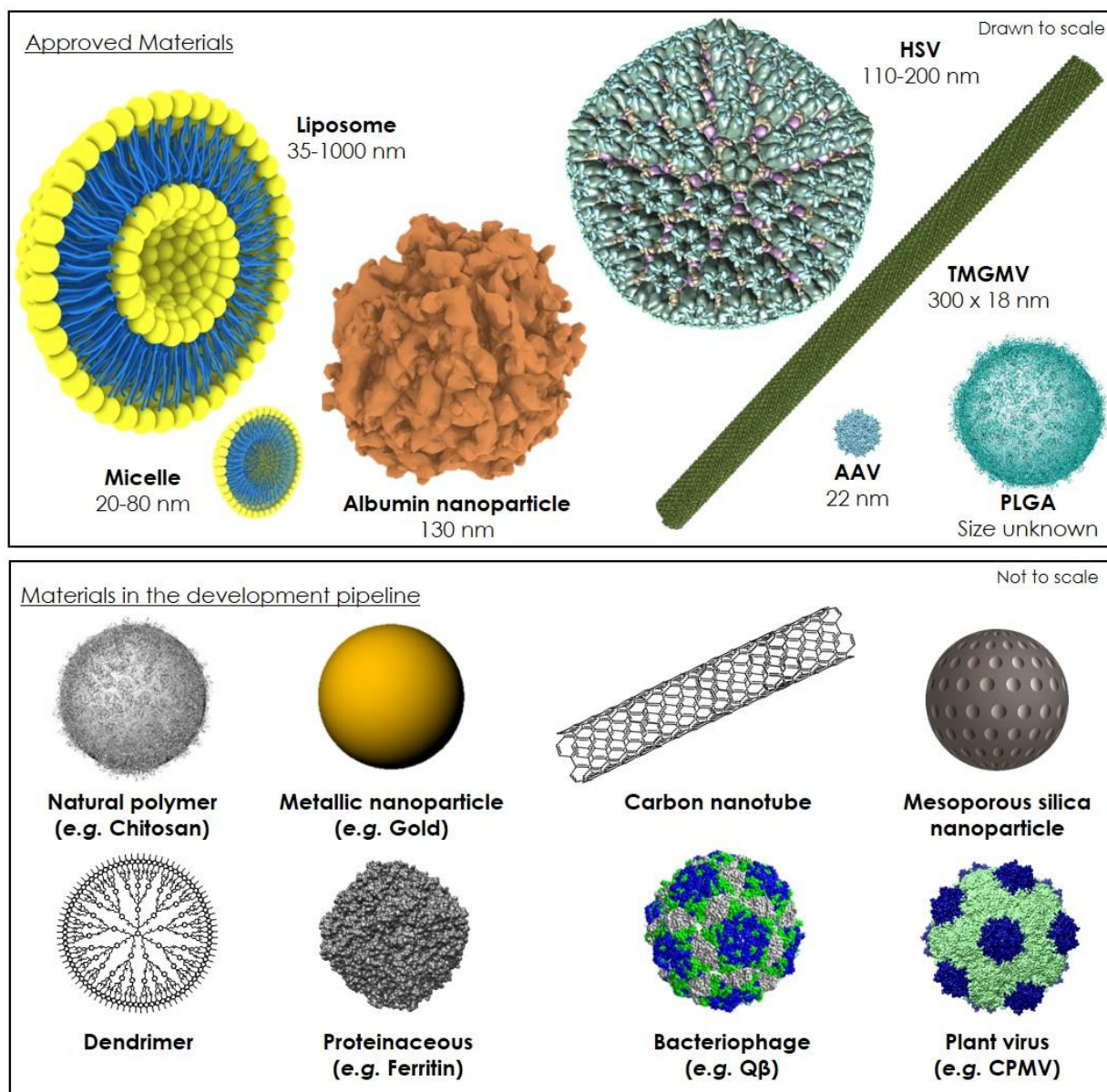


Figure 1.2. Size and structure of nanocarriers (approved and in development). Adeno-associated virus (AAV, PDB ID: 1LP3), Herpes simplex virus (HSV, PDB ID: 5ZAP), Tobacco mild green mosaic virus TMGMV (PDB ID: 1VTM), ferritin (PDB: 6BP7), bacteriophage Q β (PDB ID: 5KIP), and Cowpea mosaic virus (CPMV, PDB ID: 1NY7) were reconstructed using the UCSF Chimera software. The albumin, micelle, liposome, PLGA, chitosan polymer, mesoporous silica, and gold nanocarriers were rendered using Rhinoceros 3D v5.0. The carbon nanotube and dendrimer were drawn using ChemDraw software.

Table 1.1. FDA and EMA approved medical nanocarriers.

Liposomal nanocarriers				
Drug name (company)	Active ingredient	Nanoparticle size	Specific treatment	Year of approval
Ambisome (Gilead Sciences)	amphotericin B	80–120 nm	fungal infection	1997 [US]
Curosurf (Dey Laboratories)	poractant α	50–1000 nm	respiratory distress syndrome	1998 [US]
Dauno Xome (Calten)	daunorubicin	35–65 nm	Kaposi's sarcoma	1996 [US]
Doxil (Janssen)	doxorubicin	50–100 nm	Kaposi's sarcoma breast cancer ovarian cancer myeloma	Discontinued in 2016 1995 [US] - 1996 [EU] 1996 [EU] 2005 [US] - 1996 [EU] 2008 [US] - 1996 [EU]
Marqibo (Onco TCS)	vincristine	100 nm	acute lymphoblastic leukemia	2012 [US]
Myocet (Teva UK)	doxorubicin	150–250 nm	metastatic breast cancer	2000 [EU]
Onpattro (Alnylam Pharmaceuticals)	transferrin-directed small interfering RNA	80 nm	hereditary transthyretin-mediated amyloidosis	2018 [US] - 2018 [EU]
Onivyde (Merimack)	irinotecan	90–130 nm	pancreatic cancer	2015 [US] - 2016 [EU]
Visudyne (Novartis)	verteporfin	150–300 nm	macular degeneration	2000 [US] - 2000 [EU]
Vyxeos (Jazz Pharmaceuticals)	daunorubicin and cytarabine	100–200 nm	acute myeloid leukemia	2017 [US] - 2018 [EU]
Polymeric nanocarriers				
Drug name (company)	Active ingredient	Nanoparticle size	Specific treatment	Year of approval
Eligard (Tolmar)	leuprolide acetate in PLGA	N.A.	prostate cancer	2002 [US]
Welchol (Daichi-Sankyo)	colesvelam hydrochloride in allylamine polymer	N.A.	type 2 diabetes	2000 [US]
Micellar nanocarriers				
Drug name (company)	Active ingredient	Nanoparticle size	Specific treatment	Year of approval
Estrasorb (Novavax)	17 β -estradiol	20–80 nm	menopausal therapy	2003 [US]
Taxol (Bristol Myres Squibb)	paclitaxel	20–80 nm	ovarian cancer breast cancer Kaposi's sarcoma non-small-cell lung cancer	1992 [US] 1994 [US] 1997 [US] 1998 [US]
Taxotere (Sano fi-A ventis)	docetaxel	20–80 nm	breast cancer non-small-cell lung cancer prostate cancer gastric cancer head and neck cancer	1996 [US] - 1995 [EU] 1999 [US] - 1995 [EU] 2004 [US] - 1995 [EU] 2006 [US] - 1995 [EU] 2006 [US] - 1995 [EU]

Table 1.1. FDA and EMA approved medical nanocarriers. Continues....

Proteinaceous nanocarriers				
Drug name (company)	Active ingredient	Nanoparticle size	Specific treatment	Year of approval
Abraxane (Celgene)	albumin-bound paclitaxel	130 nm	breast cancer non-small-cell lung cancer pancreatic cancer	2005 [US] - 2008 [EU] 2012 [US] - 2005 [EU] 2013 [US] - 2008 [EU]
Ontak (Eisai)	diphtheria toxin fragments + human interleukin-2	58 kDa	cutaneous T-cell lymphoma	1999 [US] Discontinued in 2014
Viral nanocarriers				
Drug name (company)	Active ingredient	Nanoparticle size	Specific treatment	Year of approval
Glybera (UniQure)	AAV1 vector containing lipoprotein lipase gene	22 nm	lipoprotein lipase deficiency	2012 [EU] Discontinued in 2017
Imlygic (Amgen)	Herpes simplex type I	110–200 nm	melanoma	2015 [US] - 2015 [EU]
Luxturna (Spark Therapeutics)	AAV2 vector containing RPE65 cDNA	22 nm	RPE65 mutation associated retinal dystrophy	2017 [US] - 2018 [EU]
Zoigenma (Novartis)	AAV9 vector containing SMN1 gene	22 nm	spinal muscular atrophy	2019 [US]

1.3. Liposomal nanocarriers.

Liposomes are spherical vesicles comprising one or more concentric lipid bilayers with an aqueous core.⁵⁵ These amphiphilic structures are uniquely suited to entrap both lipophilic and hydrophilic compounds, making them attractive nanocarriers for a diverse range of active ingredients. Hydrophobic ingredients can be inserted into the lipid bilayer or sequestered in the core, whereas hydrophilic ingredients can be encapsulated in the core. The lipid bilayer is usually composed of phospholipids and sterols such as cholesterol, the latter controlling membrane permeability and fluidity.

In the medical and veterinary fields, conventional liposomal nanocarriers can reduce the off-target effects of active ingredients by modifying their pharmacokinetic properties and biodistribution, promoting their accumulation at the target site and avoiding non-target tissues.⁵⁶ Most liposomal nanocarriers deliver their cargo by fusing with the plasma membrane of the target cell, causing the active ingredient to be deposited in the cytoplasm. For example, Myocet is a conventional liposomal carrier approved by the EMA for the delivery of doxorubicin to metastatic breast cancer cells.⁵⁷ Commercially available liposomal nanocarriers range from 30 to 1000 nm in diameter, which makes them the largest nanocarriers used in the clinic (**Table 1.1**). The physicochemical properties of liposomes are determined by the lipid composition, sterol concentration, surface charge, and nanoparticle size.⁵⁸ Increasing the concentration of unsaturated phospholipids (*e.g.*, phosphatidylcholine) ensures that the lipid bilayer is permeable, whereas saturated phospholipids (*e.g.*, dipalmitoylphosphatidylcholine) make the barrier impermeable. By controlling the lipid composition and length of the fatty acid chains, liposomal nanocarriers can be engineered to respond to temperature and/or pH, allowing the controlled release of the active ingredient under physiological conditions that are specific to the disease site. The cellular uptake

of liposomes can be also tuned by the lipid composition, which influences the overall surface charge.^{59,60} Neutral liposomes tend to remain in circulation longer and do not readily interact with cells, promoting the release of active ingredients in the extracellular space. This strategy is used by DaunoXome (for the delivery of daunorubicin to Kaposi's sarcoma), Marqibo (for the delivery of vincristine to lymphoblastic leukemia), and Onivyde (for the delivery of irinotecan to pancreatic cancer cells).^{61,62,63} Whereas positively charged liposomes readily interact with the negative charge on the cell surface via electrostatic forces, neutral liposomes are prone to faster clearance. However, conventional liposomes of all types are rapidly eliminated from the bloodstream due to opsonization and uptake by Kupffer cells in the liver and spleen, which limits their bioavailability.⁶⁴ This has been addressed by conjugating hydrophilic polymers to the liposome surface, such as polyethylene glycol (PEG) in the case of Doxil, the first clinically approved liposome.⁶⁵ Depending on the liposome formulation, PEGylation has been shown to increase the half-life of the active ingredient from 2 h to 24 h in rodents and up to 45 h in humans, resulting in a 4–16-fold higher concentration at the target site.⁶⁶ However, PEGylation can inhibit the interaction between liposomes and the cell surface, preventing fusion and uptake. Furthermore, passive targeting is limited by the heterogeneity of the EPR effect both within the tumor environment and when comparing different types of cancer. Ligand-targeted liposomes have therefore been engineered to promote site-specific binding. Low-molecular-weight molecules such as folate, as well as peptides and monoclonal antibodies or their fragments, have been incorporated onto the surface of liposomes to achieve targeted delivery.⁶⁷ Liposomes also have the versatility to deliver multiple active ingredients simultaneously at a suitable molar ratio to maximize their synergistic interactions. The liposomal nanocarrier Vyxeos is thus far the only approved

formulation that delivers more than one active ingredient, namely cytarabine and daunorubicin (5:1 molar ratio).¹¹⁷

The first liposome formulation was approved in 1995, and since then 10 further products have been approved by the FDA/EMA for clinical use, mostly for combination cancer therapy (**Table 1.1**). Exceptionally, AmBisome (carrying amphotericin B) is indicated for fungal infections,⁶⁹ Curosurf (carrying poractant α) is indicated for respiratory distress syndrome, and Visudyne (carrying verteporfin) is indicated for macular degeneration.⁷⁰ The most recent addition is Onpattro, the first siRNA delivery formulation, approved in 2018 by the FDA.⁷¹ Onpattro encapsulates a transthyretin-directed siRNA for the treatment of amyloidosis.

Additional liposomal nanocarriers are undergoing clinical trials against a wide range of diseases, including ocular and topical applications (**Table 1.2**). Although many of the new formulations are cancer therapies, the landscape of current trials highlights the potential of nanomedicine across the field. For example, liposomal alprostadil is a potent vasodilator that increases peripheral blood flow, inhibits platelet aggregation, and induces bronchodilation (NCT02889822); liposomal cyclosporine A is also being investigated as an inhaled delivery formulation for the treatment of bronchiolitis obliterans syndrome.⁷² Another example targeting cardiovascular disease consists of sodium alendronate encapsulated in liposomes of distearoylphosphatidylglycerol, 1,2-distearoyl-*sn*-glycero-3-phosphocholine, and cholesterol. Phase II testing is underway for the treatment of *de novo* stenotic lesions in native coronary arteries in patients undergoing percutaneous coronary intervention with implantation of a bare metal stent (NCT00739466). Furthermore, a topical gel nanoliposome formulation of vitamin B12 (adenosylcobalamin) is undergoing clinical trials to treat moderate atopic dermatitis (HL-009; NCT01568489), and liposomal latanoprost is being tested as a means to lower intraocular pressure

in patients with open-angle glaucoma and ocular hypertension. Liposomal meglumine antimoniate and liposomal paromomycin are being investigated for the treatment of anthroponotic cutaneous leishmaniasis caused by *Leishmania tropica* in both humans and dogs.⁷³

Novel liposomal nanocarriers are also undergoing veterinary trials (**Table 1.4**).^{74,75} In 2006, a phase I trial of doxorubicin encapsulated into temperature-sensitive liposomes was carried out in companion dogs suffering from spontaneous tumors.⁷⁶ Injection of the nanocarrier followed by the induction of tumor hyperthermia caused 100% of the drug cargo to be released within 20 s at 41.3 °C. Of the 21 dogs enrolled in the study, 18 showed a decrease in tumor volume, including 12 with a decrease of more than 50%. Liposomal doxorubicin in combination with palliative radiotherapy improved the clinical outcome of cats with soft tissue sarcomas.⁷⁷ Clodronate encapsulated in liposomes was able to eliminate malignant histiocytosis in dogs.⁷⁸ Liposome-encapsulated amphotericin B demonstrated high efficacy in dogs infected with the blastomyces fungus while reducing the adverse effects often associated with amphotericin B.⁷⁹

Liposomes have also been used to facilitate the absorption of hydrophobic active ingredients via the cuticles of plants and insects.^{18,80} However, because they are so expensive to produce, agricultural applications are likely to be restricted for the foreseeable future. For example, Doxil costs \$1313 for 5 mg (despite being on the market for two decades and the fact that doxorubicin costs only \$8.5 for 5 mg), whereas newer formulations are even more expensive, such as Marquibo (\$15,747 per 5-mg kit) and Onpattro (\$9500 per vial, typical annual cost \$345,000). Even so, a few studies have investigated the liposomal delivery of pesticides such as entofenprox.⁸¹ An alternative and less expensive solution may be the use of liposomes comprising plant-derived lipids (or alternative nanocarrier systems). This was proposed for the delivery of Fe and Mg to

tomato plants, and 33% of the encapsulated metal was able to penetrate leaves and enter plant cells compared to 1% of the free active ingredient.⁸²

Table 1.2. Novel medical nanocarriers in clinical trials.

Liposomal nanocarriers						
Active ingredient	Nanoparticle	Specific treatment	Start	Phase	Status	ClinicalTrials.gov ID
alprostadil	liposome	cardiovascular diseases	2010	I	completed [2010]	NCT02889822
(irinotecan HCl:floxuridine)	CPX-1	colorectal neoplasms	2006	II	completed [2008]	NCT00361842
gemcitabine liposome	FF-10832	solid tumors	2018	I	recruiting	NCT03440450
alendronate	liposome	coronary artery stenosis	2008	II	completed [2015]	NCT00739466
annamycin	liposome	acute lymphocytic myelogenous leukemia	2007	I	terminated [2009]	NCT00430443
		myeloid leukemia	2018	I/II	recruiting	NCT03315039
			2018	I/II	recruiting	NCT03388749
cyclosporine A	liposome	bronchiolitis obliterans	2019	III	recruiting	NCT03657342
			2019	III	recruiting	NCT03656926
			2012	I/II	completed [2015]	NCT01650545
adenosylcobalamin	HL-009	mild to moderate atopic dermatitis	2012	II	completed [2013]	NCT01568489
latanoprost	liposome	ocular hypertension	2013	I/II	completed [2013]	NCT01987323
meglumine antimoniate and paromomycin	liposome	cutaneous leishmaniasis	2011	I	completed [2012]	NCT01050777
BoNT-A (botulinum toxin A)	liposome	interstitial cystitis	2014	IV	completed [2017]	NCT02247557
		overactive bladder	2010	II	completed [2013]	NCT01167257
docetaxel	LE-DT	pancreatic cancer	2010	II	completed [2011]	NCT01186731
		prostate cancer	2010	II	withdrawn [2011]	NCT01188408
mitoxantrone hydrochloride	liposome	metastatic breast cancer	2015	II	recruiting	NCT02596373
		neoplasms	2011	I	completed [2013]	NCT02043756
		relapsed dlbl and pt/nkcls	2015	II	recruiting	NCT02597387
		t cell lymphoma	2015	II	terminated [2019]	NCT02597153
		t-cell and nk/t-cell lymphoma	2018	II	recruiting	NCT03776279
rhenium	liposome	glioblastoma/astrocytoma	2015	I/II	recruiting	NCT01906385
SN-38	liposome	colorectal cancer	2006	II	completed [2010]	NCT00311610
		lung cancer	2016	II	withdrawn [2016]	NCT00104754
		neoplasms	2002	I	completed [2010]	NCT00046540

Table 1.2. Novel medical nanocarriers in clinical trials. Continues...

Polymeric nanocarriers						
Active ingredient	Nanoparticle	Specific treatment	Start	Phase	Status	ClinicalTrials.gov ID
chlorhexidine gluconate	chitosan nanoparticles	intra canal antiseptic	2018	N.A	active	NCT03588351
docetaxel	CriPec	solid tumor	2015	I	completed [2018]	NCT02442531
		platinum resistant ovarian cancer	2018	II	recruiting	NCT03742713
rapamycin	eRapa	prostate cancer	2018	I	recruiting	NCT03618355
cetuximab	ethylcellulose polymer coated with somatostatin analogue	colon cancer	2018	I	recruiting	NCT03774680
<i>N</i> -acetylcysteine	hydroxyl dendrimer (OP-101)	inflammation	2018	I	completed [2018]	NCT03500627
curcumin + doxorubicin	IMX-110	solid tumors	2017	I/II	recruiting	NCT03382340
paclitaxel	polyethylloxaline (PEOX)	solid tumors	2018	I	recruiting	NCT03537690
¹⁸⁸ Re	poly-l-lysine dendrimer (Imdendrim)	liver cancer	2017	N.A	recruiting	NCT03255343
docetaxel	PSMA-targeted PLA (BIND-014)	prostate cancer	2013	II	completed [2016]	NCT01812746
		non-small lung cancer	2013	II	completed [2016]	NCT01792479
		metastatic cancer	2011	I	completed [2016]	NCT01300533
		cervical cancer squamous cell carcinoma of the head and neck	2015	II	terminated [2016]	NCT02479178
Micellar nanocarriers						
Active ingredient	Nanoparticle	Specific treatment	Start	Phase	Status	ClinicalTrials.gov ID
paclitaxel	micelle (NK105)	breast cancer	2012	III	completed [2017]	NCT01644890
	NK105 + cisplatin	non-small-cell lung cancer	2016	III	active	NCT02667743
	Genexol PM	non-small-cell lung cancer	2009	III	completed [2017]	NCT01023347
		hepatocellular carcinoma	2017	II	recruiting	NCT03008512
		hepatocellular carcinoma	2017	II	recruiting	NCT03008512
		urothelial cancer	2011	II	completed [2011]	NCT01426126
	Genexol PM + carboplatin	ovarian cancer	2011	II	completed [2017]	NCT01276548
	Genexol PM + gemcitabine	pancreatic cancer	2016	II	recruiting	NCT02739633
Genexol PM + gemcitabine	pancreatic cancer	2009	I	completed [2017]	NCT00882973	
antioxidant-rich multivitamin supplement (AquADEKs)	Micelle	cystic fibrosis	2009		completed [2012]	NCT01018303
cisplatin	micelle (NC-6004) + pembrolizumab	head and neck cancer	2018	II	not recruiting	NCT03771820
	micelle (NC-6004) + 5-FU + cetuximab	head and neck cancer	2017	I	active	NCT03109158
	micelle (NC-6004) + gemcitsbine	non-small-cell lung cancer	2014	I	recruiting	NCT02240238
curcumin	micelle	metabolic syndrome	2018	N.A	recruiting	NCT03534024

Table 1.2. Novel medical nanocarriers in clinical trials. Continues...

Micellar nanocarriers						
Active ingredient	Nanoparticle	Specific treatment	Start	Phase	Status	ClinicalTrials.gov ID
curcumin	micelle	metabolic syndrome	2018	N.A	recruiting	NCT03534024
paclitaxel	micelle	psoriasis	2000	II	completed [2008]	NCT00006276
	Paxceed	rheumatoid arthritis	2003	II	completed [2008]	NCT00055133
SN-38	poly(l-glutamic acid)-PEG (NK012)	solid tumors	2007	I	completed [2013]	NCT00542958
		triple-negative breast cancer	2009	II	completed [2015]	NCT00951054
		small-cell lung cancer	2009	II	completed [2013]	NCT00951613
	poly(l-glutamic acid)-PEG (NK012) + 5-FU	colorectal cancer	2010	I	completed [2014]	NCT01238939
	poly(l-glutamic acid)-PEG (NK012) + carboplatin	triple-negative breast cancer	2010	I	completed [2014]	NCT01238952
Proteinaceous nanocarriers						
Active ingredient	Nanoparticle	Specific treatment	Start	Phase	Status	ClinicalTrials.gov ID
dodecanol alkyl ester of bendamustine (RXDX-107)	albumin nanoparticle	solid tumors	2015	I	terminated [2018]	NCT02548390
rapamycin	albumin nanoparticles (ABI-009)	<i>mTOR</i> -mutated cancer	2016	I	active	NCT02646319
		epilepsy intractable	2018	I	recruiting	NCT03646240
		glioblastoma	2018	II	recruiting	NCT03463265
		neuroendocrine tumors	2018	II	recruiting	NCT03670030
		malignant pecoma	2015	II	active	NCT02494570
		leish syndrome	2018	II	not recruiting	NCT03747328
		bladder cancer	2013	I	recruiting	NCT02009332
	ABI-009 + folfox + bevacizumab	colorectal cancer	2018	I	recruiting	NCT03439462
	ABI-009 + nivolumab	advanced sarcoma	2017	I	recruiting	NCT03190174
	ABI-009 + pazopanib	soft tissue sarcoma	2018	I	not recruiting	NCT03660930
	ABI-009 + pazopanib	soft tissue sarcomas	2018	I	active	NCT03660930
	ABI-009 + pomalidomide + dexamethasone	myeloma	2018	I	not recruiting	NCT03657420
	ABI-009 + temozolomide + irinotecan	recurrent or refractory solid tumors	2016	I	recruiting	NCT02975882

1.4. Polymeric nanocarriers.

Polymeric biomaterials are easy to produce at low cost and have therefore been developed and tested as inert shells to promote the accumulation and controlled release of active ingredients at a given target site. Natural polymers have been derived from chitosan, sodium alginate, collagen, heparin, and silk, whereas many different synthetic polymers have been tested, including, polyacrylate (PAL), PEG, polycaprolactone (PCL), polylactic acid (PLA), polyglycolic acid (PGA), polylactic-co-glycolic acid (PLGA), polyesters and polyurethanes. Natural and synthetic polymers can be biocompatible and biodegradable, and their physicochemical properties (*e.g.*, size, morphology, porosity, surface charge, surface chemistry, and hydrophilicity) are inherently flexible and can be tuned to control mechanical and physiological behavior.⁸³

For clinical and veterinary applications, the nanocarrier shell must comprise linear or branched polymers with a molecular weight in the range 0.4–40 kDa to increase the circulation time of the active ingredient while ultimately ensuring renal elimination.⁸⁴ PLGA is particularly promising as a nanocarrier material because the PLA-to-PGA ratio can be adjusted to control the rate of degradation, and thus the release rate of the active ingredient. Using this concept, Eligard was approved by the FDA in 2002 to deliver leuprolide acetate to prostate cancer cells (**Table 1.1**).⁸⁵ PLGA nanocarriers are also being tested in the veterinary field for the delivery of temozolomide to canine brain tumors (**Table 1.4**). The only other polymeric nanocarrier approved by the FDA is Welchol, an allylamine polymer that encapsulates colesevelam hydrochloride to lower the levels of sugar and low-density lipoproteins (LDL) circulating in adults suffering from type 2 diabetes and high cholesterol.⁸⁶ Although the development pipeline for polymeric drug-delivery systems is moving rapidly, there is a puzzling lack of approvals. A possible explanation is that most polymeric drug delivery systems do not improve efficacy but rather enhance safety,

and thus do not achieve significant improvements over liposomal formulations or the free drug at a lower dose.

Dendrimers are a special class of highly-branched polymeric nanocarriers with organized tree-like structures and a low polydispersity, ranging in size from 5 to 500 kDa.^{87–89} They comprise a central core that radiates a series of repeated branching units (generations), terminating with chemical groups available for functionalization. The active ingredient can be encapsulated in the core micelle via hydrophobic/electrostatic interactions, or conjugated to the surface. The greater the number of branches, the more reactive terminal groups can be coupled with the active ingredient. Branches exposed on the surface can also be functionalized to increase tissue specificity.⁹⁰ Most of the dendrimers used as nanocarriers are synthesized from hydrophilic polyamidoamine (PAMAM) or polypropylene imine units, which are not recognized by the immune system. Poly-L-lysine dendrimers are positively charged, and are therefore ideal for the delivery of nucleic acids. Other dendrimers are being developed from PEG, polyglycerol, polyglycerol-co-succinic acid, poly-2,2-bis(hydroxymethyl)propionic acid, melamine, and triazine.⁹⁰ Only two dendrimer-based nanocarriers are currently undergoing clinical trials (**Table 1.2**). The first (OP-101) consists of *N*-acetyl cysteine covalently coupled to a metabolically-stable inactive hydroxyl dendrimer, and has been administered to healthy volunteers to determine its safety, tolerability, and pharmacokinetics. The second (imdendrim) is a poly-L-lysine dendrimer that encapsulates nitro-imidazole-methyl-1,2,3-triazol-methyl-di-[2-pycolyl]amine bound to a rhenium isotope (¹⁸⁸Re), and is currently under investigation for the treatment of liver cancer.

Many other polymeric nanocarriers are undergoing clinical trials (**Table 1.2**). CriPec is a polymeric nanocarrier, 30–100 nm in diameter and of uncertain composition (Cristal Therapeutics does not disclose the details), which encapsulates docetaxel and is shielded by PEG. It is being

tested for the treatment of solid tumors and platinum-resistant ovarian cancer. PEOX is a branched polymer shell composed of polyethyloxazoline, encapsulating paclitaxel for the treatment of solid tumors. PEOX circumvents the need to solubilize paclitaxel with Kolliphor EL (formerly Cremophor EL), a toxic solvent that requires the co-administration of antihistamines to prevent an immune response.³² IMX-110 is a polymeric nanoshell encapsulating curcumin and doxorubicin for the treatment of solid tumors. Following its release in the tumor environment, curcumin targets and inhibits the activation of the transcription factors STAT3 and NF- κ B, which prevents apoptotic tumor resistance and enhances the efficacy of doxorubicin.⁹¹ Another example is eRapa, the protein kinase inhibitor rapamycin encapsulated in polymethyl methacrylate, which is undergoing clinical testing for the treatment of prostate cancer.⁹² A novel nanocarrier for the delivery of cisplatin to canine brain tumors has been developed using hyaluronic acid, a linear polymer of alternating D-glucuronic acid and *N*-acetyl-D-glucosamine residues. Hyaluronic acid is a component of the extracellular matrix and is degraded by hyaluronidase, an enzyme overexpressed in the glioma microenvironment.⁹³ Therefore, the nanocarrier accumulates in the tumor environment, where its degradation causes the local release of cisplatin to minimize systemic toxicity.

One novel formulation that did not progress beyond clinical trials is BIND-014, a PLA-PEG co-polymer displaying a ligand targeting the extracellular domain of the prostate specific membrane antigen. Early studies in rats indicated that BIND-014 could delay tumor growth by preferentially delivering docetaxel to prostate cancer xenografts, limiting the accumulation of this drug in the liver and bone marrow.⁹⁴ BIND-014 was applied in several clinical trials for the treatment of prostate cancer, non-small-cell lung cancer, cervical cancer, and head and neck cancer.⁹⁵ Unfortunately, the trials did not demonstrate sufficient efficacy, with an objective

response of only 10% in the head and neck cancer cohort. Pfizer acquired BIND Therapeutics for \$40 million in 2016 but no further clinical trials have been reported.

Various synthetic and natural biodegradable polymers have also been synthesized for the delivery of agrochemicals. The formulations have been prepared using emulsion or double emulsion strategies, as well as layer-by-layer deposition, nanoprecipitation, and solvent evaporation.^{18,96} Such formulations include nanospheres (where the active ingredient is uniformly distributed throughout the polymer matrix) and nanocapsules (where the active ingredient is encapsulated in the liquid inner core). These nanocarriers have been prepared from PEG, PCL, PAL, chitosan, or sodium alginate,¹⁸ and have been used to deliver diverse pesticides, including ametryn,⁹⁷ atrazine,⁹⁷ acephate,⁹⁸ emanectin benzoate,⁹⁹ garlic essential oil,¹⁰⁰ imidacloprid,^{101,102} lansiumamide B,¹⁰³ methomyl,¹⁰⁴ paraquat,¹⁰⁵ and simazine⁹⁷. However, these formulations are currently at an early developmental stage and are still being tested *in vitro* as well as in field trials.

Polymers have also been used to prepare other forms of active ingredient delivery system, such as hydrogels,^{18,106,107} polymer–drug conjugates,¹⁰⁸ and seed coatings.¹⁰⁹ Hydrogels are cross-linked hydrophilic polymers with a high water retention capacity. A reservoir of the active ingredient may be present at the core of the hydrogel, or it may be uniformly dispersed. The controlled release of the active ingredient is achieved by regulating the physical properties of the hydrogel matrix, such as its porosity and swelling capacity. Environmental stimuli such as temperature, pH, ionic strength, and enzyme activity are often used to control the rate of polymer degradation to achieve the slow and sustained release of the active ingredient. Examples include the FDA-approved intracanalicular implant Dextenza, a dexamethasone-loaded PEG hydrogel for the treatment of ocular pain following ophthalmic surgery,¹¹⁰ as well as hydrogel compositions containing dextran, PAL, propylene glycol, hyaluronic acid, or carboxymethyl cellulose.¹¹¹

Although not technically a nanocarrier application, active ingredients are often conjugated to PEG in a process known as PEGylation, which increases the hydrophilicity and hydrodynamic radius of small-molecule drugs and proteins, thus improving their solubility, masking them from the immune system, slowing their renal clearance, and increasing their circulation half-life while retaining their bioactivity.¹¹² Adagen, a PEGylated adenosine deaminase, was the first PEGylated formulation used in the clinic (1990) to treat severe combined immunodeficiency disease. Since then, 16 more PEGylated drugs have been approved by the FDA/EMA and the majority are indicated for cancer, hepatitis C, or hemophilia (**Supporting Tables 1.3 and 1.5**).^{108,113} To our knowledge, only one PEGylated drug has been approved for veterinary applications. This is Imrestor, a PEGylated granulocyte colony-stimulating factor, which was approved in 2016 to increase the number of circulating neutrophils in cows and thus prevent breast tissue inflammation (**Table 1.2**).¹¹⁴ Although PEGylated drugs have been successfully translated to the clinic, a growing body of literature has highlighted the increased presence of PEG-specific antibodies in the general population due to the extensive use of PEG in cosmetic and pharmaceutical products, correlating with the declining therapeutic efficacy of PEGylated active ingredients.¹¹⁵ This issue is being addressed by the development of alternative polymer-drug conjugates (**Supporting Table 1.5**).

In the agricultural industry, polymeric seed coatings are used to control pests and diseases that would otherwise inhibit germination and growth.^{109,116} Coating seeds increases their viability, reduces the risk of the active ingredient leaching into the environment, and minimizes off-target toxicity to other organisms compared to free pesticides. More than 180 coating formulations have been reported, including chitosan, polyvinyl acetate (latex), polyvinyl alcohol, PEG, ethyl cellulose, and methyl cellulose.¹⁰⁹ On the market, the majority of seed coating technologies have

been developed by Bayer Crop Science, BASF, Corteva, Monsanto, Syngenta, Incotec/Croda, and Germain.

Table 1.3. EPA approved pesticide nanocarriers.

macroencapsulation/nanoencapsulation				
product name (Company)	active ingredient (a.i)	specific treatment	year of approval	registration No.
Poridon® (Neogen Corporation)	permethrin + piperonyl butoxide	insecticide, miticide	1985	72726-1
Sump Buddy™ WT antimicrobial (Dow Chemical)	2,2-Dibromo-3-nitropropionamide	algaecide, bacteriostat, fungicide, microbicide	1989	464-624
Ezject (EZ-Ject, Inc)	glyphosate-isopropylammonium	herbicide	1989	83220-1
Whitmire PT 275 Dur-O-Cap (BASF)	chlorpyrifos	insecticide, miticide	1993	499-367
NoMate® TPW MEC (Scentry Biologicals)	(E)-4-tridecen-1-yl acetate	biochemical pesticide	1994	26638-28
ReJeX-IT AG-36 (Avian Enterprises)	methyl antranilate	repellent	1994	91897-3
Command® (FMC Corporation)	clomazone	herbicide	1995	279-3150
Sump Buddy™ MWF (Dow Chemical)	2,2-dibromo-3-nitropropionamide	microbicide	1996	464-632
Optashield® CS (BASF)	cyfluthrin	insecticide	1998	499-477
For-Mite® (Mann Lake Ltd)	formic acid	miticide	1999	61671-3
Strategy (Loveland Products)	clomazone + ethalfluralin	herbicide	2001	34704-836
CheckMate® DBM-F (Suttera LLC)	(Z)-11-hexadecenal	biochemical pesticide	2002	56336-35
Evercide® Esfenvalerate CS (McLaughlin Gormley King Company)	esfenvalerate	insecticide	2005	1021-1815
Ricemax (Riceco)	clomazone + propanil	herbicide	2006	71085-25
Apiguard® (Vita Bee Health)	thymol	insecticide, miticide	2006	79671-1
Casoron® CS (macdermid agricultural solutions)	dichlobenil	herbicide	2007	400-541
LX417 lambda-Cyhalothrin (BASF)	lambda-cyhalothrin	insecticide	2007	499-535
MGK F-2926(P) (McLaughlin Gormley King Company)	cyphenothrin	insecticide, miticide	2008	1021-1873
TC 251B (BASF)	permethrin	insecticide	2008	499-528
CSI Chlorpyrifos (Control Solutions)	chlorpyrifos	insecticide	2009	53883-264

Table 1.3. EPA approved pesticide nanocarriers. Continues...

macroencapsulation/nanoencapsulation				
product name (Company)	active ingredient (a.i)	specific treatment	year of approval	registration No.
Declare® (FMC Corporation)	gamma-cyhalothrin	insecticide	2009	279-3571
Instinct® (DOW Agrosiences)	nitrapyrin	fertilizer	2009	62719-583
Mon 63410 Herbicide (Monsanto)	acetochlor	herbicide	2010	524-591
Warrior II (Syngenta)	lambda-cyhalothrin	insecticide, miticide	2010	100-1112
MGK® Formula 2964 (McLaughlin Gormley King Company)	esfenvalerate + piperonyl butoxide + Prallethrin	insecticide	2011	1021-2574
GAT Permethrin 25 CS (FMC Corporation)	permethrin	insecticide	2011	279-9573
CSI Permethrin 25 CS (Control Solutions)	permethrin	insecticide	2011	53883-282
Trinexapac-ethyl 1 ME (Syngenta)	trinexapac-ethyl	fungicide, plant growth regulator	2011	100-1401
Permatek™ 100 Encaps (Lonza)	bifentrin	insecticide	2013	72616-8
Chlorpyrifos 42 CS (FMC Corporation)	chlorpyrifos	insecticide	2013	279-9574
Deer-Ban (TR Labs)	coyote urine	repellent	2013	91132-1
Aqua-Tec (Silversan AG)	silver	algicide	2013	91025-1
Lambdastar Urban Cap (Farmhannong America)	lambda-cyhalothrin	insecticide	2014	71532-33
Force® CS Insecticide (Syngenta)	tefluthrin	insecticide	2014	100-1253
Trupick® 0.7 (Decco US Post-harvest)	1-methylcyclopropene	pesticide	2016	2792-79
Clomazone 360 CS (Sipcam Agro USA)	clomazone	herbicide	2016	60063-58
EH-1594 Herbicide (PBI/Gordon Corporation)	2,4-D, 2-ethylhexyl ester + dicamba + mecoprop-P+ sulfentrazone	herbicide	2017	2217-1018
AiM-A Abamectin™ (Smartvet USA)	abamectin	insecticide	2017	88050-3
Oxon Clomazone 360 CS (Oxon Italia)	clomazone	herbicide	2017	35915-25
Fendona CS II (BASF)	alpha-cypermethrin	insecticide	2018	7969-425
Fenvastar™ Ecocap™ (Farmhannong America)	esfenvalerate	insecticide	2018	71532-28-91026
RightLine Pyraprop Mec (Rightline)	pyraclostrobin	fungicide	2018	93051-2

1.5. Micellar nanocarriers.

Micelles are composed of amphiphilic surfactant molecules that spontaneously aggregate into spherical vesicles in an aqueous environment. This phenomenon is only possible if the quantity of the surfactant molecules is greater than the critical micelle concentration. The core of the micelle is hydrophobic and can sequester hydrophobic active ingredients. The size of the micelle and therefore the amount of active ingredient that can be loaded in its core is dependent on the molecular size, geometry, and polarity of the surfactant.⁴⁵ The small size of polymeric micelles (20–80 nm) reduces their recognition by scavenging phagocytic and inter-endothelial cells located in the liver and spleen, respectively, and therefore increases the bioavailability of the active ingredient.¹¹⁸ Most micelles are made of block co-polymers with alternating hydrophilic and hydrophobic segments, and the ratio of drug molecules to the block co-polymers determines their properties. Micelles are often composed of PEG, PLA, PCL, polypropylene oxide, poly-L-lysine, or combinations of the above. Estrasorb was approved by the FDA in 2003 as a topical lotion, and consists of micelles designed for the transdermal delivery of 17 β -estradiol to the blood for the treatment of menopausal-related vasomotor symptoms.¹¹⁹ This administration route evades first-pass metabolism, achieving stable levels of 17 β -estradiol in the serum for 14 days. Furthermore, paclitaxel and docetaxel are commercially available formulated as micellar nanocarriers, thus avoiding the use of Kolliphor EL as a solvent.^{120,121}

Various micellar nanocarriers are currently undergoing clinical trials (**Table 1.2**). For example, NK012 is a micellar polyglutamate-PEG formulation covalently bound to the antineoplastic topoisomerase inhibitor SN-38 via an ester bond. SN-38 is slowly released from NK012 by the hydrolysis of the ester bond under physiological conditions, which increases the SN-38 half-life to 210 h. NK012 is undergoing clinical trials for the treatment of solid tumors,

triple-negative breast cancer, colorectal cancer, and small-cell lung cancer.¹²² Similarly, the NK105 micelle is being investigated for the delivery of paclitaxel to breast cancer, gastric cancer, and non-small-cell lung cancer. NK105 polymers consist of PEG as the hydrophilic segment and modified polyaspartate as the hydrophobic segment.¹²³ NK105 demonstrated efficacy in patients with advanced gastric cancer that failed to respond to chemotherapy. Genexol-PM is a micellar nanocarrier consisting of mPEG-block-D,L-PLA for the delivery of paclitaxel for the treatment of non-small-cell lung cancer, hepatocellular carcinoma, urothelial cancer, ovarian cancer, and pancreatic cancer.¹²⁴ Genexol-PM was shown to behave similarly to the FDA/EMA-approved nanocarrier Abraxane and has been approved for the treatment of metastatic breast cancer and advanced non-small-cell lung cancer in South Korea. NC-6004 is being investigated for the delivery of cisplatin to head and neck cancer as well as non-small-cell lung cancer. NC-6004 demonstrated a significant reduction in cisplatin-induced neurotoxicity and nephrotoxicity (again, the nanocarrier enhances safety not efficacy). Micelles are also being investigated for the treatment of cystic fibrosis, metabolic syndrome, psoriasis, and rheumatoid arthritis.¹²⁵

In veterinary medicine, a randomized trial was initiated in 2013 to investigate the safety and efficacy of micellar paclitaxel (Paccal Vet-CA1) for the treatment of dogs with grade II or III mast cell tumors (**Table 1.4**).¹²⁶ The micelle consisted of a surfactant derivative of retinoic acid (XR-17). Dogs treated with micellar paclitaxel showed a three-fold higher treatment response compared to a control group receiving the standard-of-care drug lomustine. However, the FDA conditional approval of Paccal Vet-CA1 was withdrawn in 2017 by the manufacturer Oasmia Pharmaceutical AB to allow them time to study lower doses in order to reduce adverse effects such as neutropenia, hepatopathy, anorexia, and diarrhea. In a different application, a micellar vitamin E has been tested as an antioxidant in race horses undergoing prolonged aerobic exercise to prevent

exercise-induced oxidative lesions, and maintained the general oxidative status to a healthy level for horses undergoing intensive training.¹²⁷

Micelles have also been developed as promising nanocarriers for the encapsulation of pesticides, helping to prevent adsorption to soil particles. Examples include the micellar encapsulation of azadirachtin,¹²⁸ carbendazim,¹²⁹ carbofuran,¹³⁰ imidacloprid,^{131,132} rotenone,¹³³ thiamethoxam,¹³⁴ and thiram.¹³⁵ These formulations are still undergoing development and have been tested *in vitro* and in the field.

Table 1.4. Nanocarriers for veterinary applications.

approved veterinary nanocarriers					
drug name (company)	active ingredient (a.i)	nanoparticle	specific treatment	year of approval	
Inrestor™ (Elanco US Inc.)	PEGylated granulocyte colony stimulating factor (Pegbovigrastim)	30 kDa protein + PEG	inflammation in the breast tissue of cows	2016 [US]	
Paccal Vet-Cal® (Oasmia Pharmaceutical AB)	paclitaxel	retinoic acid (XR-17) micelle	canine mast cell tumors	2017	discontinued
veterinary nanocarriers under clinical trials					
active ingredient (a.i)	nanoparticle	specific treatment	opening year	animal health studies ID or ref. number	
amphotericin B	liposome	dogs ingected with blastomyces fungus	1996	ref. 114	
cisplatin	hyaluronate nanoparticles	canine brain tumors	2013	AAHSD000024	
			2017	AAHSD004339	
clodronate	liposome	canine histiocytosis	2010	ref. 113	
DNA	cationic liposome-DNA complexes + losartan	canine metastatic osteosarcoma	2016	AAHSD004241	
doxorubicin	liposome	canine spontaneous tumors	2006	ref. 111	
	liposome + radiotherapy	canine soft tissue sarcoma	2010	ref. 112	
interleukin-12	GEN-1	canine brain tumors	2016	AAHSD000445	
paclitaxel	CTI 52010	canine solid tumors	2010	AAHSD000021	
SOD1 gene silencing	adeno-associated virus	canine degenerative myelopathy	2016	AAHSD004063	
temozolomide	PLGA	canine brain tumors	2015	AAHSD000385	
vitamin E	micelle	equine oxidative stress during prolonged aerobic exercise	2013	ref. 74	

1.6. Inorganic nanocarriers.

Inorganic nanocarriers include natural and synthetic materials based on silica, clay, and metals such as silver, gold, titanium, iron, copper, and zinc. These nanocarriers are physiologically compatible, resistant to microbial degradation, and environmentally friendly, which makes them suitable for medical, veterinary, and agricultural applications. Even so, their use as nanocarriers has been somewhat overshadowed by their success in other medical applications. In particular, metallic nanoparticles have been developed as theranostic and photothermal reagents, and for the treatment of iron deficiency.^{22,136,137} The first formulation approved by the FDA in 1974 was iron dextran (INFeD) for the treatment of iron deficiency. Eight more formulations have since been approved by the FDA or EMA (**Supporting Table 1.5**). We do not consider these formulations as *nanocarriers* because the treatment modalities rely entirely on the nanoparticle itself without a cargo of active ingredients. However, metallic nanocarriers have recently been proposed in which the active ingredient is attached to the surface by physical absorption, electrostatic interactions, or conjugation.¹³⁸ In particular, gold nanoparticles allow the conjugation of many biological ligands, including DNA and siRNA.¹³⁹ Thus far, only one clinical trial has been carried out using metallic nanocarriers, namely spherical nucleic acid gold nanoparticles (NU-0129) for the delivery of siRNA to patients with glioblastoma or gliosarcoma (**Supporting Table 1.1**). More advanced metallic nanocarriers are under development, including particles that can respond to external triggers, such as light, magnetic fields, and hyperthermia to release their cargo in a controlled manner. For example, gold and silver nanoparticles have been conjugated to various cancer drugs.^{140–143}

Mesoporous silica nanocarriers (MSNs) have been investigated extensively because they are stable particles with a high payload capacity due their porous structure, they have a tunable

pore diameter (2–50 nm), and surface modifications can impart new functionalities such as targeted delivery.¹⁴⁴ MSNs have already been tested in the laboratory to deliver cancer drugs such as doxorubicin and camptothecin, antibiotics such as erythromycin and vancomycin, and anti-inflammatories such as ibuprofen and naproxen, with remarkably high loading rates of up to 600 milligrams of cargo per gram of silica.¹⁴⁴ This loading capacity of up to 60% far exceeds that of liposomal and polymeric nanocarriers. For example, the liposomal formulation Doxil and the polymeric formulation Eligard achieve loading capacities of 31% and 27%, respectively. However, some silica nanoparticle formulations have been shown to cause hemolysis due to strong interactions between silanol groups on the carrier and phospholipids in the erythrocyte plasma membrane.¹⁴⁵ Another concern is their persistence *in vivo* due to the absence of renal clearance. These issues could be addressed by modifying the surface chemistry or applying coatings.

In an agricultural context, silica is already highly abundant in soil and such particles could therefore be engineered for the controlled release of active ingredients without the carrier itself causing environmental harm. For example, MSNs have been used to deliver the insecticide chlorfenapyr over a period of 20 weeks, which doubled the insecticidal activity in field tests.¹⁴⁶ The fungicide metalaxyl was also loaded into MSNs, allowing its slow release in soil and water for a period of 30 days.¹⁴⁷ Similarly, nanocarriers based on naturally occurring aluminum silicates have been formed into phyllosilicate sheets for the intercalation of antibiotics and herbicides, allowing sustained delivery.^{148,149} Several metallic nanoparticles have demonstrated antimicrobial properties, and the EPA has already approved silver nanoparticles for use as an antimicrobial agent in clothing, but not yet for the delivery of active ingredients.¹³⁹ Finally, carbon nanotubes are also being investigated for medical and agricultural uses because their shape and surface chemistry

confer unique properties, although their toxicity remains a translational barrier. I recommend the following reviews for further information.^{150–152}

1.7. Proteinaceous nanocarriers.

Over the course of evolution, nature has yielded a variety of biomaterials with great structural complexity that remains difficult to emulate. The analysis of such complexity requires the appropriate molecular methods, and for this reason the development of proteinaceous nanocarriers has lagged behind that of the simpler liposomal, polymeric, and micellar structures.^{153,154} The production of proteinaceous nanocarriers has also required the development of tools for the expression of recombinant proteins and strategies for creation or diversity, such as directed evolution, genome editing and synthetic biology. These tools have allowed the production of hierarchically organized proteinaceous structures, including albumin nanoparticles, heat shock protein cages, vault proteins, and ferritins.¹⁵⁵ These comprise repeated protein subunits forming highly organized nanostructures that are identical in size and chemical composition. Although synthetic nanoparticles can also be assembled into complex structures, the sophistication and monodispersity that can be achieved with proteins has yet to be replicated. Proteinaceous nanoparticles have been used as biocatalysts for the synthesis of novel materials, but are also useful for the delivery of active ingredients in medicine and agriculture.¹⁵⁴

The first proteinaceous nanocarriers were developed to mimic the properties of plasma proteins, thus increasing circulation times and reducing systemic side effects. In 2005, the FDA approved the proteinaceous nanoshell Abraxane, consisting of albumin-bound paclitaxel for the treatment of breast cancer. The conjugation of paclitaxel to albumin stabilized the drug even in the absence of Kolliphor EL, and enhanced the uptake of the active ingredient compared to the

Kolliphor EL formulation.³² Given the safety and efficacy of drugs conjugated to albumin, two other albumin nanocarriers are undergoing clinical trials (**Table 1.2**). The first is an albumin conjugate of the protein kinase inhibitor rapamycin (ABI-009) indicated for colorectal cancer, bladder cancer, glioblastoma, sarcoma, and myeloma.¹⁵⁶ The second is an albumin conjugate of docetaxel (ABI-008) indicated for the treatment of prostate cancer. Albumin has a long circulation half-life due to its interaction with the recycling Fc receptor. It is beneficial for the delivery of small molecules that are unstable or have low solubility in blood, as well as proteins and peptides that are rapidly cleared from the circulation. Small molecules can be chemically fused to albumin and administered as conjugate, and strategies to target small-molecule drug cargoes to albumin *in vivo* have also been developed.¹⁵⁷

Heat shock protein cages, vault proteins, and ferritins have also been investigated for the delivery of active ingredients, although no clinical trials have been reported thus far. Heat shock proteins are chaperones that promote the folding of newly synthesized proteins and the refolding of denatured ones, which means they are naturally stable and possess channels and cavities for the sequestration of cargo.¹⁵⁵ There are five families of heat shock proteins: Hsp100, Hsp90, Hsp70, and Hsp60 (which are named for the molecular mass of the proteins in kDa), and the small heat shock protein (sHsp) family, ranging in size from 12 to 43 kDa. Heat shock proteins assemble into large complexes that vary in size and shape (including rings and spheres), and they can be engineered to carry and deliver active ingredients such as doxorubicin.^{158,159} Vault nanoparticles are barrel-like ribonucleoproteins found in many eukaryotes. They are 41 x 73 nm in size and resemble the vault of a gothic cathedral. Their precise biological function remains unknown, although they are thought to play a role in nuclear transport, immunity and defense against toxins.^{160,161} Several proteins have been encapsulated in vault nanocarriers, including the lymphoid

chemokines CCL19 and CCL21, the New York esophageal squamous cell carcinoma 1 (NY-ESO-1) antigen, the precursor of adenovirus protein VI (pVI), the major outer membrane protein of *Chlamydia trachomatis*, and the egg storage protein ovalbumin.¹⁶¹ Vault Pharma is one company specializing in the development of these structures. Finally, ferritin is an iron-storage protein with 24 subunits that self-assemble into a spherical cage structure 12 nm in diameter with a molecular mass of 450 kDa.¹⁶² Each ferritin complex can sequester up to 4500 Fe²⁺ ions and convert them to Fe³⁺ to prevent oxidative stress in the cytosol, nucleus, and mitochondria. Ferritin has been investigated as an imaging reagent and vaccine platform as well as a nanocarrier.¹⁶² It has already been used to deliver cisplatin,¹⁶³ doxorubicin,¹⁶⁴ and curcumin,¹⁶⁵ and the contrast agents gadolinium¹⁶⁶ and Mn(II)¹⁶⁷.

There are few examples of proteinaceous nanocarriers used in agriculture, but nanocarriers based on maize storage proteins (zeins) are being tested for the delivery of pesticides that protect soybean crops from defoliator parasites.¹⁶⁸

The number of proteinaceous nanocarriers reaching the market will continue to grow as we learn more from nature and expand our bioengineering tools and processing capabilities, including the use of genome editing and directed evolution.¹⁶⁹ Furthermore, rather than harnessing protein complexes from nature, advances in *de novo* protein design will allow us to select customized proteins with shapes that may be difficult to obtain via the directed evolution of natural proteins.¹⁷⁰ Modular building concepts have been established to achieve the defined folding and programmed assembly of proteins into complex architectures.^{171,172} Accordingly, some synthetically designed protein-based nanoparticles have entered translational development. For example, the start-up company Tychon Bioscience is developing prosthetic antigen receptors that modulate protein

dimerization to produce self-assembling nanoscale ring structures for applications in cancer immunotherapy.

1.8. Virus-based nanocarriers.

The entirety of my dissertation relied on the use of virus-based nanocarriers (specifically plant viral nanoparticles) and their application in medicine and agriculture; they present many advantages over the other nanocarrier platforms, as described below and in all chapters of my dissertation. Viruses have evolved to deliver their genetic payload to host cells and can therefore be regarded as nature's nanocarrier systems. The structure of a virus capsid is genetically programmed so replication yields millions of identical particles, a level of monodispersity that cannot yet be achieved with synthetic nanoparticles. Viruses are proteinaceous structures, and are therefore similar to the protein cages discussed above in terms of biocompatibility. The capsids are highly symmetrical structures that come in various shapes and sizes, and they are amenable to both chemical and genetic modification to impart new functionalities, including the encapsulation or conjugation of active ingredients¹⁷³

Given the natural function of viruses, it is unsurprising that one of the first applications of virus-based nanocarriers was the delivery of nucleic acids. Mammalian viruses such as Adeno-associated virus (AAV) are established as gene delivery vectors.¹⁷⁴ The first AAV-based gene therapy vector (Glybera) was approved by the EMA in 2012 for the treatment of lipoprotein lipase deficiency, but was not approved by the FDA, and UniQure subsequently announced its withdrawal from the European market in 2017 following the treatment of only 31 patients.¹⁷⁵ The FDA has since approved two AAV-based vectors, namely Luxturna in 2017 for the treatment of patients with RPE65 mutation-associated retinal dystrophy, and Zolgensma in 2019 for the

treatment of young infants with spinal muscular atrophy. One of the major drawbacks of AAV therapies is their high cost: Luxturna treatment is estimated to cost \$850,000, whereas Zolgensma was priced at \$2.125 million by Novartis as a one-time cure. In addition to AAV nanocarriers (ssDNA, 4-kb inserts), other mammalian viruses have been developed for gene delivery including adenoviruses (dsDNA, 7.5-kb inserts), herpesviruses (dsDNA, >30-kb inserts), and lentiviruses (ssRNA, 8-kb inserts) and are undergoing clinical trials (**Supporting Table 1.2**), whereas retroviruses (ssRNA, 8-kb inserts) and alphaviruses (ssRNA, 6–8-kb inserts) remain at the preclinical development stage.^{174,176,177}

As an alternative to mammalian viruses, several plant viruses and bacteriophages have also been repurposed as nanocarriers or vaccines because they are non-infectious to humans and can be manufactured on a large scale as viral nanoparticles (VNPs, which retain the virus genome) or virus-like particles (VLPs, which are empty shells devoid of nucleic acid). For example, based on the immunostimulatory nature of VNPs/VLPs, several have been developed as *in situ* cancer vaccines, including Cowpea mosaic virus (CPMV),^{178,179} bacteriophage M13,¹⁸⁰ Potato virus X (PVX),¹⁸¹ Tobacco mosaic virus (TMV),¹⁸² and Papaya mosaic virus.¹⁸³ The CPMV system has already demonstrated efficacy in canine trials.^{184–186} The development of plant viruses or bacteriophages as vaccine candidates for infectious diseases, autoimmune disorders and cancer has been extensively reviewed.^{187–189} One of the key applications of VNP/VLP vaccine candidates is the display of heterologous epitopes.^{190–192} This protects the epitope from degradation, ensures delivery to antigen-presenting cells, provides an inbuilt adjuvant, and also generates cross-stimulatory virus-based antigens to boost humoral and cellular immunity.¹⁵⁻¹⁷ Several VNPs/VLPs presenting heterologous epitopes have been tested in human clinical trials¹⁹³ and veterinary tests.¹⁹⁴

The use of VNPs and VLPs as nanocarriers for active ingredients can be achieved by passive infusion through pores in the capsid, encapsulation during assembly, as well as chemical conjugation and/or genetic fusion of active ingredients to the outer or inner surfaces. For example, doxorubicin has been conjugated to TMV,¹⁹⁵ infused into Cucumber mosaic virus (CMV)¹⁹⁶ and Red clover necrotic mosaic virus (RCNMV),¹⁹⁷ and passively complexed with PVX.¹⁹⁸ Virus-based nanocarriers have also been used to deliver bortezomib,¹⁹⁹ cisplatin,^{200,201} 5-fluorouracil,²⁰² hygromycin,²⁰³ mitoxantrone,^{204,205} phenanthriplatin,²⁰⁶ and paclitaxel.²⁰⁷ Examples of protein delivery include TRAIL,⁴⁰ TPA,²⁰⁸ and Herceptin^{209,210}. Filamentous phages have been developed to deliver antibiotics such as chloramphenicol and neomycin to prevent the growth of *Escherichia coli*, *Streptococcus pyogenes*, and *Staphylococcus aureus*.^{211,212} Finally, siRNA has been delivered using bacteriophage MS2²¹³ and Cowpea chlorotic mosaic virus (CCMV),²¹⁴ and mRNA for the *in situ* expression of green fluorescent protein (GFP) has been successfully encapsulated into CCMV and TMV, followed by the release of the mRNA cargo into the cytosol of mammalian cells and its subsequent translation.^{215,216}

Plant VNPs have also been proposed as pesticide carriers because they are already part of the natural soil ecosystem and are harmless to humans and domestic animals.^{217,218} Compared to synthetic nanocarriers, plant viruses are highly mobile in soil and can deliver pesticides to the roots, where many pests are concentrated. TMGMV was approved by the EPA in 2007 as a bioherbicide for the treatment of the invasive tropical soda apple weed in the state of Florida, thus paving the way for the development of nanocarriers based on plant viruses.²⁸ Since then, RCNMV has been proposed for the delivery of abamectin to crops.²¹⁷ The higher stability and superior soil mobility of abamectin encapsulated in RCNMV increased the efficacy of the nematicide in tomato seedlings infested with root knot nematodes (*Meloidogyne hapla*) compared to the free chemical.

Similarly, TMGMV loaded with the anthelmintic drug crystal violet was highly toxic towards the nematode *Caenorhabditis elegans in vitro*.²¹⁸ Rational design and size and shape engineering in plant virus-based carriers may enable multi-level targeting of different soil zones.²¹⁹

1.9. Conclusions.

Nanocarriers have revolutionized the medical, veterinary, and agricultural sectors through their ability to deliver active ingredients in a targeted and controlled manner to appropriate sites, such as cancer cells or plant roots, thereby maximizing efficacy while minimizing off-target effects. Based on the current landscape of research articles, patents, clinical trials, and approved nanocarriers, I have revealed a growth trend which predicts that more formulations will be commercially available over time, allowing the targeted delivery of small molecules, peptides and proteins, as well as nucleic acids to combat pests, pathogens and diseases in animals and plants. I observed a shift away from the development of nanocarriers for small-molecule reagents and toward the delivery of peptides, proteins and nucleic acids. Advances in bioengineering have also encouraged the development of bio-inspired nanocarriers that are friendly to the environment.

Several challenges must be addressed to streamline the translation of nanocarriers from the bench to the market. In medicine, nanocarriers could greatly benefit from the incorporation of targeting ligands, aptamers, antibodies, or antibody fragments to promote their binding to receptors overexpressed on target cells or in the surrounding extracellular matrix. Additional targeted nanocarriers must undergo clinical trials before we can conclude that active targeting achieves greater therapeutic efficacy. In parallel, the development of veterinary nanocarriers has intensified with the growing public interest in animal welfare and food safety and security. Companion animals with cancer have benefited the most from nanocarriers, whereas livestock require low-

cost and prolonged treatments, such as the delivery of antibiotics. The future of veterinary nanocarriers will depend on our ability to manufacture products at a relatively low cost. Finally, precision agriculture is required to meet the growing demand for food. Nanocarriers provide the opportunity to increase crop yields in an environmentally friendly manner by delivering fertilizers and pesticides directly to plants while minimizing leaching. However, the translation of nanocarriers for agricultural applications is restricted by the lack of well-structured regulations for commercial approval. More research is therefore required to determine the fate and toxicity of nanocarriers applied in the field.

Chapter I, in full, is a reprint of the material as it appears in ACS Nano, 2020. **Chariou, P. L**, Ortega-Rivera O.A, Steinmetz N.F. *Nanocarriers for the delivery of medical, veterinary, and agricultural active ingredients*. DOI: <https://doi.org/10.1021/acsnano.0c00173>. The dissertation author was the primary investigator and author of this paper.

Chapter II: Aims of the Dissertation Work

As detailed in Chapter I, nanocarriers are revolutionizing the fields of precision medicine and precision farming by delivering active ingredients in a targeted and controlled manner to appropriate sites, such as cancer cells or plant roots, thereby maximizing efficacy while minimizing off-target effects. While viral nanocarriers are on the rise for the delivery of small molecules, peptides and proteins, nucleic acids, imaging contrast agents, or even pesticides and fertilizers, a great deal of work remains to be done to fully grasp their potential and advantages over their synthetic counterparts. In my dissertation, I specifically investigated the use of plant viruses as nanotechnology platforms for pesticide delivery, drug delivery, and immunotherapy. The specific questions addressed in my studies were the following:

Pesticide delivery and precision farming:

- **Chapter III:** Can TMGMV be engineered as a nanocarrier for the delivery of pesticides targeting nematodes?
- **Chapter IV:** How does TMGMV soil mobility compare to other nanocarriers? Can TMGMV promote the accumulation of pesticide at the root level, where nematode reside? Can we predict the soil transport behavior of nanocarriers to streamline the development of novel carriers?
- **Chapter V:** Can TMGMV be inactivated using UV light and chemical treatments to render the plant virus non-infectious for safe agricultural applications?
- **Chapter VI:** Can hydrophobic pesticides be synthesized with functional groups to promote their bioconjugation to TMGMV?

Nanomedicine: drug delivery and immunotherapy

- **Chapter VII:** How does the aspect ratio of nanocarriers affect their distribution on the tumor environment?
- **Chapter VIII:** Can TMGMV be used as a nanocarrier for the delivery of photodynamic drugs for cancer therapy?
- **Chapter IX:** Does UV or chemical inactivation of CPMV impair its efficacy as an *in situ* cancer vaccine?

In brief, I evaluated the ability of TMGMV to be used as nanocarrier for the delivery of pesticides to the roots of plants, where nematode resides (**Chapter III and IV**). I developed non-infectious TMGMV nanocarrier formulations for translation into field applications (**Chapter V**), and I laid strong basis for the conjugation of pesticides onto TMGMV (**Chapter VI**). In addition to my agricultural work, I have explored the application of TMGMV and other plant viruses for the treatment of melanoma. Specifically, I studied the effect of viral carrier aspect ratio on its ability to distribute into a cancer spheroid, to provide insight into the intratumoral distribution and ability of the carrier to deliver therapeutic cargos throughout the tumor tissue – as a function of aspect ratio (**Chapter VII**). I evaluated the loading of photodynamic drugs onto TMV and TMGMV via non-covalent charge and hydrophobic interactions to treat melanoma and cervical cancer (**Chapter VII**). Finally, I studied various methods to inactivate CPMV to render the particles non-infectious toward plants, while maintaining a anti-tumor efficacy for translation of the platform and use as *in situ* cancer vaccine applications (**Chapter VIII**).

Chapter III: Delivery of Pesticides to Parasitic Nematodes using TMGMV

3.1 Introduction.

Plant parasites are a major burden to the global agricultural industry. Among them, the United States Department of Agriculture (USDA) has highlighted several species of insects and worms (*i.e.* moths, beetles, fruit flies, grasshoppers, ants, and nematodes) as the most common and devastating parasites; they either directly injure crops by feeding on them or indirectly cause injury through the transmission of bacteria, viruses, and fungi. Specifically, crops infested by parasitic worms, including across the United States, results in an estimated \$157 billion loss each year in crop production worldwide.²²⁰ In particular, endoparasitic plant nematodes feed on the crop roots, causing distinctive root swellings commonly referred to as galls. Gall formation impairs the root conduction of water and growth nutrients into the rest of the plant, resulting in lower crop yields. In addition, galls often promote crack damages in the roots and increase the plant vulnerability to secondary infections.²²¹ The root-knot *Meloidogyne spp*, the potato cyst *Globodera spp*, and the soybean cyst *Heterodera glycines* are the most damaging and widely spread plant parasitic nematodes. Combined they can infect more than 3000 plant species, including bananas, corn, cotton, potatoes, lettuce, and tomatoes.²²² While crop nematode infestation is relatively easy to diagnose (*e.g.* dig up a few plants and examine the roots for gall formation), treatment options are limited.

In most countries, crop rotation is frequently employed to selectively control plant parasitic nematode infestations.²²³ Nonetheless, the wide host-range of root-knot nematodes limits the choice of alternate crops to a few species yielding little to no revenue. Genetically modified crops resistant to nematodes are an economically and environmentally viable alternative.²²⁴ Unfortunately, genetic resistance to plant parasitic nematodes is selective to specific nematode

species, limited to a few crops, and takes years to engineer.²²⁵ While these aforementioned control strategies can reduce the burden of plant parasitic nematodes on most crops, their efficacy and economic benefits are no match to the use of nematicides.²²⁶ The first generation of nematicides rely on highly toxic and volatile fumigants, such as methyl bromide, but their use has declined due to environmental (*e.g.* thinning of the ozone layer and indiscriminating killing of animals such as bees) and health (*e.g.* reproductive sterility and cancer) concerns.^{17,227} Alternatively, non-fumigant nematicides, such as organophosphates, carbamates, and bio-nematicides, have been employed.²²⁷ Their efficacy, however, is limited by their ability to diffuse through soil, which is dependent on the amount of organic matter, moisture, and the soil structure (*e.g.* grain size and soil density). To be effective, non-fumigant nematicides must persist long enough and in concentrations equivalent to the nematode-lethal dose at the root level. Extended persistence in such doses increases the risk of chemical contamination of crops, soil, and groundwater. Therefore, there is a critical need to resolve soil mobility issues of nematicides to enhance their agrochemical efficacy, reduce their indiscriminate use, and ensure their safe application.

To attack the problem at its roots, nanotechnology has led to the development of smart delivery systems that can be tailored to deliver pesticides in a controlled and targeted manner,¹⁸ similar to nanomedicine in humans.⁵⁰ Nanomaterials used as carriers have advantages over commonly used pesticides, such as enhanced biodegradability, thermal stability, permeability, dispersibility, wettability, and stiffness.²²⁸ When pesticide-loaded nanoparticles are spread uniformly over the soil surface, their large surface areas increase their affinity to the target pest and reduce the dose of pesticide required to effectively eradicate the infestation.²²⁹ In addition, encapsulation of nematicides in nanoparticles protect the active compound from premature biodegradation and photolysis while isolating the toxic nature of the nematicide from the end-user.

Liposomal formulations, as well as synthetic and natural polymer-based nanoparticle formulations have been employed as pesticide-delivery systems (reviewed in ref.¹⁸) While synthetic nanomaterials overcome the various challenges associated with the use of nematicides, it still remains uncertain whether their high cost of manufacturing makes them economically viable.¹⁸

In this study, I turn toward using plant viral nanoparticles (VNPs) as an economically and environmentally viable alternative to synthetic nanoparticles. VNPs can be produced in large quantities in short time for a relatively low price.¹⁷³ In addition, VNPs are exceptionally robust to the harsh environment of crop fields, yet they are biodegradable. From a human health perspective, VNPs are biocompatible and non-infectious, making them safe to use on industrial crops. From an engineering perspective, VNPs are self-assembling systems that form highly symmetrical, monodisperse structures, amenable to both chemical and genetic modifications to impart new functionalities.¹⁷³ Since plant viruses have naturally evolved to protect and efficiently deliver their payload (*i.e.*, their genome), they can be regarded as naturally occurring nanocarriers. At first glance, applying VNPs onto crops might seem counterintuitive since their natural hosts for infections are plants. However, Cao *et al.* recently introduced the concept by utilizing the red clover necrotic mosaic virus (RCNMV) to manage plant parasitic nematode infestation.²¹⁷ They demonstrated that abamectin encapsulated in RCNMV had increased stability and superior mobility in soil compared to free abamectin, which resulted in enhanced bioavailability and treatment efficacy in tomato seedlings. As expected, no viral infection in the tomato seedlings was observed, as tomato is not a RCNMV host species.

In the present work, I propose the use of tobacco mild green mosaic virus (TMGMV), also known as the U2 strain of tobacco mosaic virus (TMV), as a carrier to deliver nematicides. TMGMV self-assembles into a 300 by 18 nm rod-shaped virus with a 4 nm wide hollow channel.

The high aspect ratio soft-matter nanotube may provide a promising alternative over the spherical platform technologies, *i.e.* most synthetic nanoparticles as well as RCNMV. The nanomedicine field has demonstrated that carrier shape impacts the *in vivo* fates with elongated materials conferring advantages with enhanced margination, diffusion, and penetration through tissue.¹⁷³ Whether high aspect ratio materials perform better in soil remains to be seen. Another advantage of the TMGMV platform is the high surface area ($3.6 \times 10^{-14} \text{ m}^2$ on the exterior and $7.6 \times 10^{-15} \text{ m}^2$ on the interior), 3.9 times larger than RCNMV ($9.2 \times 10^{-15} \text{ m}^2$), which may allow for higher payload delivery.

TMGMV is already EPA-approved: Solvinix, a formulation of TMGMV mass-produced by BioProdex, is commercially available as an herbicide in the state of Florida for the treatment of the invasive weed tropical soda apple.^{28,29,230} TMGMV is not transmitted by insects, pollen, or other vectors; it is not seed borne and cannot self-disseminate. While TMGMV is capable of infecting solanaceous plants (*e.g.* tomatoes, chili peppers, and eggplants), TMGMV is unable to penetrate and infect healthy plants in the absence of a lesion wound. Furthermore, Solvinix was tested on 435 plants representing 311 species, among which only 8% of plants were killed.²⁸ It is therefore safe to conclude that TMGMV can be applied in the field with little to no risk to the environment or the crop itself. Although there are a few species of plants to which TMGMV is lethal,²⁸ it is important to remember that the remaining 3000 species infected by parasitic nematodes are not susceptible to TMGMV.

While its structure is known to atomic resolution (PDB: 1VTM),²³¹ the chemistry of TMGMV has not yet been established. Making use of the structural information and the well-established chemistries for tobacco mosaic virus (TMV),^{206,232} I developed bioconjugation techniques and non-covalent drug loading strategies for TMGMV. As a proof of concept, I used

the anthelmintic drug Crystal Violet²³³ (CV) in our studies. This therapeutic compound is fluorescent and thus streamlines development and characterization. I report, 1) the formulation and characterization of TMGMV loaded with CV (cvTMGMV), 2) the bioavailability and treatment efficacy of cvTMGMV in nematodes in liquid culture compared to free CV, and 3) the soil mobility of cvTMGMV compared to free CV.

3.2. Experimental methods.

3.2.1. Crystal Violet (CV) loading into TMGMV. TMGMV was obtained from Bioprodex. Crystal Violet (CV, G2039, Sigma Aldrich) was loaded into the interior channel of TMGMV through electrostatic interactions between the positively charged drug and the negatively-charged GLU and ASP. TMGMV (1 mg.mL⁻¹ final concentration, in 10 mM potassium phosphate (KP) buffer, pH 7.8) was incubated with CV using a molar excess of 500:1, 1000:1, 2000:1, 3000:1, 4000:1, 6000:1, 10,000:1, or 20,000:1 CV:TMGMV overnight at room temperature with agitation. The reaction mix was purified over a 40% (w/v) sucrose cushion using an Optima MAX-TL ultracentrifuge (Beckman) and a TL-55 rotor at 50,000 rpm for 1 h to yield pure cvTMGMV. Particles were resuspended in 10 mM KP buffer (pH 7.8) overnight at 4°C, and the remaining particle aggregates were removed by centrifugation at 12,000 rpm for 10 min using a table top ultracentrifuge. cvTMGMV nanoparticles were analyzed using a combination of UV/visible spectroscopy, SDS-polyacrylamide gel electrophoresis (SDS-NuPAGE), transmission electron microscopy (TEM), and size exclusion chromatography (SEC); see below. To confirm that CV was indeed interacting with GLU and ASP, chemically modified TMGMV in which the interior GLU/ASP side chains were neutralized was utilized; see below.

3.2.2. Bioconjugation of TMGMV glutamic/aspartic acid residues. First, alkynes were

conjugated to the internal TMGMV carboxylate groups using 25 e.q. of propargylamine (P50900; Sigma Aldrich) per coat protein and 45 e.q. of EDC (with 22.5 e.q. added at $t = 0$ and $t = 12$ hrs) in 10 mM HEPES buffer (pH 7.4). The reaction was allowed to proceed for 24 h at room temperature. Second, an alkyne-azide click reaction was performed by adding 2 e.q. of Sulfo-Cyanine5-azide (B3330; Lumiprobe) or 5 e.q. of biotin-azide (875770, Sigma Aldrich) per coat protein. Click reactions were conducted on ice for 30 min using $2 \text{ mg}\cdot\text{mL}^{-1}$ TMGMV in 10 mM KP buffer (pH 7.4) in the presence of 1 mM CuSO_4 (AC423615000, Fisher), 2 mM AMG (AC36891025, Fisher), and 2 mM Asc (AC352681000, Fisher). GLU/ASP-Cy5 TMGMV and GLU/ASP-Biotin TMGMV were purified using by ultracentrifugation at 50,000 rpm for 1 h on a 40% (w/v) sucrose cushion. Particles were resuspended in 10 mM KP buffer (pH 7.4) overnight at 4°C , and the remaining particle aggregates were removed by centrifugation at 12,000 rpm for 10 min using a table top ultracentrifuge. GLU/ASP-Cy5 TMGMV and GLU/ASP-Biotin TMGMV nanoparticles were analyzed using a combination of UV/visible spectroscopy, gel electrophoresis, and western blotting; see below.

3.2.3. Bioconjugation of TMGMV tyrosine residues. First, a diazonium salt was formed by reacting 75 μL of 3 M sodium nitrite (237213, Sigma Aldrich) with 25 μL of 0.68 M 3-ethylaniline (498289, Sigma Aldrich) in a final volume of 400 μL of 0.3 M P-toluenesulfonic acid monohydrate (AC139025000, Fisher) for 1 h on ice. 15 e.q. of the *in situ* formed diazonium salt as added to a $2 \text{ mg}\cdot\text{mL}^{-1}$ final concentration of TMGMV in 10 mM borate buffer (pH 8.8) for 30 min on ice. Particles were purified using by ultracentrifugation at 50,000 rpm for 1 h on a 40% (w/v) sucrose cushion. Particles were resuspended in 10 mM KP buffer (pH 7.4) overnight at 4°C , and the remaining particle aggregates were removed by centrifugation at 12,000 rpm for 10 min using a table top ultracentrifuge. Second, an alkyne-azide click reaction was performed by adding

2 e.q. of Sulfo-Cyanine5-azide (B3330; Lumiprobe) per coat protein. Particles were purified using the previously described method. TYR-Cy5TMGMV nanoparticles were analyzed using a combination of UV/visible spectroscopy and gel electrophoresis; see below.

3.2.4. UV/Visible spectroscopy. A NanoDrop Spectrophotometer (Thermo Scientific) was used to measure the UV/visible spectra of native and modified TMGMV nanoparticles. The amount of CV or Cy5 fluorophore per TMGMV coat protein was determined based on the ratio of molecule:TMGMV coat protein concentration and the use of the Beer–Lambert law. CV-, Cy5-, and TMGMV-specific extinction coefficients are as follows: TMGMV: $\epsilon(260 \text{ nm}) = 3 \text{ mL.mg}^{-1} \text{ cm}^{-1}$, molecular weight of TMGMV = $39.4 \times 10^6 \text{ g.mol}^{-1}$; Cy5: $\epsilon(651 \text{ nm}) = 270\,000 \text{ M}^{-1}.\text{cm}^{-1}$, molecular weight of Cy5 = 747 g.mol^{-1} ; CV: $\epsilon(590 \text{ nm}) = 87000 \text{ M}^{-1}.\text{cm}^{-1}$, molecular weight of CV = $407.98 \text{ g.mol}^{-1}$

3.2.5. Denaturing gel electrophoresis (SDS-NuPAGE). 20 μg of TMGMV control, CVTMGMV , $\text{GLU/ASP-BiotinTMGMV} + \text{CV}$, GLU/ASP-Cy5TMGMV , and TYR-Cy5TMGMV were denatured at 100°C for 5 min in 4 \times LDS loading dye (NP0008, Life Technologies) to obtain a final volume of 12 μL . TMGMV proteins, as well as SeeBlue Plus2 ladder (LC5925, Life Technologies), were separated for 40 min at 200 V and 120 mA using a 4–12% NuPAGE precast gel in 1 \times MOPS buffer (NP0001-02, Life Technologies). Gels were photographed before and after staining with Coomassie Blue (0.25% w/v) using the AlphaImager (Biosciences) imaging system under white light.

3.2.6. Western blotting. TMGMV and $\text{GLU/ASP-BiotinTMGMV}$ samples separated by denaturing gel electrophoresis (see above) were transferred from the gel onto a nitro-cellulose membrane under a constant voltage of 30 V for 1 h. The membrane was then incubated in blocking buffer made of 5% (w/v) milk in TBST (150 mM NaCl, 50 mM Tris HCl, 0.2% (v/v) Tween-20,

pH 7.5) overnight at 4°C. Then, the membrane was incubated with 1:2000 streptavidin-alkaline phosphatase (S2890, Sigma Aldrich) in blocking solution for 1 h at room temperature and subsequently washed 3 times in TBST. Antibody binding was visualized using Novex AP Chromogenic Substrate (BCIP/NBT) (WP20001, Invitrogen).

3.2.7. Size exclusion chromatography (SEC). Samples (200 μL of 1 $\text{mg}\cdot\text{mL}^{-1}$) were analyzed through a Superose6 column on the AKTA Explorer chromatography system (GE Healthcare) using a flow rate 0.5 $\text{mL}\cdot\text{min}^{-1}$ in 10 mM KP (pH 7.4). The absorbance at 260 nm and 280 nm was recorded.

3.2.8. Transmission electron microscopy (TEM). Drops of TMGMV particles (20 μL , 1 $\text{mg}\cdot\text{mL}^{-1}$) were added to Formvar carbon film coated copper TEM grids (FCF400-CU, Electron Microscopy Sciences) for 2 min at room temperature. The grids were washed twice with deionized water for 30 sec and subsequently stained twice with 2% (w/v) uranyl acetate in deionized water for another 45 sec. A Tecnai F30 transmission electron microscope was used to inspect samples at 300 kV.

3.2.9. CV release profile from *cv*TMGMV. The release of CV from TMGMV was evaluated using a dialysis-based assay. 1 mg of *cv*TMGMV in 10 mM KP (pH 7.8) was loaded in triplicates in Slide-A-Lyzer MINI dialysis units (69570, Fisher) with a 10,000 MW cut-off membrane. *cv*TMGMV was dialyzed against various buffer at room temperature and at 4°C for 72 hrs. At specific time points ($t = 0, 1, 3, 6, 18, 24, 48$ and 72 hrs), 10 μL was extracted from each dialysis units and analyzed using UV/Visible spectroscopy to quantify the release of CV from *cv*TMGMV.

3.2.10. *Caenorhabditis elegans* nematode culture. OP50-1 *E. coli* and *Caenorhabditis*

elegans (*C. elegans*) strain N2 were provided by the *Caenorhabditis* Genetics Center (CGC) from the University of Minnesota, which is funded by NIH office of Research Infrastructure Programs P40 OD010440. Nematodes were cultured using 100 mm x 15 mm sterile polystyrene petri dishes (FB0875712, Fisher). Plates were seeded with agar (3 g NaCl, 17 g agar (BP1425, Fisher), 2.5 g peptone (BP1420-2, Fischer) in 1 L H₂O) supplemented with 1 mL of 1M MgSO₄ (M65-500, Fisher), 1 mL of 1M CaCl₂ (BP510, Fisher), 1 mL of 5 mg.mL⁻¹ cholesterol (C3045, Sigma Aldrich), 25 mL of 1 M KPO₄, 50 mg.mL⁻¹ streptomycin (11860-038, Fisher) and subsequently cultured with OP50-1 *E. coli* at 37°C for 8 hrs. Nematodes were then cultured on the OP50-1 *E. coli* plates at 22°C.

Alternatively, nematodes were maintained in a liquid culture of S Basal (5.85 g NaCl, 1 g K₂HPO₄, 6 g KH₂PO₄, and 1 mL of 5 mg.mL⁻¹ cholesterol in 1L H₂O) supplemented with 10 mL of 1 M potassium citrate (7788-99-0, Fisher) pH 6, 10 mL of trace metals solution (N1010, US Biological), 3 mL of 1 M MgSO₄, 3 mL of 1M CaCl₂, and 50 mg.mL⁻¹ streptomycin. OP50-1 *E. coli* pellet stocks were resuspended in S basal and added to the liquid culture to provide a food source to the nematodes.

3.2.11. Bioavailability of cvTMGMV and free CV to *C. elegans*. Bioavailability of cvTMGMV and free CV to *C. elegans* was investigated in liquid culture (see above). 50 Nematodes were added to each well of a 24-well culture plate to a final volume of 1 mL. Nematodes were treated in triplicates with 0, 0.01, 0.1, 1, 10, and 100 µM of CV for a period of 24 h at 22°C. At specific time points (t = 0, 1, 3, 6, 18, and 24 hrs), nematodes were observed under a white light microscope (magnification = 5x) and their motility was classified between (1) totally immobilized nematodes, (2) nematodes with impaired mobility, and (3) completely mobilized nematodes. The percent of affected nematodes (sum of the nematodes on scale (2) and

(3)) as a function of time, and the effective concentration (EC_{50}) was determined comparing free CV, TMGMV, and cv TMGMV.

3.2.12. Soil mobility of cv TMGMV and free CV. The following soil mobility test was designed to establish the leaching of cv TMGMV and free CV in a soil column. Top Soil (5540, Garden Magic) was packed in a plastic column up to a height of 4 cm and saturated with deionized (DI) water. 1 mL aliquots of cv TMGMV or free CV (the concentration was 100 mM normalized to the drug concentration) were applied atop of the soil columns, followed by 50 elution fractions of 300 μ L DI water. Each collected elution fraction was centrifuged for 10 min at 12,000 rpm to precipitate remaining soil particles. The supernatant was subsequently analyzed by UV/visible spectroscopy (see above).

3.3. Results and discussion

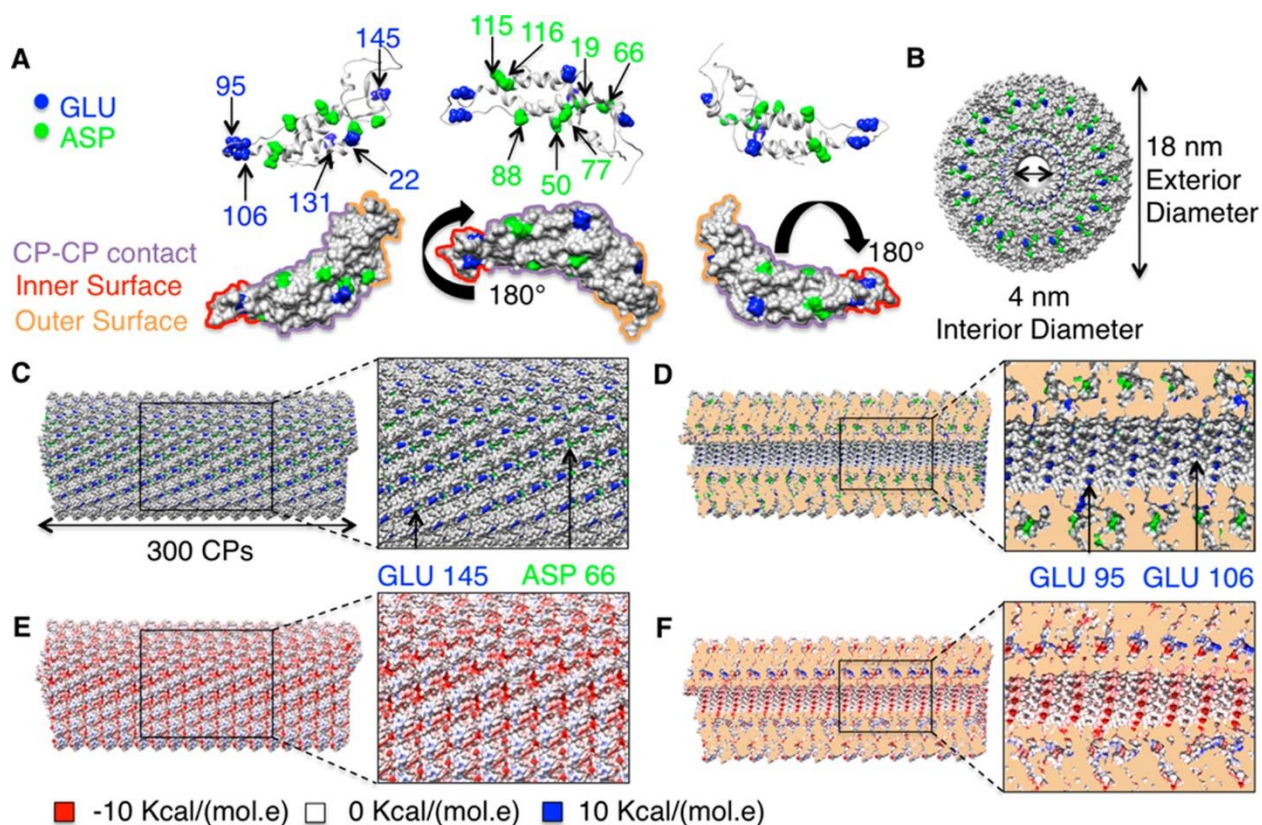


Figure 3.1. Structure of TMGMV. (A) Depiction of a single coat protein (CP) of TMGMV in various orientations highlighting surface-exposed glutamic acid (GLU, blue) and aspartic acid (ASP, green). Full-length TMGMV is formed by 2130 identical CP copies. (B) The cross-sectional orientation of the fully assembled TMGMV reveals the 4 nm-wide hollow channel of the 18 nm-wide cylindrical TMGMV. (C) Representation of a portion (300 CPs are depicted) of TMGMV in its longitudinal orientation; structural data indicate that GLU145 and ASP66 are solvent-exposed on the exterior TMGMV surface. (D) GLU95 and GLU106 appear solvent-exposed on the interior channel surface with GLU95 being more exposed than GLU106. (E+F) Coulombic surface coloring of the exterior and interior TMGMV surfaces.

3.3.1. Synthesis and characterization of TMGMV-encapsulated crystal violet (CV).

TMGMV is the U2 strain of tobacco mosaic virus (TMV); the latter has been extensively studied in plant pathology and structural biology since the 1900s and more recently in nanomedicine, biotechnology and energy research.¹⁷³ Therefore, the surface chemistry of TMV is well understood. Here I set out to establish the chemistry of TMGMV. The amino acid sequences of

the coat proteins (CPs) of TMV and TMGMV present 72% homology; also the structural overlay of a single CP of TMV and TMGMV reveals a high degree of structural similarity, only 14% of the amino acids do not overlap in the crystal structures (PDB: 2TMV for TMV; 1VTM for TMGMV; **Supporting Figure 3.1**). This is also reflected when comparing the assembled nucleoprotein complexes of TMV and TMGMV (**Figure 3.1, Supporting Figures 3.1-3.4**). Just like TMV, TMGMV forms a cylindrical structure measuring 300 by 18 nm with a 4 nm-wide hollow interior channel. The TMGMV particles consist of 2130 identical copies of CP units arranged helically around a single-stranded RNA genome (**Figure 3.1 A+B**). Analysis of the structure reveals the amino acid profile on the exterior and interior surface: because LYS, CYS, TYR, ASP, and GLU are often targeted for bioconjugation or electrostatic drug loading, I analyzed the TMGMV structure for presence of these residues. While solvent-exposed LYS and CYS side chains were not identified in TMGMV (**Supporting Figures 3.2**), several TYR, ASP and GLU residues were found to be solvent-exposed on the exterior/interior TMGMV surfaces. Structural data indicate TYR2 to be exposed on the exterior surface (**Supporting Figures 3.2**) – this is different from the structure of TMV, for which both TYR2 and to a greater extent TYR139 are solvent-exposed on the exterior surface (**Supporting Figures 3.3**). The TYR2 side chain of TMGMV could provide a potential target for bioconjugation, *e.g.* the introduction of a fluorescent label for imaging and tracking studies as described below. Further, I identified ASP66 and GLU95, 106, and 145 to be solvent exposed, with GLU145 and ASP66 located on the exterior surface and GLU95 and GLU106 on the interior surface (**Figure 3.1 C+D**). This is similar to the structure of TMV, for which GLU145, ASP64 and ASP66 are solvent-exposed on the exterior surface while GLU97 and GLU106 are solvent-exposed on the interior surface (**Supporting Figures 3.4**). However, it should be noted that previous research identified GLU97 and GLU106 to be the only

carboxylates in TMV that are reactive toward carboxylate-specific chemistries; GLU145 and ASP64 and 66 were not found to be reactive.²³⁴ The presence of GLU/ASP residues in TMGMV would allow for functionalization through bioconjugate chemistry or electrostatic loading of positively charged guest molecules, as we previously described in the case of TMV.^{206,232,235} Lastly, I analyzed the surface charge of TMGMV and determined that the inner and outer surfaces carry a net negative coulombic charge with the interior being more electronegative than the exterior (**Figure 3.1 E+F**). Together these data indicate solvent-exposed TYR side chains on the exterior surface of TMGMV and addressable carboxylates – possibly on the exterior and interior surfaces.

With the structural information in hand, I set out to develop TMGMV as a carrier for nematicide delivery. Specifically, I chose to work with crystal violet (CV) as a proof-of-concept, because this therapeutic compound is fluorescent and thus streamlines the analysis. The positively charged CV was loaded into TMGMV making use of electrostatic interactions and concepts that were previously developed to load positively charged platinum drug candidates and porphyrin derivatives into TMV.^{206,235}

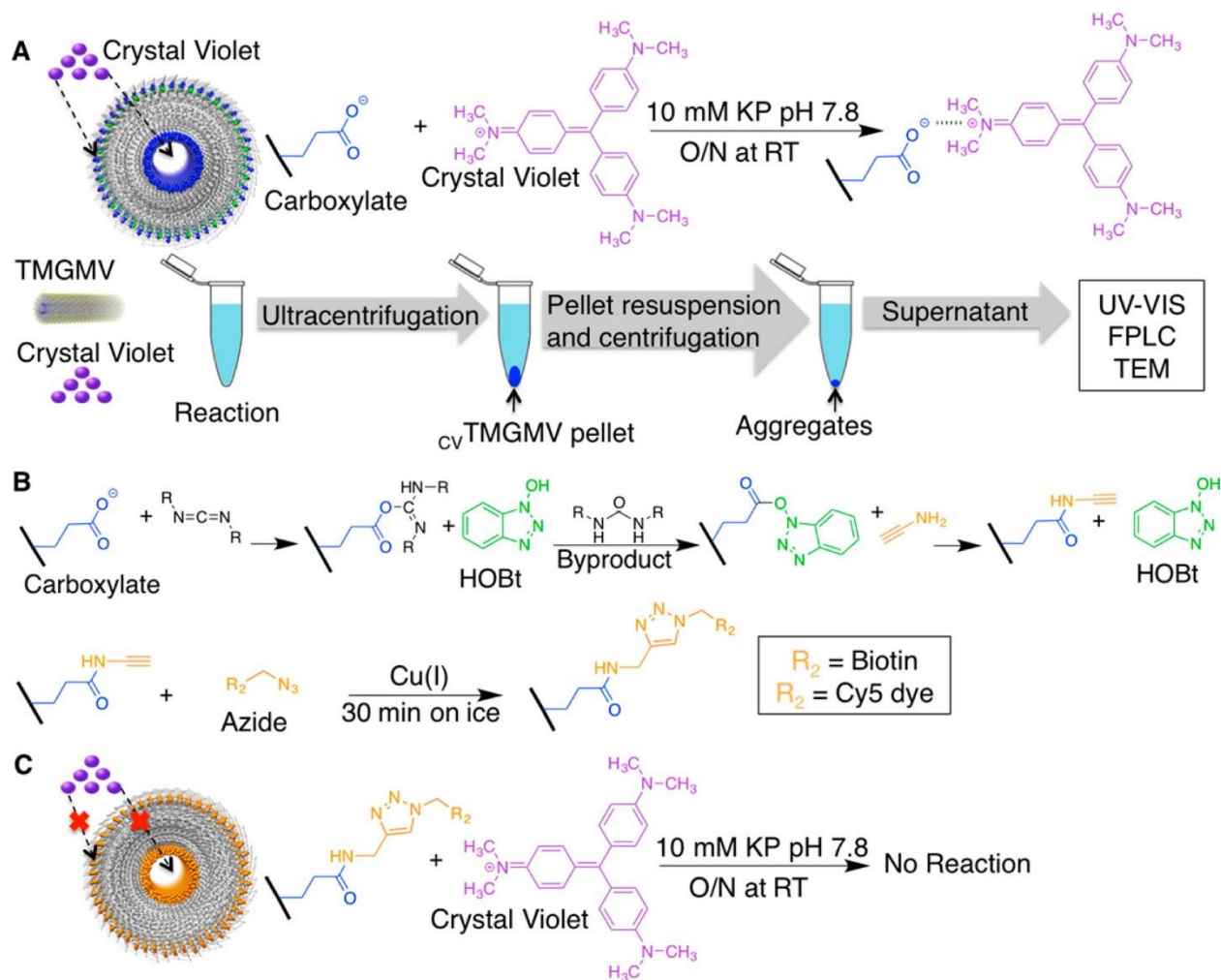


Figure 3.2. cvTMGMV conjugation and characterization. (A) Schematic of CV loading into TMGMV (shown in cross sectional orientation) and purification of cvTMGMV samples prior to analysis. (B) Chemical modification of the carboxylate groups *via* EDC and click chemistry to prevent CV loading. (C) Schematic of unsuccessful CV loading into modified GLU/ASP-Biotin TMGMV or GLU/ASP-Alkyne TMGMV.

To load CV into TMGMV, the following protocol was established: TMGMV was incubated with CV using a molar excess of 500:1, 1000:1, 2000:1, 3000:1, 4000:1, 6000:1, 10,000:1, 20,000:1 CV:TMGMV in 10 mM KP buffer (pH 7.8) overnight at room temperature with agitation (at pH 7.8 the majority of the carboxylate groups is deprotonated and thus carries a net negative charge allowing interaction with the positively charged CV guest molecule). The

reaction mix was purified by ultracentrifugation over a sucrose cushion to yield pure cv TMGMV and the degree of labeling with CV was subsequently quantified by UV/visible spectroscopy based on the Beer-Lambert law and CV-, TMGMV-specific extinction coefficients (**Figure 3.3 A+B**). CV loading efficiency in TMGMV increased with the excess of CV to TMGMV used; a plateau was not reached. Nonetheless, I observed substantial aggregate formation of free CV/ cv TMGMV when an excess of 10,000:1 or 20,000:1 CV:TMGMV mixtures were purified, therefore these samples were not considered for further evaluation. The reaction mix of 6000:1 CV:TMGMV resulted in the highest loading efficiency while still yielding dispersed TMGMV particles: 68% of the CPs were modified with a CV molecule. Assuming a full length TMGMV particle (300 by 18 nm), each TMGMV would carry ~ 1500 drug molecules. This formulation was subsequently used for all following studies.

When compared with TMV-drug formulations, the TMGMV formulation yielded comparable results: I previously reported the loading of 2,000 phenanthriplatin per TMV²⁰⁶ and 900 copies of a porphyrin derivative ZnPr per TMV.²³⁵ In those cases, the loading procedure was similar, in which a positively-charged guest molecule was loaded *via* electrostatic interaction with TMV's interior carboxylates. As in the case of TMV, the interior channel of TMGMV is lined with a dense layer of carboxylates – this, in combination with the more electronegative interior surface, may suggest that drug loading occurs on the inside channel. However further studies would be needed to rule out drug association with the exterior surface in both the cases of TMV and TMGMV. To compare the drug loading efficiency of the rod-shaped TMGMV system to the icosahedral (sphere-like) RCNMV-based nematicide carrier, the number of drug molecules was normalized to the molecular weight of the nanocarrier yielding $\sim 3.6 \times 10^{-5}$ CV per dalton of TMGMV protein, while only $\sim 1.8 \times 10^{-5}$ abamectin molecules were loaded per dalton of RCNMV

protein. In other words, when normalized per molecular weight, twice as much drug molecule can be loaded per TMGMV than compared to RCNMV.

The structural integrity of non-modified TMGMV and c_v TMGMV were assessed by size exclusion chromatography (SEC) and transmission electron microscopy (TEM). SEC measurements revealed no significant difference comparing native TMGMV and c_v TMGMV; both particles showed the same elution profile (elution at 8 mL volume) (**Figure 3.3 E+F**). Further, TEM imaging of TMGMV and c_v TMGMV revealed rod-shaped samples with no apparent differences when comparing TMGMV and c_v TMGMV (**Figure 3.3 G+H, Supporting Figure 3.5**); TEM imaging indicates that the average length of TMGMV and c_v TMGMV is comparable measuring 146 ± 97 nm and 136 ± 76 nm, respectively (**Supporting Figure 3.5**). It should be noted that short, broken particles were observed both pre- and post-drug loading. It is possible that this is an artifact from the TEM grid preparation, *i.e.* the particles may break during the drying process. However, it is important to note that there are no apparent differences comparing the TMGMV and c_v TMGMV, indicating that the nucleoprotein complex withstands the loading and purification process.

To gain insights into whether CV- loading into TMGMV is indeed *via* electrostatic interactions with GLU and/or ASP residues, chemically modified TMGMV in which the carboxylates were neutralized was prepared. To do so, EDC coupling was used to introduce alkyne ligands at the carboxylates, for subsequent addition of biotin labels using Cu(I)-catalyzed alkyne-azide cycloaddition (click chemistry) (**Figure 3.2 C+D**). The protocols are detailed in the methods and were adapted from previous methods established for bioconjugation to TMV.^{173,232} Biotinylation was confirmed by western blot (**Figures 3.3 D, Supporting Figure 3.6**), yet quantitative data could not be obtained. To quantify the degree of labeling, the fluorescent Cy5

dye was conjugated to $_{\text{GLU/ASP}}\text{TMGMV}$, yielding ~ 275 dyes per full length TMGMV, or about 13% of CPs were modified with Cy5 (**Supporting Figure 3.7**). Biotinylated and alkyne-labeled TMGMV were then used in CV-loading experiments, and I observed a 40% decrease in CV loading when using alkyne-labeled TMGMV compared to unmodified $_{\text{GLU/ASP}}\text{TMGMV}$ (**Figure 3.3 C**). Severe aggregation was observed when biotinylated TMGMV was used in CV loading experiments (**Figure 3.3 D**). This phenomenon may be explained as follows: if the chemistry of TMGMV and TMV is matched, then biotins will be displayed along the interior channel, preventing the positively charged guest molecules to be loaded and protected inside the TMGMV channel – instead CV may crosslink the particles through interactions with the while less negative, also negatively-charged exterior surface. Because the data indicate that CV-loading is mediated through the solvent-exposed GLU/ASP acids, and in light of the TMGMV structure (**Figure 3.1**) and its similarities to the known biochemistry to TMV,²³⁴ I therefore expect that interior loading of CV is achieved by this method.

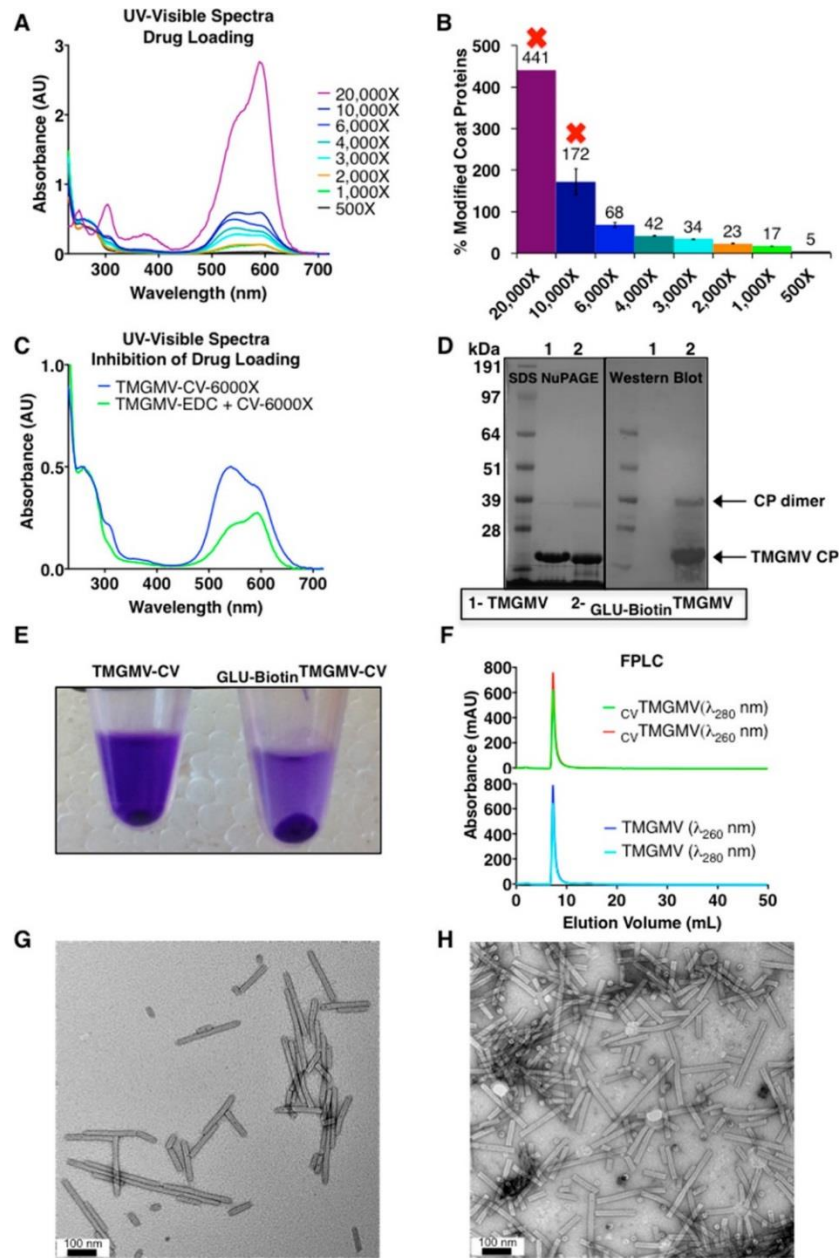


Figure 3.3. Characterization of *cv*TMGMV particles. (A) UV/visible spectra of *cv*TMGMV. Each spectrum results from a different molar excess of CV:TMGMV. Spectra were normalized to the 260 nm wavelength peak. (B) Corresponding average number of CV molecules per TMGMV. Red mark indicates reactions in which aggregation of CV and/or *cv*TMGMV post-centrifugation was high; these samples were not further considered. (C) UV/visible spectra of *cv*TMGMV (blue) and *GLU/ASP-EDC*TMGMV + CV (green). (D) SDS-NuPAGE and western blot of TMGMV and *GLU/ASP-Biotin*TMGMV, confirming covalent binding of biotin to TMGMV proteins. (E) CV loading in *GLU/ASP-Biotin*TMGMV resulted in severe aggregation compared to unmodified TMGMV (F) Size exclusion chromatography shows matched elution profiles of TMGMV and *cv*TMGMV. Both samples have an elution volume of 8 mL. RNA absorbs at 260 nm and protein at 280 nm. (G) TEM images of negatively stained (UAc) unmodified TMGMV and (H) *cv*TMGMV.

Next, I evaluated the release profile of CV from the TMGMV nanocarrier. The release rate of CV from c_v TMGMV is expected to be proportional to the pH of the bathing conditions as well as temperature. Based on thermodynamics, the rate of diffusion should increase with temperature. Furthermore, as pH decreases, a larger number of carboxylate groups become protonated and carry a net neutral charge that can no longer interact with the positively charge CV and consequently, free CV should diffuse away from TMGMV. Therefore the release rate of CV should be higher at lower pH and higher temperatures. To test this experimentally, 1 mg of a $1 \text{ mg}\cdot\text{mL}^{-1}$ solution of c_v TMGMV was prepared as described above and dialyzed against various buffers for 72 h (**Figure 3.4 A**). I tested the release profile at room temperature and 4°C to evaluate two extreme upper soil thermal conditions.²³⁶ Sodium acetate (pH 5.2) and PBS (pH 7.4) buffer solutions were chosen to mimic the acidic and neutral soil environments respectively. Diffusion of CV from c_v TMGMV was also evaluated in KP (pH 7.8) buffer, which was used during loading and storing conditions of the sample. Free CV, in a concentration matched to the concentration and number loaded into TMGMV, was also dialyzed in KP buffer (pH 7.8) at 4°C as a positive control.

As expected, increased release rates of CV from c_v TMGMV were observed at low pH and high temperature (**Figure 3.4**). Approximately half of the free CV (brown) was dialyzed within 1.6 h and complete release was observed in less than 18 hrs, while delayed release profiles were observed for the c_v TMGMV nanoparticle formulations. For c_v TMGMV, 50% of CV was released only after 5 h in acidic conditions (10 mM acetate buffer, pH 5.2) at room temperature (black), with complete release achieved after about 24 hrs. These conditions most realistically mimic the soil environment. In stark contrast, release in storing conditions (10 mM KP, pH 7.8, 4°C) was significantly slower, with 50% of CV released within 13 hrs, and complete release was not observed within 72 h. This is promising for application of these nanoparticles, however it would

be advised to prepare fresh formulations before application in the field.

We have previously reported similar results with the release of the cancer drug phenanthriplatin from TMV;²⁰⁶ half of the encapsulated chemotherapeutic was released after 1 h at pH 5 and 24 h at pH 7.4. On the other hand, encapsulated porphyrin derivatives loaded in TMV were found to be stably encapsulated for at least one month when stored at 4°C and pH 7.²³⁵ I hypothesize that the increase in stability of the porphyrin drug was due to its higher electropositivity: the compound used carries 3 positive charges. In contrast, phenanthriplatin and CV carry 2 and 1 positive charges, respectively. Compared to the previously reported RCNMV carrier, the release rate of CV from TMGMV is slightly faster than that of abamectin from RCNMV in acidic soil conditions. 50% of abamectin was released within 8 and 7 h at pH 5.2 and 7.4 respectively (vs. 50% of CV released after 5 and 7 h under the same conditions).²¹⁷

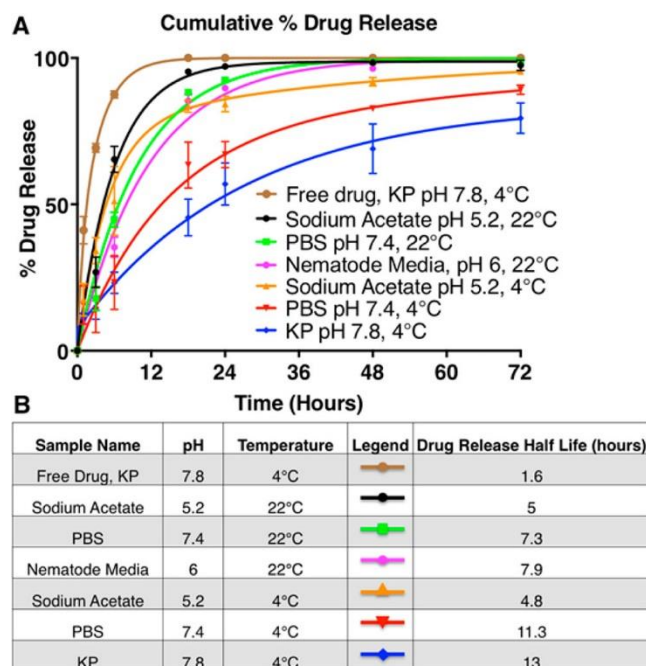


Figure 3.4. Evaluation of CV drug release from TMGMV. (A) Cumulative percent release of free CV from c_v TMGMV in various buffer conditions over 72 h. Samples conditions were as follows: CV free drug diffusion in the absence of TMGMV in KP buffer (10 mM, pH 7.8, 4°C) (brown), CV release from c_v TMGMV in sodium acetate buffer (10 mM, pH 5.2, 22°C) (black) and 4°C (orange)), CV release from c_v TMGMV in PBS (10 mM, pH 7.4, 22°C) (green) and 4°C (red), CV release from c_v TMGMV KP buffer (10 mM, pH 7.8, 4°C) (blue), and CV release from c_v TMGMV in nematode media, pH 6, 22°C (pink). (B) CV drug release half-life in the corresponding buffer conditions.

3.3.2 c_v TMGMV toxicity and interactions with *C. elegans* nematodes.

Bioavailability of c_v TMGMV and free CV in *C. elegans* was investigated in liquid culture. *C. elegans* nematode motility was classified as either (1) totally immobilized, (2) impaired motility, or (3) completely mobilized nematodes. To illustrate the data that was collected, a series of snap shots of *C. elegans* incubated with no treatment, 10 μ M CV, and 10 μ M c_v TMGMV was taken every second for 60 seconds. The corresponding videos can be found in the supporting information. **Figure 3.5 A-C** illustrates the nematodes observed after 3 h of incubation. Five nematodes were selected in each treatment regime and pseudo-colored to illustrate their motility.

Untreated *C. elegans* showed no impaired motility (**Figure 3.5 A**). For example, the nematode colored in pink moves across the frame within the 40 sec interval, while other nematodes disappear from (dark blue) or appear (light blue) in the frame during that time interval. Although the motility of these nematodes is evident, most nematodes do not travel far but rather move within a restricted area, such as the nematode colored in yellow. *C. elegans* treated with 10 μ M of CV or 10 μ M of cvTMGMV behaved differently and showed severe motility impairment (**Figure 3.5 B+C**). All pseudo-colored nematodes in **Figure 3.5 B+C** were paralyzed or dead and did not move. However, this is not true for all nematodes, as a population of nematodes showed little to no motility impairment when treated with CV or cvTMGMV. From the imaging data there were no apparent differences between the two treatment groups, free drug vs. cvTMGMV (**Figure 3.5 B+C**).

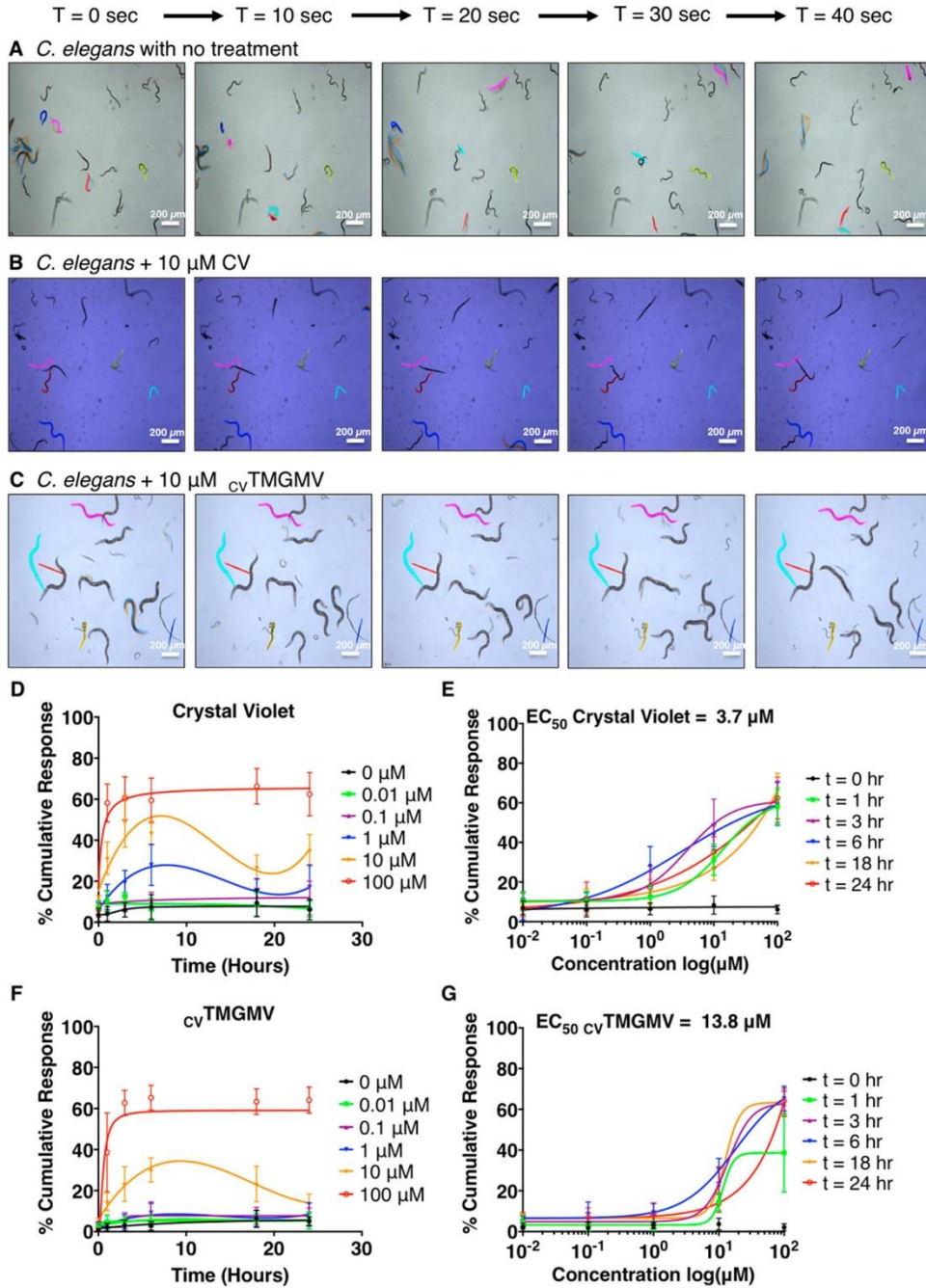


Figure 3.5. *C. elegans* motility assay. (A) Time lapse imaging of *C. elegans* in the absence of CV treatment. Images shown were taken at 10 seconds intervals. Five nematodes were pseudo-colored (dark blue, sky blue, red, pink, and yellow) to demonstrate their movement over time. (B) The 5 pseudo-colored nematodes in the presence of 10 μM of free CV and (C) 10 μM of CV loaded in $_{\text{CV}}$ TMGMV have very limited to no movement. Some non-pseudo-colored nematodes are still mobile. (D) Cumulative percent response to free CV (*C. elegans* with no or with impaired mobility) over 24 h as a function of time and (E) CV concentration. (F) Cumulative percent response to $_{\text{CV}}$ TMGMV as a function of time and (G) CV concentration.

To quantitatively analyze the motility effects of CV on *C. elegans*, nematodes were treated with various concentrations (0, 0.01, 0.1, 1, 10, and 100 μM) of free CV, cvTMGMV , or TMGMV for 24 h at 22°C. At specific time points nematodes were observed under a white light microscope and the percent of affected nematodes (sum of the nematodes on scale (2) and (3)) was quantified as a function of time. The effective concentration (EC_{50}), defined as the concentration of CV at which half of the maximum immobilization of *C. elegans* was reached, was determined for free CV and cvTMGMV (**Figure 3.5 D-G**). Sixty percent of nematodes treated with 100 μM CV were paralyzed/dead within 1 h and no further improvements were observed within 24 h (**Figure 3.5 D**). When treated with 10 μM or 1 μM of CV, only ~30% or ~15% of nematodes were paralyzed/dead within the first hour, respectively. In those cases, maximum efficacy was observed after 6 h of incubation, when ~50% (10 μM CV) and ~25% (1 μM CV) of nematodes were affected. In both treatment regimes, a decrease in efficacy was observed after 6 h of incubation – this phenomenon may be explained because remaining unaffected population of nematodes continued to progress through their life cycle; consequently eggs were laid and nematodes hatched, which led to an overall increase in population and a decrease in percent of nematodes affected by the treatment. Furthermore, it is possible that at low doses of CV, nematodes are able to recover and slowly become mobile again. At doses of CV lower than 1 μM , there was no significant effect on nematode motility compared to the untreated population. The EC_{50} , defined as the concentration of CV at which half of the maximum immobilization of *C. elegans* was reached, was quantified at various time points and was determined to be 3.7 μM .

cvTMGMV showed a similar trend to free CV (**Figure 3.5 F+G**), and, as expected, TMGMV alone did not show any nematicide properties (**Supporting Figure 3.8**) When treated with 100 μM of cvTMGMV , ~40% of nematodes were paralyzed/dead within the first hour, and

maximum efficacy (~60%) was reached in the first 3 h. Therefore the efficacy of 100 μ M of CV and c_v TMGMV is identical after 3 h of incubation. However, when the concentration of c_v TMGMV was dropped to 10 μ M, the maximum efficacy was ~30% and was reached after ~8 h of incubation. Interestingly, CV release from c_v TMGMV in nematode media conditions revealed a half-life of 8 h (**Figure 3.4**), thus supporting the idea that CV was released from TMGMV and made available to treat the nematode infestation. All studied concentrations of c_v TMGMV lower than 10 μ M led to no significant treatment of the nematode infestation compared to the untreated population. The calculated EC_{50} of c_v TMGMV is 13.8 μ M, which is approximately 4 times greater than the EC_{50} of free CV. While reduced efficacy was observed in the petri dish experiments, I envision that c_v TMGMV will outperform free CV in the field based on the enhanced drug delivery aspect (see also discussion and data presented in **Figure 3.7**).

Next, I set out to understand the biodistribution of CV in the nematodes. I prepared fluorescently labeled TMGMV and analyzed whether TMGMV would interact with or be ingested by *C. elegans*. Briefly, diazonium coupling and click chemistry was used to conjugate a Cy5 dye to TYR side chains on TMGMV, as structural studies indicated that TYR2 is solvent-exposed (**Figure 3.1, 3.6 A**). I conjugated ~160 dyes per full length TMGMV, or about 7.5% of CPs were modified with Cy5 (**Supporting Figure 3.7**). We have previously demonstrated that a minimum conjugation of Cy5 to ~8% of TMV coat proteins is sufficient to yield maximum fluorescence intensity,²³⁷ thus the prepared samples were thought to be sufficient for imaging experiments. Fluorescent $TYR-Cy5$ TMGMV was incubated with *C. elegans* nematodes for 3 h at 22°C and subsequently analyzed by fluorescent microscopy (**Figure 3.6 B+C**). Results indicate that nematodes ingest the proteinaceous TMGMV carrier and that while TMGMV distributes

throughout the entire nematode body, the majority of TMGMV accumulates in the gastrointestinal (GI) tract.

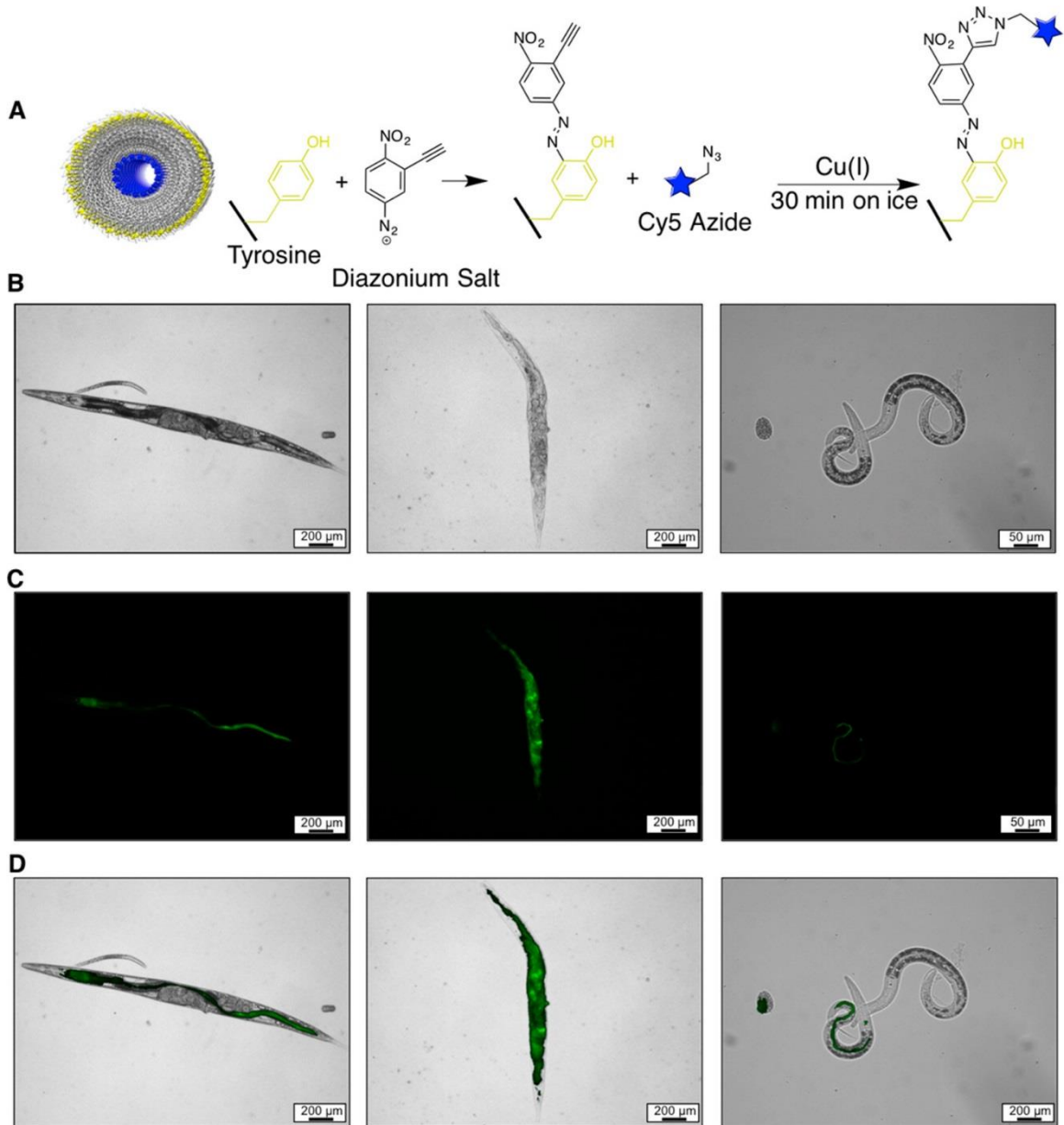


Figure 3.6. *C. elegans* ingestion of TMGMV. (A) Schematic of Cy5 conjugation to the surface exposed TYR2 groups (yellow) on the surface of TMGMV. (B) Bright field microscopy of *C. elegans* incubated with Cy5 TMGMV for 3 h. (C) Corresponding fluorescent images. (D) Bright field and fluorescent images were merged to confirm colocation.

3.3.3. Soil mobility of *c_v*TMGMV and free CV.

A soil mobility test was designed to establish the leaching of *c_v*TMGMV and free CV in soil. Briefly, top soil was packed in a plastic column up to a height of 4 cm and saturated with deionized (DI) water. *c_v*TMGMV or free CV was applied atop the soil columns, followed by DI water. Fractions were collected from the soil column, purified, and analyzed by UV/visible spectroscopy for the presence of TMGMV and CV. The λ_{260} (RNA) and λ_{280} (coat protein) wavelengths were monitored to quantify the amount of TMGMV that leached through the soil. A background 260:280 absorbance was observed in a CV soil leaching column, which most likely corresponds to the absorbance of organic matter present in top soil (**Figure 3.7 A**). *c_v*TMGMV showed enhanced mobility over free CV in the soil column, eluting from the column at high concentrations in the 5th to 15th elution fractions (**Figure 3.7 B+C**). In stark contrast, the efflux of CV from the soil column was delayed until the 25th to 50th elution fractions at a concentration 3.6 times lower than *c_v*TMGMV (**Figure 3.7 D**). CV is hydrophobic and has a strong binding affinity to soil particles ($K_{oc} = 6.1 \times 10^5$, ref: PubChem CID 11057) rendering the drug mostly immobile in soil, which explains the delayed efflux and lower concentrations eluted. Taken together, the data demonstrates the potential of TMGMV as a drug carrier to enable penetration of CV or other nematicides through soil to reach nematodes feeding on the roots of plants.

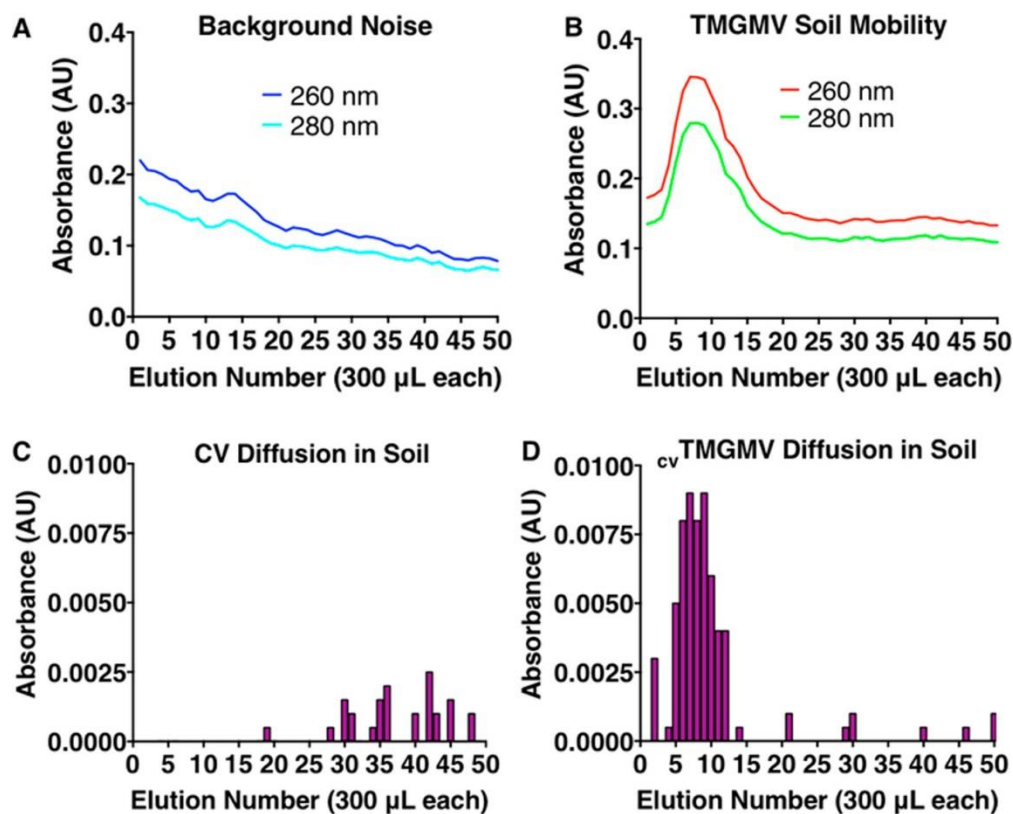


Figure 3.7. Soil mobility of cvTMGMV and free CV. UV/Visible spectrum at λ_{260} (RNA) and λ_{280} (coat proteins) from 50 elution fractions collected from the leaching of (A) CV and (B) cvTMGMV in 4 cm of top soil. The corresponding absorbance spectrum of CV (λ_{590}) was also recorded for the elution of (C) CV alone and (D) cvTMGMV.

3.4. Conclusions.

In this study, I have demonstrated the potential of tobacco mild green mosaic virus (TMGMV) as a carrier for anthelmintic drugs, such as crystal violet (CV), to treat plants infected with parasitic nematodes. After careful analysis of the TMGMV structure, I identified solvent-exposed TYR2 on the exterior surface enabling chemical modification. I also identified solvent-exposed carboxylates, GLU145 and ASP66 on the exterior surface and GLU95 and GLU106 on the interior surface, and established the chemical addressability of these residues. I also showed the potential for electrostatic encapsulation of positively charged guest molecules in TMGMV.

Further studies are needed to identify which of the identified GLU and ASP residues are chemically reactive. Electrostatic drug loading using crystal violet (CV) was achieved, yielding TMGMV carriers loaded with ~1500 CV per $_{cv}$ TMGMV nanocarrier. Treatment efficacy, while lower compared to free drug, was demonstrated using liquid *C. elegans* nematode cultures ($EC_{50} = 13.8 \mu\text{M}$ of $_{cv}$ TMGMV vs. $EC_{50} = 3.7 \mu\text{M}$ for free CV). Diffusion experiments revealed significantly increased soil mobility of $_{cv}$ TMGMV vs. free CV; the latter was unable to sufficiently diffuse and disperse through soil. Overall $_{cv}$ TMGMV demonstrates efficacy and superior soil motility, and as such makes a promising platform technology as a drug carrier targeting agricultural application.

Chapter III, in full, is a reprint of the material as it appears in ACS Nano, 2017. **Chariou, P.L.**, Steinmetz, N.F. *Delivery of Pesticides to Plant Parasitic Nematodes using Tobacco Mild Green Mosaic Virus as a Nanocarrier*. 11, 4719-4730. The dissertation author was the primary investigator and author of this paper.

Chapter IV: Soil Mobility of Synthetic and Virus-based Model Nanopesticides

4.1. Introduction.

Pesticides are needed to protect our crops and thus maximize crop yields.²³⁸ However, the efficacy of chemical pesticides is limited by their instability and strong binding to organic matter in soil, which can render them inactive or prevent their accumulation at the root level, where many pests reside.¹⁵ Large doses are applied to compensate, resulting in the accumulation of pesticide residues in soil, water and agricultural products.²³⁹ Long-term exposure to these chemicals is a risk to human health and threatens the biodiversity of an already fragile ecosystem.¹⁷ Precision farming methods are therefore needed to deliver pesticides in a more controlled manner.

Advances in nanotechnology have led to the development of more effective drug delivery and medical imaging methods (nanomedicine), and the same innovations are now being applied to smart agrochemical delivery systems, known as nanopesticides.^{18,240} These involve the use of nanomaterials for the adsorption, encapsulation or conjugation of pesticides, improving the biodegradability, stability, permeability and dispersion of the active pesticide ingredient. Nanopesticides have a much greater surface area than conventional pesticides, increasing their potential for interaction with target pests at lower doses. The encapsulation of pesticides within nanoparticles also prevents premature degradation and the risk of direct human exposure to the active ingredient. There is also evidence that nanopesticides and conventional pesticides differ in their environmental behaviour, so it is necessary to understand the fate of nanopesticides in detail in order to ensure they comply with regulatory guidelines and legislation.^{241–243}

Most of the nanopesticides investigated thus far are based on synthetic or natural polymers, metallic compounds or liposomes, which tend to persist in the environment.¹⁸ As a biodegradable

alternative, nanopesticides can be developed from plant viruses.^{217,218,244} One example, already EPA-approved, is the application of Tobacco mild green mosaic virus (TMGMV) as the herbicide Solvinix, which is produced by BioProdex for deployment against invasive tropical soda apple weed in the state of Florida.^{28,29} The safety profile and possible risks of TMGMV have been reported.²⁸ TMGMV cannot self-disseminate and is not transmitted by vectors such as insects, seeds, or pollen. Mechanical transmission through insects or contact between plants is thus the only route of transmission. Only plants of the Solanaceae are susceptible to TMGMV infections. Therefore, TMGMV offers a good safety profile for crops that are not part of the Solanaceae. Nonetheless, TMGMV as well as other plant virus-based systems could be inactivated through ultraviolet radiation for safe use on any crop.^{245,246}

To investigate the potential of plant virus nanoparticles (VNPs) and virus-like particles (VLPs) as nanopesticides in more detail, I compared the behaviour of three viruses and two synthetic particle formulations in soil column experiments and computational models, as a way to gauge their ability to deliver pesticides to the rhizosphere and thus prevent infestation by root pests (Fig. 1). I tested two VNPs, based on the rod-like TMGMV and the icosahedral Cowpea mosaic virus (CPMV), and a virus-like particle (VLP) based on *Physalis* mosaic virus (PhMV). These were compared to mesoporous silica nanoparticles (MSNPs) and a poly(lactic-co-glycolic acid) formulation (PLGA), which have already been developed as synthetic nanopesticides.^{247,248}

4.2. Experimental methods.

4.2.1. Expression and purification of nanoparticles. TMGMV was obtained from Bioprodex, DegraFluorex Fluorescent PLGA nanoparticles were purchased from Phosphorex, and MSNPs functionalized with propylcarboxylic acids were obtained from Sigma-Aldrich. I

resuspended 3 mg ml⁻¹ of PLGA and 1 mg ml⁻¹ of MSNP in distilled water and sonicated them using a Branson 2800 device (Cleanosonic) for 10 min to obtain homogeneous solutions. CPMV was propagated in Burpee black-eyed pea plants and purified as previously described.²⁴⁹ PhMV VLPs were prepared in ClearColi BL21 (DE3) cells as previously described.²⁵⁰ USDA Permits (PPQ 526) were obtained for any work with plant viruses.

4.2.2. Bioconjugation of Cy5 to TMGMV tyrosine residues. TMGMV comprises 2,130 identical coat proteins arranged helically around a single-stranded RNA genome, forming a hollow rigid rod measuring 300 × 18 nm with a 4-nm internal channel.³ The external surface features two solvent-exposed tyrosine side chains (Tyr 2 and Tyr 139), which can be functionalized using diazonium coupling reactions. I used sulfo-Cy5-azide (Lumiprobe) to modify these Tyr residues as previously described.¹⁰ Briefly, I mixed 25 µl 0.68 M 3-ethynylaniline with 75 µl 3 M sodium nitrite (both Sigma-Aldrich) in 400 µl 0.3 M *p*-toluenesulfonic acid monohydrate (Thermo Fisher Scientific) for 1 h on ice. I then added 15 equivalents of the resulting diazonium salt (DS) to 2 mg ml⁻¹ TMGMV in 10 mM borate buffer (pH 8.8) for 30 min on ice. The particles were centrifuged at 112,000 g for 1 h on a 30% (w/v) sucrose cushion to separate the TMGMV-alkyne particles from the excess DS. TMGMV-alkyne was resuspended in 10 mM KP buffer (pH 7.4) overnight before adding sulfo-Cy5-azide via a Cu(I)-catalysed alkyne-azide cyclo-addition reaction. I added two equivalents of Cy5 per coat protein to 2 mg ml⁻¹ TMGMV-alkyne in the presence of 2 mM aminoguanidine, 2 mM L-ascorbic acid sodium salt and 1 mM copper(II) sulfate (all Sigma Aldrich) in 10 mM KP buffer (pH 7.4) on ice for 30 min. The particles were again centrifuged at 112,000 g for 1 h on a 30% (w/v) sucrose cushion to remove excess Cy5, and resuspended in 10 mM KP buffer (pH 7.4) overnight. Further purification to remove aggregates involved centrifugation at 16,000 g for 10 min. TMGMV-Cy5 was eluted using PD Minitrap G-25 desalting

columns (GE Healthcare) to remove free Cy5 dye.

4.2.3. Bioconjugation of Cy5 to PhMV/CPMV lysine residues. CPMV comprises 180 coat proteins and displays a total of 300 surface-exposed lysine side chain.¹ PhMV also comprises 180 identical coat proteins, but each displays four surface-exposed lysine side chains making 720 in total.² CPMV and PhMV were labelled with sulfo-Cy5-NHS (Lumiprobe) using NHS-activated esters targeting the surface lysine residues. The reactions were carried out with a 1200-fold (CPMV) or 900-fold (PhMV) molar excess of sulfo-Cy5-NHS in 10 mM KP buffer (pH 7.0) at room temperature overnight, with agitation.

4.2.4. Bioconjugation of Cy5 to MSNP carboxylate residues. Alkynes were conjugated to carboxylate groups on the MSNP surface using 1.5 mM propargylamine (Sigma-Aldrich) per gram of MSNP and 2.5 mM EDC in 10 mM HEPES buffer (pH 7.4). The reaction was allowed to proceed for 24 h at room temperature followed by an alkyne-azide click reaction induced by adding 250 nmoles of sulfo-Cy5-azide per gram of MSNP. The components were incubated at 4°C with gentle agitation for 30 min using 1 mg ml⁻¹ MSNP in 10 mM KP buffer (pH 7.4) in the presence of 1 mM CuSO₄, 2 mM aminoguanidine and 2 mM ascorbate (all Thermo Fisher Scientific). MSNPs were purified by centrifugation at 7,000 g for 10 min and buffer exchange at least five times.

4.2.5. Encapsulation of Cy5 into TMGMV/CPMV/PhMV/MSNP particles. Encapsulated formulations were prepared by mixing 1 mg ml⁻¹ of TMGMV, CPMV or PhMV with a 5000-fold molar excess of Cy5-Amine, or by mixing 250 nmoles of Cy5 per gram of MSNP in 10 mM KP buffer (pH 7.8) overnight at room temperature with agitation.

4.2.6. UV/Vis spectroscopy. The UV/vis spectra of native and modified TMGMV, CPMV, PhMV, PLGA and MSNP nanoparticles were determined using a NanoDrop Spectrophotometer

(Thermo Fisher Scientific). The efficiency of Cy5 loading was determined based on the dye-to-carrier ratio and the Beer–Lambert law. TMGMV: $\epsilon(260 \text{ nm}) = 3 \text{ ml mg}^{-1} \text{ cm}^{-1}$, molecular weight of TMGMV = $39.4 \times 10^6 \text{ g mol}^{-1}$. CPMV: $\epsilon(260 \text{ nm}) = 8.1 \text{ ml mg}^{-1} \text{ cm}^{-1}$, molecular weight of CPMV = $5.6 \times 10^6 \text{ g mol}^{-1}$. Cy5: $\epsilon(647 \text{ nm}) = 271 \text{ 000 M}^{-1} \text{ cm}^{-1}$, molecular weight of Cy5 = 747 g mol^{-1} . PLGA dye: $\epsilon(668 \text{ nm}) = 250 \text{ 000 M}^{-1} \text{ cm}^{-1}$, molecular weight of PLGA dye = 519 g mol^{-1} .

4.2.7. Denaturing gel electrophoresis. I denatured $5 \mu\text{g}$ of native TMGMV, CPMV and PhMV at 100°C for 5 min in the presence of 4 \times LDS loading dye (Thermo Fisher Scientific). Cy5-modified particles were denatured as described above using a loading dye lacking bromophenol blue. The samples were separated on 4–12% NuPage precast gels in 1 \times MOPS buffer (Thermo Fisher Scientific) for 40 min at 200 V and 120 mA, with SeeBlue Plus2 ladder size markers (Thermo Fisher Scientific). Gels were imaged before and after staining with Coomassie Brilliant Blue (0.25% w/v) using the FluorChem R imaging system under white light and MultiFluor red light.

4.2.8. Agarose gel electrophoresis. I analysed $3 \mu\text{g}$ of native CPMV, PhMV, PLGA and MSNP particles by 1.2% (w/v) agarose gel electrophoresis (1 h at 100 V) in 1 \times TBE running buffer in the presence of Nucleic Acid Gel Stain (GoldBio) diluted 1:20 000. Gels were imaged before and after staining with Coomassie Brilliant Blue (0.25% w/v) as above.

4.2.9. Transmission electron microscopy. Formvar copper grids coated with carbon film (Electron Microscopy Sciences) were glow discharged to render the surface more hydrophilic using the PELCO easiGlow operating system. Drops of TMGMV, CPMV, PhMV or PLGA ($10 \mu\text{l}$, 1 mg ml^{-1}) were deposited onto the grids for 2 min at room temperature. The grids were then washed twice with deionized water for 30 s and subsequently stained twice with 2% (w/v) uranyl acetate for another 45 s. MSNP ($10 \mu\text{l}$, 1 mg ml^{-1}) was deposited onto grids and allowed to dry-

cast overnight. A Tecnai F-30 transmission electron microscope was used to capture images of the samples at 300 kV.

4.2.10. Dynamic light scattering. A DynaPro NanoStar instrument (Wyatt Technology) was used to measure the hydrodynamic radius of TMGMV, CPMV, PhMV, PLGA and MSNP nanoparticles. The reported hydrodynamic radii and standard derivations correspond to the average of 30 measurements, each consisting of 100 runs.

4.2.11. Size exclusion chromatography. Native and modified TMGMV, CPMV, PhMV and PLGA samples (200 μ l, 1 mg ml⁻¹) were passed through a Superose 6 Increase column on the AKTA Explorer chromatography system (GE Healthcare) at a flow rate 0.5 ml min⁻¹ in 10 mM KP buffer (pH 7.0). The absorbance at 260 nm and 280 nm was recorded for all particles, the absorbance at 647 nm was recorded to confirm Cy5 conjugation/encapsulation, and the absorbance at 668 nm was recorded to confirm dye encapsulation in the proprietary PLGA nanoparticles.

4.2.12. Fluorescent-dye release profiling. The release of Cy5 from TMGMV, PhMV, CPMV and MSNP, and dye release from PLGA, was evaluated using a dialysis-based assay. Slide-A-Lyzer MINI dialysis units (10,000 MWCO, Thermo Fisher Scientific) were loaded with 1 mg of particles in 10 mM KP buffer (pH 7.0) in triplicate. The particles were dialyzed against 10 mM KP buffer (pH 7.0) at room temperature for 96 h. At time t = 0, 1, 3, 6, 18, 24, 48, 72 and 96 h, 10 μ l was extracted from each dialysis units and the remaining dye entrapment was measured by UV/Vis spectroscopy (TMGMV, CPMV, PhMV and MSNP) or imaged under the FluorChem R imaging system (PLGA).

4.2.13. Soil mobility of TMGMV, CPMV, PhMV, PLGA, MSNP and free Cy5. *Garden Magic* Top Soil was packed at a density of 0.32 g cm⁻³ into a cylindrical column (28 mm diameter, top height 30 cm) and saturated with deionized water to remove air pockets. This was the

maximum density achievable under our experimental conditions, but the density of soil in real environments can be higher (0.6–1.6 g cm⁻³) due to compaction effects with depth and over time. I injected a bolus containing 1 mg of each formulation with and without conjugated or infused dye molecules at the top of the soil column and saturated the column with water at a constant flow rate of 1.5 cm³ min⁻¹ in 10 mM KP buffer (pH 7.0) The eluent was collected at the base of the column in 500- μ l fractions. Up to 200 fractions were collected in each trial (two trials per depth for each formulation). The elution fractions containing TMGMV, PhMV or CPMV were analysed by SDS-PAGE to determine the mass of nanoparticles recovered in each elution fraction. CPMV was analysed on 4–12% NuPage pre-cast gels in 1 \times MOPS buffer. TMGMV and PhMV were analysed on 4–12% NuPage polyacrylamide SDS gels cast according to the Surecast Handcast protocol (Invitrogen). I mixed 23 μ l of each elution fraction with 7 μ l 5 \times SDS loading buffer and separated the samples for 1 h at 200 V and 120 mA with SeeBlue Plus2 ladder size and three standards containing known amounts of nanoparticles (0.5, 1 and 2 μ g) for comparison. The gels were then incubated in 20% (v/v) methanol and 10% (v/v) acetic acid in water 30 min before staining with Coomassie Brilliant Blue (0.25% w/v) for an additional 30 min. The gels were imaged using the AlphaImager HP system (Protein Simple) under white light and the FluorChem R system under MultiFluor red light. The elution fractions containing PLGA and MSNP were imaged as 20- μ l droplets on Parafilm on the FluorChem R imaging system under MultiFluor red light in the presence of the nanoparticle standards described above.

All nanoparticles were imaged in triplicate and the images were analysed using ImageJ. The area under the curve (AUC) of the standards was used to create a linear standard curve relating the AUC of the elution samples to the total mass of nanoparticles present in the corresponding elution fraction. Finally, fractions that appeared to contain no nanoparticles were centrifuged at

160,000 g for 3 h and the pellet was resuspended in 1 mL 10 mM KP buffer (pH 7.0) for SDS-PAGE analysis to determine the recovered mass of nanoparticles.

4.3. Computational methods.

The model equations presented here are variations of those developed for other applications.²⁵¹ The nanoparticle mass density distribution in fluid (*i.e.*, interstitial soil space) changes as a function of the column depth z and time t according to Eq. (4.1):

$$\frac{\partial W_{NP}}{\partial t} + \frac{Q}{Ae} \frac{\partial W_{NP}}{\partial z} = D_{NP} \frac{\partial^2 W_{NP}}{\partial z^2} + \left(\frac{1-e}{e} \right) f R_{NPS}, \quad 0 < z < L \quad (\text{Eq. 4.1})$$

where Ω_{NP} [mg cm^{-3}] is the mass density of nanoparticles in the soil interstitial space at any location in the column, Q is the volume flow [$\text{cm}^3 \text{min}^{-1}$], e is the fluid fraction of volume (or cross-sectional area) in the column, A [cm^2] is the cross-sectional area of the column, D_{NP} [$\text{cm}^2 \text{min}^{-1}$] is the dispersion constant of the nanoparticle, and Φ [cm^{-1}] is the surface area to volume of soil. The irreversible rate of adsorption of nanoparticles onto the soil surface from the fluid is R_{NPS} [$\text{mg cm}^{-2} \text{min}^{-1}$]. With and without pesticides, the nanoparticle adsorption process is assumed to be a first-order reaction as shown in Eq. (4.2):

$$R_{NPS} = -k_{NPS} W_{NP} \quad (\text{Eq. 4.2})$$

The available soil surface, which changes negligibly, is incorporated into the rate constant k_{NPS} [cm min^{-1}]. As Ω_{NP} decreases with reaction, the nanoparticle attachment to soil increases as shown in Eq. (4.3):

$$\frac{\partial W_{NPS}}{\partial t} = -f R_{NPS} \quad (\text{Eq. 4.3})$$

where Ω_{NPS} [mg cm^{-3}] is the number density of nanoparticles bound to soil at any location in the

column.

The pesticide mass concentration C_P [mg cm^{-3}] distribution in fluid changes as shown in Eq. (4.4):

$$\frac{\partial C_P}{\partial t} + \frac{Q}{Ae} \frac{\partial C_P}{\partial z} = D_P \frac{\partial^2 C_P}{\partial z^2} - R_{PF} + \left(\frac{1-e}{e} \right) f R_{PS}, \quad 0 < z < L \quad (\text{Eq. 4.4})$$

where D_P [$\text{cm}^2 \text{min}^{-1}$] is the dispersion constant of the pesticide. The irreversible release rate R_{PF} [$\text{mg cm}^{-3} \text{min}^{-1}$] of pesticide from nanoparticles in fluid is shown in Eq. (4.5):

$$R_{PF} = -k_{PF} C_{NPF} \quad (\text{Eq. 4.5})$$

where C_{NPF} [mg cm^{-3}] is the mass concentration of pesticide bound to nanoparticles in fluid at any location in the column and k_{PF} [min^{-1}] is the rate constant of pesticide dissociation from nanoparticles in fluid. The irreversible adsorption rate R_{PS} [$\text{mg cm}^{-2} \text{min}^{-1}$] of free pesticide in fluid onto soil surface is shown in Eq. (4.6):

$$R_{PS} = -k_{PS} C_P$$

(Eq. 4.6)

where k_{PS} [cm min^{-1}] is the rate constant of pesticide absorption onto soil. The free pesticide mass concentration C_{PS} [mg cm^{-3}] bound to soil changes according to Eq. (4.7):

$$\frac{\partial C_{PS}}{\partial t} = -\phi (R_{PS} + R_P) \quad (\text{Eq. 4.7})$$

where R_P [min^{-1}] is the irreversible rate of pesticide ‘transfer’ from nanoparticles onto soil.

The concentration change of pesticide attached to nanoparticles in fluid is therefore shown in Eq. (4.8):

$$\frac{\partial C_{NPF}}{\partial t} + \frac{Q}{A\varepsilon} \frac{\partial C_{NPF}}{\partial z} = D_{NP} \frac{\partial^2 C_{NPF}}{\partial z^2} + R_{PF} + \left(\frac{1-\varepsilon}{\varepsilon} \right) \phi R_{PNP} \quad (\text{Eq. 4.8})$$

where R_{PNP} [$\text{mg cm}^{-2} \text{min}^{-1}$] is the irreversible adsorption rate of pesticide attached to nanoparticles onto the soil determined according to Eq. (4.9):

$$R_{PNP} = -k_{NPS} C_{NPF} \quad (\text{Eq. 4.9})$$

where k_{NPS} [cm min^{-1}] is the rate constant of pesticide attached to nanoparticles that adsorb to soil. This rate process has the same rate constant as the rate process of nanoparticles adsorption onto soil (R_{NPS}), as defined in Eq. (4.10):

$$-k_{NPS} = \frac{R_{PNP}}{C_{NPF}} = \frac{R_{NPS}}{W_{NP}} \quad (\text{Eq. 4.10})$$

The pesticide concentration C_{NPS} [mg cm^{-3}] in nanoparticles on soil changes according to Eq. (4.11):

$$\frac{\partial C_{NPS}}{\partial t} = \phi (R_P - R_{PNP}) \quad (\text{Eq. 4.11})$$

The irreversible rate of pesticide transfer from nanoparticles to the soil with rate constant k_P [min^{-1}] is therefore shown in Eq. (4.12):

$$R_P = -k_P C_{NPS} \quad (\text{Eq. 4.12})$$

Initially, there is no nanoparticle or pesticide in the soil space $0 < z < L$:

$$t = 0 : \Omega_{NP} = 0; \Omega_{NPS} = 0; C_{NPF} = 0; C_{NPS} = 0; C_P = 0; C_{PS} = 0;$$

At the input (top of the cylindrical column) $z = 0$, a solution of volume V_0 with nanoparticle density Ω_{NP}^0 and pesticide concentration C_{NPF}^0 is injected. The total number of nanoparticles

injected is $N_{NP}^0 = V_0 \Omega_{NP}^0$. Fluid flows through the interstitial soil space at volume rate Q . The nanoparticles are transported into the column over a time interval 0 to t_1 according to Eq. (4.13):

$$N_{NP}^0 = \int_0^{t_1} Q \Omega_{NP}^0 dt = Q \Omega_{NP}^0 t_1 \Rightarrow t_1 = \frac{N_{NP}^0}{Q \Omega_{NP}^0} \quad (\text{Eq. 4.13})$$

Therefore, at the entrance of the cylinder, mass flow rate balances must be specified for the nanoparticles and pesticide. For the nanoparticles, the input nanoparticle mass density is derived as shown in Eq. (4.14):

$$z = 0: \quad Q \Omega_{NP} = \begin{cases} Q \Omega_{NP}^0, & 0 < t \leq t_1 \\ 0, & t > t_1 \end{cases} \Rightarrow \Omega_{NP} = \begin{cases} \Omega_{NP}^0, & 0 < t \leq t_1 \\ 0, & t > t_1 \end{cases} \quad (\text{Eq. 4.14})$$

For the pesticide, which is carried by the nanoparticle, the input mass concentration is derived as shown in Eq. (4.15):

$$z = 0: \quad QC_{NPF} = \begin{cases} QC_{NPF}^0, & 0 < t \leq t_1 \\ 0, & t > t_1 \end{cases} \Rightarrow C_{NPF} = \begin{cases} C_{NPF}^0, & 0 < t \leq t_1 \\ 0, & t > t_1 \end{cases} \quad (\text{Eq. 4.15})$$

Because no dissolved pesticide enters, then $z = 0$ and $C_P = 0$. In the fluid leaving the column, the concentrations of nanoparticle, pesticide in nanoparticle, and free pesticide can be represented by X . The mass flow of X from inside the cylinder (L^-) and to outside the cylinder (L^+) is shown in Eq. (4.16):

$$z=L: \quad \left[QX - AeD \frac{\partial X}{\partial z} \right]_{L^-} = [QX]_{L^+}, \quad X \in \{ \Omega_{NP}, C_{NPF}, C_P \} \quad (\text{Eq. 4.16})$$

The volume flow rate, nanoparticle density and pesticide concentration are continuous across the output boundary of the cylinder, which implies that the gradients must vanish as shown in Eq. (4.17):

$$z = L: \quad \frac{\partial \Omega_{NP}}{\partial z} = 0, \quad \frac{\partial C_P}{\partial z} = 0, \quad \frac{\partial C_{NPF}}{\partial z} = 0 \quad (\text{Eq. 4.17})$$

For the simultaneous numerical solution of the partial differential equations, the equations were first transformed into their dimensionless form (**Supplementary Equation 4.1**).

Code Availability: These dimensionless equations were solved using partial differential equation solver function “pdepe” (MATLAB). All code was made available in **Supporting Code 4.1**.

4.4. Results and discussion.

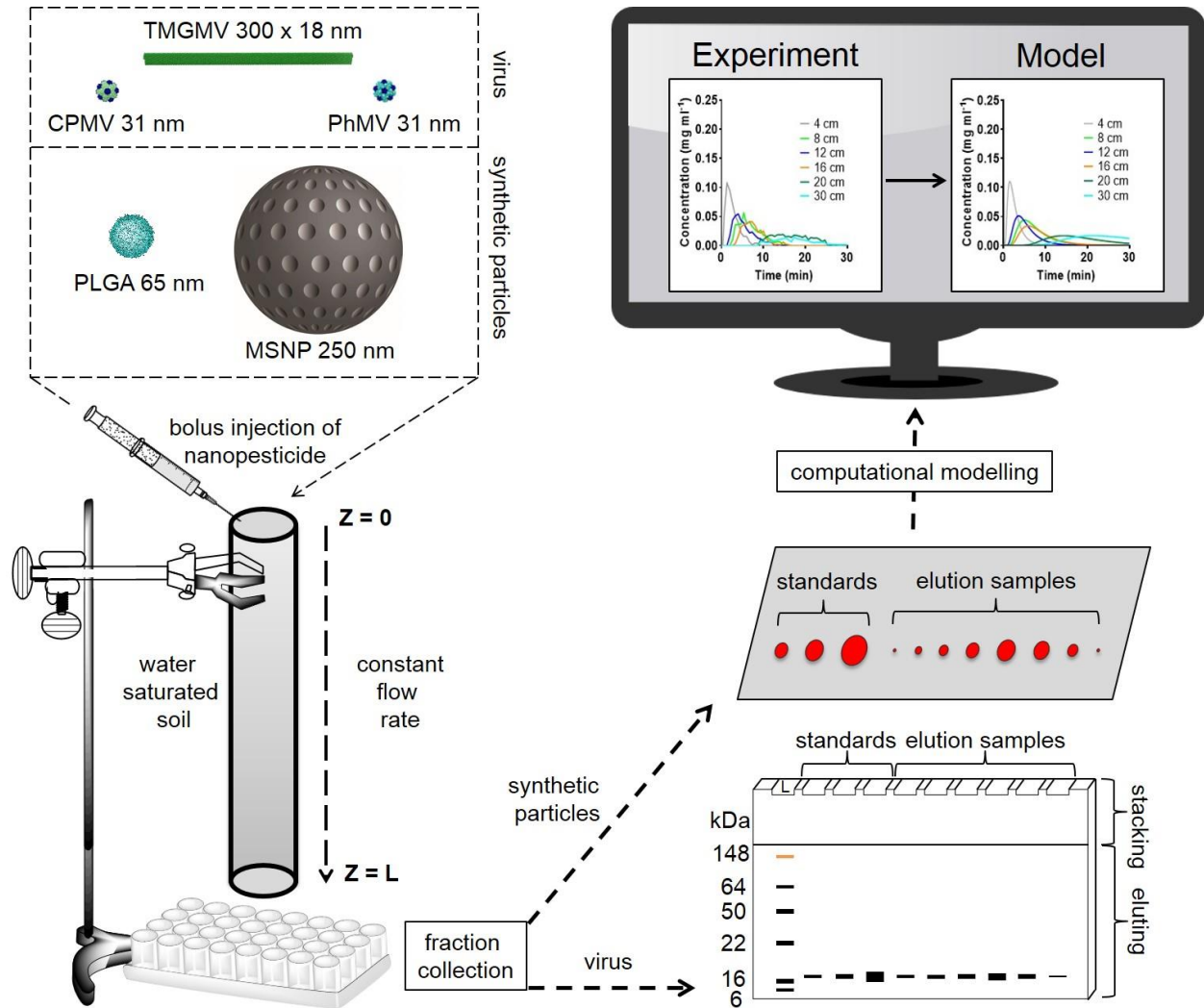


Figure 4.1. Combined experimental and computational nanopesticide transport through soil.

The virus-based and synthetic nanoparticles are depicted to scale in the top left corner. Labelled nanoparticles were injected as a bolus at the top of the soil column, and moved through the column at a constant flow rate. At the bottom of the column, particles were collected as 500- μ l fractions. The mass of the eluted virus-based nanoparticles was determined by SDS-PAGE and the synthetic nanoparticles were imaged as droplets on Parafilm using the FluorChem R imaging system under MultiFluor red light. Experimental data were imported into MATLAB for comparison with the output of the computational model.

4.4.1. Nanopesticide characterization.

The fluorophore Cyanine 5 (Cy5) has similar physicochemical properties to conventional pesticides (**Supporting Table 4.1**) but is easier to detect, so I used it as a model compound. Cy5 was either conjugated to the external surface of, or passively encapsulated within, TMGMV, CPMV, PhMV and MSNP particles (**Supporting Figure 4.1**). Degradex PLGA nanoparticles encapsulating a red fluorophore with spectral properties similar to Cy5 were obtained from Phosphorex (**Supporting Figure 4.2**). Each formulation was characterized by a combination of transmission electron microscopy (TEM), dynamic light scattering (DLS), UV/Vis spectroscopy, size exclusion chromatography (SEC) and denaturing gel electrophoresis (SDS-PAGE) or agarose gel electrophoresis, to confirm particle integrity and dye loading efficiency (**Supporting Figure 4.2, Supporting Figure 4.3, and Supporting Figure 4.4**). The capacity of TMGMV was 9.9 nmol mg⁻¹ or 390 dye molecules per TMGMV-Cy5 particle (denotes the conjugated version) but only 5.3 nmol mg⁻¹ or 210 dye molecules per TMGMV*Cy5 particle (denotes the encapsulated version). For PhMV, the corresponding loads were 12.7 nmol mg⁻¹ or 60 dye molecules per PhMV-Cy5 and 11.7 nmol mg⁻¹ or 55 dye molecules per PhMV*Cy5. For CPMV, the corresponding loads were 6.2 nmol mg⁻¹ or 35 dye molecules per CPMV-Cy5 and 2.3 nmol mg⁻¹ or 15 dye molecules per CPMV*Cy5. The synthetic MSNP formulation was similar in capacity to CPMV (6.4 nmol mg⁻¹ for MSNP-Cy5 and 4.3 nmol mg⁻¹ for MSNP*Cy5) whereas the PLGA formulation had the lowest capacity (1.2 nmol mg⁻¹ for PLGA*Dye).

The release profile of passively encapsulated Cy5 (**Figure 4.2**) was determined by dialysis. The approximate half-life, defined as the time necessary for 50% of the fluorophore to be released from its carrier, was calculated for TMGMV ($t_{1/2} = 12$ h), CPMV ($t_{1/2} = 60$ h), PhMV ($t_{1/2} = 48$ h), MSNP ($t_{1/2} = 12$ h) and PLGA ($t_{1/2} = 72$ h). Two distinct release profiles were observed, reflecting

the Cy5 entrapment methodology used in each formulation. For TMGMV and MSNP, Cy5 is not entrapped in a confined structure because the internal channel of TMGMV is uncapped at both ends and the mesopores of MSNP are similarly open to the surrounding medium, potentially explaining the faster release rate. For CPMV and PhMV, Cy5 is encapsulated within the protein shell and the PLGA nanoparticle encapsulates the dye in its hydrophobic core, hence the slower release. The observed release profiles may not precisely replicate pesticide release in a real soil environment, which is rich in various minerals and organic matter that might interact with either the carriers or the pesticide molecules, as discussed below.

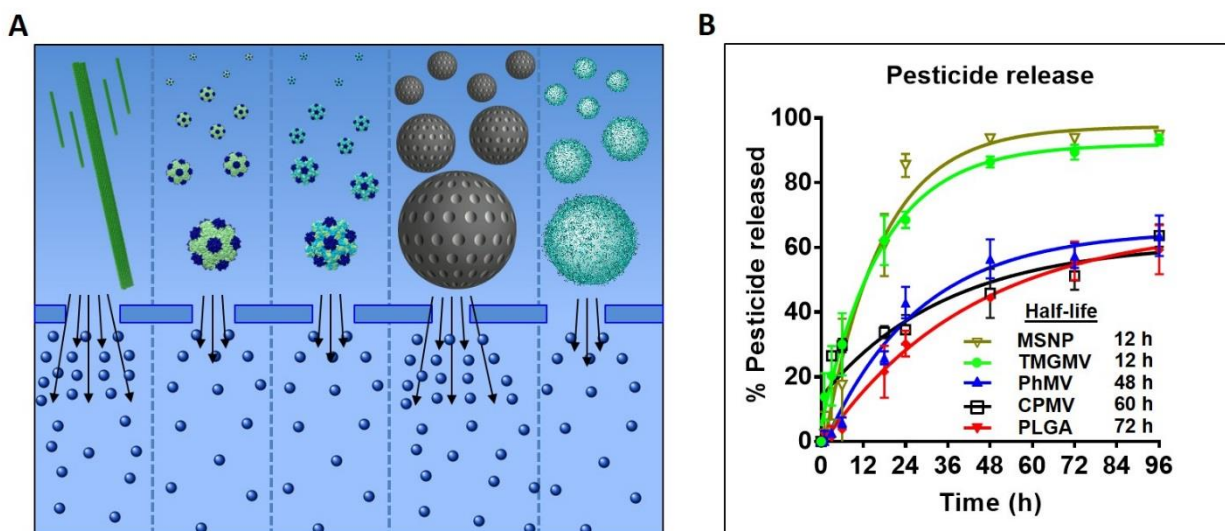


Figure 4.2. Cargo release from nanoparticles during dialysis. (A) Schematic representation of infused-dye release from (left to right) TMGMV, CPMV, PhMV, MSNP and PLGA. The dialysis membrane pores are large enough to allow the free movement of Cy5 but small enough to prevent nanoparticle diffusion. The number of arrows reflects the rate of dye release from each nanoparticle in a semi-quantitative manner. (B) Corresponding plot of Cy5 cumulative release from each nanoparticle as a function of time. The approximate half-life data (time required to release 50% of the dye) are shown at the bottom right corner of the graph. Error bars represent standard deviation (SD).

4.4.2. Soil transport behaviour.

To establish the soil transport behaviour of each formulation, I conducted mobility studies using a cylindrical column (see Methods, **Supporting Table 4.2, and Supporting Table 4.3**). As a reference, I ran 500 µg of free Cy5 through a soil column with a smaller diameter of 10 mm. Cy5 was unable to penetrate further than 4 cm through the soil because it bound strongly to the soil particles (**Supporting Figure 4.6**). About 40% of the mass of injected Cy5 was recovered from a column with a soil depth of 2 cm. These results are comparable to data reported for abamectin²¹⁷, fenamiphos and oxamyl²⁵², as well as other pesticides.²⁵³ No matter which nanoparticle type was used as a carrier, the mobility of Cy5 within the column was significantly enhanced (**Figure 4.3**). The best-performing carrier was TMGMV, which penetrated to a soil depth of 30 cm regardless of whether the cargo was conjugated or encapsulated (**Figure 4.3 A**). The spatiotemporal distribution of the nanoparticles and the Cy5 cargo was very similar, indicating that in each formulation the carrier and cargo were co-eluted (**Figure 4.3 C-E**). The quantity of encapsulated Cy5 that co-eluted with its carrier decreased with soil depth, indicating that a portion of the cargo was released over time.

To determine the quantity of particles loss from the soil transport experiment, I pooled all elution samples that showed no evidence of nanoparticles in SDS-PAGE analysis and collected any trace amounts of the virus. I found that the residual mass of nanoparticles accounted for only ~2.5% of the overall mass of particles injected (**Supporting Table 4.4**). TEM imaging of the eluted particles revealed that they remained intact (**Supporting Figure 4.7**).

In terms of soil transport behaviours, TMGMV and CPMV were able to penetrate through 30 cm of soil, whereas PhMV, MSNP and PLGA only penetrated 4, 12, and 8 cm of soil, respectively. The mobility of the carriers in soil can therefore be ranked from highest to lowest as

follows: TMGMV >> CPMV >>> MSNP > PLGA > PhMV. These data suggest that the PhMV, MSNP and PLGA formulations are not suitable for pesticide delivery deep into the soil, to target the rhizosphere, but may be suitable for the delivery of pesticides that must remain close to the surface, such as herbicides. In the latter context, PhMV demonstrated the greatest pesticide delivery capability within the first 4 cm of soil (**Figure 4.3 B**).

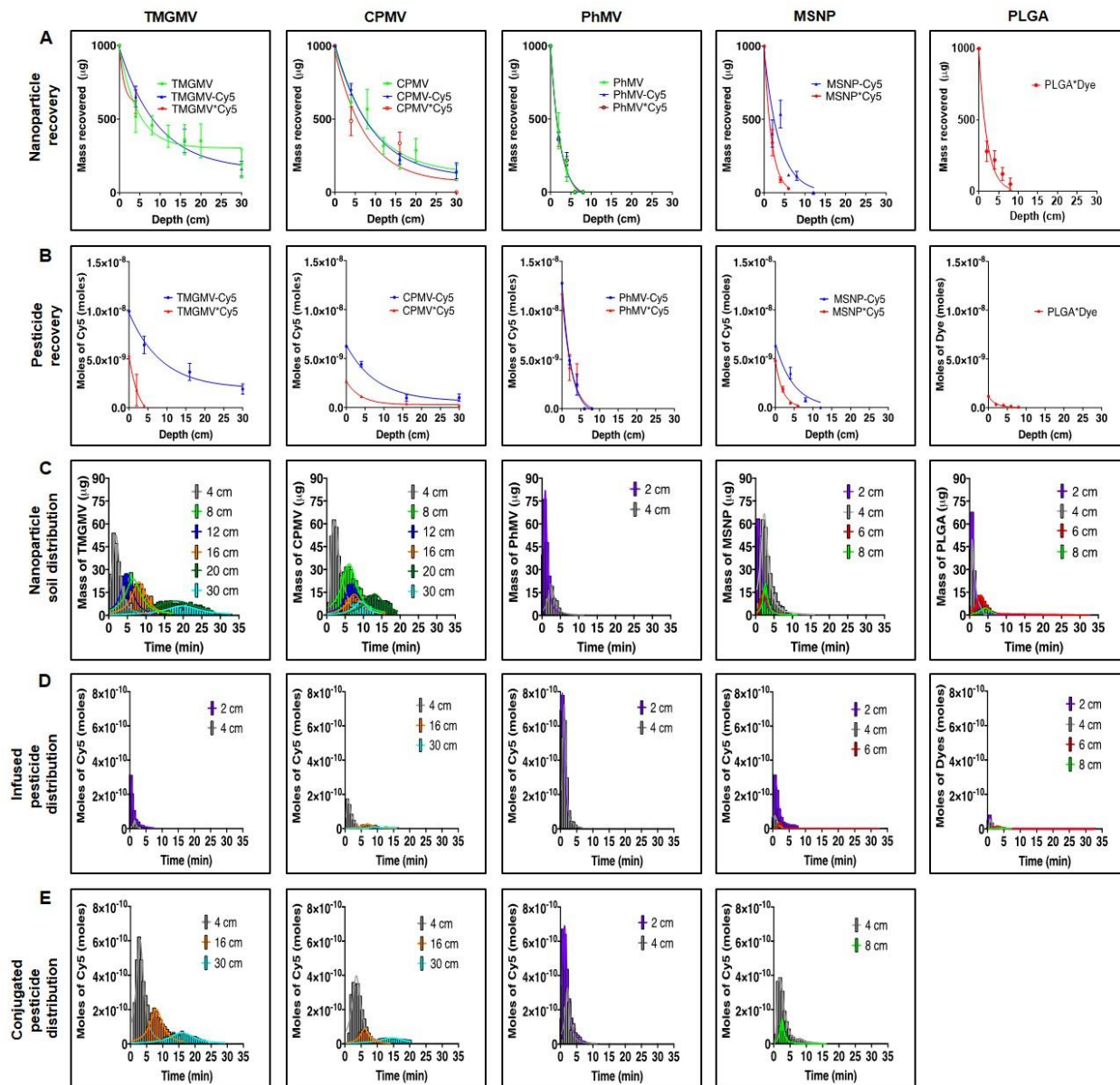


Figure 4.3. Experimental transport of nanopesticides and pesticides through soil. (A) Cumulative mass of bare (green), Cy5-conjugated (blue), and Cy5-infused (red) nanoparticles exiting the soil column as a function of soil depth. (B) Corresponding cumulative moles of conjugated Cy5 (red) and infused Cy5 (blue) exiting the soil column. Error bars represent standard derivation (SD). (C) Mass distribution of nanoparticles as a function of time at a given soil depth. (D) Corresponding mole distribution of Cy5-infused and (E) Cy5-conjugated particles as a function of time for a given soil depth.

The particle size may influence the mobility of the carriers, but there was no particular trend within the size range I tested. For example, the 250-nm MSNP particles penetrated further than the 65-nm PLGA formulation, which in turn penetrated further than the 31-nm PhMV particles, but the 31-nm CPMV particles were much more mobile than all of the above. This is interesting given that CPMV and PhMV are similar in size and geometry, so the remarkable difference in mobility must reflect their surface chemistries. Both CPMV and PhMV are proteinaceous, but the distinct amino acid sequences of their coat proteins ensure that CPMV carries a negative surface charge whereas PhMV is positive (**Supporting Figure 4.2**). Furthermore, the rod-like (300 x 18 nm) TMGMV particles were the most mobile of all, suggesting that the elongated shape may facilitate their transport through the soil. In the field of nanomedicine, elongated nanoparticles are better at margination (migration toward blood vessels) and transport through membranes than spherical particles, which improves their tumour homing and penetration characteristics.^{254–256} A high aspect ratio therefore appears to be a generally favourable property that facilitates movement between obstacles by influencing particle behaviour in flowing liquids. I therefore speculate that the field of nanopesticide delivery should further focus on designing nanoparticles with high aspect ratio in addition to the traditional spherical counterparts. Particles with overall neutral to negative surface charge should also be favoured over positively charged nanoparticles to prevent early binding to soil matter.

The concentration of Cy5 as a function of soil depth was higher when the dye was conjugated to the particles rather than encapsulated (**Figure 4.3 B**). This reflects the slower release of the conjugated dye from the carrier, allowing it to be carried further, whereas the encapsulated dye leaks more readily from the carrier and once released is rendered less mobile by its affinity for soil particles. Interestingly, Cy5 was released rapidly from the TMGMV*Cy5 and MSNP*Cy5

formulations (4 and 6 cm penetration, respectively) which suggests that the electrostatic forces between Cy5 and the carboxylate residues of (i) the TMGMV interior and (ii) the MSNP mesopores are not strong enough to overcome the attraction between Cy5 and the soil. These results agree with the rapid loss of Cy5 observed in the dialysis assay (**Figure 4.2**). Therefore, for field applications, the conjugated formulation appears superior to the encapsulated formulation.

Both TMGMV and CPMV were able to deliver Cy5 deep in the soil, but TMGMV-Cy5 showed by far the better performance. In Chapter II, I have demonstrated that nematodes ingest nematicide-loaded TMGMV particles, which resulted in the death of 60% of the nematode population in liquid cultures within 24 h.²¹⁸ To increase the efficacy, future TMGMV formulations should include cleavable linkers to promote the slow and controlled release of the pesticide at the root level. But in order to translate such pesticide formulations from the bench to the field, it is first necessary to establish the dose required to eradicate rhizosphere-dwelling pests. I therefore developed a mathematical model and validated it using our experimental data as discussed below.

4.4.3. Computational modelling of pesticide delivery.

A model column of length L [cm] and constant cross-sectional area A [cm²] was filled with a mixture of stationary soil particles and fluid (**Figure 4.1**). The input to this model was a known mass nanoparticles, with or without pesticide, introduced over a short period of time to the soil surface. The outputs were the concentrations of the nanoparticle Ω_{NP} [mg cm⁻³], the nanoparticle-pesticide formulation C_{NPS} [mg cm⁻³], and free pesticide C_P [mg cm⁻³] at the base of the soil column as a function of time for a specific depth of soil. Following the injection, fluid flow was established at top the column at a rate Q [cm³ min⁻¹]. Nanoparticles were subsequently transported through the void volume fraction ε [dimensionless] of the saturated soil column, with an adsorption surface

per soil particle volume ϕ [cm^{-1}]. The soil particle density within the column was assumed to be uniform.

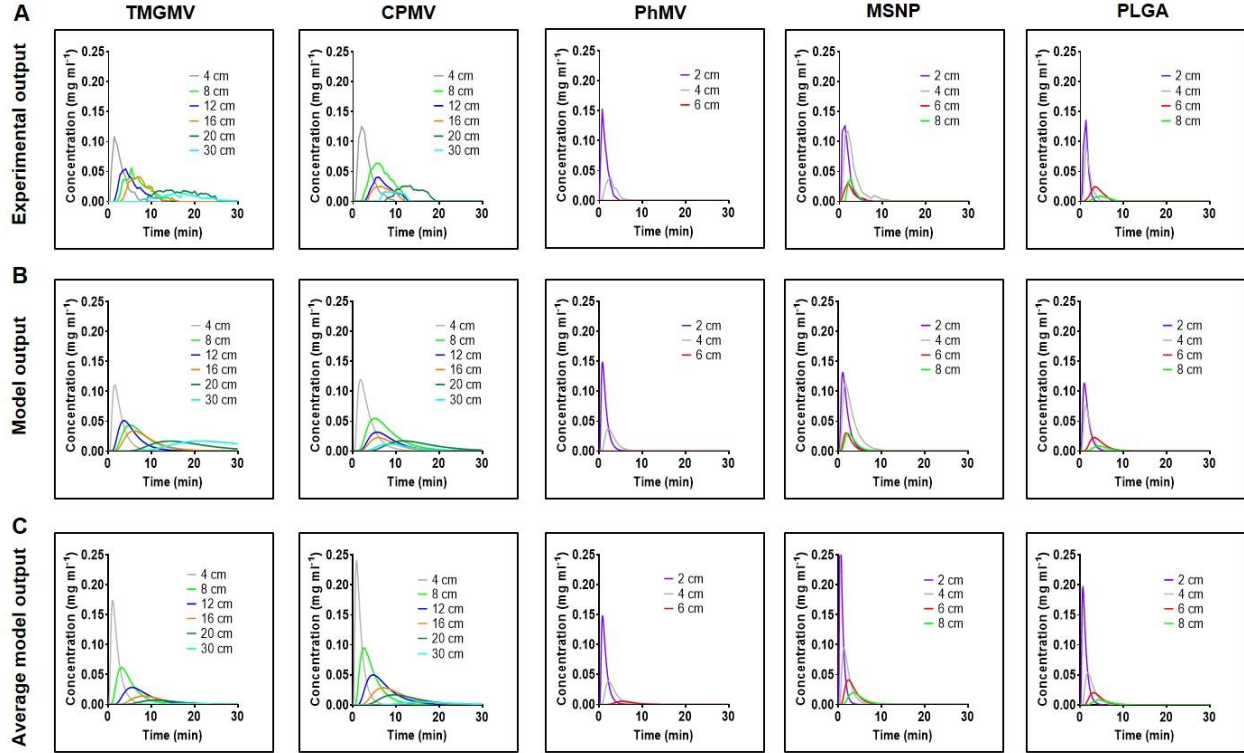


Figure 4.4. Theoretical transport of nanoparticles through soil. (A) The empirical output of TMGMV, CPMV, PhMV, MSNP and PLGA is used as a reference. (B) Computational modelling of nanoparticle transport through soil. D_{NP} and k_{NPS} were optimized for each depth. (C) Corresponding model of nanoparticle transport through soil using the average value of D_{NP} and k_{NPS} obtained in (B).

The rates of nanoparticle degradation and pesticide deactivation were assumed to be negligible during the experiment, as confirmed empirically (**Supporting Figure 4.7**). Nanoparticle binding to soil particles was modelled as a first-order irreversible reaction with rate constant k_{NPS} [cm min^{-1}] dependent on the nanoparticle size, aspect ratio and surface chemistry. The pesticide release rate was modelled as a first-order irreversible reaction with rate constant k_{PF} [min^{-1}]. While simple, using a first-order release mechanism led to comparative errors ranging from 10^{-4} to 10^{-9} between the empirical data and the model output, which are sufficiently small to be acceptable differences

(**Supporting Table 4.5**). The resulting free pesticide may bind to soil particles through a first-order irreversible reaction with rate constant k_{PS} [cm min^{-1}]. The interaction mechanisms are summarized in Supplementary Figure 8 and the corresponding partial differential equations are shown in the methods section. These equations were made dimensionless (**Supporting Equation 1**) and solved using MATLAB (**Supporting Code 1**). The system contained five unknowns: the dispersion constants of the nanoparticle D_{NP} and pesticide D_P , and the rate constants of nanoparticle absorption to soil k_{NPS} , pesticide absorption to soil k_{PS} , and pesticide release from nanoparticles in fluid k_{PF} . These values were obtained by comparing the model output to the empirical data and minimizing the error in MATLAB. This computational model is therefore semi-empirical in nature. . The resulting model outputs closely matched the empirical data (**Figure 4.4**), although the values of D_{NP} and k_{NPS} differed slightly for each depth due to experimental error caused by the need to use a new soil column in each test. Although the bulk density of the soil was kept constant across all experiments, the soil particle distribution and the soil packing may have differed from column to column. To compensate for these variables, the average values of D_{NP} and k_{NPS} at different depths were computed to model the average nanoparticle soil transport profile (**Figure 4.4 C**). The nanoparticle dispersion D_{NP} and rate of absorption to soil k_{NPS} determine the ability of a nanoparticle to carry pesticide deep in the soil. With greater mechanical dispersion, the nanoparticles become more widely distributed at a given soil depth over time. Therefore, mechanical dispersion greatly influences the concentration of nanoparticles at any given soil depth and time. The average D_{NP} of each nanoparticle can be ranked from highest to lowest as follows: TMGMV > CPMV > MSNP > PhMV > PLGA. As the absorption to the soil becomes stronger, the nanoparticles become less mobile. The average rate constant of nanoparticle absorption to soil k_{NPS} can also be ranked from highest to lowest as follows: MSNP >>> PLGA \approx PhMV >>

TMGMV > CPMV. The model confirms the superior mobility of TMGMV and its suitability to deliver pesticides to the rhizosphere.

To quantify the efficiency of pesticide delivery at the root level, I solved the model for the Cy5 dispersion constant D_p and the rate constant of Cy5 absorption to soil k_{PS} (**Supporting Figure 9**). I then used the average values of D_{NP} , k_{NPS} , D_p and k_{PS} to optimally estimate k_{PF} , (**Figure 4.5**). Again, the model output matched the empirical data closely. The rate of Cy5 release k_{PF} can be ranked from highest to lowest as follows: PhMV >>> CPMV > TMGMV >> MSNP. Interestingly, these results do not match the release profile of Cy5 in the dialysis assay (**Figure 4.2**), suggesting that the interaction between nanoparticles and soil has a major influence on the release rate.

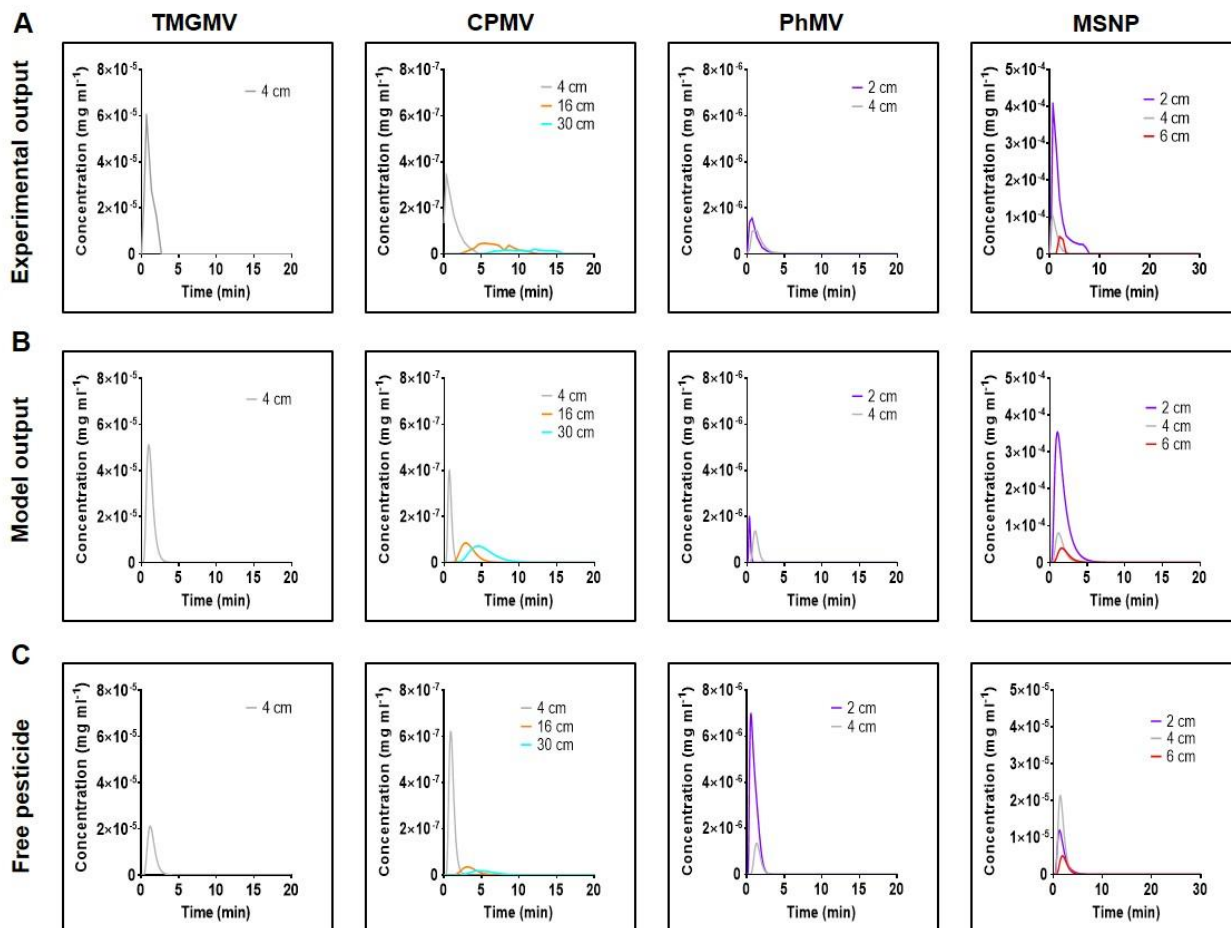


Figure 4.5. Theoretical transport of Cy5 through soil. (A) The empirical output of Cy5 infused into TMGMV, CPMV, PhMV and MSNP used as a reference. (B) Computational modelling of Cy5 transport through soil following nanoparticle infusion. (C) Corresponding model output of free Cy5 transport through soil.

Testing experimentally whether a new nanoparticle formulation is a suitable candidate for pesticide delivery to the rhizosphere is time consuming and expensive; each nanoparticle described above required 7 soil column experiments and I used an average of 100 SDS denaturing gels (each holding 10 samples) to solve the soil transport profile of the nanocarriers through 2 to 30 cm of soil depth (of note, other detection techniques would need to be developed for non-proteinaceous materials, but this is expected to be equally laborious). The model described above minimizes the time and cost required to evaluate a novel nanopesticide. In conjunction with the model, the only

experimental work required is to run the new nanocarrier candidate through a 4 cm deep soil column, a mobility test well recognized and established by the Organization for Economic Cooperation and Development.²⁵⁷ This experimental data is necessary to establish the value of D_{NP} and k_{NPS} , to predict the nanopesticides behaviour at any other soil depth (**Supporting Figure 4.10**). The VLP bacteriophage Q β , which has been investigated as a drug carrier for medical application but not for pesticide delivery,²⁵⁸ was tested for its ability to transport through soil (**Supporting Figure 4.11 and Supporting Figure 4.12**). Q β was predicted to transport through soil similarly to CPMV and TMGMV, further confirming the superior soil mobility of VNPs/VLPs over synthetic materials.

The data obtained from the six different nanoparticle tested indicate that k_{NPS} is linearly related to the surface area of MSNP, TMGMV, Q β , and CPMV; however, PLGA and PhMV behaviors are different. (**Supporting Figure 4.13**). PhMV nanoparticles have been shown to have known positive zeta potential at a pH of 7.4. On the other hand, both clay and organic matter have a net negative surface charge, which may explain the enhanced soil binding of PhMV. I suspect the polymer nature of PLGA and its strong electronegativity also promote its enhanced binding to organic matter present in the soil. The linear relationship of k_{NPS} of other nanoparticles with surface area suggests that the binding for the nanoparticles follows a mechanism that depends on the surface area such as a mechanism based on van der Waals forces. Even though such analysis is limited due to limited number of particles tested, it does suggest that the model parameters have physical basis that may be elucidated.

4.4.4. Testing the nanopesticide model in a real-life scenario.

Nematode endoparasites infect 3,000 different plant species including many crops,²²² and are most abundant ~24 cm beneath the soil surface.²⁵⁹ Based on our empirical and modelling

results, I selected TMGMV to deliver the nematicide abamectin.²⁶⁰ Abamectin is insoluble in water and binds strongly to organic matter in the top layer of soil, so its effect in the rhizosphere is limited and it is an ideal candidate for nanopesticide delivery using TMGMV. I used our nanopesticide model to determine how much TMGMV formulation must be applied to maintain the IC₅₀ concentration of abamectin 24 cm beneath the surface for at least 24 h. A conjugated formulation would be better than encapsulation to avoid premature release, and the linkage should be stable enough to allow the carrier to reach the target depth before the cargo is dispersed, such as a labile ester with a half-life release rate of 4 days.²⁶¹ The IC₅₀ value of abamectin is $1.309 \times 10^{-4} \text{ mg cm}^{-3}$, and at least this concentration must therefore be achieved in the rhizosphere.²¹⁷ I modelled various flow rates representing the typical range of crop irrigation systems, and used a common irrigation regimen of 1 h three times a week, the first irrigation taking place immediately after nanopesticide application. The values of D_{NP} and k_{NPS} for TMGMV were determined as above, and in place of abamectin I used the values for the chemically similar Cy5. I assumed complete release at the root level due to the hydrolysis of the labile ester linkage over the course of a few days. The simulation output (**Figure 4.6**) revealed that the mass of nanopesticide needed to maintain the target abamectin concentration for 24 h was dependent on the flow rate. Without no irrigation, neither free nor conjugated abamectin would achieve that concentration due to the extremely slow rate of diffusion. At a flow rate of $0.5 \text{ cm}^3 \text{ min}^{-1}$, the lowest dose of TMGMV-abamectin required to maintain the target abamectin concentration 24 cm below the surface was $0.1056 \text{ mg cm}^{-2}$. The model therefore offers a powerful tool to optimize the dose regimen that must be used to maximize the efficacy of pesticides in the rhizosphere.

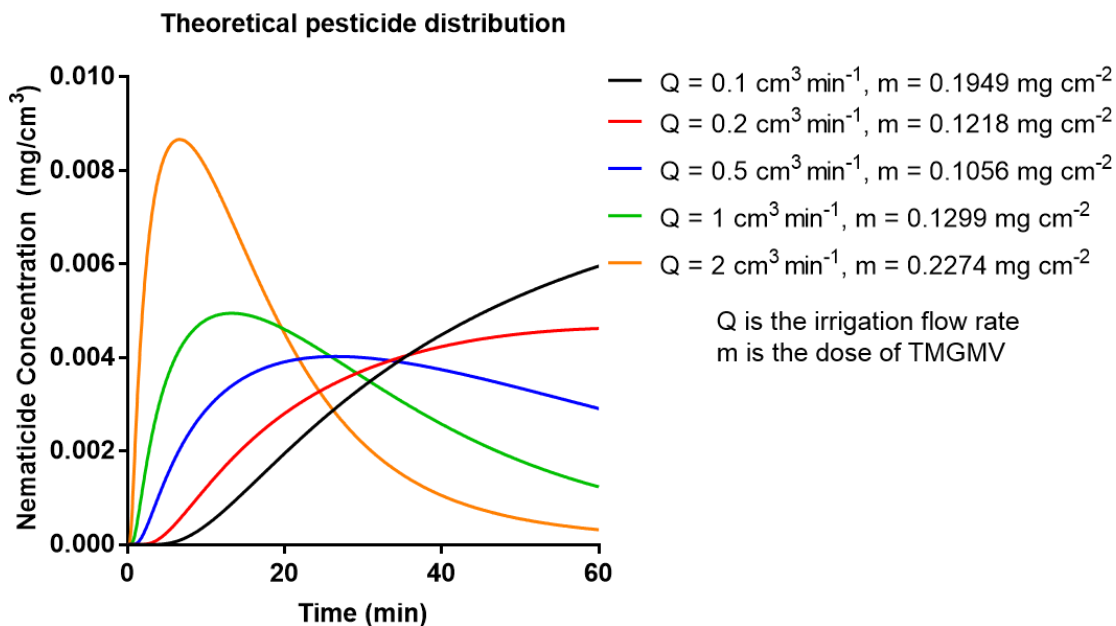


Figure 4.6. Theoretical treatment of crops infected with nematodes. Each curve represents the temporal concentration distribution of abamectin conjugated to TMGMV at a soil depth equal to 24 cm as a function of the irrigation flow rate (Q). The corresponding minimal dose of TMGMV (m) that must be applied on the crop to maintain the IC₅₀ of Abamectin is indicated.

4.5. Conclusions.

I propose the use of VNPs/VLPs as carriers to deliver pesticides to the rhizosphere, where many pest species reside. Compared to icosahedral VNPs based on CPMV and VLPs based on PhMV, and synthetic counterparts with a similar geometry (PLGA and MSNP), the rod-like VNPs based on TMGMV achieved much greater mobility in soil and also showed the highest dye loading capacity. This is the first evidence that nanoparticles with a high aspect ratio are more mobile in the soil than spherical counterparts. It remains to be determined whether VNPs/VLPs are as cost effective as some synthetic materials. To date there is only one commercial plant VNP product, namely Solvinix (Bioprodex). In conjunction with our empirical data, I developed a computational model to predict the transport behaviour of pesticides encapsulated within or conjugated to

nanoparticles. This model allowed us to calculate the optimal pesticide dose that must be applied to crops in order to achieve an effective dose at root level. This precision farming approach will increase the efficacy of pesticide applications while reducing the risk of residual chemicals to human health and the environment.

Chapter IV, in full, is a reprint of the material as it appears in Nature Nanotechnology, 2019. **Chariou, P.L.**, Dogan, A.B., Welsh, A.G., Sidel, G.M., Baskaran, H., Steinmetz, N.F. *Soil mobility of synthetic and virus-based model nanopesticides*. DOI: <https://doi.org/10.1038/s41565-019-0453-7>. The dissertation author was the primary investigator and author of this paper.

Chapter V: Chemical and UV Light Inactivation of TMGMV for Environmental Applications

5.1. Introduction.

Biological pests, including pathogens, arthropods, nematodes, and weeds are responsible for major losses in crop yields.²⁶² In modern agriculture, pest management often relies on the use of synthetic chemicals that are sparingly soluble and absorb to soil particles with high affinity. Consequently, contemporary pesticides generally have poor bioavailability, and therefore require applications in large quantities to achieve an effective dose.²³⁸ The accumulation of these chemicals in the environment contaminates both land and water sources, which leads to off-target toxicity to other species, including domestic animals and humans (*e.g.* cancer and infertility).^{16,17} As a result, an increasing number of pesticides have been withdrawn from the market due to the tightening of regulatory guidelines. The persistence of pesticide traces in the environment in concentrations below their effective dose has also resulted in the build-up of target resistance, ultimately rendering some pesticide formulations obsolete.²⁶³ Because these compounds are not being efficiently replaced, there is currently a gap in the market which threatens our food safety and security.

Advances in nanotechnology have led to the development of agrochemical nanomaterials to protect crops from various pests.^{18,240} The encapsulation or conjugation of pesticides in/to nanocarriers improves their stability and solubility, preventing their premature degradation by photolysis or biodegradation. Compared to free pesticides, nanocarriers can have enhanced soil mobility and increase the pesticide's potential for interaction with target pests at lower doses.²¹⁹ While nanocarriers can bring significant benefits to the agricultural industry, some health and environmental risks remain to be solved. The majority of nanopesticides in the development

pipeline are based on metallic compounds, synthetic or natural polymers, which tend to persist in the environment, and in some cases can cause acidification of soil, impairing its fertility.¹⁸ Thus, there is a need to design eco-friendly nanocarriers with low-toxicity and favorable biodegradation. To this end, we and others have proposed to repurpose the capsids of plant viruses for pesticide delivery applications. For example, the delivery of anthelmintic drugs to endoparasitic nematodes using the icosahedral red clover necrotic mosaic virus (RCNMV)²¹⁷ and the rod-shaped tobacco mild green mosaic virus (TMGMV)²¹⁸ has been reported. Plant viruses are already part of the natural soil ecosystem and are not known to cause adverse effects in humans or animals. We have focused on the high aspect ratio nanoparticles derived from the nucleoprotein assembly of TMGMV because the high aspect ratio offers a larger surface area to be modified with pesticide payload compared to spherical nanoparticles. More importantly, we reported enhanced soil mobility of TMGMV and accumulation at the crop root level, where nematodes reside.^{217,218}

To pave the way for environmental and field applications of TMGMV, we set out to develop non-infectious formulations thereof. Infectious TMGMV has been approved by the EPA for use as a bioherbicide; its use is restricted to its application in the state of Florida for the treatment of the invasive tropical soda apple (TSA) weed.^{28,29} While TMGMV has a rather narrow host range, it does infect solanaceous plants, including tomato, chili peppers, and eggplants. Therefore, to enable broad applicability it is desired to prepare non-infectious nanoparticle formulations.

The inactivation of plant viruses was first explored in 1936 using various chemical treatments such as formalin, hydrogen peroxide, or even sodium nitrite.²⁶⁴ Generally these chemical treatments either crosslink or oxidize the nucleic acids and/or proteins. Since then, extensive work has been reported on the use of ultraviolet (UV) radiation as an effective method

to inactivate tobamovirus using tobacco mosaic virus (TMV) and TMGMV as models.^{245,265–272} UV irradiation causes RNA-protein crosslinks as well as dimerization of adjacent uracils, both of which inhibit RNA replication and translation.²⁴⁶ TMGMV, the U2 strain of TMV, was found to be 5.5x more sensitive to UV inactivation.²⁶⁷ Since isolated RNA from TMV and TMGMV were equally sensitive to UV inactivation, the difference was attributed in differences in packaging of the RNA. While TMV and TMGMV share the same structure, both are nucleoprotein assemblies measuring 300×18 nm with a 4 nm-wide central channel, it appears that packaging of the TMV coat protein protects its RNA more efficiently from UV damage.

Nonetheless, this previous body of data relied on visual local lesion quantification to record the level of infectivity post viral inactivation; this method has now been outperformed by the far more sensitive polymerase chain reaction, which quantifies the presence of viral RNA within the inoculated leaves. Therefore, follow-up studies revisiting the UV inactivation of TMGMV were warranted. In addition to testing UV treatment, we also considered two commonly used chemical treatments, namely β PL and formalin.

β PL and formalin are more commonly used in the medical field to produce inactivated vaccines; for example, these reagents are used to produce non-virulent enterovirus 71, hepatitis A, polio, and influenza virus vaccines.^{273,274} The inactivation of TMGMV has not yet been tested using these treatment modalities. β PL induces the acylation or alkylation of nucleotides and amino acids.²⁷³ On the other hand, formalin induces chemical RNA and protein crosslinking, including RNA-protein crosslinks.²⁷⁴

Here, we compared the inactivation of TMGMV particles by UV light against that of chemical treatment using β PL or formalin. To test whether the inactivated formulation remained infective, *Nicotiana tabacum* Tennessee 86 (Tn86), *N. tabacum* Samsun-NN, and tropical soda

apple (TSA) (*Solanum viarum*) were inoculated and challenged with the various TMGMV particle preparations. Visual inspection of plants and reverse-transcription polymerase chain reaction (RT-PCR) was conducted on individual leaves to quantify infectivity with a high degree of sensitivity.

5.2. Materials and methods.

5.2.1. TMGMV inactivation using UV-light, β -propiolactone, and formalin. TMGMV was obtained from Bioproducts and inactivation was conducted using 1 mg mL⁻¹ virus samples resuspended in 10 mM potassium phosphate (KP) buffer (pH 7.0). UV-treatment was established by exposing TMGMV to 0.1, 0.2, 0.25, 0.5, 1, 5, 7.5, 10, and 15 J cm⁻² of UV light at a wavelength of 254 nm using a UVP crosslinker (Analytik Jena AG). β -propiolactone (β PL, Sigma-Aldrich) inactivation was conducted by incubating TMGMV with 1, 10, 100, 500, 750, 1000, 1500 mM of β PL for 24 h at 4°C, followed by the inactivation of β PL for 2 h at 37°C. Finally, TMGMV was exposed to 1, 10, 100, 250, 500, 750, and 1000 mM formalin (Electron Microscopy Sciences) for 5 days at 37°C. Chemically treated TMGMV was then centrifuged at 112,000 g for 1 h to remove excess β PL or formalin.

5.2.2. Plant inoculation with native and inactivated TMGMV. *Nicotiana tabacum* Tennessee 86 (Tn86), *N. tabacum* Samsun-NN, and tropical soda apple (TSA) (*Solanum viarum*) plants were seeded in 30 x 20 x 3.5 cm aluminum baking trays using SunGrow[®] Mix #3 Professional Mix (Sun Gro Horticulture) and maintained on a greenhouse bench at the USDA-ARS-U.S. Horticultural Research Laboratory, Fort Pierce, FL 34945. Seedlings were transplanted individually in 3.8 liter plastic pot and allowed to grow in the greenhouse. When the plants were about 30 days old, fully developed new leaves were mechanically inoculated by gently abrading

with a Q-tips[®] swab (Unilever United States, available in local drugstores) dipped in native or inactivated TMGMV (see above) or buffer (approximately 0.05 mL⁻¹ per application). Five plants (replicates) were inoculated for each treatment conditions in addition to a negative control (5 buffer-treated plants). Leaves were imaged and harvested individually 22 days (first trial) or 16 days (second, repeat trial) post-inoculation and stored at -80°C until further processing.

5.2.3. Viral RNA extraction. Inoculated leaves were submerged in liquid nitrogen for 1 min in a mortar and pulverized using a pestle into a thin powder. The pulverized leaves were suspended into UltraPure DNase/RNase free distilled water (Thermo Fisher Scientific) using 1 mL per gram of leaves and vortexed for 1 min prior to centrifugation at 13,000 g for 10 min to pellet down the leaf material. 500 µL of the supernatant was denatured by adding 1/4 vol. of 10 % (w/v) SDS under heating for 10 min at 60°C. Samples were then treated with 2 volumes of UltraPure phenol:chloroform:isoamylalcohol (PCI 25:24:1, v/v/v) (Thermo Fisher Scientific), mixed by vortexing for 1 min, and centrifuged at 13,000 g for 10 min. The upper phase containing the RNA was transferred into a fresh tube and the extraction was repeated an additional two times. The RNA extract was added to 2 volumes of 100% (v/v) ethanol and further purified and concentrated using the Quick-RNA[™] Miniprep kit (Zymo). The final purified RNA was suspended in 30 µL of UltraPure DNase/RNase free distilled water and stored at -80°C until further analysis. The concentration was determined by UV-visible spectroscopy at 260 nm using the extinction coefficient for single-stranded RNA: 25 ng mL⁻¹ cm⁻¹.

5.2.4. Reverse transcription polymerase chain reaction (RT-PCR). RNA from native and inactivated TMGMV was reverse-transcribed into cDNA using the SuperScript IV One-Step RT-PCR System kit (Thermo Fisher Scientific) following the manufacturer's specifications. The reaction mixture consisted of 25 µL 2X Platinum SuperFi RT-PCR Master Mix, 2.5 µL forward

primer (5'-CAATCAACTCTCCGAGCCAA-3', 10 μ M), 2.5 μ L reverse primer (5'-TCAGTATTCGGTGCGGG-3', 10 μ M), 0.5 μ L SuperScript IV RT Mix, and 1 μ g total RNA supplemented with Nuclease-free water for a final volume of 50 μ L. The RT-PCR conditions are summarized in **Table 5.1**.

Table 5.1. RT-PCR conditions.

Step	Temp ($^{\circ}$ C)	Time (min:sec)	No. Cycle
Reverse transcription	50	10:00	1
RT inactivation	98	2:00	1
Amplification	98	0:10	35
	65	0:10	
	72	0:30	
Final extension	72	5:00	1
Storage	4	∞	1

5.2.5. Agarose gel electrophoresis. All agarose gels were run in 1 \times TBE running buffer in the presence of Nucleic Acid Gel Stain (GoldBio) diluted 1:20 000 (v/v). Extracted RNA was analyzed by running 1 μ g of sample on 1.2% (w/v) agarose gels for 40 min at 110 V in the presence of a 1 kbp Plus DNA ladder (Invitrogen). Similarly, DNA amplicons were analyzed using 2.5 μ L of RT-PCR product on 1.8% (w/v) agarose gels for 35 min at 110 V in the presence of a 100 bp Plus DNA ladder (Invitrogen). Gels were imaged before and after staining with Coomassie Brilliant Blue (0.25% w/v) using the FluorChem R imaging system under UV light or white light.

5.2.6. UV/Vis spectroscopy. The UV/visible spectra of native and inactivated TMGMV were recorded using a NanoDrop Spectrophotometer (Thermo Fisher Scientific). TMGMV: $\epsilon(260 \text{ nm}) = 3.0 \text{ ml mg}^{-1} \text{ cm}^{-1}$, molecular weight of TMGMV = $39.4 \times 10^6 \text{ g mol}^{-1}$.

5.2.7. Dynamic light scattering. The hydrodynamic radius of native and inactivated TMGMV (at 1 mg mL⁻¹ in buffer 10 mM KP) was recorded using a Zetasizer Nano ZSP/Zen5600 instrument (Malvern Panalytical). The particle length was calculated as the weighted mean of the intensity distribution.

5.2.8. Transmission electron microscopy. Formvar copper grids coated with carbon film (Electron Microscopy Sciences) were glow discharged to render the surface more hydrophilic using the PELCO easiGlow operating system. 10 µL drops of TMGMV (0.5 mg mL⁻¹) were deposited onto the grids for 2 min at room temperature, followed by two wash with deionized water for 30 s and stained twice with 2% (w/v) uranyl acetate for another 45 s. Images are obtained with a Zeiss Libra 200EF transmission electron microscope operated at 80 kV.

5.2.9. Size exclusion chromatography. Native and inactivated TMGMV samples (200 µL, 1 mg mL⁻¹) were eluted through a Superose 6 Increase column on the ÄKTA Explorer chromatography system (GE Healthcare) at a flow rate 0.5 mL min⁻¹ in 10 mM KP buffer (pH 7.0) and the absorbance at 260 nm and 280 nm was recorded.

5.2.10. Denaturing gel electrophoresis. Native and inactivated TMGMV were denatured at 100°C for 5 min in the presence of 4×LDS loading dye (Thermo Fisher Scientific). Samples were run on 12% SDS-PAGE precast gels in 1× morpholinepropanesulfonic acid (MOPS) buffer (Thermo Fisher Scientific). for 40 min at 200 V and 120 mA in the presence of SeeBlue Plus2 ladder size markers (Thermo Fisher Scientific). Gels were imaged after staining for nucleic acid (GelRed, Biotium) and proteins (Coomassie Brilliant Blue (0.25% w/v)) with the FluorChem R imaging system under UV light and white light.

5.3. Results and discussion.

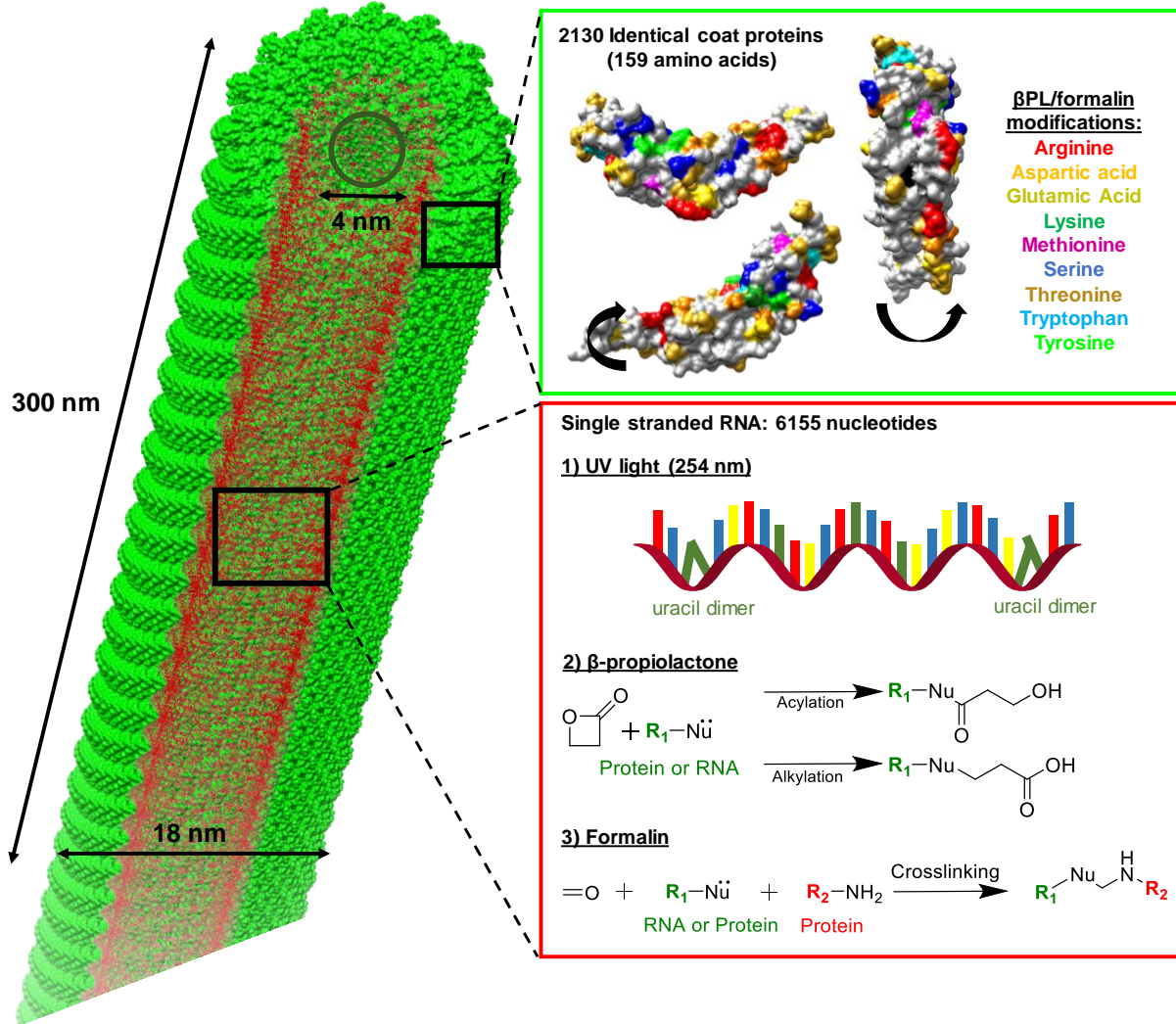


Figure 5.1. Comparing the effect of UV light, βPL, and Formalin on TMGMV. Left, structure of TMGMV using the UCSF Chimera software (PDB ID: 1VTM) depicting the coat proteins in green, and the RNA in red. To the upper right shows a single coat protein in three different orientations, highlighting amino acids that could be potentially modified by βPL and/or formalin. To the bottom right, 1) inactivation of RNA using a 254 nm wavelength UV light to promote uracil dimers. In the RNA schematic, blue = adenine, green = uracil, yellow = cytosine, and red = guanine 2) βPL induced acylation and alkylation of RNA and proteins. 3) Formalin induced cross-linking of RNA and proteins.

We set out to study the effect of UV light exposure as well as β PPL and formalin treatment on TMGMV structural integrity and its genome stability. Dose escalation studies were performed, and resulting inactivated TMGMV particles were characterized by size exclusion chromatography (SEC), dynamic light scattering (DLS), and transmission electron microscopy (TEM) to assess their physical state (**Figure 5.2 A, Supporting Figure 5.1-5.3**). Independent of the treatment modality or concentration, SEC indicated intact TMGMV particles; free or broken coat proteins were not detected (it should be noted that the resolution of the Superose 6 column does not allow to measure possible particle aggregation). The elution profile was consistent with native TMGMV and native or treated TMGMV particles eluted at \sim 8 mL from the Superose 6 column (**Supporting Figure 5.1-5.3**). As a complementary method, DLS was used to determine the hydrodynamic radius of TMGMV; DLS provides insight into the TMGMV formulation and its possible aggregation state, albeit an estimated measure given the high aspect ratio shape of TMGMV. DLS revealed signs of particle breakage when UV-TMGMV was treated with high doses of UV light (**Figure 5.2 A**). There was a trend that the average hydrodynamic radius of TMGMV decreased from 125 nm to 112, 102, 99, 91 and 78 nm with increasing UV doses of 0, 1, 5, 7.5, 10, and 15 J.cm⁻², respectively. DLS also revealed signs of particle aggregation in the β PPL-TMGMV formulations (**Figure 5.2 A**); compared to native TMGMV (125 nm average), β PPL-TMGMV recorded hydrodynamic radii between 165 and 215 nm in samples treated with 0, 100, 500, 750, 1000, and 1500 mM β PPL. In contrast, formalin treated TMGMV (Form-TMGMV) showed no signs of particle breakage nor aggregation with average lengths of 125 to 129 nm in samples treated with 0, 100, 250, 500, 750, and 1000 mM formalin (**Figure 5.2 A**).

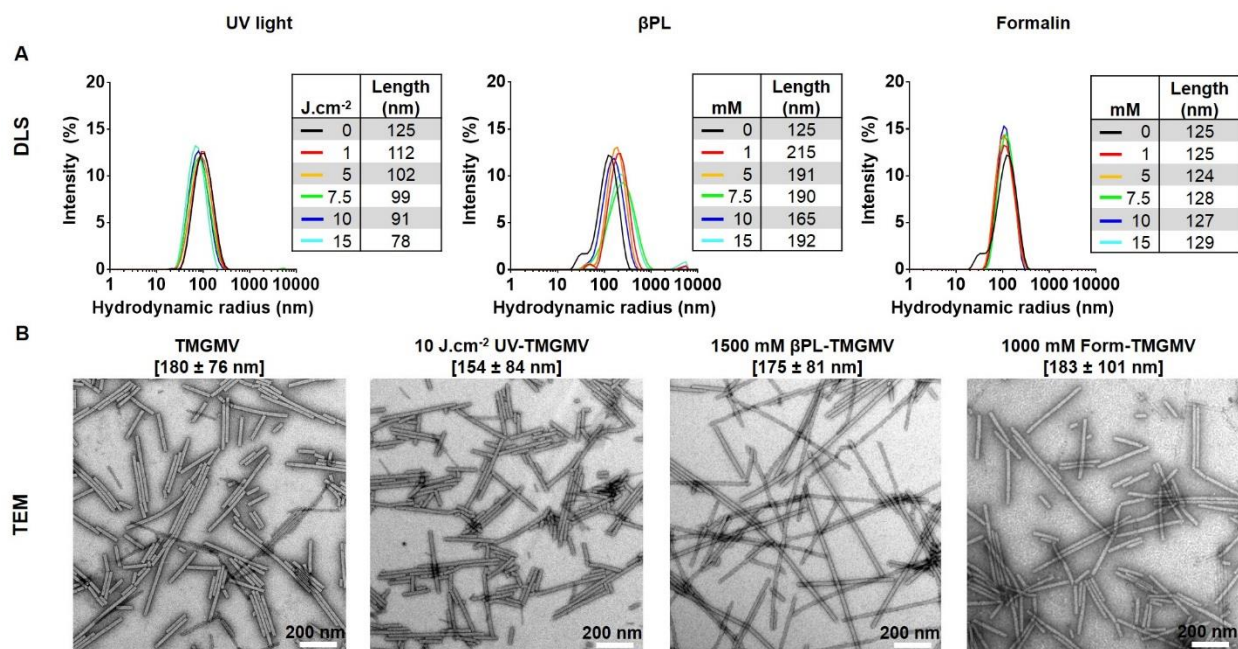


Figure 5.2. Characterization of inactivated TMGMV: part 1. (A) Dynamic light scattering of TMGMV treated with (left) UV light (0, 1, 5, 7.5, 10, and 15 J.cm⁻²), (middle) betaPL (0, 100, 500, 750, 1000, 1500 mM), and (right) formalin (0, 100, 250, 500, 750, 1000 mM). (B) TEM images of the inactivated TMGMV formulations (negatively-stained). Scale bars correspond to 200 nm.

In TEM images, the polydispersity of TMGMV was previously reported²¹⁸ and was attributed to the methods used to produce and purify TMGMV, as well as to prepare the TEM grid samples – during the drying process the particles are likely to break (**Figure 5.2 B**). TEM data concurred with the observations made by DLS. While the native TMGMV averaged a size of 180 ± 76 nm, the UV-TMGMV (154 ± 84 nm) revealed minor signs of breakage, and Form-TMGMV (183 ± 101 nm) retain its structural integrity. betaPL-TMGMV (175 ± 81 nm) did not show sign of aggregation but rather formed head-to-tail self-assembling filament. This phenomenon was previously reported using TMV assisted by aniline polymerization, and was attributed to a combination of hydrophobic interactions, electrostatic forces between the dipolar ends of adjacent particles.²⁷⁵ We hypothesize that the acylation and alkylation of amino acid residues (**Supporting Figure 5.4**) toward the opposite ends of TMGMV promotes such interactions.

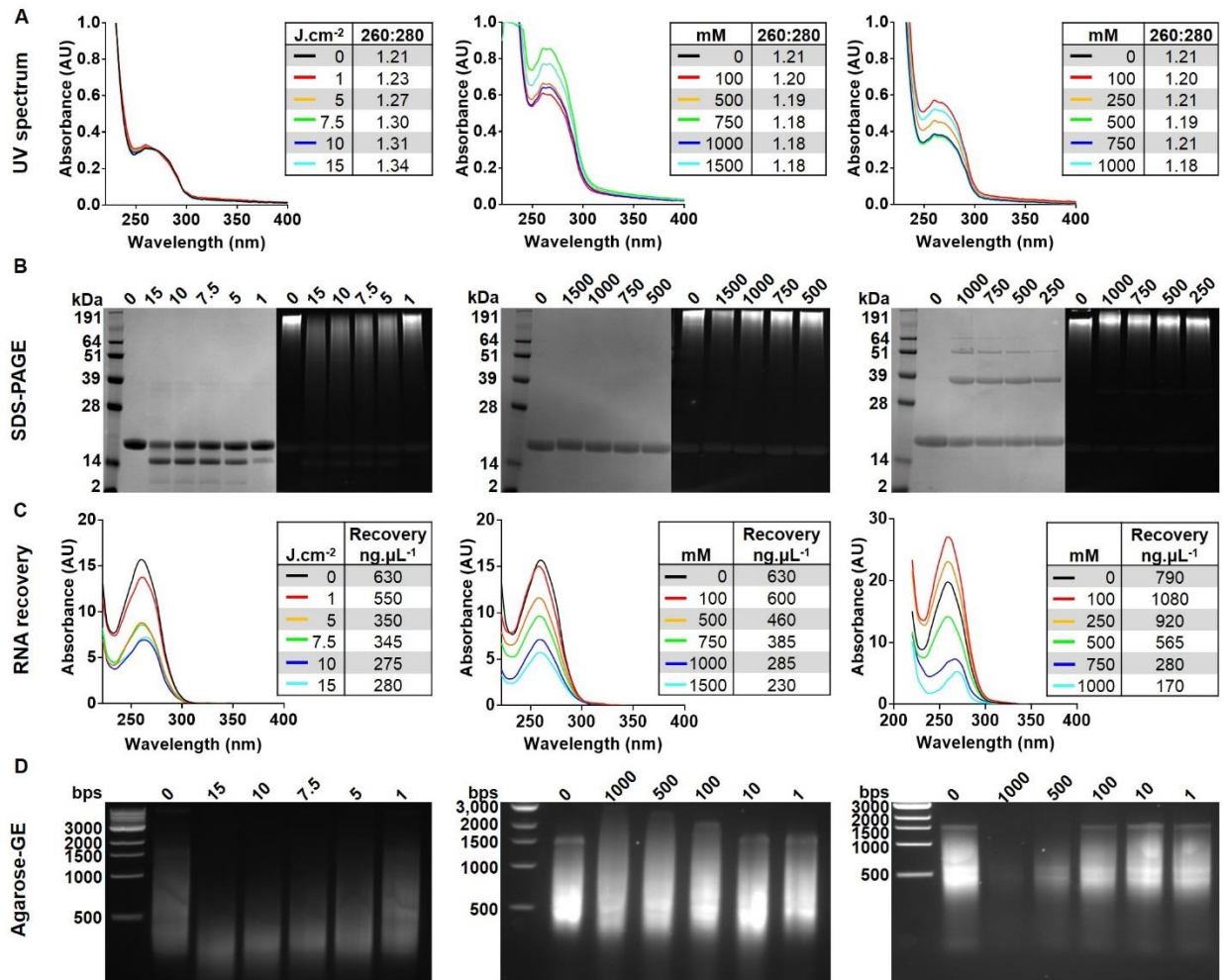


Figure 5.3. Characterization of inactivated TMGMV: part 2. (A), UV-visible light spectra of native and inactivated TMGMV. (B) Denaturing SDS-PAGE gels under white light after Coomassie staining (protein detection), and under UV light after GelRed staining (RNA detection). (C) UV-visible light spectra of RNA extracted from native and inactivated TMGMV. (D) Agarose-GE gels of the RNA extracted from UV-TMGMV, β PL-TMGMV, and formalin-TMGMV; under UV light after GelRed staining (RNA detection).

Next, we assessed the RNA state after UV, β PPL, and formalin treatment. TMGMV contains a positive-sense, single-stranded RNA genome of 6355 nucleotides and contains more than 400 sites of adjacent uracils prone to dimerization (**Supporting Table 5.1**). Overall, UV-visible spectroscopy indicated that the RNA to protein ratio (absorbance ratio at 260:280 nm) of β PPL-TMGMV and Form-TMGMV remained close to 1.2, indicating no degradation or loss of RNA – as expected (**Figure 5.3 A**). UV-TMGMV suffered from an increase in the 260:280 ratio from 1.2 to 1.3. We attribute this change to coat protein breakage, as was observed in the gel electrophoresis experiments (**Figure 5.3 B**). SDS-PAGE gels were imaged following staining for proteins and nucleic acid under white light and UV light. While the coat proteins of TMGMV are ~17 kDa in size, a second protein band (~14 kDa) was observed in the UV-TMGMV treated samples, and its intensity increased with UV dosage. It should be noted that free coat protein was not detectable by SEC (**Supporting Figure 5.1**); therefore, the smaller coat protein may be partially broken yet still be assembled in the nucleoprotein complex. We attempted to identify the amino acid sequence of the ~14 kDa and ~17 kDa bands by matrix-assisted laser desorption/ionization time-of-flight mass spectrometry (MALDI-TOF/MS), however, we were unable to clearly resolve the bands and thus could not obtain pure samples for analysis.

Denatured β PPL-TMGMV coat proteins showed no sign of protein breakage or aggregation regardless of the dose of β PPL used during the treatment. In contrast, the higher the dose of formalin, the more inter-CP crosslinking was observed, as indicated by the presence of an additional band with high molecular weight. GelRed staining of the RNA content of TMGMV particles, revealed no significant changes in RNA motility in β PPL-TMGMV and form-TMGMV samples, but signs of RNA breakage in samples treated with UV doses above 1 J.cm⁻² (**Figure 5.3 B**). The genome content of each formulation was further analyzed following RNA extraction from the TMGMV

formulations on native agarose gels (**Figure 5.3 C+D**). We observed that treatment doses higher than 1 J.cm⁻² of UV, or 10 mM of β PL and 100 mM formalin led to significant RNA damage and a decrease in total RNA recovery.

Based on these biochemical data, we hypothesized that a minimum of 5 J.cm⁻² of UV light, 100 mM β PL, and 500 mM of formalin would have been required to inactivate TMGMV; at these concentrations, the overall structural integrity of the particles was maintained, but RNA damage was visible.

5.3.1. Infectivity or lack thereof of inactivated TMGMV.

To confirm the dose of UV, β PL, or formalin required to inactivate TMGMV, we infected three plant species susceptible to TMGMV infection:

1) In *Nicotiana tabacum* Tennessee 86 (Tn86), which is a diagnostic species as well as propagation species, TMGMV elicits a strong, bright, yellow & green foliar mosaic with occasional necrotic patches (**Figure 5.4**); the symptoms are obvious by visual inspection and allow for photographic documentation.

2) *N. tabacum* Samsun-NN (Samsun-NN) is also a diagnostic species as well as propagation species; it is the propagation host used by Bioproducts to manufacture Solvinix (the TMGMV-based bioherbicide). While Samsun-NN produces high yields of TMGMV (1 to 3 mg/gram of fresh leaf tissue), the mosaic symptom in this host is mild and not always detectable by eye; it is quite difficult to photograph (**Figure 5.5**).

3) Tropical soda apple (TSA) (*Solanum viarum*), TMGMV elicits systemic necrosis that is almost invariable (**Figure 5.6**).

Tn86, Samsun-NN, and TSA were seeded and maintained in a greenhouse and challenged with native or UV/chemically treated TMGMV when the plants were about 30 days old; fully developed new leaves were mechanically inoculated by gently abrading with a Q-tips swab dipped in native or inactivated TMGMV. Five plant replicates were inoculated for each treatment condition in addition to a negative control (10 mM KP buffer). Leaves were imaged and harvested individually ~20 days post-inoculation (**Figure 5.4-5.6 and Table 5.2**).

Leaves inoculated with UV or chemically treated TMGMV showed no visual signs of infection in all three species (**Figure 5.4-5.6 and Table 5.2**). In addition to visual inspection for symptoms, RT-PCR was carried out on the total RNA content extracted from individual leaves to further attest for the presence of TMGMV infection or lack thereof (**Supporting Figures 5.5-5.7**). A total of three leaves per treatment condition was selected randomly and analyzed by RT-PCR. This method is a more sensitive assay as opposed to visual inspection of the leaves; for example, visual inspection of the leaves may indicate a lack of apparent infection when using 5 J.cm⁻² of UV, 500 mM βPL, or 500 mM formalin in either plant species tested (**Figure 5.4-5.6**). Yet, at these concentrations, the leaves were TMGMV positive in Tn86 and TSA. Agarose gel electrophoresis confirmed the inactivating UV dose was consistent amongst the 3 plant species tested (7.5 – 10 J.cm⁻²) (**Figure 5.4-5.6**). While 750 mM βPL was enough to inactivate TMGMV in Tn86 and Samsun-NN, 1500 mM was required to prevent TMGMV infection in the hyper-sensitive TSA. Therefore, one could inactivate TMGMV using 750 mM βPL and still use it as a bioherbicide with high specificity against TSA; which may be an interesting extension of the current formulation. Formalin was the least consistent treatment modality and required doses varying from 1000 mM, 250 mM, and 750 mM to inactivate Tn86, Samsun-NN, and TSA, respectively. Overall, the required treatment doses to prevent infection in all three plant species

were 10 J.cm⁻² UV, 1.5 M βPL 1 M formalin. However, given the variability of formalin dosage needed to achieve inactivation, this may be the least favorable to use for commercialization.

All three treatment modalities have their own set of advantages and disadvantages to produce inactivated TMGMV for safe agricultural and environmental applications (**Table 5.3**). UV treatment is the cheapest, fastest and most reproducible inactivation modality, but leads to shortening of the particles; 10 J.cm⁻² UV-TMGMV particles are on average 30 nm shorter than native TMGMV (or in other words 10% shorter than the native TMGMV). In contrast, βPL maintains particle integrity, although it leads to end-to-end alignment of TMGMV; furthermore, βPL is an expensive and biohazardous chemical; the chemical treatment also requires additional purification steps therefore reducing yields by 40-60%. Similarly, formalin maintains particle integrity but requires a long treatment incubation (5 days); the additional purification steps required to remove the treatment reagents are also at the cost of lower yields (40-60 %). Lastly, formalin treatment gave the least consistent inactivation results among different plant species, and therefore may require careful optimization for each species of interest. Altogether, UV inactivation may be the most suitable; it could be easily integrated into the purification process.

As previously mentioned, the inactivation of TMGMV by UV light has been reported in the 20th century using the focal lesion quantification method.^{267,271} These studies reported using different sources of UV light with various intensities and power settings, which makes it difficult to compare the results. In addition, the time of UV exposure was recorded to assess UV inactivation instead of the more accurate J.cm⁻² units of measure; for example, Ginoza *et al.* reported full inactivation of TMGMV after 2 min of UV exposure, while Streeter *et al.* stated that a 6 min exposure was required. Using our system, 2 min and 6 min of UV exposure would correspond to

~1 and ~2.5 J.cm⁻², respectively. At these concentrations, the leaves would appear symptomless but RT-PCR revealed the presence of infectious TMGMV (**Supporting Figures 5.5-5.7**).

The plant virus cowpea mosaic virus (CPMV) has been shown to be inactivated at UV doses of 2.5 J.cm⁻².²⁴⁶ CPMV consists of a bipartite ssRNA virus forming a 31 nm icosahedron with pseudo T=3 symmetry. The differences in UV dose required to yield inactivated virus preparations can be explained by differences in virus structure and assembly: CPMV's ssRNA genome is encapsulated into the internal cavity of the capsid; in contrast, TMGMV's genome is incorporated into the nucleoprotein assembly – thus the TMGMV is somewhat buried in the coat protein structure, which likely confers enhanced stability. The reported inactivation of mammalian viruses such as Influenza (ssRNA, ~1 J.cm⁻²)²⁷⁶ HIV (ssRNA, ~1 J.cm⁻²)²⁷⁷, Hepatitis A (ssRNA, ~0.3 J.cm⁻²)²⁷⁸ required lower doses, most likely due to a higher propensity for uracils in their genome to dimerize.

βPL and formalin are more commonly used to produce non-virulent mammalian virus vaccines.^{273,274} Compared to plant viruses, many mammalian viruses have a lipid envelop that can be crosslinked by formalin or acylated/alkylated by βPL; thus they generally require lower treatment doses to be inactivated. For example, the equine herpesvirus type I²⁷⁹, eastern equine encephalitis and poliomyelitis type II²⁸⁰, HIV²⁸¹, and the influenza virus²⁸² were successfully inactivated with 5-60 mM βPL. Hepatitis A²⁸³, Japanese encephalitis virus²⁸⁴, HIV²⁸¹, influenza A virus²⁸⁵, and rabies²⁸⁶ were also successfully treated with 5-120 mM of formalin. It is the structural integrity of TMGMV that makes it attractive for exploitation in nanoengineering and environmental applications; however, these same features make it harder – yet not impossible – to generate inactivated TMGMV preparations, yet the dose requires vs. mammalian vaccine development is about 10x fold higher.

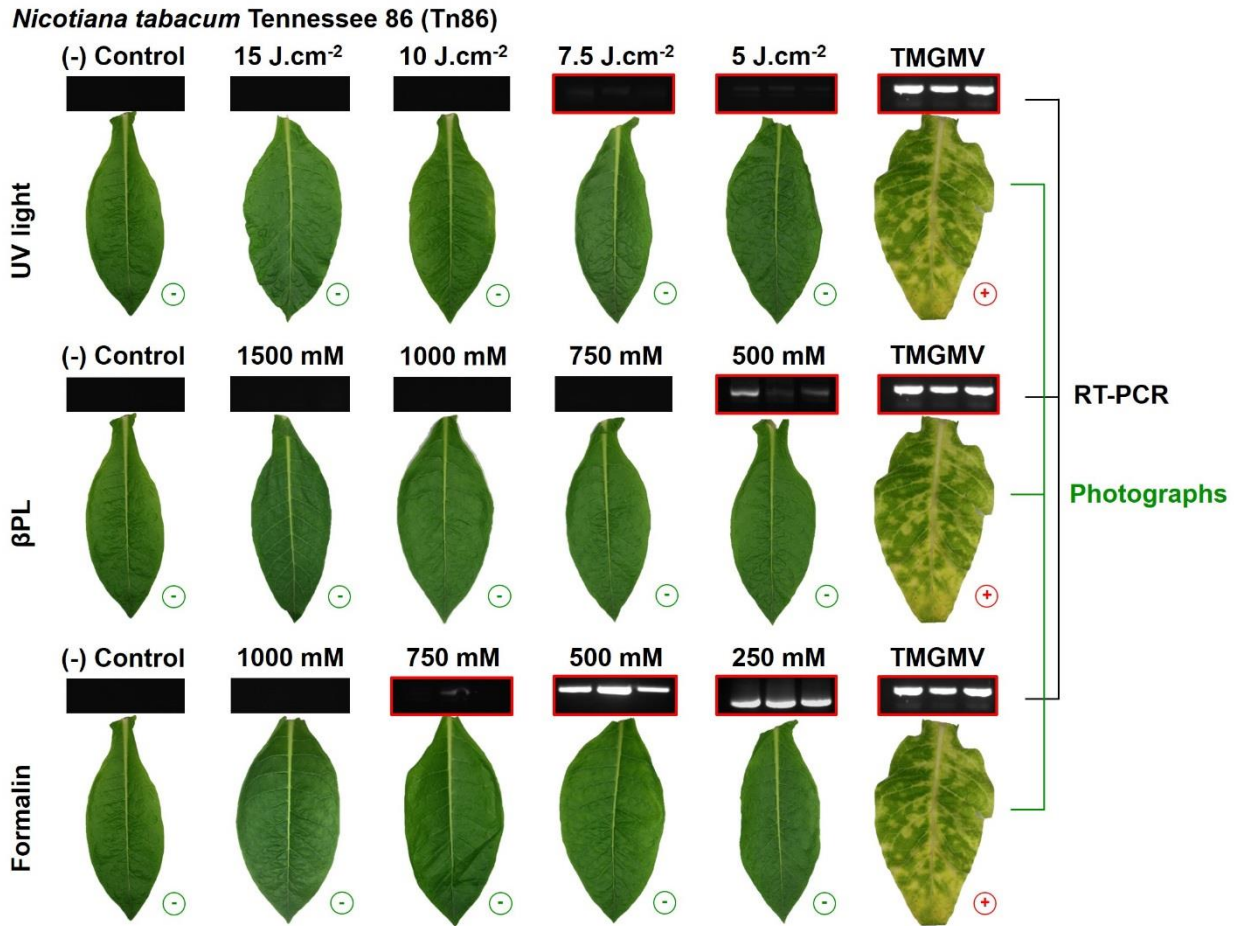


Figure 5.4. Infectivity of TMGMV v. inactivated TMGMV against Tn86. Depiction of individual leaves infected with TMGMV, UV-TMGMV, βPL-TMGMV, or Form-TMGMV at various doses. (-) indicates leaves that were visually symptomless, while (+) represents infected leaves. RNA was extracted from leaves and RT-PCR amplicons were obtained proportionally to the TMGMV infectivity level. RT-PCR results highlighted by red boxes depict conditions that were positive for TMGMV RNA within at least one leaf per condition.

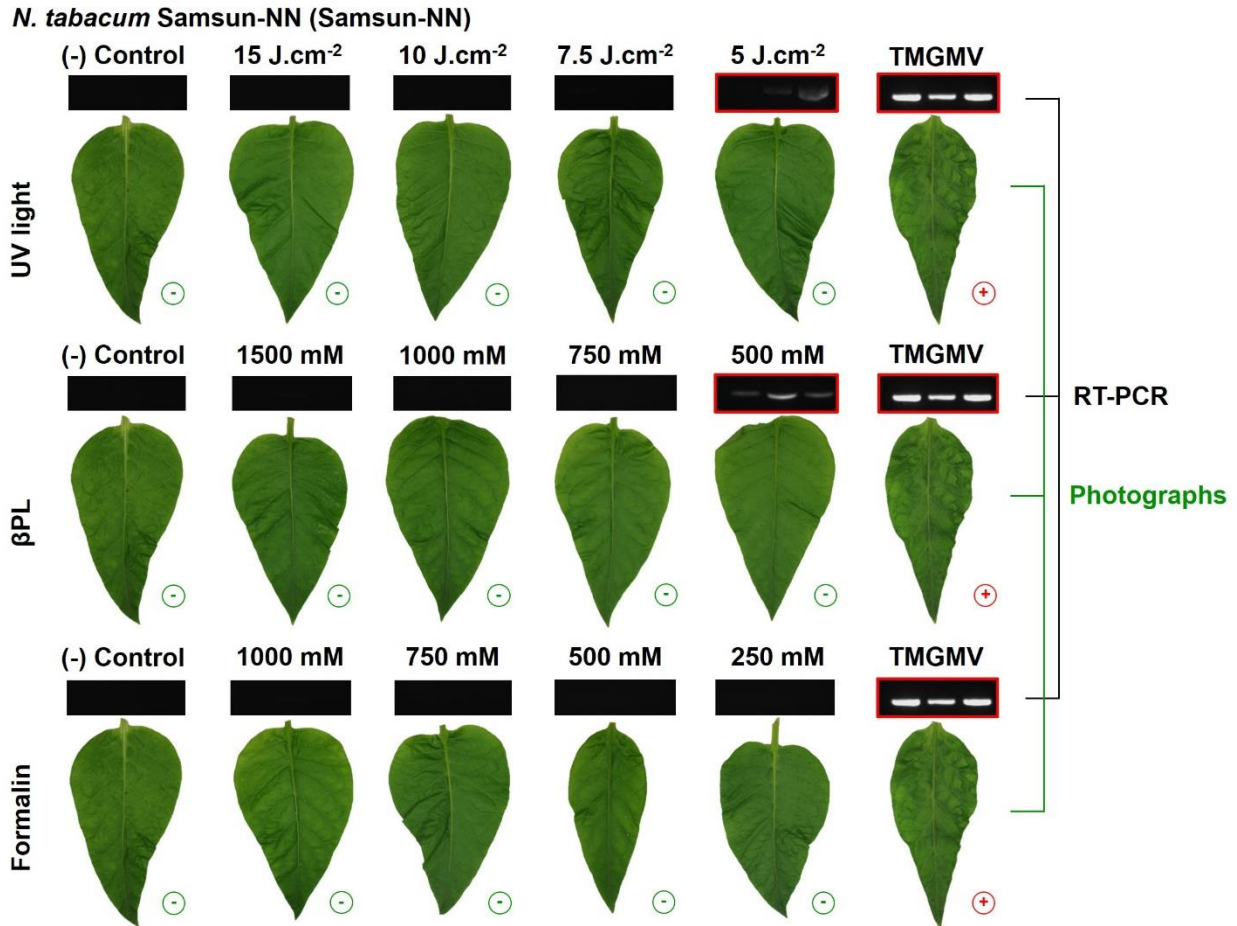


Figure 5.5. Infectivity of TMGMV v. inactivated TMGMV against Samsun-NN. Depiction of individual leaves infected with TMGMV, UV-TMGMV, βPL-TMGMV, or Form-TMGMV at various doses. (-) indicates leaves that were visually symptomless, while (+) represents infected leaves. RNA was extracted from leaves and RT-PCR amplicons were obtained proportionally to the TMGMV infectivity level. RT-PCR results highlighted by red boxes depict conditions that were positive for TMGMV RNA within at least one leaf per condition.

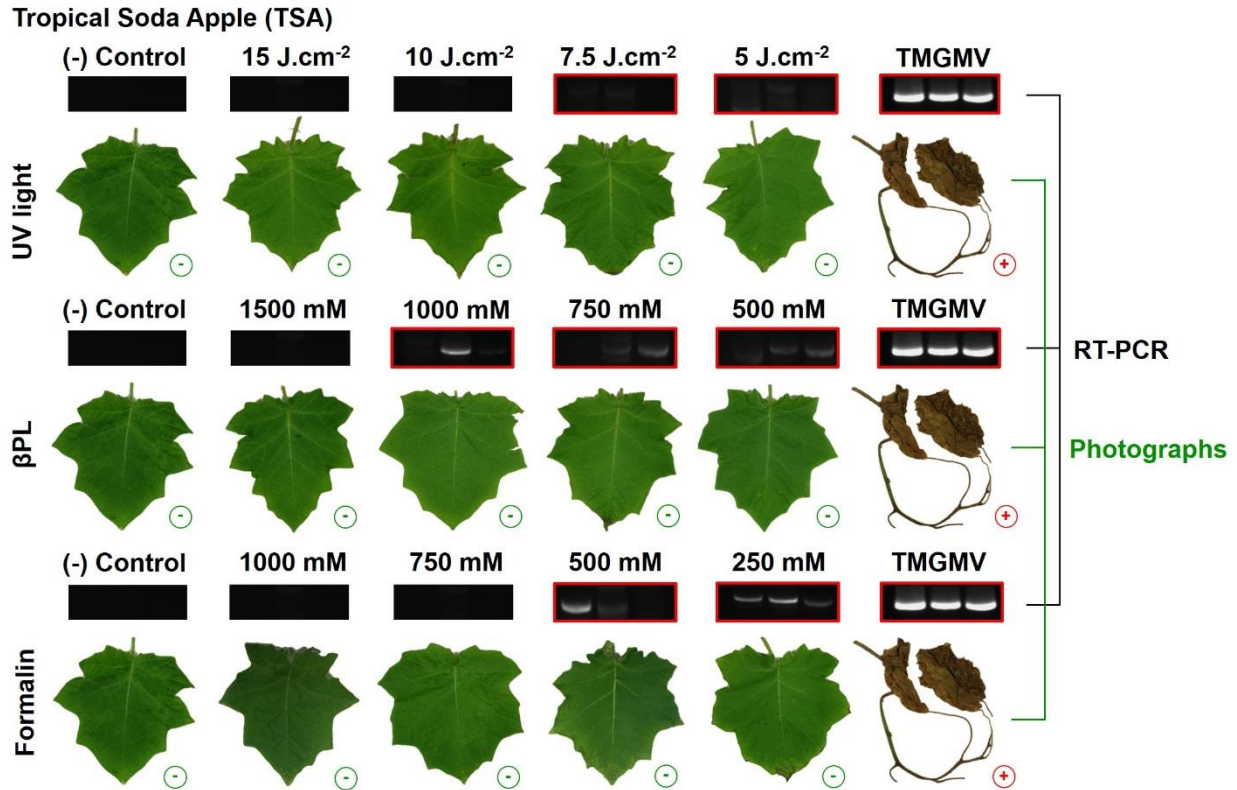


Figure 5.6. Infectivity of TMGMV v. inactivated TMGMV against TSA. Depiction of individual leaves infected with TMGMV, UV-TMGMV, βPL-TMGMV, or Form-TMGMV at various doses. (-) indicates leaves that were visually symptomless, while (+) represents infected leaves. RNA was extracted from leaves and RT-PCR amplicons were obtained proportionally to the TMGMV infectivity level. RT-PCR results highlighted by red boxes depict conditions that were positive for TMGMV RNA within at least one leaf per condition.

Table 5.2. Leaf infectivity as per visual inspection. (-) indicates no symptoms, while (+) indicates symptom level.

<i>Nicotiana tabacum</i> Tennessee 86 (Tn86)								
UV light	(-) Control	15 J.cm ⁻²	10 J.cm ⁻²	7.5 J.cm ⁻²	5 J.cm ⁻²	1 J.cm ⁻²	0.2 J.cm ⁻²	TMGMV
	-	-	-	-	-	+	-	++++
βPL	(-) Control	1500 mM	1000 mM	750 mM	500 mM	100 mM	1 mM	TMGMV
	-	-	-	-	-	+	++	++++
Formalin	(-) Control	1000 mM	750 mM	500 mM	250 mM	100 mM	1 mM	TMGMV
	-	-	-	-	-	-	++	++++
<i>N. tabacum</i> Samsun-NN (Samsun-NN)								
UV light	(-) Control	15 J.cm ⁻²	10 J.cm ⁻²	7.5 J.cm ⁻²	5 J.cm ⁻²	1 J.cm ⁻²	0.2 J.cm ⁻²	TMGMV
	-	-	-	-	-	-	-	++++
βPL	(-) Control	1500 mM	1000 mM	750 mM	500 mM	100 mM	1 mM	TMGMV
	-	-	-	-	-	++	+++	++++
Formalin	(-) Control	1000	750	500	250	100	1	TMGMV
	-	-	-	-	-	+	++	++++
Tropical Sodal Apple (TSA)								
UV light	(-) Control	15 J.cm ⁻²	10 J.cm ⁻²	7.5 J.cm ⁻²	5 J.cm ⁻²	1 J.cm ⁻²	0.2 J.cm ⁻²	TMGMV
	-	-	-	-	-	-	-	++++
βPL	(-) Control	1500 mM	1000 mM	750 mM	500 mM	100 mM	1 mM	TMGMV
	-	-	-	-	-	+++	+++	++++
Formalin	(-) Control	1000 mM	750 mM	500 mM	250 mM	100 mM	1 mM	TMGMV
	-	-	-	-	-	-	+	++++

Table 5.3. Pros and cons of TMGMV inactivation by UV, β PPL, and formalin.

	UV light	β -propiolactone	Formalin
Cost	requires a one-time purchase of a UV source (e.g. UVP crosslinker; \$2100)	requires continuous purchase of β PPL (\$302 for 10 mL)	requires continuous purchase of formaldehyde (\$23 per L of 10% solution)
Yield	100% recovery	40%-60% recovery	40%-60% recovery
Ease of application	20 min of UV treatment; could be integrated into the purification process	24 hr incubation at 4°C followed by 2 hr of β PPL inactivation at 37°C; requires additional purification	5 day incubation at 37°C; requires additional purification
Environmental health and safety	no environmental impact or health risks (no residual UV light from the samples)	hazardous compound removed during purification and rapidly inactivated at room temperature; thus considered safe	hazardous compound removed during purification and less stable at room temperature; thus considered safe
Particle integrity	some TMGMV shortening; RNA breakage above 1 J.cm ⁻²	head-to-tail particle assembly; RNA breakage and crosslinking above 10 mM β PPL	coat proteins crosslinking; RNA breakage and crosslinking above 100 mM formalin

5.4. Conclusions.

To date, TMGMV is the only EPA approved viral nanoparticle for its use as an herbicide but is limited by its application in the state of Florida. To advance and broaden the use of TMGMV as a pesticide nanocarrier, we addressed its potential risk to the environment by inactivating its infectivity, rendering it harmless to any crop. TMGMV was inactivated with 10 J.cm⁻² of UV light, 1500 mM βPL, and 1000 mM formalin, laying the ground for the development of eco-friendly and non-infectious viral pesticide nanocarriers.

Chapter V, in full, is in preparation for submission to a peer-reviewed journal, 2020. Chariou, P.L. Roskopf, E.N., Hong, J.C, Charudattan, R., Steinmetz, N.F. *Chemical and UV Light Inactivation of TMGMV for Environmental Applications*. The dissertation author was the primary investigator and author of this paper.

Chapter VI: Diffusion and Uptake of a High Aspect Ratio Nanocarriers in Tumor Tissue

6.1. Introduction.

Nanoparticle carriers are used for targeting chemotherapies and immunotherapies to tumors to increase tissue specificity and effective payload delivery with reduced systemic adverse effects. Most nanoparticle-encapsulated cancer therapeutics are delivered to the tumor site by exploiting the local tumor environment consisting of the combination of leaky vasculature and deficient lymphatic clearance, *i.e.*, enhanced permeability and retention (EPR). Some strategies also exploit the targeting of disease-specific molecular signatures, as yet no targeted nanoparticle has been translated into clinical treatment. If a target site can be identified, then the carrier diffusion and distribution of the delivered payload are critical to treatment success. Nanoparticles injected in the systemic circulation target either the vasculature or the periphery of the tumor. Limited nanoparticle-carrier diffusion can prevent drug accumulation to a lethal concentration in the tumor tissue and therefore promote cancer cell survival. Surviving cancer cells often become more aggressive and develop a drug resistance phenotype.²⁸⁷ Here, I develop the basis for quantitative analysis of nanoparticle diffusion and uptake in a solid tumor.

Nanoparticle size and shape as well as surface chemistry determine the fate of the carrier and its efficacy. A growing body of data shows increased tumor homing and tissue penetration with elongated, rather than spherical, nanomaterials.^{254,255,288} Elongated, rod-shaped or filamentous nanoparticles have enhanced margination (migration toward blood-vessel walls) and increased transport across tissue membranes. Geng et al.²⁸⁹ demonstrated that virus-like filomicelles with higher aspect ratios than spherical particles deliver the chemotherapeutic drug paclitaxel to human-derived tumor xenografts in mice more effectively and with increased

efficacy. Chauhan et al.²⁹⁰ compared the intratumoral diffusion of biostable colloidal quantum dots as nanorods and nanospheres with identical charge and surface coating. Nanorods penetrated tumors 4.1 times faster than nanospheres of the same hydrodynamic radius and occupied a tumor volume 1.7 times greater. Correspondingly, we found that filamentous potato virus X (PVX) compared to spherical cowpea mosaic virus (CPMV) has enhanced tumor homing and tissue penetration, particularly in the core of the tumor.²⁹¹ Contradictory results were obtained by Reuter et al.,²⁹² who compared sphere-like and rod-shaped nanogels using PRINT technology. They observed that smaller nanospheres had 5 fold greater tumor accumulation compared to higher aspect ratio nanorods. I hypothesize that this difference may be due to the different tumor model used. It has been previously shown that differences in tumor vasculature (*e.g.* density and leakiness) affect shape-dependent nanoparticle extravasation.²⁹³ In addition, other factors may have influenced the results, such as the differences in surface charge (CPMV has a negatively charged surface while the nanogels have a positively charged surface) and aspect ratio (PVX has an aspect ratio of 40 while the rod-shaped nanogel only has an aspect ratio of 4). Therefore, there is a need to investigate the mechanics of diffusion and accumulation of high aspect ratio nanoparticles within the tumor microenvironment.

To complement experimental work in nanoparticle therapies, mechanistic mathematical modeling and computer simulation can be used to better understand experimental results and provide quantitative guidance for more efficient design of nanotherapeutics. Optimizing carrier and drug penetration into the tumor tissue is critical to maximize the therapeutic effect. Toward this goal, I developed a mathematical model of nanoparticle diffusion and uptake in a spheroid approximation of a solid tumor segment without capillaries. Our model differs from other models that can be found in the literature^{294,295} by taking into account the effect of shape and size on the

diffusion constant of nanoparticles. Our model also builds on the previous models by incorporating the rate of endocytosis and how it is affected by size, shape, and surface modification (*e.g.*, shielding vs targeting) of nanoparticles. As the model nanoparticle, I used the nucleoprotein components of the tobacco mosaic virus (TMV). Virus-based plant nanoparticles, such as TMV, provide a unique platform for nanomedical engineering because their dimensions are known and tunable on the molecular level, which cannot readily be accomplished with synthetic nanoparticles.

Native TMV particles form a cylindrical structure measuring 300×18 nm with a 4 nm-wide hollow interior channel. TMV is composed of single-stranded RNA wrapped inside a hollow nanotube formed by 2130 identical coat proteins. TMV offers a programmable scaffold for both genetic engineering and chemical bioconjugation to impart new functionalities, *e.g.* therapeutic payloads.^{234,296} TMV virion formation can be initiated by self-assembly of coat proteins from an RNA hairpin forming sequence. This origin of assembly site (OAS) is the only sequence required to promote a bidirectional coat protein self-assembly along the template RNA. This principle has been exploited to produce TMV nanotubes with diverse shapes such as kinked nanoboomerangs or branched tetrapods.²⁹⁷ This RNA-templated self-assembly principle has also been used to produce TMV-like nanotubes with distinct longitudinal domains²⁹⁸ as well as materials of defined aspect ratio.²⁹⁹ In previous studies, we have shown that biodistribution and tumor homing is a function of the carrier's aspect ratio. With higher aspect ratio, particles avoid clearance by the mononuclear phagocyte system, resulting in increased tumor homing.²⁹⁹ Nevertheless, a balance must be established between immune evasion, tumor homing, and tissue penetration. While higher aspect-ratio materials have enhanced tumor homing, the higher molecular weight particles have slower diffusion rates. The TMV platform technology provides a high precision platform with which to specify aspect ratio and surface chemistries that affect tissue penetration in tumor

spheroids.

I chose to study TMV diffusion in a spheroidal cell-culture system with different sizes and cell densities. This 3D cellular system mimics a small segment of a solid tumor between capillaries and bridges the gap between 2D tissue culture and *in vivo* mouse models for screening therapeutics.^{294,295,300–302} In tumor tissue, the combination of leaky vasculature and deficient lymphatic clearance leads to diffusion as the driving mode of nanoparticle transport and penetration into the tumor tissue.³⁰³ For this study, I focused on ‘stealth’ TMV formulations with reduced cell uptake rates produced by coating the particle surface with polyethylene glycol (PEG). Targeted TMV formulations with molecular specificity and increased cellular uptake rates were simulated by displaying the integrin specific peptide ligand RGD on their surface. PEG and RGD are surface modifiers frequently used in nanoparticle engineering to promote immune evasion and targeted endocytosis, respectively. These coatings serve as good model systems whose results can be translated to other nanoparticle formulations.

6.2. Theoretical methods.

I developed a mathematical model of TMV diffusion and uptake in a spheroid tumor model to evaluate the effect of particle aspect ratio (maximum to minimum principal axis lengths). The input to this model was a bolus injection of a known TMV mass in the medium surrounding the tumor (**Figure 6.1 A**). TMV diffuses from the surrounding medium into the spheroid interstitial space. The rate of diffusion in the interstitial space is much slower than in the surrounding medium so that the distribution of TMV in the surrounding medium is uniform (**Supporting Equations 6.1**). In addition, the volume of the surrounding medium is much greater than the volume of the spheroid so that the changes in TMV concentration in the surrounding medium are negligible (**Supporting Equations 6.1**). The tumor cell density within the spheroid segment is uniform and

considered as a continuum. The rates of cell proliferation and death are assumed negligible relative to the other TMV rate processes so that the viable cell volume remains constant. From the interstitial space, I assume that TMV is taken up irreversibly by tumor cells at a constant rate that is dependent on the aspect ratio and surface chemistry of TMV nanorods (**Figure 6.1 B**). Furthermore, the TMV does not interact with extracellular matrix (ECM) components and cannot bind to them.

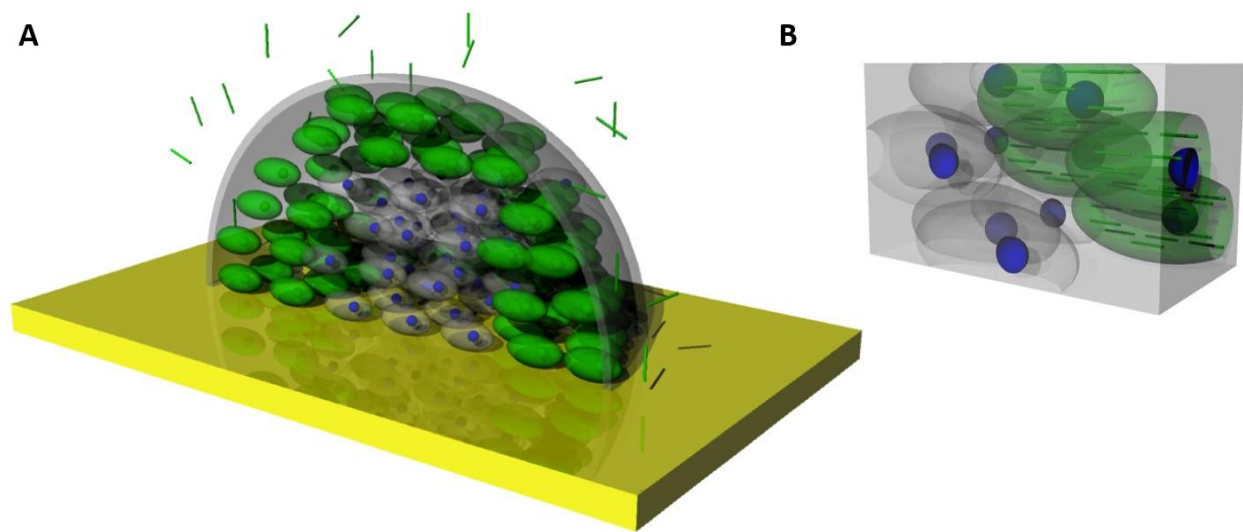


Figure 6.1. Theoretical diffusion of TMV through a tumor spheroid. (A) 3D schematic of the diffusion of high aspect-ratio nanoparticles into the tumor half spheroid model. (B) Zoom-in schematic of the interior of the spheroid. Cells in green represent cancer cells that have taken up TMV particles, while cells in gray are cancer cells without TMV inside them.

6.2.1. TMV dynamics. The dynamic mass concentration distribution of TMV within the interstitial space of a spheroid segment of radius R can be described as:

$$\frac{\partial C_s}{\partial t} = D \frac{1}{r^2} \frac{\partial}{\partial r} \left[r^2 \frac{\partial C_s}{\partial r} \right] - kC_s, \quad 0 \leq r \leq R \quad (\text{Eq. 6.1})$$

where C_s is the concentration of TMV in the interstitial space at any location in the spheroid, D is the constant TMV diffusion coefficient, and k is the constant rate at which TMV is irreversibly taken up by cells. At the interface of the surrounding medium with the spheroid, the TMV concentration is continuous with the interstitial fluid of the spheroid:

$$r = R: \quad C_s = C_M \quad (\text{Eq. 6.2})$$

Where C_M is the concentration of TMV in the surrounding medium. After a bolus injection of TMV into the surrounding medium, C_M equals the ratio of the injected mass of TMV (m_{TMV}) to the volume of the surrounding medium (V_M). At the center of the spheroid, by spherical symmetry there is no net diffusion flux so that the concentration gradient is zero:

$$r = 0: \quad \frac{\partial C_s}{\partial r} = 0 \quad (\text{Eq. 6.3})$$

Initially, there is no TMV in the interstitial space of the spheroid:

$$t = 0: \quad C_s = 0, \quad 0 \leq r \leq R \quad (\text{Eq. 6.4})$$

6.2.2. Model transformation. As described in the **Supporting Equations 6.2**, we can transform the governing equation of the spheroid into rectangular coordinates with constant coefficients by defining $g(r, t) = rC_s(r, t)$. Consequently, we obtain

$$\frac{\partial g}{\partial t} = D \frac{\partial^2 g}{\partial r^2} - kg \quad (\text{Eq. 6.5})$$

with the initial condition:

$$t = 0: \quad g = 0, \quad 0 \leq r \leq R \quad (\text{Eq. 6.6})$$

and the boundary conditions:

$$r = 0: \quad g = 0 \quad (\text{Eq. 6.7})$$

$$r = R: \quad g = RC_M \quad (\text{Eq. 6.8})$$

As described in the **Supporting Equations 6.3**, we solve these model equations by the numerical method of lines in which the spatial derivatives are discretized; consequently, the problem is expressed as an initial-value problem involving a set of differential equations. For the numerical solution, I used the MATLAB code “ode15s”.

6.2.3. Model parameter values. The model parameter values known from direct measurement are the mass of TMV (m_{TMV}) injected, the volume of the surrounding medium (V_M), and the radius of the spheroid (R). The parameters that must be estimated indirectly are the cellular uptake rate coefficient (k) and the diffusion coefficient (D). For each experiment, these coefficients are constants. This implies that free receptors are always available at the cell surface so that k is constant in any experiment. For different experiments, however, their values change depending on their surface area, shape (*i.e.*, aspect ratio) and cell density within the spheroid (ϕ). The uptake rate coefficient is directly proportional to the total cell surface area as indicated by the cell density, where $k = k_0\phi$. The diffusion coefficient is a complex function of the cell shape and cell density.

6.2.4 Diffusion coefficients. The diffusion of spherical nanomaterials can be estimated using the

Stokes–Einstein equation:

$$D_0 = \frac{k_B T}{6\pi\eta R_H} \quad (\text{Eq. 6.9})$$

where k_B is the Boltzmann constant, T is the temperature of the system, η is the solvent viscosity and R_H is the hydrodynamic radius of the particle. For cylindrical TMV nanoparticles, we consider the diffusion coefficients for axial (ν_t) and transverse (ν_r) motions³⁰⁴:

$$D_t = \frac{\left(\ln\left(\frac{L}{d}\right)\nu_t\right)k_B T}{2\pi\eta L}; D_r = \frac{\left(\ln\left(\frac{L}{d}\right)\nu_r\right)k_B T}{4\pi\eta L} \quad (\text{Eq. 6.10})$$

where L and d are the length and the diameter of TMV respectively, ν_t is the characteristic axial velocity of TMV, and ν_r is the characteristic transverse velocity of TMV. As presented in the **Supporting Equations 6.4**, the values of ν_t and ν_r for TMV were established based on the literature.³⁰⁵ For random diffusion (D_{rt}) of an elongated cylindrical nanoparticle in the surrounding medium³⁰⁴:

$$D_{rt} = \frac{\left(\ln\left(\frac{L}{d}\right)\nu\right)k_B T}{3\pi\eta L}; \nu = \frac{|\nu_t| + |\nu_r|}{2} \quad (\text{Eq. 6.11})$$

Furthermore, to evaluate the diffusion coefficient of TMV within the tumor spheroid space (D_{int}), we take into account the presence of matrix proteins, mostly collagen³⁰⁶:

$$D_{\text{int}} = D_{\text{it}} e^{\frac{-r_p \sqrt{\varepsilon}}{r_f}} \quad (\text{Eq. 6.12})$$

where ε is the volume fraction of the tumor interstitial matrix (0.06 for spheroids)²⁹⁵, r_p is the effective radius of TMV (70 nm)³⁰⁷, and r_f is the effective radius of tumor matrix proteins (20 nm for collagen)³⁰⁸. Finally, the diffusion coefficient of TMV in the porous spheroid containing cells (D), takes into account the presence of immobilized cells^{295,309}:

$$D = D_{\text{int}} (1 - \phi)^2 \quad (\text{Eq. 6.13})$$

where ϕ is the cell density. The effects of the aspect ratio on diffusion coefficients in the surrounding medium and in the spheroid are presented in the **Supporting Equations 6.5**.

6.3. Experimental methods.

6.3.1. Rate of cellular uptake. The rate of cellular uptake of RGD-modified or PEGylated TMV in cancer cells expressing $\alpha_v\beta_3$ integrins was characterized experimentally. First, the rate of cellular uptake of TMV-RGD with a length of 300 nm was quantified *in vitro*. MDA-MB-231 cells (triple negative breast cancer) were cultured in high glucose Dulbecco's modified Eagle medium (DMEM) with L-glutamine (Fisher), and supplemented with 10% (v/v) FBS and 1% (v/v) penicillin–streptomycin. Cells were grown to confluency at 37°C and 5% CO₂. MDA-MB-231 cells were collected using enzyme-free Hank's-based cell dissociation buffer (Invitrogen). 500,000 cells/200 μ L media/well were added to an untreated 96-well v-bottom plate. Triplicates of sulfo-Cyanine5 azide (Cy5)-labeled TMV-RGD (300 nm long) were added at a concentration of 100,000 particles/cell and incubated for 3 h, 1.5 h and 0.5 h at 37°C, 5% CO₂. The Cy5-TMV-RGD particles

were synthesized and characterized as described by Pitek et al.³¹⁰ Control experiments were conducted, in triplicate, with no particles present. Post-incubation with TMV nanoparticles, cells were spun down at 500 g for 4 min. Supernatant was discarded, cells were washed twice in FACS buffer (0.1 mL 0.5 M EDTA, 0.5 mL FBS, and 1.25 mL 1M HEPES pH 7.0 in Ca²⁺ and Mg²⁺ free PBS (50 mL total volume)), and fixed in 2% (v/v) paraformaldehyde in FACS buffer at room temperature for 10 min. Cells were washed twice after fixing and resuspended in PBS. Samples were transferred to a 384 flat bottom black polystyrene plate (Corning) for fluorescence analysis. The resulting fluorescence intensity (ex/em 600/665 nm) was quantified using an Infinite 200 plate reader and the software Tecan i-control (version 1.10.4.0). The number of Cy5-TMV-RGD particles internalized per cell was calculated using a standard curve. The rate of cellular uptake of PEGylated or RGD targeted TMV of various aspect ratios (L/d) of constant diameter (d = 18 nm) but distinct length (L = 300 nm, L = 135 nm, and L = 59 nm) was then extrapolated from data published by our lab²⁹⁹ by comparing the rate of cellular uptake of TMV-RGD (L = 300 nm) calculated above to the relative rate of cellular uptake of PEGylated or RGD targeted TMV.

6.4. Results and discussion.

Our tumor microenvironment system consists of a spheroidal cancer cell-culture whose diameter can vary between a few hundred micrometers to 1 mm, which corresponds to the heterogeneous spacing of capillary distribution within the tumor (**Figure 6.1**). Modeling the diffusion of nanoparticles in the tumor tissue and quantifying the time scales as a function of capillary and cell density could inform dosing and administration schedules. The physiological barriers and diffusion rates of nanoparticles also depend on nanoparticle shape, size and surface chemistry. The simulated effects of spheroid radius, cell density, and aspect ratio on the TMV

concentration distributions without cellular uptake are shown in **Figures 6.2, 6.3** and **6.4**, respectively. The parameters used in each of these figures are summarized in **Table 6.1**. These results and their significance are discussed in the following sections.

Table 6.1. Parameters used for the model simulations in Figures 6.2, 6.3 and 6.4.

	Spheroid Radius (R) [nm]	Cell Density	Aspect Ratio (L/d)	Diffusion Coefficient (D) [mm².sec⁻¹]
Figure 2	100	0.5	300/18	5.38x10 ⁻⁷
	200			
	500			
Figure 3	200	0.5	300/18	5.38x10 ⁻⁷
		0.7		
		0.9		
Figure 4	200	0.5	300/18	5.38x10 ⁻⁷
			135/18	8.98x10 ⁻⁷
			59/18	1.25x10 ⁻⁶

6.4.1. Effect of tumor spheroid radius on TMV diffusion (without cellular uptake).

The spheroid segment radius represents the distance between capillaries. The intercapillary distance is highly regulated by a fine balance between angiogenic factors that promote or inhibit vessel growth, as well as the oxygen and nutrient consumption by the surrounding cells.³¹¹ In healthy tissue, particle diffusion from the vessels to the cytoplasmic membrane of surrounding cells does not exceed 100 μm .³¹² In the tumor microenvironment, however, the oxygen consumption is lowered and the tolerance of cancer cells to hypoxic conditions is increased. Tumors with a high rate of oxygen consumption have a higher microvascular density and, therefore, a smaller intercapillary distance. On the other hand, tumors with a low rate of oxygen

consumption have a lower microvascular density and, therefore, a higher intercapillary distance.³¹³ This phenomenon is currently being investigated for nanoparticle-based antiangiogenic tumor therapy.³¹⁴ By reducing the oxygen supply to the tumor site, anti-angiogenic tumor therapies aim to prevent the growth and aggressiveness of the tumor.

To quantify the effect of different intercapillary distances within the tumor microenvironment, I simulated the diffusion of TMV in a spheroid system without cellular uptake for a range of radii in the absence of cellular uptake (**Figure 6.2**). Within the tumor cell spheroid, the simulated concentration distributions at various times of TMV with different spheroid radii are shown in two and three dimensions. The TMV concentration is highest at the interface with the surrounding medium ($r = R$) and decreases as TMV diffused to the center of the tumor spheroid ($r = 0$). A spheroid of radius $R = 100 \mu\text{m}$ corresponds to relatively low intercapillary distance as in healthy tissue, whereas $R = 500 \mu\text{m}$ corresponds to higher intercapillary distance as with tumors. For $R = 100 \mu\text{m}$, the steady-state concentration, which is equal to the concentration of TMV in the surrounding medium ($0.1 \text{ mg}\cdot\text{mL}^{-1}$), is reached at the spheroid center in less than 6 h, whereas for $R = 200 \mu\text{m}$ it takes 18 h (**Figure 6.2**). For $R = 500 \mu\text{m}$ only 68% of the initial TMV concentration reaches the spheroid center within 24 h. This poor tumor penetration correlates with increasing risks of survival of cancer cells and promotes drug resistance.²⁸⁷

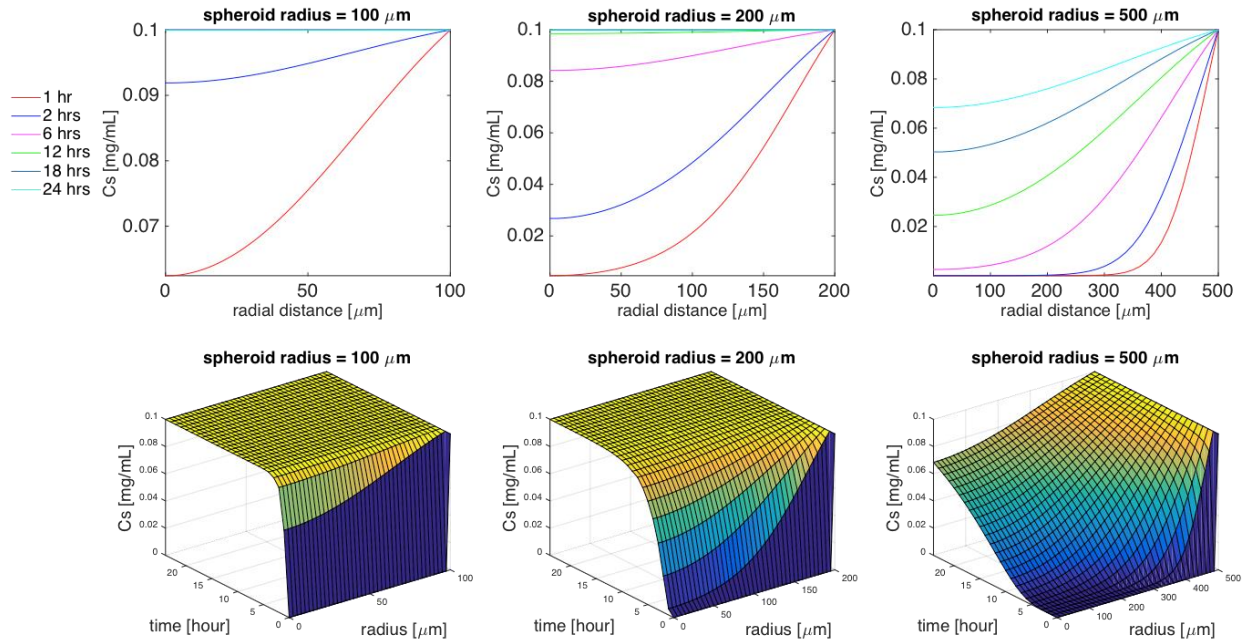


Figure 6.2. Effects of spheroid radius on TMV's distribution. Top 3 panels are 2D plots of the concentration of TMV as a function of the radial distance within the spheroid for specific time interval (1 h, 2 h, 6 h, 12 h, 18 h, 24 h), and the bottom 3 panels are the corresponding 3D plots of the concentration of TMV as a function of both time and radial distance. Cell density $\phi = 0.5$, TMV concentration in the surrounding medium $C_M = 0.1 \text{ mg}\cdot\text{mL}^{-1}$, cell uptake $k = 0$, TMV aspect ratio $L/d = 300/18$.

6.4.2. Effect of cell density on TMV diffusion (without cellular uptake).

When the tumor cell density increases, the cytotoxicity of chemotherapeutic drugs such as vincristine, bleomycin, and doxorubicin is impaired.³¹⁵ Increasing the cancer cell density within the spheroid decreases the void volume through which nanoparticles can diffuse as represented by a smaller diffusion coefficient. With high cell density, the limitation of TMV nanoparticle penetration is a major barrier to chemotherapeutic drug delivery in the deep tissue, which also correlates with increasing risks of survival of cancer cells and promotes drug resistance.²⁸⁷

The effect of cell density ϕ on the diffusion coefficient of TMV nano-rods (as expressed by Eq. 13) is computed in **Supporting Equations 6.5**. For a spheroid radius of $200 \mu\text{m}$ in the absence

of cell uptake, the simulations shown in **Figure 6.3** quantify the effect of cell density ϕ on the time required for the TMV to reach the spheroid center. When $\phi = 0.9$, the concentration at the center of the spheroid reaches 3.3% of the initial TMV concentration within 24 h. For $\phi = 0.7$, there is a 30-fold increase of TMV concentration at the center within the same time interval. A further decrease to $\phi = 0.5$ allows TMV to reach the steady-state concentration at the center of the spheroid within 18 h.

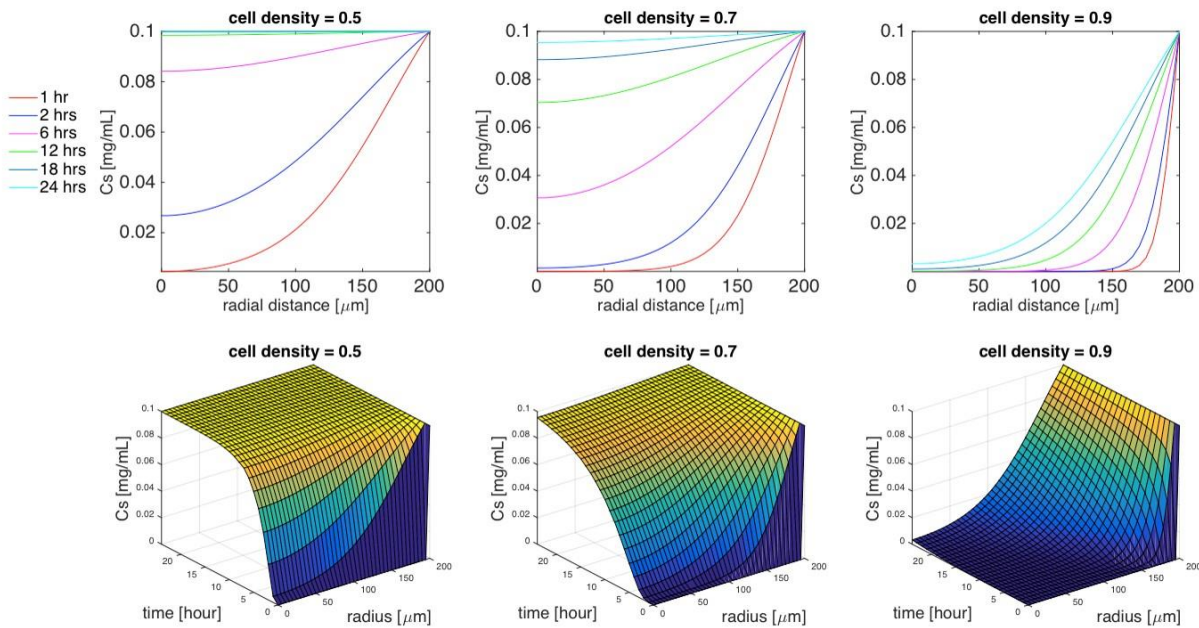


Figure 6.3. Effects of cell density on TMV's distribution. Top 3 panels are 2D plots of the concentration of TMV as a function of the radial distance within the spheroid for specific time interval (1 h, 2 h, 6 h, 12 h, 18 h, 24 h), and the bottom 3 panels are the corresponding 3D plots of the concentration of TMV as a function of both time and radial distance. Spheroid radius $R = 200 \mu\text{m}$, TMV concentration in the surrounding medium $\text{CM} = 0.1 \text{ mg}\cdot\text{mL}^{-1}$, cell uptake $k = 0$, TMV aspect ratio $L/d = 300/18$.

6.4.3. Effect of TMV aspect ratio on diffusion (without cellular uptake).

In the spheroid cell system, I investigated diffusion of TMV with different nanorod aspect ratios indicated by L/d: TL-long (300/18 ~ 16.5), TM-medium (135/18 ~ 7.5), and TS-short (59/18 ~ 3.5). The model parameters were set as follows: cell density $\phi = 0.5$, spheroid radius $R = 200 \mu\text{m}$, cell uptake $k = 0$. As observed from **Figure 6.4**, the time necessary for TMV to reach the spheroid center was reduced when the aspect ratio was decreased: TL, TM, and TS require 18, 10, and 7 h respectively to reach steady-state concentration.

While smaller aspect-ratio rod-shaped nanoparticles have higher diffusion and accumulates more easily in the deep tumor tissue, the higher aspect-ratio nanoparticles have enhanced margination toward blood-vessel walls, increased transport across tissue membranes, and reduced clearance by phagocytosis.^{254,255,288,299,316} In other words, a “one-size-fits-all” nanoparticle does not exist and a compromise must be made to optimize the diffusion and accumulation of nanoparticles within the tumor without impairing their ability to extravasate (*i.e.*, move from blood to extravascular space), cross tissue membranes, and evade the immune system. With complementary data, this model can provide a basis for predicting the aspect ratio that promotes optimal accumulation of nanoparticles injected intravenously.^{289–291} Perhaps, a better approach would be to inject intravenously a cocktail of TMV nanoparticles with various aspect ratios. In this scenario, the lowest aspect-ratio TMV are less likely to reach the tumor site, but the fraction that do penetrate the tumor can diffuse more readily than the higher aspect ratio TMV in the deep tumor tissue. In the meantime, the higher aspect ratio nanoparticles can reach the tumor site more readily, but only accumulate in the peripheral tissue of the tumor. The net result would be to improve overall drug distribution and maximize efficacy.

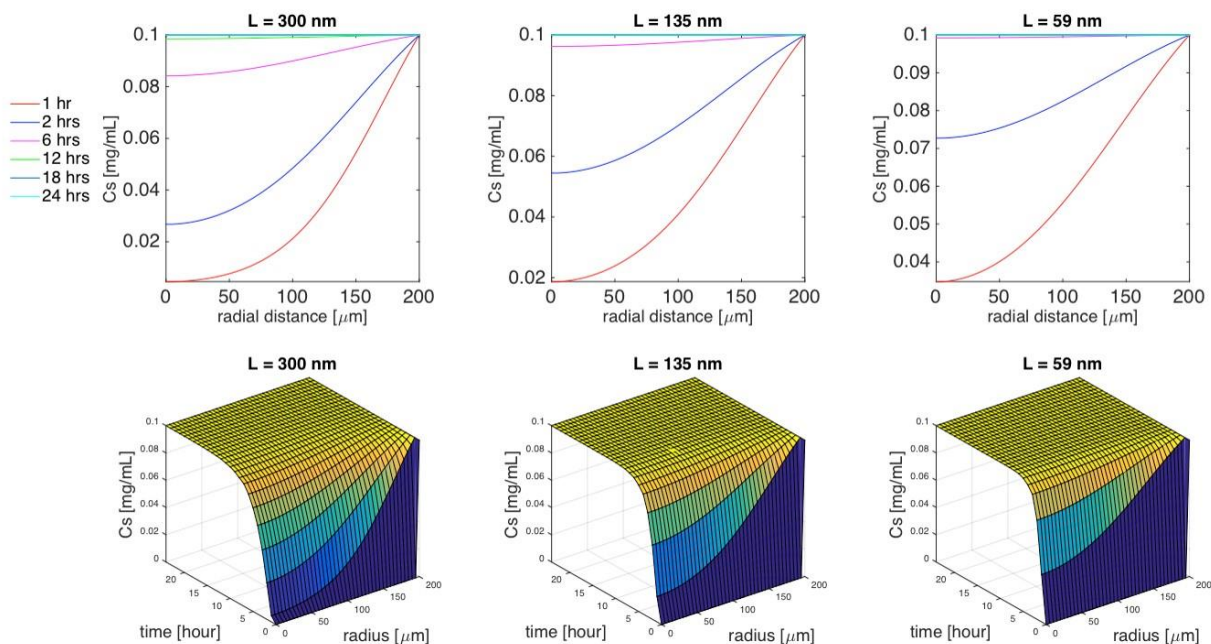


Figure 6.4. Effects of the TMV aspect ratio on TMV's distribution. Top 3 panels are 2D plots of the concentration of TMV as a function of the radial distance within the spheroid for specific time interval (1 h, 2 h, 6 h, 12 h, 18 h, 24 h), and the bottom 3 panels are the corresponding 3D plots of the concentration of TMV as a function of both time and radial distance. Cell density $\bar{f} = 0.5$, spheroid radius $R = 200 \mu\text{m}$, TMV concentration in the surrounding medium $C_M = 0.1 \text{ mg.mL}^{-1}$, cell uptake $k = 0$.

6.4.4. Effects of TMV characteristics on the rate of cell uptake.

The simulations presented above do not include TMV uptake by cells so that the effects on diffusion are not obfuscated. While targeted nanoparticle formulations can increase delivery, endocytotic clearance of targeted nanoparticle can reduce drug distribution and tumor cell access.³¹⁷ To assess the effect of cell uptake on TMV distribution throughout the spheroid, I evaluated the cell uptake rates of TMV in cancer cells experimentally: fluorescently-labeled, RGD-targeted TMV formulations were obtained as described by Pitek et al.³¹⁰ A fluorescence assay was developed to quantify TMV particle uptake cancer cells over time (**Figures 6.5 A+B**). I chose triple negative breast cancer cells (MDA-MB-231) as our model cell line for their relatively high

expression of $\alpha_v\beta_3$ integrins.³¹⁸ I determined that the targeted TMV formulation exhibits a cell uptake rate of 130 particles/h/cell. With this experimental value, we can extrapolate cell uptake rates of PEGylated and RGD-targeted TL, TM, and TS particles (**Figure 6.5 C**).²⁹⁹ These data and resulting cell uptake rates are summarized in **Table 6.2**.

Table 6.2. Rate of cellular uptake of three aspect ratios of TMV-PEG and TMV-RGD

	[TMV/h/cell] (L=300 nm)	[TMV/h/cell] (L=135 nm)	[TMV/h/cell] (L=59 nm)
TMV-RGD	130	139	178
TMV-PEG	7	5	4

While RGD-targeted formulations are readily taken up by the cells, PEGylated formulations show negligible cell interactions. The PEGylated formulations with TS and TM aspect ratios have comparable effects on uptake. The targeted formulations with TL and TM have comparable effects on uptake, but the uptake with TS increases significantly (**Table 6.2**). The experimental data (**Figure 6.5 C**)²⁹⁹ shows that TMV-PEG formulations exhibit low uptake with time. The TMV-RGD formulations, however, display a biphasic behavior: rapid cell uptake within the first 3 h followed by a plateau region with little to no cellular uptake, most likely indicating saturation. This behavior is typical of particle internalization mediated by cell surface receptors.³¹⁹

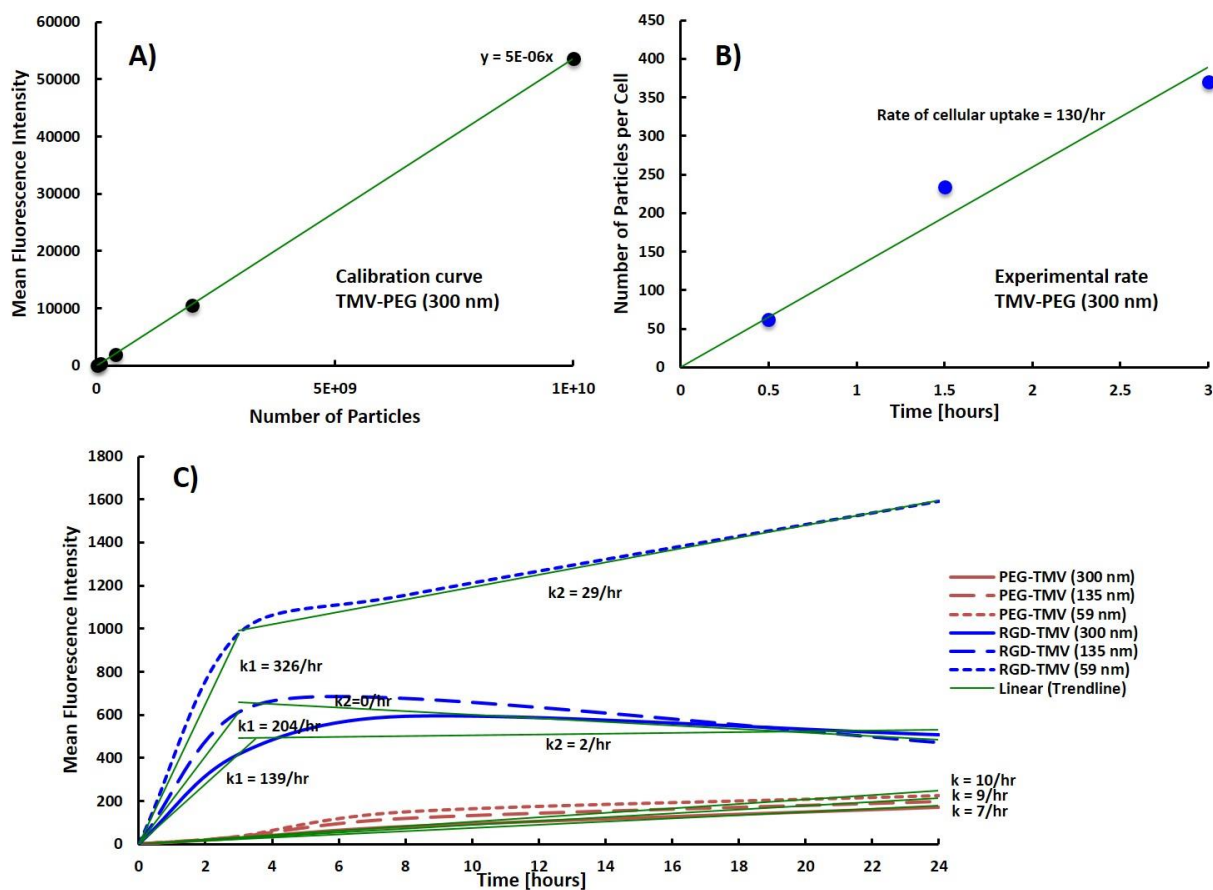


Figure 6.5. Experimental rate of cellular uptake. (A) Plate reader quantification of fluorescence intensity of Cy5-TMV-PEG (L/d = 300/18 nm) suspended in PBS solution to establish a calibration curve. (B) Resulting number of Cy5-TMV-PEG (L/d = 300/18 nm) internalized in MDA-MB-231 cells after 30 min, 1.5 h, and 3 h incubation. The slope of the curve corresponds to the rate of cellular uptake. (C) Flow cytometry quantification data from a previous study of the mean fluorescence intensity of TMV-PEG and TMV-RGD formulations, with distinct aspect ratio, which were internalized in HT-29 cells.

The rate of cellular uptake of TMV reported in this study is much smaller than the rates reported for synthetic nanoparticles. Doiron et al.³²⁰ reported that spherical polystyrene nanoparticles with diameters ranging from 20 nm to 500 nm had uptake rates ranging from 6.6×10^7 particles/h/cell to 12,000 particles/h/cell respectively within the first 3 h of incubation. In addition Huang et al.³¹⁷ reported rod-shaped gold nanocrystals (aspect ratio = 3) displaying RGD peptides

on their surface had a rate of internalization in A549 lung carcinoma cells equivalent to 4500 particles/cell/h within the first 2 h of incubation at 37°C. However, the same nanoparticles coated with single-chain variable fragment peptide to target the epidermal growth factor receptor were internalized at a slower rate of 1,250 particles/cell/h. This demonstrates that the rate of cellular uptake is dependent on nanoparticle shape, surface chemistry, as well as the nature of the molecular receptor targeted.

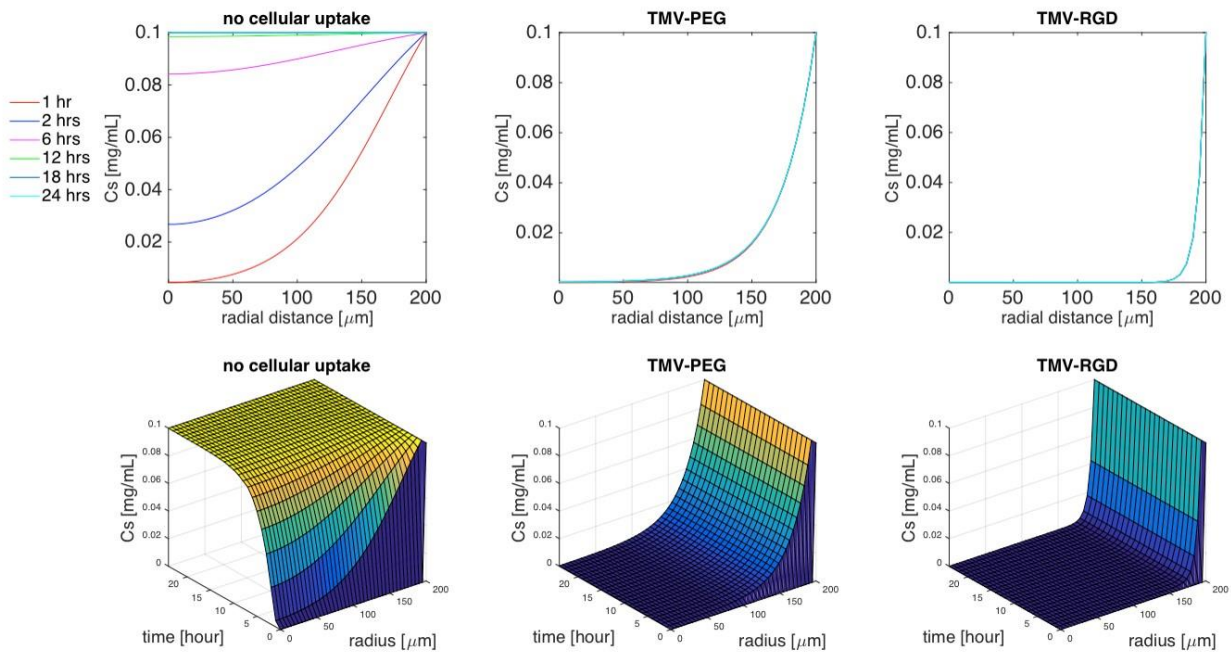


Figure 6.6. Effects of cellular uptake on on TMV's distribution. Top 3 panels are 2D plots of the concentration of TMV formulations as a function of the radial distance within the spheroid for specific time interval (1 h, 2 h, 6 h, 12 h, 18 h, 24 h), and the bottom 3 panels are the corresponding 3D plots of the concentration of TMV as a function of both time and radial distance. Cell density $\phi = 0.5$, spheroid radius $R = 200 \mu\text{m}$, TMV concentration in the surrounding medium $C_M = 0.1 \text{ mg}\cdot\text{mL}^{-1}$.

6.4.5. Model simulated uptake of TMV.

Using the evaluated cellular uptake (k) of TMV formulations (**Table 6.2**), I simulated TMV diffusion in a spheroid cell system with different rate coefficients of cell uptake (**Figure 6.6**) and aspect ratios (**Figure 6.7**). **Figure 6.6** shows the 2D and 3D responses with no uptake ($k=0$), low uptake as observed for TMV-PEG, and enhanced uptake as achieved for the TMV-RGD formulation. For these simulations, I set $L/d = 300/18$, $R=200 \mu\text{m}$, and $\phi = 0.5$. The TMV concentration decreases significantly with distance into the spheroid even at low cell uptake rate ($k=7$) associated with PEGylated particles. As characterized by the dimensionless parameter group (D/kR^2), the cellular uptake of TMV-PEG was 1,000 fold greater than its rate of diffusion (**Supporting Equations 6.1**). This prevents deep tissue penetration because cell uptake occurs at a rate much higher than diffusion. Coating TMV with RGD peptides to target integrin receptors further decreases the TMV concentration within the spheroid. Active targeting of receptors overexpressed on cancer cells (*e.g.*, TMV-RGD targets $\alpha_v\beta_3$ integrin receptors overexpressed on cancer cells) is commonly used to promote tissue specificity and accumulation. However, it is counterproductive for tissue penetration.^{321,322}

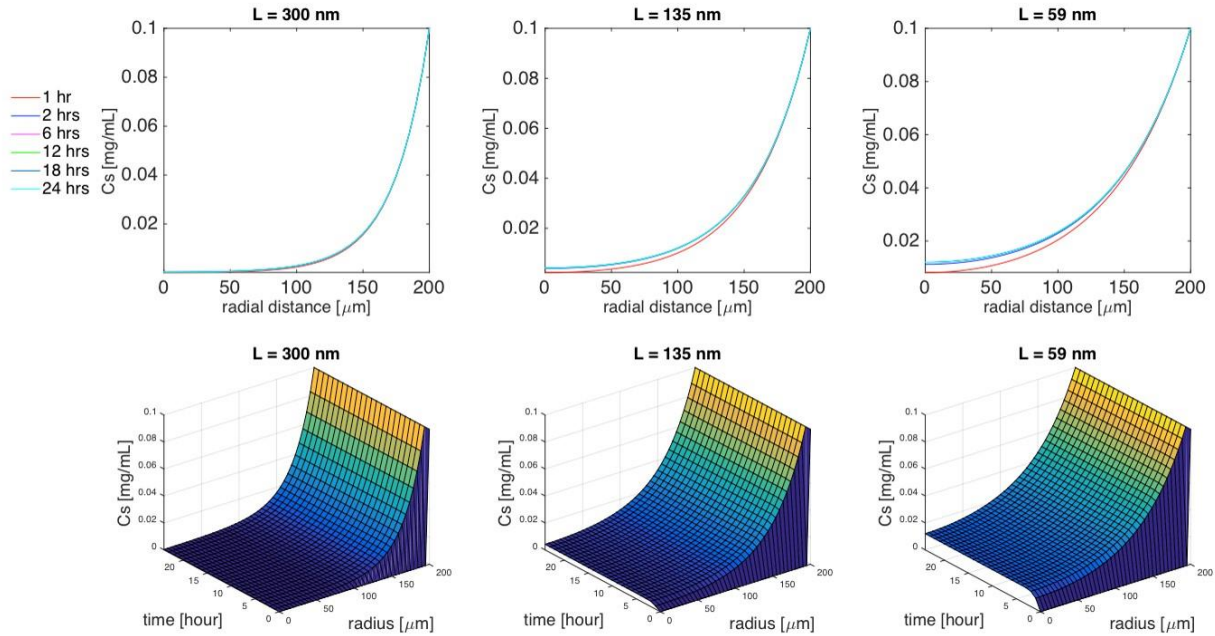


Figure 6.7. Effects of aspect ratio on TMV-PEG's distribution. Top 3 panels are 2D plots of the concentration of TMV formulations as a function of the radial distance within the spheroid for specific time interval (1 h, 2 h, 6 h, 12 h, 18 h, 24 h), and the bottom 3 panels are the corresponding 3D plots of the concentration of TMV as a function of both time and radial distance. Cell density $\phi = 0.5$, spheroid radius $R = 200 \mu\text{m}$, TMV concentration in the surrounding medium $C_M = 0.1 \text{ mg.mL}^{-1}$.

The effect of TMV aspect ratio on its concentration distribution in the spheroid with cellular uptake is shown in **Figure 6.7**. Here, we assume a TMV-PEG formulation with $R = 200 \mu\text{m}$, and $\phi = 0.5$. In 24 h, the concentration of TMV with the highest aspect ratio ($L/d = 300/18$) penetrated only $140 \mu\text{m}$ within the spheroid. For TM ($L/d = 135/18$), the TMV concentration reached the center of the tumor within 3 h. At steady state, its concentration at the center was 4% of the concentration in the surrounding medium. For TS ($L/d = 59/18$), the TMV concentration reached the center of the tumor within 3 h, but its steady-state concentration at the center was 12% of the concentration in the surrounding medium.

6.5. Conclusions.

I developed a mechanistic, mathematical model to describe the intratumoral diffusion properties and cellular interactions of PEGylated and RGD-targeted TMV nanoparticles with distinct aspect ratios. Simulations of our model quantify the effects of spheroid size, cell density aspect ratio, and cellular uptake on TMV diffusion in a spheroid tumor system. Specifically, an increase in cell density decreased the constant rate of diffusion of nanoparticles, while increasing the cellular uptake rate of TMV that prevented deep penetration. Simulations show that PEGylated TMV formulations with the lower aspect ratio accumulate further within the spheroid tumor system because they can diffuse faster than those with a higher aspect ratio. In contrast, TMV nanorods with the targeting ligand RGD of any aspect ratio were rapidly taken up and therefore could not diffuse deeply in the spheroid tumor system. Nonetheless, higher aspect-ratio nanoparticles have enhanced margination toward blood-vessel walls, increased transport across tissue membranes, and reduced clearance by phagocytosis. In that regard, a balance must be established between immune evasion, tumor homing, and tissue penetration. Although our model takes into account only some factors of tumor pathophysiology and nanoparticles design, it can be enhanced to incorporate other important factors. Together with corresponding experimental data, this model can provide an important advance in nanomedical science and engineering.

Chapter VI, in full, is a reprint of the material as it appears in the Journal of Physical Chemistry B, 2016. **Chariou, P.L.**, Lee, K.L, Pokorski, J.K, Saidel, G.M, Steinmetz, N.F. *Diffusion and Uptake of Tobacco Mosaic Virus as Therapeutic Carrier in Tumor Tissue: Effect of Nanoparticle Aspect Ratio*. 120, 6120-6129. The dissertation author was the primary investigator and author of this paper.

Chapter VII: Targeted Photodynamic Therapy Using High Aspect Ratio Plant Viral Nanoparticles

7.1. Introduction.

Photodynamic therapy (PDT) has emerged as an efficacious adjuvant treatment modality for several types of cancer.²⁵ In PDT, light is used to locally excite a photosensitizer (PS) to generate reactive oxygen species. The resulting oxidative stress disrupts organelle functions, promotes cell apoptosis, and damages the tumor vasculature that supply oxygen and nutrients required for the tumor to survive.³²³ While a few PDT therapies have received FDA approval (*i.e.*, Photofrin and aminolevulinic acid), efficient delivery of the PS to the target site remains challenging. Tumor accumulation of the PS is generally poor due to the physicochemical properties of the PS.³²⁴ Therefore, large doses are administered to compensate for the poor drug accumulation at the target site. This is particularly unfavorable because most PS suffer from slow *in vivo* clearance, which increases toxicity. For example, as skin is highly vascularized and easily exposed to light, the long circulation time of PS (*e.g.* Photofrin³²⁵ has a half-life of 452 h) promotes skin phototoxicity. As a result, patients are required to limit their exposure to the sun several weeks post-treatment. Therefore, there is a critical need to develop delivery systems with enhanced clearance that promote the accumulation of the PS in the tumor site.

To this end, I turned toward the development of plant virus-based nanoparticles (VNPs) for the delivery of PS. VNPs have been developed as carriers for the delivery of contrast agents, chemotherapeutics, protein therapies, epitopes, agro-pesticides, as well as PS⁴⁴⁻⁴⁸. Plant VNPs have several attributes that are favorable for nanomedicine delivery and in particular PS delivery. Bio-manufacturing is well established and the biologic platform offers well-defined, monodisperse structures that can be tailored with molecular precision.¹⁷³ Plant VNPs are non-infectious toward

mammals, and most importantly the proteinaceous nanoparticles are cleared rapidly from circulation and from tissue,^{299,329} thus making this a particularly attractive platform for PS delivery. Plant VNPs as well as bacteriophage-derived nanoparticles have been developed for PS delivery;¹⁷³ in most instances PS agents are covalently coupled to viral carriers. However, covalent binding of the PS to nanoparticles may impair their photoactivity due to quenching and reduced molecular freedom, and in turn limit their intracellular activity. Therefore, non-covalent drug delivery may be advantageous to enhance and control steady release of the PS within the tumor environment. This strategy relies on hydrophobic-hydrophilic and electron charge interactions between the PS and its carrier.

7.2. Results and discussion.

In this work, I utilized two high aspect ratio, soft matter tubular nanostructures for PS delivery, namely tobacco mosaic virus (TMV) and tobacco mild green mosaic virus (TMGMV). TMV and TMGMV were selected as carrier platforms based on their well-established surface chemistry and elongated shape. Elongated (rod-shaped or filamentous) nanoparticles have enhanced blood margination, transport across tissue membrane, cell adherence, and macrophage avoidance, promoting their accumulation in the tumor tissue.^{254,255} TMV and TMGMV self-assemble helically around a single-stranded RNA genome to form a 300 x 18 nm rod with a 4 nm-wide hollow interior channel (**Figure 7.1 A**). As described in chapter II, both particles are made of 2,130 identical copies of coat protein units; TMV and TMGMV share 86% sequence homology.²¹⁸ Of particular interest, the interior channels of TMV and TMGMV are covered with solvent exposed glutamic acids that are readily available for electrostatic loading of positively charged guest molecules (**Figure 7.1 A**).²¹⁸ While TMV has been extensively studied for clinical applications, including the delivery of PS,²³⁵ this is the first study investigating TMGMV for

medical applications. To probe drug loading and release, I studied the monocationic, dicationic, tricationic and tetracationic version of a zinc porphyrin photosensitizer. Lastly, we selected one formulation and developed a cancer cell targeting strategy to further enhance treatment efficacy.

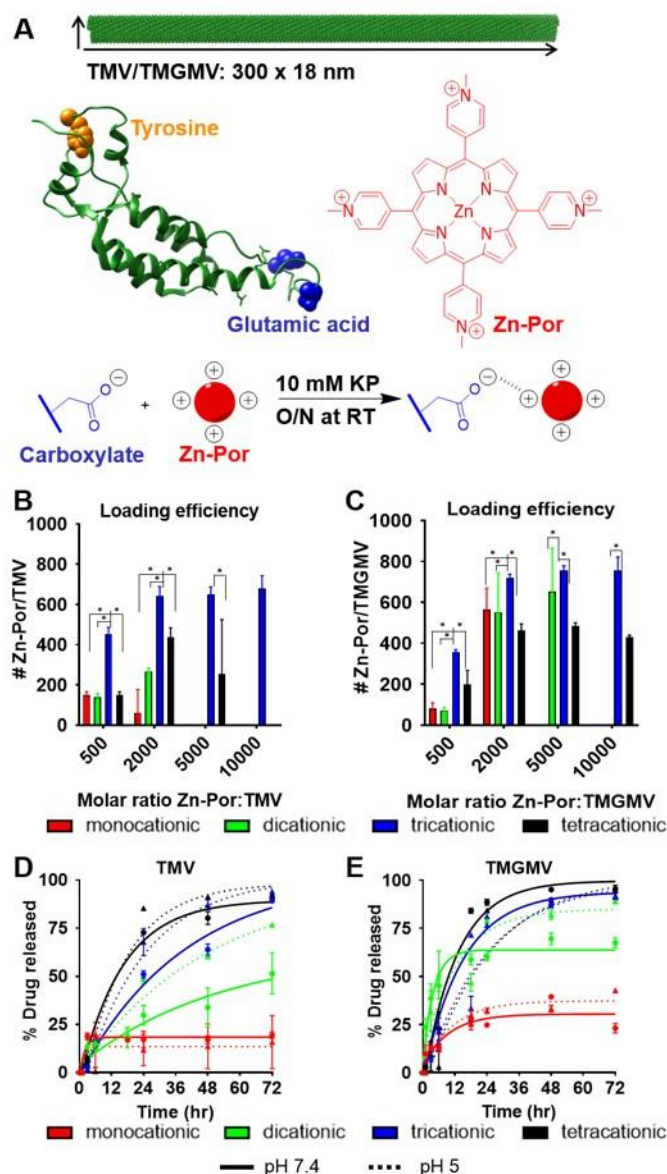


Figure 7.1. Evaluation of Zn-Por loading and release from TMV and TMGMV. (A) The full length structure of TMV/TMG MV is made of 2130 identical coat proteins. A single coat protein is depicted highlighting the exterior surface exposed tyrosine (orange) and the interior surface exposed glutamic acids (blue). The chemical structure of the cationic Zn-Por (red) is shown to the right of the coat protein. The tetracationic (4 positive charges) Zn-Por was here selected as an example. When the virus and Zn-Por are mixed together at pH 7.8, the cationic Zn-Por and the deprotonated carboxylate residue of glutamic acid form an electrostatic bond. (B) Average number of each Zn-Por formulation in TMV and (C) TMGMV as a function of the starting Zn-Por:VNP molar ratio. Statistical significance was established using an Anova test with $p < 0.01$. D) Cumulative Zn-Por release profile from TMV and E) TMGMV at physiological pH 7.4 (solid line) and endosomal/tumor environment pH 5 (dashed line).

Monocationic (Zn-Por¹⁺), dicationic (Zn-Por²⁺), tricationic (Zn-Por³⁺) and tetracationic (Zn-Por⁴⁺) drugs were synthesized using previously established protocols³³⁰ and the appropriate starting aldehydes (**Supporting Figure 7.1**). Zn-Por^{1+, 2+, 3+, 4+} were incubated with TMV and TMGMV using a molar excess of 500:1, 2,000:1, 5,000:1, 10,000:1 Zn-Por:VNP in 10 mM potassium phosphate (KP) buffer (pH 7.8) overnight at room temperature with gentle agitation (**Figure 7.1 A**). The mixture was then purified by ultracentrifugation at 112,000 g for 1 h on a 30% (w/v) sucrose cushion to separate the Zn-Por-loaded particles (VNP_{Zn-Por}) from the excess Zn-Por molecules. The resulting pellet was resuspended in 10 mM KP (pH 7.8) overnight and centrifuged at 16,000 g for 10 min to remove potential aggregates. Finally, VNP_{Zn-Por} were eluted through PD MinitrapTM G-25 desalting columns to entrap any remaining unbounded Zn-Por. The purified reaction mixtures were analyzed by UV-visible spectroscopy (UV-vis) to quantify drug loading using the extinction coefficient of Zn-Por (195,000 M⁻¹·cm⁻¹) at 440 nm (**Figure 7.1 B-C**).

The maximum drug loading, yielding ~ 600-700 Zn-Por molecules per VNP, was obtained using a 2,000 molar excess of Zn-Por. Increased molar excess did not yield increased drug loading, but rather resulted in a loss of particle recovery due to the increased formation of aggregates (**Supporting Figure 7.2 A+B**). For TMGMV, charge appeared to have little effect on loading efficiency – independent of molecular Zn-Por version used, > 500 Zn-Por molecules were incorporated into TMGMV. In stark contrast, the charge of the different Zn-Por formulations greatly influenced their loading efficiency in TMV: Zn-Por¹⁺ (~180 molecules/TMV), Zn-Por²⁺ (~250 molecules/TMV), and Zn-Por⁴⁺ (~400 molecules/TMV) all resulted in lower loading efficiency vs. ~600 molecules per TMV for Zn-Por³⁺, the latter is comparable to previously obtained data.²³⁵

The TMV results can be attributed to the combined effect of electrostatic and hydrophobic/hydrophilic interactions; the greater the positive charge the better stabilization inside the TMV interior channel. In addition, the increased hydrophobic nature of the monocationic and dicationic Zn-Por formulations in combination with their electrostatic properties led to the formation of more aggregates compared to their tricationic and tetracationic counterparts, thereby reducing the loading efficiency. Several factors may explain the differential loading results between TMGMV and TMV. In chapter II, I have previously compared the amino acids sequences of TMV and TMGMV and analyzed their distribution of charged residues on both the inner and outer surfaces of the virus.²¹⁸ While it has been shown that only two glutamic acid (Glu) residues are chemically available on TMV (Glu 97 and Glu 106), our analysis revealed that in addition to the Glu 95 and Glu 106 in the interior channel of TMGMV, Glu 145 and aspartic acid (Asp) 66 were also exposed on the outer surface and could be available for electrostatic charge interactions. The difference in the amino acid sequences of TMV and TMGMV could also play a role in the difference in loading by changing the charge and hydrophobicity surrounding the glutamic acid residues. Furthermore, the virus coat proteins are not rigid structures, and therefore small molecules could diffuse in between coat proteins. It is conceivable that TMGMV has a greater coat protein fluidity and therefore a higher loading capacity.

Based on the above studies, I prepared drug-loaded VNPs using the 2000:1 Zn-Por:VNP ratio. I studied whether changing the pH of the 10 mM KP buffer solution would influence the loading efficiency of Zn-Por into TMV and TMGMV (**Supporting Figure 7.2 C-F**). At pH 3, VNPs aggregated and disassembled, which led to lower yields. The corresponding loading efficiency was low due to the protonation of carboxylate groups, resulting in weak electrostatic interaction. At pH 5, the reaction yields and loading efficiency were improved compared to pH 3,

and reached their maximum at pH 7.8. Increasing the pH to 10 did not increase the loading yield, but rather just slightly decreased loading efficiency and reaction yields. While ~60–75% of starting materials were recovered at pH 7.8, the yield dropped to ~40% at pH 10. Based on the findings of the pH studies, I conducted the remaining experiments at pH 7.8 due to the relatively high loading efficiency and recovery observed at this pH.

Next, I analyzed the drug release profile of each Zn-Por:VNP formulation (**Figure 7.1 D-E**). 1 mg of particles was resuspended in 300 μ L PBS and loaded in triplicate in 10,000 MW cut-off Slide-A-Lyzer MINI dialysis units for 72 hrs. To mimic physiological conditions, samples were dialyzed against 3 L of PBS adjusted to pH 7.4 (physiologic conditions, *e.g.* blood pH) as well as pH 5 (acidic conditions, *e.g.* acidic tumor microenvironment or endolysosomal pH) at 37°C. At time $t = 0, 1, 3, 6, 18, 24, 48,$ and 72 h, 10 μ L was extracted from each dialysis unit and the remaining Zn-Por entrapment was measured by UV/Visible spectroscopy. The half-life $t_{1/2}$, defined as the time required for 50% of the drug to be released from the VNPs, decreases as the electropositivity of Zn-Por increases. At pH 7.4, TMV: Zn-Por⁴⁺ and TMGMV: Zn-Por⁴⁺ formulations had the lowest $t_{1/2}$ (12 and 10 h, respectively). In contrast, only 20% and 25% of Zn-Por¹⁺ was released from TMV and TMGMV respectively within 72 hrs. The release profiles of Zn-Por³⁺ were similar to that of Zn-Por⁴⁺, while the release rates of Zn-Por²⁺ were in between those of Zn-Por^{4+/3+} and Zn-Por¹⁺. While the $t_{1/2}$ values of each Zn-Por:VNP formulation were slightly lower at pH 5, the trend remained the same. These results indicate that the dominant force of interaction between TMV/TMGMV and Zn-Por is not electrostatic, but rather hydrophobic/hydrophilic interactions. Since Zn-Por becomes more hydrophobic as its electropositivity is reduced, its ability to solubilize in PBS surrounding the VNP is impaired, thereby decreasing the rate of drug release. I also tested stability of the Zn-Por:VNP formulations

under storage conditions (*i.e.* 10 mM KP, pH 7.8, 4 °C), and observed a slow and constant release of Zn-Por from TMV and TMGMV over a period of 6 weeks (**Supporting Figure 7.2 G-H**). The release rate of Zn-Por in storage conditions was ranked from highest to lowest. For TMV, Zn-Por¹⁺ > Zn-Por²⁺ = Zn-Por³⁺ > Zn-Por⁴⁺, whereas TMGMV showed a different trend: Zn-Por²⁺ = Zn-Por³⁺ > Zn-Por¹⁺ > Zn-Por⁴⁺. Specifically, 50% of Zn-Por was released from TMV:Zn-Por¹⁺ (the lowest loading efficiency ~180) and TMGMV: Zn-Por^{2+/3+} within 25-28 days. Less than 45% of Zn-Por was released from the other formulation within 6 weeks.

To evaluate *in vitro* efficacy of Zn-Por:VNP formulations, I first compared TMV and TMGMV's uptake by B16F10 melanoma cells. Melanoma was chosen as a model because PDT has shown promise in melanoma.²³⁵ While most melanomas are removed by surgery supplemented with adjuvant chemotherapy and/or immunotherapy, some melanomas remain unresponsive to these therapies. A growing body of data indicates that PDT could be applied as an adjuvant therapy for those melanomas not responsive to traditional therapies.³³¹

For cell uptake studies, TMV and TMGMV were conjugated with the fluorophore Cyanine 5 (Cy5) using solvent exposed tyrosine side chains (on the exterior TMV/TMGMV surface, **Figure 7.1 A**) click chemistry,²¹⁸ followed by the purification of the reaction mixture as previously described. The covalent attachment of Cy5 was confirmed by UV-vis and denaturing SDS-NuPAGE gel electrophoresis (**Supporting Figure 7.3 A**). We have previously demonstrated that a minimum conjugation of Cy5 to ~8% of TMV coat proteins (CPs) is sufficient to yield maximum fluorescence intensity.²³⁷ TMV and TMGMV particles displayed ~160 (7.5%) and ~490 (23%) dyes respectively. The higher dye conjugation efficiency in TMGMV could be due to differences in the chemical microenvironment (*i.e.* surrounding amino acids with different charge and

hydrophobicity) and greater surface exposure of the tyrosine side chain. The corresponding average distances between fluorophores are equal to 2.7 nm and 1.6 nm for TMV and TMGMV respectively, which are large enough to prevent quenching due to energy transfer between dye molecules and trapping by dimers.²³⁷ Therefore these Cy5-TMV and Cy5-TMGMV constructs are suitable for imaging experiments.

To assess VNP–cell interactions, B16F10 melanoma cells were incubated with 100,000 VNPs per cell at 37 °C and 5% CO₂ for 1 h and 8 h in Dulbecco’s modified Eagle’s media (DMEM) supplemented with 10% (v/v) fetal bovine serum and 1% (w/v) penicillin-streptomycin. Cells were washed thoroughly with FACS buffer (0.2% (v/v) 0.5 M EDTA, 1% (v/v) FBS and 2.5% (v/v) 1 M HEPES pH 7.0 in DPBS) and fixed with 2% (v/v) paraformaldehyde. Cells were then analyzed using a BD Accuri C6 Plus flow cytometer and 1 x 10⁴ events were recorded. Data were analyzed using FlowJo v8.6.3 software. After 1 h of incubation, 85% and 100% of TMV and TMGMV were taken up by B16F10 cells, respectively (**Figure 7.2 A**). This is reflected by an increase in mean fluorescence intensity compared to cells only (**Figure 7.2 B**). The slightly higher uptake of TMGMV may be attributed to greater particle instability during viral production and purification, which causes some of the particles to be broken²¹⁸; a shorter TMGMV rod would have a faster rate of cell penetration. Nonetheless, the cellular uptake of TMV and TMGMV reached 93% and 100%, respectively, after 8 h of incubation. This time point was selected to allow VNPs to traffic through the cells before proceeding with the photodynamic treatment. I evaluated efficacy of the drug delivery approach against B16F10 cells using previously established white light therapy.²³⁵ The following samples were tested: Drug-free VNPs, free Zn-Por, and Zn-Por-loaded VNPs, and a dark control for each sample was included. Cells were incubated with 0.001, 0.01, 0.1, 1, 5, and 10 μM of Zn-Por, Zn-Por:VNP, or controls for 8 h at 37 °C and 5% CO₂. Cells were washed to remove

any Zn-Por that was not endocytosed and samples were illuminated under white light (10 mW cm^{-2} at 430 nm) for 30 min (18.1 J cm^{-2} at 430 nm). Control samples were kept in the dark at $37 \text{ }^{\circ}\text{C}$ and 5% CO_2 . In all experiments, neither dark controls (**Figure 7.2 D+F**) nor any of the VNP only controls (not shown) showed significant cell toxicity. After illumination, plates were incubated for an additional 48 h and cell viability was assessed using the MTT cell proliferation assay according to the manufacturer's recommended protocol. The IC_{50} values of free Zn-Por¹⁺, Zn-Por²⁺, and Zn-Por³⁺ were 2.5, 0.5, and 0.03 μM , respectively. The tetracationic Zn-Por showed little to no cell toxicity. Based on these results, I selected Zn-Por¹⁺ and Zn-Por³⁺ and proceeded to repeat the experiment with the corresponding Zn-Por:VNP formulations. Zn-Por¹⁺:TMV, Zn-Por³⁺:TMV, Zn-Por¹⁺:TMGMV, and Zn-Por³⁺:TMGMV displayed IC_{50} equal to 4.7, 1.5, 7, and 1 μM , respectively.

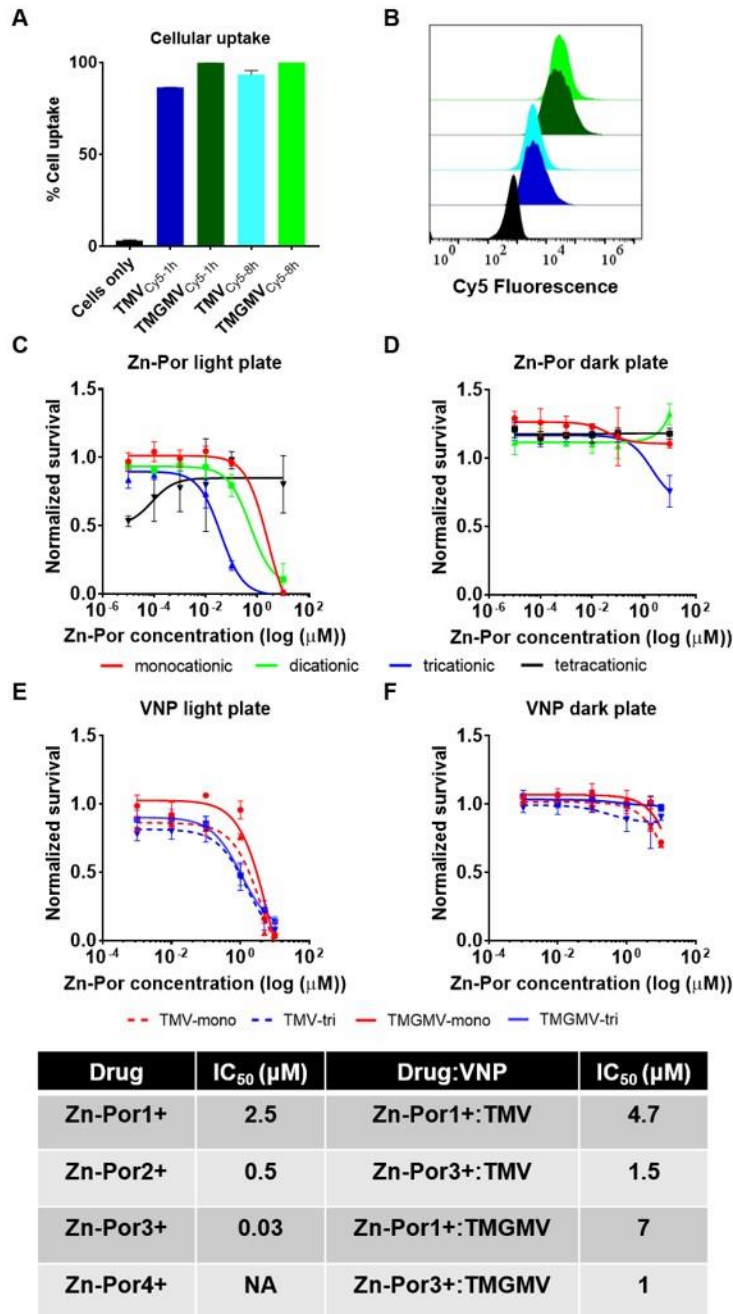


Figure 7.2. In vitro treatment of B16F10 cells. (A) Flow cytometry quantification of the percent cellular uptake of Cy5-TMV and Cy5-TMGMV in B16F10 melanoma cells after 1 h and 8 h of incubation. (B) Corresponding fluorescent intensity reading. (C) B16F10 melanoma cell viability (MTT assay) following 8 h incubation with increasing doses of Zn-Por and 30 min illumination with white light. (D) The corresponding cell viability in the absence of light treatment. The treatment was repeated using selected Zn-Por:VNP formulations with (E) and without (F) light treatment.

Free Zn-Por¹⁺ was 1.8 to 2.8-fold more effective compared its TMV/TMGMV formulation; this reduced efficacy was even more dramatic for the Zn-Por³⁺ loaded particles which showed a 30-50 fold decrease in efficacy. The decreased drug activity of VNPs loaded with Zn-Por vs. free Zn-Por is expected. The reactive oxygen species produced by PS drugs have a very short half-life and act locally from their generation site. Therefore, the subcellular localization of the PS greatly influences its phototoxicity. Like most nanoparticles, TMV and TMGMV are internalized by endocytosis and follow the endosomal-lysosomal pathway. Previous data suggest the phototoxicity of PS localized in lysosomes is significantly reduced compared to PS localized in other organelles, in particular in mitochondria.³³² On the other hand, hydrophobic PS with cationic charges such as free Zn-Por is likely to localize in mitochondria.³³² Nonetheless, TMV and TMGMV are here used to improve the bioavailability and tumor accumulation of Zn-Por while reducing non-specific tissue toxicity. TMV and TMGMV can be further chemically or genetically modified to display moieties such as cancer cell targeting ligands, cell penetrating ligands, and chemotherapeutics for combined therapy, which would further improve the treatment efficacy.

As a proof of concept, we set out to develop a targeted Zn-Por delivery system. We chose Zn-Por³⁺ and TMV, in particular we used the well-established and characterized Lys-added mutant denoted as TMV_{lys}.²⁹⁸ While TMGMV showed greater toxicity than TMGMV, the genetic engineering of TMGMV_{lys} mutant has yet to be established in the future. TMV_{lys} offers amine functional groups for bioconjugation: targeting ligands synthesized with a terminal Cys side chain can be conjugated using heterobifunctional NHS-maleimide linkers. Here we chose the F3 peptide (KDEPQRRSARLSAKPAPPKPEPKPKKAPAKK) as the ligand.³³³ The F3 peptide is a 31-amino acid fragment of the high mobility group protein HMG2N. F3 preferentially binds to nucleolin, a shuttle protein that is highly expressed on the plasma membranes of tumor cells.^{334,335} Nucleolin-

targeted delivery of drug-loaded nanoparticles using F3 peptide or nucleolin-specific aptamers has been previously demonstrated.^{336–338} For example, F3-functionalized PEG-PLA nanoparticles led to deeper tumor penetration into 3D glioma spheroids and prolonged the survival of mouse bearing intracranial C6 glioma when loaded with paclitaxel.³³⁸ In this work, we conjugated F3 to TMV_{lys} following an established protocol (**Figure 7.3 A**).³³⁹ In brief, TMV_{lys} was mixed with a maleimide-PEG₄-NHS bifunctional linker using 10 equivalents linker per TMV_{lys} coat protein in 10 mM KP buffer (pH 7.4) for 2 hrs. The mixture was then purified by ultracentrifugation at 112,000 g for 1 h on a 40% (w/v) sucrose cushion. The F3 peptide synthesized with a C-terminal Cys (GenScript) was then added to the mixture at 0.5 equivalents peptide per TMV_{lys} coat protein and reacted for 2 hrs. The final TMV_{lys}-F3 was purified with 10,000 MW cut-off Slide-A-Lyzer MINI dialysis units. A higher excess of the F3 peptides led to aggregation and a lower excess did not show sufficient conjugation yields. Cy5-labelled TMV_{lys}-F3 was also prepared for cell uptake studies. Cy5 fluorophore conjugation was carried as described above prior to F3 conjugation. Using the aforementioned protocol, SDS-NuPAGE gel electrophoresis confirmed covalent attachment of F3 peptides, as indicated by higher molecular-weight bands (**Figure 7.3 D**) The TMV coat protein has a molecular weight of ~17.5 kDa; a slightly higher molecular weight indicates the addition of F3 peptide (~4.2 kDa). ImageJ software was used to quantify the degree of F3 conjugation, and data indicate that over 20% of the TMV_{lys} coat proteins was modified with F3 peptide. The A₂₆₀:A₂₈₀ ratios (RNA:protein) of Cy5-TMV_{lys}-F3 and Zn-Por:TMV_{lys}-F3 were 1.21 and 1.29, respectively, which are indicative of intact TMV preparations (**Figure 7.3 B+C**). Furthermore, transmission electron microscopy (TEM) indicated that TMV_{lys} maintained its structural integrity post chemical modifications (**Figure 7.3 E**).

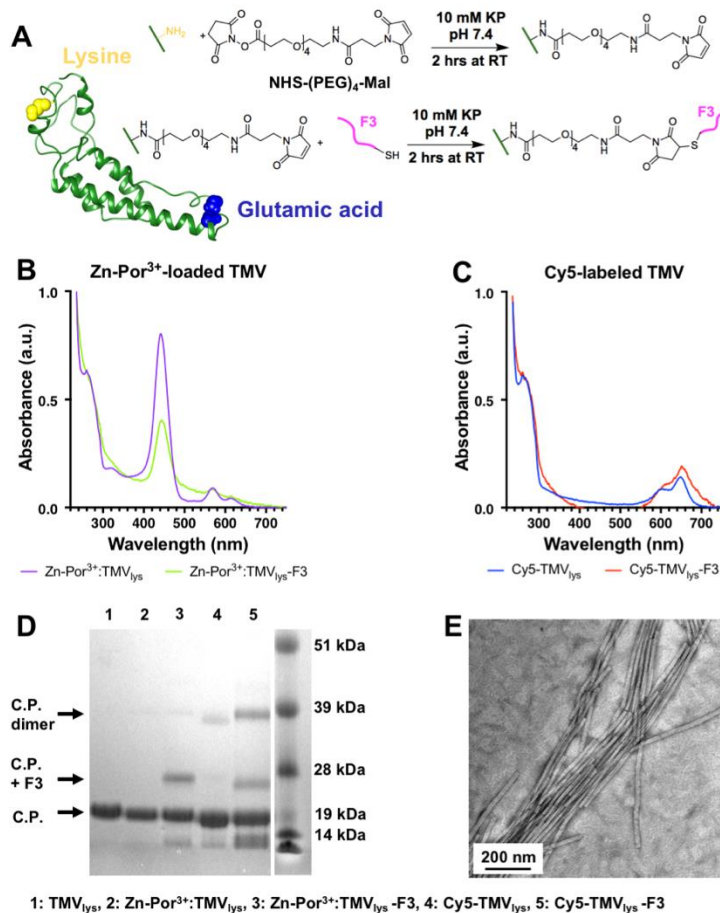


Figure 7.3. Synthesis of targeted TMV_{lys}-F3 particles. (A) Two-step conjugation scheme. A single TMV_{lys} coat protein is depicted on the left, with surface-exposed lysine (yellow) and glutamic acids (blue). The F3 peptide with C-terminal cysteine is conjugated to the exterior lysine residues of TMV_{lys} using a bifunctional PEG linker. (B) UV-vis spectra of Zn-Por³⁺-loaded and (C) Cy5-labelled TMV_{lys} and TMV_{lys}-F3, with characteristic A₂₆₀:A₂₈₀ ratio for intact TMV_{lys}; note the absorption maxima at λ₄₄₀ for Zn-Por³⁺ and λ₆₄₉ for Cy5. (D) SDS-PAGE gel image of TMV_{lys} particles, with positions for bare and conjugated coat proteins highlighted. (E) TEM image of Cy5-TMV_{lys}-F3.

To assess the targeting efficacy, we compared the cellular uptake of Cy5-labeled TMV_{lys} and TMV_{lys}-F3 particles using HeLa cells. HeLa cells were chosen because this cervical cancer cell line is known to express high levels of nucleolin.^{334,340} For cell targeting studies, HeLa cells were incubated with 150,000, 300,000, or 750,000 particles per cell at 37°C and 5% CO₂ for 3 h in DMEM supplemented with 10% (v/v) fetal bovine serum and 1% (w/v) penicillin-streptomycin.

Flow cytometry was performed as described above. Flow cytometry showed an over 50% increase in cell uptake of conjugated Cy5-TMV_{lys}-F3 particles (**Figure 7.4 A**). Compared to cells incubated with native TMV particles, the mean fluorescence intensity increased by 40-fold in the presence of nucleolin-targeted Cy5-TMV_{lys}-F3 particles (**Figure 7.4 B+C**). Because flow cytometry does not provide insights into the fates of the nanoparticles, we also used confocal microscopy to study where the particles localized within the cells. HeLa cells were incubated with 6,000,000 particles per cell for 6 h in culture medium. Then cell membranes were stained with Alexa Fluor 555-conjugated wheat germ agglutinin (1:500 dilution) and mounted with Fluoroshield™ with DAPI. Slides were imaged using a Leica TCS SPE confocal laser scanning microscope and the data was analyzed using ImageJ software. The confocal images were in agreement with flow cytometry, showing high cell interactions of the F3-targeted TMV formulation. The Cy5-TMV_{lys}-F3 particles appear bundled up at the surface of HeLa cells, where nucleolin is overexpressed (**Figure 7.4 E**). Although others have shown intracellular trafficking of F3-functionalized polymeric nanoparticles,³⁴¹ cellular uptake of Cy5-TMV_{lys}-F3 was not observed in our study. This possibly indicates that the TMV's high aspect ratio shape may not be suitable to be shuttled by nucleolin. Nevertheless, the accumulation of Cy5-TMV_{lys}-F3 particles on the cell membrane may be advantageous for PDT as cell membrane targeting may prevent trapping of zinc porphyrin in endolysosomes and therefore enhance its cytotoxic efficacy. We moved on to explore the therapeutic efficacy of the F3-targeted Zn-Por drug delivery system.

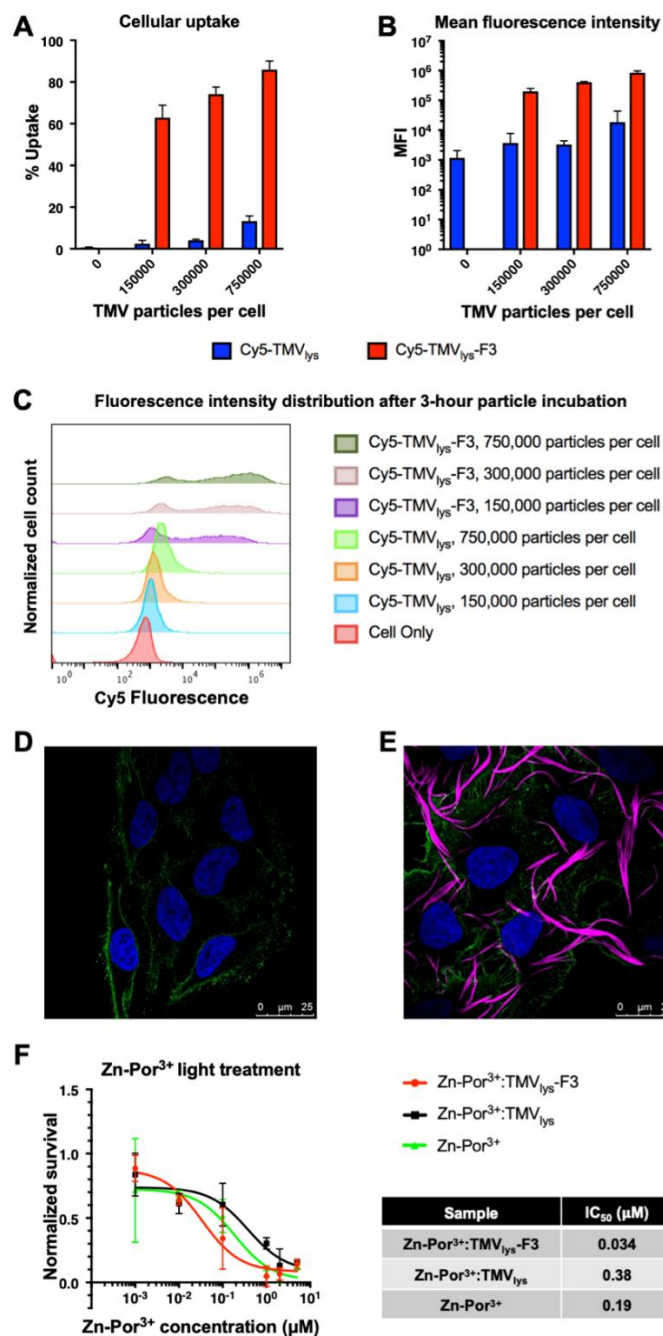


Figure 7.4. Uptake of TMV_{lys}-F3 particles by HeLa cells in vitro. Flow cytometry results showing (A) the percent cellular uptake, (B) mean fluorescence intensity and (C) corresponding fluorescence spectra of HeLa cells incubated with Cy5-labeled TMV with and without F3 ligand. (D) Confocal fluorescence microscopy image of HeLa cells stained showing DAPI (blue), AF555 conjugated wheat germ agglutinin (green) and Cy5 (magenta) after 6-hr incubation with Cy5-TMV_{lys} and (E) with Cy5-TMV_{lys}-F3. (F) HeLa cell viability (MTT assay) following 8-hr incubation with increasing doses of Zn-Por and Zn-Por loaded TMV with and without F3 ligand following 30 min illumination with white light.

The enhanced cytotoxic efficacy of Zn-Por³⁺ loaded in TMV_{lys}-F3 was reflected in the decreased survival of HeLa cells after white light treatment (**Figure 7.4 F**). TMV_{lys} particles were loaded with 2,000:1 molar excess of Zn-Por³⁺ as described above prior to the conjugation of F3 peptides. From the MTT cell proliferation assay, the IC₅₀ values for Zn-Por³⁺ in HeLa cells were equal to 0.034, 0.38 and 0.19 μM for Zn-Por³⁺-TMV_{lys}-F3, Zn-Por³⁺-TMV_{lys} and free Zn-Por³⁺ respectively. No cell killing was observed with drug-free TMV_{lys}-F3 particles at maximum concentration. Without light treatment, data indicated that Zn-Por³⁺-TMV_{lys}-F3 is non-toxic to HeLa cells (**Supporting Figure 7.4**). Compared to the data reported above, the efficacy of free Zn-Por³⁺ drug with white light treatment was 6-fold higher in B16F10 cells than in HeLa cells. This may be attributed to the biochemical differences between a mouse cell line and a human cell line. The drug activity decreased by half after loading into TMV_{lys}-F3. This level of activity decrease after loading was not as significant as our previous data with TMV and TMGMV particles in B16F10 cells, yet the trend of decreased activity after loading into VNP did agree. Meanwhile, the targeted Zn-Por³⁺-TMV_{lys}-F3 particles showed a 5-fold increase in cell killing efficacy compared to the free drug. The increase PDT activity of Zn-Por³⁺-TMV_{lys}-F3 vs. Zn-Por³⁺-TMV_{lys} may be explained as follows: i) a significantly larger amount of particles targets cancer cells when using TMV_{lys}-F3 vs. its native counterpart; and ii) TMV_{lys}-F3 targets the cell membrane, light activation may lead to cell toxicity through cell membrane disruption, and iii) it is also possible that the PS cargo is released at the cell surface, and since the Zn-Por molecule is cell permeable and positive charged, cell uptake maybe favored – in contrast TMV without the F3 ligand accumulates in the endolysosomal compartment.

7.3. Conclusions.

In summary, I have successfully investigated the loading and release profiles of Zn-Por into both, TMV and TMGMV, as a function of ionic state or charge of Zn-Por. I have shown that free Zn-Por³⁺ had the greatest cell toxicity and loading of Zn-Por into TMV and TMGMV resulted in a slightly decreased cell toxicity *in vitro*. Critically, our studies suggest that nucleolin-targeted VNP formulations carrying the Zn-Por³⁺ PS has greatest anti-cancer efficacy. The F3 nucleolin targeting ligand increases nanoparticle and therefore drug accumulation; at the same time the cellular distribution is altered with F3-targeted TMV accumulating at the cancer cell surface. Such targeted nanotechnologies hold great potential for cancer therapies with higher specificity increasing the patient's quality of life but most importantly survival.

Chapter VII, in full, is a reprint of the material as it appears in *Macromolecular Biosciences*, 2019. **Chariou, P.L.**, Wang L., Desai C., Park J., Robbins L.K., von Recum H.A., Ghiladi R.G., Steinmetz N.F. *Let there be light: targeted photodynamic therapy using high aspect ratio plant viral nanoparticles*. 1800407. The dissertation author was the primary investigator and author of this paper.

Chapter VIII: *In situ* vaccine application of inactivated CPMV nanoparticles

8.1 Introduction.

In recent years, plant virus-based nanoparticles have been investigated for vaccine and immunotherapy applications to combat infectious diseases, cancers, and autoimmune diseases.¹⁸⁸ Plant viruses are noninfectious to mammals and therefore are safer than their mammalian counterparts that are often used in oncolytic therapies.³⁴² They can be manufactured in a cost-effective manner and in large scales as viral nanoparticles (VNPs) as well as non-replicative virus-like particles (VLPs) devoid of their genomic payload.^{343,344}

Cowpea mosaic virus VNPs (CPMV) and VLPs thereof (termed empty CPMV or eCPMV³⁴⁵) have been proposed as *in situ* vaccine for cancer immunotherapy. The native form of CPMV consists of a bipartite ssRNA virus forming a 31 nm icosahedron with pseudo T = 3 symmetry. CPMV is made of 60 identical copies of a large (L, 42 kDa) and small (S, 24 kDa) coat proteins encapsidating RNA-1 (5.9 kb) and RNA-2 (3.5 kb) in separate but identical CPMV particles. When applied as *in situ* vaccine, the CPMV or eCPMV formulation is administered directly into a tumor to reprogram the tumor microenvironment and launch systemic anti-tumor immunity. While both CPMV and eCPMV demonstrated potent antitumor response in mouse models^{178,179,346,347} and canine patients,¹⁸⁴ the RNA containing CPMV formulations demonstrated higher efficacy than eCPMV through the activation of additional cytokines and immune cells, which ultimately led to an extended survival rate of tumor-bearing mice.³⁴⁸ The proteinaceous nanoparticle presents danger signals that activate the immune system through pattern recognition receptors (PRRs), and the presence of the RNA provides an additional danger signal.³⁴² RNA activates TLR7/8, and induces type I IFN secretion, which increases the potency of the CPMV-

based vaccines.^{348–350} This phenomenon was also reported using papaya mosaic virus as an *in situ* vaccine.¹⁸³

While CPMV is not infectious to mammals, it remains infectious to legumes including *Vigna unguiculata* (*i.e.* cowpea) plants. From a translational point of view, it is thus important to develop RNA laden but non-infectious CPMV that is safe from to the environment and plants. CPMV is stable in a variety of environmental conditions, such as temperature (-80°C to 60°C), pH (4.5 to 8.5), and in the presence of harsh chemicals, such as dimethyl sulfoxide.³⁵¹ CPMV particles are not sensitive to certain standard methods of virus inactivation, including peptidase or hypochlorite treatment,³⁵² but showed good response to ultra-violet (UV) light.²⁴⁶ Here we investigated UV treatment *vs.* chemical treatment of CPMV to render it non-infectious while maintaining its potent efficacy as a cancer immunotherapy. We compared β -propiolactone (β PL) or formalin treatment with the previously reported UV inactivation method. These chemical treatment modalities are commonly used to produce non-virulent vaccines such as polio, hepatitis A, enterovirus 71, and influenza viruses vaccines.^{273,274} Of particular interests, these methods do not remove the RNA from the VNP, but rather create RNA damage preventing its transcription and translation, and therefore viral replication. UV light promotes RNA-protein crosslinking and dimerization of adjacent uracils.²⁴⁶ β PL promotes the alkylation or acylation of cytidine, deoxyadenosine, and deoxyguanosine. β PL treatment also leads to a large extend of protein modifications; for example poliovirus proteins are more extensively modified by β PL than nucleic acid during viral inactivation.²⁷³ Specifically, β PL acylates and alkylates to a great extent cysteine, histidine, and methionine, and to a lesser extent with aspartic acid, glutamic acid, lysine, serine, threonine, and tyrosine.²⁷³ Lastly, formalin causes protein-protein and RNA-protein covalent crosslinking.²⁷⁴

8.2. Materials and methods.

8.2.1. Preparation of native CPMV. Native CPMV was propagated in Burpee black-eyed pea plants as previously described.³⁵³

8.2.2. CPMV inactivation using UV-light, β -propiolactone, and formalin. CPMV (1 mg.mL⁻¹) inactivation was conducted in 0.1 M potassium phosphate (KP) buffer (pH 7.0). Native CPMV was exposed to UV light at a wavelength of 254 nm (doses: 0.1, 0.2, 0.25, 0.5, 1, 5, 7.5, 10, and 15 J.cm⁻²) using a UVP crosslinker (Analytik Jena AG). Similarly, we induced the inactivation of native CPMV with β -propiolactone (β PPL, Sigma-Aldrich) (doses: 1, 10, 50, 100, and 250 mM) for 24 h at 4°C, followed by the inactivation of β PPL for 2 h at 37°C. CPMV was also exposed to formalin (Electron Microscopy Sciences) (doses: 0.1, 0.25, 0.5, 1, 10, 100, 250 mM) for 5 days at 37°C. Chemically treated CPMV was centrifuged at 112,000 g for 1 h to remove excess β PPL or formalin.

8.2.3. Black-eyed pea plants inoculation with native and inactivated CPMV. Burpee black-eyed peas were seeded in 3-1/4" square pots (Greenhouse Megastore) using Pro Mix BX soil (Greenhouse Megastore) and maintained in Conviron A1000 Reach-in growth chambers (Conviron). When the plants were 10 days old, the primary leaves were mechanically inoculated with 40 μ L (0.1 mg.mL⁻¹) of native or inactivated CPMV (see above) in the presence of a small amount of carborundum (Thermo Fisher Scientific) to promote mechanical lesions on the leaves enabling the virus infection. 10 plants were inoculated for each treatment conditions in addition to a negative control (10 non-infected plants). Leaves were imaged and harvested individually 10 days post-inoculation and stored at -80°C until further processing.

8.2.4. Viral RNA extraction. Inoculated leaves were exposed to liquid nitrogen for 30 sec

to 1 min in a mortar and subsequently pulverized into a thin powder using a pestle. The resulting leaf powder was suspended into 1 mL of UltraPure DNase/RNase free distilled water (Thermo Fisher Scientific) per gram of leaf material. The mixture was vortexed for 1 min and subsequently centrifuged at 13,000 g for 10 min. 500 μ L of the supernatant was isolated and denatured with 1/4 vol. of 10 % (w/v) SDS under heating for 10 min at 60°C. Samples were treated with 2 volumes of UltraPure phenol:chloroform:isoamylalcohol (PCI 25:24:1, v/v/v) (Thermo Fisher Scientific), vortexed for 1 min, and centrifuged at 13,000 g for 10 min. The upper phase, which contains the RNA, was collected into a fresh tube and the PCI extraction was repeated an additional two times. 2 volumes of 100% (v/v) ethanol were added to the final RNA extract prior to purification using the Quick-RNA™ Miniprep kit (Zymo). The purified RNA product was suspended in 30 μ L of UltraPure DNase/RNase free distilled water and stored at -20°C until further analysis. The concentration was determined by UV-visible spectroscopy at 260 nm using the extinction coefficient for single-stranded RNA: 25 ng mL⁻¹ cm⁻¹.

8.2.5. Reverse transcription polymerase chain reaction (RT-PCR). We used the SuperScript IV One-Step RT-PCR System kit (Thermo Fisher Scientific) according to the manufacturer's specifications. The RNA extracted from native and inactivated CPMV was reverse-transcribed and amplified into cDNA using the following reaction mixture: 2.5 μ L forward primer (5'-GGTCCCGCTTGCTTGGAGC-3', 10 μ M), 2.5 μ L reverse primer (5'-GGAGGATTATAAATGTGCG-3', 10 μ M), 25 μ L 2X Platinum SuperFi RT-PCR Master Mix, 0.5 μ L SuperScript IV RT Mix, and 1 μ g total RNA supplemented with Nuclease-free water for a final volume of 50 μ L. The RT-PCR conditions are summarized in **Table 8.1**.

Table 8.1. RT-PCR conditions.

Step	Temp (°C)	Time (min:sec)	No. Cycle
Reverse transcription	50	10:00	1
RT inactivation	98	2:00	1
Amplification	98	0:10	30
	50	0:10	
	72	0:30	
Final extension	72	5:00	1
Storage	4	∞	1

8.2.6. Bioconjugation of Cyanine 5 (Cy5) to CPMV. CPMV was labelled with sulfo-Cy5-NHS (Lumiprobe) targeting the surface lysine residues. CPMV is made of 60 copies of an asymmetric unit comprised of a small (S) and a large (L) subunits and displays a total of 300 surface-exposed lysine side chains.³⁵⁴ The reaction was carried out using 5 equivalents of sulfo-Cy5-NHS per coat protein in 0.1 M KP buffer (pH 7.0) at room temperature overnight, with agitation. The reaction mixture was then centrifuged at 112,000 g for 1 h to remove excess dyes, and resuspended in 0.1 M KP buffer (pH 7.0) overnight. Further purification to remove potential aggregates involved centrifugation at 13,000 g for 10 min. CPMV-Cy5 was eluted using PD Minitrap G-25 desalting columns (GE Healthcare) to remove excess free Cy5 dyes.

8.2.7. UV/Vis spectroscopy. The UV/vis spectra of native, inactivated CPMV, and Cy5-labeled CPMV (CPMV_{Cy5}) were obtained using a NanoDrop Spectrophotometer (Thermo Fisher Scientific). Cy5 labelling was quantified based on the dye-to-CPMV ratio and the Beer–Lambert law. CPMV: $\epsilon(260 \text{ nm}) = 8.1 \text{ ml mg}^{-1} \text{ cm}^{-1}$, molecular weight of CPMV = $5.6 \times 10^6 \text{ g mol}^{-1}$. Cy5: $\epsilon(647 \text{ nm}) = 271 \text{ 000 M}^{-1} \text{ cm}^{-1}$, molecular weight of Cy5 = 777 g mol^{-1} .

8.2.8. Dynamic light scattering (DLS). A Zetasizer Nano ZSP/Zen5600 instrument (Malvern Panalytical) was operated to measure the hydrodynamic radii of native and inactivated CPMV (1 mg.mL⁻¹) nanoparticles. The particle diameter was calculated as the weighted mean of the intensity distribution.

8.2.9. Transmission electron microscopy (TEM). Formvar copper grids coated with carbon film (Electron Microscopy Sciences) were rendered more hydrophilic using the PELCO easiGlow operating system. Drops of CPMV (10 µL, 0.5 mg mL⁻¹) were deposited onto the grids for 2 min at room temperature. The grids were then washed twice with deionized water for 30 sec and subsequently stained twice with 2% (w/v) uranyl acetate for another 45 sec. A Zeiss Libra 200EF transmission electron microscope was used to capture images of the samples at 80 kV.

8.2.10. Size exclusion chromatography (SEC). 200 µL of native and inactivated CPMV samples were eluted through a Superose 6 Increase column using the ÄKTA Explorer chromatography system (GE Healthcare). The flow rate was set to 0.5 ml min⁻¹ in 0.1 M KP buffer (pH 7.0) and the absorbance at 260 nm and 280 nm was recorded.

8.2.11. Agarose gel electrophoresis. Agarose gels were run in 1×TBE running buffer in the presence of Nucleic Acid Gel Stain (GoldBio) diluted 1:20 000 (v/v). Native and inactivated CPMV formulations were analyzed using 3 µg of sample on 1.2% (w/v) agarose gels for 45 min at 110 V. Similarly, 1 µg of RNA extracted from native or inactivated CPMV was analyzed on 1.2% (w/v) agarose gels for 35 min at 110 V in the presence of a 1 Kbp Plus DNA ladder (Invitrogen). Finally DNA amplicons were analyzed using 2.5 µL of RT-PCR product on 1.8% (w/v) agarose gels for 45 min at 110 V in the presence of a 100 bp Plus DNA ladder (Invitrogen). Gels were imaged before and after staining with Coomassie Brilliant Blue (0.25% w/v) using the FluorChem R imaging system under UV light or white light.

8.2.12. Denaturing gel electrophoresis. Native and inactivated CPMV (12 μg) were supplemented with 4 \times LDS loading dye (Thermo Fisher Scientific) and denatured at 100°C for 5 min. The L and S subunits were separated on 12% SDS-PAGE precast gels in 1 \times morpholinepropanesulfonic acid (MOPS) buffer (Thermo Fisher Scientific) for 40 min at 200 V and 120 mA in the presence of SeeBlue Plus2 ladder size markers (Thermo Fisher Scientific). Gels were stained with GelRed, (Biotium) and Coomassie Brilliant Blue (0.25% w/v) and subsequently imaged with the FluorChem R imaging system under UV light, white light, and MultiFluor red light.

8.2.13. Virus overlay binding protein assay (VOBPA). Vimentin was diluted at a concentration of 1 mg.mL⁻¹ in 4 mM HCl and incubated at 100°C for 10 min in the presence of 4 \times LDS loading dye. 5 μg of vimentin was loaded in each well of a 4-12% SDS-PAGE gel for 40 min at 200 V and 120 mA in the presence of SeeBlue Plus2 ladder size markers. The gel was then transferred to a membrane at 30V for 1 h. The resulted blotted vimentin was denatured and gently rocked for 10 min twice at room temperature using denaturing buffer (6 M Guanidine-HCl, 2 mM EDTA, 50 mM DTT, 50 mM Tris/HCl, final pH of 8.3). Then, the membrane was moved to 4°C and gently rocked for 10 min in 20 mL of renaturing buffer (10 mM Tris/HCl, 150 mM NaCl, 2 mM EDTA, 2 mM DTT, 0.1% Triton X-100, final pH 7.3) supplemented with 7.64 g of Guanidine-HCl. After 10 min, 6.5 mL of renaturing buffer was added, followed by another 13.5 mL, and 40 mL in intervals of 10 min. All solution was removed and another 20 mL of fresh renaturing buffer was added for 10 min. The membrane was then moved to room temperature and gently rocked overnight in 5% (w/v) milk solution in renaturing buffer. 100 μg of CPMV, UV-CPMV, β PL-CPMV, Form-CPMV were incubated individually with the membrane in renaturing buffer supplemented with 1% (w/v) milk and 5% (v/v) glycerol. Membranes were

washed 4 times for 5 min in TBST. A 1:5000 dilution of primary rabbit anti-CPMV antibody were added in 5% (w/v) milk/PBST and gently rocked for 1 hr. Membranes were once again washed 4 times for 5 min in TBST. A 1:5000 dilution of secondary HRP-labeled goat anti-rabbit antibody was added in 5% (w/v) milk/PBST for 1 h. Membranes were washed 4 times for 5 min in TBST. The DAB/Ni Peroxidase Substrate Kit (Vector Biolabs) was used to stain the membranes prior to imaging with the FluorChem R imaging system under white light.

8.2.14. Tissue culture. B16F10 (ATCC, mouse skin melanoma) were cultured in Dulbecco's modified Eagle medium (DMEM) with L-glutamine supplemented with 10% (v/v) fetal bovine serum (FBS) and 1% (v/v) penicillin-streptomycin. RAW-Blue™ cells (Invivogen, derived from RAW 264.7 macrophages) were maintained according to manufacturer's recommendation in DMEM with L-glutamine supplemented with 10% (v/v) heat inactivated FBS, 1% (v/v) penicillin-streptomycin, 100 $\mu\text{g mL}^{-1}$ Normocin, 200 $\mu\text{g mL}^{-1}$ Zeocin. Cells were grown at 37°C and 5% CO₂.

8.2.15. Flow cytometry. RAW-Blue™ cells were grown to 70% confluency, washed twice with PBS, and collected with a cell scraper. Cells were pelleted at 500 g for 5 min and resuspended in 1 mL of test medium (DMEM with L-glutamine supplemented with 10% (v/v) heat inactivated FBS and 1% (v/v) penicillin-streptomycin). A Countess II FL Automated Cell Counter (Thermo Scientific) was used to prepare a 1,500,000 cells mL⁻¹ stock solution in test medium. Cells (300,000 cells/200 μL media/well) were seeded on 96-well v-bottom plates, and triplicates of CPMV_{Cy5}, UV-CPMV_{Cy5}, β PL-CPMV_{Cy5}, Form-CPMV_{Cy5} were added at a concentration 100,000 particles/cell and incubated for 1h and 8h at 37°C and 5% CO₂. Cells were then washed twice in FACS buffer (0.1 mL 0.5 M EDTA, 0.5 mL FBS, and 1.25 mL 1 M HEPES pH 7.0 in Ca²⁺ and Mg²⁺ free PBS (50 mL total volume)) and fixed with 2% (v/v)

paraformaldehyde in FACS buffer for 10 min at room temperature and subsequently washed twice more. Samples were analyzed using a BD Accuri™ C6 (BD) and processed with the FlowJo software (<https://www.flowjo.com/>)

8.2.16. RAW-Blue assay. The assay was performed as per manufacturer's recommendation. RAW-Blue™ cells were grown to 70% confluency, washed twice with PBS, and collected with a cell scraper. Cells were pelleted at 500 g for 5 min and resuspended in 1 mL of test medium (DMEM with L-glutamine supplemented with 10% (v/v) heat inactivated FBS and 1% (v/v) penicillin-streptomycin). A Countess II FL Automated Cell Counter (Thermo Scientific) was used to prepare a 550,000 cells/mL stock solution in test medium. Cells (100,000 cells/200 µL media/well) were seeded on 96-well flat-bottom plates, and triplicates of CPMV, UV-CPMV, βPL-CPMV, Form-CPMV were added at a concentration 5 µg/well and incubated for 18h at 37°C and 5% CO₂. Triplicate negative controls of cells only and media only, as well as a triplicate control of 1X lipopolysaccharide (LPS, Thermo Fisher Scientific) were also tested. Subsequently, 20 µL of media per well was incubated with 180 µL of QUANTI-Blue solution (Invivogen) for 2 h at 37°C and 5% CO₂, and the SEAP level was quantified using an Infinite M200 plate reader (Tecan) at 655 nm. Statistical significance was quantified using a 1 way ANOVA test; P value < 0.0001 = ****, P value < 0.001 = ***, P value < 0.01 = **, P value < 0.1 = *, ns = non-significant data.

8.3. Results and discussion.

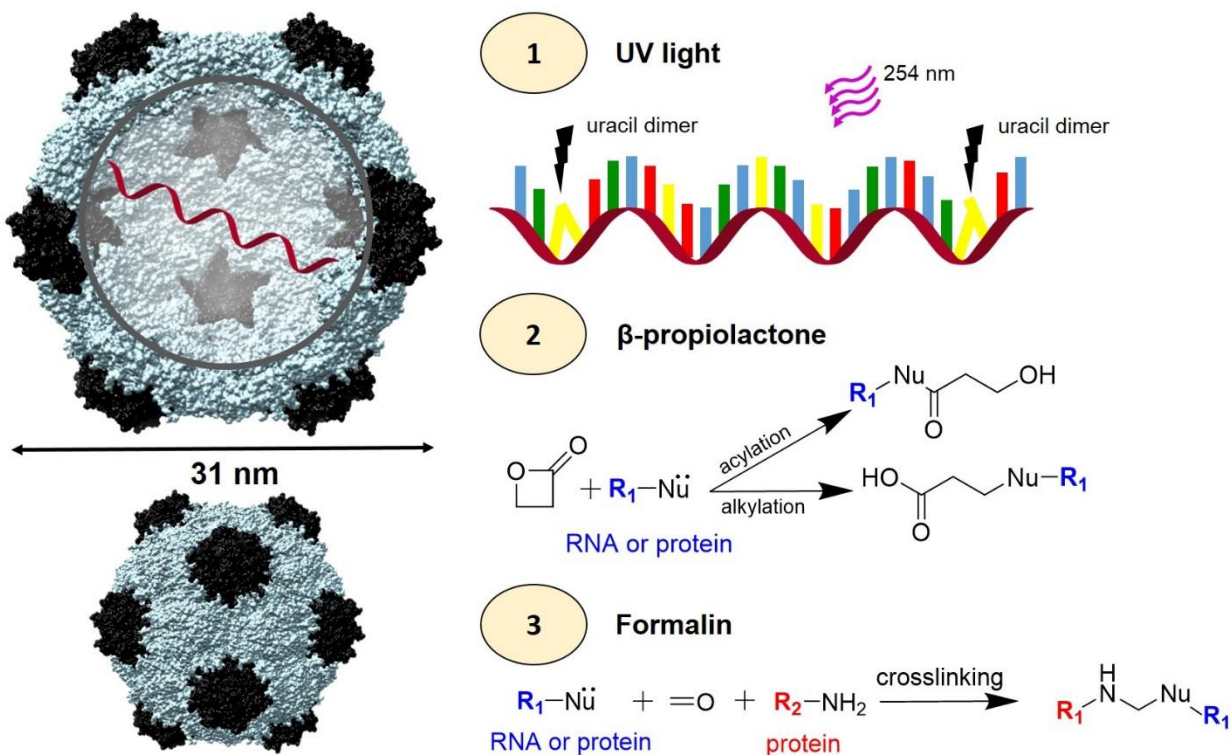


Figure 8.1. CPMV viral inactivation. Left, structure of CPMV using the UCSF Chimera software (PDB ID: 1NY7); the small coat protein is shown in black and the large coat protein is shown in grey. RNA-1 and RNA-2 are encapsidated in different but identical CPMV particles. To the right, (1) inactivation of RNA using a 254 nm wavelength UV light to promote uracil dimers. In the RNA schematic, blue = adenine, green = cytosine, yellow = uracil, and red = guanine (2) β PL induced acylation and alkylation of RNA and proteins. (3) Formalin induced cross-linking of RNA and proteins.

8.3.1. Nanoparticle characterization.

We assessed the effect of UV light, β PL, and formalin treatments on CPMV's structural integrity and genome stability (**Figure 8.1**). The potential sites of UV light mediated dimerization of adjacent uracils are highlighted in **Supporting Figure 8.1**; RNA-1 and RNA-2 of CPMV contain a total of 2905 uracil nucleotides, including more than 700 sites of adjacent uracils. Amino acid prone to β PL mediated alkylation or acylation or formalin crosslinking have also been

highlighted on the interior and exterior surface of CPMV in **Supporting Figure 8.2**. Native and treated CPMV particles were characterized by a combination of dynamic light scattering (DLS), transmission electron microscopy (TEM), and size exclusion chromatography (SEC) to assess their physical state (**Figure 8.2, Supporting Figure 8.3-8.7**). Data were consistent and indicated that CPMV particles exposed to UV, β PL or formalin remained structurally sound; 30 nm-sized particles were imaged in TEM and measured by DLS; also SEC elution profiles were in agreement. However, treatment of CPMV with UV using dosage of 7.5 J cm^{-2} and higher resulted in particle aggregation. DLS measurement indicate radii of 71, 91, and 101 nm for CPMV treated with 7.5, 10, and 15 J cm^{-2} , respectively (**Figure 8.2 A**). This was also consistent with apparent particle aggregation in the TEM images and SEC elution profiles (**Figure 8.2 B+C**). (**Supporting Figure 8.3-8.5**).

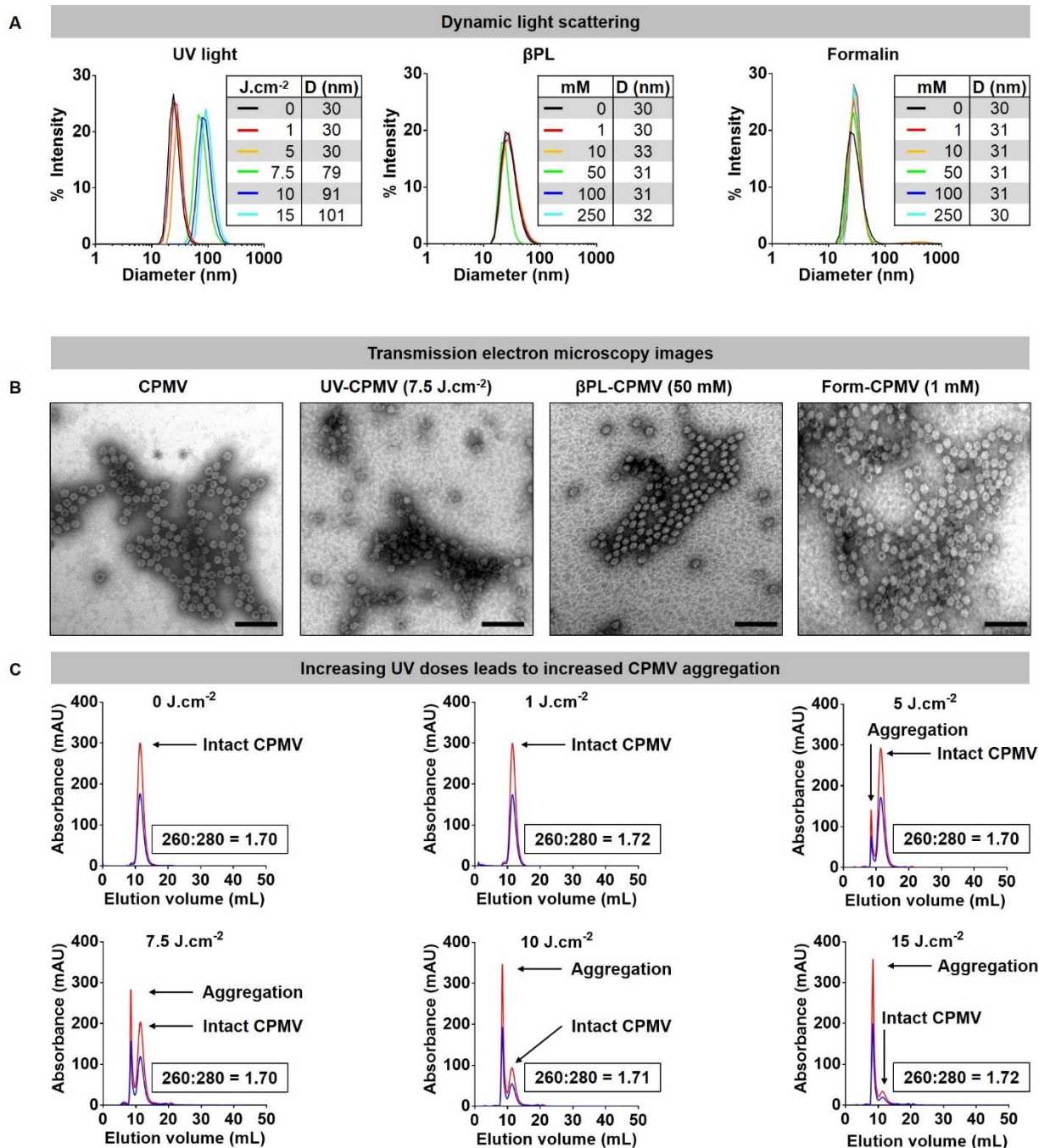


Figure 8.2. Structural integrity of UV, βPL, and Formalin inactivated CPMV particles. (A) Dynamic light scattering of CPMV treated with (left) UV light (0, 1, 5, 7.5, 10, and 15 J cm⁻²), (middle) βPL (0, 1, 10, 50, 100, 250 mM), and (right) formalin (0, 0.5, 1, 10, 100, 250 mM). Table summarizes the average hydrodynamic diameter (denoted as D) of each formulations (B) TEM images of the inactivated CPMV formulations (negatively stained). Scale bars correspond to 100 nm. (C) Size exclusion chromatography of CPMV treated UV light. blue = 260 nm, red = 280 nm. The ratio of RNA to coat protein (260:280) is included in each panel.

UV/vis spectroscopy gave insight into the RNA-to-protein ratio; for intact CPMV, the absorbance ratio at 260:280 nm is 1.7. Data revealed that the RNA to protein ratio remained close to 1.7 for most treatment conditions (**Figure 8.3 A**). There was however a decrease in the 260:280 ratio of Form-CPMV treated with 100 mM (260:280 = 1.58) and 250 mM (260:280 = 1.53) formalin. UV/vis spectroscopy and SEC were in good agreement (**Supporting Figure 8.4-8.5**). These changes however may be attributed to extensive RNA and RNA-protein crosslinking rather than RNA loss. Indeed, extensive RNA crosslinking was observed when RNA was extracted from treated CPMV and analyzed by UV/vis spectroscopy (**Figure 8.3 B**) or agarose gel electrophoresis (**Figure 8.3 C**). While treatment with 1 J cm⁻² UV light or 1 mM β PL or formalin had little effect on the RNA, RNA-1 and RNA-2 are detectable as sharp bands in the gels; at higher dosage or concentration – independent of the treatment modality, RNA crosslinking was apparent: for UV and β PPL-treated samples, extracted RNA had higher mobility and individual RNAs could not be resolved, this would indicate crosslinking, possibly intramolecular crosslinks resulting in a more compact form of the RNA thus enhancing its mobility. For the formalin-treated samples, extensive crosslinking and likely more extensive RNA-protein occurred resulting in loss of mobility of the RNA (**Figure 8.3 C**).

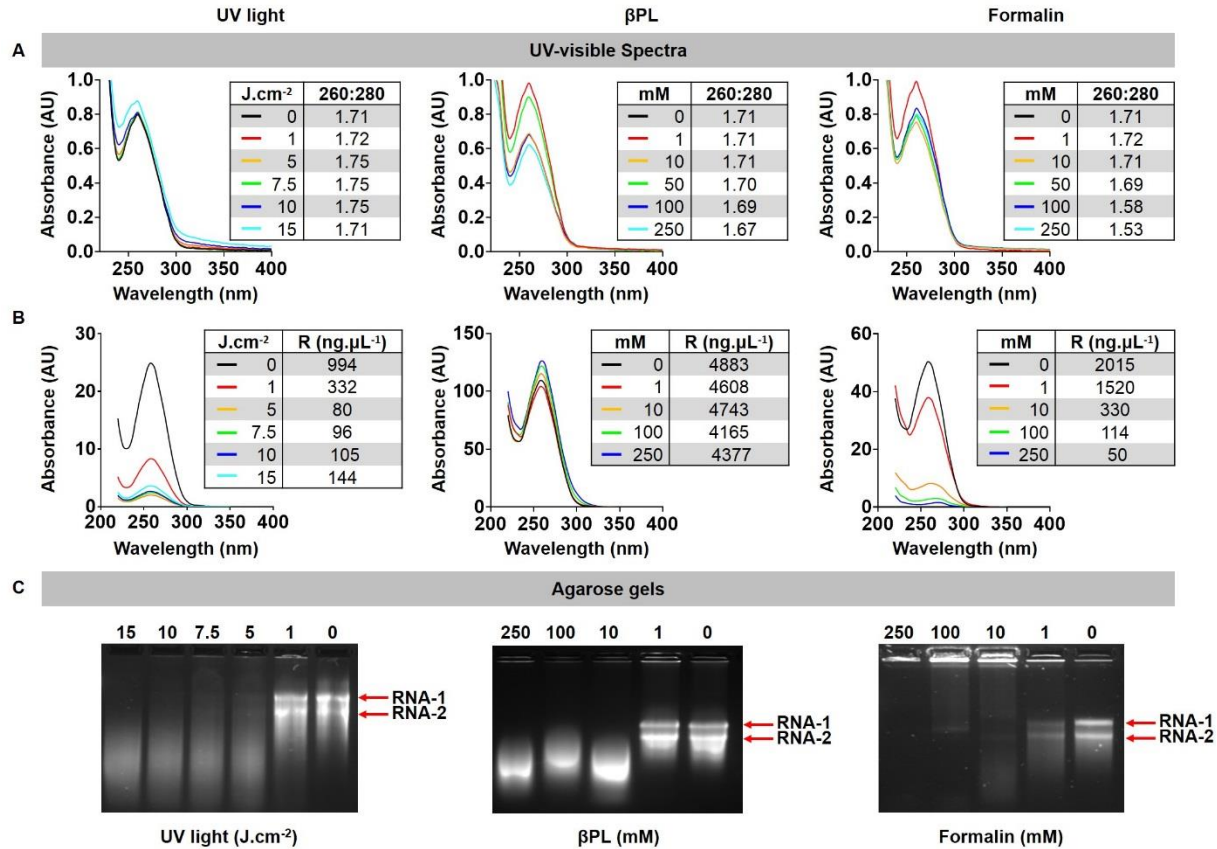


Figure 8.3. CPMV RNA integrity following UV, βPL, and Formalin treatment of CPMV. (A) UV-visible light spectra of native and inactivated CPMV and corresponding 260:280 ratio. (B) UV-visible light spectra of RNA extracted from treated CPMV and corresponding yields. (C) Agarose electrophoretic gel of the RNA extracted from UV-CPMV, βPL-CPMV, and Form-CPMV under UV light.

To gain further insights into whether and to what degree RNA-protein crosslinking occurred, intact and denatured CPMV particles pre- and post-inactivation were analyzed by native gel electrophoresis (agarose GE) and denatured samples were analyzed by SDS-PAGE. All gels were imaged after staining for proteins (Coomassie) and nucleic acid (Gel Red) under white light and UV light, respectively. In the native agarose GE, two distinctive protein bands were observed due to the presence of two electrophoretic (fast and slow) forms of CPMV particles (**Figure 8.4 A**); the fast form of CPMV is the result of a 24 amino acid loss at the C-terminus of the small coat

protein due to proteolysis in plant cells.³⁵⁵ In all samples, nucleic acids and proteins traveled through the agarose gel together, confirming the entrapment of the RNA within the CPMV particles. CPMV treated with doses of 5, 7.5, 10 and 15 J cm⁻² of UV showed signs of particle aggregation, as indicated by the presence of a smear instead of two distinct bands. Compared to CPMV, β PPL-CPMV and Form-CPMV traveled farther through the gel proportionally to the concentration of β PPL and formalin employed to inactivate CPMV. These results could reflect a change in overall particle charge due to the action of β PPL (alkylation and acylation) and formalin (crosslinking) on proteins and RNA. Samples were denatured by SDS-PAGE to separate the L and S coat protein subunits, visualized as single bands at 42 kDa and 24 kDa, respectively (**Figure 8.4 B**). The band intensity of UV-CPMV coat proteins (CP) decreased with increasing dose of UV-radiation, indicative of the presence of particle aggregates. β PPL-CPMV showed no sign of protein breakage or aggregation regardless of the dose of β PPL used during treatment. In contrast, the higher the dose of formalin, the more inter-CP crosslinking was observed at doses as low as 0.5 mM (**Supporting Figure 8.7**). GelRed staining was added to SDS-PAGE gels to assess the integrity of the RNA content of particles. RNA from UV-CPMV and Form-CPMV particles did not travel through the gel, most likely due to intra-RNA and RNA-coat protein crosslinking; the samples remained stuck in the wells. RNA from β PPL-CPMV matched the profile of that released from CPMV; however, at high β PPL concentrations RNA breakage was observed (as evident by higher mobility) – this is also consistent with UV/visible spectroscopy and SEC data as described above.

Therefore, data indicate that at doses higher than 1 J cm⁻² UV light or 1 mM β PPL or formalin RNA and protein modifications and crosslinking occur; at high concentration of UV light, CPMV particle aggregation is observed; and at high β PPL concentrations, RNA breakage is indicated.

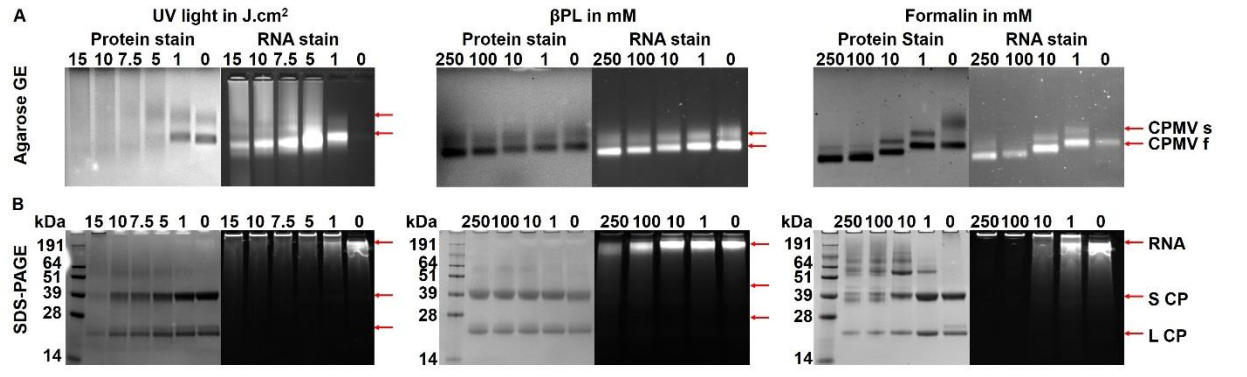


Figure 8.4 Gel electrophoretic mobility of native and inactivated CPMV. (A) Non-denaturing agarose gel electrophoresis images of CPMV treated with UV light, β PL, and formalin under white light after Coomassie staining (protein detection), and UV light after GelRed staining (RNA detection). Note that the RNA stain corresponding to the native CPMV in the upper left panel appears very faint due to the increased signal intensity of crosslinked, UV treated RNA. (B) Corresponding denaturing SDS-PAGE under white light after Coomassie staining, and under UV light after GelRed staining.

8.3.2. Treated CPMV particles exhibit diminished infectivity.

To determine the dose of UV, β PL, or formalin required to inactivate CPMV, we mechanically inoculated 40 μ g of treated CPMV formulations onto primary leaves of cowpea plants and monitored them for the appearance of symptoms after 10 days of incubation. Ten cowpea plants were inoculated in each treatment group, and a negative (not infected) and positive (infected with untreated CPMV) group were included. Necrotic or chlorotic lesions were observed in leaves infected with less than 7.5 J cm⁻² treated UV-CPMV, 10 mM treated β PL-CPMV, and 1 mM treated Form-CPMV (**Figure 8.5**). Reverse transcription (RT) polymerase chain reaction (PCR) was carried out on the total RNA content extracted from individual leaves to further attest for the presence of CPMV infection (**Supporting Figures 8.8-8.10**). One leaf from five different plants was randomly selected in each treatment group. The forward primer (5'-GGTCCCCGCTTGCTTGGAGC-3', RNA-2 nucleotide position 2630-2649) and reverse primer (5'-GGAGGATTATAAATGTGCG-3', RNA-2 nucleotide position 2823-2805) were previously

reported to yield high amounts of amplicons, 177 bps in size.³⁵⁶ Agarose gel electrophoresis confirmed that leaves infected with CPMV inactivated through UV treatment at doses of 7.5 J cm⁻² or higher were indeed effectively inactivated and CPMV infection was not detectable by RT-PCR (**Figure 8.5**). Similarly, formulations treated with 50 mM βPL-CPMV and 1 mM Form-CPMV were confirmed to be fully inactivated. It is worth mentioning that leaves inoculated with 10 mM βPL-CPMV showed no visual symptoms of infection, yet these leaves tested positive by RT-PCR – the latter is a more sensitive assay.

Based on the inactivation studies and infection assays in plants, for all subsequent experiments, we used the inactivated CPMV formulation obtained from 7.5 J cm⁻² UV, 50 mM βPL, and 1 mM formalin. At these doses (1) UV-CPMV was structurally intact but to some degree aggregated, and there was evidence of RNA-RNA and RNA-protein crosslinking. (2) βPL-CPMV remained structurally sound and monodisperse but its RNA was severely damaged. (3) Form-CPMV also retained its size and monodispersity even though protein-protein, protein-RNA, and RNA-RNA crosslinking occurred.

CPMV inactivation by UV light was previously reported and only required a dose of 2.5 J.cm⁻² to prevent infection.²⁴⁶ This difference highlights one of the hurdles to standardizing UV inactivation across systems; we employed a UVP crosslinker (Analytik Jena AG) delivering 7 mwatts.cm⁻², and samples were prepared using a 1 mg mL⁻¹ solution placed 20 cm away from the UV source. *Rae et al* relied on a Stratalinker 1800 UV Crosslinker (Stratagene) delivering 3 mWatts cm⁻², and their samples were irradiated 15 cm from the UV source at a concentration of 2 mg mL⁻¹. In addition, the volume to surface area ratio of the prepared samples could have also influenced the results. Single-stranded RNA containing mammalian viruses have also been inactivated to produce vaccines. Among them hepatitis A,²⁷⁸ HIV,²⁷⁷ and influenza²⁷⁶ reported

inactivation doses of 0.3, 1, and 1 J cm⁻², respectively. The need for use of higher dosage to inactivate the plant virus may reflect the higher stability of the plant viral nanoparticle and its requirement to remain stable in the environment when exposed to UV light. As previously stated, β PL and formalin are commonly used to produce inactivated mammalian virus vaccines.^{273,274} The dose required to inactivate CPMV using β PL (50 mM) and formalin (1 mM) is very similar to those reported in the literature for mammalian viruses. For example, the eastern equine encephalitis and poliomyelitis type II²⁸⁰, equine herpesvirus type I²⁷⁹, HIV²⁸¹, and the influenza virus²⁸² have been successfully inactivated with 5-60 mM β PL; similarly, Hepatitis A²⁸³, HIV²⁸¹, influenza A virus²⁸⁵, Japanese encephalitis virus²⁸⁴, and rabies²⁸⁶ were successfully inactivated using 5-120 mM of formalin.

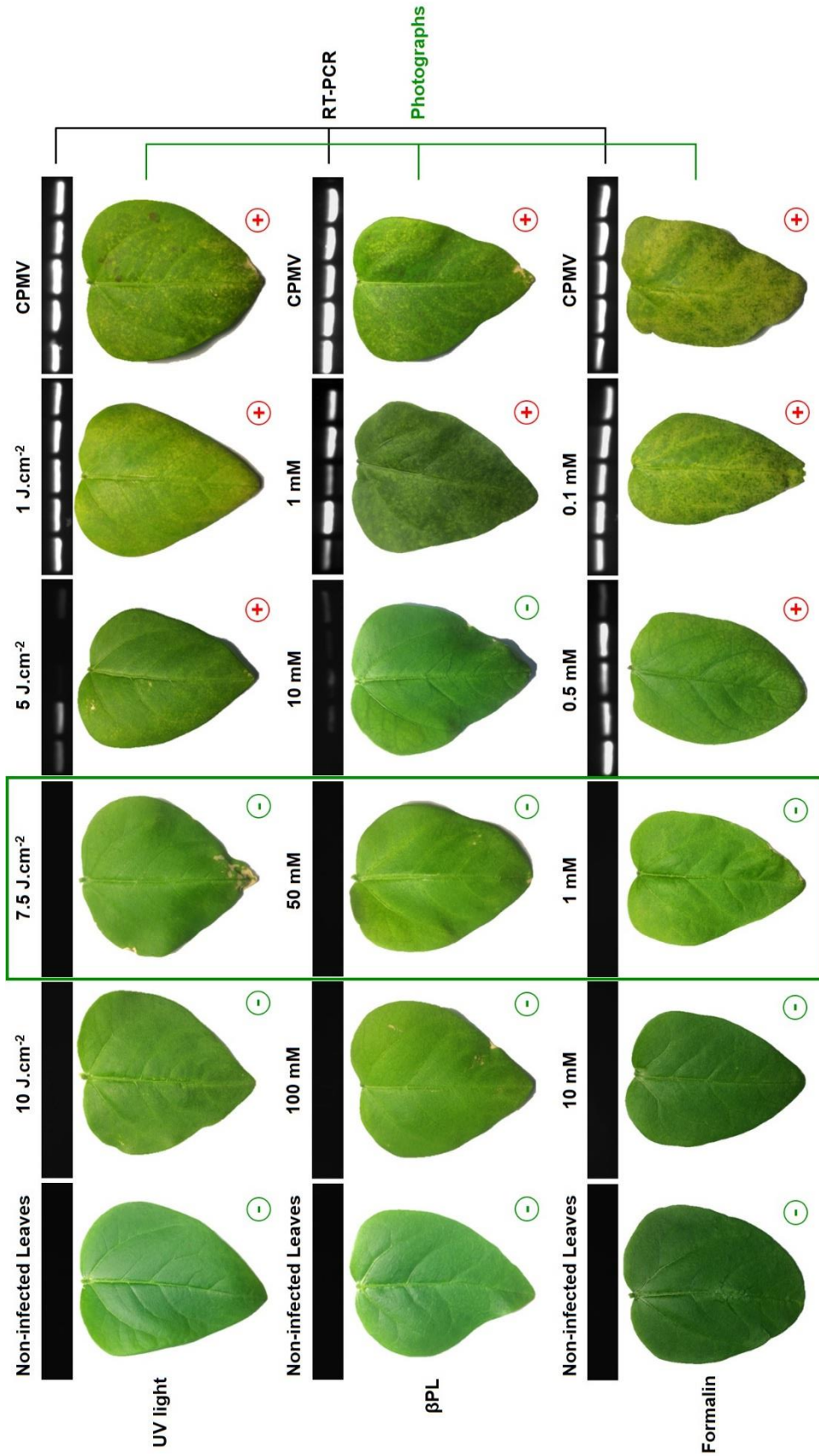


Figure 8.5. Infectivity of native and inactivated CPMV against Black eyed peas. Depiction of individual leaves infected with CPMV, UV-CPMV, βPL-CPMV, or Form-CPMV at various doses; positive red symbols represent leaves showing visual symptoms of infection, while green negative symbols depicts leaves that show no symptoms of infection. Total RNA was extracted from the leaves and RT-PCR amplicons were obtained proportionally to the CPMV infectivity level. Green box indicates minimal dose required to inactivate CPMV.

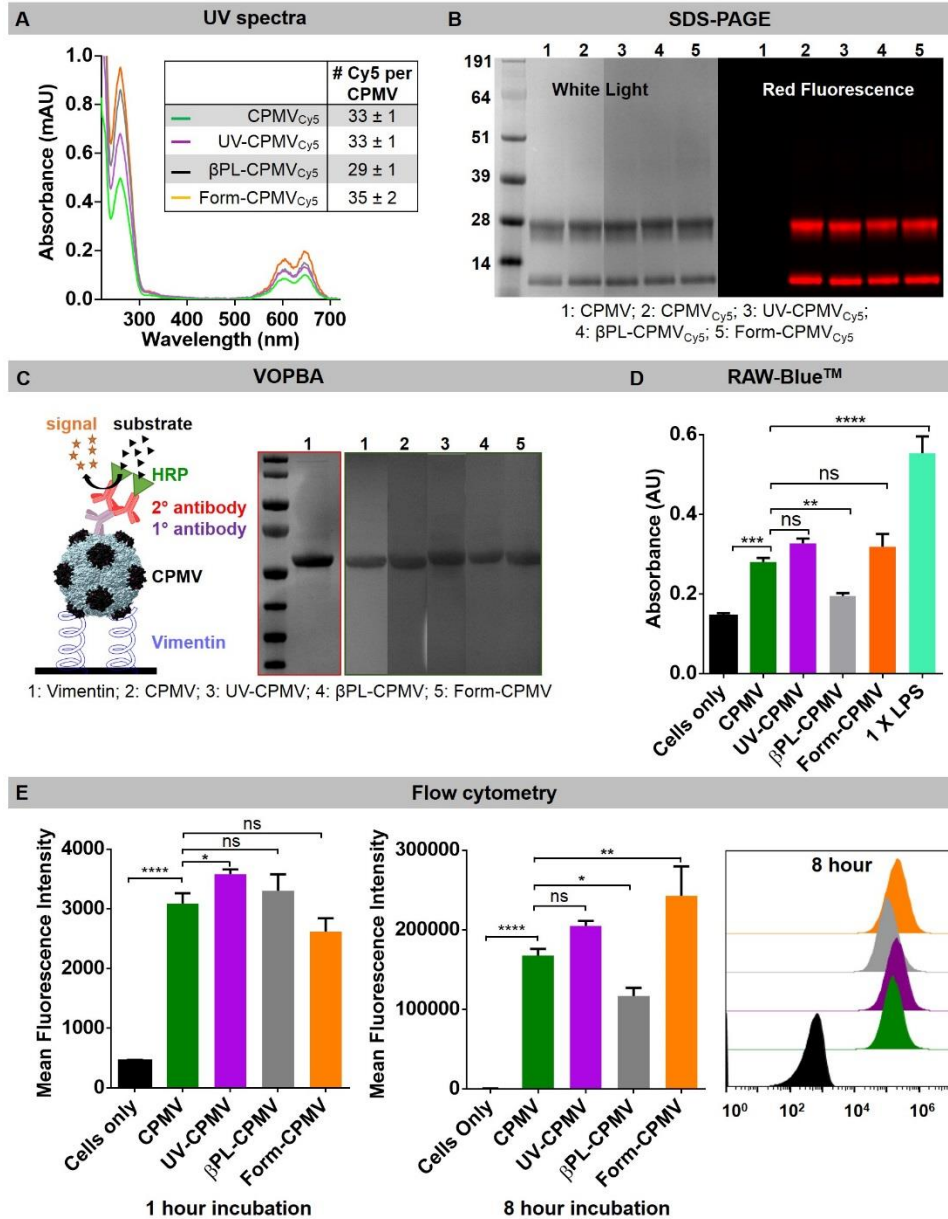


Figure 8.6. Chemical and biological reactivity of inactivated CPMV. (A) UV-visible spectra of native and inactivated CPMV conjugated to Cy5, and table reporting the number of Cy5 dye conjugated per CPMV particles. (B) Corresponding denaturing SDS-PAGE electrophoresis gels under white light after Coomassie staining, and under red fluorescent light. (C) Schematic of a VOPBA assay (on the left), SDS-PAGE gel of vimentin under with light after Coomassie staining (middle), and corresponding white light image of CPMV binding to vimentin during VOPBA assay (on the right). (D) Activation of RAW-Blue™ cells by CPMV, UV-CPMV, βPL-CPMV, and Form-CPMV. (E) Corresponding rate of cellular internalization measured by flow cytometry after 1 h and 8 h of incubation with RAW-Blue™ cells. Statistical significance was obtained using a 1 way ANOVA test; P value < 0.0001 = ****, P value < 0.001 = ***, P value < 0.01 = **, P value < 0.1 = *, ns = non-significant data.

8.3.3. Effect of inactivation on the chemical reactivity of CPMV.

CPMV viral capsids contain 300 solvent-exposed lysine residues that can be chemically modified to impart new functionalities through isothiocyanate and N-hydroxysuccinimide (NHS)-ester coupling. Examples include the conjugation of targeting ligands (*e.g.* folic acid³⁵⁷), therapeutics (*e.g.* doxorubicin³⁵⁸), and fluorescent dyes (*e.g.* Alexa Fluor dyes³⁵⁹). To verify that CPMV retained its chemical reactivity, CPMV, UV-CPMV, β PL-CPMV, and Form-CPMV were incubated with 5 molar excess of sulfo-Cyanine 5-NHS per coat protein overnight, followed by centrifugation and desalting column techniques to remove the excess dyes. The level of Cy5 labeling of the CPMV_{Cy5}, UV-CPMV_{Cy5}, β PL-CPMV_{Cy5}, and Form-CPMV_{Cy5} formulation was quantified using UV-visible spectroscopy; all samples produced dyes per particle values similar to CPMV (30 to 35 dyes per particle) (**Figure 8.6 A**). SDS-PAGE analysis further confirmed the chemical conjugation of C55 to both the L and S coat protein subunits (**Figure 8.6 B**). Thus, UV, β PL and formalin inactivated CPMV particles retain similar surface chemical reactivity.

8.3.4. Effect of inactivation on the biological activity of CPMV.

Although CPMV is a plant virus which cannot infect mammalian cells, CPMV is known to have a tropism towards vimentin; this cytoskeleton protein is surface displayed and secreted by immune cells, epithelial cells, as well as cancer cells (*e.g.* breast cancer and colon adenocarcinoma) and plays a role in inflammation and cell migration.^{359–361} These natural CPMV–vimentin interactions can be harnessed for example to target CPMV to tumor neovasculature.³⁶² We investigated whether the UV or chemical inactivation of CPMV prevented the particle from binding to vimentin using a Virus Overlay Protein Blot Assay (VOPBA) (**Figure 8.6 C**, see

method section). We report no difference in vimentin binding between CPMV, UV-CPMV, β P-CPMV and Form-CPMV, further confirming the particles retain their bio-reactivity.

To determine whether inactivated CPMV retained its strong immunogenicity, we first assayed immunogenicity using the RAW-BlueTM assay (**Figure 8.6 D**). RAW-BlueTM cells are derived from the murine RAW264.7 macrophages and express numerous pattern-recognition receptors such as toll-like receptors, nucleotide-binding oligomerization domain like receptors, retinoic acid-inducible gene-I like receptors, and C-type lectin receptors. Upon activation of the receptors, RAW-BlueTM cells secrete alkaline phosphatase (SEAP), which serves as the read-out. While this assay does not give any information about which innate pathways the CPMV particle activate, the assay provides a quantitative read out to compare whether all formulations activate innate signaling pathways to a similar or varying degree. 5 μ g of CPMV, UV-CPMV, β P-CPMV, and Form-CPMV were incubated with RAW-BlueTM cells for 18 h before the cell's SEAP secretion levels were quantified (**Figure 8.6 D**). A positive (1X LPS) and a negative control (no particles) were included. CPMV, UV-CPMV, and Form-CPMV showed significant activation in the RAW-BlueTM assay resulting in the highest and comparable signaling: while CPMV resulted in a 1.9-fold increase of SEAP level, both UV-CPMV and Form-CPMV resulted in 2.2-fold increase of SEAP levels. Yet, the difference was not statistically significant. Of note is that β P-CPMV appeared to be less effective in activating RAW-BlueTM and SEAP levels were increased only by 1.3-fold – therefore CPMV, UV-CPMV and Form-CPMV were almost 2-fold more effective (P value < 0.001).

These differences in SEAP secretion levels may be attributed to differences in rate of cellular internalization; flow cytometry indicate that all particle formulations showed similar internalization rates (**Figure 8.6 E**); 100% internalization was achieved within 8 h of incubation –

however β PL-CPMV were internalized to a lesser degree (**Figure 8.6 E**). We hypothesize that the diminished immunogenicity of β PL treated CPMV can be explained by a combination of reduced cell uptake and more severe RNA damage including RNA breakage (as indicated by shortening of the RNA and lower A260:280 nm ratios).

Based on the aforementioned results, UV treatment remains the cheapest, fastest, and safest treatment modality and could be easily integrated in the CPMV production process. While UV treatment led to particle aggregation at the required inactivation dose of 7.5 J cm^{-2} , the resulting UV-CPMV remained strongly immunogenic. In contrast, β PL treatment resulted in monodisperse particles but with severely damaged RNA which resulted in reduced immunogenicity as per RAW-BlueTM assay. Formalin could also effectively inactivate CPMV while maintaining its immunogenicity, but formalin treatment requires a long incubation step (5 days) followed by purification steps that lower the final recovery of CPMV to 40-60 % of the original stock.

In the end, selecting the most suitable inactivation modality will demand further *in vivo* testing; future work should focus on whether *in situ* vaccination with inactivated CPMV particles can still increase the tumor burden using a mice model. In a pilot study, we injected C57BL/6J mice transdermally with the murine B16F10 melanoma cell line (data not shown). Treatment (100 μg particles/10 μL) started on day 7 post tumor challenge, and was given 4 times on day 7, 12, 17, and 22. Tumor volumes was recorded every other day, and mice were sacrificed once the tumor volume reached 1000 mm^3 . The PBS control group reached the terminal tumor volume within 20 days. On the other hand, native CPMV and inactivated CPMV formulations demonstrated slower tumor growth and tumor shrinkage. In addition to the previously collected data, an additional animal study with a larger animal group ($n = 10$) is currently underway.

8.4. Conclusions and future directions.

We developed non-infectious CPMV particles using 7.5 J cm^{-2} UV, 50 mM β PL and 1 mM formalin. While particles retain their overall shape and size regardless of the treatment modality, UV treated CPMV exhibited signs of particle aggregation and RNA crosslinking. β PL treated particles were inactivated mainly through RNA breakage, while formalin inactivation resulted in RNA crosslinking to itself and to coat proteins. Inactivated CPMV particles retained their chemical and biological reactivity, but the immunogenicity of β PL-CPMV was severely impaired *in vitro*. These findings pave the way for the development of eco-friendly CPMV-based *in situ* vaccines.

Chapter VIII, in full, is in preparation for submission to a peer-reviewed journal, 2020.

Chariou, P.L. Beiss, V., Steinmetz, N.F. *In Situ Vaccine Application of Inactivated CPMV Nanoparticles*. The dissertation author was the primary investigator and author of this paper.

Chapter IX: Conclusions and Outlooks

9.1. Scope of this work.

In the past few decades, the field of nanoparticle engineering for the delivery of therapeutic payloads has found many applications in agriculture and medicine. Nanocarriers can deliver their cargo in a targeted and controlled manner to specific sites, such as cancer cells or plant roots, thereby maximizing efficacy while minimizing off-target effects. In addition to the 42 EPA approved nanopesticide formulations, 21 nanocarriers have gained FDA or EMA approval for applications ranging from cancer therapy to fungal infection (**Chapter I**). This area is growing so rapidly that 6 EPA and 6 FDA/EMA approved nanocarriers have reached the market while I have completed my dissertation.

To date, most nanocarrier materials under consideration are synthetic in nature and spherical in shape, mainly due to manufacturing restraints. Yet, advances in bioengineering have encouraged the development of bio-inspired nanocarriers that are environmentally friendly (**Chapter I**). In addition, a growing body of data has demonstrated that high aspect ratio nanoparticles, such as virus-like filomicelles, gold nanorods, PRINT nanoparticles, and rod-shaped plant viruses (*e.g.* tobacco mosaic virus (TMV) and potato virus X (PVX)), have increased transport across tissue membranes, enhanced margination, and improved tumor homing, all of which are beneficial to deliver therapeutics and increase treatment efficacy.^{254,255,288,290,291} Since nanocarriers for agricultural applications have only been explored for a decade, the effect of shape and materials' properties on their ability to deliver pesticides has not yet been elucidated. To establish this research and to gain deeper understanding of the application of high aspect ratio nanocarriers for pesticide delivery and cancer therapy, I engineered and studied the plant virus-based nanocarrier tobacco mild green mosaic virus (TMGMV). The results described in my

dissertation contribute to the field of precision farming and cancer nanomedicine through our deeper understanding of high aspect ratio viral nanocarriers. Throughout my work, I gained novel insights into the fundamental properties of TMGMV in the setting of precision farming and cancer nanomedicine; my work also led to the development of the inactivated plant virus-based nanoparticles (*i.e.* these materials are non-infectious toward their host plants) and thus paves the way for translational work. The following sections discuss the summary of the findings of the dissertation.

9.2. TMGMV as a nanocarrier for the delivery of pesticides to nematode infested crops.

In the central work of my dissertation, I demonstrated the potential of TMGMV as a carrier for anthelmintic drugs, such as crystal violet (CV), to treat plants infected with parasitic nematodes (**Chapter III**).²¹⁸ Precision agriculture using nanocarriers such as TMGMV provides the opportunity to increase crop yields in an environmentally friendly manner by delivering fertilizers or pesticides directly to plants while minimizing leaching. When I started my dissertation, most nanocarriers that had been reported in the literature for pesticide delivery were synthetic by nature (*e.g.* polylactic-co-glycolic acid nanoparticles and mesoporous silica nanoparticles) and spherical in shape.¹⁸ TMGMV was already EPA-approved and commercially available as an herbicide in the state of Florida for the treatment of the invasive weed tropical soda apple.^{28,29,230} The red clover necrotic mosaic virus (RCNMV) was the only plant viral nanocarrier under investigation for pesticide delivery,²¹⁷ and there was no mention of TMGMV as a nanocarrier for the delivery of therapeutics for either agricultural or medical purposes. Therefore, my first goal was to explore the engineering design space of TMGMV and to establish the chemical reactivity of the TMGMV platform. I identified solvent-exposed Tyr2 on its exterior surface and carboxylates Glu95 and

Glu106 on its interior surface enabling bioconjugation with small chemical modifiers (**Chapter III**).²¹⁸ Furthermore, I established protocols for electrostatic encapsulation of positively charged guest molecules, such as the anthelmintic drug CV. Up to ~1500 CV moieties could be loaded into TMGMV, and using this formulation, I demonstrated treatment efficacy against liquid *C. elegans* nematodes.²¹⁸ Early soil mobility experiments revealed significantly increased soil transport of _{CV}TMGMV vs free CV through a 4 cm soil column and these studies laid the groundwork for the development of TMGMV as a drug carrier for agricultural applications.

I further investigated the soil mobility of the TMGMV pesticide carrier to assess whether it could accumulate at root level, where nematodes reside (**Chapter IV**).²¹⁹ In order to compare TMGMV's performance to more commonly investigated nanocarrier material formulations, I evaluated the soil mobility of synthetic (*i.e.* polylactic-co-glycolic acid (PLGA)) nanoparticles, mesoporous silica nanoparticles (MSNP), and virus-based (TMGMV, physalis mottle virus-like particles (PhMV), and cowpea mosaic virus (CPMV)) nanopesticides by combining soil column experiments with computational modelling. TMGMV and CPMV could penetrate soil to a depth of at least 30 cm and could therefore be used as nematicide carriers, whereas PhMV was unable to penetrate more than 4 cm of soil and would be more useful for the delivery of herbicides. There is evidence that nanopesticides and pesticides have very different leaching and environmental behaviours, and my experiments indicated for the first time that plant viruses are superior to synthetic MSNP and PLGA for the delivery of nematicides. This study also highlighted how carrier shape and charge influence a nanoparticle's interaction with soil matter. Specifically, the rod-shape and zwitterionic nature of TMGMV facilitated its transport through soil, suggesting that similar to nanomedicine, high aspect ratio nanoparticles have enhanced soil transport compared to their traditional spherical counterparts. Importantly, the computational model I developed could

streamline the development of other synthetic and natural nanocarriers by identifying the ideal combination of particle size, shape, and surface chemistry to promote their accumulation at the pest sites.²¹⁹

Another important finding was that TMGMV-pesticide charge interactions likely are not a viable method of delivery in soil. The virus carrier was stripped of its pesticide within the first 4 cm of soil, highlighting the challenges with pesticide delivery. However, my data also showed that when the drug is conjugated and covalently attached to TMGMV, large quantities could be detected at depths up to 30 cm in the soil. Thus, for field applications, orthogonal bioconjugation of pesticides to the nanocarrier would be the preferred strategy.

Toward this goal, I initiated the development of covalent conjugation strategies to load avermectin. Avermectin is an insecticidal compound with anthelmintic properties naturally produced by fermentation of the soil bacterium *Streptomyces avermitilis*.²⁶⁰ This pesticide is commercially available in a liquid or granular formulation and has been used to control pests over a wide range of agriculturally relevant fruit, vegetable and ornamental crops.²⁶⁰ Avermectin has broad spectrum activity against nematodes by interfering with their neuromuscular transmission, resulting in paralysis and death.²⁶⁰ However, as explained in **Chapters III and IV**, avermectin suffers from poor water solubility and tends to bind to organic contents within the upper soil.³⁶³ To increase avermectin's accumulation at the root level, the pesticide has been encapsulated in several nanoparticle systems, including the plant virus RCNMV,¹⁹⁷ as well as chitosan³⁶⁴ and polymer (PLGA-PEG) nanoparticles³⁶⁵ resulting in higher pest control compared to free avermectin. My chemistry collaborators Justin Hochberg, Dr. Jon Pokorski, and Dr. Isaac Marks synthesized polymer and peptide-modified avermectin with ligation handles as shown in **Figure**

9.1. Using these compounds, I then began the bioconjugation of azide-modified avermectin to alkyne-modified TMGMV using click chemistry (**Figure 9.2**).

Following the successful synthesis of avermectin coupled to an azide (azido-avm, **Figure 9.1 A**), I tested its solubility and found that it remained insoluble in water, ethanol, methanol, DMSO, and DMF, but soluble in THF. This result was expected since the linker is made of an azide-coupled carbon rich chain; therefore, not increasing hydrophilicity. Unfortunately, this high hydrophobicity prevented the hydrolysis of the ester bond between avm and the linker, resulting in severe loss of potency against liquid cultures of *c. elegans* nematodes (data not shown). While 0.39 μM avm immobilized 50% of the nematode population within 48 hrs, 60 μM azido-avm was required to reach the same result.

I therefore tested whether the conjugation of azido-avermectin to the alkyne modified TMGMV would increase its solubility and therefore its bioavailability to nematodes in an aqueous solution. With a maximum loading efficiency of ~ 100 avm per TMGMV, I was unable to execute a nematode killing assay, which would require ~ 150 mg of TMGMV-avm. Moreover, as explained in **Chapter IV**, The IC_{50} value of avermectin against nematode is 1.309×10^{-4} mg cm^{-3} . If this concentration were to be reached at the root level of crops (~ 24 cm) using our current loading efficiency, at least 5.17×10^{-2} mg cm^{-3} of TMGMV-avermectin must be delivered by the roots and would require the application of 5.17 kg of TMGMV-avermectin per hectare of crops, which is not feasible.

We set out to replace the carbon linker with a PEG linker to increase solubility (**Figure 9.1 B**). PEG linkers for bioconjugate chemistry have been widely reported in the literature,³⁶⁶ and have led to the commercialization of numerous PEGylated drugs, as detailed in **Chapter I**. The number of repeating PEG chains could be altered to optimize loading, and functionalized PEG chains with

azide (N₃) and carboxylate (COOH) terminal groups are commercially available (*e.g.* Sigma Aldrich). We selected N₃-PEG₅₀₀-COOH (n = 10 monomers) and reacted it with avermectin via a Steglich esterification (see **Figure 9.1 B**). The synthesized product was difficult to purify and led to significant loss in final product, which prevented us to proceed with the conjugation of azido-PEG-avermectin to TMGMV.

As an alternative to PEGylation, we also tested the use of hydrophilic polypeptides as a linker. Specifically, we proposed the peptide *Cysteine-Arginine-Aspartic Acid-Arginine-Aspartic Acid-Arginine-Aspartic Acid-Lysine-Azide* which contains both positive and negative charges to strongly interact with water. The peptide was synthesized with a terminal cysteine for conjugation to maleimide modified avermectin and a terminal azide for click reaction with alkyne modified TMGMV (**Figure 9.1 C**). The hydrophobicity of avermectin prevented its successful conjugation to the zwitterionic hydrophilic peptide. Both the PEG and peptide linker synthesis were attempted only twice and future should focus on careful reaction optimization studies to maximize yields and purity of the final product.

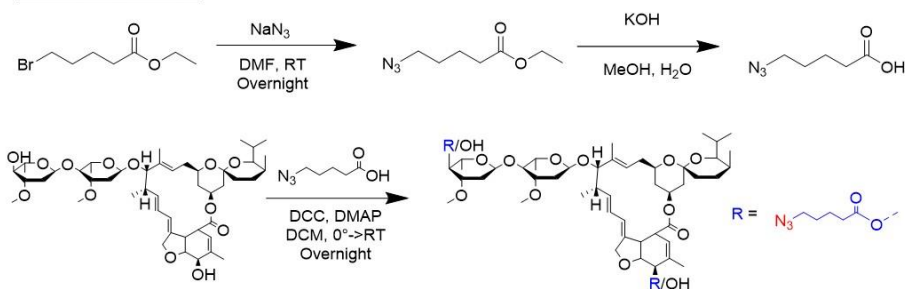
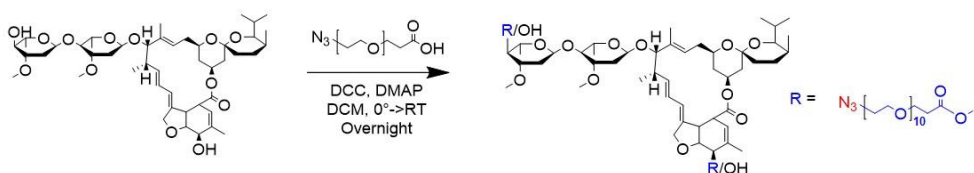
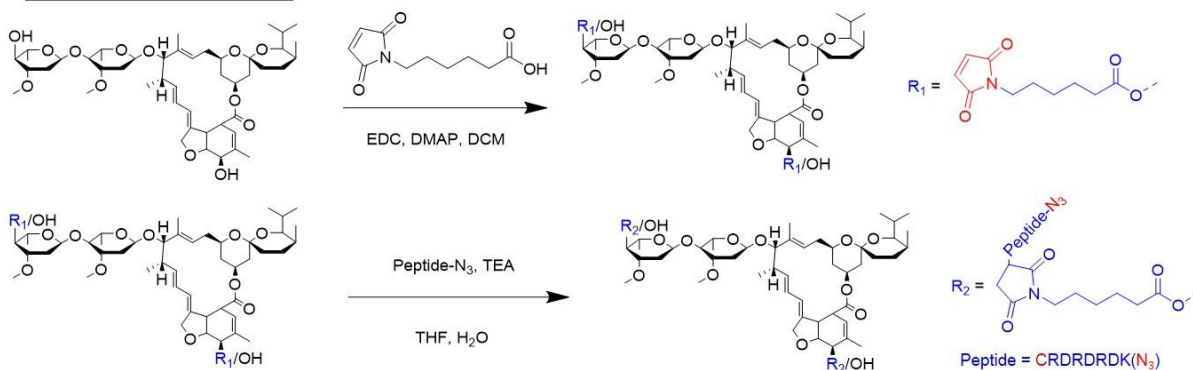
A azido-avermectin**B azido-PEG-avermectin****C azido-peptide-avermectin**

Figure 9.1. Avermectin synthesis schemes. Leading to modified azido-avermectin (A), azido-PEG-avermectin, comprised of $n = 10$ monomers (B), and azido-peptide-avermectin (C). All abbreviations are defined as follow: DMF: dimethylformamide, RT: room temperature, DCC: N,N'-dicyclohexylcarbodiimide, DMAP: 4-Dimethylaminopyridine, DCM: dichloromethane, EDC: 1-Ethyl-3-(3-dimethylaminopropyl)carbodiimide, TEA: triethylamine, THF: tetrahydrofuran.

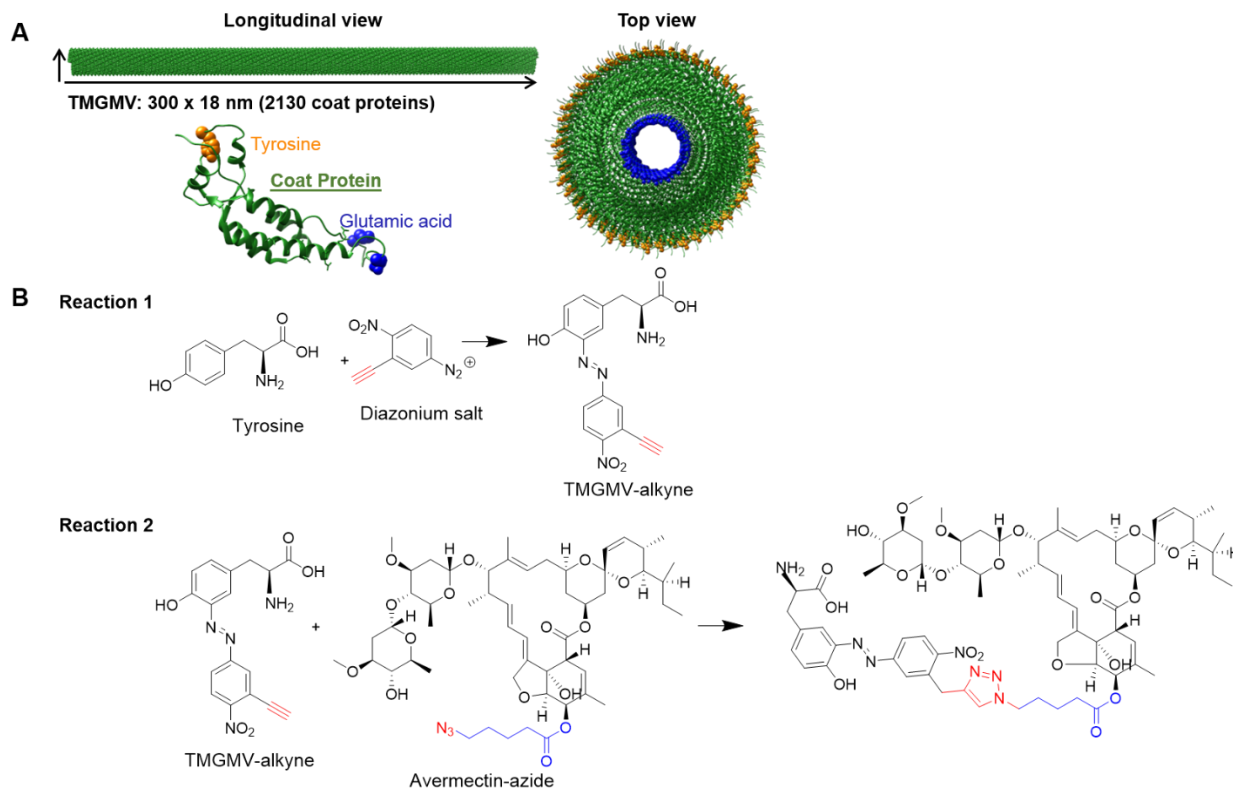


Figure 9.2. Conjugation and characterization of TMGMV-avermectin. A) Schematic representation of TMGMV (UCSD Chimera PDB ID: 1VTM) showing the dimension of the virus in its longitudinal and top view, as well as a single coat protein with the tyrosine and glutamic acid highlighted. B) Chemical conjugation scheme of azido-avermectin to TMGMV.

When thinking about translational applications in the field, we must also consider that TMGMV is infectious towards some plants. Thus, at first glance, applying VNPs to crops might seem counterintuitive since their natural hosts are plants. However, the TMGMV safety profile and possible risks of environmental contamination have been previously assessed²⁸ and showed that TMGMV infectability is limited to *Solanaceae* plants, such as tomatoes. Even so, to widely and safely apply TMGMV as a nanocarrier to crops, I developed protocols for viral inactivation using UV light (254 nm wavelength) and chemical treatments using β -propiolactone and formalin (**Chapter V**). The optimal doses are as follows: 10 J.cm⁻² UV, 1.5 M β -propiolactone, and 1 M

formalin. As discussed at length in **Chapter V**, UV treatment remains the cheapest, fastest and most reproducible inactivation modality, and could be easily integrated in the purification process. 10 J.cm^{-2} UV-TMG MV particles are on average 30 nm shorter than native TMGMV; or in other words ~10% shorter than native TMGMV. I speculate this difference would minimally influence TMGMV's soil mobility and loading capacity. While β PL maintained particle integrity, this expensive and biohazardous chemical leads to 40-60 % decrease in TMGMV yields as additional purification steps are required. Similarly, formalin maintains particle integrity but requires long treatment incubation (5 days) at the cost of lower yields (40-60 %) and shows the least consistent inactivation results among different plant species. Altogether, I would recommend UV treatment as the most suitable inactivation option.

Future developments could investigate the optimal aspect ratio for targeted delivery in soil as well as optimize the surface chemistry of TMGMV. For example, the length of TMGMV could be guided through self-assembly of the coat protein on different RNA templates – as has been done with TMV.^{182,367} Shorter, intermediate, or longer TMGMV particles might generate different soil mobility profiles that could be advantageous to control the distribution of pesticides in soil. For surface modifications, one could consider polymer coatings. For example, in the medical sector, a PEG coating is often used to increase the circulation time of nanoparticles and reduce their clearance by phagocytotic cells.¹¹² It remains to be determined whether the coating of pesticide nanocarriers with hydrophilic molecules such as PEG could decrease their interaction with soil and promote their accumulation at the root level. Other avenues not yet explored are the delivery of other types of pesticides, herbicides or fertilizers. One could consider tailoring the surface of TMGMV with positively charged molecules or peptides to reduce its soil mobility; in this approach, TMGMV could be used to deliver herbicides, which require close surface proximity.

Along these lines, I also briefly demonstrated that the non-infectious *Physalis mottle virus*-like particle (PhMV) had very poor soil mobility and could only penetrate the first 4 cm of soil (**Chapter IV**),²¹⁹ which could be advantageous to deliver herbicides, fertilizer, or pesticides against pests that remain above or close to the surface. To date, only two viruses (RCNMV and TMGMV) have been explored for agricultural applications, while dozens have been employed in nanomedicine (**Chapter I**). The work presented in this dissertation could therefore open the path to a new avenue in plant viral-based nanotechnology.

9.3. TMGMV as a nanocarrier for the delivery of therapeutics to cancer.

In cancer, nanocarriers on the market and in the development pipeline are predominantly spherical (**Chapter I**). The majority of nanocarriers rely on the enhanced permeability and retention (EPR) effect to deliver active ingredients to the tumor site.⁵ More importantly, particle properties, including size, shape, surface charge and functionalization have been tailored to optimize nanocarriers' ability to deliver therapeutics to tumor tissue.³⁶⁸ Surface charge, which is often measured by the zeta potential of nanoparticles, influences the pharmacokinetics and intratumoral cellular transport of nanocarriers. For example, neutral or slightly positively charged nanoparticles tend to internalize into cells to a greater extent than negatively charged particles.³⁶⁸ Surface functionalization of nanoparticles with PEG has a long history of enhanced circulation time, tumor accumulation, and decreased recognition by the immune system (**Chapter I**). Tumor homing of nanoparticles has been optimized using targeting ligands, aptamers, antibodies, or antibody fragments to promote their binding to receptors overexpressed on tumor cells or in the surrounding extracellular matrix.^{7,8} Size plays a major role in the biodistribution of nanoparticles; while spherical particles with a diameter near 100 nm have enhanced circulation time and tumor

accumulation, smaller particles may diffuse deeper in the tumor to promote a more uniform distribution of their therapeutic payload.³⁶⁹

A growing body of data shows increased tumor homing and tissue penetration with elongated rather than spherical nanocarriers.^{254,255,288} Elongated, rod-shaped or filamentous nanoparticles, including plant viruses such as TMV, have enhanced margination (migration toward blood-vessel walls) and increased transport across tissue membranes. For example, the effect of aspect ratio on particle biodistribution and tumor penetration was investigated in a colorectal adenocarcinoma-bearing murine model by generating TMV particles of various length.³⁶⁷ It was found that shorter rods (60 x 18 nm) had the greatest passive tumor homing whereas intermediary rods (130 x 18 nm) coated with the targeting ligand RGD achieved the greatest targeted tumor accumulation. Yet the underlying transport phenomena that explain the advantages of using high aspect ratio nanoparticles are not yet fully understood. To this end, I considered the diffusion and uptake of tobacco mosaic virus (TMV) in a spheroid system approximating a capillary-free segment of a solid tumor using a mathematical model (**Chapter VI**).³⁷⁰ At the time, no work had studied the use of TMGMV as a nanocarrier for cancer treatment, but TMV could have easily been substituted with TMGMV. Model simulations predicted TMV concentration distribution with time in a tumor spheroid for different sizes and cell densities. I quantified the effect of the TMV aspect ratio with and without cellular uptake by modulated surface chemistry. This theoretical analysis can be applied to other viral or non-viral delivery systems to complement the experimental development of the next generation of nanotherapeutics. Specifically, an increase in cell density decreased the constant rate of diffusion of nanoparticles, while increasing the cellular uptake rate of TMV prevented deep penetration. Simulations showed that PEGylated TMV formulations with lower aspect ratio accumulate further within the spheroid tumor system because they can diffuse

faster than those with a higher aspect ratio. In contrast, TMV nanocarriers with the targeting ligand RGD of any aspect ratio were rapidly taken up and therefore could not diffuse deeply in the spheroid tumor system. Nonetheless, higher aspect ratio nanoparticles have enhanced margination toward blood vessel walls, increased transport across tissue membranes, and reduced clearance by phagocytosis. In that regard, a balance must be established between immune evasion, tumor homing, and tissue penetration.

Based on these findings, I set to develop the first ever reported application of TMGMV in cancer therapy as a photosensitizer (PS) drug carrier (**Chapter VIII**).³⁷¹ Like most cancer nanocarriers summarized in **Chapter I**, the tumor accumulation of photosensitizer (PS) is generally poor due to the physicochemical properties of the PS³²⁴ and requires large doses to compensate for the poor drug accumulation. Prior to my work, viral nanoparticles (VNPs) have been developed as carriers for the delivery of contrast agents, chemotherapeutics, protein therapies, epitopes, as well as PS⁴⁴⁻⁴⁸. In most instances, PS agents were covalently coupled to the viral nanocarriers. However, covalent binding of the PS to nanoparticles may impair their photoactivity due to quenching and reduced molecular freedom and in turn limit their intracellular activity. Therefore, non-covalent drug delivery may be advantageous to enhance and control steady release of the PS within the tumor environment. This strategy relies on hydrophobic-hydrophilic and electron charge interactions between the PS and its carrier. Based on my previous experience with developing TMGMV as a pesticide carrier (**Chapter III**), I developed TMV and TMGMV based drug carriers that encapsulate the monocationic, dicationic, tricationic and tetracationic versions of porphyrin-based photosensitizer drugs (Zn-Por) (**Chapter VIII**). While TMV and TMGMV performed similarly, the maximum loading capacity and cell toxicity was achieved by loading tricationic Zn-Por into TMV. Furthermore, the functionalization of the TMV nanocarrier by my

collaborator Lu Wang with a nucleolin-targeted peptide (F3) led to increased anti-cancer efficacy. Overall TMGMV and TMV based PS nanocarriers hold great potential for cancer therapies with high specificity increasing both the patient's quality of life and survival.

Plant viruses present many advantages for biomedical applications¹⁷³: 1) They are non-infectious to humans, 2) they can be manufactured with high reproducibility and a degree of monodispersity unmatched by any synthetic nanocarriers, 3) they are easily scalable, 4) they naturally occur in a broad range of shapes and sizes, and 5) they can be chemically or genetically engineered to impart new functionalities. TMGMV has a tremendous potential in nanomedicine; as it has many suitable characteristics (*e.g.* high payload loading, enhanced margination, and tumor homing) for a diversity of medical applications (*e.g.* drug delivery or clinical imaging). TMGMV could therefore join the wide family of plant viral based nanocarriers currently on the rise for the diagnosis and treatment of cancer.¹⁷³ For example, the neoplastic drug doxorubicin has been conjugated to TMV,¹⁹⁵ infused into Cucumber mosaic virus (CMV)¹⁹⁶ and Red clover necrotic mosaic virus (RCNMV),¹⁹⁷ and passively complexed with PVX.¹⁹⁸ Virus-based nanocarriers have been successfully employed to deliver a variety of therapeutic small molecules (*e.g.* bortezomib,¹⁹⁹ cisplatin,^{200,201} 5-fluorouracil,²⁰² hygromycin,²⁰³ mitoxantrone,^{204,205} phenanthriplatin,²⁰⁶ and paclitaxel²⁰⁷), proteins (*e.g.* TRAIL,⁴⁰ TPA,²⁰⁸ and Herceptin^{209,210}), and nucleic acids (*e.g.* siRNA²¹⁴ and mRNA^{215,216}). Thus, the work presented in this dissertation will pave the way for TMGMV as a nanocarrier in medical applications.

9.4. Cancer *in situ* vaccination using inactivated CPMV.

As a standalone project, I also explored the effect of UV light and chemical inactivation on the ability of CPMV to induce a strong anti-tumor immune response (**Chapter VIII**). While

chemotherapeutic nanocarriers have limited efficacy against metastatic cancers, viral immunotherapy, if successful, triggers long-lasting and systemic anti-tumor immunity against both solid primary tumors and their metastases. Perhaps the most promising treatment approach is *in situ* (injected directly into the tumor) vaccination. Here, the virus acts as an adjuvant to stimulate the innate immune system and trigger “danger signals”. Activation of neutrophils, macrophages, and natural killer cells results in the lysing of cancer cells, as well as the recruitment of adaptive immune cells (*i.e.* T-cells) to promote a long lasting anti-tumor immune response.^{178,347} Interestingly, the source of antigen in this form of vaccination originates directly from the tumor itself. This strategy circumvents the need to generate patient-specific vaccine antigens and relies on all available tumor antigens present in the patient. Cowpea mosaic virus (CPMV) is a plant virus currently in the development pipeline for multiple biomedical applications, including immunotherapy.^{178,184} While CPMV is not infectious to mammals, it remains infectious to its host *Vigna unguiculata* (cowpea) plants (amongst other plants) and care must be taken to prevent environmental contamination. In the past, native CPMV and empty CPMV (eCPMV, non-infectious) have demonstrated potent anti-tumor responses in mouse models^{178,179} and canine patients,¹⁸⁴ but the native CPMV formulations demonstrated higher efficacy.³⁴⁸ The enhanced efficacy was attributed to the presence of the RNA, a known immune-stimulator, resulting in the activation of additional immune cells and further release of cytokines, which ultimately led to an extended survival rate of tumor-bearing mice.³⁴⁸ Therefore future translational work may consider RNA-laden but non-infectious CPMV. Therefore, I prepared inactivated CPMV. A comprehensive comparison of the viral inactivation of CPMV using UV light and the chemicals β PL and formalin was therefore carried out, and I report that 7.5 J.cm² UV, 50 mM β PL and 1 mM formalin is sufficient to inactivate CPMV viral infection. I compared the immunogenicity of native CPMV

and inactivated CPMV formulations *in vitro* using the RAW blue cell assay. Results indicate that inactivated UV and formalin treated CPMV formulations retain their immunogenicity. β PL severely reduced the immunogenicity of CPMV, most likely due to chemical alterations of important epitopes on the surface of CPMV and severe RNA damage. Further work is required to confirm the potential of inactivated CPMV to engage tumors immunologically and induce tumor regression in murine models and/or canine patients. An analysis of the cytokine and immune cell profile of treated mice would also be beneficial to fully understand the mechanism of action of the CPMV-based anti-cancer immune response. The work presented in this dissertation will facilitate the development and translation of environmentally safe CPMV-based immunotherapeutic vaccines.

9.5 Final remark.

In this dissertation, I demonstrated that plant virus-based nanocarriers hold great promises in both the agricultural and medical sectors. The work of this dissertation mainly focused on utilizing the plant virus TMGMV as a pesticide or therapeutic carrier. The rod-shape, zwitterionic, and proteinaceous nature of TMGMV confer many advantages, including 1) environmentally friendly, 2) biocompatible and non-infectious to mammals, 3) large payload capacity, 4) increased stability of hydrophobic cargos, 5) enhanced soil penetration, 5) enhanced margination and tumor homing, and) chemical and genetic engineerability. The work presented here is only a glimpse of TMGMV's true potential as biotechnological platform for medical, veterinary, or agricultural applications.

Appendix I: Supplementary Information of Chapter I

Supporting Table 1.1. Gene therapy nanocarriers undergoing clinical trials.

siRNA's target	Nanocarrier	siRNA/microRNA nanocarrier	specific treatment	opening year	phase	ClinicalTrials.gov ID
Be2L12	gold nanoparticle		Glioblastoma	2017	I	NCT03020017
CEBPA	liposome		liver cancer	2016	I	NCT02716012
ephrin type-A receptor 2	liposome		solid tumor cancer	2008	I	NCT01591356
fus1	liposome		non-small cell lung cancer	2003	I	NCT00059605
				2011	I/II	NCT01455389
growth receptor bound protein 2	liposome		leukemia	2010	I	NCT01159028
				2016	II	NCT02781883
				2016	I/II	NCT02923986
heat shock protein 47	vitamin A coupled lipid nanoparticle		extensive fibrosis	2014	I	NCT02227459
human stathmin 1	lipoplex		idiopathic Pulmonary Fibrosis	2018	II	NCT03538301
KRAS(G12D)	PLGA		Ewing's sarcoma	2016	I	NCT02736565
M2 subunit of ribonucleotide reductase	Transferrin-targeted Cyclodextrin-based polymer		metastatic cancer	2012	I	NCT01505153
MYC oncogene	lipid nanoparticle		pancreatic cancer	2012	II	NCT01676259
			solid tumor	2008	I	NCT00689065
			solid tumor, multiple myeloma, and lymphoma	2014	I	NCT02110563
			hepatocellular carcinoma	2014	I/II	NCT02314052
			solid tumor	2007	I	NCT00470613
			glioblastoma	2015	II	NCT02340156
			solid tumor	2015	I	NCT02354547
			metastatic pancreatic cancer	2015	II	NCT02340117
			central nervous system malignancies	2018	I	NCT03554707
			Adrenocortical Carcinoma	2010	I/II	NCT01262235
			Liver cancer	2011	I	NCT01437007
			advanced hepatocellular carcinoma	2014	I/II	NCT02191878
			solid cancer	2009	I	NCT00938574
			metastatic pancreatic cancer	2013	I/II	NCT01808638
			gene nanocarrier			
siRNA's target	Nanocarrier		specific treatment	opening year	phase	ClinicalTrials.gov ID
A chain of the diphtheria toxin	PEI		bladder cancer	2008	II	NCT00595088
			pancreatic cancer	2008	I/II	NCT00711997
			ovarian cancer	2009	I/II	NCT00826150
IL-2	PEG-PEI-cholesterol lipopolymer		ovarian cancer, fallopian tube cancer	2010	II	NCT01118052
REP 2139-Ca	nucleic acid polymer (REP 2139-Ca) + pegasys®		chronic hepatitis b	2016	II	NCT02726789

Supporting Table 1.2. Viral nanocarriers undergoing clinical trials.

AAV nanocarrier					
gene target	AAV specifications	specific treatment	opening year	phase	ClinicalTrials.gov ID
AAT α 1 antitrypsin	AAV1	AAT α 1 antitrypsin deficiency	2004	I	NCT00377416
			2006	I	NCT00430768
	2010		II	NCT01054339	
	2014		I	NCT02168686	
acid α -glucosidase	AAV1	Pompe disease	2010	I/II	NCT00976352
	AAV9		2017	I	NCT02240407
	AAV2/8		2018	I/II	NCT03533673
	not disclosed		2019	I/II	NCT04093349
achromatopsia CNGA3	AAV2	achromatopsia	2016	I/II	NCT02935517
	AAV2/8		2019	I/II	NCT03758404
achromatopsia CNGA3 + CNGB3	AAV2/8	achromatopsia	2017	I/II	NCT03278873
achromatopsia CNGB3	AAV2/8	achromatopsia	2005	I/II	NCT03001310
	AAV2		2015	I	NCT02599922
arylsulfatase A	AAV10	metachromatic leukodystrophy	2013	I/II	NCT01801709
aromatic L-amino acid decarboxylase	not disclosed	Parkinson's disease	2004	I	NCT00229736
	AAV2		2013	I	NCT01973543
	not disclosed		2015	I/II	NCT02418598
	AAV2		2018	II	NCT03562494
	AAV2	aromatic L-amino acid decarboxylase deficiency	2014	I/II	NCT01395641
			2016	II	NCT02926066
			2016	I	NCT02852213
α -sarcoglycan	AAVrh74	limb girdle muscular dystrophy type 2D	2013	I/II	NCT01976091
AT342	AAV8	Crigler-Najjar syndrome	2017	I/II	NCT03223194
Carcinoembryonic antigen	recombinant AAV	gastric cancer	2016	I	NCT02496273
CLN2	AAV10	Batten disease	2010	I/II	NCT01414985
CLN2	AAV10	Batten disease	2010	I	NCT01161576
CLN3	AAV9	Batten disease	2018	I/II	NCT03770572
CLN6	AAV9	Batten disease	2016	I/II	NCT02725580
Duchenne muscular dystrophy	AAVrh74	Duchenne muscular dystrophy	2015	I	NCT02376816
dysferlin	AAVrh74	dysferlin deficiency	2016	I	NCT02710500
Factor VIII	AAV5	hemophilia A	2015	I/II	NCT02576795
	recombinant AAV		2016	I/II	NCT03003533
	AAV2/6		2017	I/II	NCT03061201
	AAV2/8		2017	I	NCT03001830
	recombinant AAV		2018	III	NCT03392974
Factor IX	not disclosed	hemophilia B	2004	I/II	NCT00076557
Factor IX	AAV2/8	hemophilia B	2009	I	NCT00979238
	AAV8		2012	I/II	NCT01620801
	AAV10		2015	I/II	NCT02618915
	AAV8		2015	I/II	NCT02484092
	AAV5		2015	I/II	NCT02396342
	AAV2/6		2016	I	NCT02695160
	FLT180a		2017	I	NCT03369444
	AAV5		2018	III	NCT03569891
follistatin	AAV10	Becker muscular dystrophy sporadic inclusion body myositis	2012	I	NCT01519349
	AAV1	Duchenne muscular dystrophy	2015	I/II	NCT02354781
G11778A	AAV2	Leber's hereditary optic neuropathy	2014	I	NCT02161380
gamma-sarcoglycan	AAV1	limb girdle muscular dystrophy type 2D	2006	I	NCT01344798

Supporting Table 1.2. Viral nanocarriers undergoing clinical trials. Continues...

AAV nanocarrier					
gene target	AAV specifications	specific treatment	opening year	phase	ClinicalTrials.gov ID
Glial cell line-derived neurotrophic factor	AAV2	Parkinson's disease	2012	I	NCT01621581
glucocerebrosidase-1	AAV9	Parkinson's disease	2019	I/II	NCT04127578
Glutamic Acid Decarboxylase	not disclosed	Parkinson's disease	2003	I	NCT00195143
			2008	II	NCT00643890
human apolipoprotein E2	AAV10	alzheimer disease	2019	I	NCT03634007
human N-sulfoglucosamine sulfohydrolase + sulfatase modifying factor 1	AAV10	mucopolysaccharidosis III A	2013	I/II	NCT02053064
human N-sulfoglucosamine sulfohydrolase	AAV10	mucopolysaccharidosis III A	2018	II/III	NCT03612869
	AAV9		2019	I/II	NCT04088734
human RPE65	AAV2	Leber congenital amaurosis	2007	I/II	NCT00481546
	AAV2		2016	I	NCT02781480
human telomerase reverse transcriptase	AAV2	critical limb ischemia	2019	I	NCT04110964
IL-1Ra	AAV2	rheumatoid arthritis	2019	I	NCT02790723
lysosomal enzyme tripeptidyl peptidase 1	AAV2	late infantile neuronal ceroid lipofuscinosis	2005	I	NCT00151216
lysosome-associated membrane protein 2 isoform B (LAMP2B)	AAV9	Danon disease	2019	I	NCT03882437
microRNA targeting human HTT	AAV5	Huntington disease	2019	I/II	NCT04120493
NADH-ubiquinone oxidoreductase chain 4	AAV2	Leber hereditary optic neuropathy	2016	III	NCT02652767
			2016	III	NCT02652780
			2018	III	NCT03293524
nerve growth factor	AAV2	Alzheimer disease	2004	I	NCT00087789
			2009	II	NCT00876863
neurturin	AAV2	Parkinson's disease	2005	I	NCT00252850
			2006	II	NCT00400634
			2009	I/II	NCT00985517
NF-κB and IFN-β	AAV5	rheumatoid arthritis	2016	I	NCT02727764
			2018	I	NCT03445715
NTF3	AAV1	Charcot-Marie-Tooth neuropathy type 1A	2019	I/II	NCT03520751
N-sulfoglucosamine sulfohydrolase	AAV9	mucopolysaccharidosis III A	2016	I/II	NCT02716246
N-sulfoglucosamine sulfohydrolase + sulfatase modifying factor-1	AAV10	mucopolysaccharidosis III A	2011	I/II	NCT01474343
ornithine transcarbamylase	AAV8	ornithine transcarbamylase deficiency	2016	I	NCT02991144
porphobilinogen daminase	AAV2/5	acute intermittent porphyria	2012	I	NCT02082860
Rab escort protein 1	AAV2	choroideremia	2011	I/II	NCT01461213
			2015	II	NCT02553135
			2015	I/II	NCT02077361
			2015	I/II	NCT02341807
			2016	II	NCT02407678
			2016	II	NCT02671539
			2017	II	NCT03507686
			2018	III	NCT03496012
		X-linked retinoschisis	2018	I/II	NCT03316560
sarco/endoplasmic reticulum Ca2+-ATPase	AAV1	ischemic cardiomyopathy	2012	II	NCT01643330
			2015	I/II	NCT02346422
small synthetic dystrophin	AAV9	Duchenne muscular dystrophy	2017	I/II	NCT03368742
	AAVrh74		2017	I/II	NCT03375164
truncated human dystrophin	AAV2	Duchenne muscular dystrophy	2006	I	NCT00428935
	AAV9		2018	I	NCT03362502
tgAAC09	AAV2	HIV infections	2005	II	NCT00888446
tumor necrosis factor receptor immunoglobulin (IgG1)	AAV2	rheumatoid arthritis	2005	I/II	NCT00126724
UGT1A1	AAV8	Crigler-Najjar syndrome	2018	I/II	NCT03466463
X-linked retinoschisis	AAV2	X-linked retinoschisis	2015	I/II	NCT02416622
			2015	I/II	NCT02317887
			2017	I/II	NCT03199469
			2017	I/II	NCT03252847
	AAV8		2017	II/III	NCT03116113

Supporting Table 1.2. Viral nanocarriers undergoing clinical trials. Continues...

Adenovirus nanocarrier				
Gene cargo	specific treatment	Opening year	Phase	ClinicalTrials.gov ID
adenylyl cyclase 6	congestive heart failure	2008	I/II	NCT00787059
	reduced left ventricular ejection fraction	2017	III	NCT03360448
CD40	bladder cancer	2009	I/II	NCT00891748
fibroblast growth factor	myocardial Ischemia	2016	III	NCT02928094
GM-CSF	breast cancer	2009	I	NCT00880464
	colorectal cancer	2013	I	NCT01952730
interferon β	colorectal cancer	2005	I/II	NCT00107861
	pleural mesothelioma	2006	I	NCT00299962
interferon α -2b	bladder cancer	2012	II	NCT01687244
IL-12	prostate cancer	2005	I	NCT00110526
	breast cancer	2006	I	NCT00301106
	prostate cancer	2006	I	NCT00406939
	prostate cancer	2015	I	NCT02555397
	metastatic pancreatic cancer	2017	I	NCT03281382
p53	non-small cell lung cancer	2003	I	NCT00003649
	oral carcinoma	2003	I/II	NCT00064103
	bladder cancer	2003	I	NCT00003167
	ovarian cancer	2003	I	NCT00003450
	liver cancer	2004	I	NCT00003147
	ovarian cancer	2004	I	NCT00003588
	ovarian cancer	2004	I	NCT00002960
	brain tumor	2004	I	NCT00004080
	malignant glioma	2004	I	NCT00004041
metastatic breast cancer	2009	I	NCT00849459	
pigment epithelium-derived factor	neovascular age-related macular degeneration	2005	I	NCT00109499
REIC protein	prostate cancer	2013	I/II	NCT01931046
Thymidine kinase	primary brain tumor	2004	I	NCT00002824
	stage IV melanoma	2004	I	NCT00005057
	hepatocellular carcinoma	2006	II	NCT00300521
	prostate cancer	2007	II	NCT00583492
	malignant glioma	2008	I	NCT00751270
	malignant glioma	2008	II	NCT00589875
	pancreatic cancer	2008	I	NCT00638612
	hepatocellular carcinoma	2009	I	NCT00844623
	ovarian cancer	2009	I	NCT00964756
	high grade glioma	2009	II	NCT00870181
	prostate cancer	2013	I/II	NCT01913106
	non-small cell lung cancer	2016	II	NCT02831933
	non-small cell lung cancer	2017	I	NCT03029871
	hepatocellular carcinoma	2017	III	NCT03313596
	reccurent glioblastoma	2018	I/II	NCT03596086
reccurent glioblastoma	2018	I/II	NCT03603405	

Supporting Table 1.2. Viral nanocarriers undergoing clinical trials. Continues...

Adenovirus nanocarrier				
Gene cargo	specific treatment	Opening year	Phase	ClinicalTrials.gov ID
TNF- α	esophageal cancer	2003	II	NCT00051480
VEGF	refractory angina pectoris	2017	II	NCT03039751
		2019	I/II	NCT04125732
Lentivirus nanocarrier				
Gene cargo	Specific treatment	Opening year	Phase	ClinicalTrials.gov ID
adenosine deaminase	adenosine deaminase deficiency	2018	I/II	NCT03765632
arylsulfatase A	metachromatic leukodystrophy	2018	NA	NCT03725670
β A-T87Q-globin	transfusion-dependent β -thalassemia	2016	III	NCT02906202
	β -thalassemia major and Sickle cell disease	2014	I/II	NCT02151526
	β -Thalassemia major	2012	I/II	NCT01745120
	transfusion-dependent β -thalassemia	2017	III	NCT03207009
Herpes Simplex viral nanocarrier				
Gene cargo	Specific treatment	Opening year	Phase	ClinicalTrials.gov ID
collagen VII	dystrophic epidermolysis bullosa	2018	II	NCT03536143
preproenkephalin	cancer pain	2008	I	NCT00804076

Supporting Table 1.3. FDA and EMA approved polymer-protein conjugates.

polymer-protein conjugates				
drug name (company)	active ingredient	nanoparticle size	specific treatment	year of approval
Adagen® (Sigma Tau Pharmaceuticals)	adensine deaminase	41 kDa enzyme 5 kDa PEG	severe combined immunodeficiency diseases (SCID)	1990 [FDA]
Adynovate® (Baxalta)	coagulation factor VIII	280 kDa factor 20 kDa PEG	hemophilia	2015 [FDA]
Asparlas® (Servier)	L-asparaginase	31 kDa enzyme 5 kDa PEG	acute lymphoblastic leukemia	2018 [FDA]
Cimzia® (UCB)	certolizumab (target: TNF α)	48 kDa Fab 40 kDa PEG	Crohn's disease rheumatoid arthritis psoriatic arthritis ankylosing spondylitis moderate-to-severe plaque psoriasis	2008 [FDA] - 2009 [EMA] 2009 [FDA] - 2009 [EMA] 2013 [FDA] - 2009 [EMA] 2013 [FDA] - 2009 [EMA] 2018 [FDA] - 2019 [EMA]
Esperoct® (Novo Nordisk)	factor VIII	330 kDa factor 40 kDa PEG	hemophilia A	2019 [FDA]
Jivi (Bayer)	factor VIII	330 kDa factor 60 kDa PEG	hemophilia A	2018 [FDA] - 2018 [EMA]
Krystexxa® (Savient Pharmaceuticals)	urate oxidase	34 kDa enzyme 10 kDa PEG	chronic gout (hyperuricemia)	2010 [FDA] - 2013 [EMA]
Macugen® (Pfizer)	vascular endothelial growth factor antagonist	30 kDa aptamer 20 kDa PEG	macular degeneration	2004 [FDA] - 2006 [EMA]
Mircera® (Roche)	epoetin β	30 kDa hormone 30 kDa PEG	anemia associated with chronic renal failure	2007 [FDA] - 2007 [EMA]
Neulasta® (Amgen)	filgrastim	19 kDa filgrastim 20 kDa PEG	chemotherapy induced neutropenia	2002 [FDA] - 2002 [EMA]
Oncaspar® (Enzon Pharmaceuticals)	L-asparaginase	31 kDa enzyme 5 kDa PEG	acute lymphoblastic leukemia	2006 [FDA] - 2016 [EMA]
Palyngiq (Biomarin)	phenylalanine ammonia lyase	62 kDa enzyme 20 kDa PEG	phenylketonuria	2018 [US]
Pegasys® (Roche)	interferon α -2a	19 kDa inteferon 40 kDa PEG	hepatitis C	2002 [FDA] - 2002 [EMA]
Peg-Intron (Shering-Plough)	interferon α -2a	19 kDa inteferon 12 kDa PEG	hepatitis C	2001 [FDA] - 2000 [EMA] Discontinued in 2015
Plegridy® (Biogene)	interferon β -1a	24 kDa Inteferon 20 kDa PEG	multiple sclerosis	2014 [FDA] - 2014 [EMA]
Rebiny® (Novo Nordisk)	factor IX	56 kDa factor 40 kDa PEG	hemophilia B	2017 [FDA]
Somavert® (Pfizer)	recombinant DNA protein	22 kDa protein 5 kDa PEG	acromegaly	2003 [FDA] - 2002 [EMA]

Supporting Table 1.4. Polymer-protein conjugates undergoing clinical trials.

polymer-protein conjugates						
active ingredient	nanoparticle	specific treatment	opening year	phase	status	ClinicalTrials.gov ID
arginine deiminase	PEG (ADI-PEG 20)	small cell lung cancer	2010	II	terminated [2017]	NCT01266018
		hepatocellular carcinoma	2011	III	completed [2018]	NCT01287585
		hepatocellular carcinoma	2014	I	recruiting	NCT02102022
		argininosuccinate synthetase deficiency	2012	I	completed [2014]	NCT01528384
		metastatic melanoma	2012	I	completed [2016]	NCT01665183
		triple negative breast cancer	2013	I	completed [2016]	NCT01948843
		non-hodgkins' lymphoma	2013	II	completed [2018]	NCT01910025
		myeloid leukemia	2013	II	active	NCT01910012
		myeloid leukemia	2016	I	recruiting	NCT02875093
		pancreatic cancer	2014	I	active	NCT02101580
		liver cancer	2014	I	completed [2016]	NCT02101593
carboxyhemoglobin bovine	PEG	solid tumors	2017	I	recruiting	NCT03254732
		soft tissue carcinoma	2018	II	recruiting	NCT03449901
IFN α -2b	PEG	acute severe anemia	2016	I	completed [2017]	NCT02754999
		non-hodgkin's lymphoma	2004	II	completed [2013]	NCT00006039
		melanoma	2007	II	completed [2017]	NCT00025031
			2008	II	completed [2011]	NCT00623402
			2014	II	completed [2018]	NCT00701298
		hepatitis C	2007	II	completed [2017]	NCT00512278
		lymphoma	2008	N.A	terminated [2018]	NCT00724061
		solid tumors	2008	I	terminated [2014]	NCT02155322
		myeloid leukemia	2012	II	completed [2017]	NCT01725204
			2013	II	recruiting	NCT02001818
		squamous cell carcinoma	2014	II	active	NCT02218164
renal cell carcinoma	2014	II	active	NCT02089685		
	2015	II	completed [2017]	NCT02447887		
IFN α	PEG	hepatitis C	2011	III	withdrawn [2012]	NCT01447394
			2012	III	completed [2015]	NCT01616524
		hepatitis D	2016	II	completed [2019]	NCT02765802
oxyntomodulin (MOD-6031)	PEG	obesity	2016	I	completed [2018]	NCT02692781
proline-IFN α -2b	PEG	polycythemia vera	2015	III	completed [2016]	NCT02523638
somatropin	PEG	growth hormone deficiency	2011	II	completed [2017]	NCT01342146
			2015	IV	recruiting	NCT02380235
			2017	IV	recruiting	NCT03249480
synthetic human C-peptide (CBX129801)	PEG	type I diabetes	2012	II	completed [2015]	NCT01681290
irinotecan	PEG (NKTR 102)	ovarian cancer	2008	II	completed [2014]	NCT00806156
		colorectal cancer	2008	II	completed [2014]	NCT00598975
		bevacizumab-resistant high grade glioma	2012	II	completed [2016]	NCT01663012
		small cell lung cancer	2013	II	active	NCT01876446
		breast cancer	2014	II	active	NCT02312622

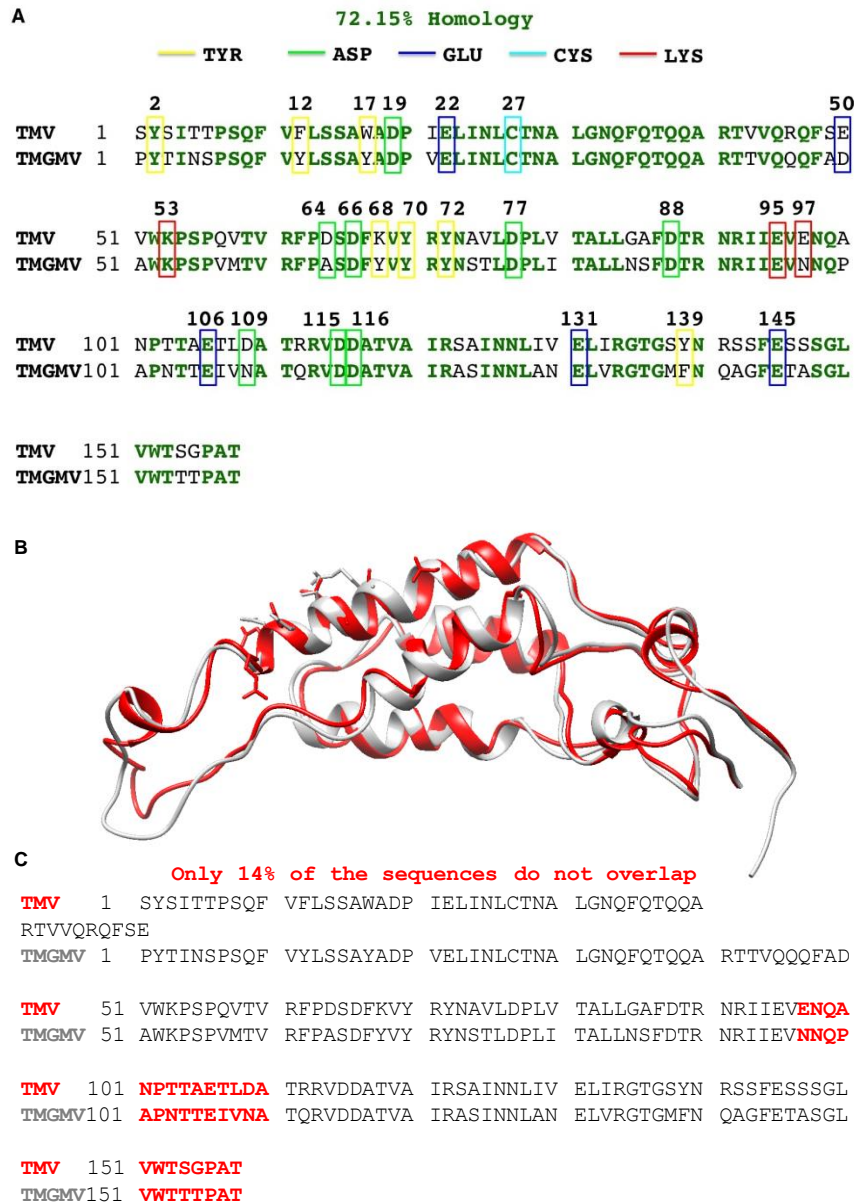
Supporting Table 1.4. Polymer-protein conjugates undergoing clinical trials. Continues...

polymer-protein conjugates						
active ingredient	nanoparticle	specific treatment	opening year	phase	status	ClinicalTrials.gov ID
human hyaluronidase	PEG (PEGPH20)	solid tumors	2010	I	completed [2014]	NCT01170897
		pancreatic cancer	2011	II	completed [2018]	NCT01453153
		pancreatic cancer	2013	I	active	NCT01959139
		pancreatic cancer	2013	II	completed [2018]	NCT01839487
		pancreatic cancer	2014	N.A	completed [2017]	NCT02241187
		pancreatic cancer	2016	II	terminated [2019]	NCT02910882
		pancreatic cancer	2018	I	recruiting	NCT03481920
		pancreatic cancer	2018	II	not yet recruiting	NCT03634332
		gastric cancer	2015	I	active	NCT02563548
		non-small cell lung cancer	2015	I	terminated [2019]	NCT02346370
		breast cancer	2016	I	active	NCT02753595
paclitaxel	poliglumex (Xyotax)	cholangiocarcinoma gallbladder adenocarcinoma	2017	I	active	NCT03267940
		ovarian cancer	2003	II	completed [2013]	NCT00017017
		ovarian cancer	2003	II	completed [2015]	NCT00060359
		prostate cancer	2007	II	completed [2017]	NCT00446836
		prostate cancer	2007	II	terminated [2017]	NCT00459810
		breast cancer	2005	II	completed [2007]	NCT00148707
		breast cancer	2005	I	completed [2013]	NCT00270907
		breast cancer	2005	II	completed [2016]	NCT00265733
		breast cancer	2010	II	withdrawn [2017]	NCT00017018
		non-small cell lung cancer	2006	II	terminated [2016]	NCT00352690
		non-small cell lung cancer	2007	II	completed	NCT00487669
esophageal cancer	2007	II	completed [2013]	NCT00522795		
camptothecin	cyclodextrin nanoparticle (crxl01)	non-small cell lung cancer	2011	II	completed [2017]	NCT01380769
		ovarian/tubal/peritoneal cancer	2012	II	completed [2018]	NCT01652079
		solid tumors	2006	I	completed [2017]	NCT00333502
	crxl01 + bevacizumab	ovarian cancer	2012	II	completed [2018]	NCT01652079
	crxl01 + bevacizumab	renal cell carcinoma	2014	II	completed [2017]	NCT02187302
	crxl01 + capecitabine	rectal cancer	2013	I	active	NCT02010567
	crxl01 + enzalutamide	prostate cancer	2018	II	recruiting	NCT03531827
	crxl01 + olaparid	small cell lung cancer	2016	I	recruiting	NCT02769962
	crxl01 + paclitaxel	ovarian cancer	2015	I	terminated [2019]	NCT02389985
	cyclodextrin nanoparticle + enzalutamide	prostate cancer	2018	II	recruiting	NCT03531827
cyclodextrin nanoparticle + olaparib	small cell lung cancer	2016	I	recruiting	NCT02769962	

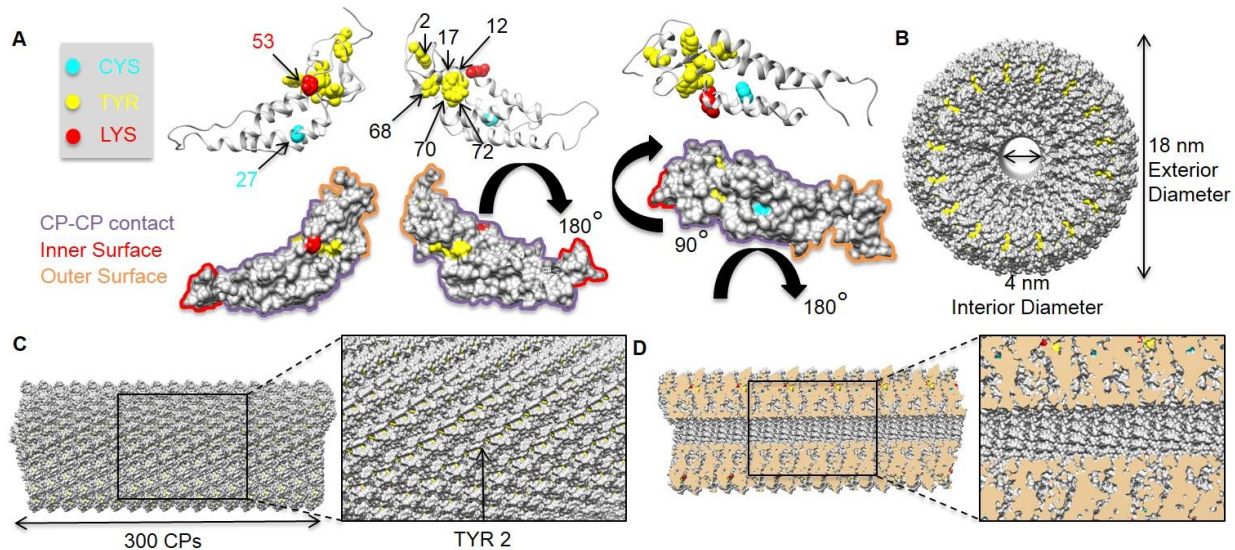
Supporting Table 1.5. FDA and EMA approved inorganic nanoparticles.

inorganic nanocarriers				
drug name (company)	active ingredient	nanoparticle size	specific treatment	year of approval
Dexferrum - DexIron® (Luitpold Pharmaceuticals)	dextran coated ferric oxyhydroxide	35 x 4.5 nm	iron deficiency anemia	1996 [US]
Feraheme™ (AMAG pharmaceuticals)	polyglucose sorbitolcarboxymethylether coated SPION	17 - 31 nm	iron deficiency anemia	2009 [US] - 2012 [EU]
Feridex® - Endorem® (AMAG Pharmaceuticals)	dextran coated SPION	120 - 180 nm	MRI contrast agent	1996 [US] Discontinued in 2008
Ferlecit® (Sanofi Avertis)	sodium ferric gluconate	<10 nm	iron deficiency anemia	1999 [US]
GastroMARK™ (AMAG pharmaceuticals)	silicone coated SPION	400 nm	MRI contrast agent	1996 [US] - 1996 [EU] Discontinued in 2012
INFeD® (Allergan Pharmaceuticals)	iron dextran	<10 nm	iron deficiency anemia	1974 [US]
Injectafer® - Ferinject® (Luitpold Pharmaceuticals)	ferric carboxymaltose	<10 nm	iron deficiency anemia	2013 [US]
Resovist®	carboxydextran coated SPION	60 nm	MRI contrast agent	2001 [EU] Discontinued in 2009
Venofer® (Luitpold Pharmaceuticals)	polynuclear iron (III)-hydroxide	<10 nm	iron deficiency anemia	2000 [US]

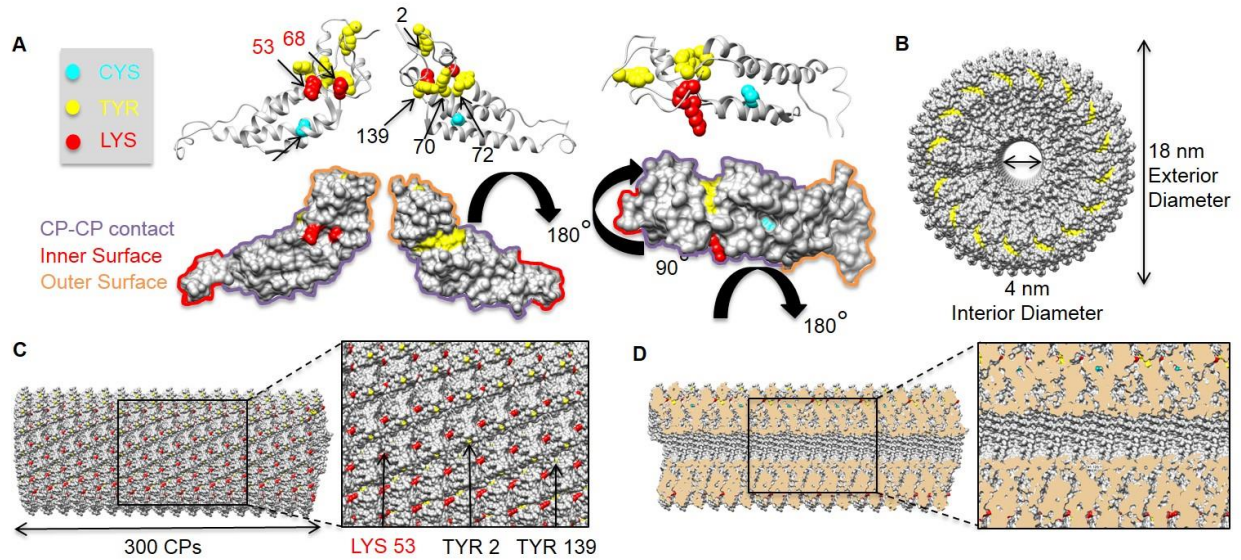
Appendix II. Supplementary Information of Chapter III



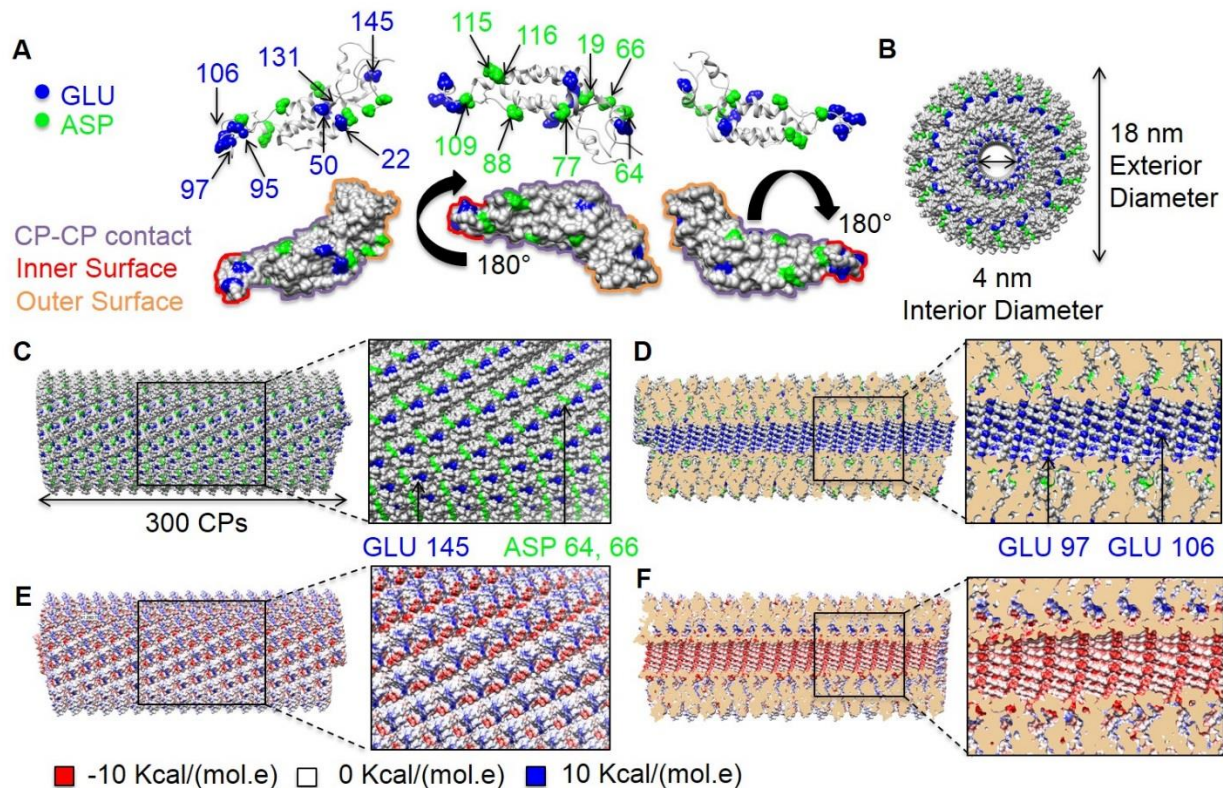
Supporting Figure 3.1. TMV and TMGMV sequence and structural comparisons. (A) Alignment of the 158 amino acid sequence of TMV and TMGMV. Amino acids that are identical in both sequences are highlighted in green. The position of TYR (yellow), ASP (green), GLU (blue), CYS (cyanine), and LYS (red), which are often targeted for bioconjugation or electrostatic drug loading, are also indicated. (B) The overlay of a single coat protein of TMV (red) and TMGMV (grey) indicates 86% homology; only 14% of the amino acids (highlighted in red in panel (C)) do not overlap.



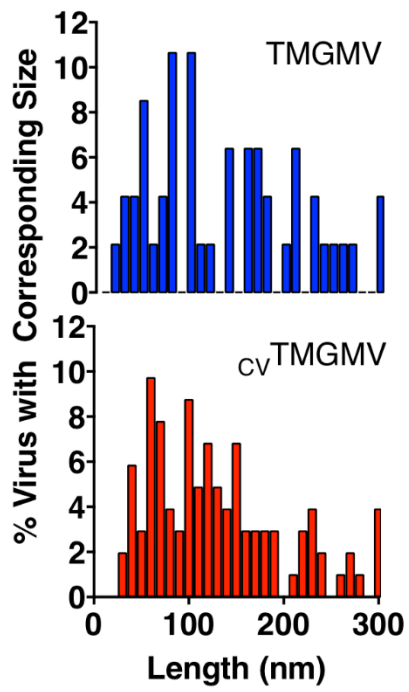
Supporting Figure 3.2. Positioning of cysteine, tyrosine, and lysine residues on TMGMV. (A) Depiction of a single coat protein (CP) of TMGMV in various orientations highlighting surface-exposed cysteine (CYS, cyanine), tyrosine (TYR, yellow), and lysine (LYS, red). (B) The cross-sectional orientation of the fully assembled TMGMV reveals the 4 nm-wide hollow channel of the 18 nm-wide cylindrical TMGMV. (C) Representation of a portion (300 CPs are depicted) of TMGMV in its longitudinal orientation; structural data indicate that TYR2 is solvent-exposed on the exterior TMGMV surface; no CYS or LYS residues are mapped. (D) No CYS, TYR, or LYS are solvent-exposed on the interior surface of TMGMV.



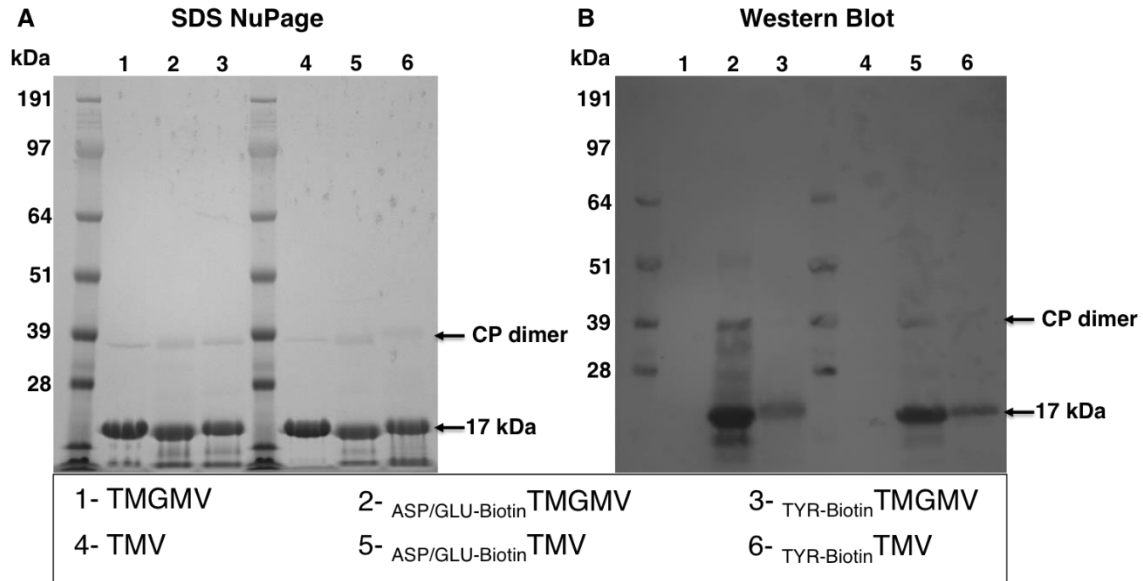
Supporting Figure 3.3. Positioning of cysteine, tyrosine, and lysine residues on TMV. (A) Depiction of a single coat protein (CP) of TMV in various orientations highlighting surface-exposed cysteine (CYS, cyanine), tyrosine (TYR, yellow), and lysine (LYS, red). (B) The cross-sectional orientation of the fully assembled TMV reveals the 4 nm-wide hollow channel of the 18 nm-wide cylindrical TMV. (C) Representation of a portion (300 CPs are depicted) of TMV in its longitudinal orientation; structural data indicate that TYR2 and TYR139 are solvent-exposed on the exterior TMV surface; no CYS or LYS residues are mapped. (D) No CYS, TYR, or LYS are solvent-exposed on the interior surface of TMV.



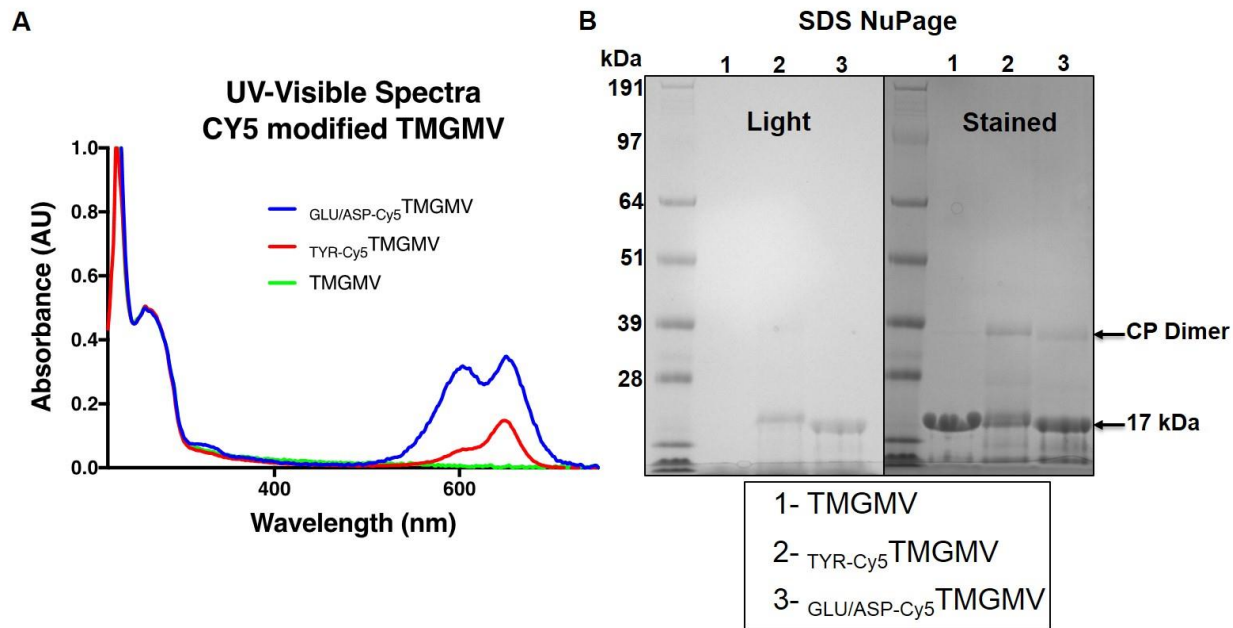
Supporting Figure 3.4. Structure of TMV. (A) Depiction of a single coat protein (CP) of TMV in various orientations highlighting surface-exposed glutamic acid (GLU, blue) and aspartic acid (ASP, green). Full-length TMV is formed by 2130 identical CP copies. (B) The cross-sectional orientation of the fully assembled TMV reveals the 4 nm-wide hollow channel of the 18 nm-wide cylindrical TMGMV. (C) Representation of a portion (300 CPs are depicted) of TMV in its longitudinal orientation; structural data indicate that GLU145, ASP64, and ASP66 are solvent-exposed on the exterior TMV surface – *nevertheless previous data indicate that these residues are not chemically addressable.*¹ (D) GLU97 and GLU106 appear solvent-exposed on the interior channel surface with GLU97 being more exposed compared to GLU106. (E, F) Coulombic surface coloring of the exterior and interior TMV surfaces.



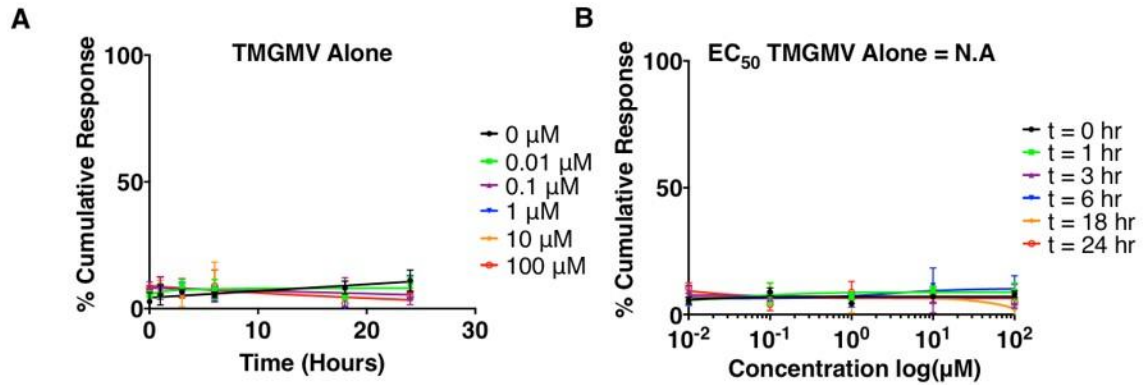
Supporting Figure 3.5. Size distribution analysis from TEM images. (A) TMGMV and (B) cvTMGMV.



Supporting Figure 3.6. Reactivity of ASP/GLU/TYR residues on TMV and TMGMV. (A) SDS NuPAGE gel of 1) native TMGMV, 2) ASP/GLU-Biotin TMGMV, 3) TYR-Biotin TMGMV, 4) native TMV, 5) ASP/GLU-Biotin TMV, 6) TYR-Biotin TMV. (B) Corresponding Western blot probed with streptavidin conjugated to alkaline phosphatase.



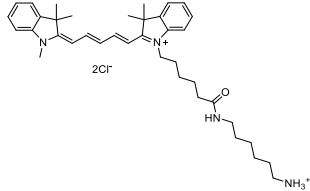
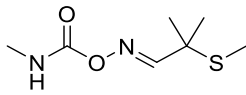
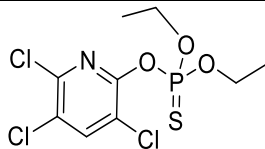
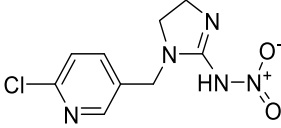
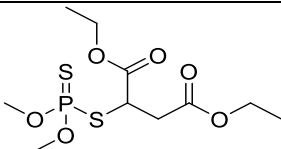
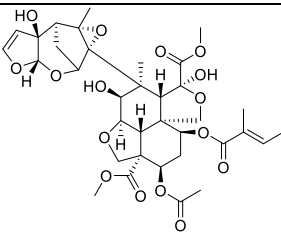
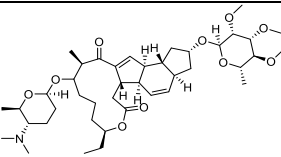
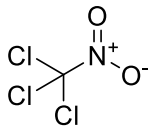
Supporting Figure 3.7. Characterization of modified TMGMV. (A) UV/ visible spectra of native TMGMV (green), TYR-Cy5 TMGMV (red) and GLU/ASP-Cy5 TMGMV (blue) nanoparticles. Spectra are normalized to the 260 nm wavelength peak. Based on the ratio of Cy5:TMGMV coat protein concentration, 7.5 % and 13% of the TYR-Cy5 TMGMV and GLU/ASP-Cy5 TMGMV coat proteins were modified respectively. (B) SDS NuPAGE gel of 1) native TMGMV, 2) TYR-Cy5 TMGMV and 3) ASP/GLU-Cy5 TMGMV under white light before and after Coomassie staining.

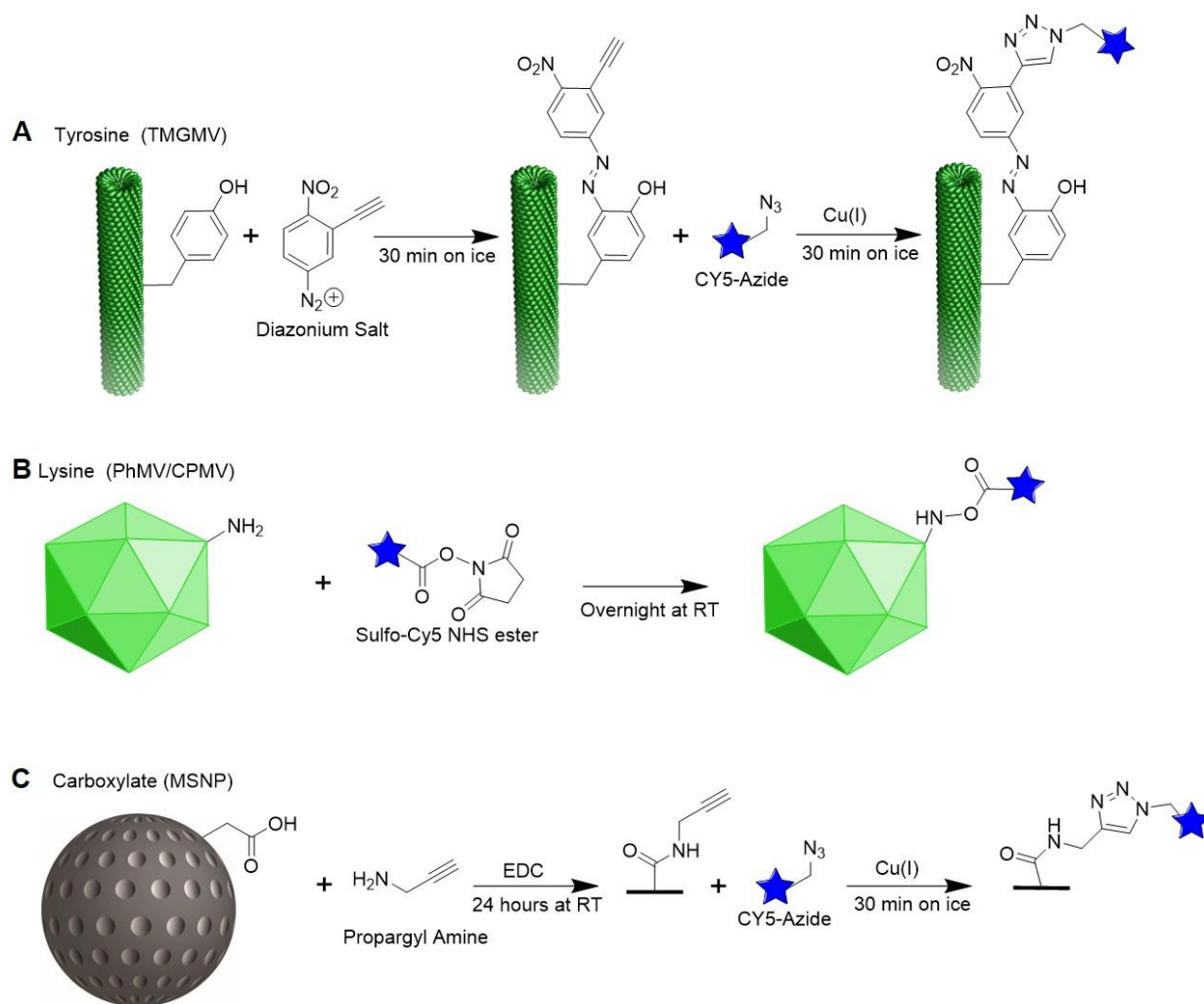


Supporting Figure 3.8. *C. elegans* neutralization assay with TMGMV alone. (A) Cumulative percent response over 24 h to various doses of TMGMV. The indicated molar concentration corresponds to the theoretical CV concentration used for the groups: free CV and TMGMV-delivered TMV. The concentrations correspond to 0.26 – 2600 μg per mL of proteome concentration. (B) Corresponding cumulative percent response as a function of theoretical CV concentration for given time of exposure to TMGMV.

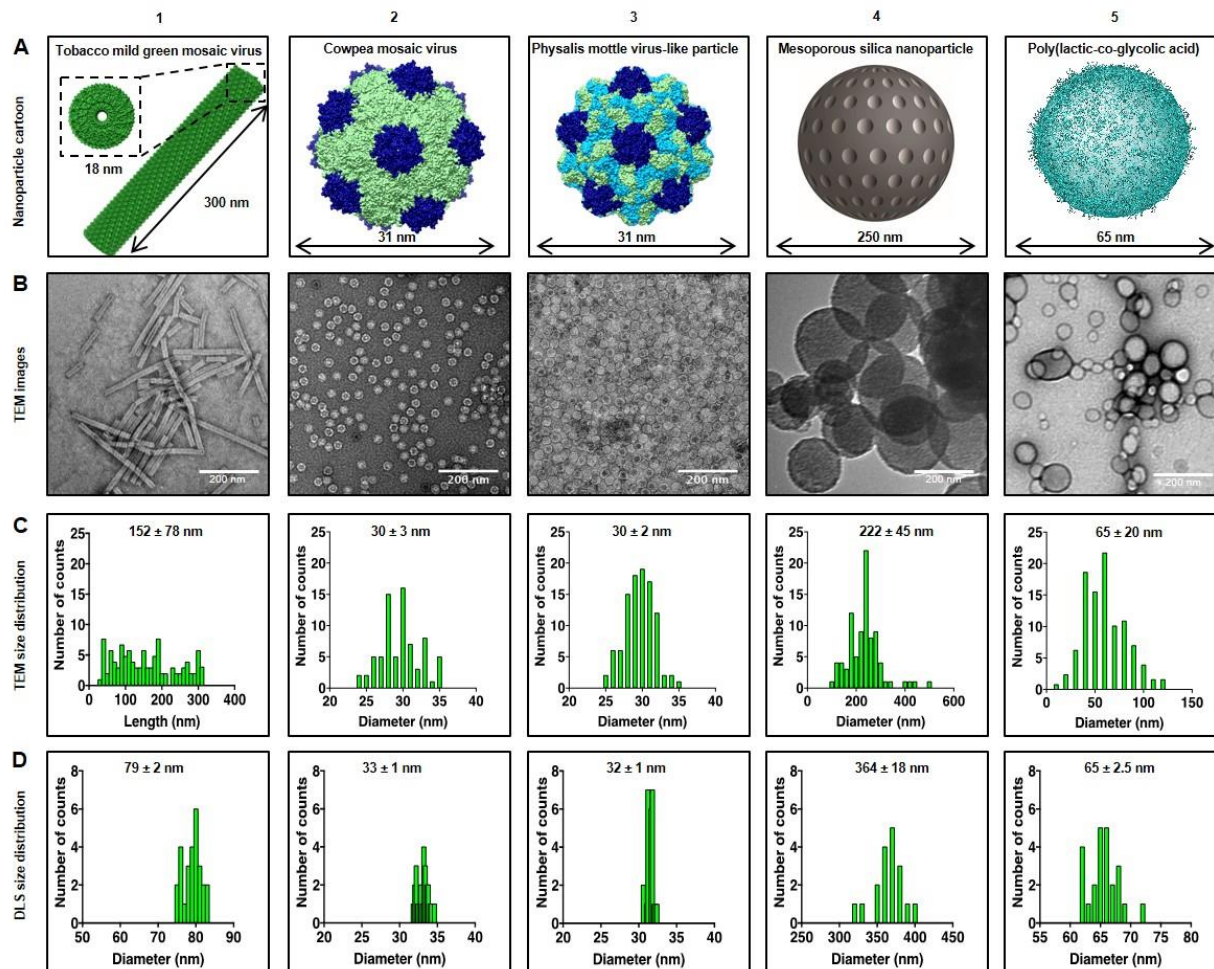
Appendix III: Supplementary Information of Chapter IV

Supplementary Table 4.1. Comparison of conventional pesticides to the model drug Cy5.

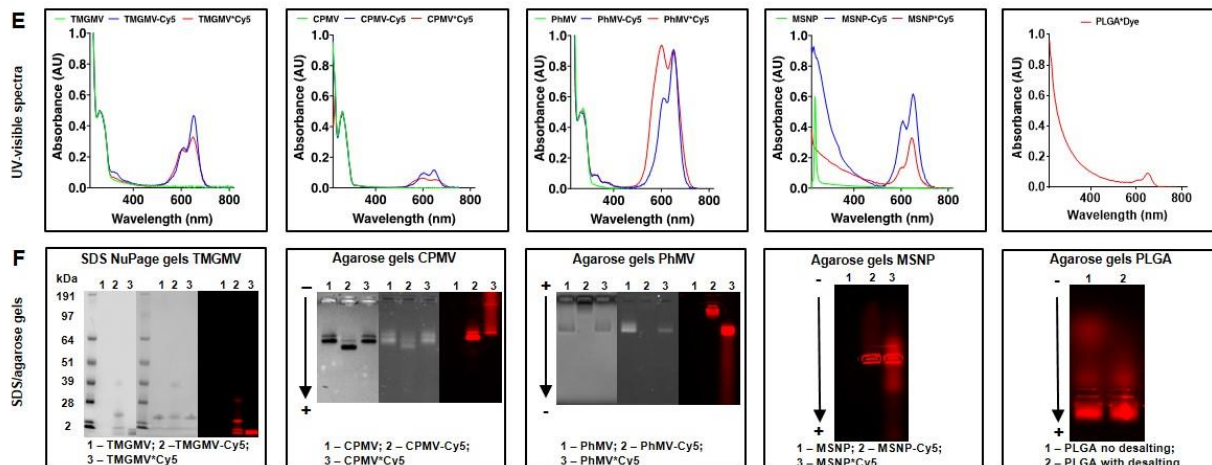
Root pests	Pesticide	Log P (oct/aqu)	Molecular weight (g/mol)	Chemical structure
Model pesticide	Cyanine 5	3.2	747	
Nematode	Aldicarb	1.13	190.3	
	Chlorpyrifos	4.96	350	
Beetle grubs	Imidacloprid	0.57	255.6	
	Melathion	2.36	330.4	
Moths caterpillars root aphids	Azadirachtin	1.09	720.7	
	Spinosad	2.8	731.9	
Root fungus	Chloropicrin	2.09	164.4	



Supporting Figure. 4.1. Cy5 conjugation to TMGMV, PhMV, CPMV and MSNP. The schematics show chemical conjugation of Cy5 to (A) the surface-exposed tyrosine residues of TMGMV using diazonium chemistry followed by click chemistry, (B) the surface exposed lysine residues of PhMV and CPMV using NHS chemistry, and (C) the carboxylate groups of MSNP via EDC and click chemistry.



Supporting Figure. 4.2. Nanoparticle characterization. (A) Simplified representation of (1) TMGMV (PDB ID: 1VTM), (2) CPMV (PDB ID: 1NY7), (3) PhMV (PDB ID: 1QJZ), (4) MSNP, and (5) PLGA. (B) Corresponding TEM images obtained using a Tecnai F-30 transmission electron microscope. Scale bar = 200 nm. (C) Size distribution analysis of the TEM images. (D) Particle size distribution obtained by dynamic light scattering (DLS).

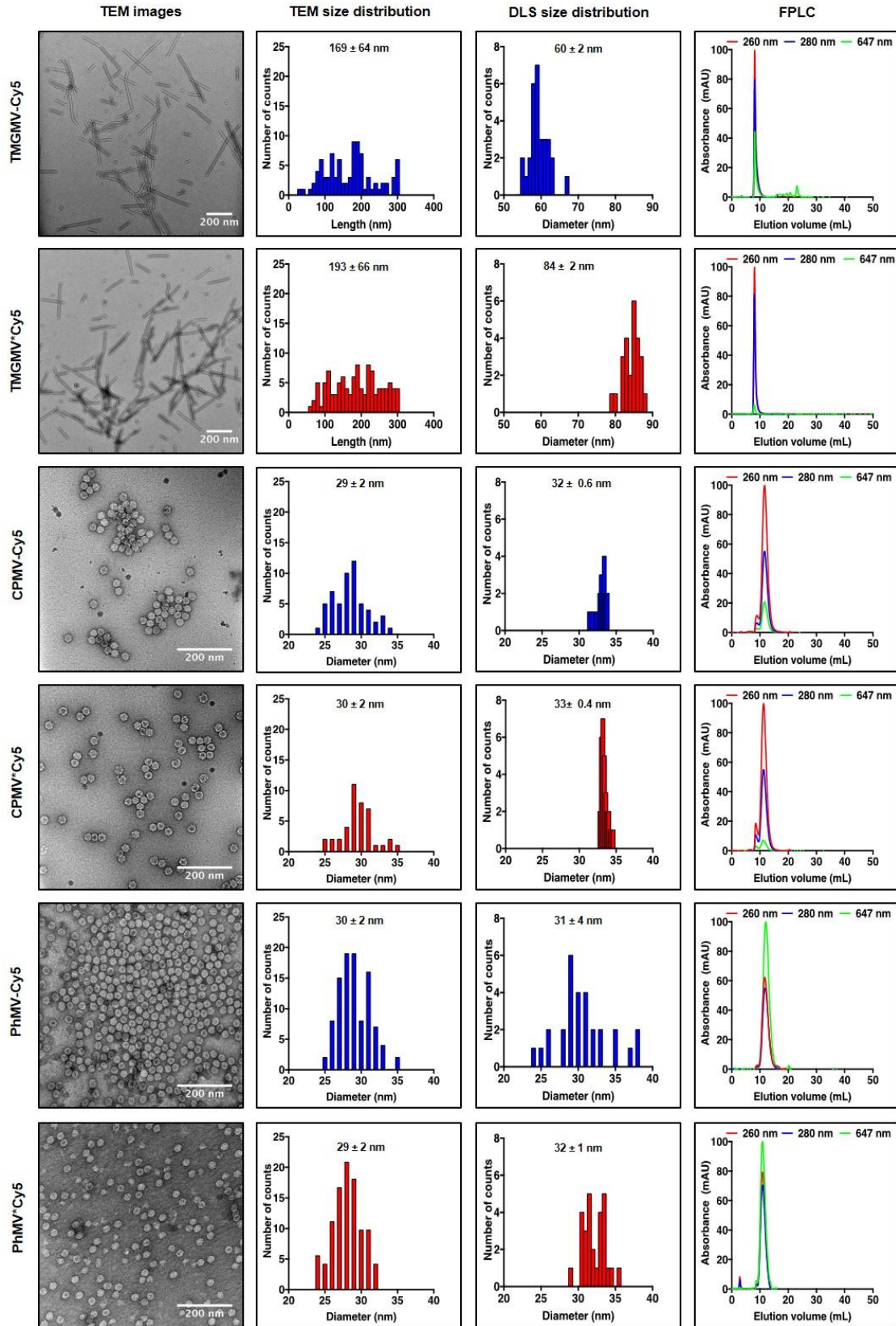


Supporting Figure. 4.2. Nanoparticle characterization continues. (E) UV/Vis spectra of bare nanoparticles (green), Cy5-conjugated nanoparticles (blue), and Cy5-infused nanoparticles (red). Spectra were normalized to the 260 nm wavelength peak. (F) SDS-PAGE analysis of the different TMGMV formulations. Left to right gels were imaged under white light before staining, white light after staining, and under red fluorescence, respectively. In addition, agarose gels of the CPMV, PhMV, MSNP and PLGA formulations are shown. Left to right agarose gels were imaged under white light after staining, UV light, and under red fluorescence.

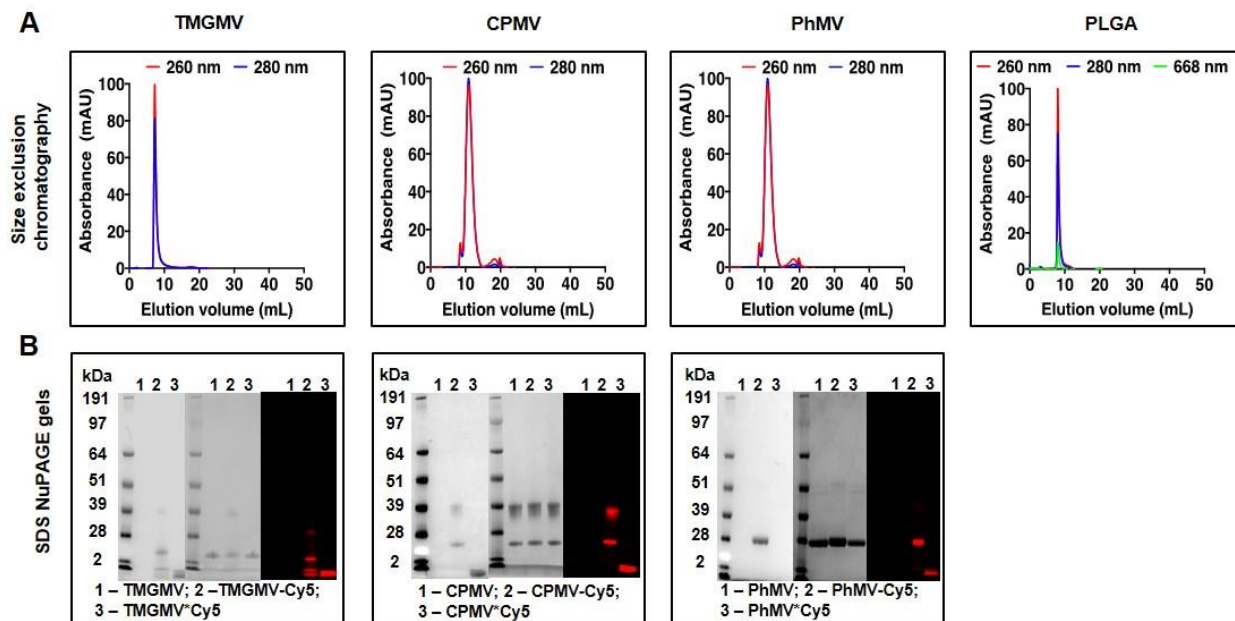
Characterization results. TEM imaging revealed monodisperse CPMV (30 ± 3 nm) and PhMV (30 ± 2 nm) samples, but polydisperse TMGMV (152 ± 78 nm), MSNP (222 ± 45 nm), and PLGA (65 ± 20 nm) samples (**Supporting Figure 4.2 B+C**). Plant viruses are naturally produced as identical copies and therefore are highly monodisperse. This level of quality control has yet to be achieved using synthetic nanoparticles such as MSNP and PLGA. The polydispersity of TMGMV has been reported²¹⁸ and is attributed to greater particle instability during virus production and purification and due to the TEM grid preparation, when the particles may break. DLS was also used to measure the hydrodynamic radii of TMGMV (79 ± 2 nm), CPMV (33 ± 1 nm), PhMV (32 ± 2 nm), MSNP (364 ± 18 nm), and PLGA (65 ± 2.5 nm), in agreement with the TEM data (**Supporting Figure 4.2 D**). The hydrodynamic radius of TMGMV is inaccurate because of the rod-like shape of the particle, but the data can still be used to semi-quantify the

degree of polydispersity of the TMGMV sample. I attribute the increased hydrodynamic radius of MSNP to its physicochemical properties (many carboxylate residues on the surface, which may promote the formation of a water shell around the nanoparticle). Particles were further characterized post-conjugation or after the encapsulation of Cy5. TEM and DLS results revealed no apparent differences in size and polydispersity between the nanoparticles with and without Cy5 (**Supporting Figure 4.3**). The dye loading efficiency was quantified by UV/Vis spectroscopy using the Beer–Lambert law and specific extinction coefficients (**Supporting Figure 4.2 E**). Overall, the dye loading efficiency (nmol of dye per mg of nanoparticle) was higher when the fluorophore was conjugated to the nanoparticle (denoted as nanoparticle-Cy5) rather than passively encapsulated (denoted as nanoparticle*Cy5). Specifically, the loading efficiencies of TMGMV-Cy5 (9.9 nmol mg⁻¹ or 390 dyes per TMGMV), CPMV-Cy5 (6.2 nmol mg⁻¹ or 35 dyes per CPMV), PhMV-Cy5 (12.7 nmol mg⁻¹ or 60 dyes per PhMV), and MSNP-Cy5 (6.4 nmol mg⁻¹) were higher than corresponding encapsulated formulations TMGMV*Cy5 (5.3 nmol mg⁻¹ or 210 dyes per TMGMV), CPMV*Cy5 (2.3 nmol mg⁻¹ or 15 dyes per CPMV), PhMV*Cy5 (11.7 nmol mg⁻¹ or 55 dyes per PhMV), MSNP*Cy5 (4.3 nmol mg⁻¹), and PLGA*Dye (1.2 nmol mg⁻¹). The loading efficiency can be ranked from highest to lowest as follows: PhMV > TMGMV > CPMV > MSNP > PLGA. Agarose gel electrophoresis, SDS-PAGE and SEC (**Supporting Figure 4.4**) confirmed the covalent attachment or encapsulation of Cy5, as indicated by the presence of fluorescence under red light (**Supporting Figure 4.2 F and 4.4**). SDS-PAGE only works with protein samples, so PLGA and MNSP were characterized in agarose gels only. Due to its shape and size, TMGMV has no mobility in agarose gels and therefore was only characterized by SDS-PAGE. On the agarose gels, free Cy5 moves toward the anode due to its overall positive charge. Because of their net electronegativity, CPMV, PLGA and MSNP move toward the cathode,

whereas the positively charged PhMV particles move toward the anode. The Cy5-conjugated nanoparticle samples showed no apparent sign of free fluorophores. On the other hand, the formulation containing Cy5 passively encapsulated in the nanoparticles revealed that a portion of the Cy5 was indeed released during gel electrophoresis. In addition to the red light, agarose gels loaded with viruses were imaged under white light after staining with Commassie Brilliant Blue, and under UV light to check for the presence of RNA. Both PhMV and CPMV samples revealed the presence of encapsulated RNA. The presence of RNA in PhMV is the result of “junk” RNA encapsulation during the capsid self-assembly in the bacterial culture. Denaturing SDS-PAGE gels further confirmed the covalent attachment or encapsulation of Cy5 (**Supporting Figure 4.2 F and 4.4**). The TMGMV and PhMV coat proteins are ~17 kDa and ~26 kDa, respectively. CPMV is composed of 60 coat proteins, each comprising a small (24 kDa) and a large (42kD) subunit. Cy5 has a molecular weight of ~650 Da, which is too small to cause a visible shift of the coat protein electrophoretic mobility. Nonetheless, the covalently bound Cy5 co-localize with the coat proteins of TMGMV, PhMV and CPMV, whereas the encapsulated dye travels freely to the anode. In the Cy5 conjugated virus samples, a portion of the Cy5 travelled freely to the anode. Because the samples were meticulously desalted prior to the experiment to remove any remaining free Cy5, this result indicates that the dye molecules detached from the coat proteins during sample preparation.



Supporting Figure. 4.3. Characterization of Cy5-labelled viruses.



Supporting Figure. 4.4. SEC and SDS-PAGE analysis of Cy5-labelled viruses. (A) Size exclusion chromatography of TMGMV, CPMV, PhMV and PLGA. (B) SDS-PAGE analysis of viruses. From left to right, gels were imaged under white light before staining, after staining with Coomassie Brilliant Blue, and under red light.

Supporting Table 4.2. Soil composition.

Analysis was contracted to Western Laboratories, Parma, ID.

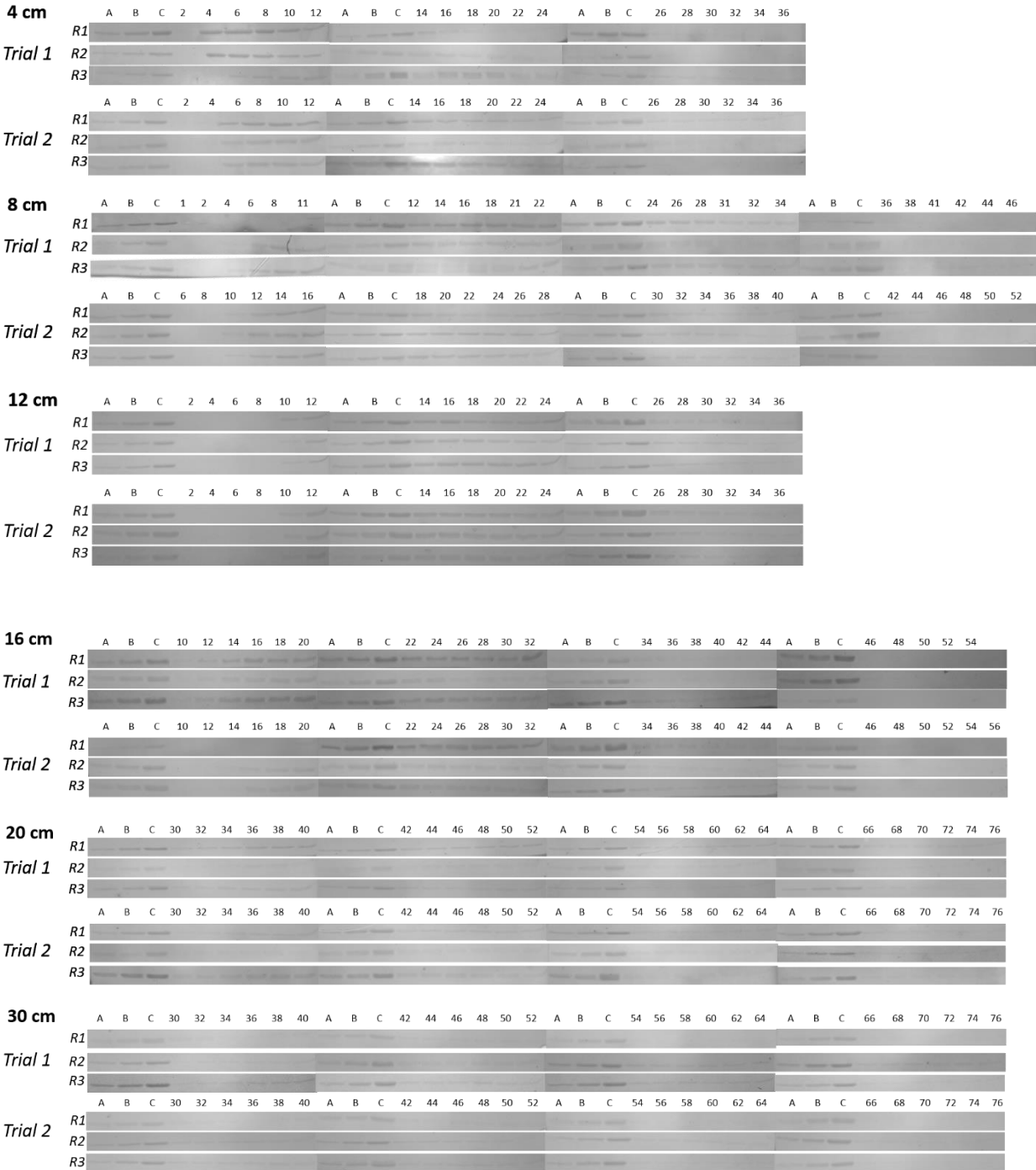
ELEMENT	ANSWER	INTERP	SHOULD BE	ELEMENT	ANSWER	INTERP	SHOULD BE
pH-Soil	6.7	Neutral Soil		Sulfur-ppm	12	Low	20 +
pH-SMP				Calcium-ppm	3567	High	1,800 +
Soluble Salts	0.30	Optimum	< 1.5	Magnesium-ppm	674	Very High	250 +
% Lime	0	No lime		Sodium-ppm	29	Optimum	< 225
% Organic Matter	36.55	Very High		Zinc-ppm	0.5	Very Low	1.0 - 3.0
Nitrates-ppm	27	Optimum	10 - 35	Copper-ppm	0.8	Low	0.8 - 2.5
Ammonium-ppm	6	Optimum	5 +	Manganese-ppm	4	Low	6 - 30
Phosphorus-ppm	7	Very Low	25 - 40	Iron-ppm	11	Medium	25 +
Phos-ppm-Bray			50 - 100	Boron-ppm	0.3	Very Low	0.7 - 1.5
Potassium-ppm	125	Low	300 +	TBS%	0		
Texture	Water Holding Capacity/foot			Bulk Density			
Cation Exchange Capacity - CEC	7	P Index			Fertilizer Suggestions in Pounds per Acre for the whole season		
Percent Base Saturation	98						
BASES		IDEAL	YOURS		NO3 ppm	NH4 ppm	Crop
Calcium-% of CEC	65-80	73	1 Ft	27	6		Yield Goal
Magnesium-% of CEC	10-20	23	2 Ft				Past Crop
Potassium-% of CEC	2-6	1	3 Ft				Acres
Sodium-% of CEC (ESP)	< 5	1	Total N PPM		33		Nitrogen
Hydrogen-% of CEC	< 15	2	Lbs N / Acre		99		Phosphate
Ratio	Ideal	Yours	Evaluation	Recommendations			Add Phos for P INDEX
Ca:Mg	6-20:1	5 :1	Low	Watch Ca			Potash
Ca:K pH >7	15:1	:1					P.F. Sulfur
Ca:K pH <7	10:1	29 :1	Low				Elemental Sulfur
Ca:P pH >7	100:1	:1					Gypsum
Ca:P pH <7	40:1	510:1	High	Watch P			Lime
P:Zn	15:1	14 :1	OK				Dolomite
P:Mn	4:1	2:1	OK				Magnesium
P:Cu	25:1	9 :1	OK				Zinc
Zn:Cu	3:1	1 :1	OK				Manganese
Mn:Zn	3:1	8 :1	High	Watch Zn			Copper
Mn:Cu	7:1	5 :1	OK				
K:B	200:1	417 :1	High	Watch B			
Mg:K	2:1	5 :1	High	Watch K			

Supporting Table 4.3. Soil particle size distribution.

Adsorption surface per particle volume ϕ .			Distribution				
Particle Size (μm)	Surface area (μm^2)	Volume (μm^3)	Read 1	Read 2	Average	Φ (μm^{-1})	Weighted average Φ (μm^{-1})
1000	3140000	523333333	0.72	1.34	1.03	0.0060	0.0000618
500	785000	65416667	8.29	8.60	8.45	0.0120	0.0010134
250	196250	8177083	14.31	13.69	14.00	0.0240	0.00336
200	125600	4186667	5.46	5.34	5.40	0.0300	0.00162
150	70650	1766250	7.55	7.47	7.51	0.0400	0.003004
125	49063	1022135	5.03	5.00	5.02	0.0480	0.0024072
100	31400	523333	6.28	6.27	6.28	0.0600	0.003765
75	17663	220781	7.92	7.92	7.92	0.0800	0.006336
62.5	12266	127767	4.68	4.70	4.69	0.0960	0.0045024
50	7850	65417	5.27	5.29	5.28	0.1200	0.006336
40	5024	33493	4.72	4.74	4.73	0.1500	0.007095
30	2826	14130	5.29	5.29	5.29	0.2000	0.01058
20	1256	4187	6.18	6.14	6.16	0.3000	0.01848
19	1134	3590	0.69	0.68	0.69	0.3158	0.002163158
18	1017	3052	0.69	0.68	0.69	0.3333	0.002283333
17	907	2571	0.71	0.71	0.71	0.3529	0.002505882
16	804	2144	0.73	0.72	0.73	0.3750	0.00271875
15	707	1766	0.75	0.74	0.75	0.4000	0.00298
14	615	1436	0.77	0.76	0.77	0.4286	0.003278571
13	531	1150	0.79	0.79	0.79	0.4615	0.003646154
12	452	904	0.81	0.81	0.81	0.5000	0.00405
11	380	697	0.85	0.85	0.85	0.5455	0.004636364
10	314	523	0.88	0.88	0.88	0.6000	0.00528
9	254	382	0.92	0.91	0.92	0.6667	0.0061
8	201	268	0.97	0.96	0.97	0.7500	0.0072375
7	154	180	1.02	1.02	1.02	0.8571	0.008742857
6	113	113	1.09	1.09	1.09	1.0000	0.0109
5	79	65	1.15	1.14	1.15	1.2000	0.01374
4	50	33	1.22	1.22	1.22	1.5000	0.0183
3	28	14	1.27	1.26	1.27	2.0000	0.0253
2	13	4	1.32	1.32	1.32	3.0000	0.0396
1.5	7	2	0.67	0.67	0.67	4.0000	0.0268
1	3	1	0.65	0.66	0.66	6.0000	0.0393
0.5	1	0	0.35	0.35	0.35	12.0000	0.042
0.01	0	0	0.00	0.00	0.00	600.0000	0
0	0	0	0.00	0.00	0.00		0
ΣSum			100.0	100.0	100.0		0.34012337
Sand			60.2	60.3			
Silt			38.1	38.0			
Clay			1.7	1.7			
$\Sigma\sqrt$			100.0	100.0			
NRCS Soil Texture			sandy loam	sandy loam			

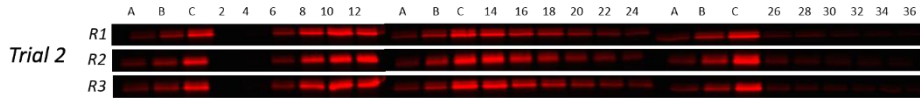
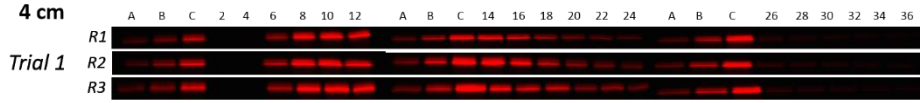
Supporting Figure. 4.5. SDS-PAGE and dot blot analysis of nanoparticle elution fractions.

TMGMV

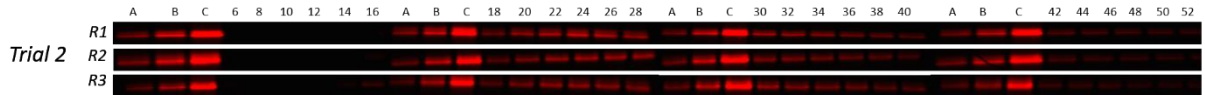
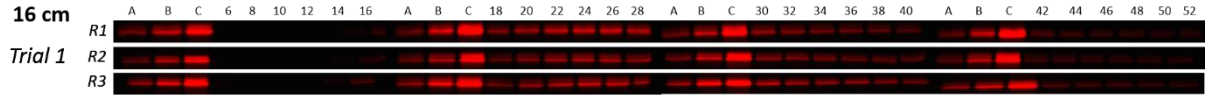


TMGMV-Cy5

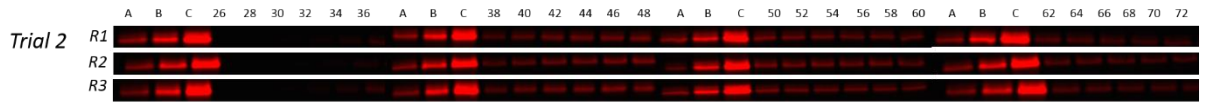
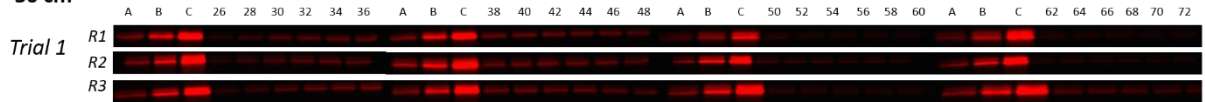
4 cm



16 cm

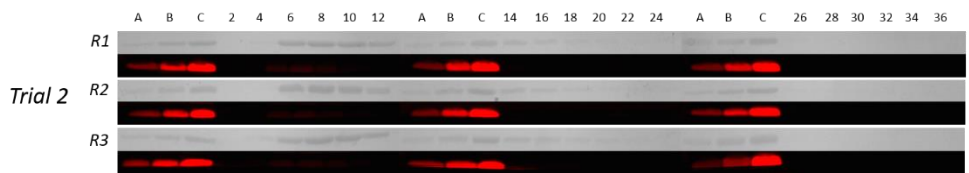
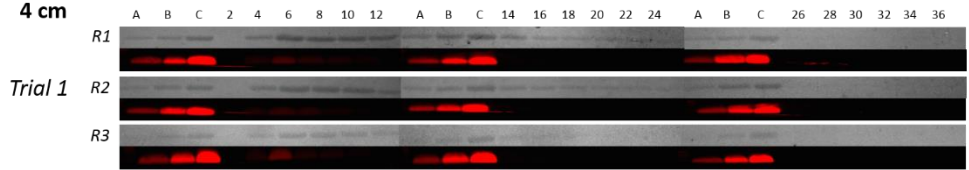


30 cm



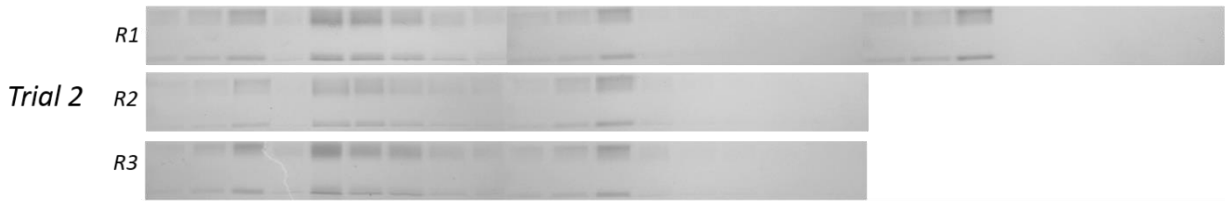
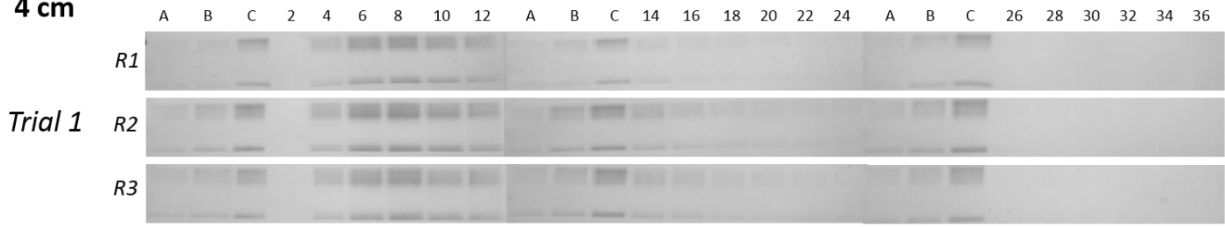
TMGMV*Cy5

4 cm

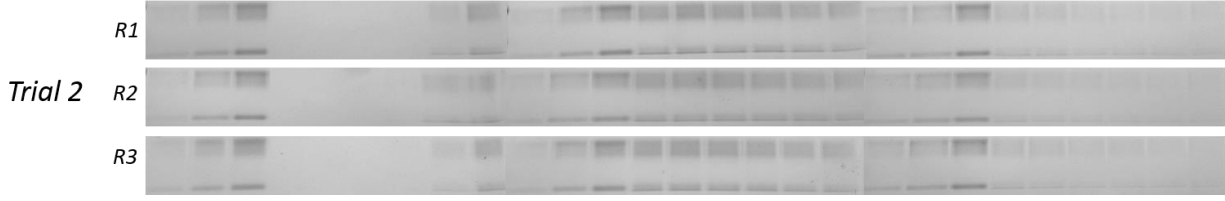
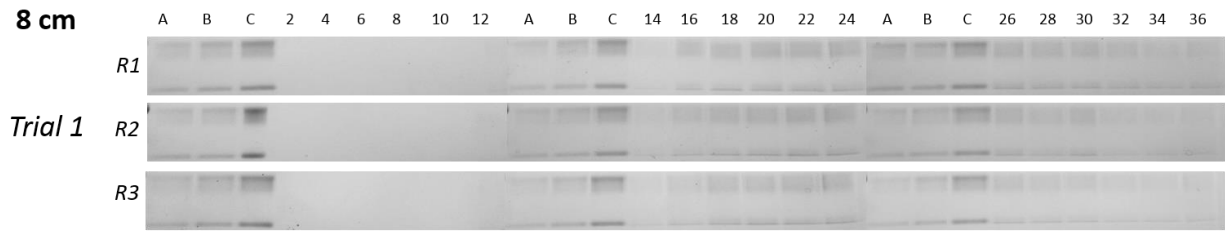


CPMV

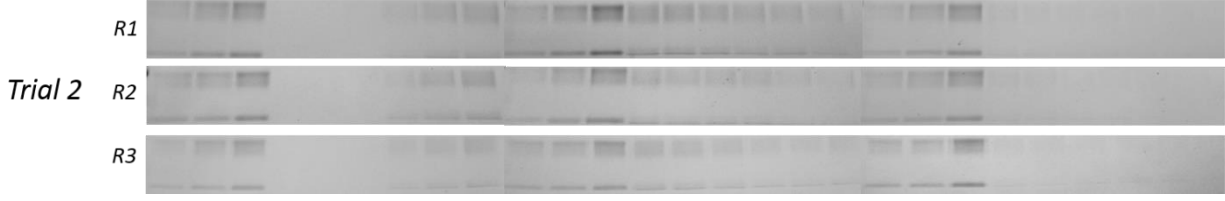
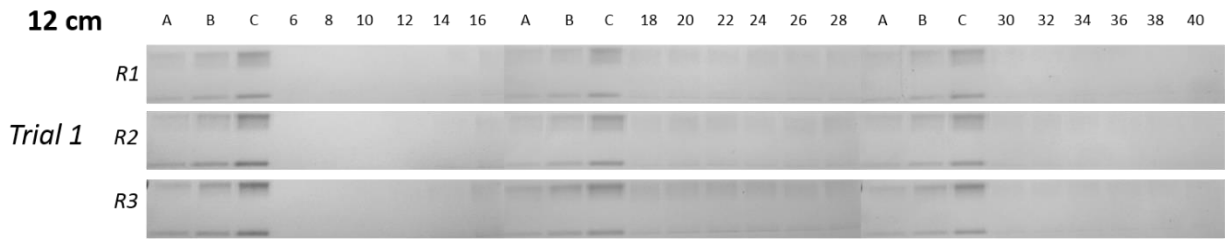
4 cm



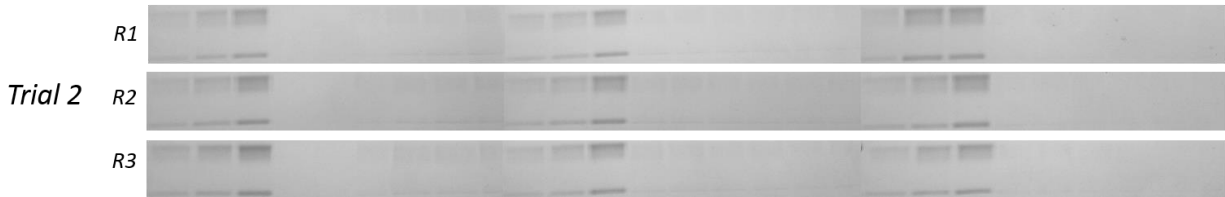
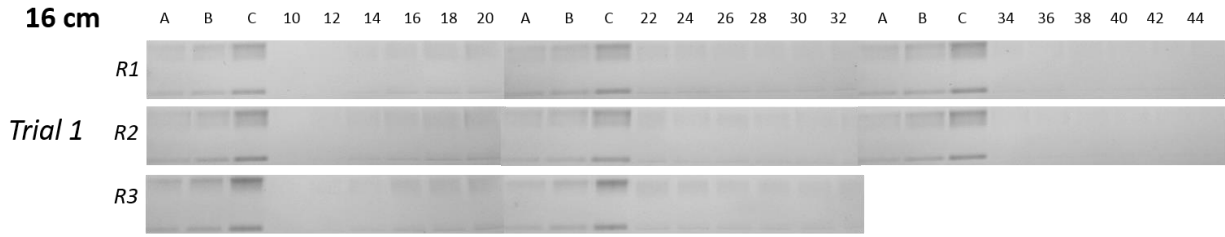
8 cm



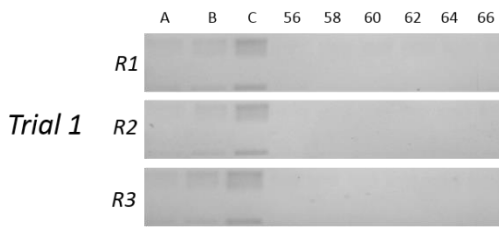
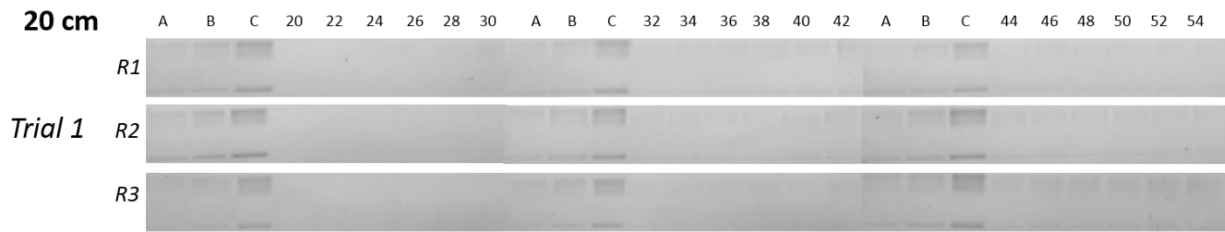
12 cm



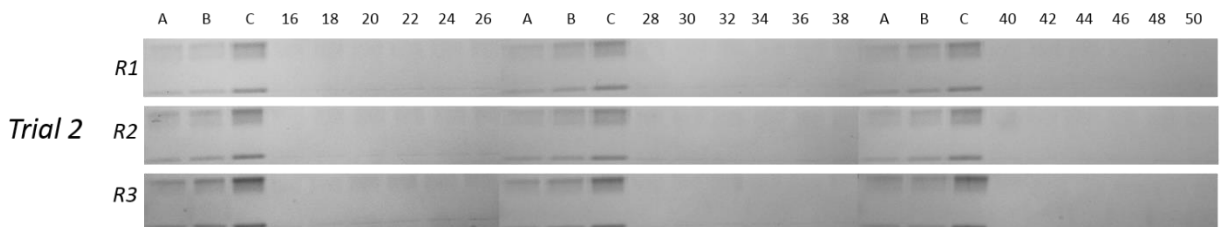
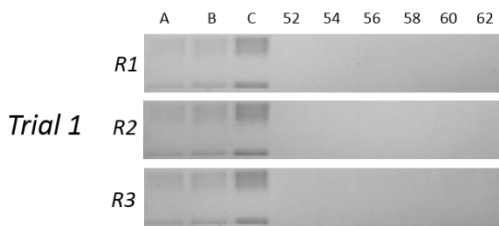
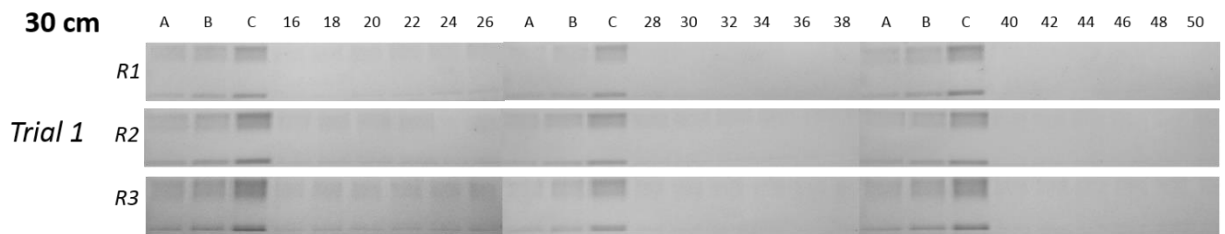
16 cm



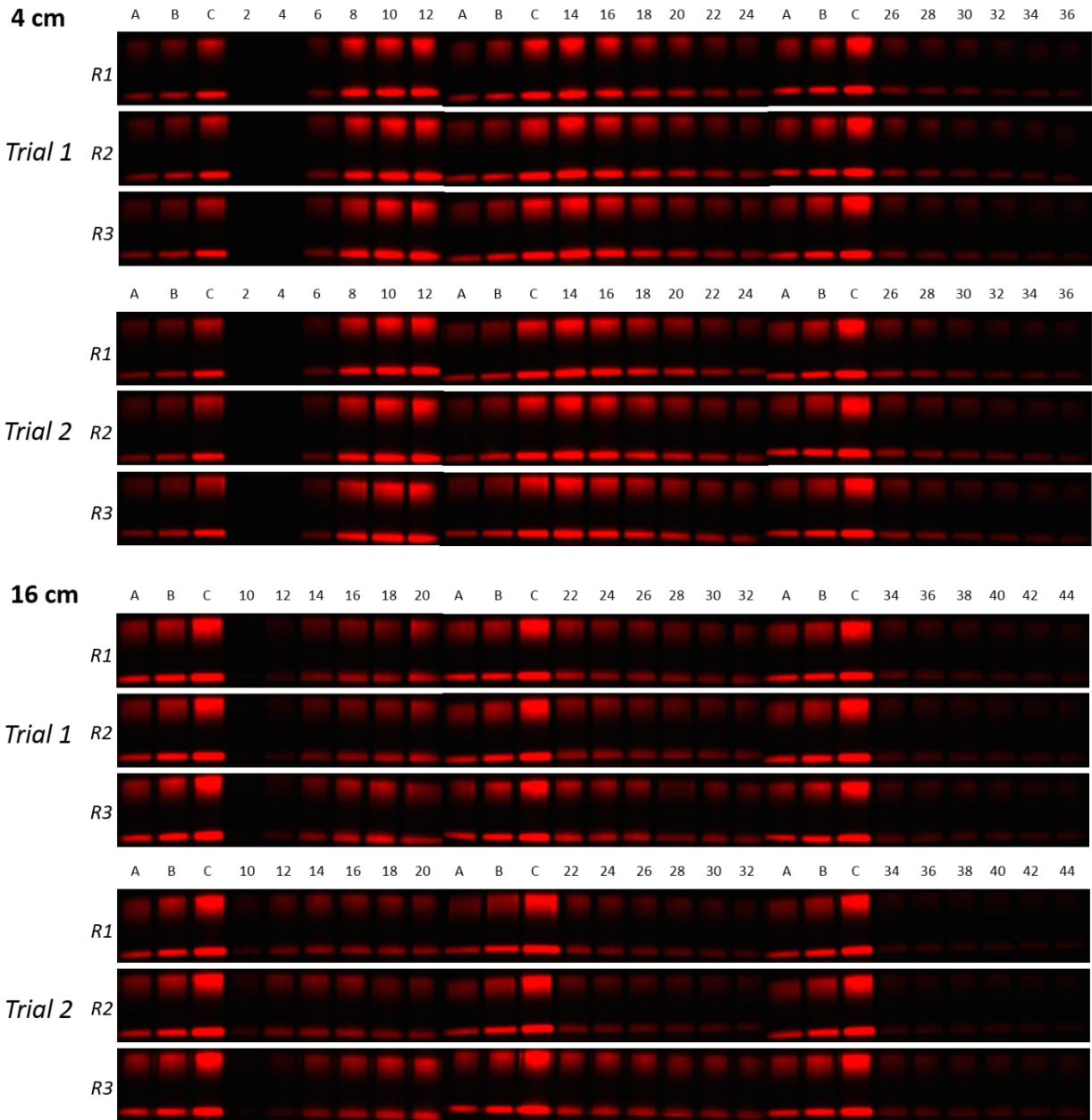
20 cm

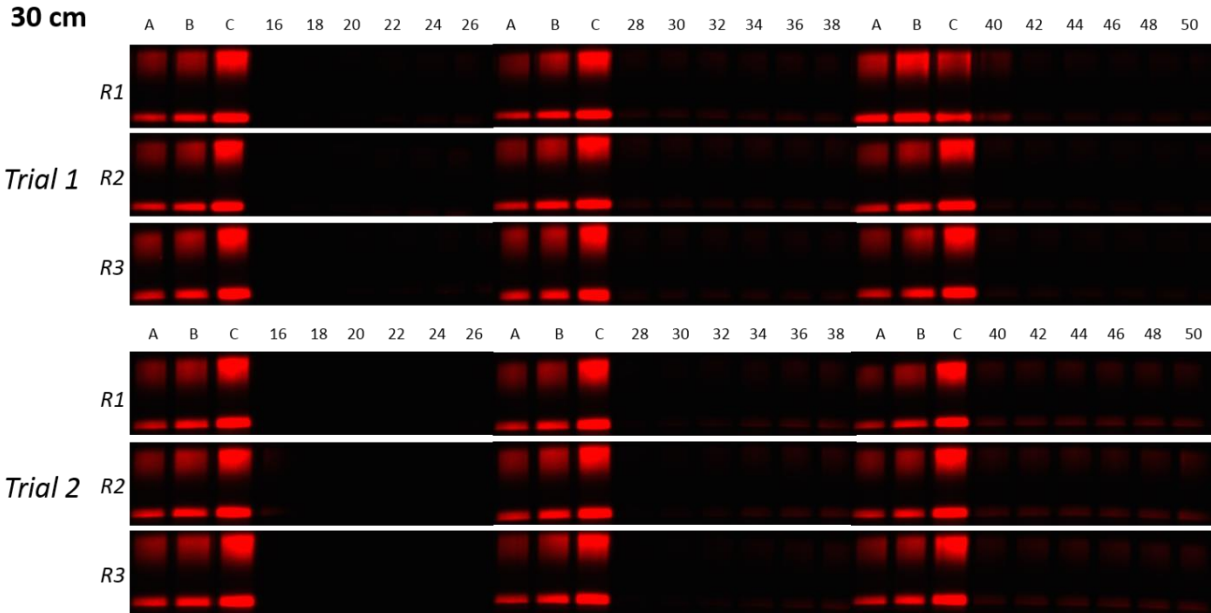


30 cm

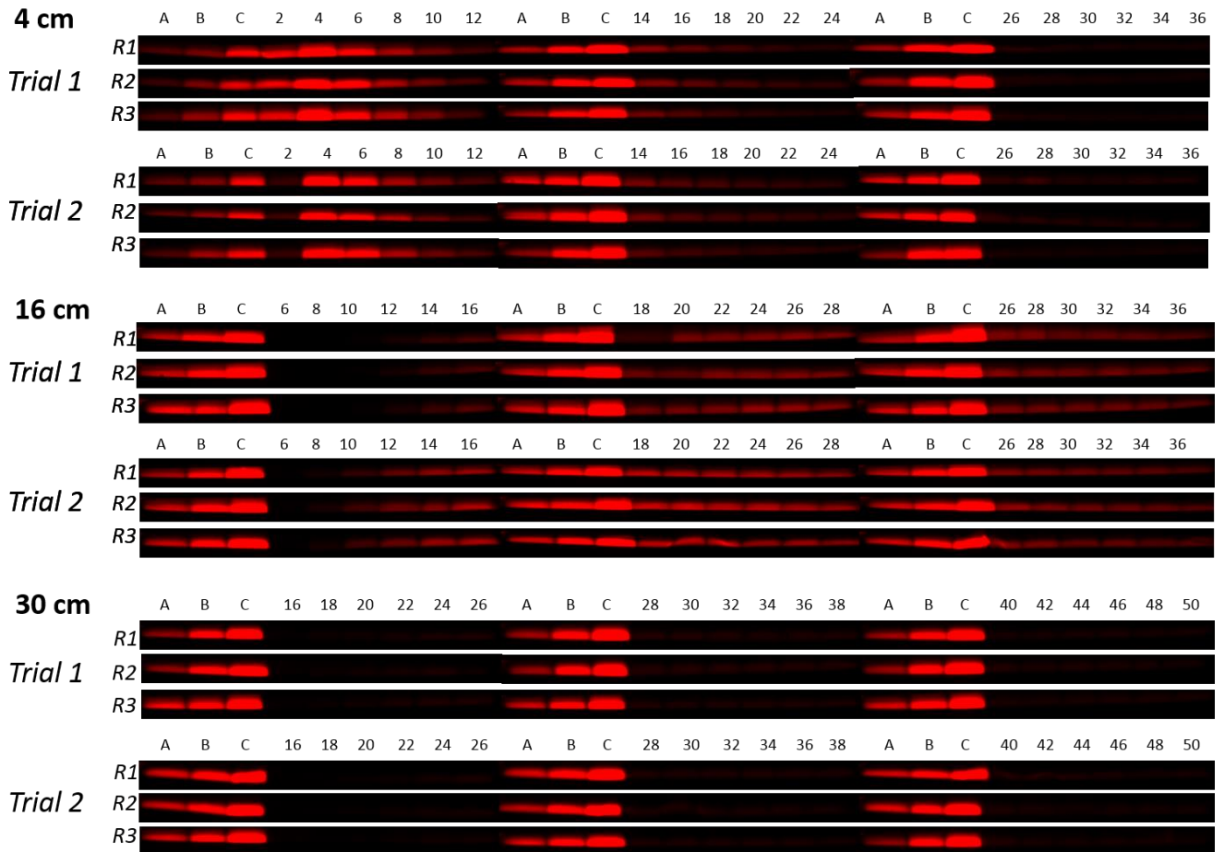


CPMV-Cy5



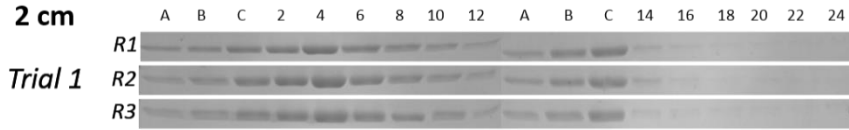


CPMV*Cy5

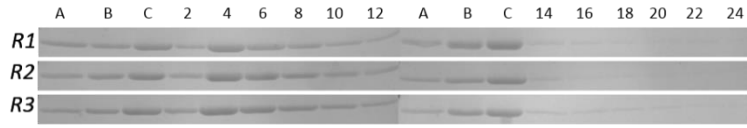


PhMV

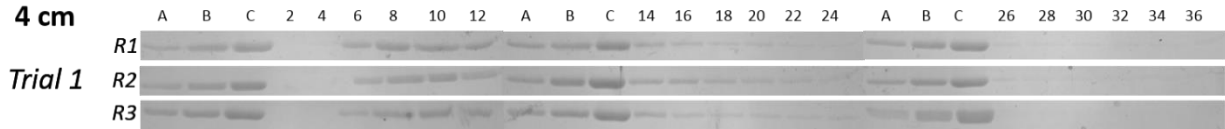
2 cm



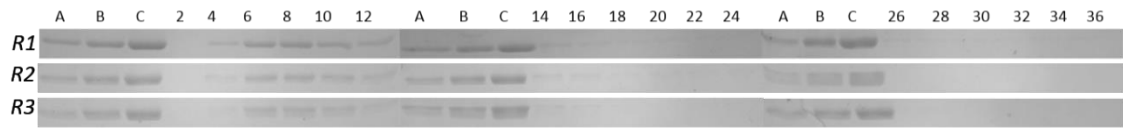
Trial 2



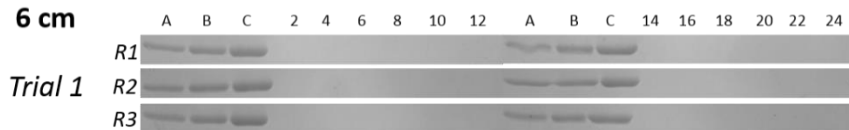
4 cm



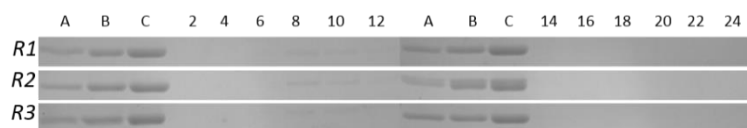
Trial 2



6 cm

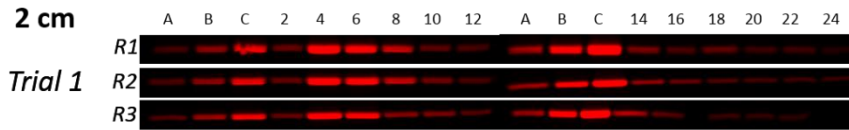


Trial 2

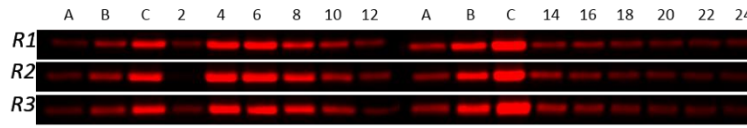


PhMV-Cy5

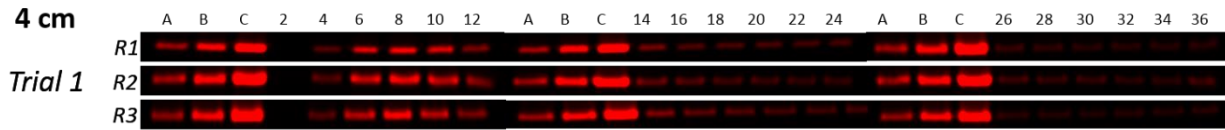
2 cm



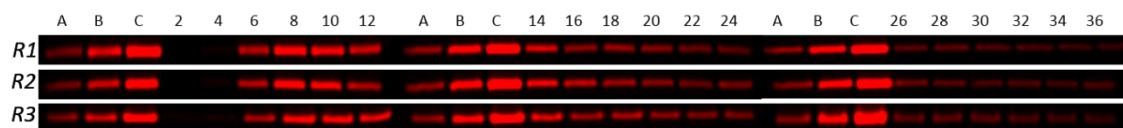
Trial 2



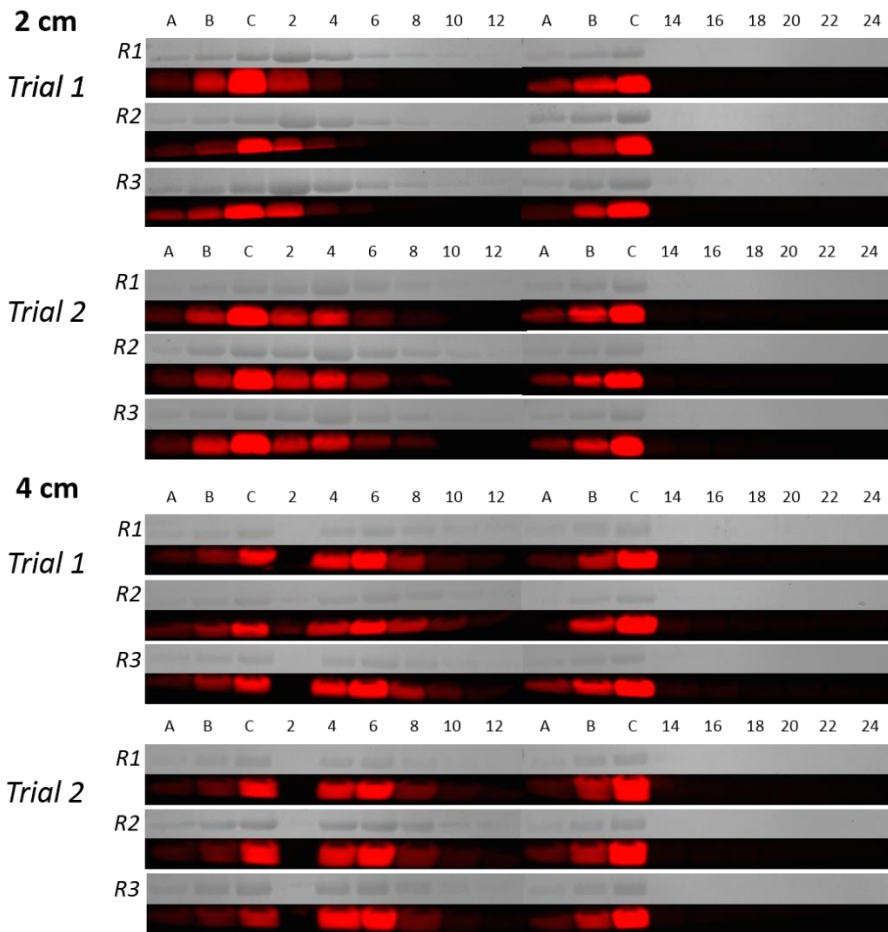
4 cm



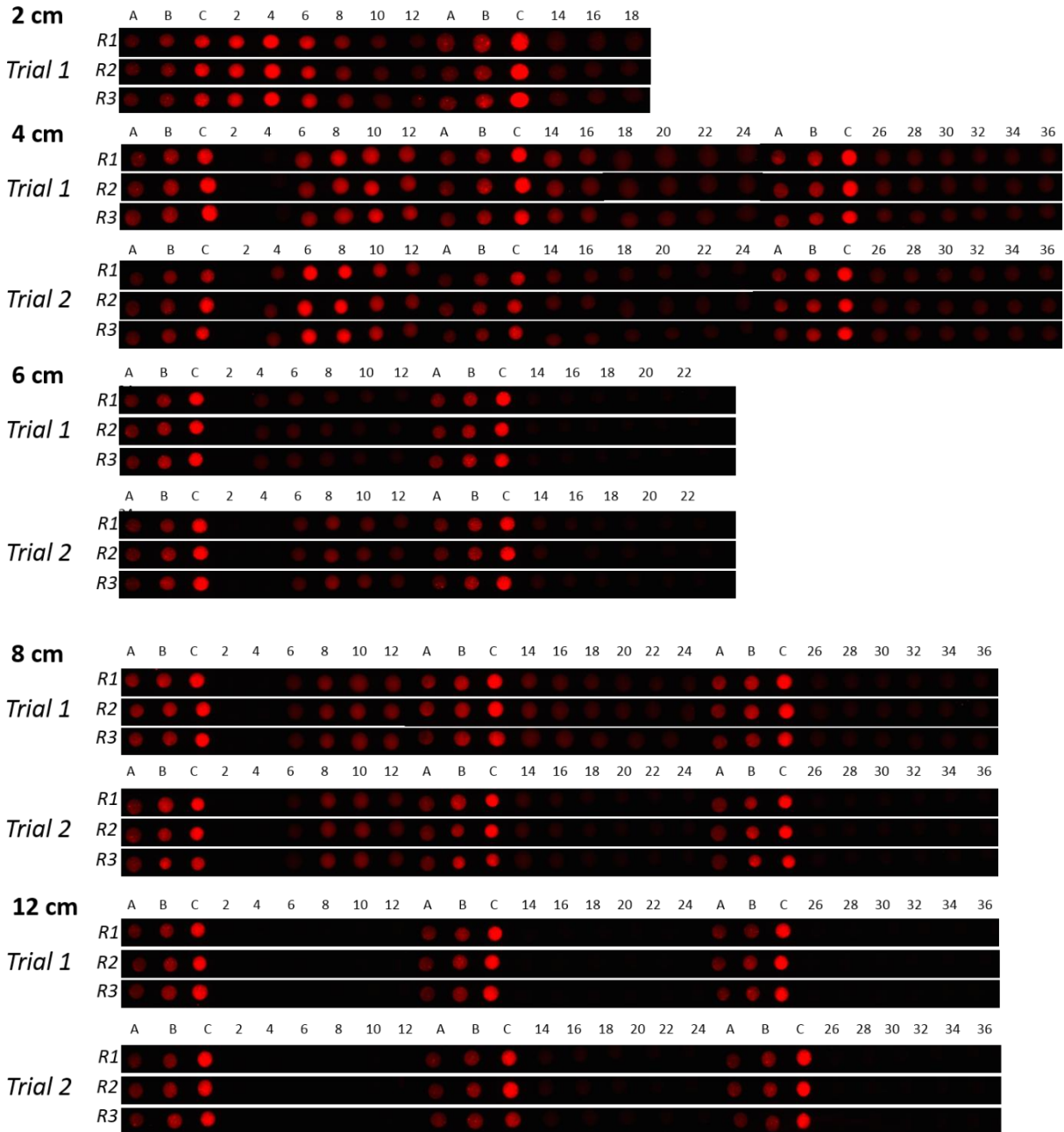
Trial 2



PhMV*Cy5

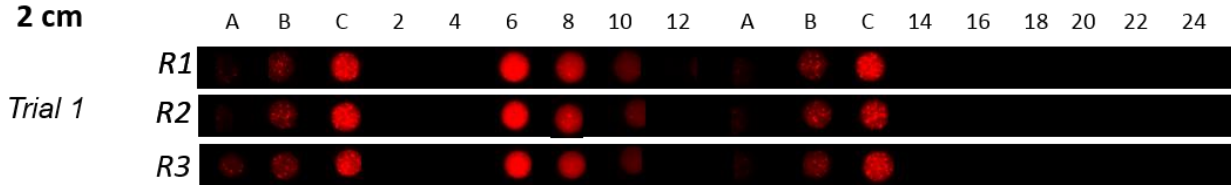


MSNP-Cy5

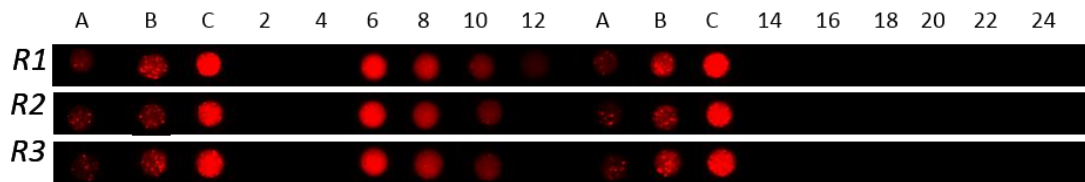


MSNP*Cy5

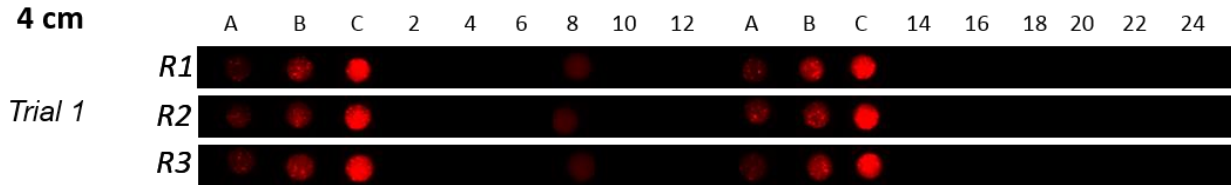
2 cm



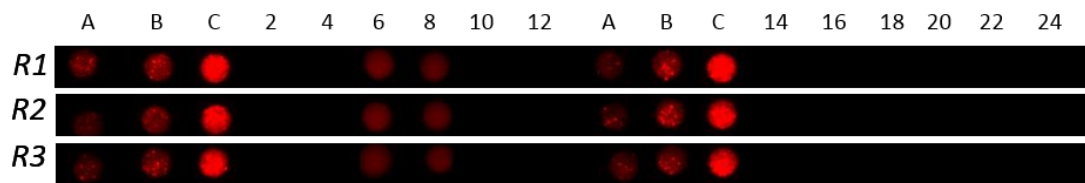
Trial 2



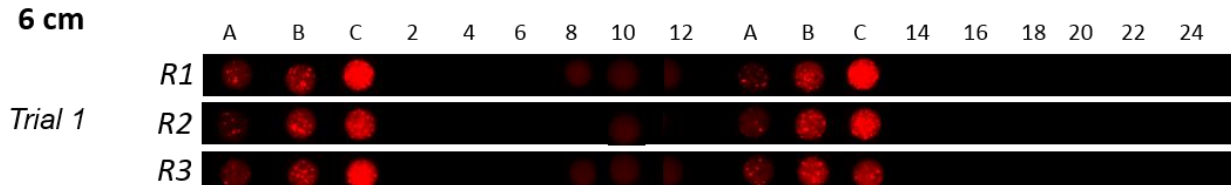
4 cm



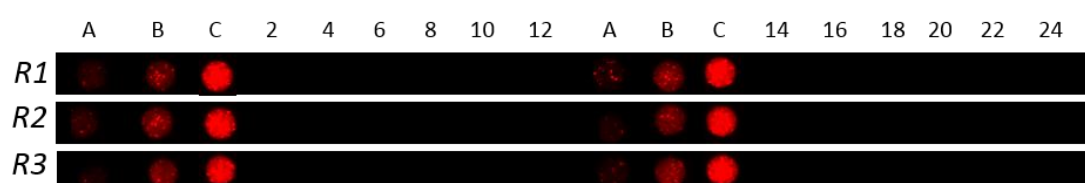
Trial 2



6 cm

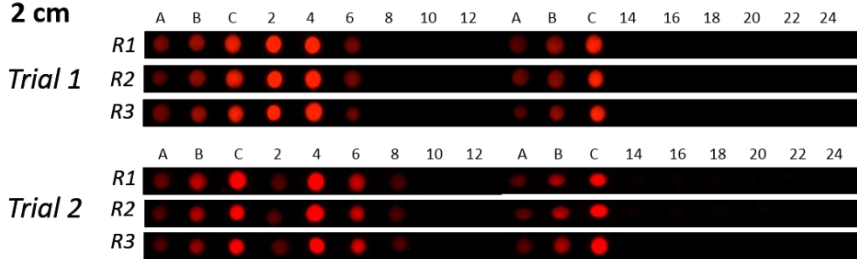


Trial 2

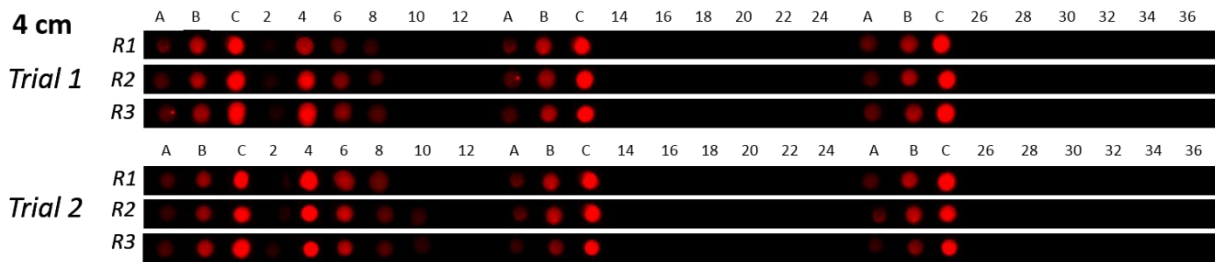


PLGA*Cy5

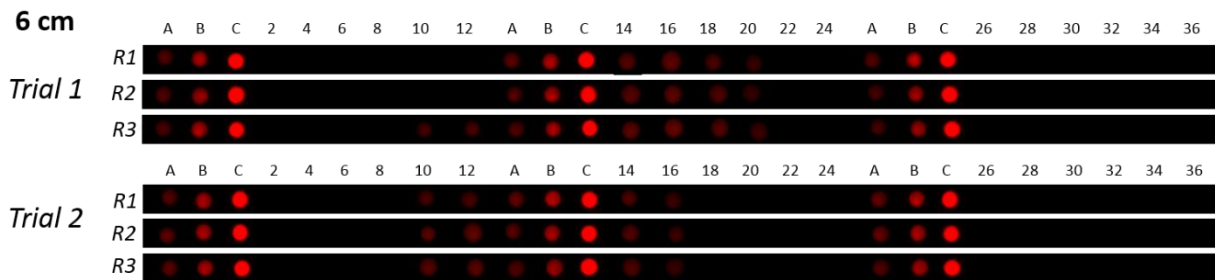
2 cm



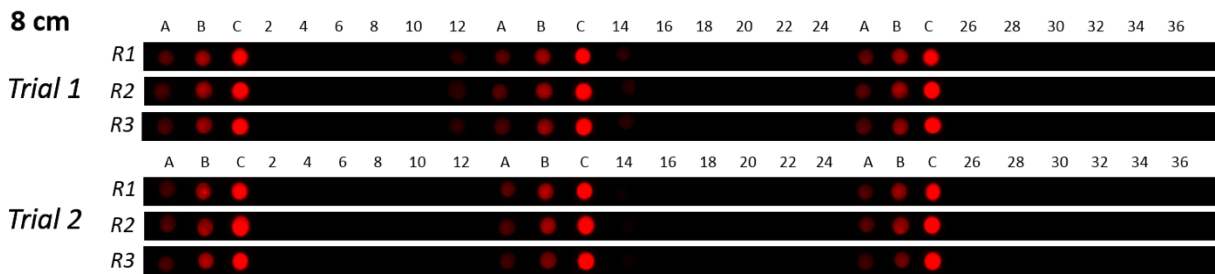
4 cm

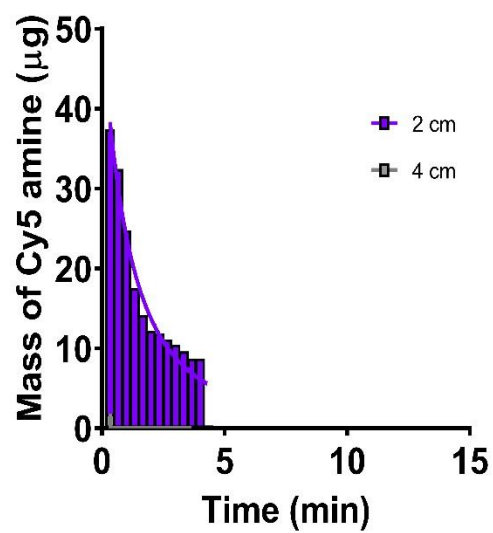


6 cm



8 cm





Supporting Figure 4.6. Distribution of free Cy5 in the soil.

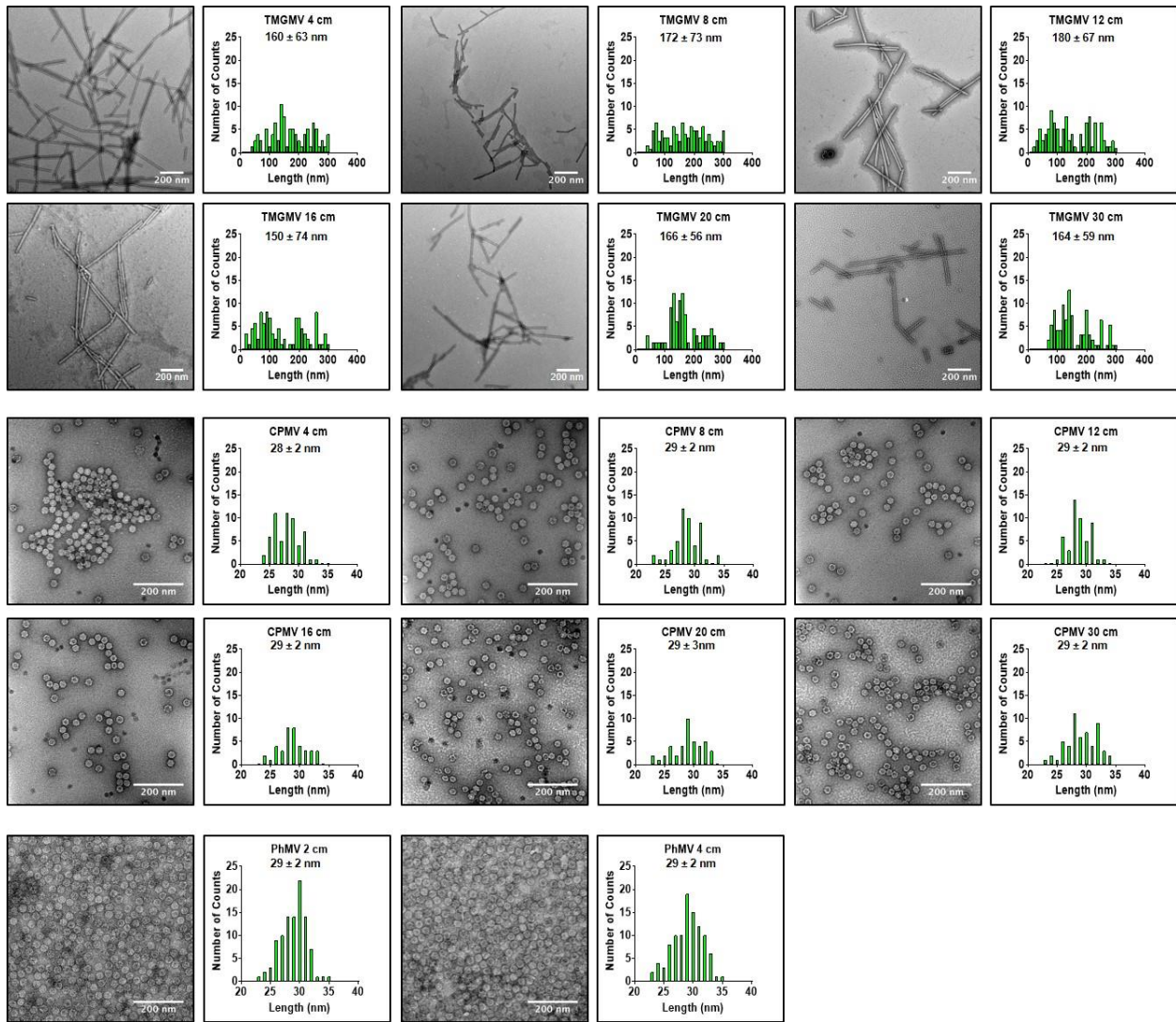
Supporting Table 4.4. Tables of virus recovery from the empty elution samples.

Elution samples lacking viral mass according to SDS-PAGE analysis were pooled and centrifuged at 112,000 g for 3 h to collect any trace amounts of virus. The concentrated solutions were analysed by SDS-PAGE gels to determine the residual mass of experimentally lost nanoparticles.

TMGMV			CPMV			PhMV		
	Average Loss (ug)	% loss		Average Loss (ug)	% loss		Average Loss (ug)	% loss
4 cm	16	1.6	4 cm	25	2.5	2 cm	0	0
8 cm	10	1	8 cm	22	2.2	4 cm	0	0
12 cm	44	4.4	12 cm	43	4.3	6 cm	0	0
16 cm	37	3.7	16 cm	32	3.2	8 cm	0	0
20 cm	26	2.6	20 cm	26	2.6			
30 cm	28	2.8	30 cm	40	4			

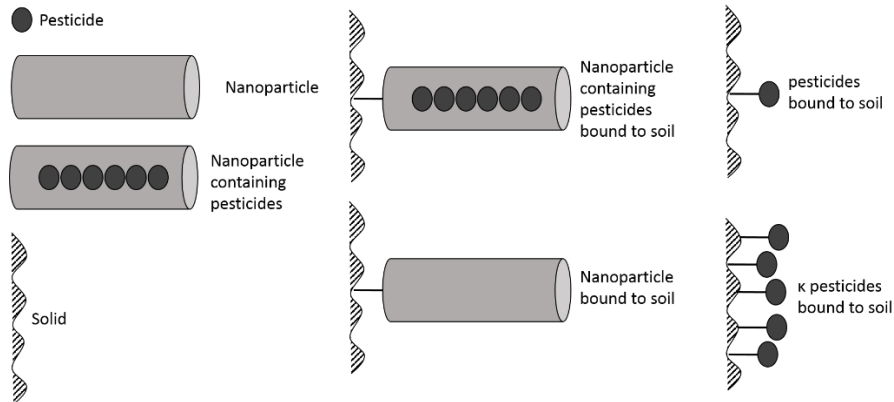
TMGMV-Cy5			CPMV-Cy5			PhMV-Cy5		
	Average Loss (ug)	% loss		Average Loss (ug)	% loss		Average Loss (ug)	% loss
4 cm	16	2.4	4 cm	26	2.6	2 cm	19	1.9
16 cm	37	6	16 cm	31	3.1	4 cm	35	3.5
30 cm	28	8.3	30 cm	15	1.5			

TMGMV-Cy5-Amine			CPMV-Cy5-Amine			PhMV-Cy5-Amine		
	Average Loss (ug)	% loss		Average Loss (ug)	% loss		Average Loss (ug)	% loss
2 cm	35	3.5	4 cm	24	2.4	2 cm	1.2	0.12
4 cm	20	3	16 cm	16	1.6	4 cm	1.8	0.18
			30 cm	19	1.9			

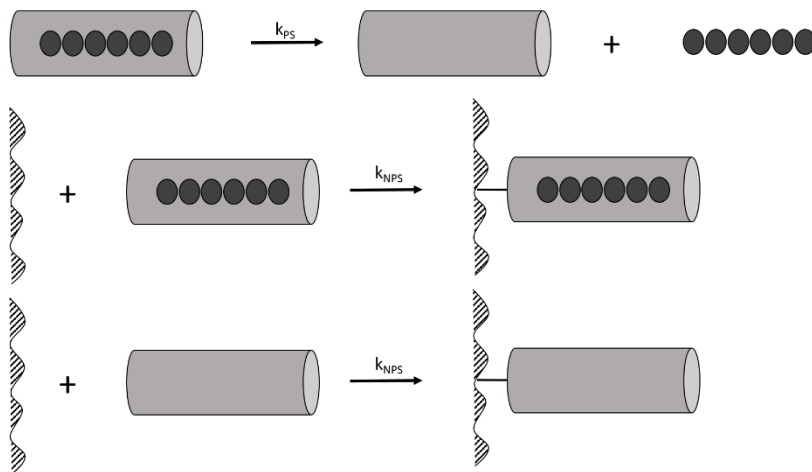


Supporting Figure. 4.7. TEM images of viruses that were leached through soil.

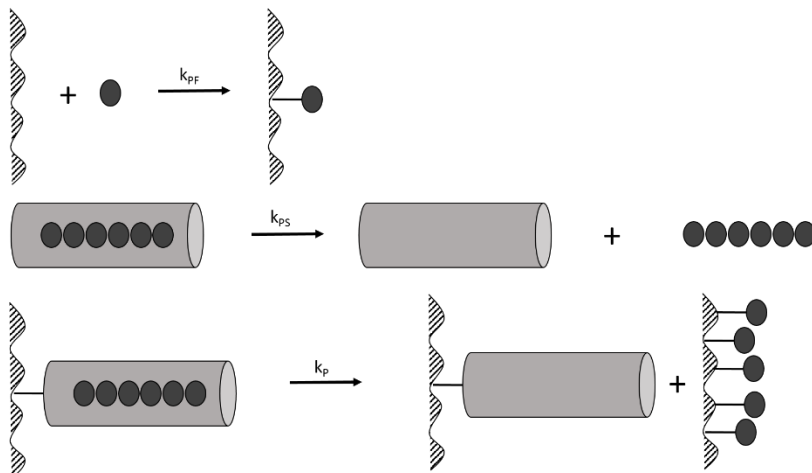
Reaction Mechanisms of Pesticide, Nanoparticle, Soil Interactions
Definitions



Reactions involving nanoparticle



Reactions involving pesticide



Supporting Figure. 4.8. Reaction mechanisms of nanoparticles and pesticides in soil.

Supporting Equation 4.1. model of nanopesticide transport through the soil.

For the numerical solution of simultaneous partial differential equations, I used the MATLAB code “pdepe”. For numerical stability, I added a “false” diffusion term for equations involving the soil particles:

$$\frac{\partial \Omega_{\text{NPS}}}{\partial t} = D_F \frac{\partial^2 \Omega_{\text{NPS}}}{\partial z^2} + \phi k_{\text{NPS}} \Omega_{\text{NP}}$$

$$\frac{\partial C_{\text{NPS}}}{\partial t} = D_F \frac{\partial^2 C_{\text{NPS}}}{\partial z^2} + \phi (R_P - R_{\text{PNP}})$$

$$\frac{\partial C_{\text{PS}}}{\partial t} = D_F \frac{\partial^2 C_{\text{PS}}}{\partial z^2} - \phi (R_{\text{PS}} - R_P)$$

where the coefficient D_F [$\text{cm}^2 \text{min}^{-1}$] is given an arbitrarily small value. The boundary conditions for these modified equations are

$$z = 0: \Omega_{\text{NPS}} = 0; C_{\text{NPS}} = 0; C_{\text{PS}} = 0$$

$$z = L: \frac{\partial \Omega_{\text{NPS}}}{\partial z} = 0; \frac{\partial C_{\text{NPS}}}{\partial z} = 0; \frac{\partial C_{\text{PS}}}{\partial z} = 0$$

Dimensionless forms

We can express the nanoparticle density as a function of fluid volume within the soil column in dimensionless form by defining the dimensionless variables:

$$t' = \frac{Q}{LAe} t \quad z' = \frac{z}{L}$$

where Q is the constant volume flow of species through voids in soil, t is the time variable, L is the column length, and A is the constant cross-sectional area of the column.

Also, the dimensionless forms of pesticide concentration and nanoparticle density are:

$$\Omega'_{NP} = \frac{\Omega_{NP}}{\Omega_{NP}^0}; \quad \Omega'_{NPS} = \frac{\Omega_{NPS}}{\Omega_{NP}^0}; \quad C'_{NPF} = \frac{C_{NPF}}{C_{NPF}^0}; \quad C'_{NPS} = \frac{C_{NPS}}{C_{NPF}^0}; \quad C'_P = \frac{C_P}{C_{NPF}^0}; \quad C'_{PS} = \frac{C_{PS}}{C_{NPF}^0}$$

Starting with the equation for nanoparticle mass density in fluid:

$$\frac{\partial \Omega_{NP}}{\partial t} + \frac{Q}{A\varepsilon} \frac{\partial \Omega_{NP}}{\partial z} = D_{NP} \frac{\partial^2 \Omega_{NP}}{\partial z^2} + \left(\frac{1-\varepsilon}{\varepsilon} \right) \phi R_{NPS}, \quad 0 < z < L$$

we substitute the dimensionless variables:

$$\frac{Q\Omega_{NP}^0}{LA\varepsilon} \frac{\partial \Omega'_{NP}}{\partial t'} + \frac{Q\Omega_{NP}^0}{LA\varepsilon} \frac{\partial \Omega'_{NP}}{\partial z'} = \frac{\Omega_{NP}^0 D_{NP}}{L^2} \frac{\partial^2 \Omega'_{NP}}{\partial z'^2} - \left(\frac{1-\varepsilon}{\varepsilon} \right) \phi \Omega_{NP}^0 k_{NPS} \Omega'_{NP}, \quad 0 < z' < 1$$

Dividing by the coefficient of the first term yields

$$\frac{\partial \Omega'_{NP}}{\partial t'} + \frac{\partial \Omega'_{NP}}{\partial z'} = \left[\frac{A\varepsilon D_{NP}}{QL} \right] \frac{\partial^2 \Omega'_{NP}}{\partial z'^2} - \left[\frac{LA\phi k_{NPS}}{Q} \right] \left[\frac{1-\varepsilon}{\varepsilon} \right] \Omega'_{NP}, \quad 0 < z' < 1 \quad (1)$$

Starting with the equation for mass density of nanoparticles attached to soil particles:

$$\frac{\partial \Omega_{NPS}}{\partial t} = D_F \frac{\partial^2 \Omega_{NPS}}{\partial z^2} + \phi k_{NPS} \Omega_{NP}, \quad 0 < z < L$$

we substitute the dimensionless variables:

$$\frac{Q\Omega_{NP}^0}{LA\varepsilon} \frac{\partial \Omega'_{NPS}}{\partial t'} = \frac{D_F \Omega_{NP}^0}{L^2} \frac{\partial^2 \Omega'_{NPS}}{\partial z'^2} + \phi k_{NPS} \Omega_{NP}^0 \Omega'_{NP}, \quad 0 < z' < 1$$

Dividing by the coefficient of the first term yields:

$$\frac{\partial \Omega'_{NPS}}{\partial t'} = \left[\frac{D_F A\varepsilon}{QL} \right] \frac{\partial^2 \Omega'_{NPS}}{\partial z'^2} + \left[\frac{LA\phi k_{NPS}}{Q} \right] \Omega'_{NP}, \quad 0 < z' < 1 \quad (2)$$

The equation for pesticide dissolved in fluid can be written as:

$$\frac{\partial C_p}{\partial t} + \frac{Q}{A\varepsilon} \frac{\partial C_p}{\partial z} = D_p \frac{\partial^2 C_p}{\partial z^2} - R_{PF} + \left(\frac{1-\varepsilon}{\varepsilon} \right) \phi R_{PS}, \quad 0 < z < L$$

$$\frac{QC_{NPF}^0}{LA\varepsilon} \frac{\partial C'_p}{\partial t'} + \frac{QC_{NPF}^0}{LA\varepsilon} \frac{\partial C'_p}{\partial z'} = \frac{D_p C_{NPF}^0}{L^2} \frac{\partial^2 C'_p}{\partial z'^2} + k_{PF} C_{NPF}^0 C'_{NPF} - \left(\frac{1-\varepsilon}{\varepsilon} \right) \phi [k_{PS} C_{NPF}^0] C'_p \quad 0 < z' < 1$$

After the substitution of dimensionless variables, we find:

Dividing by the coefficient of the first term yields:

$$\frac{\partial C'_p}{\partial t'} + \frac{\partial C'_p}{\partial z'} = \left[\frac{A\varepsilon D_p}{QL} \right] \frac{\partial^2 C'_p}{\partial z'^2} + \left[\frac{LA\varepsilon k_{PF}}{Q} \right] C'_{NPF} - \left[\frac{LA\varepsilon \phi k_{PS}}{Q} \right] \left[\frac{1-\varepsilon}{\varepsilon} \right] C'_p, \quad 0 < z' < 1 \quad (3)$$

The equation for pesticide attached to nanoparticles in fluid can be written as:

$$\frac{\partial C_{NPF}}{\partial t} + \frac{Q}{A\varepsilon} \frac{\partial C_{NPF}}{\partial z} = D_{NP} \frac{\partial^2 C_{NPF}}{\partial z^2} + R_{PF} + \left(\frac{1-\varepsilon}{\varepsilon} \right) \phi R_{PNP}, \quad 0 < z < L$$

After the substitution of dimensionless variables, we find:

$$\frac{QC_{NPF}^0}{LA\varepsilon} \frac{\partial C'_{NPF}}{\partial t'} + \frac{QC_{NPF}^0}{LA\varepsilon} \frac{\partial C'_{NPF}}{\partial z'} = \frac{D_{NP} C_{NPF}^0}{L^2} \frac{\partial^2 C'_{NPF}}{\partial z'^2} - k_{PF} C_{NPF}^0 C'_{NPF} - \left(\frac{1-\varepsilon}{\varepsilon} \right) \phi k_{NPS} C_{NPF}^0 C'_{NPF}$$

Dividing by the coefficient of the first term yields:

$$\frac{\partial C'_{NPF}}{\partial t'} + \frac{\partial C'_{NPF}}{\partial z'} = \left[\frac{A\varepsilon D_{NP}}{QL} \right] \frac{\partial^2 C'_{NPF}}{\partial z'^2} - \left[\frac{LA\varepsilon k_{PF}}{Q} \right] C'_{NPF} + \left[\frac{LA\varepsilon \phi k_{NPS}}{Q} \right] \left(\frac{1-\varepsilon}{\varepsilon} \right) C'_{NPF}, \quad 0 < z' < 1 \quad (4)$$

The equation for pesticide attached to nanoparticles on soil particles:

$$\frac{\partial C_{NPS}}{\partial t} = D_F \frac{\partial^2 C_{NPS}}{\partial z^2} + \phi (R_P - R_{PNP})$$

After the substitution of dimensionless variables, we find:

$$\frac{QC_{NPF}^0}{LA\varepsilon} \frac{\partial C'_{NPS}}{\partial t'} = \frac{D_F C_{NPF}^0}{L^2} \frac{\partial^2 C'_{NPS}}{\partial z'^2} - \phi \left(k_P C_{NPF}^0 C'_{NPS} - k_{NPS} C_{NPF}^0 C'_{NPF} \right)$$

Dividing by the coefficient of the first term yields:

$$\frac{\partial C'_{NPS}}{\partial t'} = \left[\frac{D_F A \varepsilon}{QL} \right] \frac{\partial^2 C'_{NPS}}{\partial z'^2} - \left[\frac{LA\varepsilon\phi k_P}{Q} \right] C'_{NPS} + \left[\frac{LA\varepsilon\phi k_{NPS}}{Q} \right] C'_{NPF} \quad (5)$$

The equation for pesticide adsorbed by soil particles can be written as:

$$\frac{\partial C_{PS}}{\partial t} = D_F \frac{\partial^2 C_{PS}}{\partial z^2} - \phi (R_{PS} - R_P)$$

After the substitution of dimensionless variables, we find:

$$\frac{QC_{NPF}^0}{LA\varepsilon} \frac{\partial C'_{PS}}{\partial t'} = \frac{D_F C_{NPF}^0}{L^2} \frac{\partial^2 C'_{PS}}{\partial z'^2} + \phi \left(k_{PS} C_{NPF}^0 C'_P + k_P C_{NPF}^0 C'_{NPS} \right)$$

Dividing by the coefficient of the first term yields:

$$\frac{\partial C'_{PS}}{\partial t'} = \left[\frac{D_F A \varepsilon}{QL} \right] \frac{\partial^2 C'_{PS}}{\partial z'^2} + \left[\frac{LA\varepsilon\phi k_{PS}}{Q} \right] C'_P + \left[\frac{LA\varepsilon\phi k_P}{Q} \right] C'_{NPS} \quad (6)$$

Equations 1-6 can be written as:

$$\frac{\partial \Omega'_{NP}}{\partial t'} + \frac{\partial \Omega'_{NP}}{\partial z'} = \frac{1}{Pe_{NP}} \frac{\partial^2 \Omega'_{NP}}{\partial z'^2} - Da_{NP} \left[\frac{1-\varepsilon}{\varepsilon} \right] \Omega'_{NP} \quad (1)$$

$$\frac{\partial \Omega'_{NPS}}{\partial t'} = \frac{1}{Pe_{NPS}} \frac{\partial^2 \Omega'_{NPS}}{\partial z'^2} + Da_{NP} \Omega'_{NP} \quad (2)$$

$$\frac{\partial C'_P}{\partial t'} + \frac{\partial C'_P}{\partial z'} = \frac{1}{\text{Pe}_D} \frac{\partial^2 C'_P}{\partial z'^2} + \text{Da}_{PF} C'_{NPF} - \text{Da}_{PS} \left[\frac{1-\varepsilon}{\varepsilon} \right] C'_P \quad (3)$$

$$\frac{\partial C'_{NPF}}{\partial t'} + \frac{\partial C'_{NPF}}{\partial z'} = \frac{1}{\text{Pe}_{NP}} \frac{\partial^2 C'_{NPF}}{\partial z'^2} - \text{Da}_{PF} C'_{NPF} + \text{Da}_{NP} \left(\frac{1-\varepsilon}{\varepsilon} \right) C'_{NPF} \quad (4)$$

$$\frac{\partial C'_{NPS}}{\partial t'} = \frac{1}{\text{Pe}_{NPS}} \frac{\partial^2 C'_{NPS}}{\partial z'^2} - \text{Da}_P C'_{NPS} + \text{Da}_{NP} C'_{NPF} \quad (5)$$

$$\frac{\partial C'_{PS}}{\partial t'} = \frac{1}{\text{Pe}_{NPS}} \frac{\partial^2 C'_{PS}}{\partial z'^2} + \text{Da}_{PS} C'_P + \text{Da}_P C'_{NPS} \quad (6)$$

Supporting Code 4.1. MATLAB code.

Part 1: Model for nanoparticle transport through soil

% Last edited: 07/21/18

```
function NanoparticlesPdepe
```

```
tic
```

```
clc
```

```
clear
```

```
%% Defining the constants
```

```
E = 0.45; % Volume fraction of fluid [1 = 100% fluid]
```

```
rsf = (1-E)/E; % Particle-to-fluid volume ratio [dimensionless]
```

```
Q = 1.5; % Flow rate [cm3/min]
```

```
Phi = 3401; % Adsorption surface per particle volume [cm-1]
```

```
radius = 1.4; % Radius of the soil column [cm]
```

```
A = pi*radius2; % Cross sectional Area of the column [cm2]
```

```
massparticle = 1; % Mass of particle injected in the system [mg]
```

```
volumeinj = 0.3; % Volume of particle injection [cm3]
```

```
OmegaVfinitial = massparticle/volumeinj; % Initial nanoparticle concentration [mg/cm3]
```

```
%% Experimental data
```

```
ExpData = xlsread('ExperimentalDataMatlab_TMGMVnodelay'); % Importing the experimental data
```

```
% ~~First row is the depth value~~
```

```
Depth = ExpData (1,:); % Creating the array of soil depth data
```

```
Time = ExpData (2:end,1,:); % Creating the array of time data.
```

```
MassNP = ExpData (2:end,2:end,:); % Creating the array of experimental mass of nanoparticles
```

```
ConcNP = MassNP /500; % Converting the mass into concentration of nanoparticles
```

```
%% Initialization of parameters
```

```
Cerror = zeros (length (Depth)-1);
```

```
individualparams= zeros (length (Depth)-1, 2); % We currently only have a Peclet number and a Damkohler number as parameters (2 parameters)
```

```
global optimj
```

```
global L
```

```
%% Parameters estimation STARTS
```

```
for optimj = 1: length(Depth)-1
```

```
    %% Non dimensionalization of the time and length
```

```
    L = Depth(optimj+1);
```

```
    KT= Q/(L*A*E); % Dimensionless constant of time
```

```
    tinj=volumeinj/Q/2*KT; % Initial time of particle injection into the system
```

```
    TimeD = Time * KT; % Dimensionless time
```

```
    depthD = Depth/L; % Dimensionless depth
```

```
%% Defining dimensionless time and length for the PDEPE function
```

```
m = 0; % The symmetry of the problem. m can be slab = 0, cylindrical = 1, or spherical = 2.
```

```
x = linspace(0,1,1000); % Dimensionless
```

```

tmin = 0;
tmax = ceil(max(TimeD));
t = linspace(tmin,tmax,1001); % Dimensionless

%% Experimental data as a function of t for specific x values
ConcNPD = ConcNP./OmegaVfinitial; % Dimensionless concentration
fitobject = fit(TimeD,ConcNPD(:,optimj),'smoothingspline'); % Creating a curve fit to the
experimental data
FittedConc = fitobject (t); % Extracting more points from the curve fit of the experimental
data
for i = 1: length (Time)-1
    OmegaNPF_exp(i+1,:)=ConcNPD(i+1,:); % The first index is the depth row
end

%% Parameter estimation function
options1 = optimoptions('fmincon','Display','iter','Algorithm','sqp') % Options for the fmincon
function
[optparams Error2] = fmincon(@objfun, [0.2 2],[[],[],[],[],[0.05 0],[5 15],[[], options1) %
Estimating the value of the Peclet number and a Damkohler number of the nanoparticle
individualparams(optimj,:) = optparams % Returns the optimized parameter for each depth
Dv (optimj) = (individualparams(optimj,1)*Q*L)/(A*E) % Computing the value of the
dispersion coefficient of the nanoparticle
kvfp (optimj) = (individualparams(optimj,2)*Q)/(L*A*E*Phi) % Computing the value of the
rate of binding to soil of the nanoparticle
ERROR (optimj) = Error2 % Returns the absolute error between the model and the experimental
data for each depth (~~Scaled by 1000X~~)
Averageparameters = mean (individualparams); % Returns the average value of the Peclet
number and Damkohler number
Standardparameters = std (individualparams); % Returns the standard derivation value of the
Peclet number and Damkohler number

%% Figures of the results
maxth = max(OmegaVfinitial.*OmegaNPF_x(:,1)); maxexp = max(smooth(ConcNP(:,1))); %
The highest peak is the first depth
MaxY = max ([maxexp maxth]); % To normalize graph with dimension to the highest peak

maxthD = max(OmegaNPF_x(:,1)); maxexpD = max(smooth(ConcNPD(:,1)));
MaxYD = max ([maxexpD maxthD]); % To normalize dimensionless graphs to the highest
peak

figure(1) % Nanoparticles transport in fluid
bx1 = subplot (2,1,1);
plot (TimeD/KT, (ConcNP(:,optimj)), 'Color',[0.15*optimj, 0,1])
hold on
xlabel('Time [min]'); ylabel('\Omega_N_P_F [mg/cm^3]');title ('Experimental Data'); axis
tight;

```

```

bx2 = subplot (2,1,2);
plot(t/KT, OmegaVfinitial*OmegaNPF_x(:,optimj), 'Color', [0.15*optimj, 0, 1]);
hold on
xlabel('Time [min]'); ylabel('\Omega_N_P_F [mg/cm^3]'); title ('Model Output'); axis tight
bx1.YLim = [0, MaxY]; bx2.YLim = [0, MaxY];
bx2.XLim = [0, max(Time)];

%% Exporting results in an Excel sheet
EXP = [Time, ConcNP]';
Time_m = (t/KT)';
Model(optimj, 1:length(Time_m)) = Time_m;
Model(length(Depth)-1+optimj, 1:length(OmegaNPF_x)) =
OmegaVfinitial*OmegaNPF_x(:,optimj);
xlswrite('Particlemodel.xlsx', Model); % Model output
xlswrite('Particleexp.xlsx', EXP); % Experimental Ddata

end

function Error = objfun (params)
%% UNKNOWN parameter to fit
Pev_inv = params(1); % a Peclet number of nanoparticles
Dav = params(2); % a Damkohler number of nanoparticles

%% Solving the PDEPE
% options2=odeset('RelTol', 1e-5); % sets the relative tolerance to 10^-5
sol = pdepe(m, @pdeNPSoil, @pdeNPSoilic, @pdeNPSoilbc, x, t);
OmegaNPF = sol(:, :, 1); % Model output of nanoparticles in fluid in time and space

% OmegaNPF as a function of t at the exit of the column
OmegaNPF_x(:, optimj) = OmegaNPF(:, length(x));

%% Comparing concentrations and calculating error for specific time points
Cerror(optimj) = 0;
for xi = 1 : length (t)
    Cerror(optimj) = Cerror(optimj) + (OmegaNPF_x(xi, optimj) - FittedConc(xi, :))^2;
end
Error = Cerror(optimj) * 1000

%% Inner Functions
function [c, f, s] = pdeNPSoil(x, t, u, DuDx)
% Defining c, f, and s to solve the PDEPE function
c = [1]; % Coefficients in front of DuDt term (none here so all ones)
f = [Pev_inv * DuDx(1)]; % Coefficients for the second derivative
s = [-DuDx(1) - Dav * rsf * u(1)]; % Reaction term
end

```

```

%% Initial Conditions
function u0 = pdeNPSoilic(x)
    u0 = [0];
end
% Boundary conditions
function [pl,ql,pr,qr] = pdeNPSoilbc(xl,ul,xr,ur,t)
    OmegaVfi = 1 - 1/(1+exp(-50*(t-tinj)));
    pl = [ul(1)-OmegaVfi];
    ql = [0];
    pr = [0];
    qr = [1];
end
end

%%
WarnWave = [sin(1:.6:400), sin(1:.7:400), sin(1:.4:400)]; % Produces a sound alert when code is
done running
Audio = audioplayer(WarnWave, 22050);
play(Audio);
toc

end

```


Part 2: Model for pesticides transport through soil

% Last edited: 07/21/18

```
function DrugonlyPdepe1
tic
clc
clear
%% Defining the constants
E = 0.45; % Volume fraction of fluid [1 = 100% fluid]
rsf = (1-E)/E; % Particle-to-fluid volume ratio [dimensionless]
Q = 1.5; % Flow rate [cm3/min]
Phi = 3401; % Adsorption surface per particle volume[cm-1]
radius = 0.5; % Radius of the soil column [cm]
A = pi*radius2; % Cross sectional Area of the column[cm2]
massparticle = 0.5; % Mass of particle injected in the system [mg]
volumeinj = 0.3; % Volume of particle injection [cm3]
OmegaVfinitial = massparticle/volumeinj; % [mg/cm3]

%% Experimental Data
ExpData = xlsread('ExperimentalDataMatlab_DRUGnodelay'); % Importing the experimental
data
% ~~First row is the depth value~~
Depth = ExpData (1,:); % Creating the array of soil depth data
Time = ExpData (2:end,1,:); % Creating the array of time data.
MassNP = ExpData (2:end,2:end,:); % Creating the array of experimental mass of pesticides
ConcNP = MassNP /500; % converting the mass into concentration of pesticides

%% Initialization of parameters
Cerror = zeros (length (Depth)-1);
individualparams= zeros (length (Depth)-1, 2); % We currently only have a Peclet number and a
Damkohler number as parameters (2 parameters)
global optimj
global L

%% Parameters estimation STARTS
for optimj = 1: length(Depth)-1
    %% Non dimensionalization of the time and length
    L = Depth(optimj+1);
    KT= Q/(L*A*E); % Dimensionless constant of time
    tinj=volumeinj/Q/2*KT; % Initial time of particle injection into the system
    TimeD = Time * KT; % Dimensionless time
    depthD = Depth/L; % Dimensionless depth

    %% Defining dimensionless time and length for the PDEPE function
    m = 0; % The symmetry of the problem. m can be slab = 0, cylindrical = 1, or spherical = 2.
```

```

x = linspace(0,1,1000); % Dimensionless
tmin = 0;
tmax = ceil(max(TimeD));
t = linspace(tmin,tmax,1001); % Dimensionless

%% Experimental data as a function of t for specific x values
ConcNPD = ConcNP./OmegaVfinitial; % Dimensionless concentration
fitobject = fit(TimeD,ConcNPD(:,optimj),'smoothingspline');% Creating a curve fit to the
experimental data
FittedConc = fitobject (t); % Extracting more points from the curve fit of the experimental
data
for i = 1: length (Time)-1
    OmegaNPF_exp(i+1,:)=ConcNPD(i+1,:); % The first index is depth row
end

%% Parameter estimation function
options1 = optimoptions('fmincon','Display','iter','Algorithm','sqp') % Options for the fmincon
function
[optparams Error2] = fmincon(@objfun, [0.05 0.01],[[],[],[],[],[0 0.001],[5 15],[], options1) %
Estimating the value of the Peclet number and a Damkohler number of the nanoparticle
    individualparams(optimj,:) = optparams % Returns the optimized parameter for each depth
ERROR (optimj) = Error2 % Returns the absolute error between the model and the experimental
data for each depth (~~Scaled by 1000X~~)

%% Figures of the results
maxth = max(OmegaVfinitial.*OmegaNPF_x(:,1)); maxexp = max(smooth(ConcNP(:,1))); %
The highest peak is the firts depth
MaxY = max ([maxexp maxth]); % To normalize graph with dimension to the highest peak

maxthD = max(OmegaNPF_x(:,1)); maxexpD = max(smooth(ConcNPD(:,1)));
MaxYD = max ([maxexpD maxthD]); % To normalize dimensionless graphs to the highest
peak

figure(1) % Pesticide transport in fluid
bx1 = subplot (2,1,1);
plot (TimeD/KT, (ConcNP(:,optimj)),'Color',[0.15*optimj, 0,1])
hold on
xlabel('Time [min]'); ylabel('\Omega_D_F [mg/cm^3]');title ('Experimental Data'); axis tight;

bx2 = subplot (2,1,2);
plot(t/KT,OmegaVfinitial*OmegaNPF_x(:,optimj),'Color',[0.15*optimj, 0,1]);
hold on
xlabel('Time [min]'); ylabel('\Omega_D_F [mg/cm^3]');title ('Model Output'); axis tight
bx1.YLim = [0,MaxY];bx2.XLim = [0,max(Time)];
bx2.YLim = [0,MaxY];bx2.XLim = [0,max(Time)];

```

```

%% Exporting results in an Excel sheet
EXP = [Time, ConcNP]';
Time_m = (t/KT)';
Model(optimj,1:length(Time_m))= Time_m;
Model(length(Depth)-1+optimj ,1:length(OmegaNPF_x))=
OmegaVfinal*OmegaNPF_x(:,optimj);
xlswrite('DRUGmodel.xlsx',Model');
xlswrite('DRUGexp.xlsx',EXP);

end

function Error = objfun (params)
%% UNKNOWN parameter to fit
Ped_inv = params(1); % a Peclet number of pesticides
Dad = params(2); % a Damkohler number of pesticides

%% Solving the PDEPE
% options2=odeset('RelTol',1e-5); % sets the relative tolerance to 10^-5
sol = pdepe(m,@pdeNPSoil,@pdeNPSoilc,@pdeNPSoilbc,x,t);
OmegaNPF = sol(:,,1); % Model output of pesticides in fluid in time and space

% OmegaDF as a function of t at the exit of the column
OmegaNPF_x(:,optimj)=OmegaNPF(:,length(x));

%% Comparing concentrations and calculating error for specific time points
Cerror(optimj)=0;
for xi = 1 : length (t)
    Cerror(optimj) = Cerror(optimj)+ (OmegaNPF_x(xi,optimj)-FittedConc(xi,:))^2;
end
Error=Cerror(optimj)*1000

%% Inner Functions
function [c,f,s] = pdeNPSoil(x,t,u,DuDx)
% Defining c, f, and s to solve the PDEPE function
c = [1]; % Coefficients in front of DuDt term (none here so all ones)
f = [Ped_inv*DuDx(1)]; % Coefficients for the second derivative
s = [-DuDx(1) - Dad*rsf*u(1)]; % Reaction term
end

%% Initial Conditions
function u0 = pdeNPSoilc(x)
u0 = [0];
end

% Boundary conditions
function [pl,ql,pr,qr] = pdeNPSoilbc(xl,ul,xr,ur,t)
OmegaVfi = 1- 1/(1+exp(-50*(t-tinj)));

```

```
    pl = [ul(1)-OmegaVfi];
    ql = [0];
    pr = [0];
    qr = [1];
end
end
%%
WarnWave = [sin(1:.6:400), sin(1:.7:400), sin(1:.4:400)]; % Produces a sound alert when code is
done running
Audio = audioplayer(WarnWave, 22050);
play(Audio);
toc
%%
end
```

Part 3: Model of pesticide release from nanoparticles

% Last edited: 07/23/18

```
function DruginNanoparticlesPdepe
tic
clc
clear
%% Defining the constants
E = 0.45; % Volume fraction of fluid [1 = 100% fluid]
rsf = (1-E)/E; % Particle-to-fluid volume ratio [dimensionless]
Q = 1.5; % Flow rate [cm3/min]
Phi = 3401; % Adsorption surface per particle volume[cm-1]
radius = 1.4; % Radius of the soil column [cm]
A = pi*radius2; % Cross sectional Area of the column[cm2]
massparticle = 1; % Mass of particle injected in the system [mg]
MWDDrug = 653.77; % Molecular weight of pesticide (g/mol)
% moleDrug = 2.67857142e-009 ; % (CPMV) moles of pesticide added to the system (mol)
% moleDrug = 5.32995e-009 ; % (TMGMV) moles of pesticide added to the system (mol)
% moleDrug = 1.17021e-008 ; % (PHMV) moles of pesticide added to the system (mol)
moleDrug = 4.77922e-009 ; % (MSNP) moles of pesticide added to the system (mol)
massDrug = MWDDrug * moleDrug * 1000; % Mass of pesticide injected in the system [mg]
volumeinj = 0.3; % Volume of particle injection [cm3]
OmegaVfinitial = massparticle/volumeinj; % [mg/cm3]
OmegaDfinitial1 = massDrug/volumeinj; % [mg/cm3]
OmegaDfinitial = massDrug/volumeinj; % [mg/cm3]

%% Experimental Data
ExpData = xlsread('ExperimentalDataMatlab_MSNP2nodelay'); % Importing the experimental
data of nanoparticles through soil
ExpData_D = xlsread('ExperimentalDataMatlab_DRUGinMSNPnodelay'); % Importing the
experimental data of pesticide in nanoparticles through soil
NPParamData = xlsread('MSNPparameters'); % Importing the parameter optimization from
nanoparticles
DrugParamData = xlsread('DRUGparameters2'); % Importing the parameter optimization from
pesticide

%first row is the depth value
Depth = ExpData_D (1,:,:) % Creating the array of soil depth data
NPDepth = ExpData (1,:,:) % Creating the array of soil depth data
Time = ExpData_D (2:end,1,:); % Creating the array of time data.
MassNP = ExpData (2:end,2:end,:); % Creating the array of experimental mass of nanoparticles
ConcNP = MassNP /500; % Converting the mass into concentration of nanoparticles
MassD = ExpData_D (2:end,2:end,:)*1000; % Creating the array of experimental mass of
pesticide
```

```

ConcD = MassD /0.5; % Converting the mass into concentration of pesticide

% Creating the vectors of Peclet numbers and for each depth
Pev_inv = NPParamData (:,1); % Peclet number of nanoparticles
Dav = NPParamData (:,2); % a Damkohler number
Ped_inv1 = DrugParamData (:,1); % Peclet number of pesticide
Dad1 = DrugParamData(:,2)*(A/0.7854); % a Damkohler number
kd = (Dad1*Q)/(2*A*E*Phi)
Dd = (Q*2*Ped_inv1)/(A*E)
%% Initialization of parameters
Cerror = zeros (length (Depth)-1);
individualparams= zeros (length (Depth)-1, 1); % We currently only pesticide rate of release
from nanoparticles as parameters (1 parameter)
global optimj
global L

%% Parameters Estimation STARTS
for optimj = 1: length(Depth)-1
    %% Non dimensionalization of the time and length
    L = Depth(optimj+1);
    Dad = (kd*L*A*E*Phi)/Q
    Ped_inv = (Dd*A*E)/(Q*L)
    KT= Q/(L*A*E); % Dimensionless constant of time
    tinj=volumeinj/Q/2*KT; % Initial time of particle injection into the system
    TimeD = Time * KT; % Dimensionless time
    depthD = Depth/L; % Dimensionless depth

    %% Defining dimensionless time and length for the PDEPE function
    m = 0; % The symmetry of the problem. m can be slab = 0, cylindrical = 1, or spherical = 2.
    x = linspace(0,1,1000); % Dimensionless
    tmin = 0;
    tmax = ceil(max(TimeD));
    t = linspace(tmin,tmax,1001); % Dimensionless

    %% Experimental data as a function of t for specific x values
    ConcNPD = ConcNP./OmegaVfinitial; % Dimensionless concentration of nanoparticles
    ConcDD = ConcD./OmegaDfinitial; % Dimensionless concentration of nanoparticles

    fitobject = fit(TimeD,ConcNPD(:,optimj),'smoothingspline'); % Creating a curve fit to the
    experimental data of nanoparticles
    FittedConc = fitobject (t); % Extracting more points from the curve fit of the experimental data
    of pesticide
    fitDRUG = fit(TimeD,ConcDD(:,optimj),'smoothingspline'); % Creating a curve fit to the
    experimental data

```

```

FittedConcD = fitDRUG (t); % Extracting more points from the curve fit of the experimental
data of pesticide

    for i = 1: length (Time)-1
        OmegaNPF_exp(i+1,:)=ConcNPD(i+1,:); % The first index is depth row (experimental data of
nanoparticles)
    end

    for i = 1: length (Time)-1
        OmegaDF_exp(i+1,:)=ConcDD(i+1,:); % The first index is depth row (experimental data of
pesticide)
    end

%% Parameter estimation function
options1 = optimoptions('fmincon','Display','iter','Algorithm','sqp') % Options for the fmincon
function
[optparams Error2] = fmincon(@objfun, [20],[,],[,],[,],[,],[0],[100],[,], options1)
    individualparams(optimj,:) = optparams % returns the optimized parameter for each depth
ERROR (optimj) = Error2 % returns the absolute error between the model and the experimental
data for each depth

%% Figures of the results
maxth = max(OmegaVfinitial.*OmegaNPF_x(:,1)); maxexp = max(smooth(ConcNP(:,1)));
maxthDF = max(OmegaDfinitial.*OmegaDF_x(:,1));
maxDexp = max(smooth(ConcD(:,1))); maxthDNPF =
max(OmegaDfinitial.*OmegaDNPF_x(:,1));% the highest of nanoparticles peak is the first depth
    MaxY = max ([maxexp maxth]); % to normalize nanoparticle graph with dimension to the
highest peak
    MaxDY = max ([maxthDF maxDexp maxthDNPF]);
    figure(1) % Nanoparticles Transport in FLuid
    bx1 = subplot (2,1,1);
    for xi = 1 : length (Depth)-1
        plot (Time, (ConcNP(:,find(NPDepth == Depth (xi+1))-1)), 'Color',[0.15*optimj, 0,1])
        hold on
    end
xlabel("Time [min]"); ylabel("\Omega_N_P_F [mg/cm^3]");title ('Nanoparticle experimental
data'); axis tight;

    bx2 = subplot (2,1,2);
    plot(t/KT,OmegaVfinitial*OmegaNPF_x(:,optimj),'Color',[0.15*optimj, 0,1]);
    hold on
    xlabel("Time [min]"); ylabel("\Omega_N_P_F [mg/cm^3]");title ('Nanoparticle model Output');
axis tight
    bx1.YLim = [0,MaxY]; bx2.YLim = [0,MaxY];
    bx2.XLim = [0,max(Time)];

```

```

figure(2) % pesticide Transport in FLuid
dx1 = subplot (3,1,1);
plot (TimeD/KT, (ConcD(:,optimj)), 'Color',[0.15*optimj, 0,1])
hold on
xlabel('Time [min]'); ylabel('C_D_F [mg/cm^3]');title ('Pesticide in nanoparticle experimental
data'); axis tight;

dx2 = subplot (3,1,2);
plot(t/KT, OmegaDfinitia*OmegaDNPF_x(:,optimj), 'Color',[0.15*optimj, 0,1]);
hold on
xlabel('Time [min]'); ylabel('C_D_F [mg/cm^3]');title ('Pesticide in nanoparticle model
output');
axis tight

dx3 = subplot (3,1,3);
plot(t/KT, OmegaDfinitia*OmegaDF_x(:,optimj), 'Color',[0.15*optimj, 0,1]);
hold on
xlabel('Time [min]'); ylabel('C_F [mg/cm^3]');title (' Free pesticide model output'); axis tight
dx1.YLim = [0,MaxDY]; dx2.YLim = [0,MaxDY]; dx3.YLim = [0,MaxDY];
dx1.XLim = [0,max(Time)]; dx2.XLim = [0,max(Time)]; dx3.XLim = [0,max(Time)];

%% Exporting results in an Excel sheet
EXP = [Time, ConcD]';
Time_m = (t/KT)';
Model(optimj,1:length(Time_m))= Time_m;
ModelD(optimj,1:length(Time_m))= Time_m;
Model(length(Depth)-1+optimj ,1:length(OmegaDNPF_x))=
OmegaDfinitia*OmegaDNPF_x(:,optimj);
ModelD(length(Depth)-1+optimj ,1:length(OmegaDF_x))=
OmegaDfinitia*OmegaDF_x(:,optimj);
xlswrite('DruginParticleExp.xlsx',EXP);% Experimental pesticide in nanoparticle Data
xlswrite('DruginParticlemodel.xlsx',Model); % Model pesticide in nanoparticles output
xlswrite('Freepesticidemodel.xlsx',ModelD); % Model free pesticide output
end

function Error = objfun (params)
%% UNKNOWN parameter to fit
DaDNP = params(1) % Rate constant of pesticide release from nanoparticles [min^-1]

%% Solving the PDEPE
% options2=odeset('RelTol',1e-5); % sets the relative tolerance to 10^-5
sol = pdepe(m,@pdeNPSoil,@pdeNPSoilc,@pdeNPSoilbc,x,t);
OmegaNPF = sol(:, :,1); % model output of Nanoparticles in fluid in time and space
OmegaDF = sol(:, :,2); % model output of pesticide in fluid in time and space

```



```
OmegaDNPF = sol(:,3); % model output of pesticide attached to virus in fluid in time and space
```

```
% OmegaVF as a function of t at the exit of the column
```

```
OmegaNPF_x(:,optimj)=OmegaNPF(:,length(x));
```

```
% OmegaDF as a function of t at the exit of the column
```

```
OmegaDF_x(:,optimj)=OmegaDF(:,length(x));
```

```
% OmegaDNPF as a function of t at the exit of the column
```

```
OmegaDNPF_x(:,optimj)=OmegaDNPF(:,length(x));
```

```
%% MODIFIED Simpson's Integration to calculate area under the curve
```

```
% Total area under the pesticide in fluid at the exit
```

```
C_x = zeros (length(OmegaDNPF_x),1);
```

```
te = 0;
```

```
for num = 1: length (t)
```

```
    C_x (num) = (OmegaDNPF_x (num) + OmegaDF_x (num)) ;
```

```
end
```

```
for i = 2:2:length(t)-2
```

```
    te = te + 4*C_x (i) + 2*C_x (i+1);
```

```
end
```

```
te = te + C_x (1) + C_x (length(t)) + 4*C_x (length(t)-1);
```

```
areaE = te * (tmax-tmin)/(length(t)-1)/3;
```

```
AUC = areaE;
```

```
masspesticide = AUC*OmegaDfinitial*L*A*E
```

```
massDrug
```

```
% Total area under the pesticide stuck in soil
```

```
%% Comparing concentrations and calculating error for specific time points
```

```
Cerror(optimj)=0;
```

```
for xi = 1 : length (t)
```

```
    Cerror(optimj) = Cerror(optimj)+ (OmegaDNPF_x(xi,optimj)-FittedConcD(xi,:))^2;
```

```
end
```

```
Error=Cerror(optimj)*10^3
```

```
%% Inner Functions
```

```
function [c,f,s] = pdeNPSoil(x,t,u,DuDx)
```

```
    % Defining c, f, and s to solve the PDEPE function
```

```
    c = [1;1;1]; % Coefficients in front of DuDt term (none here so all ones)
```

```
f = [Pev_inv(optimj)*DuDx(1);Ped_inv*DuDx(2); Pev_inv(optimj)*DuDx(3) ]; % Coefficients for the second derivative
```

```
s = [-DuDx(1) - Dav(optimj)*rsf*u(1);-DuDx(2) - Dad*rsf*u(2) + DaDNP * u(3); -DuDx(3) - Dav(optimj)*rsf*u(3) - DaDNP * u(3)]; % Reactive term
```

```

end

%% Initial Conditions
function u0 = pdeNPSoilic(x)
    u0 = [0; 0; 0];
end
%% Boundary Conditions
function [pl,ql,pr,qr] = pdeNPSoilbc(xl,ul,xr,ur,t)
    OmegaVfi = 1- 1/(1+exp(-50*(t-tinj)));
    pl = [ul(1)-OmegaVfi; ul(2); ul(3)-OmegaVfi];
    ql = [0;0;0];
    pr = [0;0;0];
    qr = [1;1;1];
end
end

%%
WarnWave = [sin(1:.6:400), sin(1:.7:400), sin(1:.4:400)]; % Produces a sound alert when code is
done running
Audio = audioplayer(WarnWave, 22050);
play(Audio);
toc

end

```

Part 4: Theoretical treatment of a crop infected by nematodes

```
% Last edited: 09/04/18
%% Scenario:
% Root-knot nematodes have infected the roots of a crop.
% Analysis of the soil reveals that their highest density is located 24 cm deep from the surface.
% To treat the crop, the drug Abamectin is to be used. The IC50 of Abamectin is  $1.309 \times 10^{-4}$ 
mg.cm-3.
% The TMGMV-Abamectin formulation is explored.
```

```
%QUESTION: what is the concentration of TMGMV-Abamectin that must be applied on the
crop to reach the
IC50 concentration 24 cm deep in the soil?
%%
```

```
function NematodeTreatment
```

```
tic
clc
clear
```

```
%% Defining the constants
```

```
E = 0.45; % Volume fraction of fluid [1 = 100% fluid]
rsf = (1-E)/E; % Particle-to-fluid volume ratio [dimensionless]
Phi = 3401; % Adsorption surface per particle volume[cm-1]
radius = 1.4; % Radius of the soil column [cm]
A = pi*radius2; % Cross sectional Area of the column[cm2]
volumeinj = 0.3; % Volume of particle injection [cm3]
Lz=24; % Target location [cm]
MWDrug = 873; % Molecular weight of Abamectin (g/mol)
ICfifty = 1.309 * 10-4; % Concentration of Abamectin that must be
reached at Lz [mg/cm3]
moleDrug = 1e-008 ; % (TMGMV) moles of Abamectin in 1 mg of TMGMV (mol)
massDrug = MWDrug * moleDrug * 1000; % Mass of pesticide injected in the
system [mg]
```

```
%% Optimized parameters of Nanoparticle and pesticide
```

```
NPPParamData = xlsread('TMGMVaverage'); % Importing the parameter
optimizations from nanoparticles
DrugParamData = xlsread('DRUGaverage'); % Importing the parameter
optimizations from pesticide
Time = (0:.1:60); %irrigation for one hour
Q = [0.1 0.2 0.5 1 2];
for fl = 1: length (Q)
Pev_inv = NPPParamData (1); % Peclet number of nanoparticle
Dav = NPPParamData (2); % a Damkohler number of nanoparticle
```

```

Ped_inv1 = DrugParamData(:,1);% Peclet number of pesticide
Dad1 = DrugParamData(:,2)*(A/0.7854); % a Damkohler number
kd = (Dad1*Q(fl))/(2*A*E*Phi);
Dd = (Q(fl)*2*Ped_inv1)/(A*E);
DaDNP = NPPParamData(3); % a a Damkohler number of pesticide release from nanoparticle

```

```
%% Parameters Estimation STARTS
```

```
%% Defining dimensionless time and length for the PDEPE function
```

```
L = 300; % Depth of the nematodes
```

```
Dad = (kd*L*A*E*Phi)/Q(fl);
```

```
Ped_inv = (Dd*A*E)/(Q(fl)*L);
```

```
KT= Q(fl)/(L*A*E); % Dimensionless constant of time
```

```
tinj=volumeinj/Q(fl)/2*KT; % Initial time of particle injection into the system
```

```
TimeD = Time * KT; % Dimensionless time
```

```
m = 0; % The symmetry of the problem. m can be slab = 0, cylindrical = 1, or spherical = 2.
```

```
x = linspace(0,1,1000); % Dimensionless
```

```
tmin = 0;
```

```
tmax = max(TimeD);
```

```
t = linspace(tmin,tmax,1001); % Dimensionless
```

```
%% UNKNOWN parameter to fit
```

```
maxi = 1.5; % [mg]
```

```
increment = .2;
```

```
j = 1;
```

```
Cerror = 0;
```

```
AUC = 0;
```

```
for iparam = .2:increment:maxi
```

```
    massparticle = iparam; % Initial concentration of nanoparticle applied
```

```
    massparticles(j) = massparticle; % [mg]
```

```
    OmegaVfinitial = massparticle/volumeinj; % [mg/cm^3]
```

```
    OmegaDfinitial = (massDrug/volumeinj) * massparticle ; % [mg/cm^3]
```

```
%% Solving the PDEPE
```

```
% options2=odeset('RelTol',1e-5); % sets the relative tolerance to 10^-5
```

```
sol = pdepe(m,@pdeNPSoil,@pdeNPSoilic,@pdeNPSoilbc,x,t);
```

```
OmegaNPF = sol(:,:,1); % model output of Nanoparticles in fluid in time and space
```

```
OmegaDF = sol(:,:,2); % model output of pesticide in fluid in time and space
```

```
OmegaDNPF = sol(:,:,3); % model output of pesticide attached to virus in fluid in time
```

and

```
space
```

```
OmegaNPS = sol(:,:,4); % model output of Nanoparticles bound to soil in time and space
```

```
OmegaDS = sol(:,:,5); % model output of pesticide bound to soil in time and space
```

```
%calculate length array position for Lz
```

```

nLz=round((length(x)-1)*Lz/L);

%calculate variables as a function of t at z=Lz

% OmegaNPF as a function of t at Lz
OmegaNPF_x(:)=OmegaNPF(:,nLz);

% OmegaDF as a function of t at Lz
OmegaDF_x(:)=OmegaDF(:,nLz);

% OmegaDNPF as a function of t at L
OmegaDNPF_x(:)=OmegaDNPF(:,nLz);

% OmegaNPS as a function of t at Lz
OmegaNPS_x(:)=OmegaNPS(:,nLz);

% OmegaDS as a function of t at Lz
OmegaDS_x(:)=OmegaDS(:,nLz);

%% MODIFIED Simpson's Integration to calculate area under the curve
% Total area under the pesticide in fluid
C_x = zeros (length(OmegaDNPF_x),1);
Cmin = 0;
te = 0;
for num = 1: length (t)
    C_x (num) = (OmegaDNPF_x (num) + OmegaDF_x(num))*OmegaDfinitial ; %C_x is
dimensional
end

for i = 2:2:length(t)-2
    te = te + 4*C_x (i) + 2*C_x (i+1);
end

te = te + C_x (1) + C_x (length(t)) + 4*C_x (length(t)-1);
area = te * (tmax-tmin)/(length(t)-1)/3/KT; %area is dimensional

tnematode = 24*max(Time);
AUC(j) = area
Cerror(j) = ((AUC(j)-ICfifty*tnematode)^2 )*1000
j = j+1;

end
minerror = min(Cerror);

```

```

masstoinject(fl) = massparticles(find (Cerror == minerror))/A
MinError (fl) = Cerror(find (Cerror == minerror))
for i = 1: length (massparticles)
    IC1 (i) = ICfifty;
end
figure (3)
plot (massparticles, IC1*tnematode,'r')
hold on
plot (massparticles, AUC,'b')
hold off

%% Figures
figure(1) % Nanoparticles Transport in FLuid
bx1 = subplot (5,1,1);
plot(t/KT,OmegaVfinitial*OmegaNPF_x);
xlabel('Time [min]'); ylabel('\Omega_N_P_F [mg/cm^3]');title (' Free nanoparticle model
Output');
axis tight
bx2 = subplot (5,1,2);
plot(t/KT,OmegaVfinitial*OmegaNPS_x);
xlabel('Time [min]'); ylabel('\Omega_N_P_S [mg/cm^3]');title ('bound nanoparticle model
Output');
axis tight
bx3 = subplot (5,1,3);
plot(t/KT,OmegaDfinitial*OmegaDNPF_x);
xlabel('Time [min]'); ylabel('C_D_N_P_F [mg/cm^3]');title ('Pesticide in nanoparticle
model
output'); axis tight
bx4 = subplot (5,1,4);
plot(t/KT,OmegaDfinitial*OmegaDF_x);
xlabel('Time [min]'); ylabel('C_F [mg/cm^3]');title (' Free pesticide model output'); axis
tight
bx5 = subplot (5,1,5);
plot(t/KT,OmegaDfinitial*OmegaDS_x);
xlabel('Time [min]'); ylabel('C_S [mg/cm^3]');title (' Bound
pesticide model output'); axis tight

totaldrug = OmegaDfinitial*OmegaDNPF_x + OmegaDfinitial*OmegaDF_x;
for i = 1: length (t)
    IC (i) = ICfifty;
end
figure (2)
plot (t/KT,IC, 'r')
hold on
plot(t/KT,totaldrug, 'k')
hold off

```

```

xlabel('Time [min]'); ylabel('Pesticide distribution [mg/cm^3]');title (' Treatment of
nematodes');
axis tight

end

%% Inner Functions
function [c,f,s] = pdeNPSoil(x,t,u,DuDx)
    % Defining c, f, and s to solve the PDEPE function
    c = [1;1;1;1;1]; % Coefficients in front of DuDt term (none
here so all ones)
    f = [Pev_inv*DuDx(1);Ped_inv*DuDx(2); Pev_inv*DuDx(3);
Pev_inv*DuDx(1)/1000; Ped_inv*DuDx(2)/1000 ]; % Coefficients
for the second derivative
    s = [-DuDx(1) - Dav*rsf*u(1);-DuDx(2) - Dad*rsf*u(2) + DaDNP * u(3); -DuDx(3) -
Dav*rsf*u(3) - DaDNP * u(3); Dav*u(1); Dad*u(2) ]; % Reactive term
end

%% Initial Conditions
function u0 = pdeNPSoilic(x)
    u0 = [0; 0; 0; 0; 0];
end

%% Boundary Conditions
function [pl,ql,pr,qr] = pdeNPSoilbc(xl,ul,xr,ur,t)
    OmegaVfi = 1- 1/(1+exp(-50*(t-tinj)));
    pl = [ul(1)-OmegaVfi; ul(2); ul(3)-OmegaVfi; ul(4); ul(5)];
    ql = [0;0;0;0;0];
    pr = [0;0;0;0;0];
    qr = [1;1;1;1;1];
end

%%
WarnWave = [sin(1:.6:400), sin(1:.7:400), sin(1:.4:400)]; % Produces a sound alert when code
is done
running
Audio = audioplayer(WarnWave, 22050);
play(Audio);
toc

end

```

Part 5: Code used to calculate nanoparticle transport through soil based on average value of D_v and k .

Note: Can also be used for the prediction of nanoparticle transport through soil based on 4 cm depth data.

```
function AveragePdepe
tic
clc
clear
%% Defining the constants
E = 0.45; % Volume fraction of fluid [1 = 100% fluid]
Q = 1.5; % Flow rate [cm3/min]
Phi = 3401; % Adsorption surface per particle volume[cm-1]
radius = 1.4; % Radius of the soil column [cm]
A = pi*radius2; % Cross sectional Area of the column[cm2]
massparticle = 1; % mass of particle injected in the system [mg]
volumeinj = 0.3; % volume of particle injection [cm3]
OmegaVfinitial = massparticle/volumeinj; % [mg/cm3]

%% Estimated Paramters
Kvfp = 3.73*10-5; % Rate constant of particle absorbtion to soil [min-1]
Dv = 3.02; % Dispersion coefficient of nanoparticles in fluid

%% Experimental Data
ExpData = xlsread('ExperimentalDataMatlab_TMGMVnodelay'); % Importing the experimental
data
%first row is the depth value
Depth = ExpData (1,:); % creating the array of soil depth data
Time = ExpData (2:end,1,:); % creating the array of time data.
MassNP = ExpData (2:end,2:end,:); % creating the array of experimental mass of nanoparticles
ConcNP = MassNP /500; % converting the mass into concentration of nanoparticles

for optimj = 1: length(Depth)-1
    %% Non dimensionalization of the time and length
    L = Depth(optimj+1);
    KT= Q/(L*A*E); % dimensionless constant of time
    tinj=volumeinj/Q/2*KT; % Initial time of particle injection into the system%% Non-
Dimensionalization of Experimental Data
    TimeD = Time * KT; % Dimensionless time
    depthD = Depth/L;
    %% Defining dimensionless time and length for the PDEPE function
    m = 0; % the symmetry of the problem. m can be slab = 0, cylindrical = 1, or spherical = 2.
    x = linspace(0,1,1000); % dimensionless
    tmin = 0;
    tmax = ceil(max(TimeD));
```



```

t = linspace(tmin,tmax,1001); % dimensionless
Index = round(1+ TimeD./(tmax-tmin)*(length (t)-1));

%% Experimental data as a function of t for specific x values
ConcNPD = ConcNP./OmegaVfinitial; % Dimensionless concentration
for i = 1: length (Time)-1
    OmegaNPF_exp(i+1,:)=ConcNPD(i+1,:); %the first index is depth row
end

%% Defining the Dimensionless Parameters
% Equation 1
KA = (A*E*Dv)/(Q*L);
KB = (L*A*Kvfp*Phi*(1-E))/(Q);
%% Solving the PDEPE

% options2=odeset('RelTol',1e-5); % sets the relative tolerance to 10^-5
sol = pdepe(m,@pdeNPSoil,@pdeNPSoilc,@pdeNPSoilbc,x,t);
OmegaNPF = sol(:,1); % model output of Nanoparticles in fluid in time and space

% OmegaVF as a function of t at the exit of the column
OmegaNPF_x(:,optimj)=OmegaNPF(:,length(x));

%% Figures of the results
maxth = max(OmegaVfinitial.*OmegaNPF_x(:,1)); maxexp = max(smooth(ConcNP(:,1))); %
the highest peak is the first depth
MaxY = max ([maxexp maxth]); % to normalize graph with dimension to the highest peak

maxthD = max(OmegaNPF_x(:,1)); maxexpD = max(smooth(ConcNPD(:,1)));
MaxYD = max ([maxexpD maxthD]); % to normalize dimensionless graphs to the highest
peak

figure(1) % With Dimensions
bx1 = subplot (2,1,1);
plot (TimeD/KT, (ConcNP(:,optimj)), 'Color',[0.15*optimj, 0,1])
hold on
xlabel("Time [min]"); ylabel("\Omega_N_P_F [mg/cm^3]");title ('Experimental Data'); axis
tight;
legend (int2str(optimj), 'Location', 'northeast');legend ('boxoff')

bx2 = subplot (2,1,2);
plot(t/KT,OmegaVfinitial*OmegaNPF_x(:,optimj), 'Color',[0.15*optimj, 0,1]);
hold on
xlabel("Time [min]"); ylabel("\Omega_N_P_F [mg/cm^3]");title ('Model Output'); axis tight
legend(int2str(optimj), 'Location', 'northeast');legend ('boxoff')
bx1.YLim = [0,MaxY]; bx2.YLim = [0,MaxY];
bx2.XLim = [0,32];

```

```

EXP = [Time, ConcNP]';
Time_m = (t/KT)';
Model(optimj,1:length(Time_m))= Time_m;
Model(length(Depth)-1+optimj ,1:length(OmegaNPF_x))=
OmegaVfinal*OmegaNPF_x(:,optimj);
xlswrite('Average.xlsx',Model);
end

%% Inner Functions
function [c,f,s] = pdeNPSoil(x,t,u,DuDx)
    % Defining c, f, and s to solve the PDEPE function
    c = [1]; % coefficients in front of DuDt term (none here so all ones)
    f = [KA*DuDx(1)]; % coefficients for the second derivative
    s = [-DuDx(1) - KB*(u(1))];
end

%% Initial Conditions
function u0 = pdeNPSoilic(x)
    u0 = [0];
end

%% Boundary conditions
function [pl,ql,pr,qr] = pdeNPSoilbc(xl,ul,xr,ur,t)
    OmegaVfi = 1 - 1/(1+exp(-50*(t-tinj)));
    pl = [ul(1)-OmegaVfi];
    ql = [0];
    pr = [0];
    qr = [1];

end

WarnWave = [sin(1:.6:400), sin(1:.7:400), sin(1:.4:400)]; % produces a sound alert when code is
done running
Audio = audioplayer(WarnWave, 22050);
play(Audio);
toc
end

```

Supporting Table 4.5. Optimized parameters.

k_{NPS} [cm min^{-1}]: rate constant of nanoparticle absorption to soil.

D_{NP} [$\text{cm}^2 \text{min}^{-1}$]: dispersion constant of nanoparticles in the interstitial space.

k_{PS} [cm min^{-1}]: rate constant of pesticide absorption to soil.

D_P [$\text{cm}^2 \text{min}^{-1}$]: dispersion constant of pesticide in the interstitial space.

k_{PF} [min^{-1}]: rate constant of pesticide release from nanoparticles.

		TMGMV	CPMV	PhMV	MSNP	PLGA
2 cm	k_{NPS}			9.69×10^{-05}	7.00×10^{-2}	9.81×10^{-05}
	D_{NP}			0.72	0.50	0.51
4 cm	k_{NPS}	4.53×10^{-05}	1.53×10^{-05}	1.07×10^{-4}	3.95×10^{-2}	1.22×10^{-4}
	D_{NP}	1.55	1.35	0.75	1.43	1.60
6 cm	k_{NPS}				2.13×10^{-1}	8.92×10^{-5}
	D_{NP}				2.07	0.98
8 cm	k_{NPS}	2.81×10^{-05}	1.88×10^{-05}		1.7×10^{-1}	1.06×10^{-4}
	D_{NP}	1.34	1.44		2.9758	1.08
12 cm	k_{NPS}	5.36×10^{-05}	3.89×10^{-06}			
	D_{NP}	5.08	2.71			
16 cm	k_{NPS}	3.92×10^{-05}	5.11×10^{-05}			
	D_{NP}	4.91	4.42			
20 cm	k_{NPS}	2.07×10^{-05}	2.58×10^{-05}			
	D_{NP}	2.22	2.95			
30 cm	k_{NPS}	4.26×10^{-05}	5.39×10^{-05}			
	D_{NP}	6.39	10.17			
Average	k_{NPS}	3.82×10^{-05}	2.3×10^{-05}	1.02×10^{-04}	1.236×10^{-01}	1.04×10^{-04}
	D_{NP}	3.58	2.57	0.73	1.75	1.04
STD	k_{NPS}	1.19×10^{-05}	1.76×10^{-05}	6.93×10^{-06}	8.12×10^{-02}	1.4×10^{-05}
	D_{NP}	2.14	1.26	0.02	1.04	0.45

		Cy5
2 cm	k _{PS}	1.37 x 10 ⁻⁰⁴
	D _p	1.73

		TMGMV*Cy5	CPMV*Cy5	PhMV*Cy5	MSNP*Cy5
2 cm	k _{PF}			5.18 x 10 ⁻⁰³	5.08 x 10 ⁻⁰⁵
4 cm	k _{PF}	5.89 x 10 ⁻⁰⁴	2.27 x 10 ⁻⁰⁴	1.26 x 10 ⁻⁰³	3.75 x 10 ⁻⁰⁴
6 cm	k _{PF}				1.18 x 10 ⁻⁰⁴
16 cm	k _{PF}		5.46 x 10 ⁻⁰⁴		
30 cm	k _{PF}		3.49 x 10 ⁻⁰⁴		
Average	k _{PF}	5.89 x 10 ⁻⁰⁴	1.05 x 10 ⁻⁰³	3.22 x 10 ⁻⁰³	2.03 x 10 ⁻⁰⁴
STD	k _{PF}	NA	8.63 x 10 ⁻⁰⁴	1.96 x 10 ⁻⁰³	1.33 x 10 ⁻⁰⁴

To quantify how well the computational outputs matched the empirical data, I calculated the difference (error) as follows:

$$\frac{\partial \Omega_{NP}}{\partial t} + \frac{Q}{A\varepsilon} \frac{\partial \Omega_{NP}}{\partial z} = D_{NP} \frac{\partial^2 \Omega_{NP}}{\partial z^2} + \left(\frac{1-\varepsilon}{\varepsilon} \right) \phi R_{NPS}, \quad 0 < z < L$$

$$\text{Error}(z) = \text{SUM}(\text{OmegaNPF}_x(t,z) - \text{OmegaNPF}_x(t,z))^2;$$

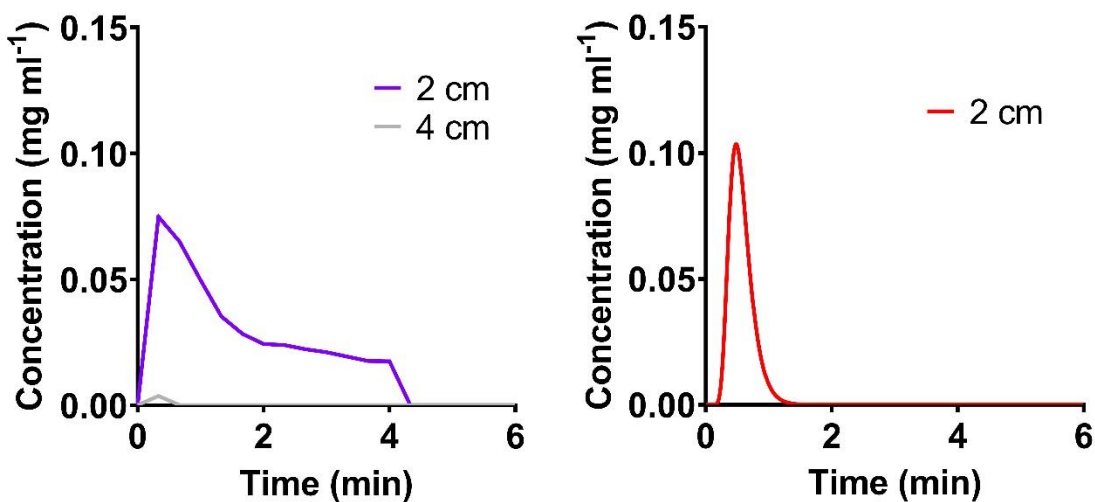
	TMGMV	CPMV	PhMV	MSNP	PLGA
2 cm			3.07×10^{-3}	1.31×10^{-3}	1.67×10^{-3}
4 cm	7.76×10^{-4}	1.03×10^{-3}	7.7×10^{-5}	7.48×10^{-4}	2.98×10^{-4}
6 cm				7.58×10^{-5}	8.56×10^{-5}
8 cm	1.98×10^{-4}	2.06×10^{-3}		1.91×10^{-4}	9.3×10^{-6}
12 cm	9.96×10^{-5}	6.71×10^{-4}			
16 cm	7.48×10^{-4}	3.07×10^{-4}			
20 cm	7.35×10^{-4}	1.86×10^{-3}			
30 cm	2.44×10^{-3}	4.36×10^{-4}			

Error (z) = SUM(OmegaNPF_x(t,z)- OmegaNPF_x(t,z))^2);

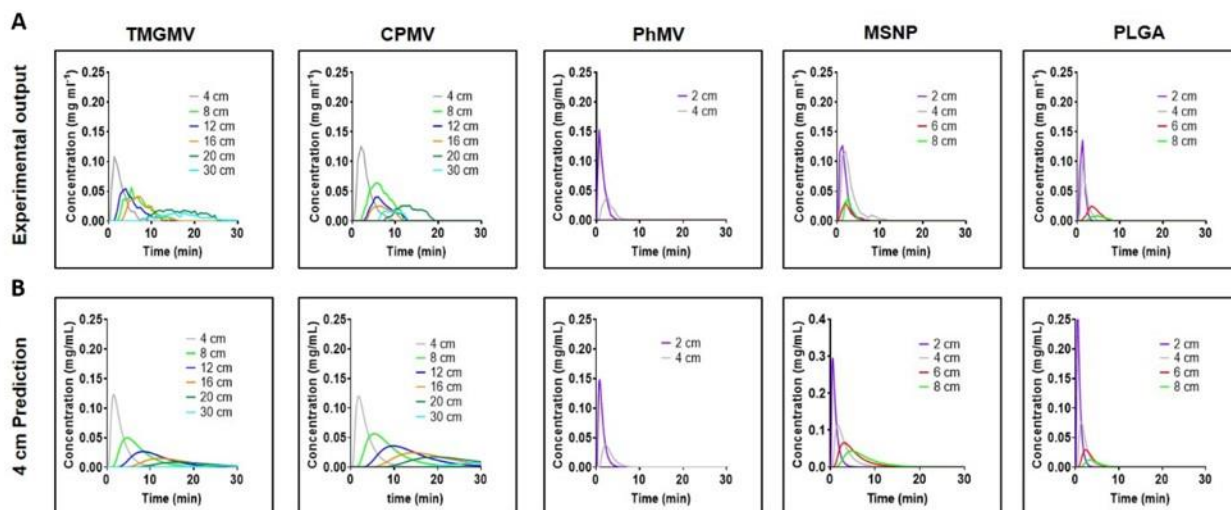
	Cy5
2 cm	7.2×10^{-05}

$$\text{Error}(z) = \text{SUM}(\text{OmegaNPF}_x(t,z) - \text{OmegaNPF}_x(t,z))^2;$$

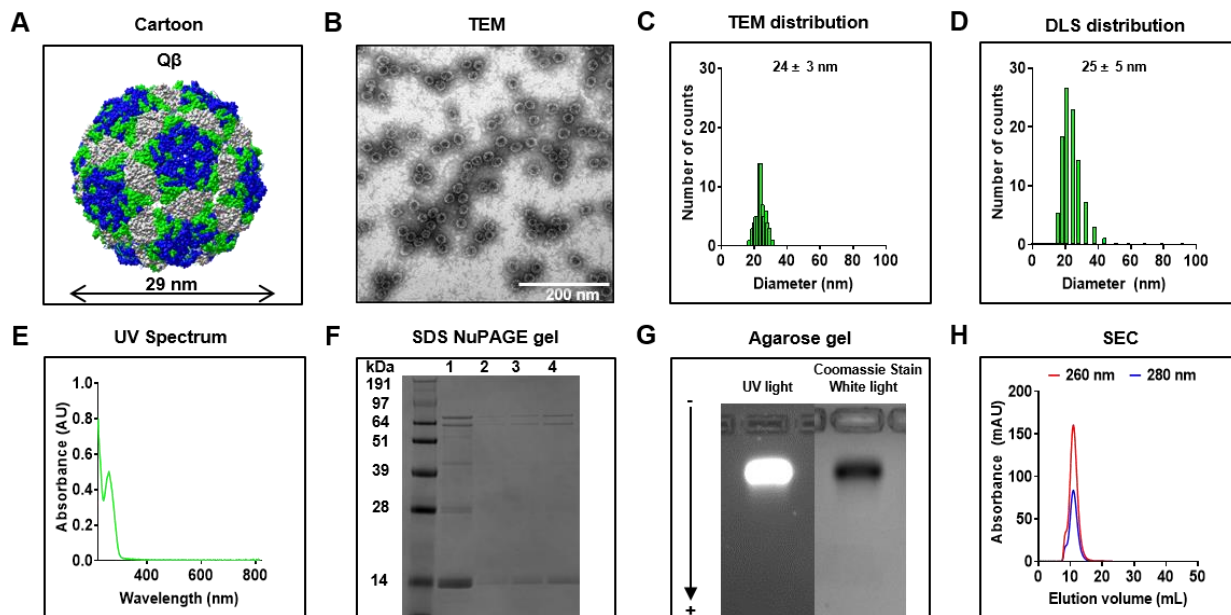
	TMGMV*Cy5	CPMV*Cy5	PhMV*Cy5	MSNP*Cy5
2 cm			6.56×10^{-8}	2.27×10^{-3}
4 cm	6.59×10^{-5}	3.66×10^{-8}	1.24×10^{-8}	6.66×10^{-4}
6 cm				1.65×10^{-4}
16 cm				
		7.82×10^{-9}		
30 cm				
		1.71×10^{-8}		



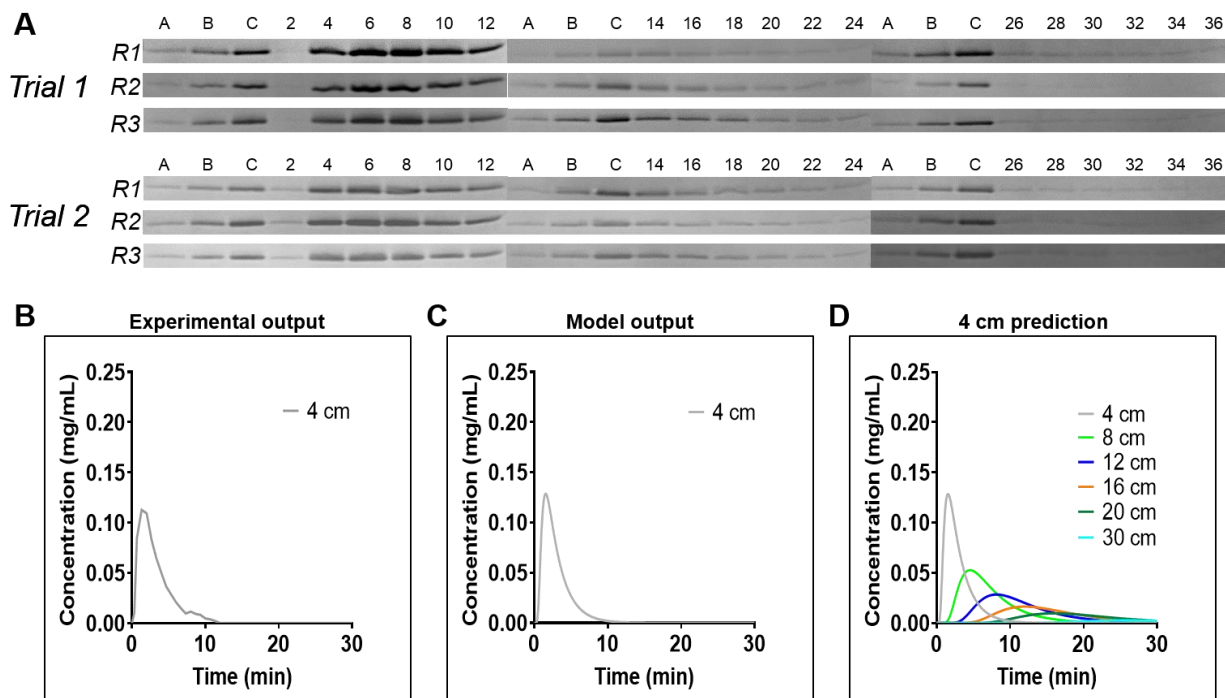
Supporting Figure. 4.9. Free Cy5 from experimental (left) and model output (right).



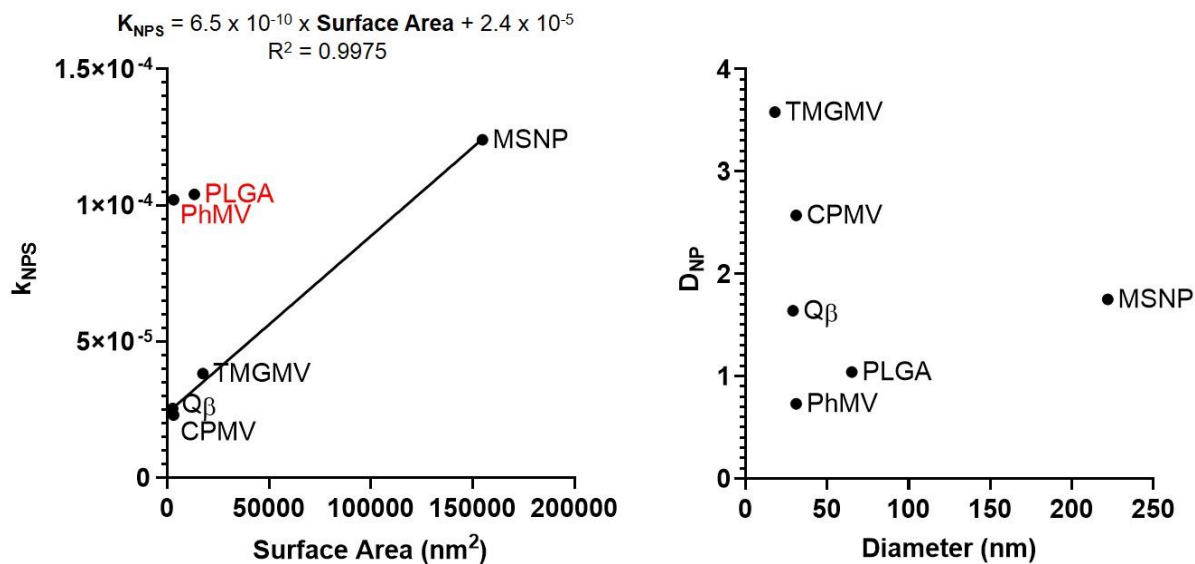
Supporting Figure. 4.10. Nanoparticle soil transport prediction using a 4 cm soil column. (A) The empirical output of TMGMV, CPMV, PhMV, MSNP and PLGA is used as a reference. (B) Computational prediction of nanoparticle transport through soil. D_{NP} and k_{NPS} were optimized from the empirical data obtained from the 4 cm soil column.



Supporting Figure. 4.11. Q β characterization. (A) Simplified representation of (1) Q β (PDB ID: 5KIP). (B) Corresponding TEM images, Scale bar = 200 nm. (C) Size distribution analysis of the TEM images. (D) Particle size distribution obtained by dynamic light scattering (DLS). (E) UV/Vis spectrum of bare Q β . (F) SDS-PAGE gel of Q β imaged under white light after Coomassie staining. Sample 1, 2, 3, and 4 correspond to 10, 0.5, 1, and 2 μ g of Q β , respectively; higher mobility bands correspond to dimers and multimers. (G) agarose gel electrophoretic separation of Q β ; gels were imaged under UV light and under white light after Coomassie staining to visualize the RNA (random cellular RNA) and protein. (H) Size exclusion chromatography of Q β .

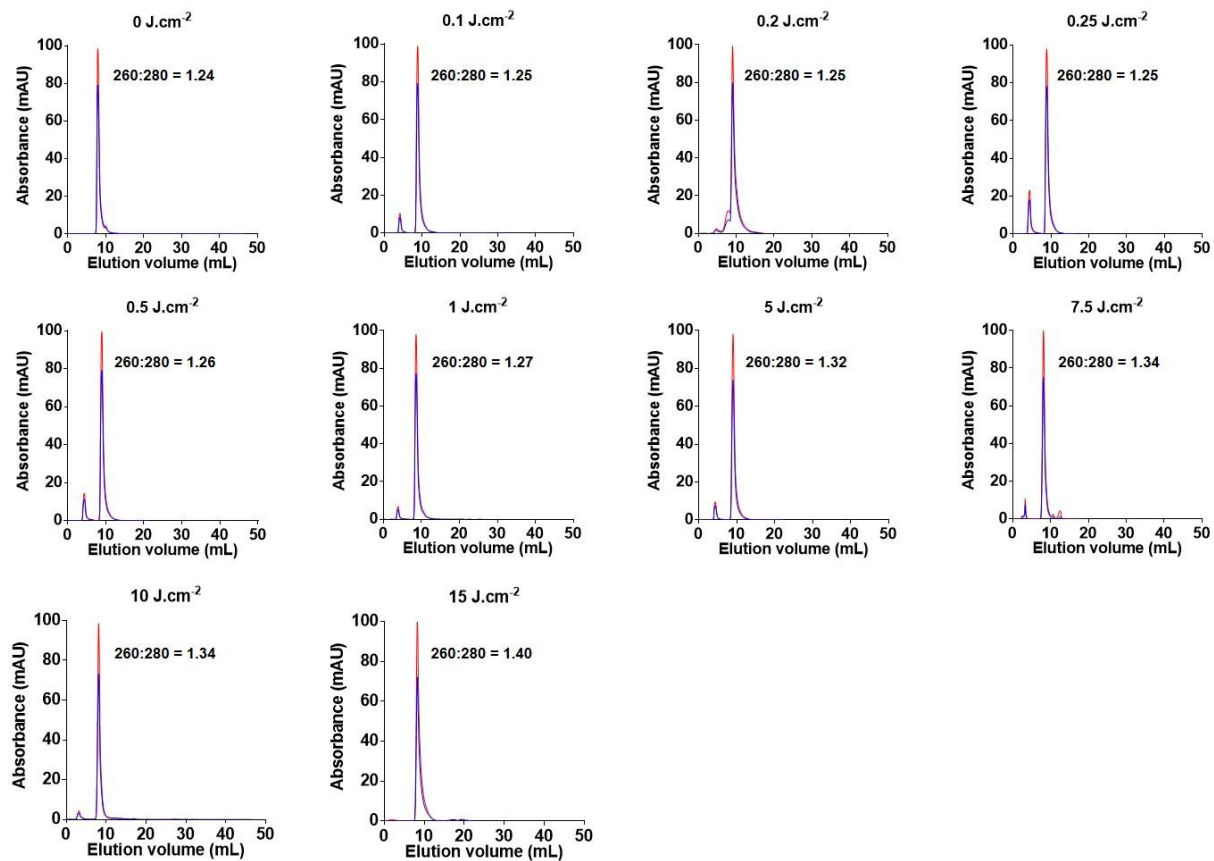


Supporting Figure 4.12. Q β transport through soil. (A) SDS-PAGE analysis of Q β elution fractions exiting the 4 cm-deep soil column. (B) The empirical output of Q β is used as a reference. (C) Computational modelling of Q β nanoparticle transport through 4 cm of soil. (D) Computational prediction of nanoparticle transport through soil columns of various length. D_{NP} and k_{NPS} were optimized from the empirical data obtained from the 4 cm soil column: $D_{NP_Q\beta} = 1.64 \text{ cm}^2 \text{ min}^{-1}$ and $k_{NP_Q\beta} = 2.54 \times 10^{-5} \text{ cm min}^{-1}$.

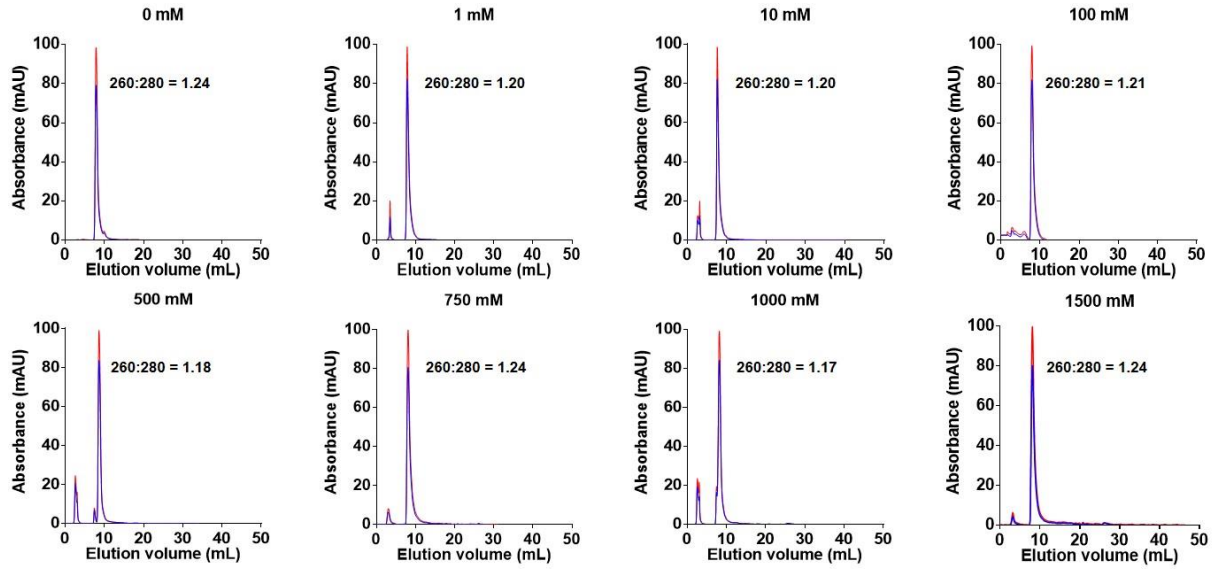


Supporting Figure. 4.13. Parameter correlation. A linear correlation between the surface area of TMGMV, CPMV, MSNP, and Q β with the constant of binding rate k_{NPS} was obtained. No linear correlation could be obtained for the dispersion constant D_{NP} .

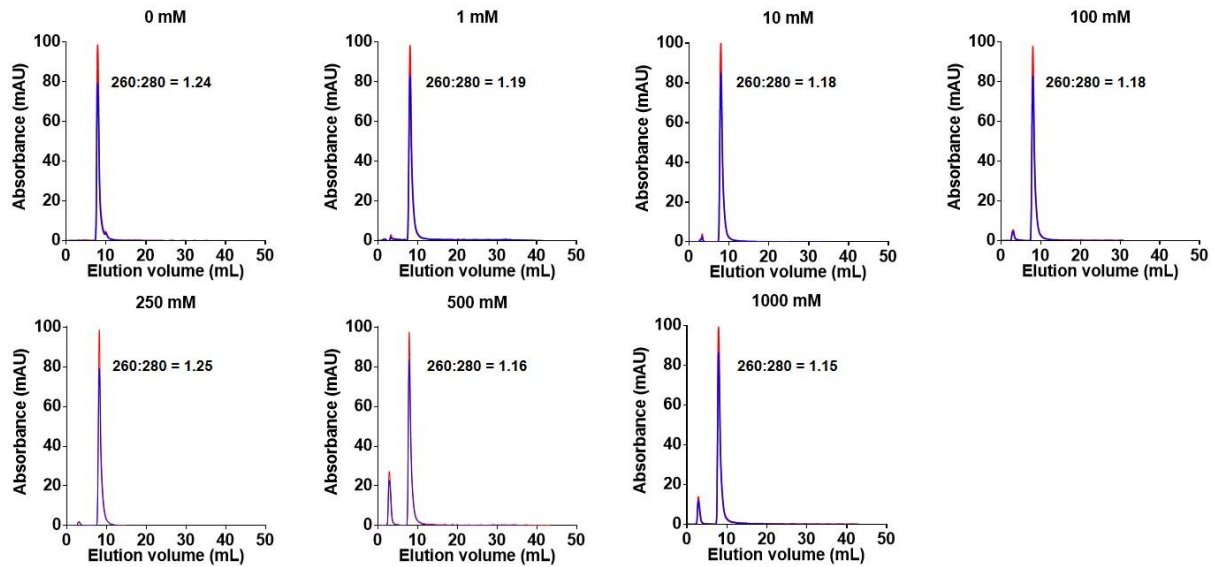
Appendix IV: Supplementary Information of Chapter V



Supporting Figure 5.1. Size exclusion chromatography of TMGMV after UV treatment. blue = 260 nm, red = 280 nm. The ratio of RNA:coat protein (260:280) is included in each panel.

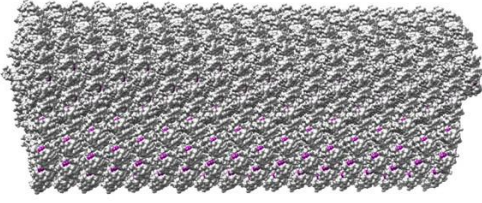


Supporting Figure 5.2. Size exclusion chromatography of β PL-TMG MV. blue = 260 nm, red = 280 nm. The ratio of RNA:coat protein (260:280) is included in each panel.

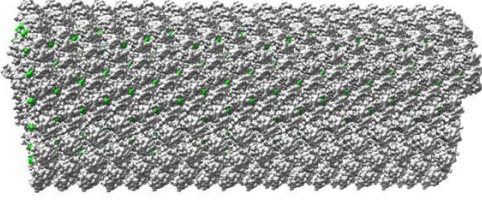


Supporting Figure 5.3. Size exclusion chromatography of form-TMG MV. blue = 260 nm, red = 280 nm. The ratio of RNA:coat protein (260:280) is included in each pa

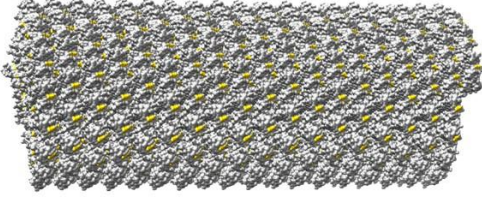
Methionine



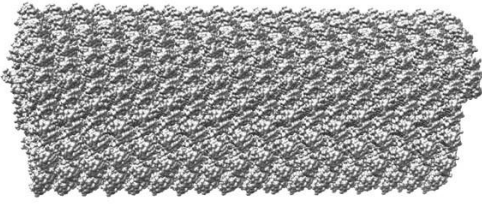
Lysine



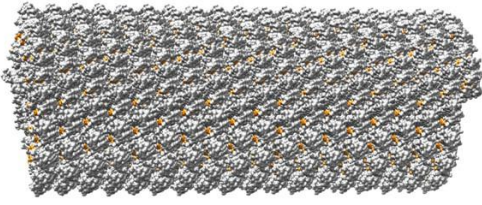
Glutamic acid



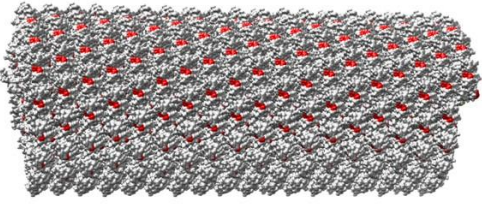
Cysteine



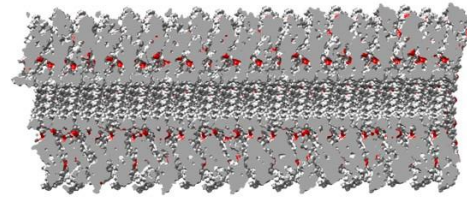
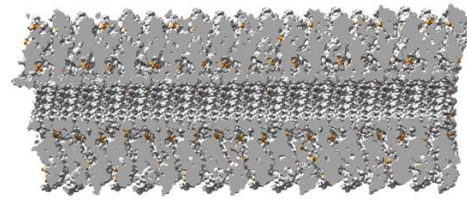
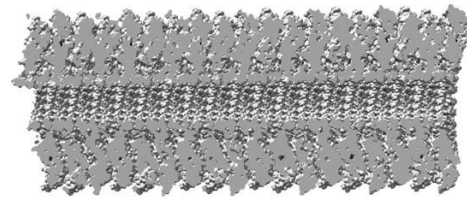
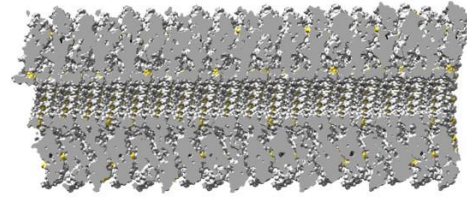
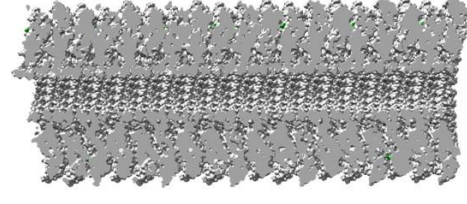
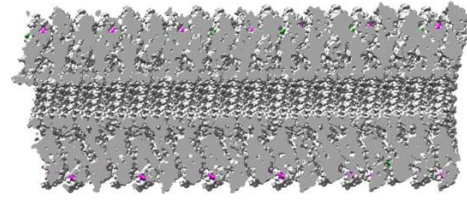
Aspartic acid



Arginine

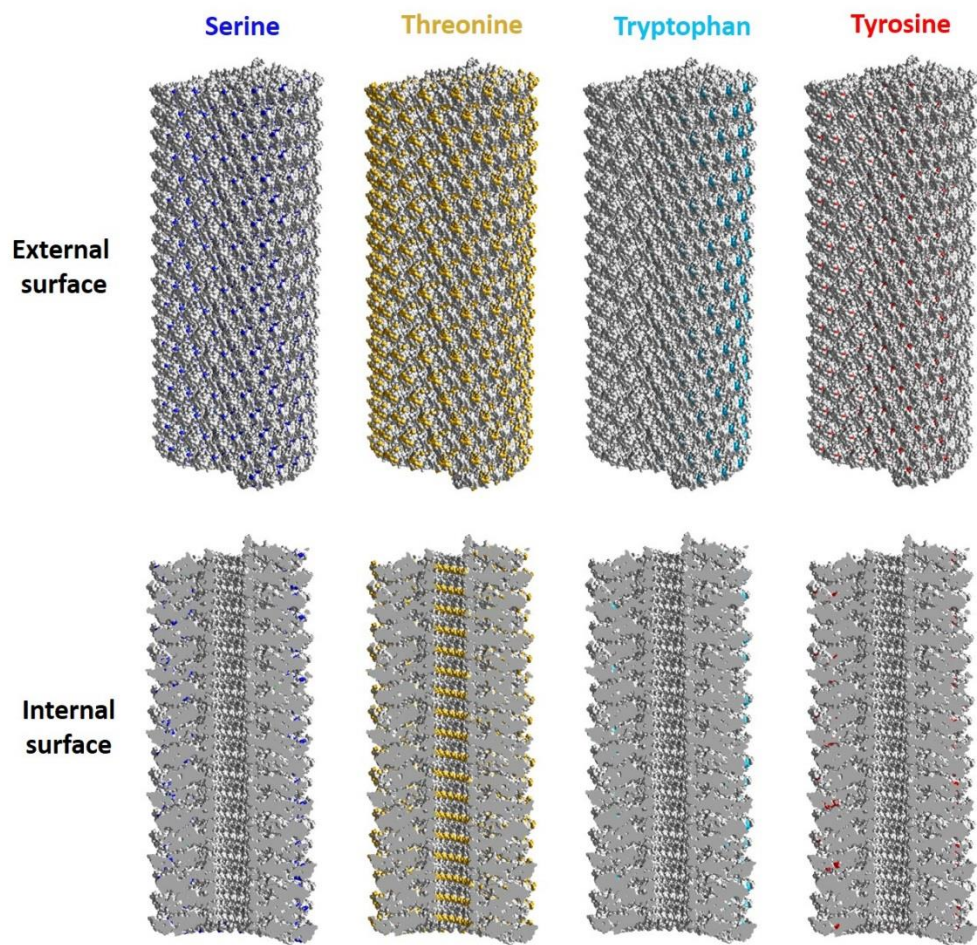


External surface

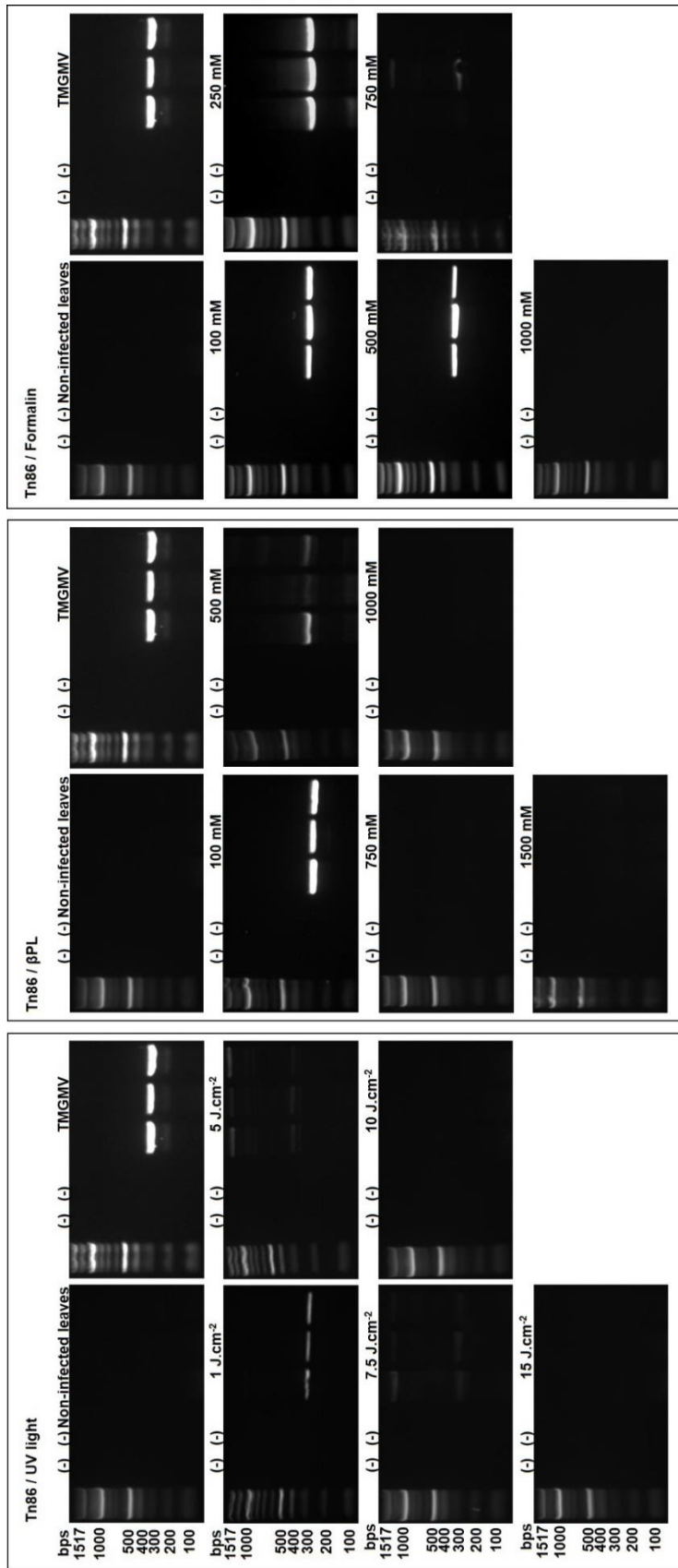


Internal surface

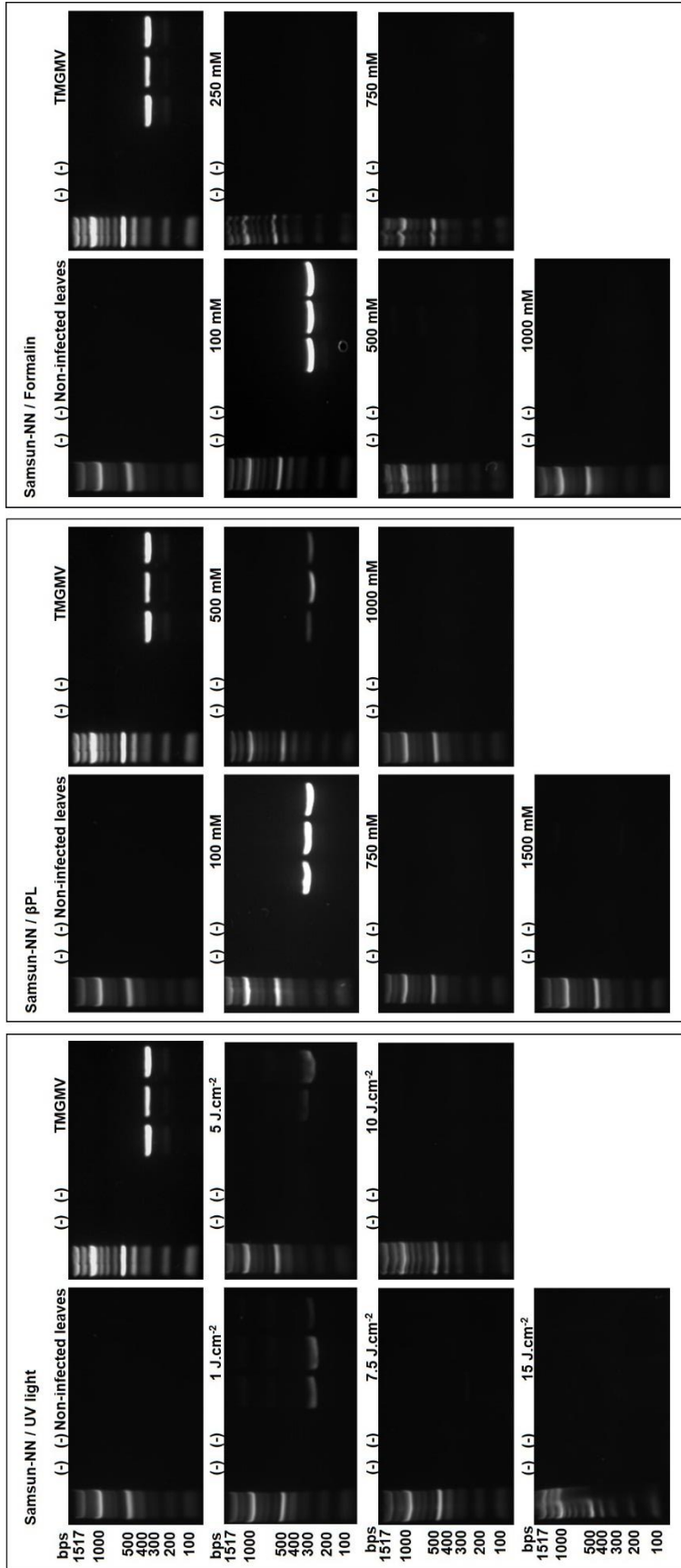
Supporting Figure 5.4. Surface exposition of various amino acids on the surface of TMGMV prone to β PPL and Formalin treatment.



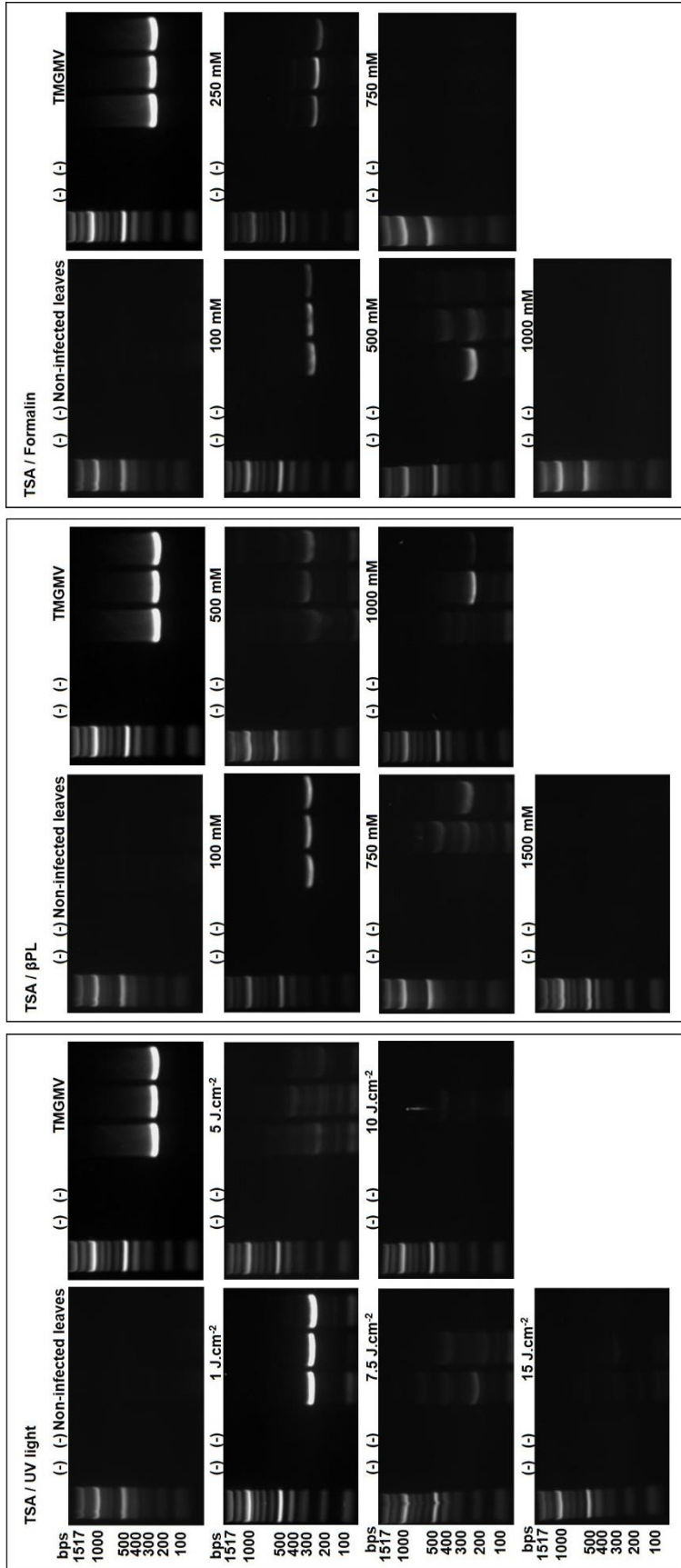
Supporting Figure 5.4 continues.



Supporting Figure 5.5. Agarose gels from the RT-PCR run on RNA extract from Tn86.



Supporting Figure 5.6. Agarose gels from the RT-PCR run on RNA extract from Samsun-NN.



Supporting Figure 5.7. Agarose gels from the RT-PCR run on RNA extract from TSA.

Appendix V: Supplementary Information of Chapter VI

Supporting Equations 6.1. Characteristic rates of diffusion and cellular uptake.

To determine the relationship between the cellular uptake rate (k) and the rate of TMV diffusion (D) in the spheroid, we expressed the dynamic mass concentration distribution of TMV within the spheroid in dimensionless form by defining the dimensionless variables:

$$\tau = kt; \quad \xi = \frac{r}{R}$$

where k is the constant rate of TMV cellular uptake, t is the time variable, r is the radial distance into the spheroid, and R is the radius of the spheroid. Subsequently, we obtained

$$\frac{\partial C_s}{\partial \tau} = \left(\frac{D}{kR^2} \right) \frac{1}{\xi^2} \frac{\partial}{\partial \xi} \left[\xi^2 \frac{\partial C_s}{\partial \xi} \right] - C_s \quad (\text{Sup. Eq 6.1})$$

where C_s is the concentration of TMV in the interstitial space at any location in the spheroid and D is the constant TMV diffusion coefficient. The values of the dimensionless parameter group (in parentheses) for various aspect ratios of TMV can be found in Table 6.1. In this table, R was maintained to $200 \mu m$ and the cell density was kept to 0.5. In our simulations, the rate of endocytosis is a thousand to a hundred times greater than the rate of TMV diffusion through the spheroid (see **Supporting Table 6.1**).

Supporting Table 6.1. Computation of the order of magnitude difference between the rate of endocytosis and the rate of diffusion of TMV.

TMV aspect ratio (L/d)	Dimensionless parameter $\frac{\alpha D \bar{c}}{kR^2 \theta}$
300/18	2.8×10^{-3}
135/18	6.4×10^{-3}
59/18	1.1×10^{-2}

In general, the rate of TMV mass loss from the surrounding medium equals the rate of diffusion into the spheroid:

$$V_M \frac{dC_M}{dt} = -4\pi R^2 D \left. \frac{dC_S}{dr} \right|_{r=R} \quad (\text{Sup. Eq 6.2})$$

where V_M is the constant volume of the surrounding medium, C_M is the concentration of TMV in the surrounding medium and N is the diffusion rate of TMV into the spheroid from the surrounding medium: $N = -4\pi R^2 D$

To determine if the TMV concentration in the surrounding medium changes significantly over the expected course of an experiment, I also expressed this equation in dimensionless form:

$$\frac{dC_M}{d\tau} = - \left(\frac{4\pi R D}{k V_M} \right) \left. \frac{dC_S}{d\xi} \right|_{\xi=R} \quad (\text{Sup. Eq 6.3})$$

In this case, the dimensionless parameter group (in parentheses) is approximately 10^{-6} (**Supporting Table 6.2**). Therefore, over the time course of our experiment, we can assume that the changes in concentration of TMV in the surrounding medium are negligible.

Supporting Table 6.2. Computation of the order of magnitude difference between the rate of TMV diffusion in the surrounding medium and the spheroid interspace.

TMV aspect ratio (L/d)	Dimensionless parameter $\frac{4\rho RD}{kV_M}$
300/18	6.98×10^{-7}
135/18	1.59×10^{-6}
59/18	2.76×10^{-6}

Supporting Equations 6.2. Model transformation. I transformed the governing equation of the spheroid into rectangular coordinates with constant coefficients by defining $g(r, t) = rC_s(r, t)$

$$\frac{\partial C_s}{\partial r} = \frac{1}{r} \frac{\partial}{\partial r} \left(\frac{g}{r} \right) = \frac{1}{r} \frac{\partial g}{\partial r} - \frac{g}{r^2} \Rightarrow r^2 \frac{\partial C_s}{\partial r} = r \frac{\partial g}{\partial r} - g \quad (\text{Sup .Eq. 6.4})$$

$$\frac{\partial}{\partial r} \left[r^2 \frac{\partial C_s}{\partial r} \right] = r \frac{\partial^2 g}{\partial r^2} + \frac{\partial g}{\partial r} - \frac{\partial g}{\partial r} = r \frac{\partial^2 g}{\partial r^2} \Rightarrow \frac{1}{r^2} \frac{\partial}{\partial r} \left[r^2 \frac{\partial C_s}{\partial r} \right] = \frac{1}{r} \frac{\partial^2 g}{\partial r^2} \quad (\text{Sup .Eq. 6.5})$$

$$\frac{\partial C_s}{\partial t} = \frac{1}{r} \frac{\partial g}{\partial t} \quad (\text{Sup .Eq. 6.6})$$

$$\frac{\partial C_s}{\partial t} = D \frac{1}{r^2} \frac{\partial}{\partial r} \left[r^2 \frac{\partial C_s}{\partial r} \right] - kC_s \Rightarrow \frac{\partial g}{\partial t} = D \frac{\partial^2 g}{\partial r^2} - kg \quad (\text{Sup .Eq. 6.4 = 7})$$

Supporting Equations 6.3. Method of lines. I defined a discrete spatial domain $i = 0, 1, 2, 3, \dots, N$ corresponding to the continuous spatial domain $0 \leq r \leq R$, where N is the number of spatial intervals of size $\Delta = R/N$. The relationship between the continuous and discrete spatial variable is given as $r_i = i\Delta$ and $g_i(t) = g(r_i, t)$. Thus, the discretized equations become

$$\frac{dg_i}{dt} = D \left[\frac{g_{i+1} - 2g_i + g_{i-1}}{\Delta^2} \right] - kg_i \quad (i = 1, 2, 3, \dots, N-1) \quad (\text{Sup. Eq 6.8})$$

The boundary condition at the center of the spheroid becomes

$$i = 0 : g_0 = 0 \quad (\text{Sup. Eq 6.9})$$

which can be incorporated into the governing equation for $i=1$:

$$\frac{dg_1}{dt} = D \left[\frac{g_2 - 2g_1}{\Delta^2} \right] - kg_1 \quad (\text{Sup. Eq 6.10})$$

The boundary conditions at the interface become

$$i = N : g_N = RC_M \quad (\text{Sup. Eq 6.11})$$

which can be incorporated into the governing equation for $i = N-1$:

$$\frac{dg_{N-1}}{dt} = D \left[\frac{RC_M - 2g_{N-1} + g_{N-2}}{\Delta^2} \right] - kg_{N-1} \quad (\text{Sup. Eq 6.12})$$

The initial conditions become

$$t = 0 : g_i = 0 \quad (i = 1, 2, 3, \dots, N) \quad (\text{Sup. Eq 6.13})$$

Conversion to original variables

$$C_s(r_i, t) = \frac{g_i(t)}{r_i} = \frac{g_i(t)}{i\Delta} \quad (i = 1, 2, 3, \dots, N); \quad C_M = \frac{g_N}{R} \quad (\text{Sup. Eq 6.14})$$

From the boundary condition, we see that

$$r = 0 : \frac{\partial C_s}{\partial r} = 0 \Rightarrow C_s(r_0, t) = C_s(r_1, t) = \frac{g_1(t)}{r_1} = \frac{g_1(t)}{\Delta} \quad (\text{Sup. Eq 6.15})$$

Supporting Equations 6.4. Characteristic axial and transverse velocity of TMV.

The equations of the axial (v_t) and transverse (v_r) velocity of TMV, which were obtained from a study by Broersma,³⁰⁵ are displayed below. I computed the value of the axial and transverse velocity for specific TMV aspect ratios (L/d) (see **Supporting Table 6.3**).

$$v_t = -.114 - \frac{.15}{\ln\left(2\frac{L}{d}\right)} - \frac{13.5}{\ln^2\left(2\frac{L}{d}\right)} + \frac{37}{\ln^3\left(2\frac{L}{d}\right)} - \frac{22}{\ln^4\left(2\frac{L}{d}\right)} \quad (\text{Sup. Eq. 6.16})$$

$$v_r = -.886 - \frac{.15}{\ln\left(2\frac{L}{d}\right)} - \frac{8.1}{\ln^2\left(2\frac{L}{d}\right)} + \frac{18}{\ln^3\left(2\frac{L}{d}\right)} - \frac{9}{\ln^4\left(2\frac{L}{d}\right)} \quad (\text{Sup. Eq. 6.17})$$

Supporting Table 6.3. Computation of the axial and transverse velocity of specified TMV dimensions.

	(300/18)	(135/18)	(59/18)
Axial velocity of TMV (v_t)	0.5421	0.5562	0.2065
Transverse velocity of TMV (v_r)	0.5224	0.4451	0.4828

Supporting Equations 6.5. Diffusion coefficients in the surrounding medium and in the spheroid.

The values of the diffusion coefficient of TMV in the surrounding medium (D_{rt}) were computed from equation (12) for specific aspect ratios of TMV. The corresponding values of the diffusion coefficient of TMV in the spheroid (D_{int}), which takes into account the presence of ECM proteins, are also calculated from equation (13) (**Supporting Table 6.4**).

Supporting Table 6.4. Diffusion coefficients of TMV in the surrounding medium (D_{rt}), and in the presence of ECM proteins (D_{int}).

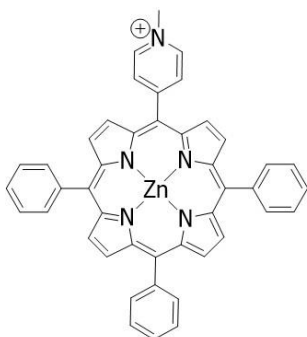
TMV aspect ratio (L/d)	Diffusion coefficient of TMV in the surrounding medium (D_{rt}) [mm ² .sec ⁻¹]	Diffusion coefficient of TMV in the spheroid (D_{int}) [mm ² .sec ⁻¹]
300/18	5.07x10 ⁻⁶	2.15x10 ⁻⁶
135/18	8.47x10 ⁻⁶	3.59x10 ⁻⁶
59/18	1.18x10 ⁻⁵	5.01x10 ⁻⁶

The final diffusion coefficients of TMV (D) were obtained from equation (14) and take into account the shape and the dimensions of the nanoparticle, the presence of ECM proteins, and the presence of cells in the spheroid (see **Supporting Table 6.5**).

Supporting Table 6.5. Diffusion coefficient of TMV in the porous spheroid containing cells.

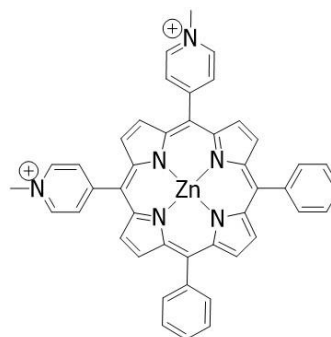
Cell density	D [mm².sec⁻¹] (300/18)	D [mm².sec⁻¹] (125/18)	D [mm².sec⁻¹] (59/18)
0.4	7.74x10 ⁻⁷	1.29x10 ⁻⁶	1.80x10 ⁻⁶
0.5	5.38x10 ⁻⁷	8.98x10 ⁻⁷	1.25x10 ⁻⁶
0.6	3.44x10 ⁻⁷	5.75x10 ⁻⁷	8.01x10 ⁻⁷
0.7	1.94x10 ⁻⁷	3.23x10 ⁻⁷	4.51x10 ⁻⁷
0.8	8.60x10 ⁻⁸	1.44x10 ⁻⁷	2.00x10 ⁻⁷
0.9	2.15x10 ⁻⁸	3.59x10 ⁻⁸	5.00x10 ⁻⁸

Appendix VI: Supplementary Information of Chapter VII.



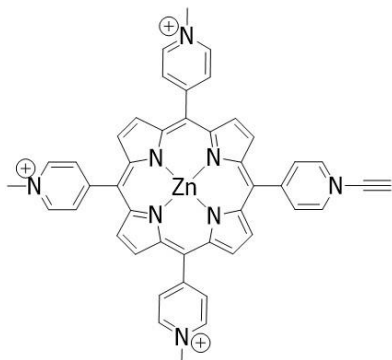
Monocationic

5,10,15-Triphenyl-20-(1-methylpyridinium-4-yl)porphyrin iodide



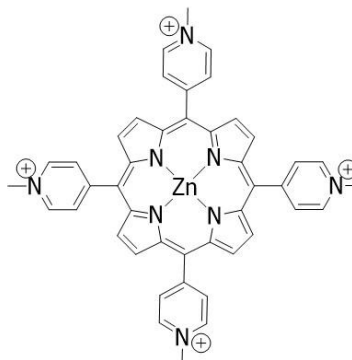
Dicationic

5,10-Bis(1-methylpyridinium-4-yl)-15,20-diphenylporphyrin diiodide



Tricationic

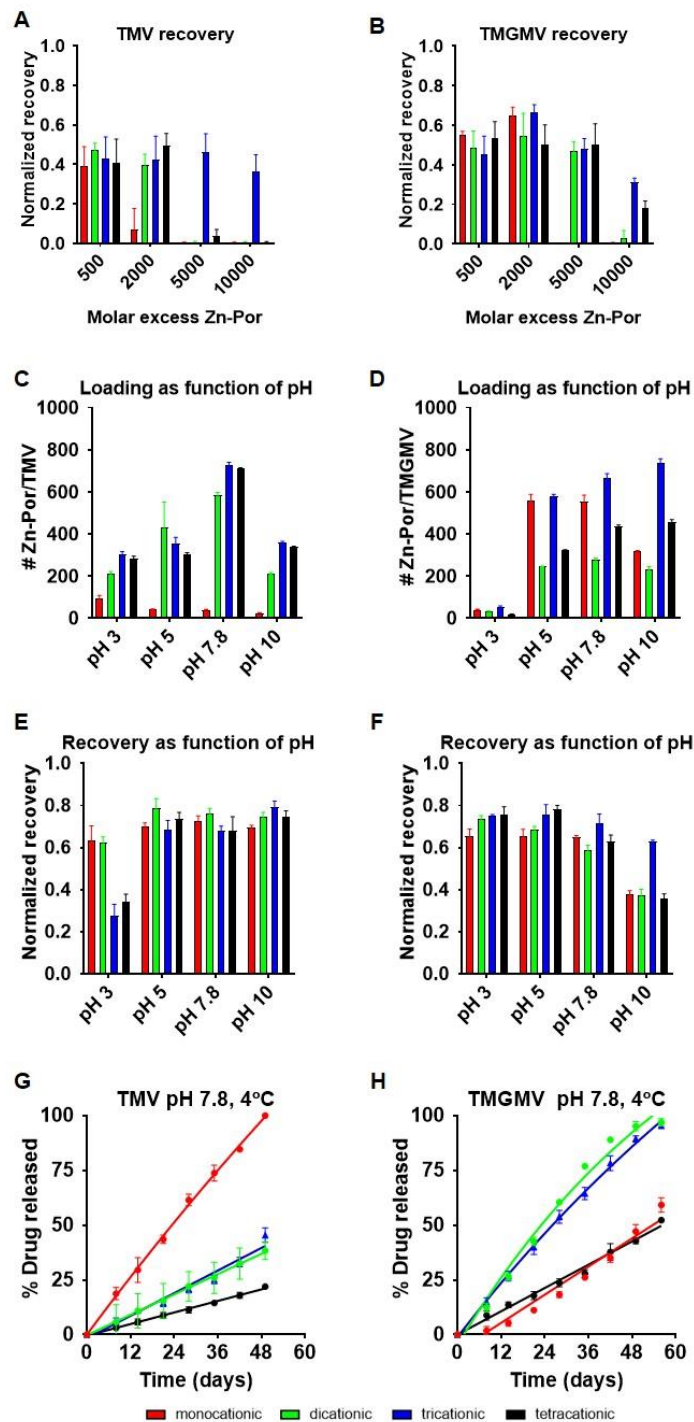
5-(4-ethynylphenyl)-10,15,20-tris(4-methylpyridinium-4-yl)porphyrin-zinc(II) triiodide



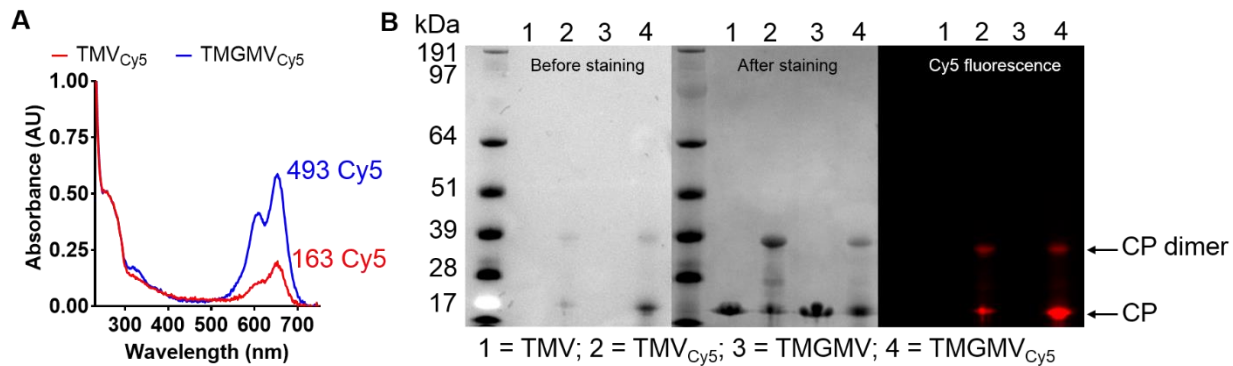
**Tetracationic
Zn-TMPyP**

5,10,15,20-Tetrakis(1-methylpyridinium-4-yl)porphyrin tetraiodide

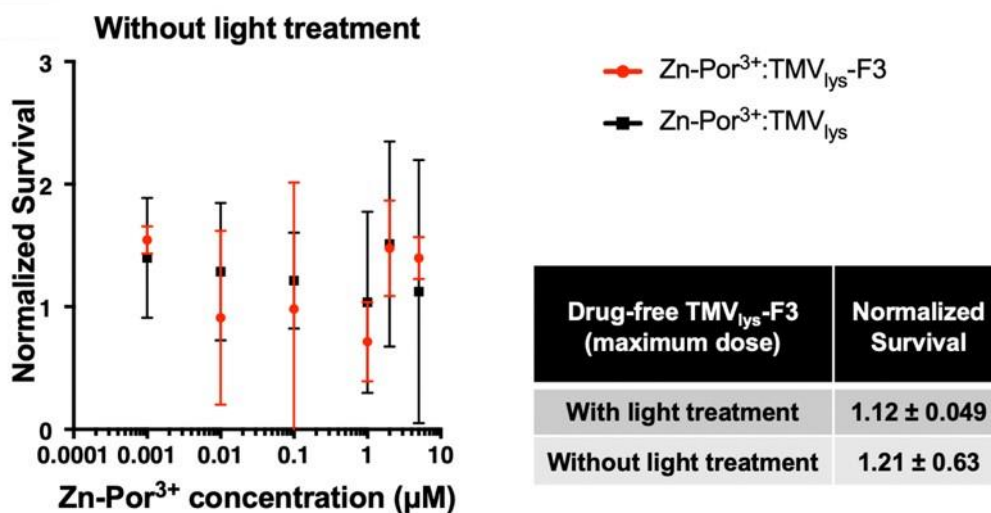
Supporting Figure 7.1. Chemical structure of the monocationic, dicationic, tricationic and tetracationic Zn-Porphyrin molecules.



Supporting Figure 7.2. Evaluation of Zn-Por loading and release from TMV and TMGMV. (A) TMV and (B) TMGMV recovery (1 = 100% recovery) as a function of the starting Zn-Por:VNP molar excess. (C) Average number of each Zn-Por per TMV and (D) TMGMV as a function of the buffer pH. The corresponding normalized recovery (normalized to 1 mg of starting viral material) of TMV and TMGMV are depicted in (E) and (F) respectively. (G) Zn-Por release from TMV and (H) TMGMV under storing conditions (10 mM KP, pH 7.8 at 4°C) over a period of 6 weeks.



Supporting Figure 7.3. Characterization of fluorescently labeled TMV and TMGMV. (A) UV/visible spectra of TMV (red) and TMGMV (blue) modified with Cyanine5 (Cy5). The number of Cy5 conjugated to each VNP was calculated using the Beer-Lambert law and the known extinction coefficient of Cy5, TMV, and TMGMV. (B) Particles after electrophoretic separation on 4-12% SDS-NuPage gel visualized with white light before and after Coomassie staining, and under red fluorescent light; arrows indicate the coat protein (CP) and its dimer.



Supporting Figure 7.4. MTT viability assay of HeLa cells treated with TMV_{lys}-F3 particles. HeLa cell viability was examined after 8-hr incubation with increasing doses of Zn-Por and Zn-Por loaded TMV with and without F3 ligand. Without light treatment, cell growth was observed when treated drug-loaded particles. No cell killing was observed with drug-free TMV_{lys}-F3 particles at maximum dose administered.

Appendix VII: Supplementary Information of Chapter VIII.

Supporting Figure 8.1. Nucleotide sequence of the RNA-1 and RNA-2. Highlighting in green the potential site of uracil dimerization.

RNA-1 (5.89 kbp)

```

1 uaUUaaaaauc aaucacaggUU UUgauaaaaag cgaacgugga gaaauccaaa ccUUUcUUUc
61 UUUccucaau cucUUcaaUU gCGaacgaaa uccaagcUUU ggUUUUgcug aaacaaauac
121 acaacguaua cugaaUUUgg caaaUUUcuc ucucucucuc ugUCAUUUUc UUUcUUcugu
181 cgggacUUUc UUagucUUga cccaacaugg gucuccaga auaugaggcc gauagugagg
241 cUUUaUUaag ucaacucacu aucgaaUUca caccggcau gacagUUUcU UcaUUgUUgg
301 cacaagucac cacuaaugac UUUcacagug ccaUUgagUU UUUUgcugca gaaaaagcag
361 uagacaUUga gggcgUUcaU Uacaauugcu auaugcaaca aaUUaggaaa aaccuagUU
421 UaUUacgcAU UUccguggua gcUUaugcUU UccacgUUUc agacauggua gcugagacca
481 ugucUUauga ugUUUaugaa UUUcuguaua aacaUUaugc ccUUUUcauc ucuaaucugg
541 ugaccagaac acucagaUUU aaagagcUUU UgcugUUcug uaagcagcaa UUUcuggaga
601 aaaugcaagc UUcaauaguc ugggcuccgg aacUUgagca auaucUUcaa gUUgaagggg
661 augcuguggc ucaaggagUU UcacaacugU Uauacaagau ggucacUUgg gugccacUU
721 UUgucagagg agcaguagac uggagcgUUg augcgaUUUU ggucagUUUc aggaaacaUU
781 UUgaaaagau ggUUcaggag uaugugcca uggcucaucg cgUUUgcagU Uggcugagcc
841 aacuauggga uaagaucgug caauggaucu cacaagcaag ugagaccaug ggUUggUUUc
901 uagauggUUg ucgggaUUUg augacUUggg gaaUUgccac ucucgcaaca uguagugcuc
961 ucucccuggU Ugagaagcug UUagucgcaa ugggUUUUcu ggUUgagccU UUcggcUUga
1021 guggaaucUU cUUgCGgacg ggagUUgUUg cggcagcUUg UUauaacuau gggacuaaUU
1081 cuaagggUUU Ugccgagaug auggcUUUgU UgucaUUggc ggCUaacugu gucucuacag
1141 UUauagUUgg uggcUUUUuc ccuggugaaa aggacaaugc acagaguagu ccugUUaucc
1201 ucUUagaagg aUUggcuggg cagaugcaaa acUUUUguga gacuacacUU gucagugUUg
1261 ggaaaacaug cacugccguc aaugcuauU caacaugUUg ugggaucug aaagcacugg
1321 ccggaaggau cUUgggcaug cucagagaUU UUaucuggaa gacUUUggg UUgagacca
1381 gaUUUcuag agaugcaucU UUgcUUUUug gcgaggauU Ugauggagg cucaaagcaa
1441 ucagugaucu gcgagaucaa UUUaUUgcca aaucuaucug UUcgaggau gagaugc
1501 agaUUUUggu gUUgcUUgaa aagggaaggc agaugcggaa aaguggucUU Ucuaaaggag
1561 gcaUUUcucc ugcuaucaUU aaucugaUUc ucaaagggaU UaaugaucUU gaacaaUUga
1621 accgcagcug UUcagugcaa ggaguaagag gagUUaggaa aaugccaUUU accaUUUUcU
1681 Uccaaggaaa gucacgcacu gguaagagUU Ugcugaugag ucaggUUaca aaggaUUUUc
1741 aggaucacua uggaUUgggu ggagaaacug uguacaguag aaauccUUgu gaucaauaUU
1801 ggaguggaua ucggcggcaa ccUUUUgugc ugauggauga UUUUgcccgc gUUgUUacug
1861 agccgucugc ugaggcucag augaucaauc ugaUUUcuag ugcuccauau ccUUUgaaua
1921 uggcuggacU Ugaagaaaaa ggaaUUUgUU UUgaUUcuca aUUUgUUUUU gUUUccacca
1981 acUUcUUgga aguaucuccu gaagccaaag UUagggacga ugaggcUUUc aagaacagga
2041 gacaugugaU UgUUcaggUU Ucaaaugauc cugccaaagc auaugaugcu gcaaaUUUUg
2101 cuagcaacca aaUUUacacc aUUUUggcau ggaaggauGg ucgauacaac accgugugcg
2161 UUaUUgagga cuaugaugag cugguggcau aUUUgUUgac uaggagucaa cagcaugcug
2221 aagagcagga gaagaauUcU gcuaacauga ugaagagugc uacaUUUgaa agucaUUUca
2281 aaagUUUagU UgaaguccUU gagcucggUU cuaugauauc ugcuggUUUU gauaucaUUc
2341 ggccagaaaa acUUccuagu gaagcuaagg agaagagagu ccUUUacagu aUUccuaca
2401 auggggagaa UUguaaugca cucaUUgaurg acaaUUaca ugUUacUUc UUggggug
2461 agugugUUgg uaauccugag cagcucuaa aguacaguga aaagaugcUU UUgggugcUU
2521 augaaUUUcU UcugugUUcu gagagcUUga augUUgaaU UcaggcacaU UUgaaggaaa
2581 uggUUUgccc ucaccaUUau gacaaggagc ucaaUUUUaU Uggcaagaua ggagagaccu
2641 acuaucacaa ucagauggUU Ucaaaauaug gcucuaugca gaaauggcau cgugccaUUc
2701 ugUUUggaaU UggggUUcuc UUgggaaagg aaaaagagaa gacaugguac caagUUcagg
2761 UUgccaauG Uaaacaagcu cUUUacgaca uguacacuaa ggagaUUcgu gaUUggccca
2821 ugccgaucAA agucaccugu ggaaUUgucU UggcagcuaU Uggggguagu gccUUUUgga
2881 aagugUUUca acaacuagug ggaagcggaa auggucagU aUUgaugggu guggcugcug

```

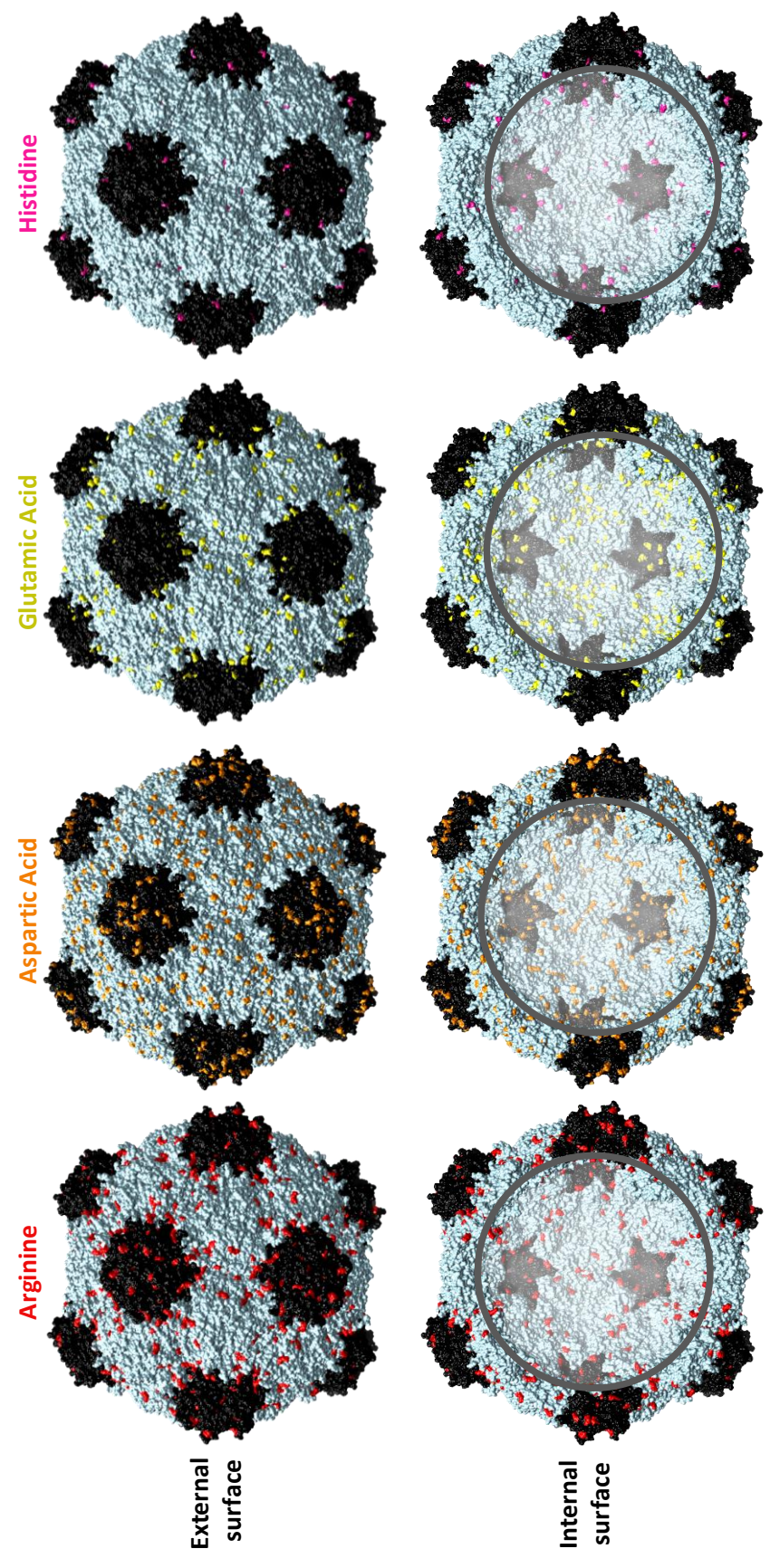
2941 gagcaUUcag ugcugagccu caaaguagaa agcccaauag gUUUgauaug cagcaauaca
3001 gguacaacaa ugUUccucuc aagagaagag UUUgggcaga cgcacaaaug ucUUUggauc
3061 agaguagugU Ugcuaucag ucuaagugua gggcuaaucu ggUUUUugga ggcacuaaUU
3121 Ugcaaaauagu caugguacca ggaagacgcu UUUUUggcaug caaacaUUUc UUcaccacaca
3181 uaaagaccaa aUUgcgugug gaaauagUUa uggauuggaag aagguacuau caucuaUUUg
3241 auccugcaaa uaUUUaugau auaccugaUU cugagUUggu cUUguacucc cauccuagcU
3301 UggaaagacgU UUcccaUUcu ugcugggauc ugUUcugUUg ggaccagac aaagaaUUgc
3361 cUUcaguaUU UggagcggaU UUcUUgagUU guaaaucaca caagUUUggg ggUUUUuaug
3421 aggcgcaaua ugcugauauc aaagugcgca caaagaaaga augccUUacc auacagagug
3481 guaaUUaugu gaacaaggug ucucgcuauc UUGaguauga agcuccuacu aucccugagg
3541 aUUguggauc ucUUgugaua gcacacaUUg gugggaagca caagaUUgug ggugUUcaug
3601 UUGcugguaU Ucaagguaag auaggaugug cUUccUUaUU gccaccaUUg gagccaauag
3661 cacaaagcga aggugcugag gaaucUUUg aUUUUcUUcc agcugaagag auagaaUUcUU
3721 cuggaguggc uaugguagca ggacucaaac aaggagUUUa cauaccaUUa cccacaaaa
3781 cagcgcuagu ggagaccccc uccgaguggc aUUUggacac accaugugac aaagUUccua
3841 gcaUUUUagU Ucccacggau ccccgaUUc cugcgcaaca ugaaggauau gauccugcua
3901 agaguggggU UUccaaguaU Ucccagccua ugucugcucu ggaccugag UUacUUggcg
3961 agguggcuaa ugaugUUcuc gagcuauggc augacugcgc uguagaUUgg gacgaUUUUg
4021 gugaaguguc ucuggaggaa gcUUUgaaug gaugugaagg aguggaaauau auggaaagga
4081 UUccaUUagc aacUUcugag ggcUUUccgc acaUUcUUUc uagaaauggg aaagaaaagg
4141 ggaaaagacg gUUUgUUcag ggagaugaUU gugUUgucuc acuaaUUcca ggaacuacug
4201 uagccaaagc UUAaugaggag UUGgaagcaa gugcacacag aUUUgUUccc gcucUUgUUg
4261 ggaUUgaau uccaaaagau gagaagUUgc cuaugagaaa ggUUUUugau aagccuaaga
4321 ccaggugUUU UaccaUUUUg ccaauggaau auaaUUUggu cgUUcguagg aagUUUcuga
4381 aUUUUgugcg cUUUaucaug gccaaucguc acagacucag UUgucaagug gguaUUaauc
4441 cauaUUcaau ggaauggagu cgcUUagcag caaggaugaa agagaaaggc aaugaugucU
4501 UgugUUguga UUauagcuca UUcgauggcU UgcUUUcuaa gcaagugaug gaugucaUUg
4561 cuagcaugau caaugaacUU Ugugguggag aggaucaacu caaaaugca aggcgaaacU
4621 UgUUaauggc gugUUgcucu aggUUggcua UUUgcaagaa uacaguaugg agagUUgagu
4681 guggaUUcc UUcagggUUU ccaaugacag ugaUUgugaa uagcaUUUUUc aaugagaUUc
4741 ucaUUcgcuca ucaUUacaag aaacucaug cgaacaaca agcuccugaa cugaugguac
4801 agagUUUUga uaaacucaua gggcugguga cUUaugguga ugauaaucug aUUUcaguga
4861 augcugUUgu gacaccuaU UUUgauggga agaaaUUgaa gcaaucUUUg gcucagggug
4921 gugugacuau cacugauggu aaggacaaaa caagUUUgga acUUccUUUU cgcagaUUgg
4981 aagaauguga UUUUcuaag agaacUUUUg UUcagaggag caguaccauc ugggacgcuc
5041 cagaggauaa ggcaagUUUg uggucgcagc UUcaUUaugU UaaUUgcaac aaUUgugaga
5101 aagaagUUgc UUAUUUgacu aaugUUgUUa augUUcUUcg ugaacUUUau augcauaguc
5161 cucgggaagc cacagaaUUU agggaggaagg ucUUaaagaa ggucagUUgg aucacuagug
5221 gagaUUUgcc uacUUUggca caaUUgcaag agUUcuauga guaccagcgg cagcaaggug
5281 gggcagacaa caaugacacU UgugacUUgU Uaacaagugu agacUUgcua gguccuccUU
5341 UgucUUUUga gaaagaagcg augcacggau gcaauguguc ugaagaauc gucaccaaga
5401 aUUUggcaua UUacgaUUUc aaaaggaaag gugaggauga agugguaUUUcugUUcaaua
5461 cgcucuaucc ucagagUUca UUgccugaug ggugucacuc ugugaccugg ucucagggua
5521 guggaagggg aggUUUgcc acacaaagUU ggauagcua uaaauaaagc aggaaagaUU
5581 cuaauauctaa caagaUUaUU agaacugcug UUUcUUcgaa gaaacgagug auaUUcugug
5641 cucgugauaa uauggUUccu gUUaacaUUg uagcUUUgcu cugugcugUU agaaacaagc
5701 ugaugcccac ugcuguaucu aaugcuacac UUGucaaggu gauggaaaau gccaaagcUU
5761 ucaagUUUUU accagaagag UUcaaUUUcg cUUUUucuga ugUUUaggua aaauaugcUU
5821 augUUUUUgU UUgcuccugU UUagcagguc gUUccUUcag caagaacaac aaaaaaugu
5881 gUUUUuaUU

RNA-2 (3.48 kbp)

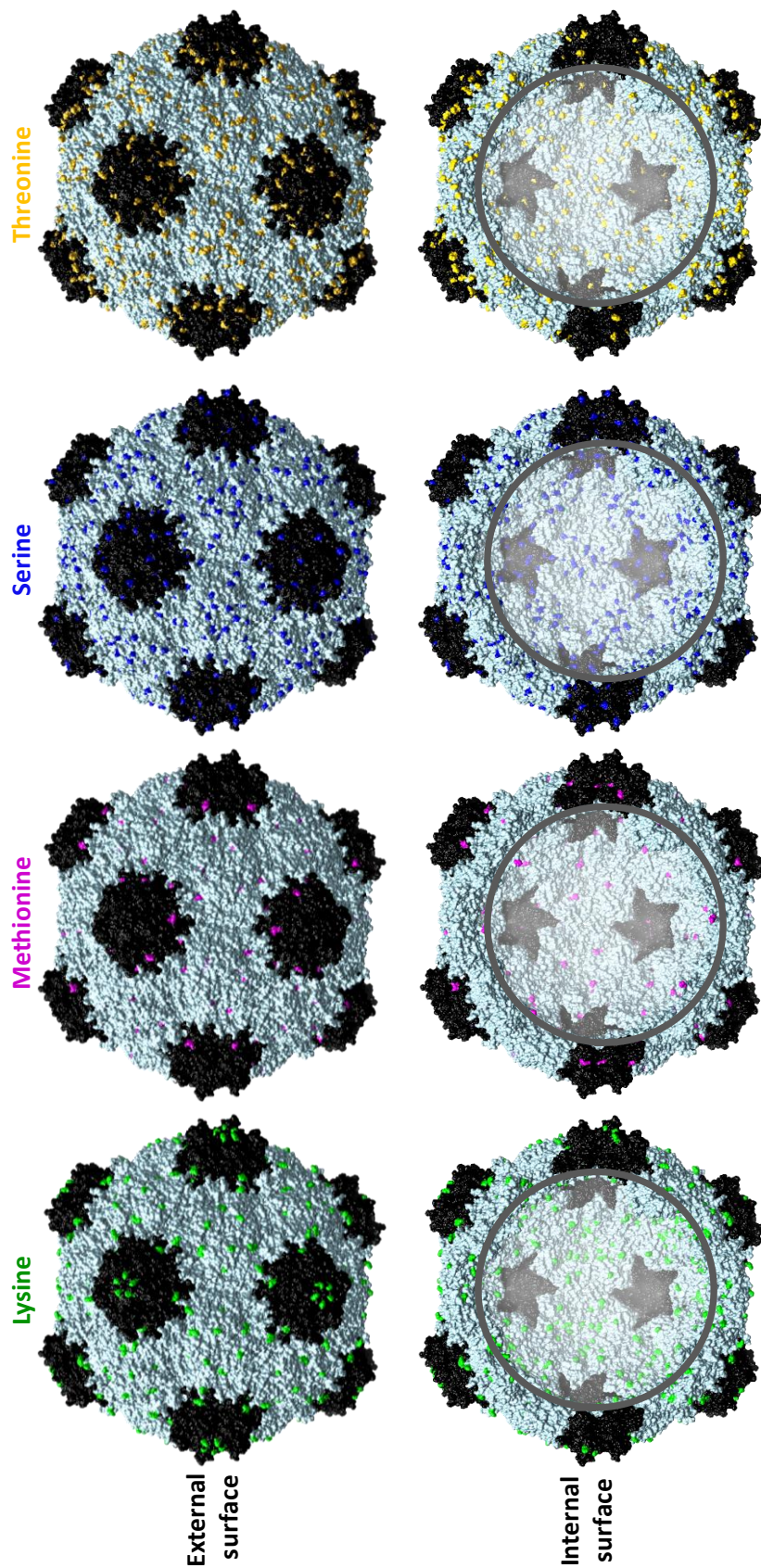
1 uaUUaaaauc UUaaauaggUU UUgauaaaaag cgaacguggg gaaacccgaa ccaaaccUUc
61 UUcuaaaaUUc ucucucucaucu cucUUaaagc aaacUUcucu cUUgucUUUc UUgcaugagc
121 gaucUUcaac gUUgucagau cgugcUUcgg caccaguaca augUUUUcUU ucacugaagc
181 gaaaucaaaag aucucUUUgu ggacacguag ugcggcgcca UUaaauaacg uguacUUguc
241 cuaUUcUUgu cggugugguc UUgggaaaag aaagcUUgcu ggaggcugcu gUUcagcccc
301 auacaUUacU UgUUacgaUU cugcugacUU Ucgggcgug gcauaucucu acUUcugcUU
361 gacgagguaU UgUUgcccugu acUUcUUUUc UUcUUcUUcUU gcugaUUggU Ucuauaagaa
421 aucuaguaUU UUcUUUgaaa cagagUUUUc ccguggUUUU cgaacUUgga gaaagaUUgu
481 uaagcUUcug uauaUUcugc ccaaaUUUga aauggaaagc aUUaugagcc gugguaUUcc
541 UUcaggaaUU UUggaggaaa aagcuaUUca gUUcaaacgu gccaaagaag ggaauaaacc
601 cUUgaaggau gagaUUccca agccugagga uauguaugug ucucacacUU cuaaauggaa
661 ugugcucaga aaaaugagcc aaaagacugu ggauUUUUc aaagcagcug cugggauggg
721 aUUcaucaau aagcauagc UUacgggcaa caucUUggca caaccaaca cagucUUgga
781 uaUUcccgc acaaaggau aaacacUUgc gauggccagu gaUUUUaUUc gUUgcaUUc
841 ccuaagacU UcugccaUUc acaUUggagc aaUUgagaUU aUUauccaga gcUUUgcUUc
901 cccugaagu gaUUUgugg gaggcUUUUU gcUUguggaU UUcUUacaca cugauacagc
961 uaaugcuaUU cguagcaUUU UUgUUgcucc aaugcgggga ggaagaccag ucagaguggu
1021 gaccUUccca aaucacugc caccuguauc augugaucug aacaauagaU Ucaagcucau
1081 UUgcucaUUg ccaaacugug auaUUgucca gguagccaa guagcagaag ugaguguaaa
1141 ugUUgcagga ugugcuacUU ccuagagaa aucucacacc ccUUcccaU Uguauacaga
1201 ggaaUUUgaa aaggagggug cugUUgUUgu agaauacUUa ggcagacaga ccuaUUgugc
1261 ucagccuagc aaUUUaccca cagaagaaa acUUcggucc cUUaagUUUg acUUUcaugU
1321 Ugaacaacca aguguccuga agUUauccaa UUccugcaau ggcacUUUg ucaagggaga
1381 aagUUUgaaa uacucuaUUU cuggcaaaga agcagaaaac caugcagUUc augcuacugu
1441 ggucucucga gaaggggcUU cugcggcacc caagcaauau gauccuaUUU ugggacgggu
1501 gcuggaucca cgaaauggga auguggcUUU Uccacaaug gagcaaacU UgUUUgcccU
1561 UUcUUUggau gauacaagcu cagUUcgugg UUcUUUgcUU gacacaaaaU Ucgcaaaaac
1621 ucgagUUUUg UUgucceaag cuauggcugg uggugaugug UUaUUggaug aguaucucua
1681 ugaugugguc aauggacaag aUUUUagagc uacugucgcU UUUUugcgca ccaugUUau
1741 aacaggcaaa auaaagguga cagcuaccac caacaUUUcu gacaacucgg gUUgUUgUUU
1801 gaugUUggcc auaaaugug gugugagggg uaaguauagu acugaugUUU auacuacug
1861 cucucaagc uccaugacgu ggaaccagc gugcaaaaag aacUUcucgu ucacaUUUaa
1921 uccaaaccU UguggggaUU cUUggucgc ugagaugua agucgaagca gagUUaggau
1981 gcagUUaUU ugugUUUcgg gauggaccUU aucuccuacc acagauguga UUgccaagcu
2041 agacugguca aUUgucaaug agaaauguga gccaccaUU UaccacUUgg cugaUUguca
2101 gaaUUggUUa ccccUUaauc gUUggauggg aaaaUUgacU UUUccccagg gugugacaag
2161 ugaggUUcga aggaugccuc UUUCuauagg aggcggugcu ggugcgacuc aagcUUUcUU
2221 ggccaauaug cccaaUUcau ggauaucaau guggagauaU UUUagaggug aacUUcacUU
2281 ugaagUUacu aaaaugagcu cuccaauaU Uaaagccacu gUUacaUUUc ucuaugcUUU
2341 UgguaaucUU agugaugccU UUggUUUUua ugagagUUUU ccucauagaa UUgUUcaaUU
2401 ugcugaggUU gaggaaaaau guacUUUggU UUUCucccaa caagagUUUg ucacugcUUg
2461 gucaacacaa guaaacccca gaaccacacU Ugaagcagau ggUUgucCCU accuauaugc
2521 aaUUaUUcau gauaguacaa cagguacaau cuccggagaU UUUaaucUUg gggucaagcu
2581 UgUUggcaUU aaggaUUUUu gugguauagg UUcuaaucg gguaUUgaug gUUcccgcUU
2641 gcUUggagcu auagcacaag gaccugUUUg ugcugaagcc ucagaugugu auagcccag
2701 uaugauagcu agcacuccuc cugcuccaUU UUcagacgUU acagcaguaa cUUUUgacUU
2761 aaucaacggc aaaauaacuc cugUUgguga ugacaaUUgg aaucgcaca UUUauaauc
2821 uccaaUUaug aaugucUUgc guacugcugc UUggaaaucu ggaacuaUUc augUUcaacU
2881 UaaugUUagg ggugcuggug ucaaaagagc agaUUggggu gguaagucu UUgUUaccu
2941 gcgcagucc augaacCCug aaagUUauga ugcgcggaca UUUgugaucU cacaaccgg
3001 UUcugccaug UUgaacUUcu cUUUUgauau cauagggcg aauagggau UUgaaUUUgc
3061 cgaaugccca ugggccaauc agaccaccug guaucUUgaa ugugUUgcu ccauuccag
3121 acaauacag caaUUUgagg ucaacaugc cUUcgauccu aaUUUcaggg UUgcccgcaa
3181 uauccugaug cccccaUUUc cacugucaac ggaaacucca ccgUUaUUaa agUUUaggUU
3241 UcgggauaUU gaacgcucca agcguagugu uauggUUgga cacacugcua cugcugcUUa

3301 acucuggUUU caUUaaaUUU UcUUUagUUU gaaUUUacug UUAUUUggug ugcaUUUcua
3361 ugUUUgguga gcggUUUUcu gUGCUCagag ugugUUUaUU UUAUGuaaUU UaaUUUCUUU
3421 gugagcuccu gUUUagcagg ucGUcccUUC agcaaggaca caaaaagaUU UUaaUUUUaU
3481 U

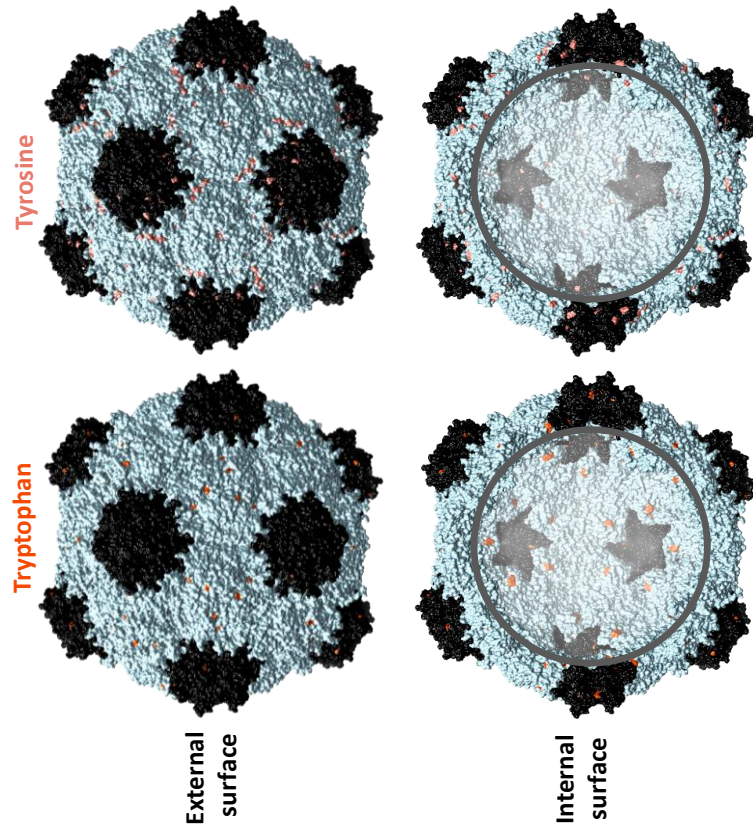
Supporting Figure 8.2: Chemical addressability of various amino acids on the surface of CPMV.

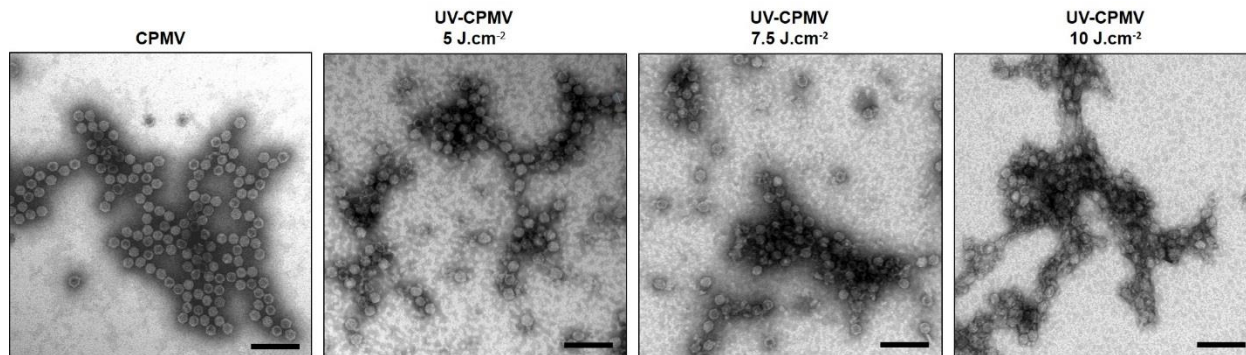


Supporting Figure 8.2: Chemical addressability of various amino acids on the surface of CPMV. Continues

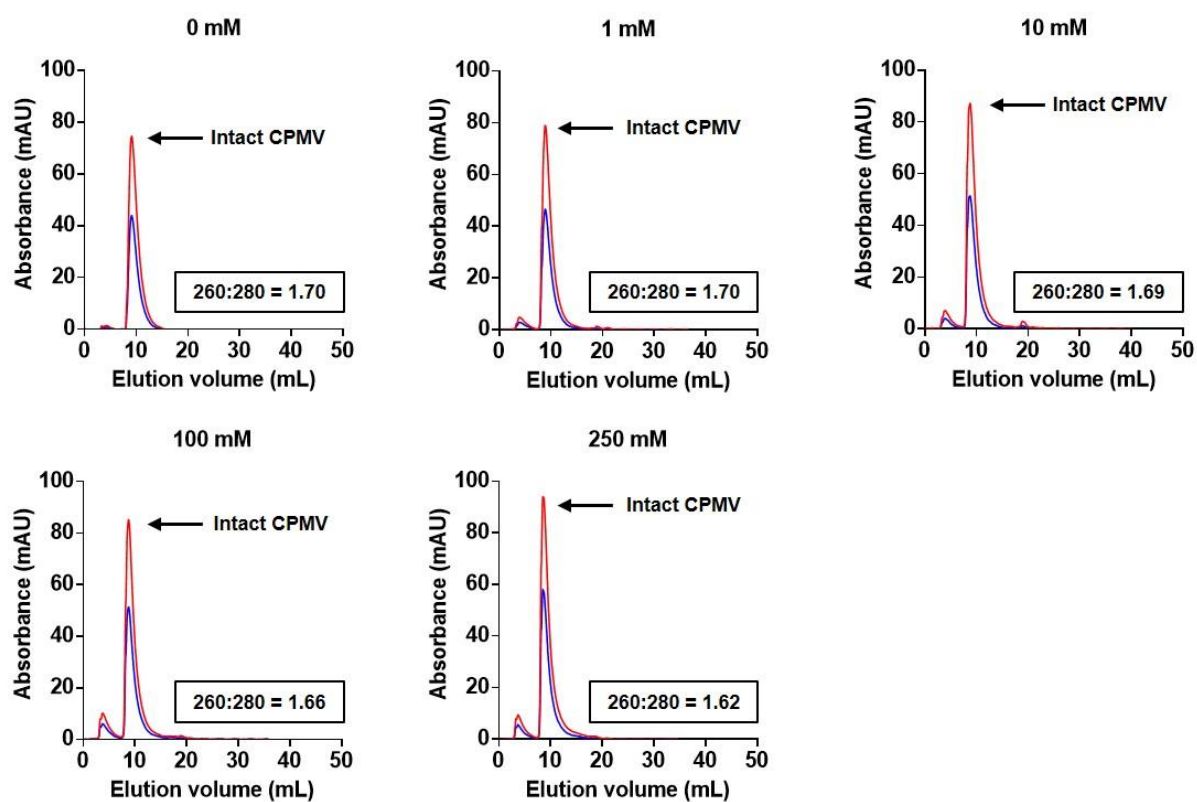


Supporting Figure 8.2: Chemical addressability of various amino acids on the surface of CPMV. Continues

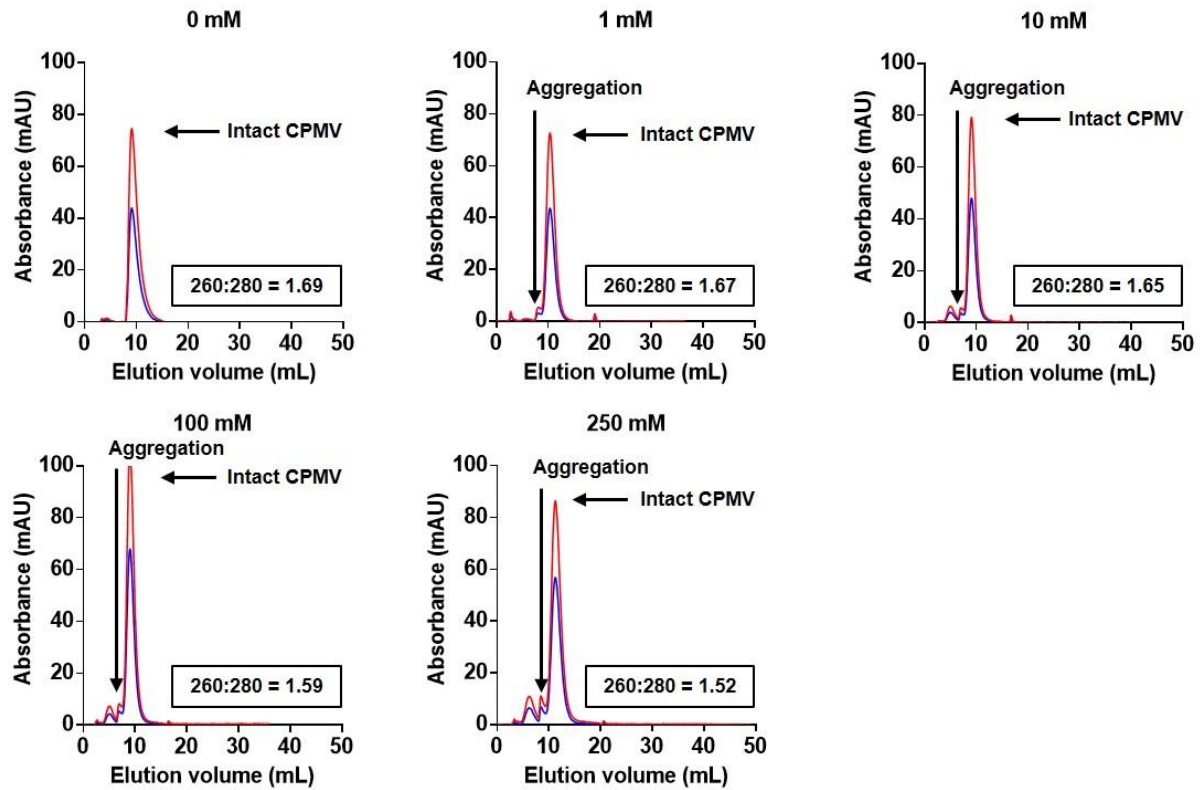




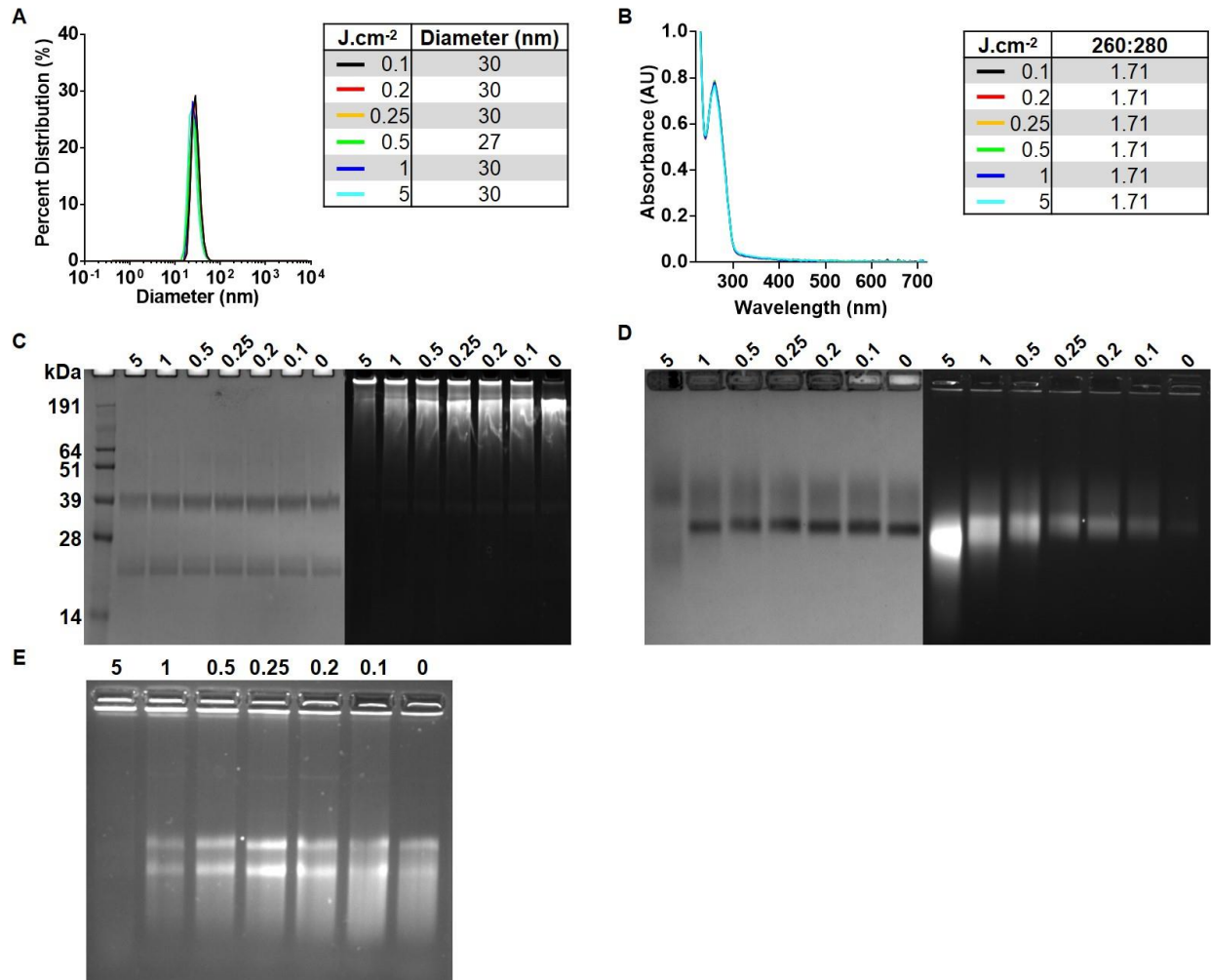
Supporting Figure 8.3. TEM images of native and UV inactivated CPMV. Scale bars represent 100 nm.



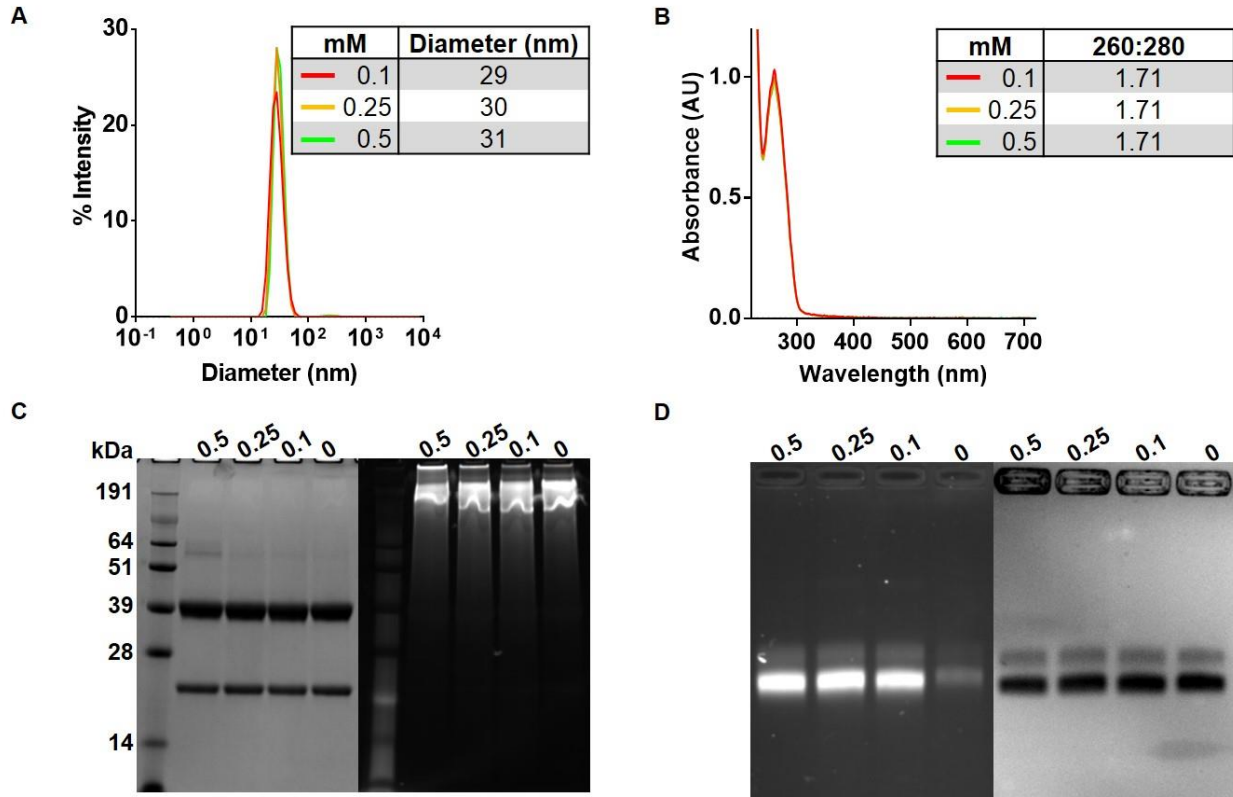
Supporting Figure 8.4. Size exclusion chromatography of CPMV treated with β PL. blue = 260 nm, red = 280 nm. The ratio of RNA:coat protein (260:280) is included in each panel.



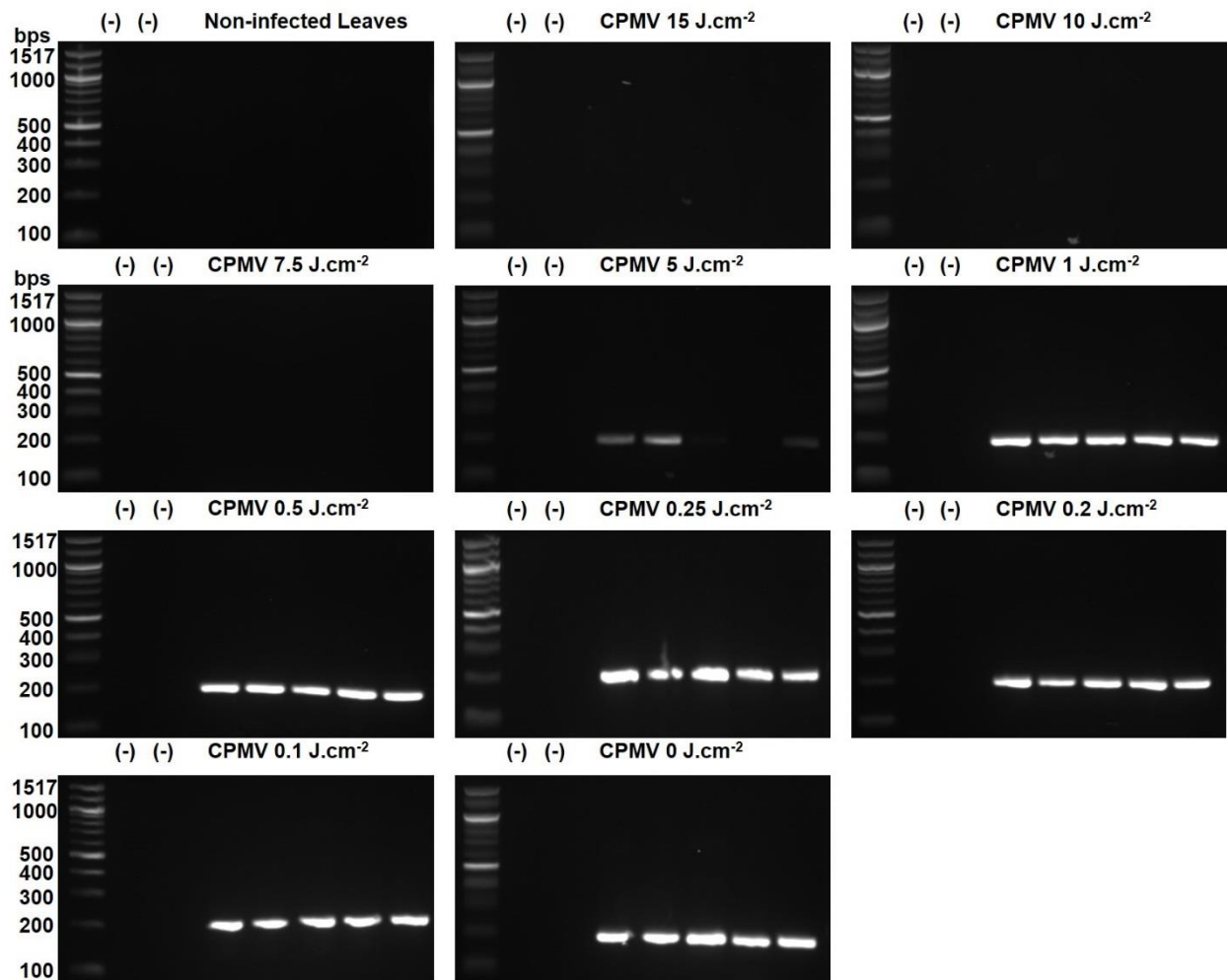
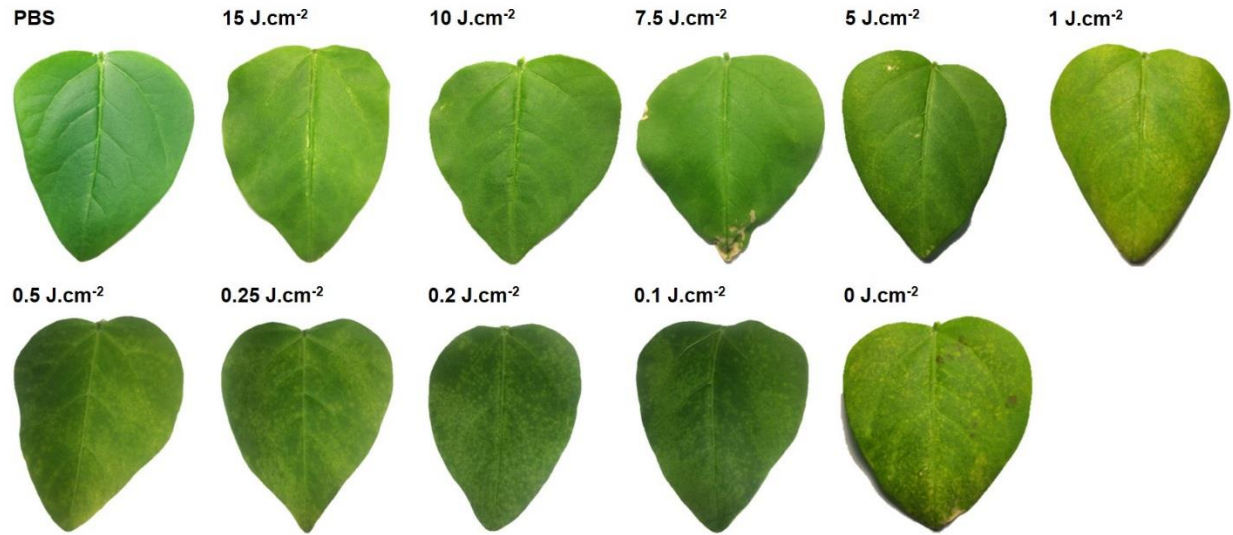
Supporting Figure 8.5. Size exclusion chromatography of CPMV treated with formalin.
 blue = 260 nm, red = 280 nm. The ratio of RNA:coat protein (260:280) is included in each panel.



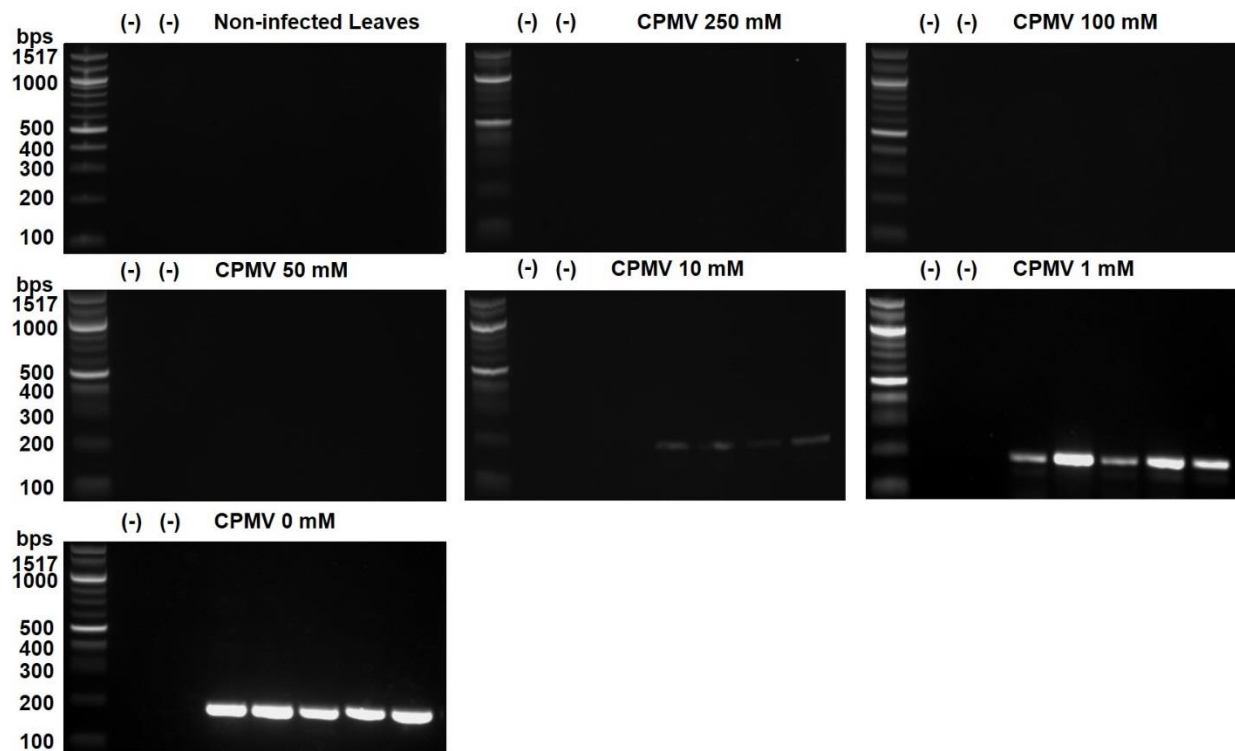
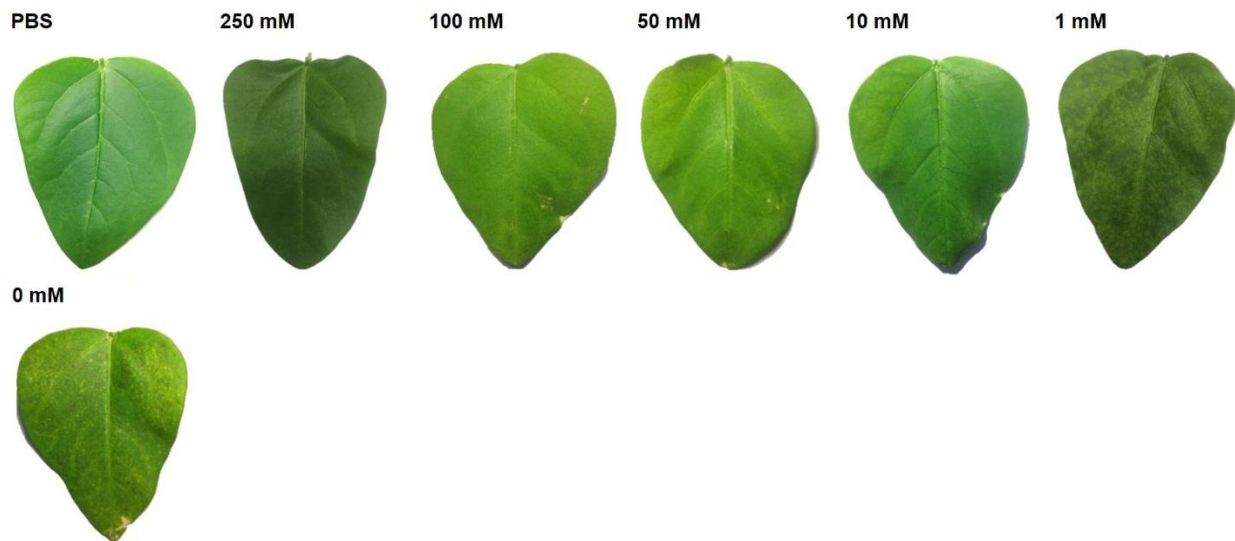
Supporting Figure 8.6. CPMV treated with low concentrations of UV. (A) Dynamic light sizes of CPMV treated with 0, 0.1, 0.2, 0.25, 0.5, 1 and 5 J.cm⁻² of UV light (B), Corresponding UV-visible light spectra. (C) Denaturing SDS-NuPAGE electrophoresis gels under white light after Coomassie staining, and under UV light after GelRed staining. (D) Corresponding non-denaturing agarose gel electrophoresis images under white light after Coomassie staining, and UV light after GelRed staining. (E) Agarose electrophoretic gel of the RNA extracted from UV-CPMV.



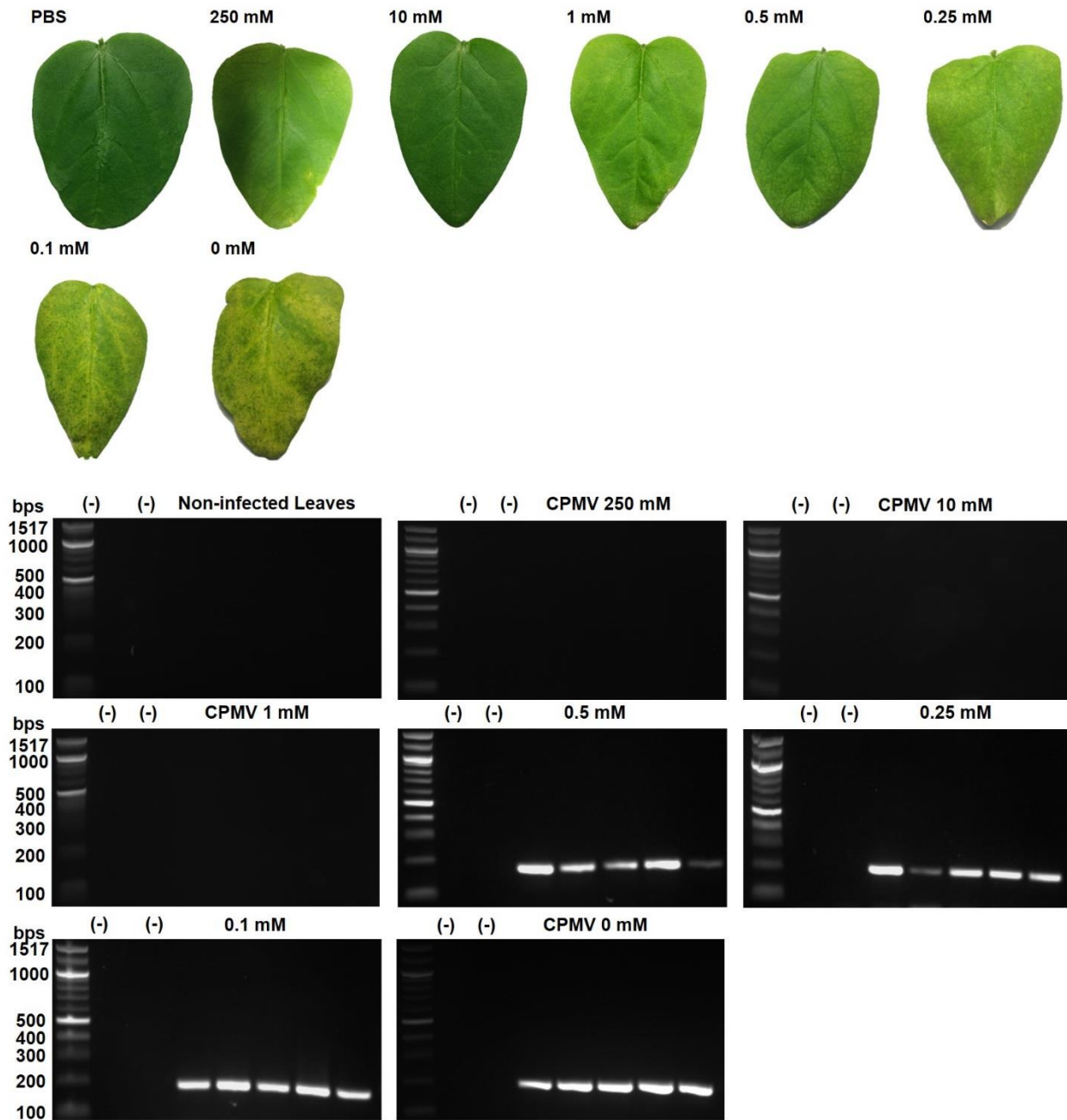
Supporting Figure 8.7. CPMV treated with low concentrations of formalin. (A) Dynamic light sizes of CPMV treated with 0, 0.1, 0.25, 0.5 mM of formalin (B), Corresponding UV-visible light spectrum. (C) Denaturing SDS-NuPAGE electrophoresis gels under white light after Coomassie staining, and under UV light after GelRed staining. (D) Corresponding non-denaturing agarose gel electrophoresis images under white light after Coomassie staining, and UV light after GelRed staining.



Supporting Figure 8.8. UV-CPMV infection on black-eyed peas leaves, and corresponding RT-PCR amplicons.



Supporting Figure 8.9. β PL-CPMV infection on black-eyed peas leaves, and corresponding RT-PCR amplicons.



Supporting Figure 8.10. Form-CPMV infection on black-eyed peas leaves, and corresponding RT-PCR amplicons.

References

1. Eder, J. & Herrling, P. L. Trends in modern drug discovery. in *New approaches to drug discovery* (eds. Nielsch, U., Fuhrmann, U. & Jaroch, S.) 3–22 (Springer International Publishing, 2016). doi:10.1007/164_2015_20.
2. Hogan, G. & Tangney, M. The who, what, and why of drug discovery and development. *Trends Pharmacol. Sci.* **39**, 848–852 (2018).
3. Holohan, C., Van Schaeybroeck, S., Longley, D. B. & Johnston, P. G. Cancer drug resistance: an evolving paradigm. *Nat. Rev. Cancer* **13**, 714–726 (2013).
4. Mansoori, B., Mohammadi, A., Davudian, S., Shirjang, S. & Baradaran, B. The different mechanisms of cancer drug resistance: A brief review. *Adv. Pharm. Bull.* **7**, 339–348 (2017).
5. Maeda, H., Tsukigawa, K. & Fang, J. A retrospective 30 years after discovery of the enhanced permeability and retention effect of solid tumors: next-generation chemotherapeutics and photodynamic therapy—problems, solutions, and prospects. *Microcirculation* **23**, 173–182 (2016).
6. Nakamura, Y., Mochida, A., Choyke, P. L. & Kobayashi, H. Nanodrug delivery: Is the enhanced permeability and retention effect sufficient for curing cancer? *Bioconjug. Chem.* **27**, 2225–2238 (2016).
7. Bazak, R., Hourri, M., Achy, S. E., Kamel, S. & Refaat, T. Cancer active targeting by nanoparticles: a comprehensive review of literature. *J. Cancer Res. Clin. Oncol.* **141**, 769–784 (2015).
8. Muhamad, N., Plengsuriyakarn, T. & Na-Bangchang, K. Application of active targeting nanoparticle delivery system for chemotherapeutic drugs and traditional/herbal medicines in cancer therapy: a systematic review. *Int. J. Nanomedicine* **13**, 3921–3935 (2018).
9. Witchev-Lakshmanan, L. C. & Li, Y. Chapter 9: Controlled drug delivery and the companion animal. in *Controlled Release Veterinary Drug Delivery* 249–267 (Elsevier Science, 2000).
10. McDowell, A. & Rathbone, M. J. Veterinary drug delivery. *J. Pharm. Bioallied Sci.* **6**, 1 (2014).
11. *American Pet Products Association: pet industry market size.* (2019).

12. Sekhon, B. S. Nanotechnology in agri-food production: an overview. *Nanotechnol. Sci. Appl.* **7**, 31–53 (2014).
13. Schwab, F. *et al.* Barriers, pathways and processes for uptake, translocation and accumulation of nanomaterials in plants – Critical review. **3**, 257–278 (2016).
14. Tsuji, K. Microencapsulation of pesticides and their improved handling safety. *J Microencapsulation* **18**, 137–147 (2001).
15. Lamberth, C., Jeanmart, S., Luksch, T. & Plant, A. Current challenges and trends in the discovery of agrochemicals. *Science* **341**, 742–746 (2013).
16. Nicolopoulou-Stamati, P., Maipas, S., Kotampasi, C., Stamatis, P. & Hens, L. Chemical pesticides and human health: The urgent need for a new concept in agriculture. *Front. Public Health* **4**, (2016).
17. Damalas, C. A. & Eleftherohorinos, I. G. Pesticide exposure, safety issues, and risk assessment indicators. *Int J Environ Res Public Health* **8**, 1402–1419 (2011).
18. Nuruzzaman, Md., Rahman, M. M., Liu, Y. & Naidu, R. Nanoencapsulation, nano-guard for pesticides: A new window for safe application. *J. Agric. Food Chem.* **64**, 1447–1483 (2016).
19. Boverhof, D. *et al.* Comparative assessment of nanomaterial definitions and safety evaluation considerations. *Regulatory Toxicology and Pharmacology* **73**, 137–150 (2015).
20. Chen, J., Guo, Z., Tian, H. & Chen, X. Production and clinical development of nanoparticles for gene delivery. *Mol. Ther. - Methods Clin. Dev.* **3**, 16023 (2016).
21. Velpurisiva, P., Gad, A., Piel, B., Jadia, R. & Rai, P. Nanoparticle design strategies for effective cancer immunotherapy. *J. Biomed. Syd. NSW* **2**, 64–77 (2017).
22. Gun'ko, Y. K. Nanoparticles in Bioimaging. *Nanomaterials* **6**, 105 (2016).
23. Jain, K. K. The role of nanobiotechnology in drug discovery. *Drug Discov. Today* **10**, 1435–1442 (2005).
24. Jaque, D. *et al.* Nanoparticles for photothermal therapies. *Nanoscale* **6**, 9494–9530 (2014).

25. Agostinis, P. *et al.* Photodynamic therapy of cancer: an update. *CA. Cancer J. Clin.* **61**, 250–281 (2011).
26. Taniguchi, N. On the basic concept of nano-technology. in *Proceedings of the international conference of production engineering* 245 (1974).
27. Caster, J. M., Patel, A. N., Zhang, T. & Wang, A. Investigational nanomedicines in 2016: a review of nanotherapeutics currently undergoing clinical trials. *Wires: Nanomedicine and Nanobiotechnology* **9**, (2016).
28. Charudattan, R. & Hiebert, E. A plant virus as a bioherbicide for tropical soda apple, *solanum viarum*. *Outlooks Pest Manage* 167–171 (2007).
29. Charudattan, R., Pettersen, M. S. & Hiebert, E. Use of tobacco mild green mosaic virus (TMGMV) mediated lethal hypersensitive response (HR) as a novel method of weed control. (2009).
30. Shang, Y. *et al.* Applications of nanotechnology in plant growth and crop protection: a review. *Molecules* **24**, (2019).
31. Zhao, N., C Woodle, M. & Mixson, A. J. Advances in delivery systems for doxorubicin. *J. Nanomedicine Nanotechnol.* **09**, 519 (2018).
32. Ma, P. & Mumper, R. J. Paclitaxel nano-delivery systems: a comprehensive review. *J. Nanomedicine Nanotechnol.* **4**, 1000164 (2013).
33. Lee, C.-T., Huang, Y.-W., Yang, C.-H. & Huang, K.-S. Drug delivery systems and combination therapy by using vinca alkaloids. *Curr. Top. Med. Chem.* **15**, 1491–1500 (2015).
34. Zaioncz, S., Khalil, N. & Mainardes, R. Exploring the role of nanoparticles in amphotericin B delivery. *Curr. Pharm. Des.* **23**, 509–521 (2017).
35. Lameire, N. Nephrotoxicity of recent anti-cancer agents. *Clin. Kidney J.* **7**, 11–22 (2014).
36. Varricchi, G. *et al.* Antineoplastic drug-induced cardiotoxicity: a redox perspective. *Front. Physiol.* **9**, 167 (2018).

37. Van Bulck, M., Sierra-Magro, A., Alarcon-Gil, J., Perez-Castillo, A. & Morales-Garcia, J. A. Novel approaches for the treatment of Alzheimer's and Parkinson's disease. *Int. J. Mol. Sci.* **20**, 719 (2019).
38. Teleanu, D. M., Chircov, C., Grumezescu, A. M., Volceanov, A. & Teleanu, R. I. Blood-brain delivery methods using nanotechnology. *Pharmaceutics* **10**, (2018).
39. Lee, B. *et al.* Antimicrobial peptide-loaded gold nanoparticle-DNA aptamer conjugates as highly effective antibacterial therapeutics against *Vibrio vulnificus*. *Sci. Rep.* **7**, 13572 (2017).
40. Le, D. H. T., Commandeur, U. & Steinmetz, N. F. Presentation and delivery of tumor necrosis factor-related apoptosis-inducing ligand via elongated plant viral nanoparticle enhances antitumor efficacy. *ACS Nano* **13**, 2501–2510 (2019).
41. Mitchell, M. J., Wayne, E., Rana, K., Schaffer, C. B. & King, M. R. TRAIL-coated leukocytes that kill cancer cells in the circulation. *Proc. Natl. Acad. Sci.* **111**, 930 (2014).
42. McKeage, K. & Perry, C. M. Trastuzumab. *Drugs* **62**, 209–243 (2002).
43. Singh, S. *et al.* Monoclonal antibodies: a review. *Curr. Clin. Pharmacol.* **13**, 85–99 (2018).
44. Birrer, M. J., Moore, K. N., Betella, I. & Bates, R. C. Antibody-drug conjugate-based therapeutics: state of the science. *JNCI J. Natl. Cancer Inst.* **111**, 538–549 (2019).
45. Carter, T., Mulholland, P. & Chester, K. Antibody-targeted nanoparticles for cancer treatment. *Future Medicine* **8**, 941–958 (2016).
46. Slastnikova, T. A., Ulasov, A. V., Rosenkranz, A. A. & Sobolev, A. S. Targeted intracellular delivery of antibodies: The state of the art. *Front. Pharmacol.* **9**, 1208 (2018).
47. Guo, C. *et al.* Liposomal nanoparticles carrying anti-IL6R antibody to the tumour microenvironment inhibit metastasis in two molecular subtypes of breast cancer mouse models. *Theranostics* **7**, 775–788 (2017).
48. Yoo, J., Park, C., Yi, G., Lee, D. & Koo, H. Active targeting strategies using biological ligands for nanoparticle drug delivery systems. *Cancers* **11**, 640 (2019).

49. Rosenblum, D., Joshi, N., Tao, W., Karp, J. M. & Peer, D. Progress and challenges towards targeted delivery of cancer therapeutics. *Nat. Commun.* **9**, 1410 (2018).
50. Wilhelm, S. *et al.* Analysis of nanoparticle delivery to tumours. *Nat. Rev. Mater.* **1**, (2016).
51. Chaudhary, V., Jangra, S. & Yadav, N. R. Nanotechnology based approaches for detection and delivery of microRNA in healthcare and crop protection. *J. Nanobiotechnology* **16**, 40 (2018).
52. Cunningham, F. J., Goh, N. S., Demirer, G. S., Matos, J. L. & Landry, M. P. Nanoparticle-mediated delivery towards advancing plant genetic engineering. *Trends Biotechnol.* **36**, 882–897 (2018).
53. Hwang, H.-H., Yu, M. & Lai, E.-M. Agrobacterium-mediated plant transformation: biology and applications. *Arab. Book* **15**, (2017).
54. Ismagul, A. *et al.* A biolistic method for high-throughput production of transgenic wheat plants with single gene insertions. *BMC Plant Biol.* **18**, (2018).
55. Bangham, A. D., Standish, M. M. & Watkins, J. C. Diffusion of univalent ions across the lamellae of swollen phospholipids. *J. Mol. Biol.* **13**, 238-IN27 (1965).
56. Bulbake, U., Doppalapudi, S., Kommineni, N. & Khan, W. Liposomal formulations in clinical use: an updated review. *Pharmaceutics* **9**, (2017).
57. Swenson, C. E., Perkins, W. R., Roberts, P. & Janoff, A. S. Liposome technology and the development of Myocet (liposomal doxorubicin citrate). *The Breast* **2**, 1–7 (2001).
58. Signorell, R. D., Luciani, P., Brambilla, D. & Leroux, J.-C. Pharmacokinetics of lipid-drug conjugates loaded into liposomes. *Eur. J. Pharm. Biopharm. Off. J. Arbeitsgemeinschaft Pharm. Verfahrenstechnik EV* **128**, 188–199 (2018).
59. Fröhlich, E. The role of surface charge in cellular uptake and cytotoxicity of medical nanoparticles. *Int. J. Nanomedicine* **7**, 5577–5591 (2012).
60. Krasnici, S. *et al.* Effect of the surface charge of liposomes on their uptake by angiogenic tumor vessels. *Int. J. Cancer* **105**, 561–567 (2003).

61. Piccaluga, P. *et al.* Liposomal daunorubicin (DaunoXome) for treatment of relapsed meningeal acute myeloid leukemia. *Leukemia* **16**, 1880–1881 (2002).
62. Silverman, J. A. & Deitcher, S. R. Marqibo® (vincristine sulfate liposome injection) improves the pharmacokinetics and pharmacodynamics of vincristine. *Cancer Chemother. Pharmacol.* **71**, 555–564 (2013).
63. Lamb, Y. N. & Scott, L. J. Liposomal irinotecan: a review in metastatic pancreatic adenocarcinoma. *Drugs* **77**, 785–792 (2017).
64. Sercombe, L. *et al.* Advances and challenges of liposome assisted drug delivery. *Front. Pharmacol.* **6**, (2015).
65. Duggan, S. T. & Keating, G. M. Pegylated liposomal doxorubicin: a review of its use in metastatic breast cancer, ovarian cancer, multiple myeloma and AIDS-related Kaposi's sarcoma. **18**, 2531–2558 (2011).
66. Gabizon, A. *et al.* Prolonged circulation time and enhanced accumulation in malignant exudates of doxorubicin encapsulated in polyethylene-glycol coated liposomes. *Cancer Res.* **54**, 987–992 (1994).
67. Deshpande, P. P., Biswas, S. & Torchilin, V. P. Current trends in the use of liposomes for tumor targeting. *Nanomed.* **8**, 1509–1528 (2013).
68. Blair, H. A. Daunorubicin/Cytarabine liposome: a review in acute myeloid leukaemia. *Drugs* **78**, 1903–1910 (2018).
69. Stone, N. R., Bicanic, T., Salim, R. & Hope, W. Liposomal amphotericin B (AmBisome®): a review of the pharmacokinetics, pharmacodynamics, clinical experience and future directions. *Drugs* **76**, 485–500 (2016).
70. Fenton, C. & Perry, C. M. Verteporfin: a review of its use in the management of subfoveal choroidal neovascularisation. *Drugs Aging* **5**, 421–425 (2006).
71. Weng, Y., Xiao, H., Zhang, J., Liang, X.-J. & Huang, Y. RNAi therapeutic and its innovative biotechnological evolution. *Biotechnology Advances* **5**, 801–825 (2019).
72. Behr, J. *et al.* Lung deposition of a liposomal cyclosporine A inhalation solution in patients after lung transplantation. *J. Aerosol Med. Pulm. Drug Deliv.* **22**, 121–130 (2009).

73. da Silva, S. M. *et al.* Efficacy of combined therapy with liposome-encapsulated meglumine antimoniate and allopurinol in treatment of canine visceral leishmaniasis. *Antimicrob. Agents Chemother.* **56**, 2858–2867 (2012).
74. Bai, D.-P., Lin, X.-Y., Huang, Y.-F. & Zhang, X.-F. Theranostics aspects of various nanoparticles in veterinary medicine. *Int. J. Mol. Sci.* **19**, 3299 (2018).
75. Sadozai, H. & Saeidi, D. Recent developments in liposome-based veterinary therapeutics. *ISRN Vet. Sci.* **2013**, 167521 (2013).
76. Hauck, M. L. *et al.* Phase I trial of doxorubicin-containing low temperature sensitive liposomes in spontaneous canine tumors. *Clin. Cancer Res. Off. J. Am. Assoc. Cancer Res.* **12**, 4004–4010 (2006).
77. Kleiter, M., Tichy, A., Willmann, M., Pagitz, M. & Wolfesberger, B. Concomitant liposomal doxorubicin and daily palliative radiotherapy in advanced feline soft tissue sarcomas. *Vet. Radiol. Ultrasound* **51**, 349–355 (2010).
78. Hafeman, S., London, C., Elmslie, R. & Dow, S. Evaluation of liposomal clodronate for treatment of malignant histiocytosis in dogs. *Cancer Immunol. Immunother.* **59**, 441–452 (2010).
79. Krawiec, D. R. *et al.* Use of an amphotericin B lipid complex for treatment of blastomycosis in dogs. *J. Am. Vet. Med. Assoc.* **209**, 2073–2075 (1996).
80. Taylor, T. M., Weiss, J., Davidson, P. M. & Bruce, B. D. Liposomal nanocapsules in food science and agriculture. *Crit. Rev. Food Sci. Nutr.* **45**, 587–605 (2005).
81. Hwang, I. C. *et al.* Insecticidal effect of controlled release formulations of Etofenprox based on nano-bio technique. *J. Fac. Agr* **56**, 33–40 (2011).
82. Karny, A., Zinger, A., Kajal, A., Shainsky-Roitman, J. & Schroeder, A. Therapeutic nanoparticles penetrate leaves and deliver nutrients to agricultural crops. *Sci. Rep.* **8**, 7589 (2018).
83. Honey, J., Rijo, J., Anju, A. & Anoop, K. R. Smart polymers for the controlled delivery of drugs – a concise overview. *Acta Pharmaceutica Sinica B* **2**, 120–127 (2014).

84. Knop, K., Hoogenboom, R., Fischer, D. & Schubert, U. S. Poly(ethylene glycol) in drug delivery: pros and cons as well as potential alternatives. *Angew. Chem. Int. Ed.* **49**, 6288–6308 (2010).
85. Sartor, O. Eligard: Leuprolide acetate in a novel sustained-release delivery system. *Urology* **61**, 25–31 (2003).
86. Avitabile, N., Banka, A. & Fonseca, V. A. Safety evaluation of colesevelam therapy to achieve glycemic and lipid goals in type 2 diabetes. *Expert Opin. Drug Saf.* **10**, 305–310 (2011).
87. Madaan, K., Kumar, S., Poonia, N., Lather, V. & Pandita, D. Dendrimers in drug delivery and targeting: Drug-dendrimer interactions and toxicity issues. *J. Pharm. Bioallied Sci.* **6**, 139–150 (2014).
88. Palmerston Mendes, L., Pan, J. & Torchilin, V. P. Dendrimers as nanocarriers for nucleic acid and drug delivery in cancer therapy. *Mol. J. Synth. Chem. Nat. Prod. Chem.* **22**, (2017).
89. Kannan, R. M., Nance, E., Kannan, S. & Tomalia, D. A. Emerging concepts in dendrimer-based nanomedicine: from design principles to clinical applications. *J. Intern. Med.* **276**, 579–617 (2014).
90. Kesharwani, P. & Lyer, A. K. Recent advances in dendrimer-based nanovectors for tumor-targeted drug and gene delivery. *Drug Discov. Today* **20**, 536–547 (2015).
91. Wilken, R., Veena, M. S., Wang, M. B. & Srivatsan, E. S. Curcumin: A review of anti-cancer properties and therapeutic activity in head and neck squamous cell carcinoma. *Mol. Cancer* **10**, 12 (2011).
92. Hasty, P. *et al.* eRapa restores a normal life span in a FAP mouse model. *Cancer Prev. Res. Phila. Pa* **7**, 169–178 (2014).
93. Jeong, Y. *et al.* Cisplatin-incorporated hyaluronic acid nanoparticles based on ion-complex formation. *J. Pharm. Sci.* **97**, 1268–1276 (2008).
94. Hrkach, J. *et al.* Preclinical development and clinical translation of a PSMA-targeted docetaxel nanoparticle with a differentiated pharmacological profile. *Sci. Transl. Med.* **4**, 128–139 (2012).

95. Autio, K. A. *et al.* Safety and efficacy of BIND-014, a docetaxel nanoparticle targeting prostate-specific membrane antigen for patients with metastatic castration-resistant prostate cancer: A phase 2 clinical trial. *JAMA Oncology* **4**, 1344–1351 (2018).
96. Perlatti, B., Luísa de Souza Bergo, P., das Graças Fernandes da Silva, M. F., Fernandes, J. B. & Forim, M. R. *Polymeric nanoparticle-based insecticides: A controlled release purpose for agrochemicals*. (INTECH Open Access, 2013).
97. Grillo, R. *et al.* Poly(ϵ -caprolactone)nanocapsules as carrier systems for herbicides: Physico-chemical characterization and genotoxicity evaluation. *Journal of Hazardous Materials* **231–232**, 1–9 (2012).
98. Pradhan, S. *et al.* Entomotoxicity and biosafety assessment of PEGylated acephate nanoparticles: A biologically safe alternative to neurotoxic pesticides. *J. Environ. Sci. Health Part B* **48**, 559–569 (2013).
99. Shang, Q., Shi, Y., Zhang, Y., Zheng, T. & Shi, H. Pesticide-conjugated polyacrylate nanoparticles: novel opportunities for improving the photostability of emamectin benzoate. *Polym. Adv. Technol.* **24**, 137–143 (2013).
100. Yang, F.-L., Li, X.-G., Zhu, F. & Lei, C.-L. Structural characterization of nanoparticles loaded with garlic essential oil and their insecticidal activity against *Tribolium castaneum*. *J. Agric. Food Chem.* **57**, 10156–10162 (2009).
101. Kumar, S., Bhanjana, G., Sharma, A., Sidhu, M. C. & Dilbaghi, N. Synthesis, characterization and on field evaluation of pesticide loaded sodium alginate nanoparticles. *Carbohydr. Polym.* **101**, 1061–1067 (2014).
102. Guan, H., Chi, D., Yu, J. & Li, X. A novel photodegradable insecticide: Preparation, characterization and properties evaluation of nano-Imidacloprid. *Pestic. Biochem. Physiol.* **92**, 83–91 (2008).
103. Yin, Y., Guo, Q., Han, Y., Wang, L. & Wan, S. Preparation, characterization and nematicidal activity of lansiumamide B nano-capsules. *Journal of Integrative Agriculture* **11**, 1151–1158 (2012).
104. Yin, Y. *et al.* One-pot synthesis of biopolymeric hollow nanospheres by photocrosslinking. *Chem. Commun.* **46**, 8222 (2010).

105. Silva, M. dos S. *et al.* Paraquat-loaded alginate/chitosan nanoparticles: Preparation, characterization and soil sorption studies. *J. Hazard. Mater.* **190**, 366–374 (2011).
106. Li, J. & Mooney, D. J. Designing hydrogels for controlled drug delivery. *Nat. Rev. Mater.* **1**, (2016).
107. Hoare, T. R. & Kohane, D. S. hydrogels in drug delivery: progress and challenges. *Polymer* **49**, 1993–2007 (2008).
108. Ekladios, I., Colson, Y. L. & Grinstaff, M. W. Polymer–drug conjugate therapeutics: advances, insights and prospects. *Nat. Rev. Drug Discov.* **18**, 273–294 (2019).
109. Pedrini, S., Merritt, D. J., Stevens, J. & Dixon, K. Seed coating: science or marketing spin? *Trends Plant Sci.* **22**, 106–116 (2017).
110. Blizzard, C., Desai, A. & Driscoll, A. pharmacokinetic studies of sustained-release depot of dexamethasone in beagle dogs. *J. Ocul. Pharmacol. Ther.* **32**, 595–600 (2016).
111. Narayanaswamy, R. & Torchilin, V. P. Hydrogels and their applications in targeted drug delivery. *Molecules* **24**, (2019).
112. Greenwald, R. B., Choe, Y. H., McGuire, J. & Conover, C. D. Effective drug delivery by PEGylated drug conjugates. *Adv. Drug Deliv. Rev.* **55**, 217–250 (2003).
113. Alconcel, S. N. S., Baas, A. S. & Maynard, H. D. FDA-approved poly(ethylene glycol)–protein conjugate drugs. *Polym. Chem.* **2**, 1442 (2011).
114. Zinicola, M. *et al.* Effects of pegbovigrastim administration on periparturient diseases, milk production, and reproductive performance of Holstein cows. *Journal of Dairy Science* **101**, 11199–11217 (2018).
115. Zhang, P., Sun, F., Liu, S. & Jiang, S. Anti-PEG antibodies in the clinic: Current issues and beyond PEGylation. *14th Ed. Eur. Symp. Control. Drug Deliv. Egmond Aan Zee Neth. April 13-15 2016* **244**, 184–193 (2016).
116. Sharma, K. K., Singh, U. S., Sharma, P., Kumar, A. & Sharma, L. Seed treatments for sustainable agriculture-A review. *J. Appl. Nat. Sci.* **7**, 521–539 (2015).

117. Croy, S. R. & Kwon, G. S. Polymeric micelles for drug delivery. *Current Pharmaceutical Design* **12**, 4669–4684 (2006).
118. Lu, Y. & Park, K. Polymeric micelles and alternative nanonized delivery vehicles for poorly soluble drugs. *Int. J. Pharm.* **453**, 198–214 (2013).
119. Simon, J. A. Estradiol in micellar nanoparticles: the efficacy and safety of a novel transdermal drug-delivery technology in the management of moderate to severe vasomotor symptoms. *The Journal of The North American Menopause Society* **13**, 222–231 (2006).
120. Hart, M. & Acott, S. Physical and chemical stability of Taxotere® (docetaxel) one-vial (20 mg/ml) infusion solution following refrigerated storage. *ecancermedicalscience* **4**, (2010).
121. Scripture, C., Szebeni, J., Loos, W. J., Figg, II, W. & Sparreboom, A. Comparative in vitro properties and clinical pharmacokinetics of paclitaxel following the administration of Taxol® and Paxene®. *Cancer Biol. Ther.* **4**, 555–560 (2005).
122. Hamaguchi, T. *et al.* A phase II study of NK012, a polymeric micelle formulation of SN-38, in unresectable, metastatic or recurrent colorectal cancer patients. *Cancer Chemother. Pharmacol.* **82**, 1021–1029 (2018).
123. Hamaguchi, T. *et al.* NK105, a paclitaxel-incorporating micellar nanoparticle formulation, can extend in vivo antitumour activity and reduce the neurotoxicity of paclitaxel. *Br. J. Cancer* **92**, 1240–1246 (2005).
124. Kim, D.-W. *et al.* Multicenter phase II trial of Genexol-PM, a novel Cremophor-free, polymeric micelle formulation of paclitaxel, with cisplatin in patients with advanced non-small-cell lung cancer. *Ann. Oncol.* **18**, 2009–2014 (2007).
125. Plummer, R. *et al.* A Phase I clinical study of cisplatin-incorporated polymeric micelles (NC-6004) in patients with solid tumours. *Br. J. Cancer* **104**, 593–598 (2011).
126. Vail, D. M. *et al.* A randomized trial investigating the efficacy and safety of water soluble micellar Paclitaxel (Paccal Vet) for treatment of nonresectable grade 2 or 3 mast cell tumors in dogs. *J. Vet. Intern. Med.* **26**, 598–607 (2012).
127. Rey, A. I., Segura, J., Arandilla, E. & López-Bote, C. J. Short- and long-term effect of oral administration of micellized natural vitamin E (D- α -tocopherol) on oxidative status in race horses under intense training¹. *J. Anim. Sci.* **91**, 1277–1284 (2013).

128. Feng, B.-H. & Peng, L.-F. Synthesis and characterization of carboxymethyl chitosan carrying ricinoleic functions as an emulsifier for azadirachtin. *Carbohydr. Polym.* **88**, 576–582 (2012).
129. Koli, P., Singh, B. B., Shakil, N. A., Kumar, J. & Kamil, D. Development of controlled release nanoformulations of carbendazim employing amphiphilic polymers and their bioefficacy evaluation against *Rhizoctonia solani*. **9**, 674–681.
130. Shakil, N. A. *et al.* Development of poly(ethylene glycol) based amphiphilic copolymers for controlled release delivery of carbofuran. *J. Macromol. Sci. Part A* **47**, 241–247 (2010).
131. Adak, T., Kumar, J., Shakil, N. A. & Walia, S. Development of controlled release formulations of imidacloprid employing novel nano-ranged amphiphilic polymers. *J. Environ. Sci. Health Part B* **47**, 217–225 (2012).
132. Adak, T., Kumar, J., Dey, D., Shakil, N. A. & Walia, S. Residue and bio-efficacy evaluation of controlled release formulations of imidacloprid against pests in soybean (*Glycine max*). *J. Environ. Sci. Health Part B* **47**, 226–231 (2012).
133. Lao, S.-B., Zhang, Z.-X., Xu, H.-H. & Jiang, G.-B. Novel amphiphilic chitosan derivatives: Synthesis, characterization and micellar solubilization of rotenone. *Carbohydr. Polym.* **82**, 1136–1142 (2010).
134. Sarkar, D. J., Kumar, J., Shakil, N. A. & Walia, S. Release kinetics of controlled release formulations of thiamethoxam employing nano-ranged amphiphilic PEG and diacid based block polymers in soil. *J. Environ. Sci. Health Part A* **47**, 1701–1712 (2012).
135. Kaushik, P. *et al.* Development of controlled release formulations of thiram employing amphiphilic polymers and their bioefficacy evaluation in seed quality enhancement studies. *J. Environ. Sci. Health Part B* **48**, 677–685 (2013).
136. Pinto, A. & Pocard, M. Photodynamic therapy and photothermal therapy for the treatment of peritoneal metastasis: a systematic review. *Pleura Peritoneum* **3**, (2018).
137. Anselmo, A. C. & Mitragotri, S. A review of clinical translation of inorganic nanoparticles. *AAPS J.* **17**, 1041–1054 (2015).
138. Lin, G., Mi, P., Chu, C., Zhang, J. & Liu, G. Inorganic nanocarriers overcoming multidrug resistance for cancer theranostics. *Adv. Sci.* **3**, (2016).

139. Mei, W. & Wu, Q. Applications of metal nanoparticles in medicine/metal nanoparticles as anticancer agents. in *Metal Nanoparticles* 169–190 (Wiley-VCH Verlag GmbH & Co. KGaA, 2017). doi:10.1002/9783527807093.ch7.
140. Chen, Y.-H. *et al.* Methotrexate conjugated to gold nanoparticles inhibits tumor growth in a syngeneic lung tumor model. *Mol. Pharm.* **4**, 713–722 (2007).
141. Wang, F. *et al.* Doxorubicin-tethered responsive gold nanoparticles facilitate intracellular drug delivery for overcoming multidrug resistance in cancer cells. *ACS Nano* **5**, 3679–3692 (2011).
142. Brown, S. D. *et al.* Gold nanoparticles for the improved anticancer drug delivery of the active component of Oxaliplatin. *J. Am. Chem. Soc.* **132**, 4678–4684 (2010).
143. Duraipandy, N. *et al.* Caging of plumbagin on silver nanoparticles imparts selectivity and sensitivity to plumbagin for targeted cancer cell apoptosis. *Metallomics* **6**, 2025–2033 (2014).
144. Bharti, C., Nagaich, U., Pal, A. K. & Gulati, N. Mesoporous silica nanoparticles in target drug delivery system: A review. *Int. J. Pharm. Investig.* **5**, 124–133 (2015).
145. Kettiger, H., Québatte, G., Perrone, B. & Huwyler, J. Interactions between silica nanoparticles and phospholipid membranes. *Biochim. Biophys. Acta BBA - Biomembr.* **1858**, 2163–2170 (2016).
146. Song, M.-R. *et al.* Dispersible silica nanoparticles as carrier for enhanced bioactivity of chlorfenapyr. *J. Pestic. Sci.* **37**, 258–260 (2012).
147. Wanyika, H. Sustained release of fungicide metalaxyl by mesoporous silica nanospheres. *J. Nanoparticle Res.* **15**, 1831 (2013).
148. Park, M. *et al.* Hybridization of the natural antibiotic, cinnamic acid, with layered double hydroxides (LDH) as green pesticide. *Environ. Sci. Pollut. Res.* **17**, 203–209 (2010).
149. Zobir bin Hussein, M., Hj Yahaya, A., Zainal, Z. & Hee Kian, L. Nanocomposite-based controlled release formulation of an herbicide, 2,4-dichlorophenoxyacetate encapsulated in zinc–aluminium-layered double hydroxide. *Sci. Technol. Adv. Mater.* **6**, 956–962 (2005).
150. Elhissi, A. M. A., Ahmed, W., Hassan, I. U., Dhanak, Vinod. R. & D’Emanuele, A. Carbon nanotubes in cancer therapy and drug delivery. *J. Drug Deliv.* **2012**, 1–10 (2012).

151. Guo, Q., Shen, X., Li, Y. & Xu, S. Carbon nanotubes-based drug delivery to cancer and brain. *Curr. Med. Sci.* **37**, 635–641 (2017).
152. Mahajan, S. *et al.* Functionalized carbon nanotubes as emerging delivery system for the treatment of cancer. *Int. J. Pharm.* **548**, 540–558 (2018).
153. Matthews, B. Tools for protein science. *Protein Sci. Publ. Protein Soc.* **27**, 6–9 (2018).
154. Niemeyer, C. M. Nanoparticles, proteins, and nucleic acids: biotechnology meets materials science. *Angew. Chem. Int. Ed.* **40**, 4128–4158 (2001).
155. Rong, J., Niu, Z., Lee, L. A. & Wang, Q. 2.06 - Chemistry and materials development of protein-based nanoparticles. in *Comprehensive nanoscience and technology* (eds. Andrews, D. L., Scholes, G. D. & Wiederrecht, G. P.) 153–174 (Academic Press, 2011). doi:10.1016/B978-0-12-374396-1.00081-7.
156. Hawkins, M., Soon-Shiong, P. & Desai, N. Protein nanoparticles as drug carriers in clinical medicine. *Advanced Drug Delivery Reviews* **60**, 876–885 (2008).
157. Larsen, M. T., Kuhlmann, M., Hvam, M. L. & Howard, K. A. Albumin-based drug delivery: harnessing nature to cure disease. *Mol. Cell. Ther.* **4**, 3–3 (2016).
158. Sauvage, F., Messaoudi, S., Fattal, E., Barratt, G. & Vergnaud-Gauduchon, J. Heat shock proteins and cancer: How can nanomedicine be harnessed? *J. Controlled Release* **248**, 133–143 (2017).
159. Flenniken, M. L. *et al.* Selective attachment and release of a chemotherapeutic agent from the interior of a protein cage architecture. *Chem. Commun.* **4**, 447–449 (2005).
160. Rother, M., Nussbaumer, M. G., Renggli, K. & Bruns, N. Protein cages and synthetic polymers: a fruitful symbiosis for drug delivery applications, bionanotechnology and materials science. *Chem. Soc. Rev.* **45**, 6213–6249 (2016).
161. Muñoz-Juan, A., Carreño, A., Mendoza, R. & Corchero, J. L. Latest advances in the development of eukaryotic vaults as targeted drug delivery systems. *Pharmaceutics* **11**, (2019).
162. Truffi, M. *et al.* Ferritin nanocages: A biological platform for drug delivery, imaging and theranostics in cancer. *Pharmacol. Res.* **107**, 57–65 (2016).

163. Yang, Z. *et al.* Encapsulation of platinum anticancer drugs by apoferritin. *Chem. Commun.* 3453–3455 (2007) doi:10.1039/B705326F.
164. Zhen, Z. *et al.* RGD-modified apoferritin nanoparticles for efficient drug delivery to tumors. *ACS Nano* **7**, 4830–4837 (2013).
165. Chen, L. *et al.* Encapsulation of curcumin in recombinant human H-chain ferritin increases its water-solubility and stability. *Food Res. Int.* **62**, 1147–1153 (2014).
166. Sánchez, P. *et al.* MRI relaxation properties of water-soluble apoferritin-encapsulated gadolinium oxide-hydroxide nanoparticles. *Dalton Trans.* 800–804 (2009) doi:10.1039/B809645G.
167. Kálmán, F. K., Geninatti-Crich, S. & Aime, S. Reduction/dissolution of a β -MnOOH nanophase in the ferritin cavity to yield a highly sensitive, biologically compatible magnetic resonance imaging agent. *Angew. Chem. Int. Ed.* **49**, 612–615 (2010).
168. Ristroph, K. D., Astete, C. E., Bodoki, E. & Sabliov, C. M. Zein nanoparticles uptake by hydroponically grown soybean plants. *Environ. Sci. Technol.* **51**, 14065–14071 (2017).
169. Adli, M. The CRISPR tool kit for genome editing and beyond. *Nat. Commun.* **9**, 1911 (2018).
170. Chevalier, A. *et al.* Massively parallel de novo protein design for targeted therapeutics. *Nature* **550**, 74–79 (2017).
171. Ljubetič, A. *et al.* Design of coiled-coil protein-origami cages that self-assemble in vitro and in vivo. *Nat. Biotechnol.* **35**, 1094 (2017).
172. Modica, J. A., Lin, Y. & Mrksich, M. Synthesis of cyclic megamolecules. *J. Am. Chem. Soc.* **140**, 6391–6399 (2018).
173. Wen, A. M. & Steinmetz, N. F. Design of virus-based nanomaterials for medicine, biotechnology, and energy. *Chem. Soc. Rev.* **45**, 4074–4126 (2016).
174. Naso, M. F., Tomkowicz, B., Perry, W. L. & Strohl, W. R. Adeno-associated virus (AAV) as a vector for gene therapy. *Biodrugs* **31**, 317–334 (2017).

175. Ylä-Herttuala, S. Endgame: Glybera finally recommended for approval as the first gene therapy drug in the European Union. *Mol. Ther.* **20**, 1831–1832 (2012).
176. Keeler, A. M. & Flotte, T. R. Recombinant adeno-associated virus gene therapy in Light of Luxturna (and Zolgensma and Glybera): where are we, and how did we get here? *Annu. Rev. Virol.* **6**, 601–621 (2019).
177. Lundstrom, K. Viral vectors in gene therapy. *Diseases* **6**, (2018).
178. Lizotte, P. H. *et al.* In situ vaccination with cowpea mosaic virus nanoparticles suppresses metastatic cancer. *Nat. Nanotechnol.* **11**, 295–303 (2016).
179. Kerstetter-Fogle, A. *et al.* Plant virus-like particle in situ vaccine for intracranial glioma immunotherapy. *Cancers* **11**, 515 (2019).
180. Eriksson, F. *et al.* Tumor-specific bacteriophages induce tumor destruction through activation of tumor-associated macrophages. *J. Immunol.* **182**, 3105 (2009).
181. Lee, K. L. *et al.* Combination of plant virus nanoparticle-based in situ vaccination with chemotherapy potentiates antitumor response. *Nano Lett.* **17**, 4019–4028 (2017).
182. Murray, A. A., Wang, C., Fiering, S. & Steinmetz, N. F. In situ vaccination with cowpea vs tobacco mosaic virus against melanoma. *Mol. Pharm.* **15**, 3700–3716 (2018).
183. Lebel, M.-È. *et al.* Potentiating cancer immunotherapy using papaya mosaic virus-derived nanoparticles. *Nano Lett.* **16**, 1826–1832 (2016).
184. Hoopes, P. J. *et al.* Treatment of canine oral melanoma with nanotechnology-based immunotherapy and radiation. *Mol. Pharm.* **15**, 3717–3722 (2018).
185. Hoopes, P. J. *et al.* Effect of intra-tumoral magnetic nanoparticle hyperthermia and viral nanoparticle immunogenicity on primary and metastatic cancer. *Proc. SPIE-- Int. Soc. Opt. Eng.* **10066**, (2017).
186. Hoopes, P. J. *et al.* Hypo-fractionated Radiation, Magnetic Nanoparticle Hyperthermia and a Viral Immunotherapy Treatment of Spontaneous Canine Cancer. *Proc. SPIE-- Int. Soc. Opt. Eng.* **10066**, (2017).

187. Donaldson, B., Lateef, Z., Walker, G. F., Young, S. L. & Ward, V. K. Virus-like particle vaccines: immunology and formulation for clinical translation. *Expert Rev. Vaccines* **17**, 833–849 (2018).
188. Balke, I. & Zeltins, A. Use of plant viruses and virus-like particles for the creation of novel vaccines. *Adv. Drug Deliv. Rev.* 119–129 (2018) doi:10.1016/j.addr.2018.08.007.
189. Crisci, E., Bárcena, J. & Montoya, M. Virus-like particle-based vaccines for animal viral infections. *Inmunología* **32**, 102–116 (2013).
190. Mohsen, M. O., Zha, L., Cabral-Miranda, G. & Bachmann, M. F. Major findings and recent advances in virus-like particle (VLP)-based vaccines. *Interact. Nanoparticles Immune Syst. Advant. Disadv.* **34**, 123–132 (2017).
191. Mohsen, M. O., Speiser, D. E., Knuth, A. & Bachmann, M. F. Virus-like particles for vaccination against cancer. *Wiley Interdiscip. Rev. Nanomed. Nanobiotechnol.* e1579 (2019) doi:10.1002/wnan.1579.
192. Lee, K. L., Twyman, R. M., Fiering, S. & Steinmetz, N. F. Virus-based nanoparticles as platform technologies for modern vaccines. *Wiley Interdiscip. Rev. Nanomed. Nanobiotechnol.* **8**, 554–578 (2016).
193. Huang, X., Wang, X., Zhang, J., Xia, N. & Zhao, Q. Escherichia coli-derived virus-like particles in vaccine development. *Npj Vaccines* **2**, 3 (2017).
194. Fettelschoss-Gabriel, A. *et al.* Treating insect-bite hypersensitivity in horses with active vaccination against IL-5. *J. Allergy Clin. Immunol.* **142**, 1194-1205.e3 (2018).
195. Bruckman, M. A., Czapar, A. E., VanMeter, A., Randolph, L. N. & Steinmetz, N. F. Tobacco mosaic virus-based protein nanoparticles and nanorods for chemotherapy delivery targeting breast cancer. *J. Control. Release Off. J. Control. Release Soc.* **231**, 103–113 (2016).
196. Zeng, Q. *et al.* Cucumber mosaic virus as drug delivery vehicle for doxorubicin. *Biomaterials* **34**, 4632–4642 (2013).
197. Cao, J. *et al.* Loading and release mechanism of red clover necrotic mosaic virus derived plant viral nanoparticles for drug delivery of doxorubicin. *Small* **10**, 5126–5136 (2014).

198. Le, D. H. T., Lee, K. L., Shukla, S., Commandeur, U. & Steinmetz, N. F. Potato virus X, a filamentous plant viral nanoparticle for doxorubicin delivery in cancer therapy. *Nanoscale* **9**, 2348–2357 (2017).
199. Min, J., Moon, H., Yang, H., Hong, S. & Kang, S. Development of P22 viral capsid nanocomposites as anti-cancer drug, bortezomib (BTZ), delivery nanoplatfoms. *Macromol. Biosci.* **4**, 557–64 (2014).
200. Franke, C. E., Czapar, A. E., Patel, R. B. & Steinmetz, N. F. Tobacco mosaic virus-delivered cisplatin restores efficacy in platinum-resistant ovarian cancer cells. *Mol. Pharm.* **15**, 2922–2931 (2017).
201. Liu, X. *et al.* Glyco-decorated tobacco mosaic virus as a vector for cisplatin delivery. *J. Mater. Chem. B* **5**, 2078–2085 (2017).
202. Ashley, C. E. *et al.* Cell-specific delivery of diverse cargos by bacteriophage MS2 virus-like particles. *ACS Nano* **5**, 5729–5745 (2011).
203. Bar, H., Yacoby, I. & Benhar, I. Killing cancer cells by targeted drug-carrying phage nanomedicines. *BMC Biotechnol.* **8**, 37 (2008).
204. Lam, P., Lin, R. D. & Steinmetz, N. F. Delivery of mitoxantrone using a plant virus-based nanoparticle for the treatment of glioblastomas. *J. Mater. Chem. B* **6**, 5888–5895 (2018).
205. Lin, R. D. & Steinmetz, N. F. Tobacco mosaic virus delivery of mitoxantrone for cancer therapy. *Nanoscale* **10**, 16307–16313 (2018).
206. Czapar, A. E. *et al.* Tobacco mosaic virus delivery of Phenanthriplatin for cancer therapy. *ACS Nano* **10**, 4119–4126 (2016).
207. Wu, W., Hsiao, S. C., Carrico, Z. M. & Francis, M. B. Genome-free viral capsids as multivalent carriers for Taxol delivery. *Angew. Chem. Int. Ed.* **48**, 9493–9497 (2009).
208. Pitek, A. S. *et al.* Elongated plant virus-based nanoparticles for enhanced delivery of thrombolytic therapies. *Mol. Pharm.* **14**, 3815–3823 (2017).

209. Esfandiari, N., Arzanani, M. K., Soleimani, M., Kohi-Habibi, M. & Svendsen, W. E. A new application of plant virus nanoparticles as drug delivery in breast cancer. *Tumor Biol.* **37**, 1229–1236 (2016).
210. Rothwell, W. *et al.* Intrathecal viral vector delivery of trastuzumab prevents or inhibits tumor growth of human HER2-positive xenografts in mice. *Cancer Res.* **78**, 6171–6182 (2018).
211. Yacoby, I., Bar, H. & Benhar, I. Targeted drug-carrying bacteriophages as antibacterial nanomedicines. *Antimicrob. Agents Chemother.* **51**, 2156–2163 (2007).
212. Yacoby, I., Shamis, M., Bar, H., Shabat, D. & Benhar, I. Targeting antibacterial agents by using drug-carrying filamentous bacteriophages. *Antimicrob. Agents Chemother.* **50**, 2087–2097 (2006).
213. Galaway, F. A. & Stockley, P. G. MS2 virus-like particles: a robust, semisynthetic targeted drug delivery platform. *Mol. Pharm.* **10**, 59–68 (2013).
214. Lam, P. & Steinmetz, N. F. Delivery of siRNA therapeutics using cowpea chlorotic mottle virus-like particles. *Biomater. Sci.* **7**, 3138–3142 (2019).
215. Azizgolshani, O., Garmann, R. F., Cadena-Nava, R., Knobler, C. M. & Gelbart, W. M. Reconstituted plant viral capsids can release genes to mammalian cells. *Virology* **441**, 12–17 (2013).
216. Zhou, Y., Maharaj, P. D., Mallajosyula, J. K., McCormick, A. A. & Kearney, C. M. In planta production of flock house virus transencapsidated RNA and its potential use as a vaccine. *Mol. Biotechnol.* **57**, 325–336 (2015).
217. Cao, J. *et al.* Development of abamectin loaded plant virus nanoparticles for efficacious plant parasitic nematode control. *ACS Appl. Mater. Interfaces* **7**, 9546–9553 (2015).
218. Chariou, P. L. & Steinmetz, N. F. Delivery of pesticides to plant parasitic nematodes using tobacco mild green mosaic virus as a nanocarrier. *ACS Nano* **11**, 4719–4730 (2017).
219. Chariou, P. L. *et al.* Soil mobility of synthetic and virus-based model nanopesticides. *Nat. Nanotechnol.* (2019) doi:10.1038/s41565-019-0453-7.

220. Abad, P. *et al.* Genome sequence of the metazoan plant-parasitic nematode *Meloidogyne incognita*. *Nat. Biotechnol.* **26**, 909–915 (2008).
221. Williamson, V. M. & Gleason, C. A. Plant–nematode interactions. *Curr. Opin. Plant Biol.* **6**, 327–333 (2003).
222. Quentin, M., Abad, P. & Favery, B. Plant parasitic nematode effectors target host defense and nuclear functions to establish feeding cells. *Front. Plant Sci.* **4**, 53 (2013).
223. Nusbaum, C. J. & Ferris, H. The Role of cropping systems in nematode population management. *Annu. Rev. Phytopathol.* **11**, 423–440 (1973).
224. Fuller, V. L., Lilley, C. J. & Urwin, P. E. Nematode resistance. *New Phytol.* **180**, 27–44 (2008).
225. Cook, R. Genetic resistance to nematodes: where is it useful? *Australias. Plant Pathol.* **33**, 139–150 (2004).
226. Sikora, R. & Fernandez, E. *Plant nematodes in tropical and subtropical agriculture*. (CABI Publishing, 2005).
227. Chitwood, D. J. *Nematicides*. vol. 3 (John Wiley & Sons, 2003).
228. Bordes, P., Pollet, E. & Averous, L. Nano-biocomposites: Biodegradable polyester/nanoclay systems. *Prog. Polym. Sci.* **34**, 125–155 (2009).
229. Yan, J. Study on anti-pollution nano-preparation of dimethomorph and its performance. *Chin. Sci. Bull.* **50**, 108 (2005).
230. Ferrell, J., Charudattan, R., Elliott, M. & Hiebert, E. Effects of selected herbicides on the efficacy of tobacco mild green mosaic virus to control tropical soda apple (*Solanum viarum*). *Weed Sci* **56**, 128–132 (2008).
231. Pattanayek, R. & Stubbs, G. Structure of the U2 strain of tobacco mosaic virus refined at 3.5 Å resolution using X-ray fiber diffraction. *J. Mol. Biol* **228**, 516–528 (1992).
232. Bruckman, M. A. & Steinmetz, N. F. Chemical modification of the inner and outer surfaces of tobacco mosaic virus (TMV). *Methods Mol. Biol. Clifton NJ* **1108**, 173–185 (2014).

233. Docampo, R. & Moreno, S. N. J. The metabolism and mode of action of gentian violet. *Drug Metab. Rev.* **22**, 161–178 (1990).
234. Schlick, T. L., Ding, Z., Kovacs, E. W. & Francis, M. B. Dual-surface modification of the tobacco mosaic virus. *J. Am. Chem. Soc.* **127**, 3718–3723 (2005).
235. Lee, K. L., Carpenter, B. L., Wen, A. M., Ghiladi, R. A. & Steinmetz, N. F. High aspect ratio nanotubes formed by tobacco mosaic virus for delivery of photodynamic agents targeting melanoma. *ACS Biomater. Sci. Eng.* **2**, 838–844 (2016).
236. Mount, H. R. & Paetzold, R. F. The temperature regime for selected soil in the United-States. *National Soil survey Center: Lincoln NE* (2002).
237. Wen, A. M. *et al.* Interface of physics and biology: engineering virus-based nanoparticles for biophotonics. *Bioconjug. Chem.* **26**, 51–62 (2015).
238. Aktar, Md. W., Sengupta, D. & Chowdhury, A. Impact of pesticides use in agriculture: Their benefits and hazards. *Interdiscip. Toxicol.* **2**, 1–12 (2009).
239. Atwood, D. & Paisley-Jones, C. *U.S. Environmental Protection Agency.* (2017).
240. Vurro, M., Miguel-Rojas, C. & Pérez-de-Luque, A. Safe nanotechnologies for increasing the effectiveness of environmentally friendly natural agrochemicals. *Pest Manag. Sci.* **0**, (2019).
241. Kah, M., Kookana, R. S., Gogos, A. & Bucheli, T. D. A critical evaluation of nanopesticides and nanofertilizers against their conventional analogues. *Nat. Nanotechnol.* **13**, 677–684 (2018).
242. Kookana, R. S. *et al.* Nanopesticides: Guiding principles for regulatory evaluation of environmental risks. *J. Agric. Food Chem.* **62**, 4227–4240 (2014).
243. Walker, G. W. *et al.* Ecological risk assessment of nano-enabled pesticides: A perspective on problem formulation. *J. Agric. Food Chem.* **66**, 6480–6486 (2018).
244. Guenther, R. H., Lommel, S. A., Opperman, C. H. & Sit, T. L. Plant virus-based nanoparticles for the delivery of agronomic compounds as a suspension concentrate. in *Virus-Derived Nanoparticles for Advanced Technologies: Methods and Protocols* (eds. Wege, C. &

- Lomonosoff, G. P.) 203–214 (Springer New York, 2018). doi:10.1007/978-1-4939-7808-3_13.
245. Umekawa, M. & Oshima, N. Sensitivity of tobacco mosaic virus to ultraviolet irradiation. *Jpn. J. Microbiol.* **16**, 441–443 (1972).
246. Rae, C. *et al.* Chemical addressability of ultraviolet-inactivated viral nanoparticles (VNPs). *PLoS ONE* **3**, e3315 (2008).
247. Mir, M., Ahmed, N. & Asim ur, R. Recent applications of PLGA based nanostructures in drug delivery. *Colloids and Surfaces B: Biointerfaces* **159**, 217–231 (2017).
248. Torney, F., Trewyn, B. G., Lin, V. S.-Y. & Wang, K. Mesoporous silica nanoparticles deliver DNA and chemicals into plants. *Nat. Nanotechnol.* **2**, 295–300 (2007).
249. Steinmetz, N. F. & Manchester, M. *Viral nanoparticles: Tools for materials science and medicine*. (Pan Stanford Publishing, 2015).
250. Masarapu, H. *et al.* Physalis mottle virus-like particles as nanocarriers for imaging reagents and drugs. *Biomacromolecules* **18**, 4141–4153 (2017).
251. Ultman, J. S., Baskaran, H. & Saidel, G. M. Biomedical mass transport and chemical reaction : physicochemical principles and mathematical modeling. <http://public.ebib.com/choice/publicfullrecord.aspx?p=4517662> (2016).
252. Hassan, M. E. M., Zawam, I Hanaa S., El-Nahas, S. E. M. & Desoukey, A. F. Comparison study between silver nanoparticles and two nematicides against meloidogyne incognita on tomato seedlings. **15**, 144–151 (2016).
253. Pestovsky, Y. S. & Martínez-Antonio, A. The use of nanoparticles and nanoformulations in agriculture. *J. Nanosci. Nanotechnol.* **17**, 8699–8730 (2017).
254. Truong, N. P., Whittaker, M. R., Mak, C. W. & Davis, T. P. The importance of nanoparticle shape in cancer drug delivery. *Expert Opin. Drug Deliv.* **12**, 129–142 (2015).
255. Barua, S. & Mitragotri, S. Challenges associated with penetration of nanoparticles across cell and tissue barriers: A review of current status and future prospects. *Nano Today* **9**, 223–243 (2014).

256. Toy, R. The effect of particle size and shape on the in vivo journey of nanoparticles. (Case Western Reserve University, 2014).
257. OECD. *Test No. 312: Leaching in Soil Columns*. (2004).
258. Chen, Z., Li, N., Chen, L., Lee, J. & Gassensmith, J. J. Dual functionalized bacteriophage Q β as a photocaged drug carrier. *Small* **12**, 4563–4571 (2016).
259. Godfrey, G. H. The depth distribution of the root-knot nematode, *heterodera radiculicola*, in Florida soils. *J. Agric. Res.* **7** (1925).
260. Putter, I. *et al.* Avermectins: novel insecticides, acaricides and nematicides from a soil microorganism. *Experientia* **37**, 963–964 (1981).
261. Schoenmakers, R. G., van de Wetering, P., Elbert, D. L. & Hubbell, J. A. The effect of the linker on the hydrolysis rate of drug-linked ester bonds. *J. Controlled Release* **95**, 291–300 (2004).
262. Culliney, T. W. Crop losses to arthropods. in *Integrated pest management: pesticide problems, Vol.3* (eds. Pimentel, D. & Peshin, R.) 201–225 (Springer Netherlands, 2014). doi:10.1007/978-94-007-7796-5_8.
263. Hawkins, N. J., Bass, C., Dixon, A. & Neve, P. The evolutionary origins of pesticide resistance. *Biol. Rev.* **94**, 135–155 (2019).
264. Ross, A. F. & Stanley, W. M. The partial reactivation of formalized tobacco mosaic virus protein. *J. Gen. Physiol.* **22**, 165–191 (1938).
265. Bawden, F. C. & Kleczkowski, A. The behaviour of some plant viruses after exposure to ultraviolet radiation. *J. Gen. Microbiol.* **8**, 145–156 (1953).
266. Cartwright, T. E., Ritchie, A. E. & Lauffer, M. A. The reaction of tobacco mosaic virus with formaldehyde: III. Kinetics of the Loss of Infectivity. *Virology* **2**, 689–702 (1956).
267. Ginoza, W., Siegel, A. & Wildman, S. G. Sensitivity to ultra-violet light of infectious tobacco mosaic virus nucleic acid. *Nature* **178**, 1117–1118 (1956).
268. McLaren, A. D. & Takahashi, W. N. Inactivation of infectious nucleic acid from tobacco mosaic virus by ultraviolet light. *Radiat. Res.* **6**, 532–542 (1957).

269. Rushizky, G. W., Knight, C. A. & McLaren, A. D. A comparison of the ultraviolet-light inactivation of infectious ribonucleic acid preparations from tobacco mosaic virus with those of the native and reconstituted virus. *Virology* **12**, 32–47 (1960).
270. Goddard, J., Streeter, D., Weber, C. & Gordon, M. P. Studies on the inactivation of tobacco mosaic virus by ultraviolet light. *Photochem. Photobiol.* **5**, 213–222 (1966).
271. Streeter, D. G. & Gordon, M. P. Ultraviolet photoinactivation studies on hybrid viruses obtained by the cross-reconstitution of the protein and RNA components of U(1) and U(2) strains of TMV. *Photochem. Photobiol.* **6**, 413–421 (1967).
272. Kleczkowski, A. & McLaren, A. D. Inactivation of infectivity of RNA of tobacco mosaic virus during ultraviolet-irradiation of the whole virus at two wavelengths. *J. Gen. Virol.* **1**, 441–448 (1967).
273. Uittenbogaard, J. P., Zomer, B., Hoogerhout, P. & Metz, B. Reactions of beta-propiolactone with nucleobase analogues, nucleosides, and peptides: implications for the inactivation of viruses. *J. Biol. Chem.* **286**, 36198–36214 (2011).
274. Wilton, T., Dunn, G., Eastwood, D., Minor, P. D. & Martin, J. Effect of formaldehyde inactivation on poliovirus. *J. Virol.* **88**, 11955 (2014).
275. Niu, Z. *et al.* Study and characterization of tobacco mosaic virus head-to-tail assembly assisted by aniline polymerization. *Chem. Commun.* 3019–3021 (2006)
doi:10.1039/B603780A.
276. Furuya, Y. *et al.* Effect of inactivation method on the cross-protective immunity induced by whole ‘killed’ influenza A viruses and commercial vaccine preparations. *J. Gen. Virol.* **91**, 1450–1460 (2010).
277. Henderson, E. E., Tudor, G. & Yang, J.-Y. Inactivation of the human immunodeficiency virus type I (HIV-1) by ultraviolet and X radiation. *Radiation Research* **131**, 169–176 (1992).
278. Jean, J., Morales-Rayas, R., Anoman, M.-N. & Lamhoujeb, S. Inactivation of hepatitis A virus and norovirus surrogate in suspension and on food-contact surfaces using pulsed UV light (pulsed light inactivation of food-borne viruses). *Food Microbiol.* **28**, 568–572 (2011).
279. Campbell, T. M., Studdert, M. J. & Blackney, M. H. Immunogenicity of equine herpesvirus type 1 (EHV1) and equine rhinovirus type 1 (ERhV1) following inactivation by betapropiolactone (BPL) and ultraviolet (UV) light. *Vet. Microbiol.* **7**, 535–544 (1982).

280. Logrippo, G. A. Investigations of the use of beta-propiolactone in virus inactivation. *Ann. N. Y. Acad. Sci.* **83**, 578–594 (1960).
281. Race, E. *et al.* A multistep procedure for the chemical inactivation of human immunodeficiency virus for use as an experimental vaccine. *Vaccine* **13**, 1567–1575 (1995).
282. Budowsky, E. I., Friedman, E. A., Zheleznova, N. V. & Noskov, F. S. Principles of selective inactivation of viral genome. VI. Inactivation of the infectivity of the influenza virus by the action of β -propiolactone. *Vaccine* **9**, 398–402 (1991).
283. Frösner, G. G., Stephan, W. & Dichtelmüller, H. Inactivation of hepatitis A virus added to pooled human plasma by beta-propiolactone treatment and ultraviolet irradiation. *Eur. J. Clin. Microbiol.* **2**, 355–357 (1983).
284. Fan, Y.-C., Chiu, H.-C., Chen, L.-K., Chang, G.-J. J. & Chiou, S.-S. Formalin inactivation of Japanese encephalitis virus vaccine alters the antigenicity and immunogenicity of a neutralization epitope in envelope protein domain III. *PLoS Negl. Trop. Dis.* **9**, e0004167 (2015).
285. Takada, A., Matsushita, S., Ninomiya, A., Kawaoka, Y. & Kida, H. Intranasal immunization with formalin-inactivated virus vaccine induces a broad spectrum of heterosubtypic immunity against influenza A virus infection in mice. *Vaccine* **21**, 3212–3218 (2003).
286. Kissling, R. E. & Reese, D. R. Anti-rabies vaccine of tissue culture origin. *J. Immunol.* **91**, 362 (1963).
287. Tredan, O., Galmarini, C. M., Patel, K. & Tannock, I. F. Drug resistance and the solid tumor microenvironment. *JNCI J. Natl. Cancer Inst.* **99**, 1441–1454 (2007).
288. Durymanov, M. O., Rosenkranz, A. A. & Sobolev, A. S. Current approaches for improving intratumoral accumulation and distribution of nanomedicines. *Theranostics* **5**, 1007–1020 (2015).
289. Geng, Y. *et al.* Shape effects of filaments versus spherical particles in flow and drug delivery. *Nat. Nanotechnol.* **2**, 249–255 (2007).
290. Chauhan, V. P. *et al.* Fluorescent nanorods and nanospheres for real-time in vivo probing of nanoparticle shape-dependent tumor penetration. *Angew. Chem. Int. Ed Engl.* **50**, 11417–11420 (2011).

291. Shukla, S. *et al.* Increased tumor homing and tissue penetration of the filamentous plant viral nanoparticle Potato virus X. *Mol. Pharm.* **10**, 33–42 (2013).
292. Reuter, K. G. *et al.* Targeted PRINT hydrogels: The role of nanoparticle size and ligand density on cell association, biodistribution, and tumor accumulation. *Nano Lett.* **15**, 6371–6378 (2015).
293. Smith, B. R. *et al.* Shape matters: intravital microscopy reveals surprising geometrical dependence for nanoparticles in tumor models of extravasation. *Nano Lett.* **12**, 3369–3377 (2012).
294. Goodman, T. T., Chen, J., Matveev, K. & Pun, S. H. Spatio-temporal modeling of nanoparticle delivery to multicellular tumor spheroids. *Biotechnol. Bioeng.* **101**, 388–399 (2008).
295. Gao, Y. *et al.* Predictive models of diffusive nanoparticle transport in 3-dimensional tumor cell spheroids. *AAPS J.* **15**, 816–831 (2013).
296. Bruckman, M. A. *et al.* Surface Modification of Tobacco Mosaic Virus with “Click” Chemistry. *ChemBioChem* **9**, 519–523 (2008).
297. Eber, F. J., Eiben, S., Jeske, H. & Wege, C. RNA-controlled assembly of tobacco mosaic virus-derived complex structures: from nanoboomerangs to tetrapods. *Nanoscale* **7**, 344–355 (2015).
298. Geiger, F. C. *et al.* TMV nanorods with programmed longitudinal domains of differently addressable coat proteins. *Nanoscale* **5**, 3808 (2013).
299. Shukla, S. *et al.* The impact of aspect ratio on the biodistribution and tumor homing of rigid soft-matter nanorods. *Adv. Healthc. Mater.* **4**, 874–882 (2015).
300. Dufau, I. *et al.* Multicellular tumor spheroid model to evaluate spatio-temporal dynamics effect of chemotherapeutics: application to the gemcitabine/CHK1 inhibitor combination in pancreatic cancer. *BMC Cancer* **12**, 15 (2012).
301. Fayad, W. *et al.* Restriction of cisplatin induction of acute apoptosis to a subpopulation of cells in a three-dimensional carcinoma culture model. *Int. J. Cancer* **125**, 2450–2455 (2009).

302. Frankel, A., Man, S., Elliott, P., Adams, J. & Kerbel, R. S. Lack of multicellular drug resistance observed in human ovarian and prostate carcinoma treated with the proteasome inhibitor PS-341. *11*.
303. Jain, R. K. Transport of molecules, particles, and cells in solid tumors. *Annu. Rev. Biomed. Eng.* **1**, 241–263 (1999).
304. Tirado, M. M., Martínez, C. L. & de la Torre, J. G. Comparison of theories for the translational and rotational diffusion coefficients of rod-like macromolecules. Application to short DNA fragments. *J. Chem. Phys.* **81**, 2047–2052 (1984).
305. Tirado, M. M. Viscous force and torque constants for a cylinder. *J Chem Phys* (1981).
306. Pluen, A., Netti, P. A., Jain, R. K. & Berk, D. A. Diffusion of macromolecules in agarose gels: comparison of linear and globular configurations. *Biophys. J.* **77**, 542–552 (1999).
307. Lee, K. L. *et al.* Shape matters: the diffusion rates of TMV rods and CPMV icosahedrons in a spheroid model of extracellular matrix are distinct. *Biomater. Sci.* **1**, 581 (2013).
308. Levick, J. R. Flow through interstitium and other fibrous matrices. *Q. J. Exp. Physiol.* **72**, 409–437 (1987).
309. Westrin, B. A. & Axelsson, A. Diffusion in gels containing immobilized cells: A critical review. *Biotechnol. Bioeng.* **38**, 439–446 (1991).
310. Pitek, A. S., Wen, A. M., Shukla, S. & Steinmetz, N. F. The protein corona of plant virus nanoparticles influences their dispersion properties, cellular interactions and in vivo fates. *Small Weinh. Bergstr. Ger.* **12**, 1758–1769 (2016).
311. Yoshii, Y. & Sugiyama, K. Intercapillary distance in the proliferating area of human glioma. **48**, 2938–2941 (1988).
312. Baish, J. W. *et al.* Scaling rules for diffusive drug delivery in tumor and normal tissues. *Proc. Natl. Acad. Sci. U. S. A.* **108**, 1799–1803 (2011).
313. Majeesh, N. & Amir, S. Hypoxia-inducible factor (HIF) in human tumorigenesis. *Histol. Histopathol.* 559–572 (2007) doi:10.14670/HH-22.559.

314. Banerjee, D., Harfouche, R. & Sengupta, S. Nanotechnology-mediated targeting of tumor angiogenesis. *Vasc. Cell* **3**, 3 (2011).
315. Kobayashi, H., Takemura, Y. & Ohnuma, T. Relationship between tumor cell density and drug concentration and the cytotoxic effect of doxorubicin and vincristine: Mechanism of inoculum effects. *Cancer Chemother Pharmacol* **31**, 6–10 (1992).
316. Champion, J. A. & Mitragotri, S. Role of target geometry in phagocytosis. *Proc. Natl. Acad. Sci.* **103**, 4930–4934 (2006).
317. Huang, X. *et al.* A Reexamination of active and passive tumor targeting by Using rod-shaped gold nanocrystals and covalently conjugated peptide ligands. *ACS Nano* **4**, 5887–5896 (2010).
318. Taherian, A., Li, X., Liu, Y. & Haas, T. A. Differences in integrin expression and signaling within human breast cancer cells. *BMC Cancer* **11**, 293 (2011).
319. Krippendorff, B.-F., Kuester, K., Kloft, C. & Huisinga, W. Nonlinear pharmacokinetics of therapeutic proteins resulting from receptor mediated endocytosis. *J. Pharmacokinet. Pharmacodyn.* **36**, 239–260 (2009).
320. Doiron, A. L., Clark, B. & Rinker, K. D. Endothelial nanoparticle binding kinetics are matrix and size dependent. *Biotechnol. Bioeng.* **108**, 2988–2998 (2011).
321. Thurber, G. M., Schmidt, M. M. & Wittrup, K. D. Antibody tumor penetration. *Adv. Drug Deliv. Rev.* **60**, 1421 (2008).
322. Thurber, G. M. & Wittrup, K. D. Quantitative spatiotemporal analysis of antibody fragment diffusion and endocytic consumption in tumor spheroids. *Cancer Res.* **68**, 3334–3341 (2008).
323. Felsher, D. W. Cancer revoked: oncogenes as therapeutic targets. *Nat. Rev. Cancer* **3**, 375–379 (2003).
324. Wang, W., Moriyama, L. T. & Bagnato, V. S. Photodynamic therapy induced vascular damage: an overview of experimental PDT. *Laser Phys. Lett.* **10**, 023001 (2013).
325. Alonso, M. J. & Garcia-Fuentes, M. *Nano-oncologicals: new targeting and delivery approaches.* (Springer, 2014).

326. Brasch, M. *et al.* Encapsulation of phthalocyanine supramolecular stacks into virus-like particles. *J. Am. Chem. Soc.* **133**, 6878–6881 (2011).
327. Ma, Y., Nolte, R. J. M. & Cornelissen, J. J. L. M. Virus-based nanocarriers for drug delivery. *Adv. Drug Deliv. Rev.* **64**, 811–825 (2012).
328. Alemzadeh, E., Dehshahri, A., Izadpanah, K. & Ahmadi, F. Plant virus nanoparticles: Novel and robust nanocarriers for drug delivery and imaging. *Colloids Surf. B Biointerfaces* **167**, 20–27 (2018).
329. Shukla, S. *et al.* Biodistribution and clearance of a filamentous plant virus in healthy and tumor-bearing mice. *Nanomed.* **9**, 221–235 (2014).
330. Feese, E., Sadeghifar, H., Gracz, H. S., Argyropoulos, D. S. & Ghiladi, R. A. Photobactericidal porphyrin-cellulose nanocrystals: synthesis, characterization, and antimicrobial properties. *Biomacromolecules* **12**, 3528–3539 (2011).
331. Zhao, B. & He, Y.-Y. Recent advances in the prevention and treatment of skin cancer using photodynamic therapy. *Expert Rev. Anticancer Ther.* **10**, 1797–1809 (2010).
332. Castano, A. P., Demidova, T. N. & Hamblin, M. R. Mechanisms in photodynamic therapy: part one—photosensitizers, photochemistry and cellular localization. *Photodiagnosis Photodyn. Ther.* **1**, 279–293 (2004).
333. Porkka, K., Laakkonen, P., Hoffman, J. A., Bernasconi, M. & Ruoslahti, E. A fragment of the HMGN2 protein homes to the nuclei of tumor cells and tumor endothelial cells in vivo. *Proc. Natl. Acad. Sci.* **99**, 7444–7449 (2002).
334. Hovanesian, A. G. *et al.* Surface expressed nucleolin is constantly induced in tumor cells to mediate calcium-dependent ligand internalization. *PLoS One* **5**, e15787 (2010).
335. Huang, Y. The angiogenic function of nucleolin is mediated by vascular endothelial growth factor and nonmuscle myosin. *Blood* **107**, 3564–3571 (2006).
336. Hwang, D. W. *et al.* A nucleolin-targeted multimodal nanoparticle imaging probe for tracking cancer cells using an aptamer. *J. Nucl. Med. Off. Publ. Soc. Nucl. Med.* **51**, 98–105 (2010).

337. Winer, I. *et al.* F3-targeted cisplatin-hydrogel nanoparticles as an effective therapeutic that targets both murine and human ovarian tumor endothelial cells in vivo. *Cancer Res.* **70**, 8674–8683 (2010).
338. Hu, Q. *et al.* F3 peptide-functionalized PEG-PLA nanoparticles co-administrated with tLyp-1 peptide for anti-glioma drug delivery. *Biomaterials* **34**, 1135–1145 (2013).
339. M. Gulati, N., S. Pitek, A., F. Steinmetz, N. & L. Stewart, P. Cryo-electron tomography investigation of serum albumin-camouflaged tobacco mosaic virus nanoparticles. *Nanoscale* **9**, 3408–3415 (2017).
340. Grinstein, E. *et al.* Nucleolin as activator of human papillomavirus type 18 oncogene transcription in cervical cancer. *J. Exp. Med.* **196**, 1067–1078 (2002).
341. Qin, M., Zong, H. & Kopelman, R. Click conjugation of peptide to hydrogel nanoparticles for tumor-targeted drug delivery. *Biomacromolecules* **15**, 3728–3734 (2014).
342. Bachmann, M. F. & Jennings, G. T. Vaccine delivery: a matter of size, geometry, kinetics and molecular patterns. *Nat. Rev. Immunol.* **10**, 787–796 (2010).
343. D'Aoust, M.-A. *et al.* The production of hemagglutinin-based virus-like particles in plants: a rapid, efficient and safe response to pandemic influenza. *Plant Biotechnol. J.* **8**, 607–619 (2010).
344. Tschofen, M., Knopp, D., Hood, E. & Stöger, E. Plant molecular farming: much more than medicines. *Annu. Rev. Anal. Chem.* **9**, 271–294 (2016).
345. Montague, N. P. *et al.* Recent advances of cowpea mosaic virus-based particle technology. *Hum. Vaccin.* **7**, 383–390 (2011).
346. Patel, R., Czapar, A. E., Fiering, S., Oleinick, N. L. & Steinmetz, N. F. Radiation therapy combined with cowpea mosaic virus nanoparticle in situ vaccination initiates immune-mediated tumor regression. *ACS Omega* **3**, 3702–3707 (2018).
347. Wang, C., Fiering, S. N. & Steinmetz, N. F. Cowpea mosaic virus promotes anti-tumor activity and immune memory in a mouse ovarian tumor model. *Adv. Ther.* **2**, 1900003 (2019).

348. Wang, C., Beiss, V. & Steinmetz, N. F. Cowpea mosaic virus nanoparticles and empty virus-like particles show distinct but overlapping immunostimulatory properties. *J. Virol.* **93**, e00129-19 (2019).
349. Kranz, L. M. *et al.* Systemic RNA delivery to dendritic cells exploits antiviral defence for cancer immunotherapy. *Nature* **534**, 396–401 (2016).
350. Albakri, M. M., Veliz, F. A., Fiering, S. N., Steinmetz, N. F. & Sieg, S. F. Endosomal toll-like receptors play a key role in activation of primary human monocytes by cowpea mosaic virus. *Immunology* **159**, 183–192 (2020).
351. Wang, Q., Kaltgrad, E., Lin, T., Johnson, J. E. & Finn, M. G. Natural supramolecular building blocks: wild-type cowpea mosaic virus. 7.
352. Rae, C. S. *et al.* Systemic trafficking of plant virus nanoparticles in mice via the oral route. *Virology* **343**, 224–235 (2005).
353. Wen, A. M. *et al.* Interior engineering of a viral nanoparticle and its tumor homing properties. *Biomacromolecules* **13**, 3990–4001 (2012).
354. Chatterji, A. *et al.* New addresses on an addressable virus nanoblock: uniquely reactive Lys residues on cowpea mosaic virus. *Chem. Biol.* **11**, 855–863 (2004).
355. Saunders, K., Sainsbury, F. & Lomonossoff, G. P. Efficient generation of cowpea mosaicvirus empty virus-like particles by the proteolytic processing of precursors in insect cells and plants. *Virology* **393**, 329–337 (2009).
356. Steinmetz, Nicole. F. Viral capsids as programmable nanobuilding blocks. (John Innes Centre, 2007).
357. Lu, Y. & Low, P. S. Folate-mediated delivery of macromolecular anticancer therapeutic agents. *Adv. Drug Delivery. Rev.* **64**, 342–352 (2012).
358. Aljabali, A. A. A., Shukla, S., Lomonossoff, G. P., Steinmetz, N. F. & Evans, D. J. CPMV-DOX Delivers. *Mol. Pharm.* **10**, 3–10 (2013).
359. Leong, H. S. *et al.* Intravital imaging of embryonic and tumor neovasculature using viral nanoparticles. *Nat. Protoc.* **5**, 1406–1417 (2010).

360. Beatty, P. H. & Lewis, J. D. Cowpea mosaic virus nanoparticles for cancer imaging and therapy. *Biomater. Based Phages Viruses* **145**, 130–144 (2019).
361. Koudelka, K. J. *et al.* Endothelial targeting of cowpea mosaic virus (CPMV) via surface vimentin. *PLoS Pathog.* **5**, e1000417 (2009).
362. Steinmetz, N. F. *et al.* Intravital imaging of human prostate cancer using viral nanoparticles targeted to gastrin-releasing peptide receptors. *Small* **7**, 1664–1672 (2011).
363. Krogh, K. A., Søbørg, T., Brodin, B. & Halling-Sørensen, B. Sorption and mobility of ivermectin in different soils. *J. Environ. Qual.* **37**, 2202–2211 (2008).
364. Li, Y. *et al.* Preparation, characterization, and insecticidal activity of avermectin-grafted-carboxymethyl chitosan. *BioMed Res. Int.* **2016**, (2016).
365. Fu, Z. *et al.* Spherical and spindle-like abamectin-loaded nanoparticles by flash nanoprecipitation for southern root-knot nematode control: preparation and characterization. *Nanomaterials* **8**, (2018).
366. Zalipsky, S. Functionalized poly(ethylene glycols) for preparation of biologically relevant conjugates. *Bioconjug. Chem.* **6**, 150–165 (1995).
367. Shukla, S. *et al.* The impact of aspect ratio on the biodistribution and tumor homing of rigid soft-natter nanorods. *Adv. Healthc. Mater.* **4**, 874–882 (2015).
368. Wang, Z., Wu, Z., Liu, J. & Zhang, W. Particle morphology: an important factor affecting drug delivery by nanocarriers into solid tumors. *Expert Opin. Drug Deliv.* **15**, 379–395 (2018).
369. Ernsting, M. J., Murakami, M., Roy, A. & Li, S.-D. Factors controlling the pharmacokinetics, biodistribution and intratumoral penetration of nanoparticles. *J. Controlled Release* **172**, 782–794 (2013).
370. Chariou, P. L., Lee, K. L., Pokorski, J. K., Saidel, G. M. & Steinmetz, N. F. Diffusion and uptake of tobacco mosaic virus as therapeutic carrier in tumor tissue: Effect of nanoparticle aspect ratio. *J. Phys. Chem. B* **120**, 6120–6129 (2016).
371. Chariou, P. L. *et al.* Let there be light: Targeted photodynamic therapy using high aspect ratio plant viral nanoparticles. *Macromol. Biosci.* **19**, e1800407 (2019).